1985-10

Anisotropy of Heat Conduction in Fibre-Reinforced Composites

Grove, SM

ANISOTROPY OF HEAT CONDUCTION IN FIBRE-REINFORCED COMPOSITES

by

Stephen Michael Grove

Department of Mechanical Engineering
Plymouth Polytechnic

A thesis submitted to the Council for National Academic Awards
in partial fulfilment of the requirements for the degree of
Doctor of Philosophy

October 1985

ANISOTROPY OF HEAT CONDUCTION IN FIBRE-REINFORCED COMPOSITES

S. M. Grove

ABSTRACT

Fibre-reinforced composites usually exhibit anisotropy of thermal as well as mechanical properties. For example, in a unidirectional carbon fibre-reinforced plastic of 60% volume fraction, the longitudinal thermal conductivity may be greater than that in the transverse direction by a factor of 50, and greater than that of the unreinforced polymer by more than two orders of magnitude.

In order to evaluate the engineering applications of thermal anisotropy, this thesis concentrates on the development and validation of a generalised finite element model of heat conduction in an anisotropic medium. This uses a variational formulation of the anisotropic time-dependent heat conduction equation, and is implemented for two and three-dimensional quadratic finite elements. The model may be used for the solution of problems having any combination of steady or time-dependent boundary conditions (fixed temperature, convection, radiation, heat flux and internal heat generation), as well as nonlinear properties. Anisotropy is specified by the components of the two or three-dimensional thermal conductivity tensor; efficient representation of nonhomogeneous materials is achieved by the specification of properties at element integration points.

Theoretical validation of the model is carried out by means of a number of mathematical solutions to orthotropic and anisotropic problems. Experimental validation is performed by comparison of calculations with measured steady-state surface temperatures on a cylindrical specimen of unidirectional carbon fibre-reinforced epoxy resin. The thermal property data for this exercise are obtained from measurements of principal thermal conductivities on absolute and comparative steady-state apparatus.

The use of the finite element model in two industrial applications is briefly described. These concern thermal cycling during composite fabrication with reinforced thermoplastic tape, and an analysis of heat transfer in a composite propeller blade.

PERMISSION TO COPY

I hereby give permission for my thesis, entitled 'Anisotropy of Heat Conduction in Fibre-Reinforced Composites', to be made available for consultation by readers at the British Library or Plymouth Polytechnic, or to be sent away on temporary loan if requested by other institutions.

The thesis is made available on the understanding that the reader will not publish in any form either the whole or any part of it without written permission from both the holding library and the author. Where the regulations of the CNAA and the holding library allow, the thesis may be photocopied in whole or in part for the purposes of private study.

Signed: 

Date: 14/10/85

ACKNOWLEDGEMENTS

I am very grateful to David Short, my Director of Studies, for his patient guidance and understanding throughout my time at Plymouth Polytechnic. I would also like to thank Prof David Fussey and Max Bacon for their involvement in my work, in particular for their valuable comments on the thesis, and Dr Tony Vallis (now at Sheffield Polytechnic) for his help in the early stages of the project.

The work described here owes much to the technical skill and ingenuity of Brian Lord. My thanks also to Terry Richards and Tony To for their help with specimen preparation. Geoff Bouch and Jon Warbrick have provided valuable advice concerning the use of the Prime computer.

I am particularly grateful to Dr Frank Willmouth (New Science Group, ICI Petrochemicals and Plastics Division) and Roy McCarthy (Composites Manager, Dowty Rotol Ltd) for interesting discussions and for permission to include material in Chapter 8.

The experimental work received financial support from the Science and Engineering Research Council (grant number GR/B/84367, 1981-83).

My wife, Penny, has typed this thesis with the utmost skill and dedication, despite the conflicting demands of the rest of my family.

CONTENTS

NOMENCLATURE

Symbol	Definition	Chapter
a_{ij}	cofactor of determinant	2
a	unit cell dimension	2
a_{ij}	matrix coefficient	5
a	rectangle dimension	6
A	packing factor	2
A	cross-sectional area	3
A^e	element area	5
b	unit cell dimension	2
b	rectangle dimension	6
$\underline{B}$	matrix of shape function derivatives	5
c_{ij}	direction cosines	4
$\underline{c}^e$	element capacitance matrix	5
$\bar{C}, C_p$	specific heat	1
$\underline{C}$	global capacitance matrix	5
$\underline{d}$	matrix of temperature derivatives	5
$\bar{d}$	correction vector	5
$\underline{D}$	property matrix	5
e	(as superscript) referring to element	5
e	(as subscript) effective	1
e_{ij}	matrix coefficient	5
f	(as subscript) referring to fibre	
f,F	arbitrary functions	4,5
f^e	element force vector	5
$\bar{F}$	global force vector	5
F	shape factor	5
$\dot{g}$	rate of heat generation	4
h	fibre dimension	2
h	heat transfer coefficient	4
h_R	heat transfer coefficient for radiation	5
h,h'	enthalpy	5
I	integral	5
$\underline{J}$	Jacobian matrix	5
$\bar{k}$	thermal conductivity	
$k_{\parallel}, k_{\perp}$	conductivity parallel and perpendicular to unidirectional reinforcement	
$\bar{k}$	thermal conductivity tensor	4
k_{ij}	components of conductivity tensor	2
$\underline{k}^e$	element stiffness matrix	5
K_1, K_2, K_3	principal thermal conductivities	1
K	reference conductivity	4
$\underline{K}$	global stiffness matrix	5
ℓ	mean free path	1
ℓ	space scale	1
	length of element side	5
m	(as subscript) referring to matrix	1
M	(as subscript) measured value	3
n	normal direction	4
N_i	shape function	5
Ox,Oy,Oz	cartesian axes	4
p	ratio $k_{\parallel}/k_{\perp}$	2
q	heat flux (units W/m^2)	1
Q	rate of heat input (units W)	3
r	radial coordinate	4
r	local element coordinate	5

$\underline{r}$	residual vector	5
$\overline{R}_{ij}$	coefficient of resistivity tensor	2
s	fibre dimension	2
s	local element coordinate	5
S^e	element surface	5
S	adjusted rms deviation	6
$S_{nm...}$	error in weighted mean	3
t	time	
t	local element coordinate	5
T	temperature	
T_∞	temperature of surrounding medium for convective heat transfer	5
$\overline{v}$	mean group velocity	1
V	volume	5
W_i	weight coefficient	5
x,y,z	cartesian coordinates	
X,Y,Z	principal axes of conductivity	4
X_i, Y_i	global coordinates of node i	5
$X_{nm...}$	weighted mean	3
α	thermal diffusivity	1
α	temperature coefficient	4
β	eigenvalues	6
γ	square root of ratio of principal thermal conductivities	3
δ	O or 1	4
δ	error	6
Δ	determinant of conductivity coeffs.	2
ε	normalised conductivity (k_{ij}/k_{11})	4
ε	conductivity ratio (k_r/k_θ)	4
ε	emissivity	5
η	dimensionless coordinate (x/y)	4
η	local variable	5
ϕ	fibre volume fraction	1
ϕ	specimen orientation angle	7
Φ	normalised temperature	7
ρ	density	
σ	Stefan's constant	5
θ	circular coordinate	
θ	fibre orientation angle	3
τ	time scale	1
ω	weighting factor	5
χ	ratio of temperature gradients	3

CHAPTER 1 : INTRODUCTION

There are many possible definitions of a composite, but at the macrostructural level it may be regarded as consisting of two or more physically distinct materials which have been combined in some controlled manner. The resulting mixture is characterised by properties which are, according to previously-defined criteria, more useful than those possessed by any one of the constituents in isolation. The concept dates from the earliest of the ancient civilisations, when straw and other fibrous material was used for reinforcement and crack prevention in the manufacture of clay pottery and bricks. In addition, many naturally-occurring materials are composites, such as wood, bone and muscle. In this thesis, 'composite materials' are taken to be polymer-based compounds containing gaseous, particulate or fibrous matter. The range of such materials which has found applications across the spectrum of engineering disciplines is vast, ranging from foamed plastics in building and packaging to high-performance carbon fibre-reinforced resins in the aerospace industry.

Polymers are conveniently divided into two broad categories. End-to-end joining of basic molecules (mers) produces a long, chain-like linear polymer. The individual chains are not chemically bonded, and the so-called 'thermoplastic' polymer will melt on heating. The commonest examples are polyethylene (PE), polypropylene (PP), polyvinylchloride (PVC), and polystyrene (PS); together these account for about 90% of thermoplastics production in the U.K. (Central Statistical Office, 1984). Network polymers are based on mers which form chemical bonds at sites in addition to the ends of the molecules, thus giving rise to covalently-bonded three-dimensional networks. Cross-linking of the polymer chains may be effected by heating or by chemical means, and the process is irreversible. Among the 'thermoset' and 'chemiset' plastics are phenolic and epoxy resins, urea-formaldehyde and polyurethane. Rubber polymers are examples of a network system, and the curing or 'vulcanizing' process uses sulphur to form a bridge between long molecules which

would otherwise be thermoplastic in character.

1.1 MECHANICAL PROPERTIES OF POLYMERS AND COMPOSITES

Several attributes of polymers are responsible for their importance as engineering materials. They display a useful range of durability in environments hostile to many traditional materials; they are of low density, leading to valuable weight reduction in certain components; they are easily processed, being formed into products of complex shape at low cost. Stiffness and strength, however, are not characteristic features of plastics; typical elastic moduli are of the order of 10^9 N/m^2 and tensile strengths are only about 10^7 N/m^2. (In metals, tensile moduli and strengths are greater by factors of 50-200 and 10-50 respectively.)

There are two broad approaches to the problem of achieving higher performances, both of which require considerable skill on the part of the engineer. The first requires detailed analysis of stresses and loads in a particular structure, and leads to the design of a component which possesses the necessary strength or stiffness by virtue of its geometry, rather than the inherent properties of the material. The processing characteristics of plastics are of particular importance here, since stiffening features such as ribs or struts may be incorporated with ease. There are many examples of this approach in such mass-produced items as stacking crates, trays and furniture.

An alternative (or, in some cases, complementary) technique of increasing stiffness and strength is to incorporate stiff, strong fibres. Glass fibres are commonly used, being cheap and readily available, and have moduli between 50 and 100 times that of the polymer; carbon fibres have moduli of more than 200 x 10^9 N/m^2, although their relatively high cost limits their application. However, fibre reinforcement achieves its function most effectively when loads are applied in the direction of the longitudinal axis, and the ultimate performance of a composite depends critically on the degree of alignment of the fibres. Moreover, a composite

of highly aligned fibres will display considerable anisotropy - for loads applied at right angles to the longitudinal axis, the modulus may be only slightly higher than the unreinforced plastic.

Powell (1983) has emphasised the two extremes which are to be found in designing with composites. One is to reduce the directionality by distributing fibres randomly in the plane of a sheet material, thus reducing the anisotropy and enabling isotropic analysis to be used in design. Although simple in concept, the utilisation of fibres is highly inefficient, since most will be loaded at an angle to their axis. Such materials also have poor out-of-plane properties, and interlaminar shear must be avoided. The second approach involves both detailed analysis and careful control of production technique - fibres are positioned to respond most efficiently to particular applied loads, and the response of a component in any given circumstances will have been predicted beforehand. The essential difference between the two approaches is that the former seeks to minimise the anisotropy of fibre-reinforced composites, while the latter regards the directional properties as a positive design feature which may be exploited for the effective and efficient use of material.

1.2 HEAT TRANSFER IN COMPOSITES

Fibre reinforcement has found widespread application as a means for improving the mechanical properties of plastics. Accordingly, most of the research into such materials may be regarded as composite mechanics, and is concerned with the theoretical and experimental analysis of anisotropic elasticity and strength. In recent years, however, there has been a growing awareness of the importance of heat transfer in composite materials. The impetus for many recent investigations in this area has been supplied by the aerospace industry, where novel materials, selected for their superior mechanical properties such as strength-to-weight ratio, began to find applications in which their thermal properties were also of direct relevance, such as rocket nozzles and heat shields. This led to a number of

research programmes, particularly in the U.S.A., which sought to develop the theoretical approach to heat conduction in composites and to evaluate their performance in severe thermal environments, such as space re-entry vehicles (Clayton and others, 1968).

More recently, attention has turned to the processing of polymers and composites, prompted by the growing real cost of energy and by the introduction of new techniques (Edwards and Ellis, 1982). At least one cycle of heating and cooling is necessary in the manufacture of many polymer-based materials, whether to promote cross-linking in a thermosetting resin, or to mould or weld a thermoplastic. A knowledge of the thermal properties of both polymers and composites, together with suitable models of relevant heat transfer processes, are prerequisites for the design of efficient manufacturing and processing plant.

It is relevant at this point to emphasise the fundamental difference between the thermosetting and thermoplastic materials and, in consequence, the rather different problems associated with heat transfer. Thermosets are usually liquid at room temperature, and become solid only after a suitable process which combines the addition of a chemical catalyst and an increase of temperature to allow rapid cross-linking of the long molecules. This chemical process is irreversible, and it is necessary that curing should occur uniformly; in some moulding techniques excess resin must be expelled while still a liquid, and, particularly if a reinforcement is present, it will require unimpeded passage through the mould. Having cured, the resin must be cooled, and this process must also be carefully controlled to avoid residual stresses. Thermoplastics, on the other hand, are characterised by a melting temperature (typically 80-120^{o}C for high-volume plastics such as polyethylene, but exceptionally 300-400^{o}C for some advanced engineering plastics). On heating to its melting temperature, the plastic softens, and may then be moulded into the required shape or welded to similar material. On cooling, the moulded shape is retained, but again the rate must be controlled, since rapid cooling may prevent the formation of crystalline regions in some

polymers, and hence affect the mechanical properties. Measurement and analysis are thus important both in the design and operation of processing equipment and in the effects of the process on the material itself.

1.3 ANISOTROPY OF THERMAL CONDUCTIVITY

Just as a mechanically-anisotropic composite results from fibre and matrix having different stiffnesses and strengths, so thermal properties may be direction-dependent. The property in question is thermal conductivity (k), which, according to the Fourier law of conduction, relates the magnitude of the heat flux vector ($\underline{q}$) to the temperature gradient $\underline{\nabla}T$:

$$-\underline{q} = k\underline{\nabla}T \qquad (1.1)$$

Fig. 1.1 shows a section through a composite containing long, straight fibres, which are regularly-spaced and perfectly bonded to the polymer matrix. This is an orthotropic lamina, having different but independent thermal conductivities in the three principal directions shown: parallel (1) and perpendicular (2) to the fibres, and through the lamina (3). In this idealisation, it is possible to relate the thermal conductivities in each of the principal directions (K_1, K_2 and K_3) to those of the fibre (k_f) and the matrix (k_m) and to the fibre volume fraction (ϕ). In the longitudinal direction, thermal resistance is provided by continuous lengths of fibre and matrix in parallel, and simple mixture theory gives

$$K_1 = \phi k_f + (1-\phi)k_m \simeq \phi k_f \quad \text{if} \quad k_f \gg k_m \qquad (1.2)$$

In the two transverse directions, the situation is more complicated, since the thermal resistance to heat flow arises from a combination of material in series and parallel, and is thus dependent on the precise packing geometry. A lower bound to the effective thermal conductivity is obtained by assuming a completely series arrangement:

$$K_2 \simeq K_3 \geqslant \frac{k_f k_m}{(1-\phi)k_f + \phi k_m} \simeq \frac{k_m}{1-\phi} \text{ if } k_f \gg k_m \qquad (1.3)$$

To a good approximation, the lamina may be considered isotropic in the plane perpendicular to the reinforcement.

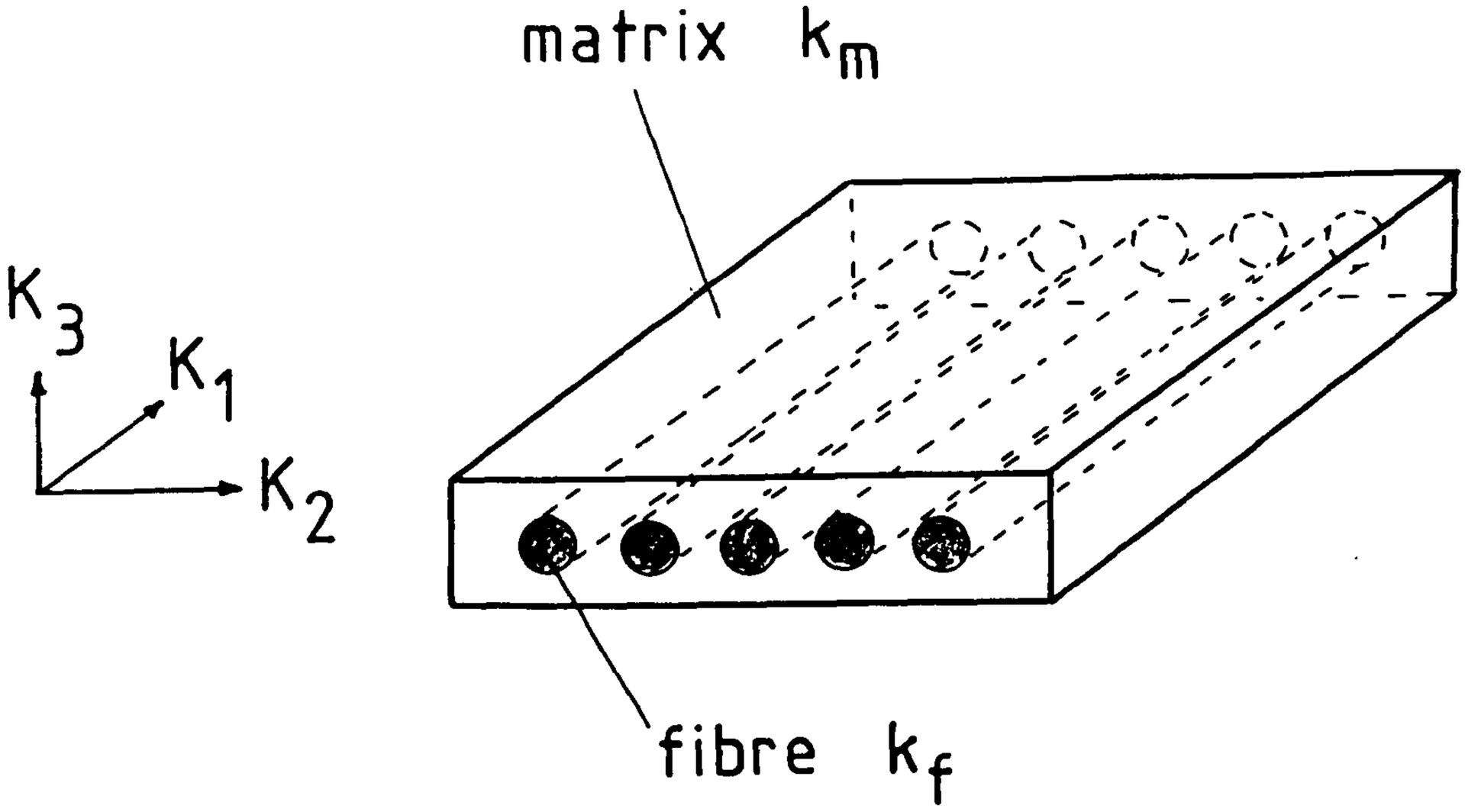

Fig. 1.1

Directions of the three mutually perpendicular principal thermal conductivities (K_1, K_2 and K_3) in an orthotropic lamina.

Laminated composites comprise a bonded stack of laminae, and the directions of fibres in adjacent sheets may be different. Several authors (for example, Tsou and others, 1974, and Harris, 1980) have applied mixture theories to such materials showing that, provided that the thickness of each lamina is small, the laminate may be regarded as a homogeneous solid with three (macroscopic) principal thermal conductivities.

As a result of anisotropy, the heat flux produced in response to a given temperature gradient depends on the direction within the solid. Moreover, in cases where a temperature difference is applied 'off-axis' (that is, not parallel to any of the principal axes), the heat flux is not necessarily in the same direction as the temperature gradient. The situation is similar to the coupling between direct stress and shear strain when an anisotropic laminate is loaded off-axis.

Polymers are generally classified as poor conductors of heat, and as shown in Fig. 1.2, the thermal conductivity at room temperature is between 0.1 and 0.5 W/m K, with semi-crystalline polymers having somewhat higher values than amorphous types. The axial thermal conductivity of a high modulus carbon fibre, on the other hand, may be a few hundred W/m K. A plastic reinforced with long, unidirectional carbon fibres may thus display considerable thermal anisotropy, with $k_{\parallel} / k_{\perp} \simeq 50$; the longitudinal thermal conductivity of such a composite may be comparable with a mild steel, being some 200-300 times greater than that of the polymer. Glass fibre-reinforced plastics generally display an anisotropy ratio of less than 2, due to the much lower thermal conductivity of glass.

1.4 THEORY OF HEAT CONDUCTION IN POLYMERS AND FIBRES

Elementary kinetic theory gives the thermal conductivity of an ideal gas from the Debye equation:

$$k = \frac{1}{3} C \bar{v} \ell \qquad (1.4)$$

where C is the specific heat of the constituent particles, $\bar{v}$ their mean group velocity and ℓ their mean free path. In solids, the gas is thought of as a 'gas' of phonons (energy

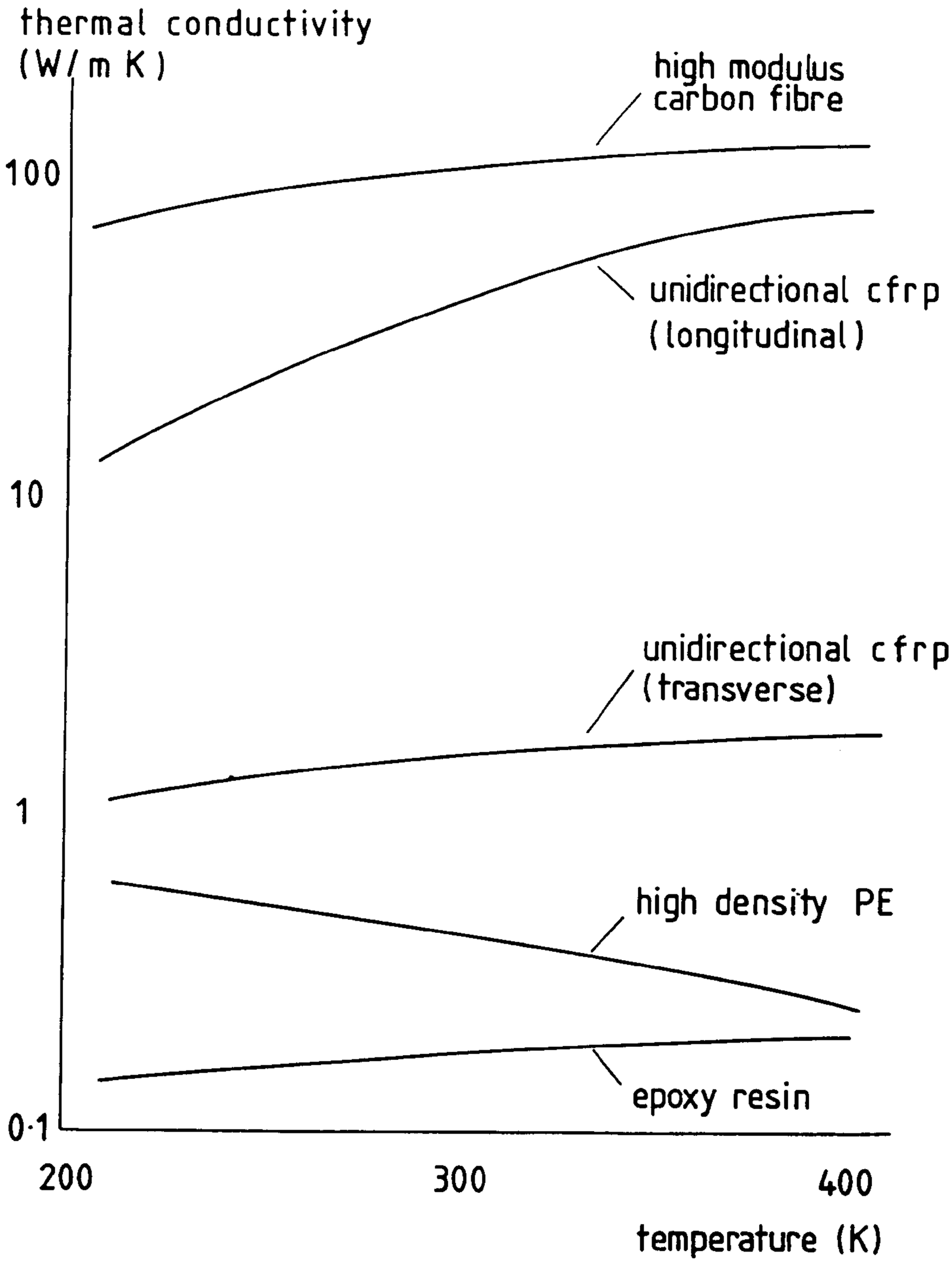

Fig. 1.2

Typical thermal conductivities of carbon fibre, polymer and composite.

quanta of lattice vibrations) which drift down the temperature gradient, colliding with one another and with any irregularity which may be present in the solid. The values of C and $\bar{v}$ are roughly comparable in all solids, so the very low values of k in polymers (and amorphous materials in general) can be explained by low values of the mean free path which in turn result from the disorder in the solid. $\bar{v}$ is equivalent to the velocity of sound in the solid.

In crystalline materials, the regularity of the atomic structure leads to much larger mean free paths, so that values of thermal conductivity are considerably higher than in amorphous materials. Semi-crystalline polymers have a range of thermal conductivity which is approximately double that found in amorphous polymers, and this is broadly consistent with predictions based on a simple law of mixtures. Drawing or extrusion of a polymer may result in crystallite or molecular orientation in the direction of elongation, and results in an anisotropy of thermal conductivity which is an order of magnitude greater for semi-crystalline polymers than for amorphous ones. Parallel to the orientation direction, the conductivity is proportional to the draw ratio (Greig, 1982).

A detailed explanation of the temperature dependence of thermal conductivity in polymers relies on more sophisticated arguments, but it is interesting to note that all amorphous solids can be represented by the same relationship between k and temperature (Choy, 1977). This is because, at all normal temperatures (above a few K) the mean free path is roughly the same as the magnitude of the disorder; as shown above, the thermal conductivity is determined by the product of the specific heat and the velocity of sound, both of which are approximately the same for all solids. The thermal conductivity of an amorphous polymer is thus proportional to specific heat, and hence approximately constant from room temperature to the melting point. In crystalline materials, the mean free path increases more rapidly than the specific heat falls with decreasing temperature, resulting in an increase of thermal conductivity at lower temperatures.

Carbon fibres are produced from various organic precursors, such as polyacrylonitrile (PAN) or rayon, which are subjected to a controlled heat treatment at temperatures up to a few thousand K. A vital stage of the process is stretching or spinning, which promotes a high degree of orientation of the graphite crystals; in the axial direction the strong covalent bonds between carbon atoms predominate, giving a theoretical tensile modulus of almost 10^{12} N/m^2. In practice, the degree of perfection and alignment depends on the details of the manufacturing conditions, and these may be varied to optimise particular properties; commercial fibres are usually categorised as 'high modulus', with tensile moduli between 300 and 690 GN/m^2 and strengths of 1.9 to 2.8 GN/m^2, or 'high strength', with moduli between 140 and 260 GN/m^2 and strengths of 1.4 to 4.2 GN/m^2 (Lovell and Pamington, 1982). As a result of the crystal structure, the fibres are highly anisotropic, and, perpendicular to the longitudinal axis, moduli may be lower by a factor of 20 or 30.

Johnson and Watt (1967) pointed out that other physical properties are influenced by the crystal orientation, in particular the thermal conductivity. Graphite is a lattice conductor, so Equation 1.4 applies, and the authors were able to deduce a longitudinal thermal conductivity of about 60 W/m K for a high modulus (400 x 10^9N/m^2) carbon fibre. Transverse thermal conductivities are between $\frac{1}{3}$ and $\frac{1}{5}$ of the longitudinal value, and this is roughly what would be expected from the smaller scale of crystal structure (and hence lower mean free path) in this direction.

1.5 MACROSCOPIC HOMOGENEITY

It will be assumed in this thesis that the microstructural scale of a fibre-reinforced plastic is small enough for the material to be regarded as macroscopically homogeneous. Although, in reality, the composite is a heterogeneous mixture of two very different substances, the typical dimensions of interest in engineering applications ($\simeq 10^{-2}$ m and above) are several orders of magnitude greater than the scale of the mixture itself (reinforcing fibres have a

diameter of a few tens of microns, that is of the order of 10^{-5}m). The fibre-reinforced plastic is thus considered as a thermally anisotropic but homogeneous material; the details of the microstructure, such as variable void content, are only of interest insofar as they influence the macroscopic thermal properties. There is, however, an intermediate scale at which inhomogeneity will be considered, and is typified by a composite containing curved or divergent long fibres. In such cases, the thermal conductivity becomes dependent on position within the solid, which may be regarded as macroscopically homogeneous, yet non-uniform.

A few authors, such as Balageas and Luc (1983), have paid particular attention to the assumptions of macroscopic homogeneity, partly because they are concerned with applications of composites in particularly severe environments involving very large thermal shocks. They emphasise the importance of determining the limits of validity of the homogeneous model, and, if necessary, progressively increasing the level of sophistication. Some situations involving severe transient heating may require, for example, a model in which each component of the composite is considered separately homogeneous, with the interface characterised by a coupling term.

Fig. 1.3 shows a section through an idealised one-dimensional composite, comprising equal amounts of fibre and matrix. As indicated in 1.3, various mixture theories may be invoked to derive an effective thermal conductivity (k_e) and heat capacity ($(\rho C_p)_e$) for transient conduction parallel to the reinforcement (the x-direction in Fig. 1.3). The question arises as to whether an effective thermal diffusivity, defined by $\alpha_e = k_e/(\rho C_p)_e$, is physically valid. Theoretical and experimental studies on these simplified systems (for example, Horvay and others, 1973; Truong and Zinsmeister, 1978) have indicated that the use of an average diffusivity can lead to significant errors in calculated temperature distributions close to a boundary condition which is periodic and changing at a high frequency. Similar discrepancies may be expected a short time after a thermal shock at a boundary, such as a step change in temperature or heat flux.

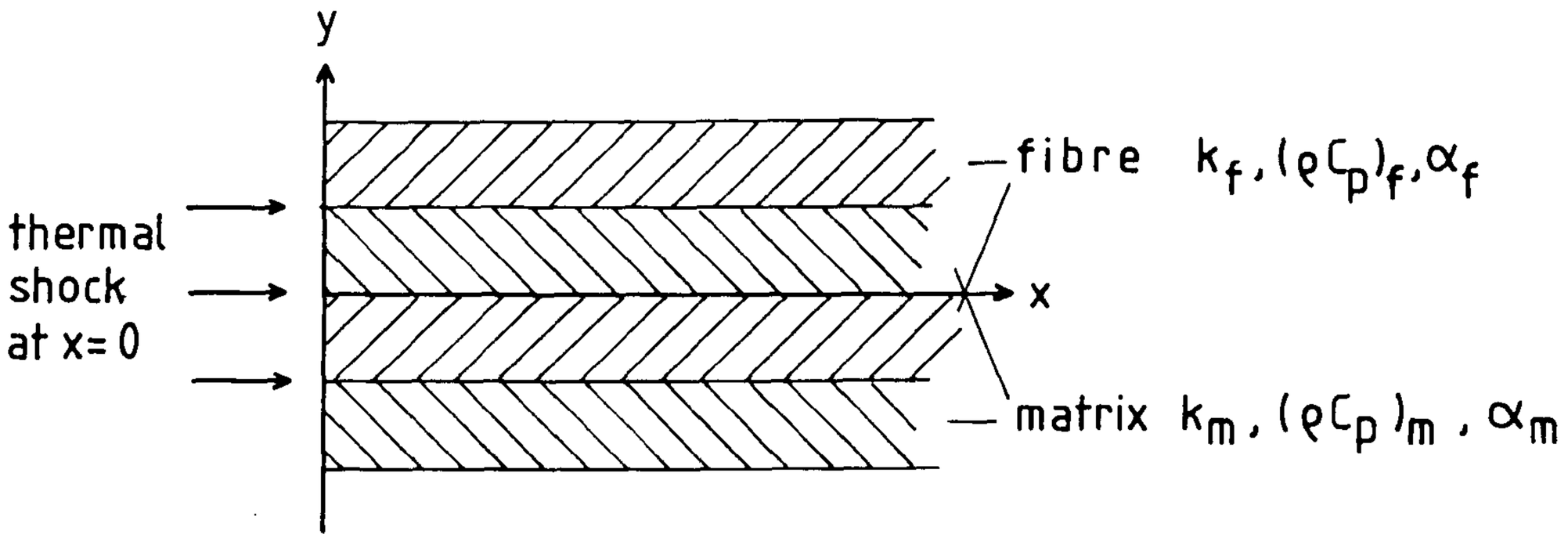

Fig. 1.3

Section through idealised one-dimensional composite, consisting of equal volumes of fibre and matrix.

The validity of the homogeneous assumption in transient situations may be examined by considering a time scale (τ) characteristic of heat transfer perpendicular to the laminate. With typical thermal diffusivities of fibre and matrix of $\alpha_f \simeq 10^{-5}\,m^2/s$ and $\alpha_m \simeq 10^{-7}\,m^2/s$, and assuming the transverse dimension of the microstructure to be $\ell \simeq 10^{-5}\,m$, time scales appropriate for fibre and matrix are

$$\tau_f = \frac{\ell^2}{\alpha_f} \simeq 10^{-5}\,s, \text{ and } \tau_m = \frac{\ell^2}{\alpha_m} \simeq 10^{-3}\,s$$

This suggests that macroscopic homogeneity will be a reasonable assumption in such a composite for time $t \geqslant 10^{-3}\,s$, when the lateral temperature gradient will have decayed sufficiently for the use of a one-dimensional effective thermal diffusivity to be valid.

1.6 OBJECTIVES AND SCOPE OF THE PROBLEM

The primary objective of the work described in this thesis is the development of a numerical model of heat conduction in two and three-dimensional anisotropic materials, with the aim of analysing the temperature distribution in engineering composite components. The ability of carbon fibres not only to increase the thermal conductivity of a polymer matrix but also to impart highly directional properties was thought to be of considerable importance, and not yet fully exploited by polymer engineers in industry. It was felt that in addition to a thermal analysis of existing composite components, such a model could serve as a generalised design tool, and encourage the use of carbon fibre-reinforced plastic as a heat transfer material in its own right. For these reasons, effort was directed towards a model which was specific to the problems of heat transfer, yet general in its potential applications.

Fig. 1.4 is an attempt to depict the various areas of study relevant to heat conduction in composites, and the ways in which they are interrelated.

Both mathematical analyses and experimental measurements may contribute directly to an understanding of heat transfer in a composite component (as indicated by the broken lines in Fig. 1.4), but their use in the present context is confined

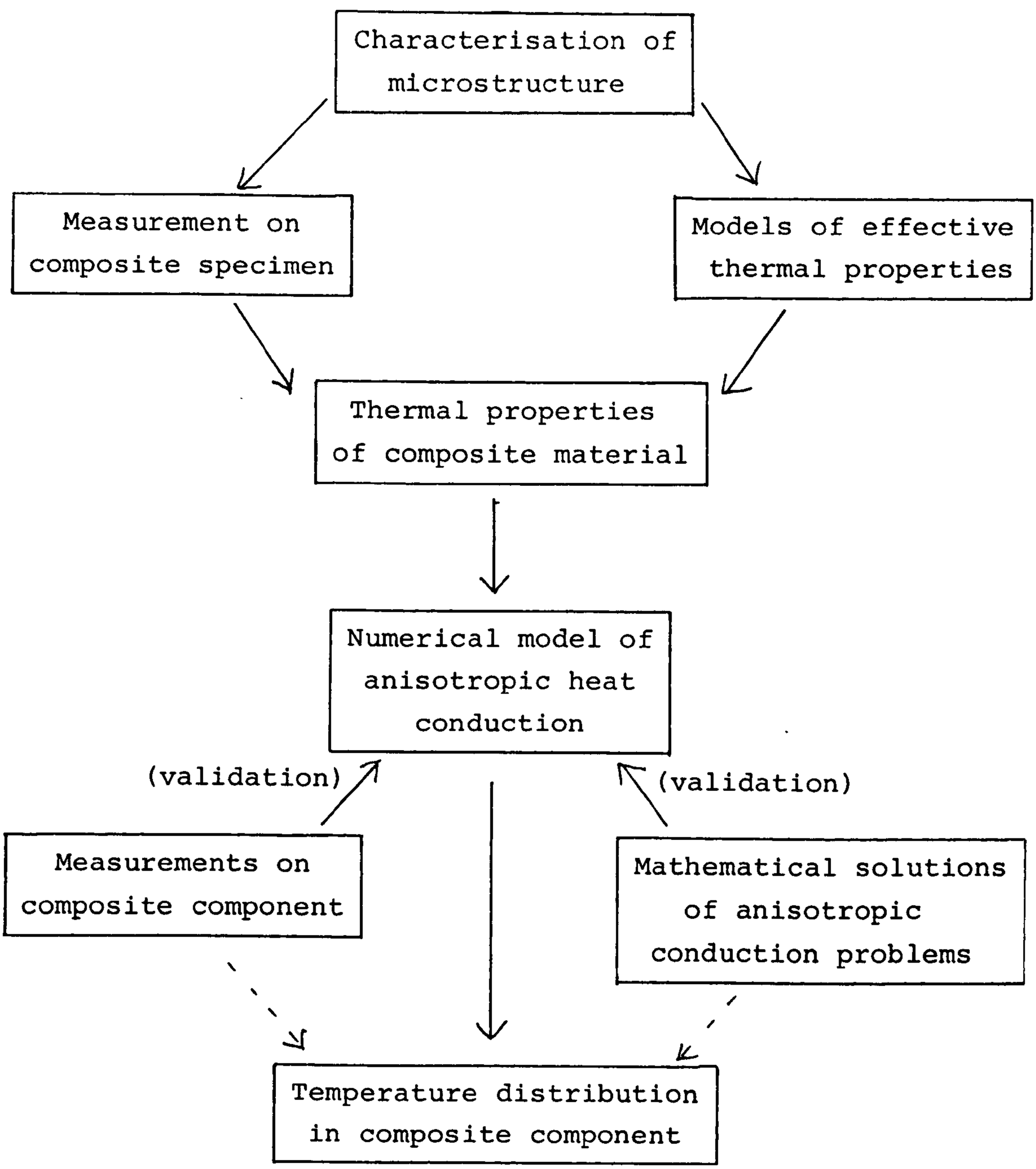

Fig. 1.4

Related areas of study in heat conduction in composites.

to validation of the numerical model. Before the introduction of modern composite materials in the 1960's, the mathematical theory of heat conduction in anisotropic solids had found only limited application in the study of crystals. Since the early 1970's, however, many solutions to initial-value and boundary-value problems have appeared in the literature, and, although of limited use in practical engineering situations, they are of considerable importance in the validation of numerical techniques. Experimental measurements on actual components can give insight to specific problems, but results are often difficult to generalise and may be both expensive and time-consuming to obtain.

A knowledge of composite thermal properties is essential both for numerical modelling itself and for the interpretation of experimental data in the context of validation. As indicated in Fig. 1.4, these may be obtained from direct measurements on the composite material, or derived from models of the effective macroscopic properties of the system. In an anisotropic material, two or three mutually perpendicular thermal conductivities may be required, together with specific heat and density over the temperature range of interest. If the anisotropy ratio is high, different experimental techniques, using specimens of different geometry, may be necessary to measure conductivities differing by a factor up to 50. Polymer processing involves changes of phase, and measurements of, for example, latent heats of crystallisation are required. Other thermal properties may be different in the molten phase, demanding yet another measurement technique. Apart from problems associated with the vast range of material combinations in composites, there is also the question of the representativeness of a single specimen. A given manufacturing process may result in material of variable quality, and it is important to subject all specimens to detailed microstructural classification, since misalignment of fibres or the presence of voids in the matrix can have a large effect on thermal properties.

The microstructure of the composite material is also an

important parameter in models which relate effective thermal properties to those of the constituents. There are useful analogies between thermal and mechanical properties (Springer and Tsai, 1967), although many current theories derive from the early work of Maxwell, who related permeability and electromagnetic field strength. A definitive assessment of rival models is hampered by the inadequacy of experimental data, in which the scatter may be greater than the difference between different theories. Some of the necessary data simply does not exist, such as a direct measurement of the transverse thermal conductivity of carbon fibres.

1.7 THESIS OUTLINE

Chapter 2 contains a brief review of the basic principles of thermal conductivity measurement, and a discussion of the particular problems associated with measurements in anisotropic solids. Published thermal conductivities of fibre-reinforced plastics are surveyed, and although the particular interest in this thesis is carbon fibres, other reinforcements are included. Overall, a substantial number of conductivity measurements have been reported, but the range of matrix and reinforcement materials is so large that there are few data available on any one particular composite. Moreover, the 'standard carbon fibre' does not exist, and the products of different manufacturers all possess slightly different properties. Further experimental scatter arises from the variable quality with which composite specimens are manufactured, and also from different designs of measurement techniques; it is thus possible only to identify a range of values for the principal thermal conductivities of carbon fibre-reinforced plastics.

In order to interpret experimental measurements on a suitable composite for the purposes of validating a numerical model, reliable values of thermal conductivity are required. Chapter 3 thus describes the laboratory manufacture of specimens of unidirectional high strength carbon fibre-reinforced epoxy resin composites, and the design of a steady-state apparatus to measure longitudinal thermal conductivity around room temperature. Specimens were also prepared for

complementary measurements of transverse thermal conductivity on a commercial instrument.

The mathematical basis of heat conduction in an anisotropic medium is presented in Chapter 4, and the available literature surveyed in order to extract analytic solutions to problems which may serve in the validation of the numerical model. The application of the finite element method to thermal problems is discussed in this chapter, and a number of advantages over other numerical techniques are identified.

Chapter 5 contains the derivation of a finite element model of transient, anisotropic conduction in two and three space dimensions, based on variational principles. (The implementation of these models as computer programs is discussed in appendices to the thesis.) As indicated above, generality of application to thermal problems was an important criterion, and the model includes facilities for spatial variation and temperature-dependence of material properties.

As the first stage of validation, the finite element model was used to generate solutions to some of the idealised conduction problems identified in Chapter 4. Comparisons between analytic and numerical solutions are evaluated in Chapter 6; only two-dimensional problems are discussed in detail, but they include examples of steady and transient conduction in non-linear and non-uniform (spatially-variable conductivity) anisotropic media.

Chapter 7 describes an experiment to measure the steady-state temperature distribution in a large specimen of carbon fibre-reinforced plastic in response to controlled boundary conditions. Using the measured thermal conductivity of this material (Chapter 3) the results provide not only additional support for the validity of the numerical model, but also give confidence that the composite material is in reasonable conformity with its homogeneous idealisation.

Chapter 8 discusses two recent industrial applications of the finite element model. The first concerns the tape-laying of a carbon fibre-reinforced thermoplastic in which the

model was used to investigate the effect of the process on the thermal history of the semi-crystalline polymer during fabrication of thin sheet sections of unidirectional composite. The second is the calculation of the temperature distribution in a composite turbopropeller blade, in response to convective heating in an exhaust gas stream.

The thesis concludes (Chapter 9) with a summary of the findings and a discussion of avenues for future research and development.

CHAPTER 2 : REVIEW OF THERMAL CONDUCTIVITY MEASUREMENT IN COMPOSITES

This chapter contains a general review of the principles of thermal conductivity measurement, followed by a discussion of the particular considerations arising from the use of anisotropic materials. In 2.2 a survey is made of theoretical models describing the relationship between the macroscopic thermal properties of a composite and those of its constituent materials. Finally, published data on the thermal conductivity of fibre-reinforced plastics are reviewed, with the emphasis on carbon fibre composites.

2.1 PRINCIPLES OF THERMAL CONDUCTIVITY MEASUREMENT

The measurement of thermal conductivity in solids has concerned scientists for at least two centuries; experiments to compare the ability of different materials to transmit heat had taken place long before Fourier's classical presentation of the mathematics of conduction in 1822. One of the earliest practical investigations appears to have been by Inger-Hansz (1789), who coated the surface of various rods with wax, placed one end in a furnace, and measured the different lengths over which the wax melted.

Techniques of thermal conductivity measurement are conveniently classified under the fundamental headings 'static' and 'dynamic'. The basis of the former category is Fourier's law of heat conduction (Equation 1.1), and a value of thermal conductivity is obtained from measurements of the heat flux and the temperature gradient (in the direction of the heat flux) under steady conditions. In dynamic methods of measurement, the temperature distribution in the sample varies with time; this requires a solution to the complete differential equation of heat conduction, and the technique generally yields a value of the diffusivity ($\alpha = k/\rho C_p$). Some dynamic methods also give a measure of the specific heat, so that the thermal conductivity can be obtained indirectly.

The choice of the most suitable measurement technique is determined by many factors, the most important of which are

the temperatures at which data are required and the magnitude of the thermal conductivity to be measured. Parrott and Stuckes (1975) have provided a concise survey of alternative methods, and their main conclusions are summarised below. Detailed treatments of apparatus design are given by, for example, Laubitz (1969) and Powell and Tye (1960) for steady-state methods, and Danielson and Sidles (1969) for dynamic methods.

2.1.1 Static Methods

The simplest form of static method involves one-dimensional heat flow down a sample of uniform cross-section (Fig. 2.1). The heater is usually electrical, so the rate of heat supplied to the sample may be measured with considerable accuracy. The measurement of temperature difference is less straightforward however, and the following points require attention:

(i) thermometers must be installed without disturbance to the heat flow, and heat leakage down connecting leads must be avoided;

(ii) the temperature difference must be large enough to be measured with acceptable accuracy, but small enough to ascribe a meaningful average temperature to the measurement.

In addition, the apparatus must incorporate features to ensure that all the energy dissipated by the heater passes down the sample, and that lateral heat losses are negligible (otherwise the assumption of one-dimensional heat flow is invalid). For this reason, the heater is usually surrounded by a guard, the temperature of which can be matched to the heater. The sample itself is surrounded by a shield (see Fig. 2.1 b), down which the temperature gradient is matched to that in the sample.

Laubitz (1969) performed a range of analytic and numerical calculations on the basic linear, steady-state method, and on the basis of these, made a number of general recommendations for the design of such apparatus. He suggested a ratio of sample length to diameter of about 10, with the outside

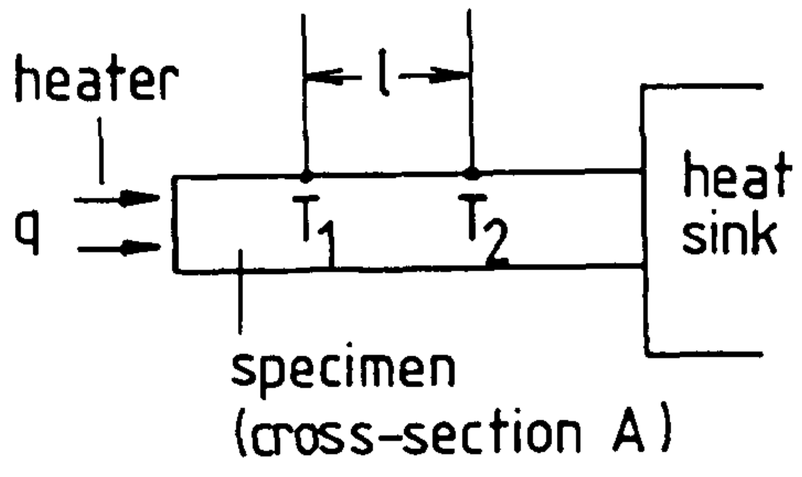

(a)

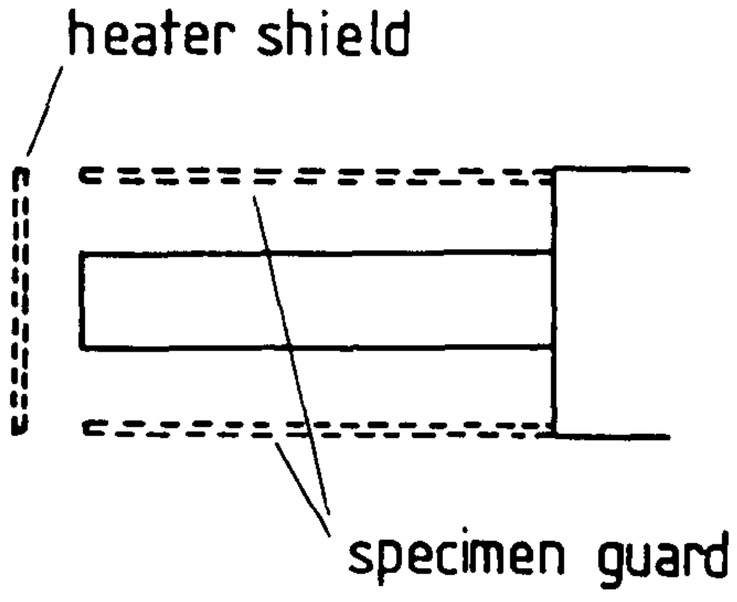

(b)

Fig. 2.1

(a) One dimensional steady-state heat flow for measurement of thermal conductivity. $k = \frac{q\ell}{T_1 - T_2}$

(b) Location of heater shield and specimen guard to ensure one-dimensional heat flow.

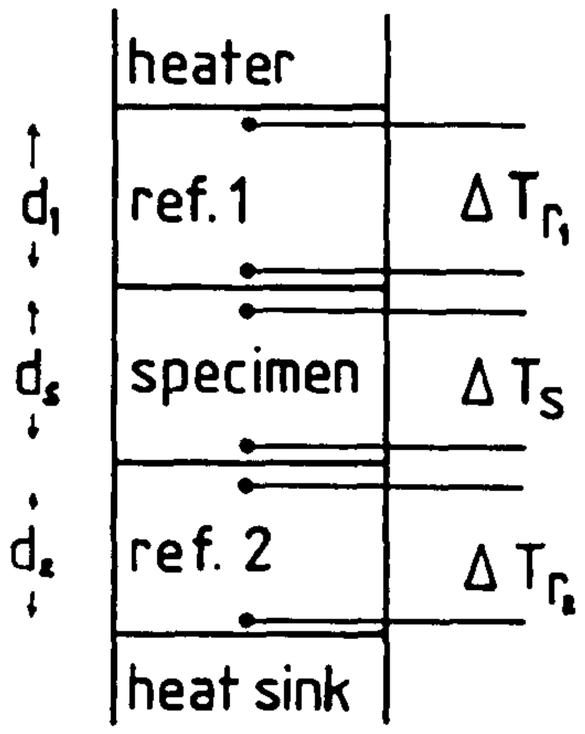

Fig. 2.2

Comparative measurement of thermal conductivity.

$$k = \frac{d_s}{2\Delta T_s}\left(\frac{k_{r_1}\Delta T_{r1}}{d_1} + \frac{k_{r2}\Delta T_{r2}}{d_2}\right)$$

diameter of the guard about twice that of the sample. The space between sample and guard should be filled with an insulator, and the ratio of sample conductivity to that of the insulator should be between 10^2 and 10^3; this implies a lower limit of about 1 W/m K to the value which can be measured with this configuration.

The above arrangement is known as an absolute measurement, since the value of thermal conductivity is obtained directly from a heat flux and a temperature gradient. In comparative measurements, the sample is inserted between two standard materials of known (but similar) conductivity, and the unknown conductivity is obtained by comparison of the three temperature gradients (Fig. 2.2). This method is particularly advantageous when samples are not sufficiently long for the absolute system. However, the location of thermometers between the samples is critical, and large errors may arise from contact resistances (and hence spurious temperature gradients) at the interfaces between sample and measuring point. One way of avoiding this error is to install miniature temperature sensors in the surfaces of the samples themselves, provided that this can be achieved without disturbing the linear heat flow.

The measurement of low thermal conductivity (less than about 1 W/m K) requires the use of thin samples in order to obtain a suitably small temperature gradient. The standard method is the 'guarded hot plate', and is the subject of BS 874 (1973) and ASTM C177 (1974). Two identical samples are sandwiched either side of a heater, between two water-cooled heat sinks (Fig. 2.3). The main heater is surrounded by an annular guard heater in order to eliminate radial heat losses. For measurements above room temperature, auxiliary heaters may be inserted between the samples and the heat sinks, and the entire stack surrounded by a cylindrical guard heater. The apparatus is capable of better than 1% accuracy, but the requirements for precision of construction and temperature control are considerable.

The problem of lateral heat losses in the linear static methods described above may be eliminated by providing heat

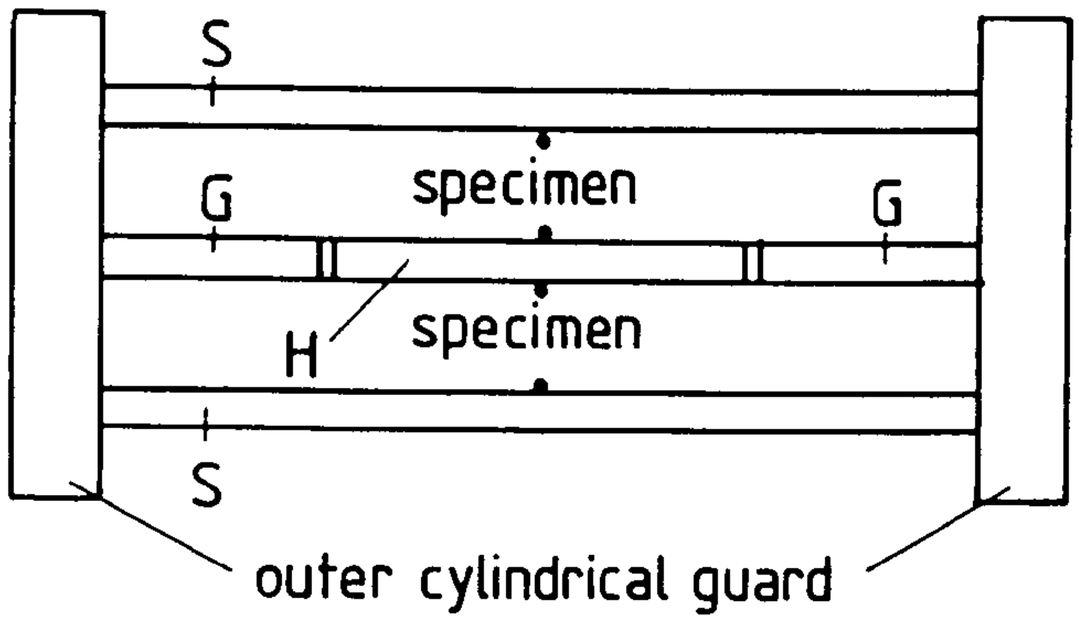

H - heater
S - sink
G - heater guard
• - temperature measurements

Fig. 2.3

Guarded hot plate apparatus for thermal conductivity measurement.

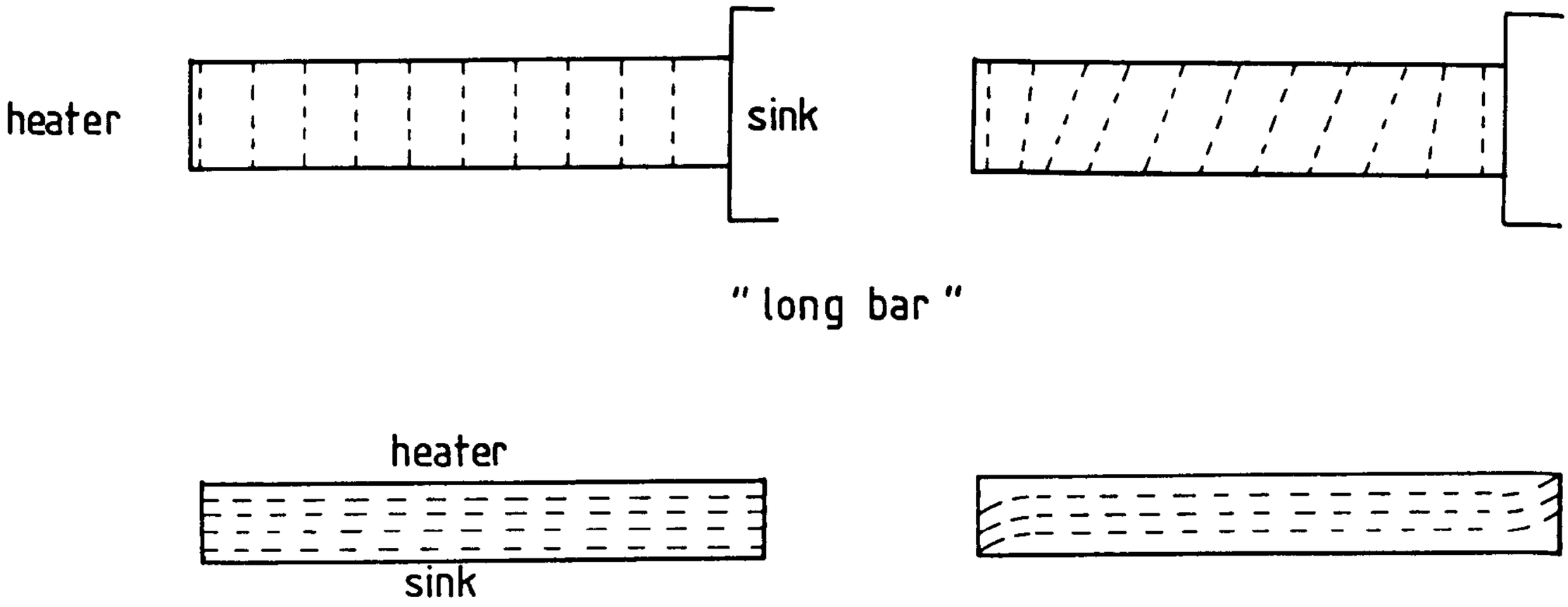

Fig. 2.4

Schematic isotherms in isotropic (left) and anisotropic (right) materials.

along the axis of a long cylindrical specimen, and measuring a radial temperature gradient. However, as discussed in 2.1.3, this configuration is not suitable for materials with anisotropic thermal properties in a cartesian geometry.

2.1.2 Dynamic Methods

Although steady-state methods of thermal conductivity measurement are capable of a high degree of accuracy, dynamic methods offer several advantages. Most importantly, heat losses have less influence on the measured value, since the experiment is performed over a short period of time (typically of the order 10-100 sec.). Often, measurements of power input to the sample are not required, and thermal diffusivity is calculated from relative (as opposed to absolute) changes in temperature as a function of position and time. In consequence, temperature sensors are required to have a linear response over small ranges, but need not be accurately calibrated, since absolute measurements are not required. The thermal inertia of the monitoring system is, however, of importance, and temperature sensors should have suitably small response times.

Dynamic methods may be classified as 'periodic' or 'transitory', depending on the manner in which energy is supplied to the specimen. In the former category, one end of a sample is heated at a known frequency, while measurement of the amplitude and either the phase or the velocity of the resultant 'temperature wave' enables the diffusivity to be calculated. Transitory methods require the sample to be initially in equilibrium with its environment, and then subjected to a change in heat flux at some point; the diffusivity is calculated either from the time rate of change of temperature at a single point in the sample, or from the difference in temperature between two points at a given time. The change in heat flux may be in the form of a step change or a single pulse of known duration.

In dynamic methods, it is not possible to guard the sample against heat losses by matching temperature gradients. For measurements on low conductivity materials, the sample should

be in the form of a flat slab, which is relatively thin in the direction of heat flow; in this case it may be regarded as an infinite plate and the one-dimensional heat flow equation is applicable. An alternative approach is to include appropriate heat losses in the differential equation describing the experimental configuration. Heat loss coefficients then appear in the solution, and may be eliminated by making a number of measurements under different experimental conditions.

2.1.3 Measurements in Anisotropic Solids

The mathematical theory of heat conduction in an anisotropic solid is considered in some detail in Chapter 4. For the present it will be sufficient to state the general expression for the cartesian components of the heat flux, namely

$$-q_x = k_{11}\frac{\partial T}{\partial x} + k_{12}\frac{\partial T}{\partial y} + k_{13}\frac{\partial T}{\partial z}$$

$$-q_y = k_{21}\frac{\partial T}{\partial x} + k_{22}\frac{\partial T}{\partial y} + k_{23}\frac{\partial T}{\partial z} \qquad (2.1)$$

$$-q_z = k_{31}\frac{\partial T}{\partial x} + k_{32}\frac{\partial T}{\partial y} + k_{33}\frac{\partial T}{\partial z}$$

where the quantities k_{ij} are the components of a second order tensor. As shown by Carslaw and Jaeger (1959), Equation 2.1 may be solved for the temperature gradients in terms of the heat fluxes, giving

$$-\frac{\partial T}{\partial x} = R_{11}\,q_x + R_{12}\,q_y + R_{13}\,q_z$$

$$-\frac{\partial T}{\partial y} = R_{21}\,q_x + R_{22}\,q_y + R_{23}\,q_z \qquad (2.2)$$

$$-\frac{\partial T}{\partial z} = R_{31}\,q_x + R_{32}\,q_y + R_{33}\,q_z$$

The constants R_{ij} are known as the resistivity coefficients. A general expression relating resistivity and conductivity coefficients is given by Ozisik (1980) as

$$R_{ij} = (-1)^{i+j}\frac{a_{ij}}{\Delta} \qquad (2.3)$$

where Δ is a determinant defined by

$$\Delta = \begin{vmatrix} k_{11} & k_{12} & k_{13} \\ k_{21} & k_{22} & k_{23} \\ k_{31} & k_{32} & k_{33} \end{vmatrix}$$

and a_{ij} is a cofactor of Δ, obtained by omitting the i th row and the j th column. For example,

$$R_{12} = (-1)^3 \frac{\begin{vmatrix} k_{21} & k_{23} \\ k_{31} & k_{33} \end{vmatrix}}{\Delta} = \frac{k_{23}k_{31} - k_{21}k_{33}}{\Delta} \qquad (2.4)$$

As shown in 4.1, both resistivity and conductivity tensors obey the reciprocity relation $R_{ij} = R_{ji}$ and $k_{ij} = k_{ji}\,(i \neq j)$.

In the fundamental experiment of linear heat flow down a long rod, illustrated in Fig. 2.1, the heat flux is confined to only one dimension. Putting $q_y = q_z = 0$ in Equation 2.2 gives

$$-\frac{\partial T}{\partial x} = R_{11}\,q_x \;;\; -\frac{\partial T}{\partial y} = R_{21}\,q_x \;;\; -\frac{\partial T}{\partial z} = R_{31}\,q_x \qquad (2.5)$$

so that measurement of the heat flux and the temperature gradient (in the direction of the flux) yields not a conductivity, but a resistivity. If the sample is an orthotropic solid, having three independent (principal) thermal conductivities in mutually perpendicular directions, and if these principal axes are aligned with the cartesian axes, then the above expressions simplify to

$$-\frac{\partial T}{\partial x} = \frac{1}{K_1} q_x \qquad (2.6)$$

where K_1 is the principal conductivity in the direction of the heat flux.

A similar generalisation may be applied to the 'guarded hot plate' configuration (Fig. 2.3). In this case, because the sample is relatively thin, the direction of the temperature gradient is fixed, so that, for example, $\frac{\partial T}{\partial y} = \frac{\partial T}{\partial z} = 0$. Equation 2.1 becomes

$$-q_x = k_{11}\,\frac{\partial T}{\partial x} \;;\; -q_y = k_{21}\,\frac{\partial T}{\partial x} \;;\; -q_z = k_{31}\,\frac{\partial T}{\partial x} \qquad (2.7)$$

and the measurement of heat flux and temperature gradient yields a value for the coefficient k_{11}. As before, on a suitably orientated orthotropic specimen the measurement gives one of the principal conductivities.

Thus, the basic measurement techniques described in 2.1.1 and 2.1.2 will be applicable to anisotropic materials, provided that (i) the geometry of the experiment is consistent with the anisotropy of the specimen, and (ii) measurements are made in the direction of the principal thermal conductivity axes.

The first point implies that methods which are based on the radial flow of heat in a cylindrical sample would not be appropriate for a material with anisotropic thermal properties in a cartesian geometry (such as a unidirectional, long fibre-reinforced plastic), since the temperature gradient would not, in general, be perpendicular to the heat flux. The experimental consequences of the second point are indicated by Fig. 2.4, which shows the temperature distributions in the 'long bar' and 'thin slab' configurations for anisotropic materials (compare Figs 2.1 and 2.3). In the former case, the temperature will vary around the circumference of the specimen (since $\frac{\partial T}{\partial y} \neq 0$), making it difficult to match the longitudinal temperature gradient in a sample shield. In the thin slab arrangement, the isotherms become distorted at the edges of the specimen, if the boundary condition of no lateral heat loss is maintained, and the sample aspect ratio must be sufficient for the presence of the edges not to influence the measurement of the temperature gradient.

A further experimental inconvenience arises from the magnitude of the difference in principal conductivities in some fibre-reinforced composites. As discussed in the introduction, the thermal conductivity parallel to the reinforcement in a composite containing high modulus carbon fibres may be 30 or 40 times greater than in the transverse direction. In some cases, more than one experimental configuration may be required to deal with this range of values. In any case, the estimates of experimental accuracy will have to be

revised to take the directional nature of heat flow into account; a specimen prepared for the measurement of a low, transverse thermal conductivity would be liable to greater lateral heat losses than a similar isotropic specimen.

2.2 EFFECTIVE THERMAL CONDUCTIVITY OF COMPOSITES

Much of the experimental work to be reviewed in 2.3 has been used to test various models of heat conduction in composite materials. The motivation behind such analyses is clear - if the macroscopic thermal properties of a material which is microscopically inhomogeneous can be reliably predicted from a knowledge of the constituents, then a great deal of tedious experimental work could be avoided. Alternatively, thermal property measurements could be used as a (non-destructive) method of quality assessment, since defects such as delamination or high void content would be apparent through anomalous thermal properties.

Consider a composite material containing long, continuous fibres (Fig. 1.1). In the direction of the reinforcement, direct analogy may be made with a parallel electrical resistance network; this implies that the effective thermal conductivity may be obtained by adding the component conductivities in proportion to the volume fraction of the reinforcements (ϕ). This leads to the simple expression

$$k_e^{\parallel} = \phi k_f + (1 - \phi) k_m \qquad (2.8)$$

As long as matrix and reinforcement are continuous, Equation 2.8 is generally accepted to be valid, and, as discussed in 2.3, has been widely used for the estimation of the longitudinal thermal conductivity of fibres.

At right angles to the reinforcement the situation is more complicated, since in this plane the composite presents many discontinuous paths for the passage of heat. The literature abounds with theoretical approaches to the problem, and a comprehensive review was made by Progelhof and others (1975). Dawson and Briggs (1981) have categorised the models into three basic groups, namely 'flux law', 'Ohm's law' and

'empirical'. The first group of models derive from the classical work of J.C. Maxwell, who used potential theory to obtain an exact expression for the effective conductivity of randomly distributed, non-interacting spheres in a continuous medium. The critical assumption here is 'non-interacting' which requires that the composite be only sparsely-filled. The theory has been applied to a regular array of particles which may be in contact or dispersed, but the models are of simplified geometry.

The Ohm's Law models derive from an analogy to a system of electrical resistances, which comprises various components in series and parallel, depending on the dispersion of the reinforcement and its geometrical cross-section. If it is assumed that the series and parallel components are arranged randomly, then the geometric mean equation is appropriate:

$$k_e^{\perp} = k_f^{\phi} k_m^{(1-\phi)} \qquad (2.9)$$

Dawson and Briggs (1981) found this the most accurate prediction of the thermal conductivity of porous alumina. A lower bound to the effective conductivity is obtained by assuming both components to be arranged in series. In this case the Ohm's Law analogy gives

$$\frac{1}{k_e^{\perp}} = \frac{\phi}{k_f} + \frac{(1-\phi)}{k_m} \qquad (2.10)$$

The final group of models take the form of equations derived either from experimental measurements on composites, or, more recently, from numerical calculation of the heat flux across an appropriate 'unit cell'.

Some of the models which have been or could be applied to fibre-reinforced composites are briefly described here. It is important to note that not all are suitable either for high reinforcement volume fractions or for composites in which the filler has a thermal conductivity much greater than the matrix.

In the following formulae, k_e, k_f and k_m denote the thermal conductivity of the composite, fibre and resin matrix

respectively; ϕ is the volume fraction of reinforcement, and $p = k_f/k_m$.

Ashton and others (1969) presented what is generally referred to as the Halpin-Tsai model, although it derives from the classical work of Rayleigh (1892). For circular or square fibres:

$$k_e = \left(\frac{1 + \eta\phi}{1 - \eta\phi}\right) k_m, \text{ where } \eta = \frac{p-1}{p+1} \qquad (2.11)$$

Lewis and Nielsen (1968) and Nielsen (1974) modified the Halpin-Tsai equation to include the effect of different packing modes:

$$k_e = \left(\frac{1 + AB\phi}{1 - B\phi\psi}\right) k_m \qquad (2.12)$$

where $B = \frac{p-1}{p+A}$ and $\psi = 1 + \frac{(1-\phi_m)\phi}{\phi_m^2}$.

Perpendicular to uniaxial fibres, A = 0.5. The quantity ϕ_m represents the maximum possible volume fraction in different packing geometries:

hexagonal, close packing	$\phi_m = 0.907$
simple cubic packing	$\phi_m = 0.785$
random packing	$\phi_m = 0.82$

For composites containing bunched fibres, a better value of A was given as 0.84.

Springer and Tsai (1967) used an analogy with longitudinal shear loading, and obtained the formula

$$\frac{k_e}{k_m} = \left(1 - \frac{s}{2b}\right) + \frac{a}{b}\int_0^s \frac{dy}{(2a-h) + h\, k_m/k_f} \qquad (2.13)$$

where s is the maximum dimension of the fibre in the y direction, and h is the width of the fibre (a function of y). Parameters a and b define the 'unit cell' as shown in Fig. 2.5. For a cylindrical filament in square packing (a = b)

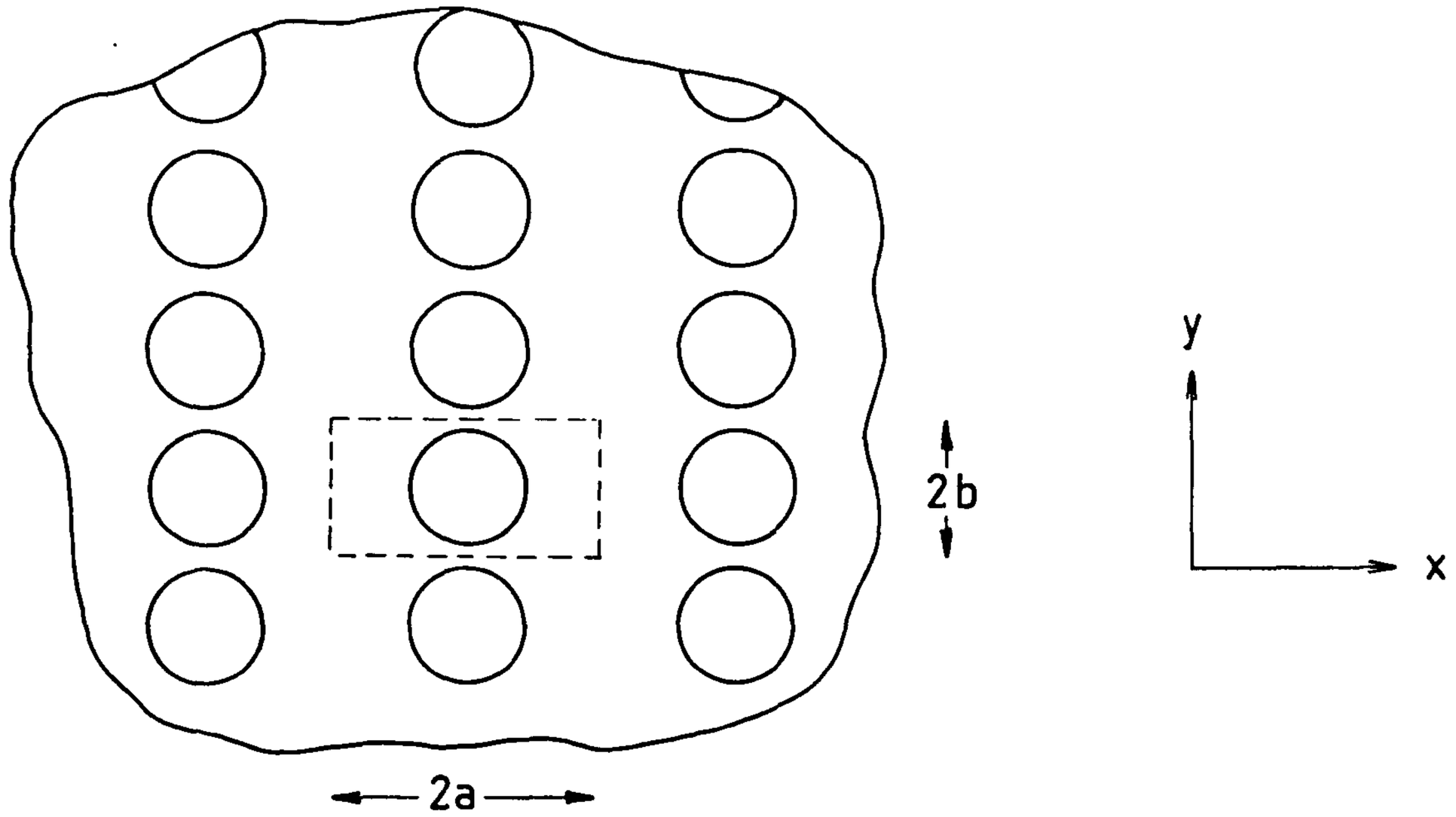

Fig. 2.5

Dimensions of unit cell in idealised composite section.

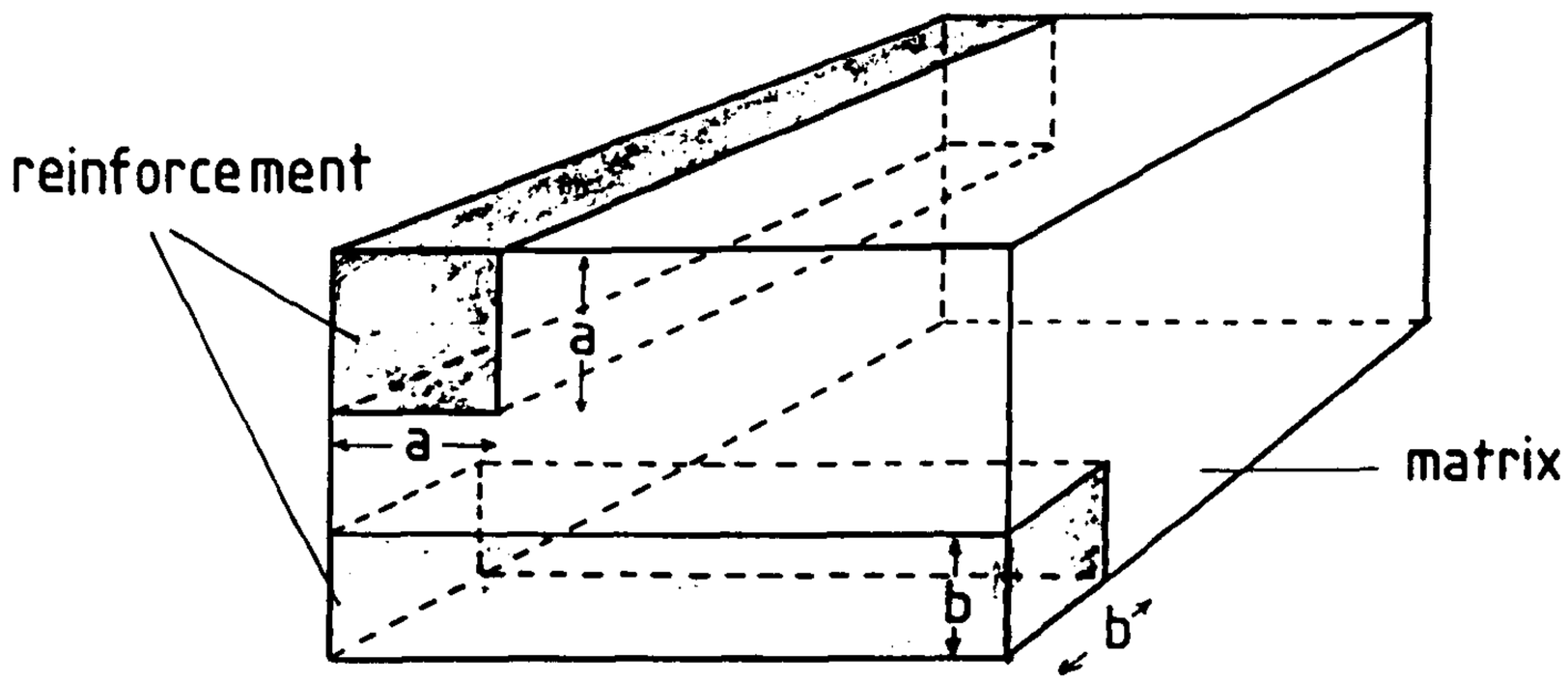

Fig. 2.6

Model of cross-ply mat with reinforcement of square section (Knappe and Martinez-Freire, 1965).

$$\frac{k_e}{k_m} = 1 - 2\sqrt{\frac{\phi}{\pi}} + \frac{1}{B}\left[\pi - \frac{4}{\sqrt{1-\frac{B^2\phi}{\pi}}} \tan^{-1}\left(\frac{\sqrt{1-\frac{B^2\phi}{\pi}}}{1+\sqrt{\frac{B^2\phi}{\pi}}}\right)\right]$$

$$\text{where } B = \frac{2}{p}(1-p) \qquad (2.14)$$

Knappe and Martinez-Freire (1965) considered a unit volume of a cross-ply mat, with square-section fibre-reinforcement in two solid prisms at right angles (see Fig. 2.6). For a unidirectional fibre-reinforcement, their expression reduces to

$$k_e = \frac{a\ k_f k_m}{a\ k_m + (1-a)\ k_f} + (1-a)k_m \qquad (2.15)$$

$$\text{where } a = \sqrt{\phi}$$

Bruggeman (1935) based a derivation on the work of Maxwell, using different assumptions for permeability and field strength, and obtained the following (implicit) equation for a dilute suspension of spheres:

$$1 - \phi = \left(\frac{k_f - k_e}{k_f - k_m}\right)\left(\frac{k_m}{k_e}\right)^{1/3} \qquad (2.16)$$

Clayton (1971) adapted Bruggeman's formula for heat flow at right angles to fibres:

$$\left(\frac{k_e}{k_m}\right)^{1/2} = \frac{\left[(1-\phi)^2(p-1)^2 + 4p\right]^{1/2} - (1-\phi)(p-1)}{2} \qquad (2.17)$$

Several authors (such as Donea, 1972 and Willis, 1977) have used a variational approach to determine upper and lower bounds on the effective thermal conductivity. Examples of the empirical approach are provided by Schneider and Romilly (1979) and Han and Cosner (1981), who all used numerical techniques to solve the steady-state heat conduction problem in an appropriate 'unit cell' of the material. Correlations were given in the form

$$k_e = \text{fn}(\phi,\ k_f/k_m,\ \text{packing geometry}). \qquad (2.18)$$

Zimmerman (1980) adopted a semi-empirical approach, using Han and Cosner's data to apply correcting factors to the Halpin-Tsai/Rayleigh model (Equation 2.11).

A comparison of the analytical equations is made in Fig. 2.7, where k_e/k_m is plotted as a function of ϕ. Calculations assumed $k_f/k_m = 30$, a value much higher than typical of glass fibre-reinforced plastics, but probably representative of carbon fibres. The geometric mean and series models appear to give the extreme predictions, but there is reasonable agreement between most of the other models. However, differences are more apparent if the effective conductivity is plotted as a function of fibre conductivity, as in Fig. 2.8, for a volume fraction of $\phi = 0.6$. All models approach an asymptotic value as k_f/k_m increases, except for the geometric mean model, which increases monotonically. The difference between the theoretical models (excluding geometric mean and series) at large k_f/k_m is as much as 70%.

As will be shown in the following section, and in Chapter 3, typical values for k_e/k_m in unidirectional carbon fibre-reinforced composites (measured at right angles to the reinforcement) may be as high as 3 or 4 for high strength and up to 6 or 7 for high modulus fibres. There is considerable difficulty in deducing values of k_f/k_m from these data - in the first case the value of k_e/k_m occurs at the flat region of the curves, leading to a large uncertainty in k_f/k_m. In the case of high modulus fibres, the value of k_e/k_m is greater than the asymptotic values predicted by all except the geometric mean model.

In their empirical study, Han and Cosner (1981) found that the effective conductivity was very sensitive to fibre packing geometry, all other factors being equal, and concluded that many of the theoretical models are likely to be inaccurate for $k_f/k_m \gg 1$, since this variable is seldom included. Their results are illustrated in Fig. 2.9, which gives effective conductivities in a rectangular packing array at a volume fraction of $\phi = 0.6$. Three curves are shown, each with different values of the complementary angle

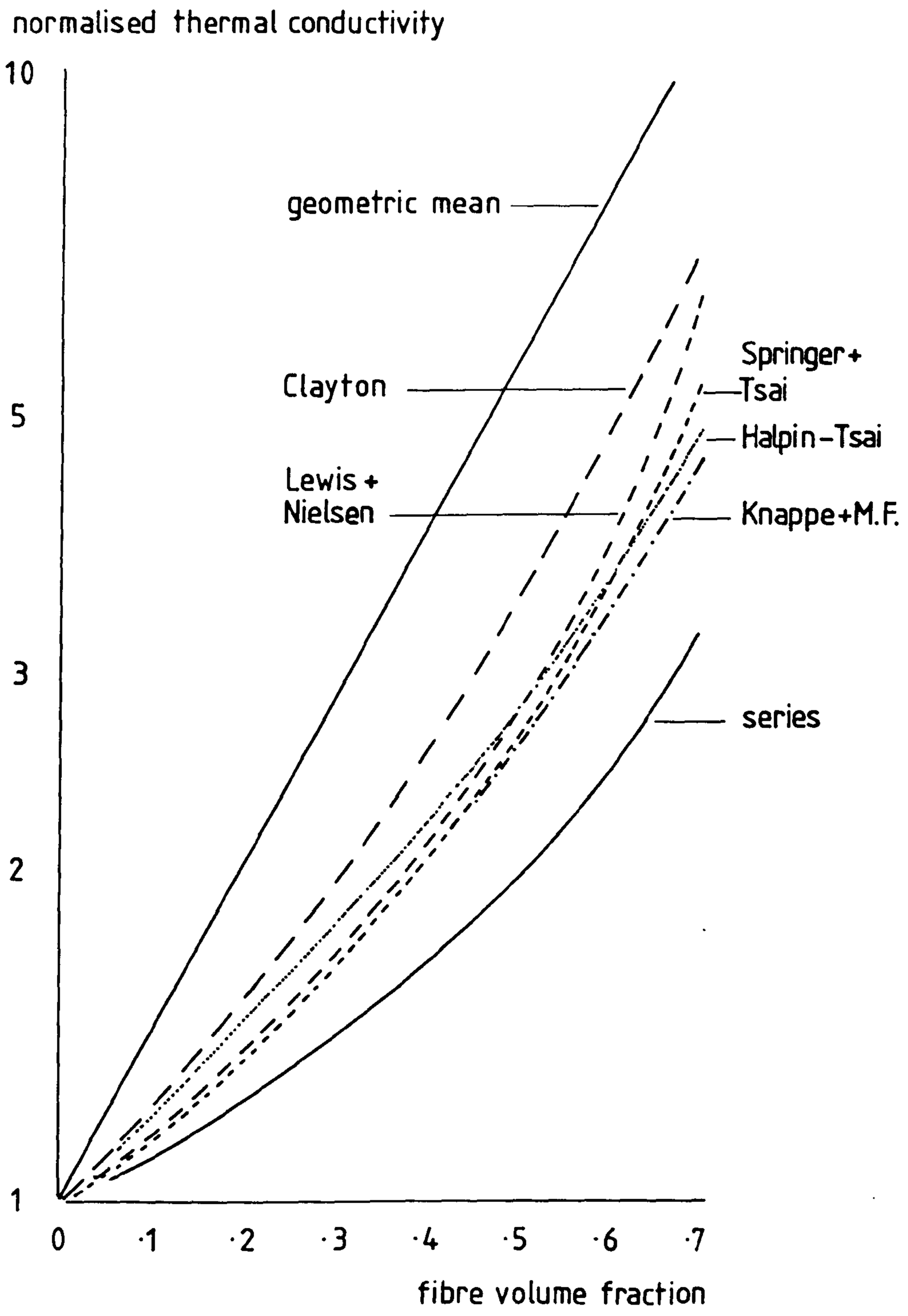

Fig. 2.7

Comparison of analytic models of normalised effective thermal conductivity (k_e/k_m) as a function of fibre volume fraction with $k_f/k_m = 30$.

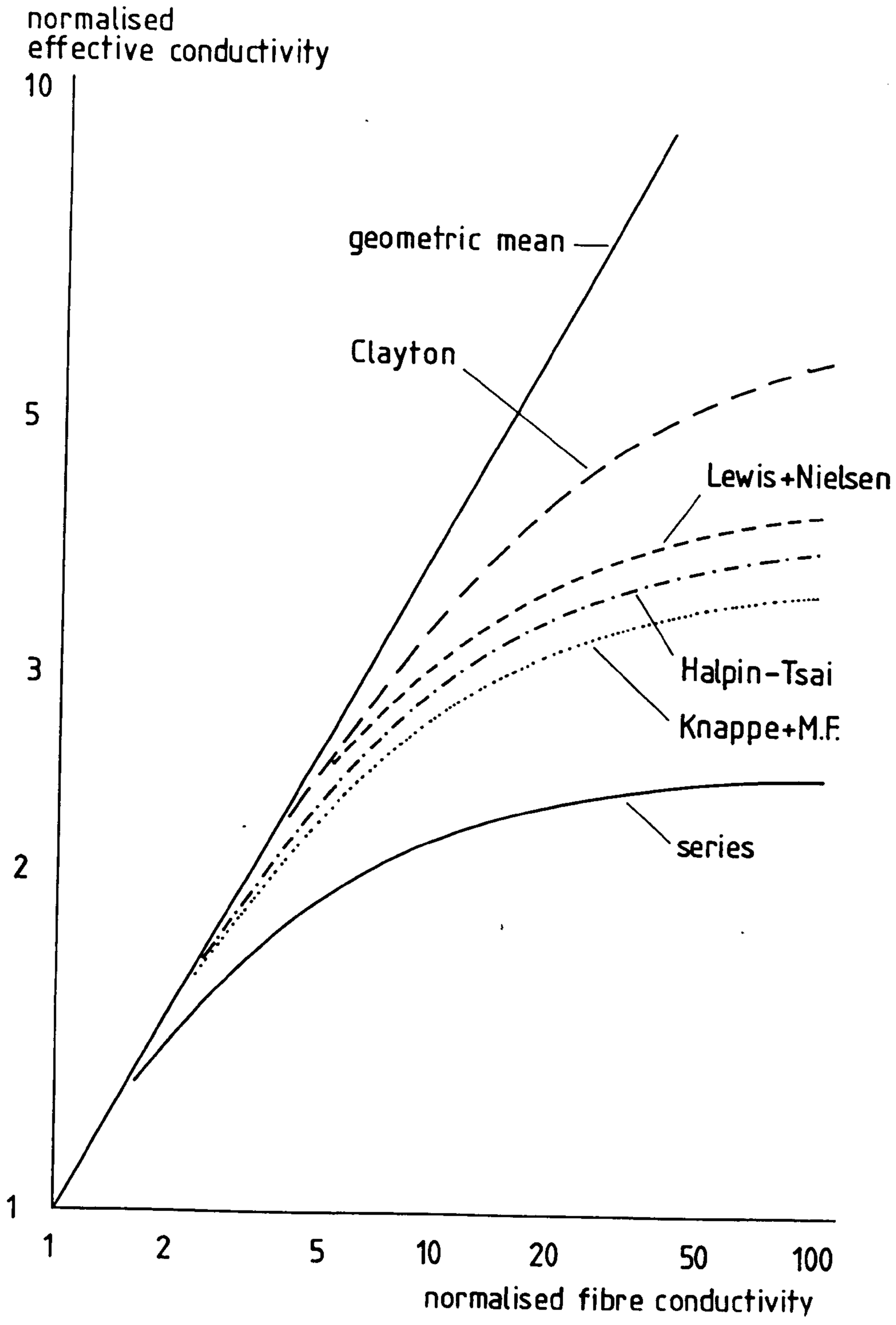

Fig. 2.8

Analytic models of effective thermal conductivity as a function of fibre conductivity (both normalised with respect to k_m). Fibre volume fraction 0.6.

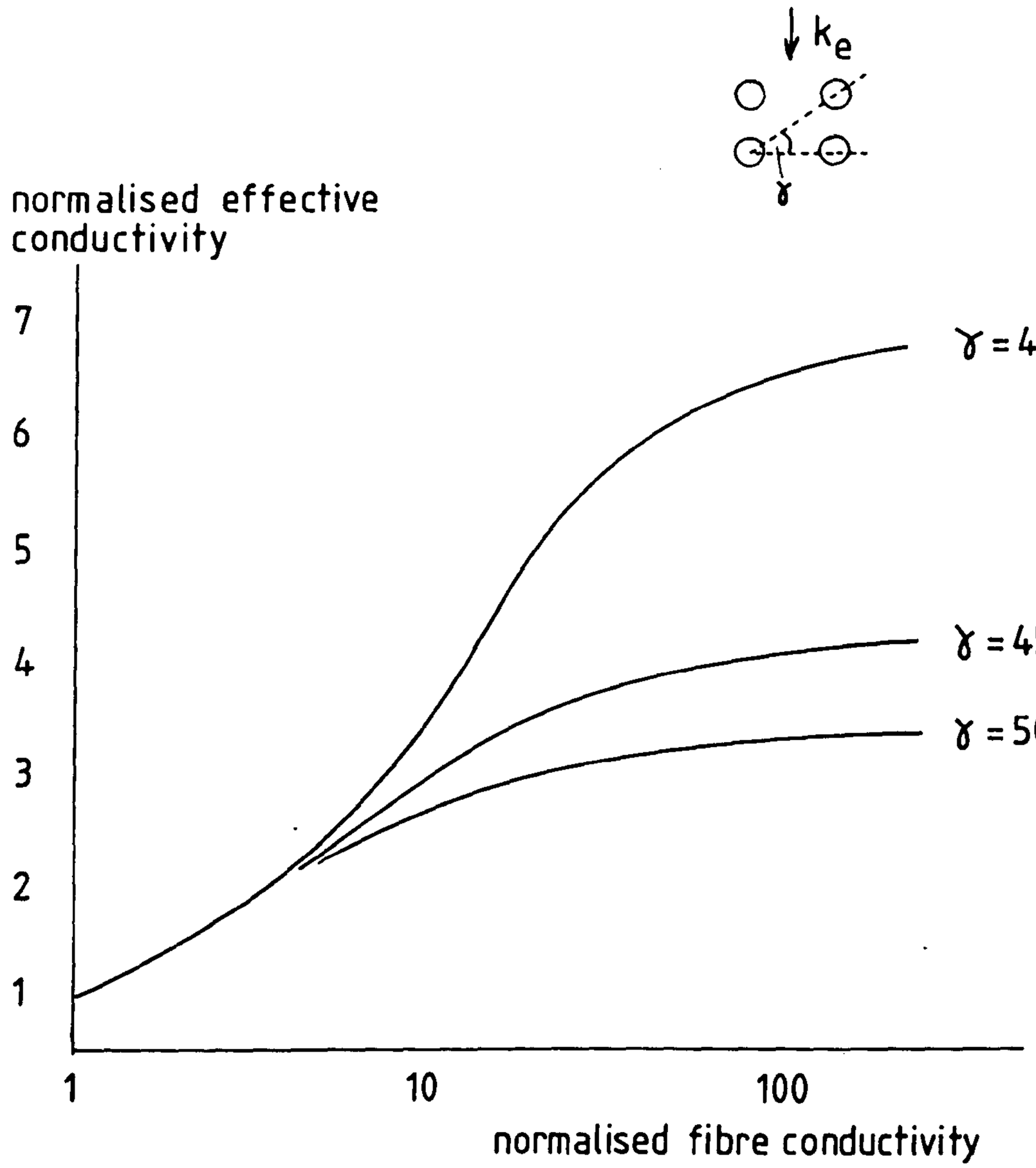

Fig. 2.9

Empirical model of effective thermal conductivity in a composite with rectangular packing. Fibre volume fraction 0.6. (Han and Cosner, 1981.)

γ. A change of only 10^{o} in this angle has the effect of doubling the asymptotic effective conductivity. It appears that empirical models may yield more realistic values for high conductivity fibre composites, but it is unlikely to be a simple matter to select the most appropriate packing geometry in a real material.

2.3 THERMAL PROPERTY MEASUREMENTS IN COMPOSITES

Composite materials considered in this review generally consist of a glass or carbon fibre-reinforcement in a polymeric matrix (abbreviated GRP or CFRP). Published work on other non-homogeneous solids, such as foamed plastics or particulate-filled metals, is beyond the scope of this review, and reference to it has only been made where experimental techniques are of special interest.

2.3.1 Glass Fibre-Reinforced Polymers

It is convenient to consider measurements on GRP as a separate category for several reasons. Firstly, glass has a longer history of use than carbon fibre as a reinforcing material, and considerably more data are available. Secondly, the thermal anisotropy of GRP is relatively small, and experimental values span a much smaller range.

Touloukian and Ho (1977) reviewed 93 sets of experimental data giving the thermal conductivity of glass fibre or fabric-reinforced epoxy resin. The data include a large number of different reinforcement types (mainly E-glass or S-glass) and volume fractions, but above about 300K most reported values of thermal conductivity lie between 0.3 and 1.0 W/m K. Commonly, the reinforcements were in the form of cloth laminates or woven rovings rather than unidirectional fibres, but in all cases the ratio of thermal conductivity parallel and perpendicular to the reinforcement was less than 1.5.

Many of these data were obtained by Thornburg and Pears who, in 1965, reported thermal conductivity measurements on a range of filled plastics, containing quartz fibre and carbon, graphite and quartz fabric. In order to account for heat

flow at right angles to the laminae, they extended the simple electrical analogue model to allow for the different orientations of the fabric layers, having estimated volume fractions for the various continuous and discontinuous phases. Their theoretical predictions agreed with experimental data to within 10%, but they stress that the models would need to be modified for reinforcements of high conductivity. They also noted the influence of voids at high reinforcement volume fractions, and point out that in certain circumstances the conductivity of the composite could decrease as the addition of more filler resulted in a higher proportion of voids.

Ratcliffe (1965) described a steady-state apparatus used at the National Physical Laboratory, with an electrically-heated hot plate and two water-cooled heat sinks. Measurements were made on a number of matrix materials (melamine, epoxy, phenolic, silicone and polyester) with reinforcements of paper, cotton and asbestos, as well as glass fabric and mat. For the last of these, thermal conductivities at room temperature were between 0.27 and 0.44 W/m K, depending on density and matrix material.

Knappe and Martinez-Freire (1965) used a "stationary twin-panel method without protective ring" (presumably corresponding to an unguarded hot plate apparatus) to measure thermal conductivities in glass fabric-reinforced epoxy composites. Their model of transverse conduction is briefly described in 2.2.

Kim (1972) measured the thermophysical properties of E-glass and boron-reinforced epoxy and polyamide resins, using a commercial guarded hot plate instrument for thermal conductivity. Variations considered in the specimens were fabric type and resin content by weight, and measurements were made from room temperature up to about 135°C. Experimental data were compared with several theoretical predictions, and the model of Thornburg and Pears (1965) gave results closest to the observations. Ziebland (1977) noted two anomalies in Kim's reported values of the temperature coefficient of thermal conductivity; these were consistent with the

increasing effect of transmission through the specimen by radiation at higher temperatures. Ziebland also considered the data of Knappe and Martinez-Freire (1965), and found the geometric mean model to be a better predictor of transverse thermal conductivity than the authors' own model (see 2.2).

Kozhevnikov and Kudryacheva (1974) reported the thermal conductivities parallel and perpendicular to the laminae in four different GRPs, from 90-470 K. They used a transient method with a linear heat source, but the experimental description is sparse. As the density of GRP reduced, so the anisotropy was observed to increase, as a result of increasing porosity in the resin.

Maries (1976) compared experimental measurements on five GRPs with some common models of composite thermal conductivity. He used a double-sided hot plate apparatus, operating at mean temperatures of 20°C and 55°C, and estimated the experimental error to be ±3%. The most successful of the models considered was that of Knappe and Martinez-Freire (1965), and the author expressed confidence that conductivities may be predicted with sufficient accuracy given the data normally available from manufacturers of the composite constituents.

Ott (1981) reported the thermal conductivity of various reinforced polymers from -180 to 140°C, and included much of the data originally published by Knappe and others (1978). Twenty different fibre-filled materials were used in a quasi-stationary "two-plate" apparatus comprising a sandwich of heater/temperature probe/sample/copper heat store with guard ring/sample/probe/heater. The complete assembly was placed in an adiabatic enclosure and was subject to continuous heating. The calibration method allowed for elimination of contact resistances and the effect of the specific heat of the samples. The thermal conductivity of several glass types were also measured. The author found good agreement between his results and the theoretical models of Cheng and Vachon (1969) and Russell (1935).

A summary of the available data is difficult, due to the

considerable range of reinforcements, volume fractions and experimental reliability. Fig. 2.10 is an attempt to present representative values of thermal conductivity taken from the publications reported above. The smooth curve gives the typical values for a 35% E-Glass fabric/epoxy resin composite, measured perpendicular to the fabric, as deduced from the data reviewed by Touloukian and Ho (1977). A key to Fig. 2.10 is given in Table 2.1. There is good agreement in the literature concerning the thermal conductivity of pure epoxy resin; all reported values are between 0.20 and 0.24 W/m K, and the variation with temperature between 200 and 450 K is negligible.

2.3.2 Carbon Fibre-Reinforced Polymers

Kalnin and others (1972) sought to produce a high modulus carbon fibre with a low thermal conductivity, by experimenting with various temperature treatments and surface coatings. As a preliminary, they calculated the thermal conductivity of a number of existing carbon fibres from measurements on reinforced epoxy resin specimens. A commercial steady-state apparatus was used, but found to be too inaccurate at low conductivities. In consequence, they developed a dry fibre 'thermoconductometer', the operation of which was based on the heating effect of an electric current passing through a bundle of fibres. The experimental difficulties associated with lateral heat losses from fibres with a high surface area-to-volume ratio and with poor contact between specimen and thermometer were considerable, but reasonable agreement was eventually achieved with the composite measurements.

Direct measurement of the thermal conductivity of carbon fibres was performed by Volga and others (1973) who reported experiments on a roving of more than 1000 carbon monofilaments over the temperature range 80 to 320 K, although little information is given concerning their technique. Conductivity was found to increase monotonically over this temperature range, and the values were also highly dependent on the graphitisation temperature at which the fibres were obtained from the PAN precursor. These characteristics are broadly consistent with the theory of graphite as a lattice conductor, as discussed in Chapter 1.

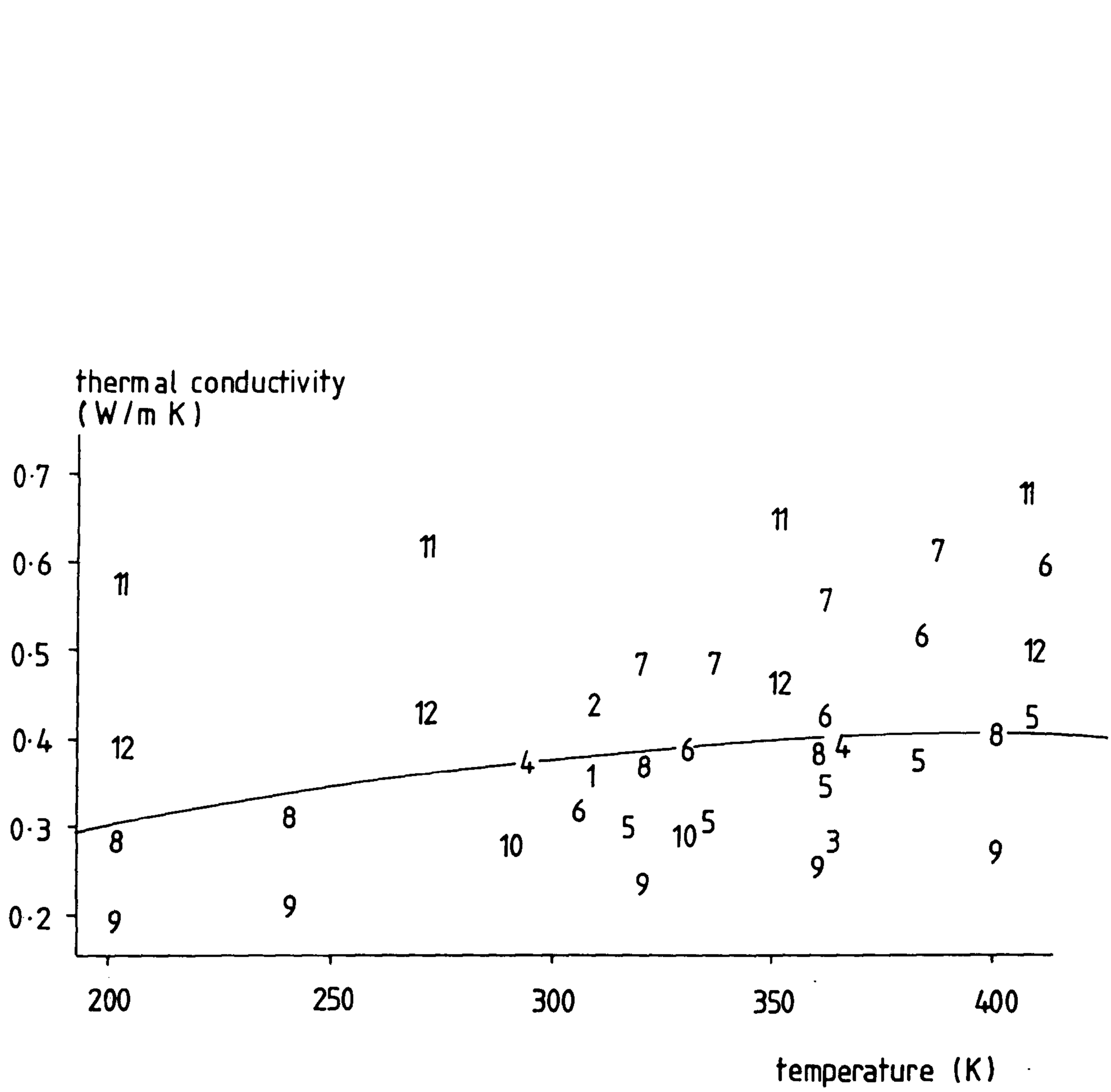

Fig. 2.10

Reported values of thermal conductivity in glass fibre-reinforced plastics. Sources of data given in Table 2.1.

Table 2.1

Source of grp thermal conductivity data in Fig. 2.10

Symbol	Reference			Fibre Volume Fraction
1	Ratcliffe (1965)			(ρ = 1.7)
2	"			(ρ = 1.85)
3	Knappe & Martinez-Freire (1965)			.21
4	"			.43
5	Kim (1972)			.20
6	"			.38
7	"			.48
8	Kozhevinikov & Kudryacheva (1974)		∥	(ρ = 1.48)
9	"		⊥	"
10	Maries (1976)			.31
11	Ott (1981)	u.d. rovings	∥	.59
12	"	"	⊥	"
smooth curve	Touloukian & Ho (1977)			.35

Unless otherwise stated, measurements were made perpendicular to the laminae of woven glass fabric or mat/epoxy resin composite.

Graphite and carbon fabrics were among the various reinforcements considered by Thornburg and Pears (1965), who measured thermal conductivities parallel and perpendicular to the reinforcement in phenolic resin composites, using a comparative bar apparatus. They quote manufacturers' data for the graphite and carbon fabrics as being 144 and 5.8 W/m K respectively, although it is not clear how the conductivity of a fabric is defined.

Clayton and others (1968) were concerned with the thermophysical properties of carbon-reinforced phenolic resin used as ablative char in rocket nozzle throats. In addition, they used a steady-state comparative disc technique to measure the thermal conductivity of the 'virgin' materials over a large temperature range. Specimens were prepared from satin-weave carbon fabric and square-weave graphite cloth impregnated with carbon-filled (~10%) phenolic resin. Measurements were made at various angles to the plane of the lamination.

Knibbs and others (1971) measured longitudinal and transverse thermal conductivities in a number of Type I (high modulus) and Type II (high strength) carbon/epoxy resin composites, in which the reinforcement was in the form of long, unidirectional fibres. Longitudinal measurements were carried out on 10 cm long samples by a comparative method; for the transverse measurement, the specimens were thin discs, with heat flow measured by calorimetry. Accuracies of ±5% and ±20% were quoted for the two methods. Values for the longitudinal conductivities of the fibres were deduced by extrapolating the values at different volume fractions, according to Equation 2.8. They are 102 W/m K (Type I) and 22 W/m K (Type II).

Lee and Taylor (1975) used a transient method known as the flash or pulse technique, in which a sudden heat flux is applied to one face of a specimen by laser irradiation. They measured the thermal diffusivity of graphite and carbon fibres, both as fibre bundles and as unidirectional reinforcement in epoxy resin, and also measured thermal conductivity by an absolute steady-state method. In the transient method,

it was found possible to determine directly the diffusivity of the fibre from measurements on the composite if the temperature sensor was positioned at the termination of a fibre bundle. Their techniques were verified on reference composite specimens of copper wire embedded in epoxy resin.

Further diffusivity measurements using similar apparatus were made by Taylor and Procter (1981) on various carbon fibre/carbon matrix composites. Two of these materials had a three-dimensional reinforcement structure, with fibres parallel to the x, y and z cartesian axes, while a third contained fibre in an 8-harness satin weave. Samples were also available containing unidirectional fibre reinforcement. They analysed their experimental data in the light of Springer and Tsai's (1967) one-dimensional composite model, and extended Knappe and Martinez-Freire's (1965) geometric model into three dimensions; this enabled them to derive values for fibre conductivity in general agreement with other published data. More detail of the experimental procedure was given by Deshpande and others (1981).

Assem and Daniels (1977) set out to measure the thermal conductivity in a laminated sheet material comprising three layers of long, unidirectional carbon fibre-reinforced epoxy resin. The fibres in each layer were positioned at an angle of 60^{o} relative to the adjacent layer during fabrication, resulting in a material which was pseudo-isotropic in the plane of the reinforcement (designated the x-y plane). Thermal conductivity normal to this plane was an order of magnitude lower, so that two distinct designs of apparatus were required. These experiments highlighted the dominating influence of the thermal resistance of the contact layer between specimen and heat sink. The final measurements quoted were $k_z = 0.61 \pm 0.18$ W/m K and $k_{xy} = 6.4 \pm 1.0$ W/m K.

The review by Ziebland (1977) included measurements of the thermal conductivity of discontinuous carbon fibre composites (both high modulus and high strength) between $20^{o}C$ and $120^{o}C$, with samples manufactured from uniaxially aligned mat and felt. Longitudinal values were only about 25% lower than previously-reported measurements on continuous fibre

composites. Results were shown to be in reasonable agreement with the geometric mean model of transverse conductivity. It is interesting, however, that the transverse conductivities are higher for the discontinuous fibre composites of a given volume fraction than for comparable specimens with continuous fibres. This is explained by the fact that discontinuous fibres are more likely to deviate from the ideal uniaxial alignment.

Pilling and others (1979) used a steady-state apparatus (described in detail by German, 1976) which could be adapted for high conductivity bar specimens or low conductivity disc specimens. They measured thermal conductivity between 80 and 270 K on a series of unidirectional and bidirectional carbon fibre/epoxy resin composites. Their results demonstrate the considerable temperature dependence of thermal conductivity of both high modulus and high strength fibres. Values of transverse conductivity of high strength fibres were deduced using several of the available theoretical models. They eventually used an elastic analogue equation in the form

$$\frac{k_f}{k_m} = \frac{k_m\,(1-\phi) - k_e\,(1+\phi)}{k_e\,(1-\phi) - k_m\,(1+\phi)} \qquad (2.19)$$

which is equivalent to the Halpin-Tsai/Rayleigh model (Equation 2.11) and gives k_f = 6.0 W/m K at 270 K.

Han and Boyes (1983) described a combined transient and steady-state apparatus, in which two identical specimens were heated electrically up to a steady temperature. Analysis of the initial rate of temperature increase gave a thermal diffusivity, while the steady-state measurement defined the conductivity. They made measurements parallel and perpendicular to the reinforcement in a unidirectional carbon fibre/epoxy composite.

Several workers have used a thermal probe technique (described by Muller, 1967) to measure the anisotropy ratio in stretched polyethylenes (Kilian & Pietralla, 1978) and reinforced polymers (Voronkov & others,1980). A point heat source

is applied to a plane surface of the material, and observation of the subsequent temperature distribution indicates the directional nature of the thermal conductivity in that plane. In an isotropic material, the isotherms in the vicinity of the probe are circles, but when anisotropy is present, they appear as ellipses, with the square of the ratio of the principal axes equal to the anisotropy ratio. Berrie and others (1981) used a soldering iron with a 1 mm diameter tip for the probe, and observed isotherms with an infra-red imaging system. They report data for a carbon fibre composite of unspecified composition.

Almost all the 22 sets of data reviewed by Touloukian and Ho (1977) were taken from the work of Knibbs and others (1971). In addition, measurements by Gille (1969) and Hertz and others (1972) contribute to the authors' "provisional" representative data for a 50% volume fraction graphite fibre/epoxy composite. These data (for conductivity parallel and perpendicular to the reinforcement), appear in Fig. 2.11 as continuous lines. Some of the other data reviewed above are plotted, with Table 2.2 providing a key.

Although the data on carbon fibre composites extend over two orders of magnitude (and include almost no values above room temperature) it is possible to identify typical regions on the graph, and the following characteristic values of thermal conductivity near room temperature in a 50% volume fraction carbon fibre/epoxy resin may be suggested:

(i) high modulus fibres, parallel to reinforcement:
30 - 60 W/m K

(ii) high modulus fibres, perpendicular to reinforcement:
1 - 1.5 W/m K

(iii) high strength fibres, parallel to reinforcement:
5 - 11 W/m K

(iv) high strength fibres, perpendicular to reinforcement:
0.6 - 1 W/m K

Fig. 2.12 shows the available data on the thermal conductivity of carbon fibres themselves. As indicated in Table 2.3,

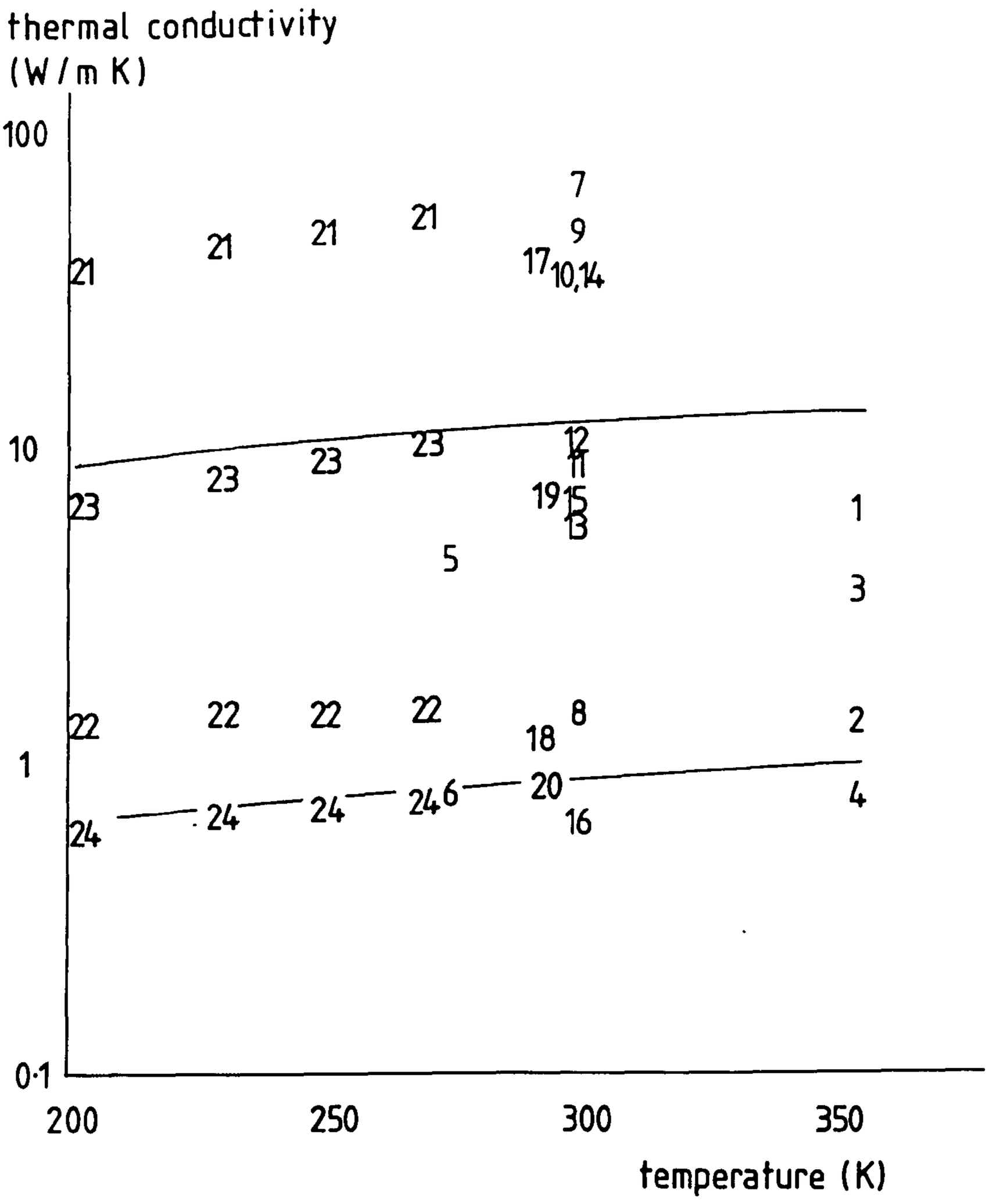

Fig. 2.11

Reported values of thermal conductivity in carbon fibre-reinforced plastics. Sources of data given in Table 2.2.

Table 2.2

Source of cfrp thermal conductivity data in Fig. 2.11

Symbol	Reference	Material		Fibre Volume Fraction
1	Thornburg & Pears (1965)	WCA graphite fabric/ phenolic resin	∥	.67
2	"		⊥	
3	"		∥	.47
4	"		⊥	
5	Clayton & others (1968)	Square weave graphite cloth/phenolic resin	∥	(ρ = 1.5)
6	"		⊥	
7	Knibbs & others (1971)	Morganite Type I u.d./ epoxy	∥	.60
8	"		⊥	
9	Kalnin & others (1972)	Courtaulds HMS/epoxy	∥	.49
10	"	Thornel 50	∥	.64
11	"	Courtaulds HTS	∥	.57
12	"	Morganite II	∥	.50
13	Lee & Taylor (1975)	Morganite II/epoxy		.38
14	"	Thornel 50-S		.54
15	Assem & Daniels (1977)	Laminated sheet	∥	
16	"	(see text)	⊥	
17	Ziebland (1977)	HMS fibres discontinuous	∥	.50
18	"		⊥	
19	"	HTS	∥	
20	"		⊥	
21	Pilling & others (1979)	HMS u.d./epoxy	∥	.61
22	"		⊥	.58
23	"	HTS	∥	.58
24	"		⊥	.59
25	Han & Boyes (1983)	Hercules AS-1/epoxy	∥	.60
26	"		⊥	

(The data of Taylor and Proctor (1981) have not been included, since they used a high conductivity carbon matrix.)

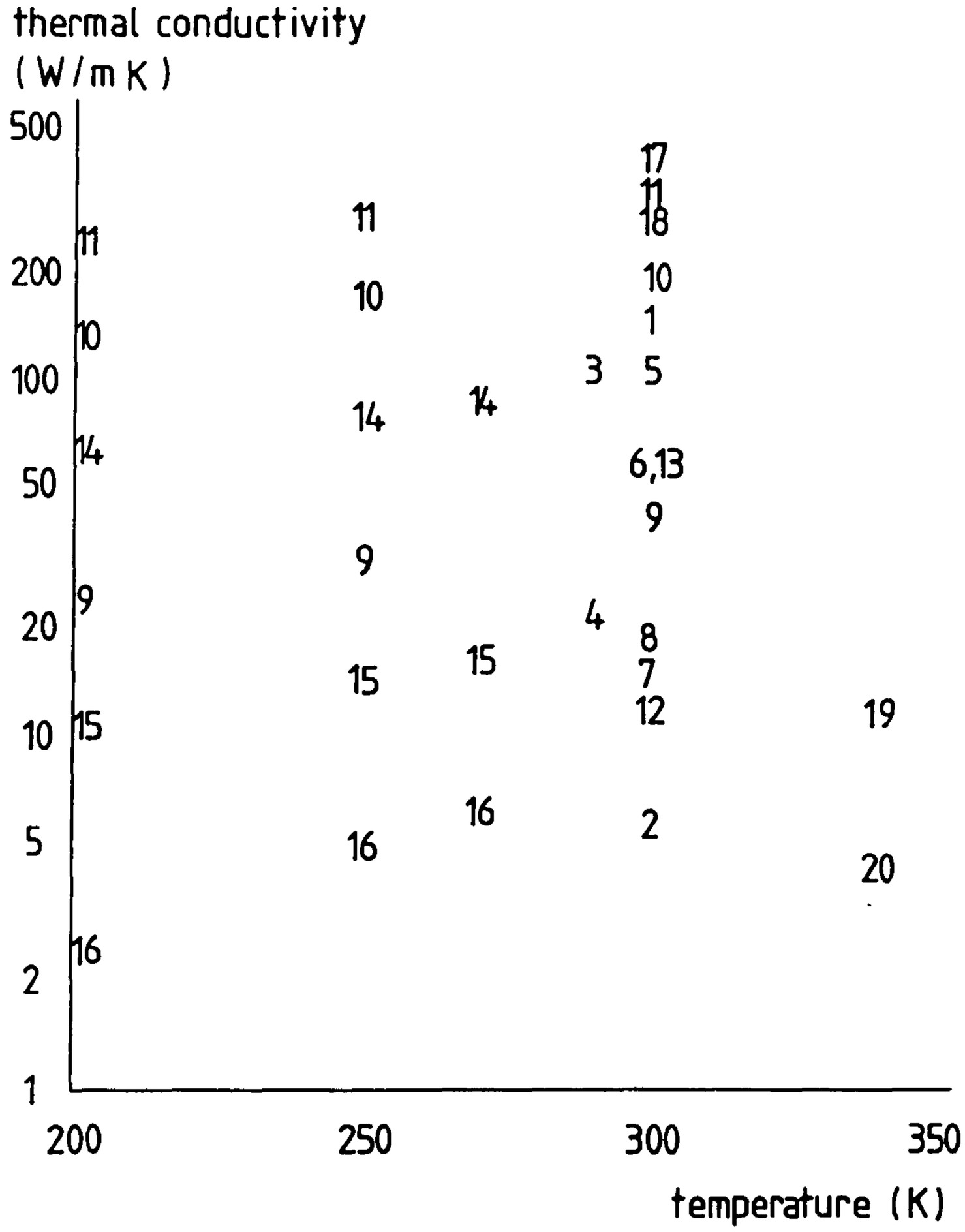

Fig. 2.12

Reported values of thermal conductivity of carbon fibres.
Sources of data given in Table 2.3.

Table 2.3

Sources of carbon fibre thermal conductivity data in Fig. 2.12

Symbol	Reference	Material	Density
1	Thornburg & Pears (1965)	WCA Graphite	1.5
2	"	Carbon (unspecified)	1.5
3	Knibbs & others (1971)	Morganite Type I	
4		Morganite Type II	
*5	Kalnin & others (1972)	Courtaulds HMS	1.88
*6	"	Union Carbide Thornel 50	1.63
*7	"	Courtaulds HTS	1.68
*8	"	Morganite II	1.82
	Volga & others (1973)	Carbon fibre (PAN precursor)	
*9	"	graphitisation temp. 1400 °C	
*10	"	2600 °C	
*11	"	2800 °C	
*12	Lee & Taylor (1975)	Morganite II	1.82
*13	"	Thornel 50-S	1.66
14	Pilling & others (1979)	Morganite HMS (graphitisation temp. 2600 °C)	
15	"	HTS (graphitisation temp. 1500 °C)	
16	"	HTS (transverse)	
17	Taylor & Proctor (1981)	Fibre 'F'	1.92
18	"	High modulus	1.66
19	Han & Boyes (1983)	Hercules AS-1	1.83
20	"		

The symbol '*' indicates a direct measurement of conductivity. Except where indicated, values refer to the longitudinal direction.

these include direct measurement, and calculation from values obtained on composites. It has already been pointed out that as a result of their oriented structure, carbon fibres are themselves thermally anisotropic. Calculation of the transverse thermal conductivity is particularly prone to error for two reasons: firstly, there is uncertainty as to which of the available theoretical models is most appropriate (especially in the case where the conductivity of the reinforcement is much greater than that of the matrix), and secondly, the calculation is based on a measurement of composite conductivity which may be in error by as much as ± 20% (Knibbs and others, 1971).

Again, generalisation is difficult. There is clearly a correlation between thermal conductivity and graphitisation temperature, but it is not possible to quantify the relationship.

2.3.3 Other Composite Materials

Although not within the scope of this thesis, work on other composite materials has some relevance to the understanding of thermal anisotropy, and to the prediction and measurement of heat transfer in heterogeneous materials. Attention has been concentrated on fibrous reinforcements, although there is a large body of literature concerned with porous and particle-filled materials.

Griffin (1974) was concerned with methods of improving the thermal conductivity of thermoplastics to enable their use as a material for injection-moulded bearings. He used metal particles as an additive, and further improved their heat transfer capabilities by aligning them in a magnetic field during the moulding process. The need for a large number of thermal conductivity measurements led to the use of a transient 'hot finger' technique, which used the change in temperature of an electric point heat source when brought into contact with the specimen. At a volume fraction of about 15%, the author was able to increase the thermal conductivity of low density polyethylene by a factor of 4.

Tanaeva and others (1980) summarised measurements on several reinforced epoxy resin composites, including a glass/carbon hybrid, over a large temperature range (4.2 - 400 K). Little experimental detail was given, beyond the fact that a transient technique with an internal heat source was used.

Gogol and Furmanski (1980) compared theoretical values of transverse thermal conductivity in a unidirectional fibre-reinforced composite with a large-scale model and with a copper fibre/epoxy resin composite, finding good agreement between measurement and calculation.

Brennan and others (1982) used measurements on silicon carbide-reinforced glass-ceramic composites to calculate the thermal conductivity and diffusivity of the fibres themselves. Perpendicular to the unidirectional reinforcement, the authors used Bruggeman's (1935) formula to deduce the transverse fibre thermal conductivity.

Composites of Kevlar 49 fibre have been examined by Harris and others (1982). They adapted the apparatus used by Pilling and others (1979), with specimens in the form of a thin disc. Data were used to predict a longitudinal thermal conductivity of the fibre.

2.4 CONCLUSIONS

A considerable diversity of materials is included in the category 'fibre-reinforced composites', and there is no general agreement as to typical or representative thermal properties. In terms of thermal conductivity models, there is an important distinction to be made between low and high conductivity reinforcements - most authors found that the effective thermal conductivity of GRP was adequately predicted by one or more of the simpler models, but several difficulties arise in applying them to high conductivity carbon fibre-reinforcements. Firstly, most models predict an asymptotic value of k_e with increasing k_f which is less than experimental data; secondly, carbon fibres are thermally anisotropic, and there are no direct measurements of transverse properties. Empirical models may correspond

more closely with experiment, but here the overriding difficulty is the characterisation of the packing geometry. Analysis is further complicated by the considerable dependence of the thermal conductivity of carbon fibres on their graphitisation temperature. As with other properties of composite materials, manufacturing technique and specimen quality are important factors, and it appears that applications or investigations which require an accurate knowledge of thermal conductivity must include property measurements on the material in question.

CHAPTER 3 : MEASUREMENTS OF THE THERMAL CONDUCTIVITY OF CARBON FIBRE-REINFORCED EPOXY RESIN

This chapter describes laboratory measurements on samples of high modulus carbon fibre/epoxy resin composite materials, with the objective of obtaining values of thermal conductivity around room temperature. These data are required for the experimental validation of the finite element model, to be discussed in Chapter 7. Two pieces of apparatus were used; one for absolute measurements parallel to the heat flux in a 'long rod' specimen, and a commercial instrument for comparative measurements in 'thin slab' specimens.

3.1 MEASUREMENTS PARALLEL TO HEAT FLUX

3.1.1 Design of Apparatus

The general principles of the absolute measurement of thermal conductivity in moderate conductors of heat are outlined in 2.1.1, and embodied in the design illustrated in Fig. 3.1.

The specimen (25 mm x 25 mm square cross-section and approximately 250 mm long) was secured at one end in a copper heat sink, around which were soldered three turns of 5 mm copper pipe through which cooling water was to be circulated. The recess in the heat sink was milled out approximately 5 mm oversize, and the specimen was held in place by introducing a low melting point fusible alloy {1}* in molten form into the gap. The same technique was used for fixing the copper heater block onto the other end of the specimen.

An estimate of the necessary heating power was made by requiring a temperature gradient down the specimen of at least 1 K/cm. In a material with a thermal conductivity of 50 W/m K, this would be achieved by a heat flux of 5000 W/m^2, which is equivalent to a power of about 3 W into a sample of 25 mm square cross-section. Suitable resistance wire was wound around the outside of the specimen heater into a continuous groove milled in the surface (see Fig. 3.2).

---

* The figures in brackets refer to Table 3.1, which gives the specifications and suppliers of components and materials.

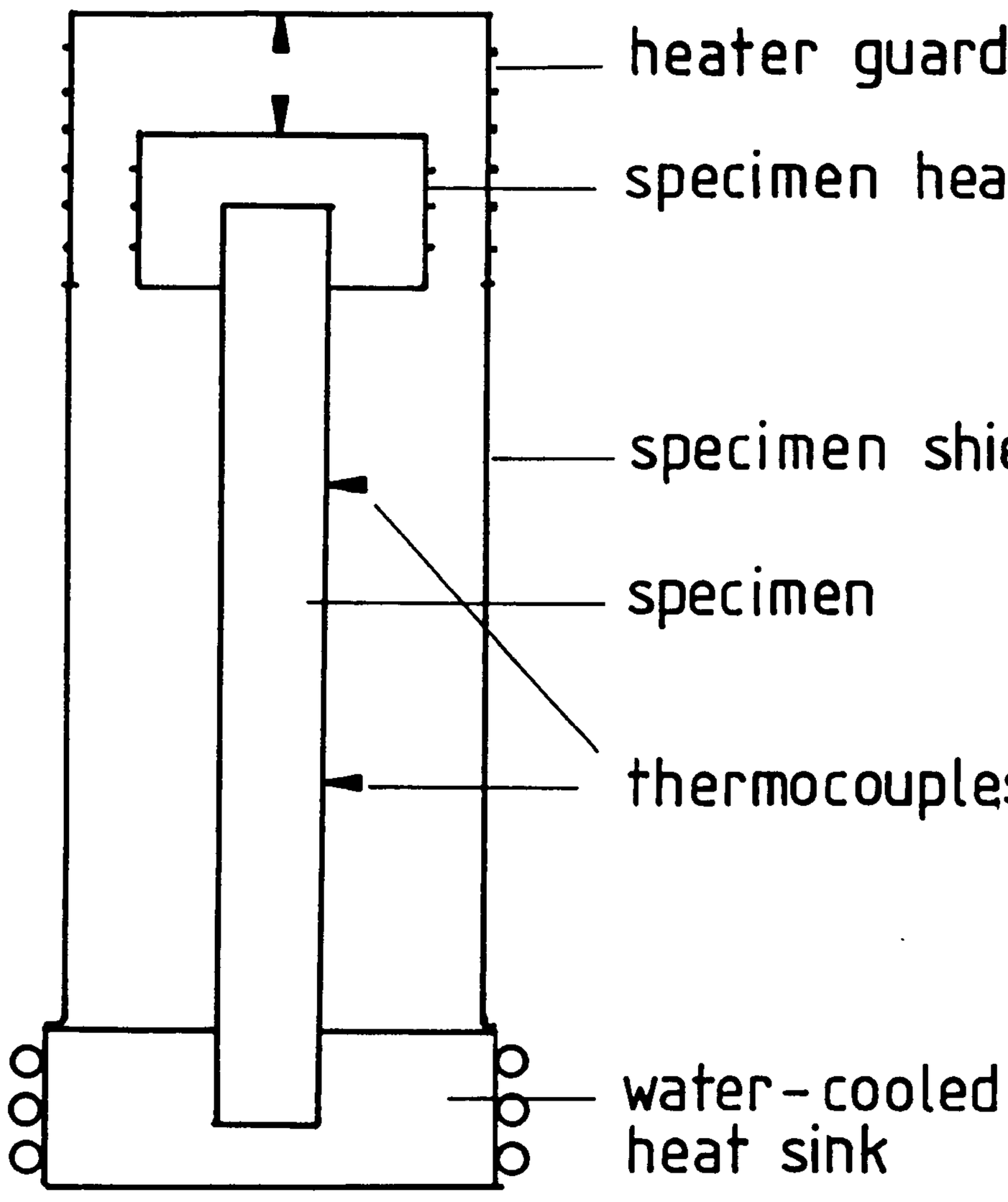

Fig. 3.1

Schematic diagram of steady-state thermal conductivity apparatus.

Table 3.1

Materials and components used in thermal conductivity measurements

Ref.	Item	Supplier
1	Fusible alloy MCP 96	Mining & Chemical Products Ltd.
2	Constantan wire, Isonel varnish	Labfacility Ltd.
3	Expanded PS beads	Metal Closures Poron Ltd.
4	Type W/T thermocouples	Labfacility Ltd.
5	Thermometer 1179, -5/105 °C, graduation 0.1	H. Stout & Co. Ltd.
6	PCI 1002 thermocouple converter	CIL Microsystems Ltd.
7	Digital Multimeter DM 131	Farnell Electronic Components Ltd.
8	Metal chemical analysis	BSC Sheffield Laboratories
9	Grafil EHM-S/DX 210 BF 400 prepreg.	Fothergill Rotorway Composites Ltd.
10	Comparative Thermal Conductivity Instrument TCFCM	Dynatech R/D Co., USA
11	Exposed junction, butt-welded thermocouples	Labfacility Ltd.

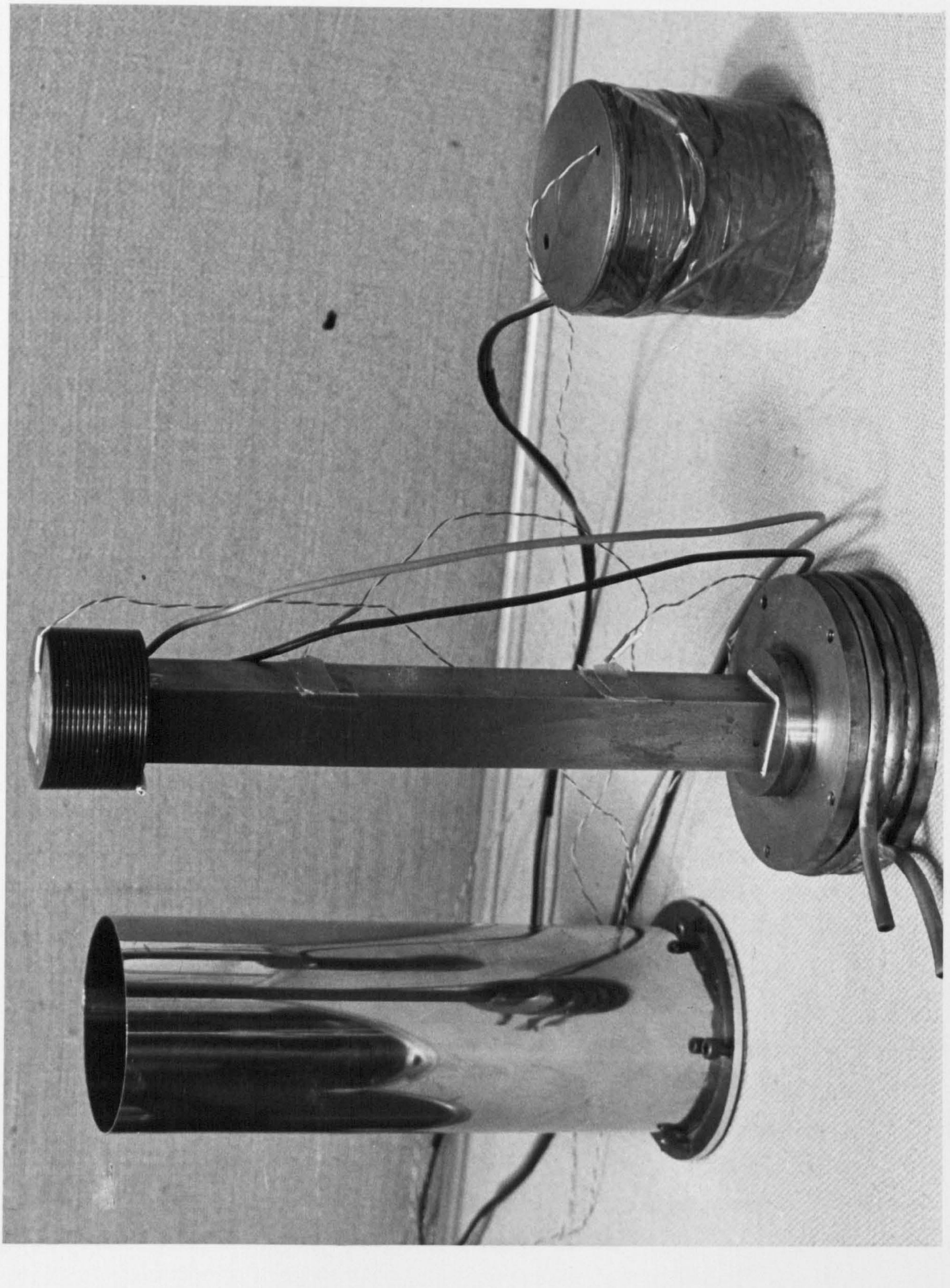

Fig. 3.2

Components of thermal conductivity apparatus.

Constantan wire {2} of diameter 0.005 inch was used, a length of 2.5 m giving a nominal resistance of 100Ω. The surface of the heater was coated with electrical insulating varnish before attaching the resistance wire, the ends of which were held in place with small quantities of epoxy resin adhesive.

The sample guard was constructed from 0.6 mm stainless steel sheet, formed into a cylinder 250 mm long and 80 mm in diameter. One end was flanged, so that it could be screwed securely onto the heat sink (see Fig. 3.2). The heater guard comprised a copper cylinder and cap, sized to fit inside the sample guard cylinder, and attached by 12 self-tapping screws.

The heater guard was intended to be maintained at the same temperature as the heater itself, and so was provided with resistance wire wound onto the outer surface, after coating with insulating varnish. The power input to the guard was first estimated by assuming no heat loss to the surroundings and that the temperature gradient down the shield was the same as in the sample (1 K/cm) - this amounted to about 5 W. The heater guard also dissipates energy to the surroundings, so it was required to produce at least twice this power. A nominal resistance of 15Ω was obtained, using 0.508 mm constantan wire.

The heater guard contained holes in the top surface to allow the passage of heater and thermocouple wires, as well as the introduction of loose-fill insulation {3} to the space between specimen and guard cylinder. These wires are attached both physically and thermally to the guard to avoid possible heat leakage from the specimen.

During operation, the temperature of the guard was matched to that of the sample heater. This was achieved by manual adjustment of the guard voltage until the signal from a differential thermocouple pair, with sensors attached to the top of the heater and the inner surface of the guard, was zero. It was found that only occasional adjustment was required during the course of an experimental measurement.

This arrangement eliminated the requirement for costly control equipment, and yet maintained the temperature difference within ±0.2 K.

In order to minimise the disturbance to heat flow in the specimen, self-adhesive surface thermocouples {4} were used to measure temperature gradient. Fig. 3.3 shows a magnified view of the sensing junction; the thermocouple leads are attached to flattened wires which allow good thermal contact with the specimen. The main disadvantage of this type of sensor is that it responds to an average surface temperature over its finite width, rather than indicating the temperature at a point. This uncertainty is taken into account in the calculation of temperature gradient (3.1.2). Thermocouples were used in preference to alternative temperature sensors due to their small size and the ease with which temperature differences may be measured. By using easily-detachable thermocouples, their calibration could be checked before and after each experiment; this was done by immersion in a stirred water bath, the temperature of which was measured by a mercury-in-glass thermometer {5}, itself calibrated by the British Standards Institution.

The temperature monitoring system comprised a commercial analogue-to-digital thermocouple convertor {6}, linked to a Commodore CBM 3032 microcomputer. This allowed sequential scanning of up to 12 thermocouple inputs with a further 2 channels available for voltage inputs in the range ±1V. As supplied, the instrument was configured for copper-constantan (type T) thermocouples, giving 12 bit resolution in the temperature range -270 to 212°C (i.e. 0.12 K per bit). Cold junction compensation was carried out internally, by means of a platinum resistance element attached to the terminal block. The resolution of this channel was considerably better, using 4000 bits for the range 0 - 100°C (i.e. 0.025 K per bit). By replacement of thermocouple sockets and compensating leads, two channels were converted for millivolt inputs, with a resolution of about 5μV.

The analogue-to-digital converter was initially calibrated

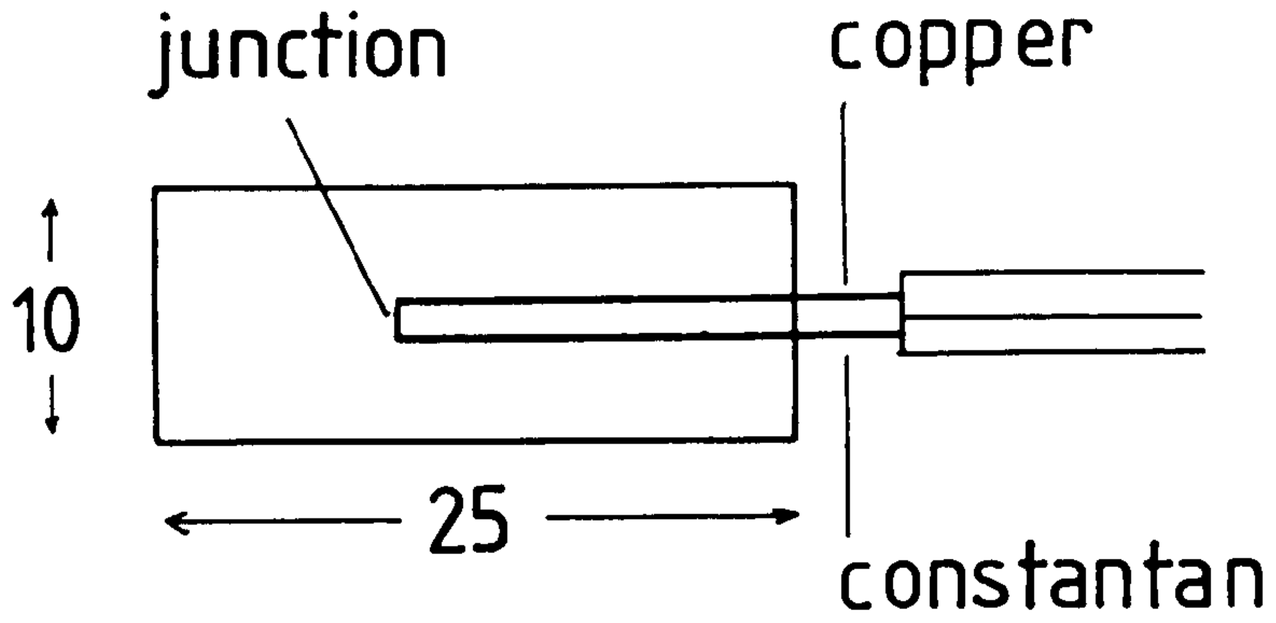

Fig. 3.3

Self-adhesive patch thermocouple. Dimensions in mm.

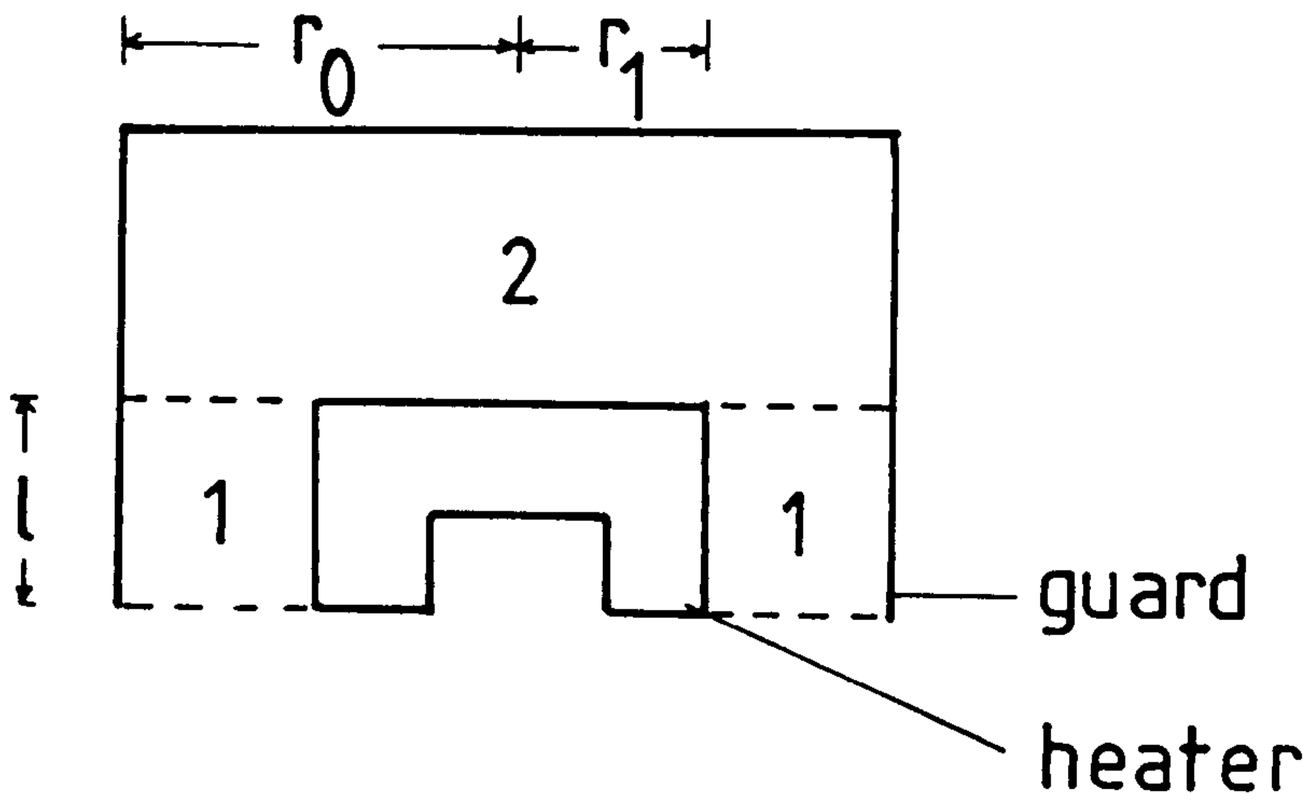

Fig. 3.4

Geometry of heater and guard in thermal conductivity apparatus. r_o = 40 mm r_1 = 25 mm ℓ = 30 mm

according to the manufacturer's instructions, setting each temperature channel with a thermocouple immersed in melting ice. Problems of long-term drift and non-linearity were reduced by ensuring that thermocouples were used in the same input channels in which they had been calibrated.

Sampling rate, cold junction compensation and data manipulation and storage were all controlled by a generalised BASIC program running on the Commodore microcomputer. This program is listed in Appendix III.

3.1.2 Experimental Errors

It is convenient to separate random errors, arising from the limited accuracy or resolution of measurement devices, and systematic errors, which may be due to a design fault in the apparatus. The former type of error leads to a band of uncertainty either side of the measured value of thermal conductivity, while the latter may result in a consistent bias.

In the 'long bar' configuration, the measured thermal conductivity is given by

$$k_M = \frac{q}{\partial T/\partial x} \qquad (3.1)$$

where both the heat flux and the temperature gradient are measured in the x-direction. The heat flux is given by

$$q = Q/A$$

where A is the cross-sectional area of the specimen and Q is the total rate of energy dissipation by the heater (all of which passes through the specimen). The temperature gradient may be written

$$\frac{\partial T}{\partial x} = \frac{\Delta T}{\ell}$$

where ℓ is the longitudinal distance over which the temperature difference ΔT is measured. Assigning appropriate uncertainties to each of the measured values, the resulting

fractional error in the measured thermal conductivity is

$$\frac{\delta k_M}{k_M} = \frac{\delta q}{q} + \frac{\delta \ell}{\ell} + \frac{\delta A}{A} + \frac{\delta(\Delta T)}{\Delta T} \qquad (3.2)$$

(i) The power input to the specimen heater is given by the product of voltage across and current through the resistance wire. Both quantities were measured by digital multimeters {7} with maximum errors of about 0.2% and 1.3% respectively. The combined error in the power measurement was therefore no greater than 1.5%.

(ii) The cross-sectional area of the specimens was determined from micrometer measurements, and averaged over the length of the sample. Micrometer readings involved an error of less than 0.1%, but as discussed in 3.1.4, the specimens were not precisely uniform in cross-section, the area varying by up to ±1% over a length of 250 mm.

(iii) In addition to the resolution of the thermocouple converter, further errors in a measurement of temperature arise from the calibration procedure (3.1.3). These are a combination of the scatter observed in a calibration run and the accuracy with which the reference temperature was measured. The total error in the measurement of (absolute) temperature was estimated to be ±0.3 K, while a direct measure of temperature difference involved an error of ±0.4 K.

(iv) Measurement of thermocouple separation (ℓ) was subject to a relatively large error, due to the size of the sensor junction (see Fig. 3.3). The maximum uncertainty in ℓ was taken as ±2 mm, or about ±2% of a typical separation of 100 mm.

The resultant random error in the measured thermal conductivity is thus dependent on the magnitude of the temperature gradient; for values of 10 K in 100 mm, the total error is about ±8%.

Systematic errors may result from various unanticipated heat flows within the apparatus; the possible effect of these will

now be quantified.

Temperature imbalance between specimen heater and guard will result in an error in the calculated heat flux down the specimen, either due to an additional heat flow outwards or a parasitic flow inwards from the guard. The magnitude of this effect may be estimated by an idealised geometry (Fig. 3.4), in which the space between heater and guard contains an insulating material of conductivity 0.035 W/m K. The conduction heat transfer across region (1) is estimated from the expression

$$Q_1 = k\Delta T 2\pi \ell / \ln(r_o/r_i)$$

in which r_o and r_i refer to the outer and inner radii of two concentric cylinders, length ℓ. Inserting appropriate dimensions, $Q_1 = 0.016\Delta T$ W, where ΔT is the temperature difference between heater and guard. Across region (2), heat transfer may be approximated by $Q_2 = k\Delta T\pi r^2/h$, where r is the mean value of heater and guard radii, and h is the separation. Using the dimensions shown in Fig. 3.4 gives $Q_2 = .002\Delta T$ W. The total rate of heat transfer between heater and guard is thus estimated as $0.02\Delta T$ W, assuming conduction to be the only mechanism. As discussed in 3.1.1, the value of ΔT was maintained at less than ±0.2 K; allowing for the maximum experimental error in the measurement of temperature difference, the heat transfer rate between heater and guard becomes about 0.01 W, or 0.4% of the heat flux down the specimen.

Heat losses from the specimen itself may be estimated in a similar manner, by approximating the sample and its shield to two concentric cylinders of radii 12 mm and 40 mm respectively. The average rate of heat loss over the length of the specimen is then $0.037\Delta T$, where ΔT is an average temperature difference; if, as above, temperatures are matched to about ±0.5 K, then lateral heat losses from the specimen will be less than 1% of the longitudinal heat flux.

However, it will be appreciated that the apparatus does not incorporate separate temperature control of the shield, and

although matched at the level of heater and heat sink, the temperature gradients down the specimen and its shield may be markedly different, due to different contact resistances, and the different material thermal conductivities. The possible effects of this error were investigated in two ways, as described in 3.1.3, by measurements on a reference material, and also by evacuating the space between specimen and shield.

A potential source of error is the conduction of heat down the thermocouple leads, which could affect the measured temperature gradient by providing a heat path between the guard and the specimen. The conduction rate down a wire of conductivity k, cross-section A and length ℓ is given by $Q = kA\ \Delta T/\ell$ where the maximum value of ΔT will be about 20 K. Inserting quantities appropriate to a 0.3 mm diameter copper wire gives $Q \simeq 4 \times 10^{-3}$ W (about 0.1% of the specimen heat flux).

(It is common practice when attaching surface temperature probes to ensure that connecting leads close to the junction are placed parallel to the isotherms. This avoids temperature gradients in the leads and prevents heat conduction away from the sensor. In anisotropic materials, however, this will not always be possible, since, in general, the isotherms are not perpendicular to the heat flux. Only in the case of heat flow parallel to one of the principal thermal conductivity axes can the orientation of isotherms be determined immediately.)

3.1.3 Measurements on Reference Material

Unidirectional carbon fibre-reinforced plastic at about 60% volume fraction has a thermal conductivity in the range 30-70 W/m K parallel to the reinforcement (see Fig. 2.11). A suitable reference material was considered to be a mild steel, having a thermal conductivity of about 50 W/m K. Woolman and Mottram (1964) gave the following correlation for the thermal conductivity of steel at 0°C, as a function of its chemical composition:

$$\frac{1}{k} = 5.80 + 1.6C + 4.15Si + 1.4Mn + 5.0P + 1.0Ni + 0.6Cr + 0.6Mo \qquad (3.3)$$

In Equation 3.3, the symbols have their conventional meaning, and refer to percentage composition by weight. The units of k are cal/cm s K. The correlation was derived from data obtained at the National Physical Laboratory (British Iron and Steel Research Association, 1953), and agreed with measured values to within 5%; for 14 of the 18 steels tested, the deviation was within 3%.

A sample of mild steel of appropriate dimensions was obtained, and a small quantity (approximately 25 mm cube) was sent for chemical analysis at the laboratories of the British Steel Corporation {8}. The resulting composition, together with the calculation of thermal conductivity, is given in Table 3.2. On the basis of the steels reported by the BISRA (1953), the value at 50 °C is approximately 1% lower than 0°C.

A total of 7 measurements were made on the mild steel sample, at various levels of power input. The thermocouples were calibrated before, after, and mid-way through the set of measurements. Fig. 3.5 shows typical calibration data for two sensors, in which the actual thermocouple output is compared to the reference value at the temperature in question. The two calibrations for each channel were separated by a period of about 4 weeks, and show differences in the necessary correction of as much as 3 K.
It is not clear whether these changes in thermocouple output have their origin in the sensor or in the measurement system - in any case, this problem was avoided by frequent calibration checks, and by ensuring that each thermocouple was always used with the same input channel.

The theory of the conductivity measurement demands a steady state. In practice, these conditions were assumed to prevail when the temperatures at all points on the specimen had changed by not more than 0.3 K over a period of 1 hour. Having established a satisfactory steady state, temperatures were recorded as 1 minute mean values, and subsequently

Table 3.2

Percentage composition by weight of mild steel specimen

Carbon	C	.18
Silicon	Si	.24
Manganese	Mn	.78
Phosphorus	P	.017
Sulphur		.046
Chromium	Cr	.10
Molybdenum	Mo	.04
Nickel	Ni	.17
Aluminium		.033
Arsenic		.026
Boron		<.0005
Copper		.26
Tin		.025

By Equation 3.3, $k = (8.503)^{-1}$ = 0.117606 cal/cm s K
= 49.2 W/m K (at 0^{o}C)

Estimated value at 50^{o}C : 48.7 W/m K
Maximum error : ±2.4 W/m K

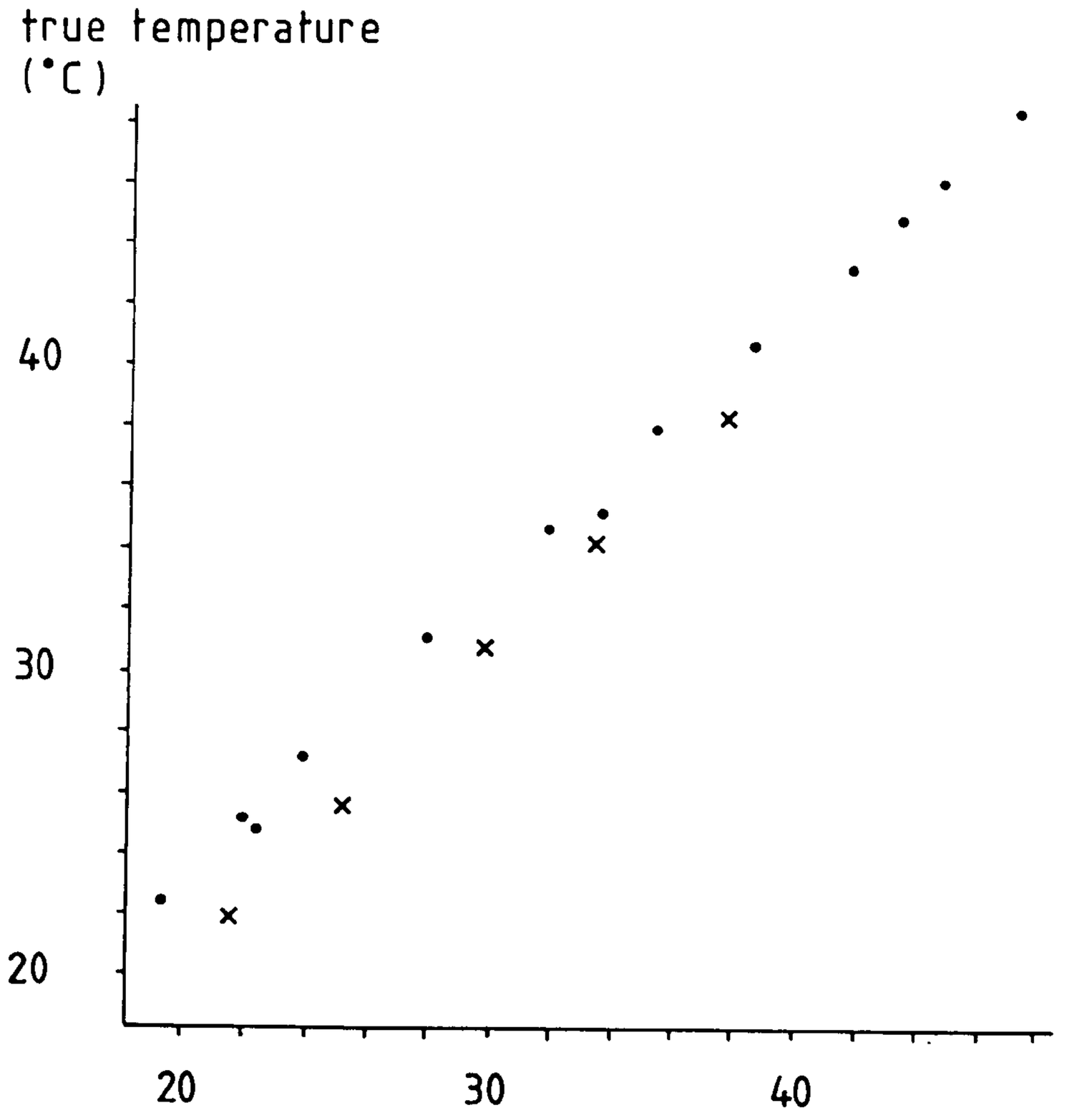

Fig. 3.5

Example of thermocouple calibration data. 'x' obtained about 4 weeks after '.'

averaged over a period of ½ hour. The mild steel specimen required between 3 and 5 hours to attain equilibrium, depending on the input power.

The conductivity measurements on mild steel are summarised in Table 3.3, and plotted against temperature gradient and heating power in Fig. 3.6. The weighted mean of the 7 measurements has been calculated; for a series of values $X_n \pm S_n$, $X_m \pm S_m$, etc., the weighted mean is $X_{nm...} \pm S_{nm...}$, where

$$X_{nm...} = \frac{1}{S_n^{-2} + S_m^{-2} + ...} \left(\frac{X_n}{S_n^2} + \frac{X_m}{S_m^2} + \cdots \right)$$

and $$S_{nm}^{-2} = S_n^{-2} + S_m^{-2} + ...$$

Averaged over these measurements, the agreement with the calculated thermal conductivity at room temperature is considered satisfactory, although the scatter of experimental values is too great for any temperature dependence to be evident.

3.1.4 Preparation of CFRP Specimens

Bar specimens of unidirectional carbon fibre-reinforced epoxy resin were manufactured by hot compression moulding from pre-impregnated fibre sheets ('prepreg') {9}. Preliminary moulding trials were made with a glass fibre-reinforced MY 750 epoxy resin system, but this proved inconvenient to handle, having a low viscosity at room temperature, and it was difficult to remove the prepreg backing paper without disturbing the fibres. The Shell DX 210 resin system is considerably more viscous at room temperature, and was adopted for the CFRP specimens.

Fig. 3.7 shows the steel mould used for manufacture, all sections of which could be separately dismantled for easy removal of specimens.

Prepreg was supplied at a mould thickness of 0.02 inch for a nominal fibre volume fraction of 60% - a specimen of cross-section 25 mm square thus required 49 prepreg layers. These

Table 3.3

Results of thermal conductivity measurements on mild steel

Heating Power W	dT/dx K/m	k W/m k	$\overline{T}$ K
4.54	157.6	45.9 ± 3.2*	312
3.24	119.2	43.3 ± 3.9*	304
4.63	152.3	48.4 ± 2.9	309
3.26	94.7	54.5 ± 4.4	301
2.73	80.8	53.8 ± 4.3	302
4.63	159.6	46.2 ± 3.7	311
3.32	109.9	48.1 ± 2.9*	303
Weighted mean value		48.1 ± 1.3	

* denotes measurement under vacuum

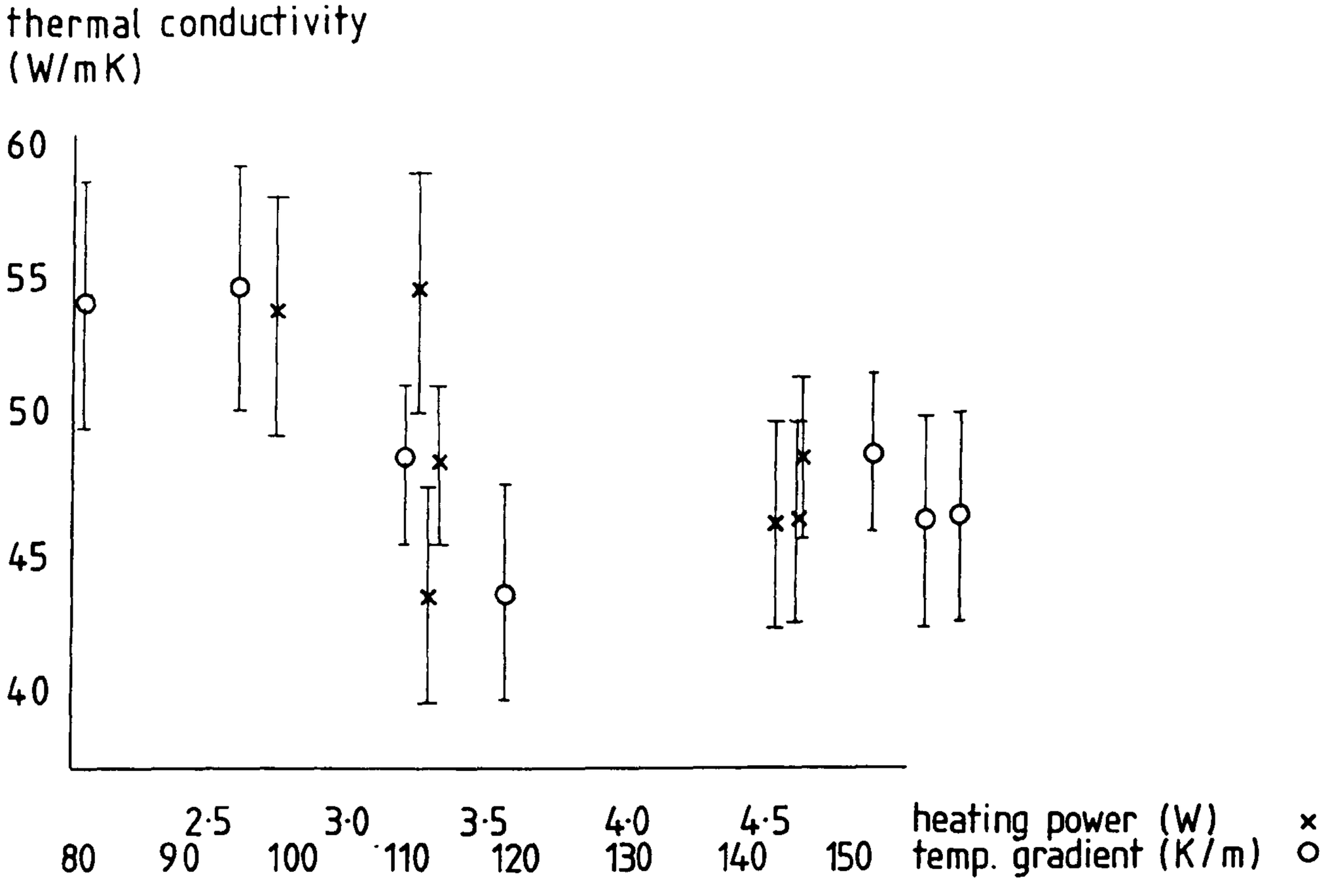

Fig. 3.6

Mild steel thermal conductivity measurements, plotted against heating power and temperature gradient.

were cut to size from larger sheets and placed in the assembled mould, which had been previously treated with a mould-releasing agent. The top of the mould was then located on its guiding pins, and hand pressure applied for initial consolidation of the layers.

In order to reduce the likelihood of air being trapped within the material during the curing process, the mould was raised to a temperature of about 80° C in a vacuum oven and the pressure was then reduced to about 0.1 atmosphere. The mould was left in this condition for about 15 hours. On removal from the oven, the mould was placed between heated platens, at a nominal temperature of 160°C. Pressure was applied very gradually to the mould, by locating the platens within an Avery-Davison Universal Test Machine, such that the top of the mould was lowered to within a few mm of its closing stops over a period of 20-30 minutes. During this time, excess resin was steadily expelled from the holes in the ends of the mould (see Fig. 3.7). The emerging resin was regularly checked for signs of gelation, and when this occurred (typically 40-50 minutes after placing the mould between the platens) the final closing pressure was applied. The force necessary to close the mould was usually between 30 and 40 kN (equivalent to pressures of up to 5300 kN/m^2. At this stage, the platen heaters were switched off, and the mould was allowed to cool naturally (although still under pressure) for 2 to 3 hours. After removal from the mould, the specimen was given a post-cure heat treatment for 2 hours at 180°C.

Fig. 3.8 shows a number of examples of both glass and carbon fibre-reinforced epoxy resin specimens produced by this method. Inspection indicated that the fibres tended to be distorted near the ends of the specimen, curving upwards due to the flow of excess resin being expelled from the mould. The mould length was 30 cm, thus allowing for the removal of 2.5 cm from each end of the specimens. These end sections were mounted in quick-setting resin, and their faces progressively polished on 14, 6 and 1 micron diamond wheels to enable examination of the composite microstructure.

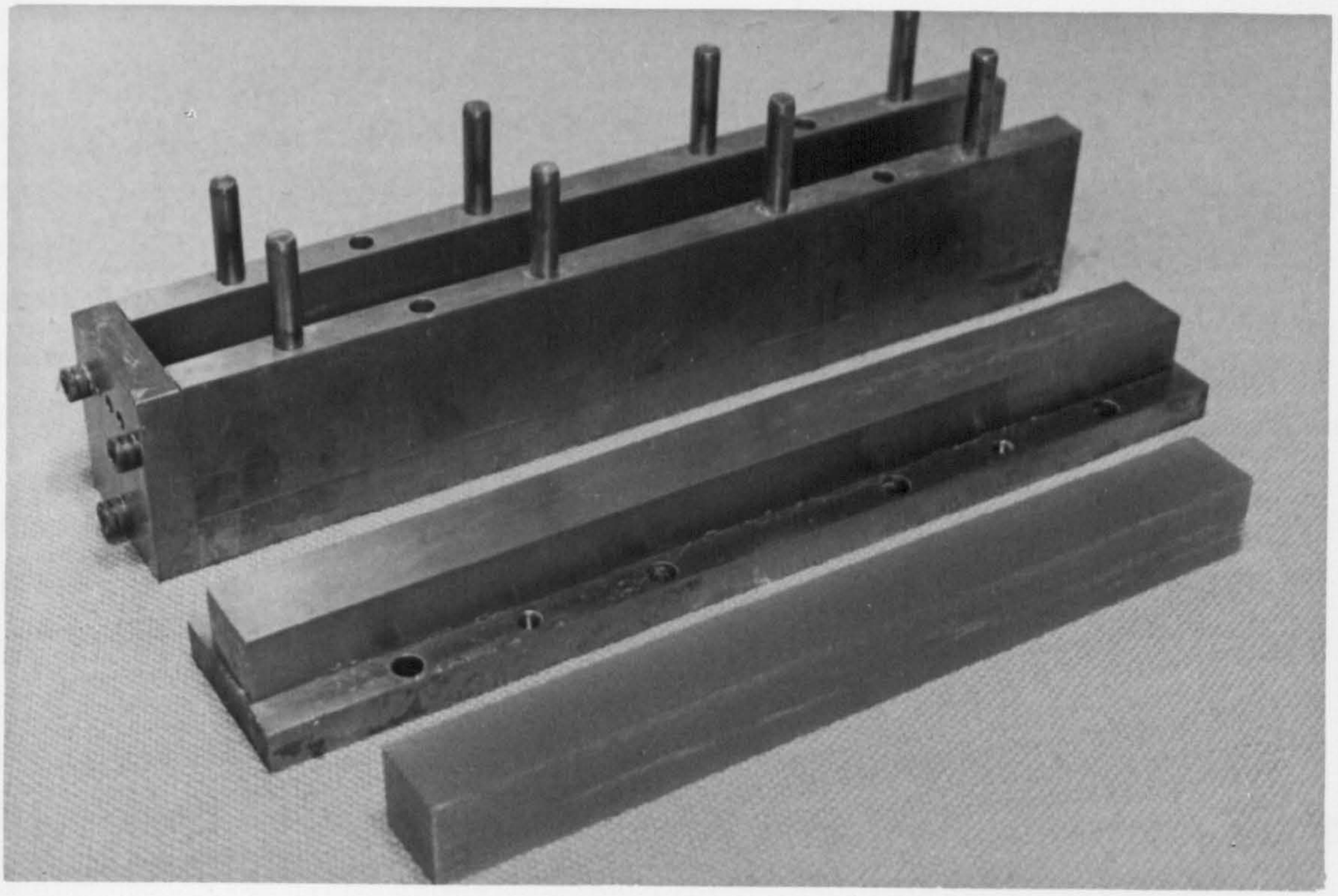

Fig. 3.7

Steel matched mould for manufacture of bar specimens.

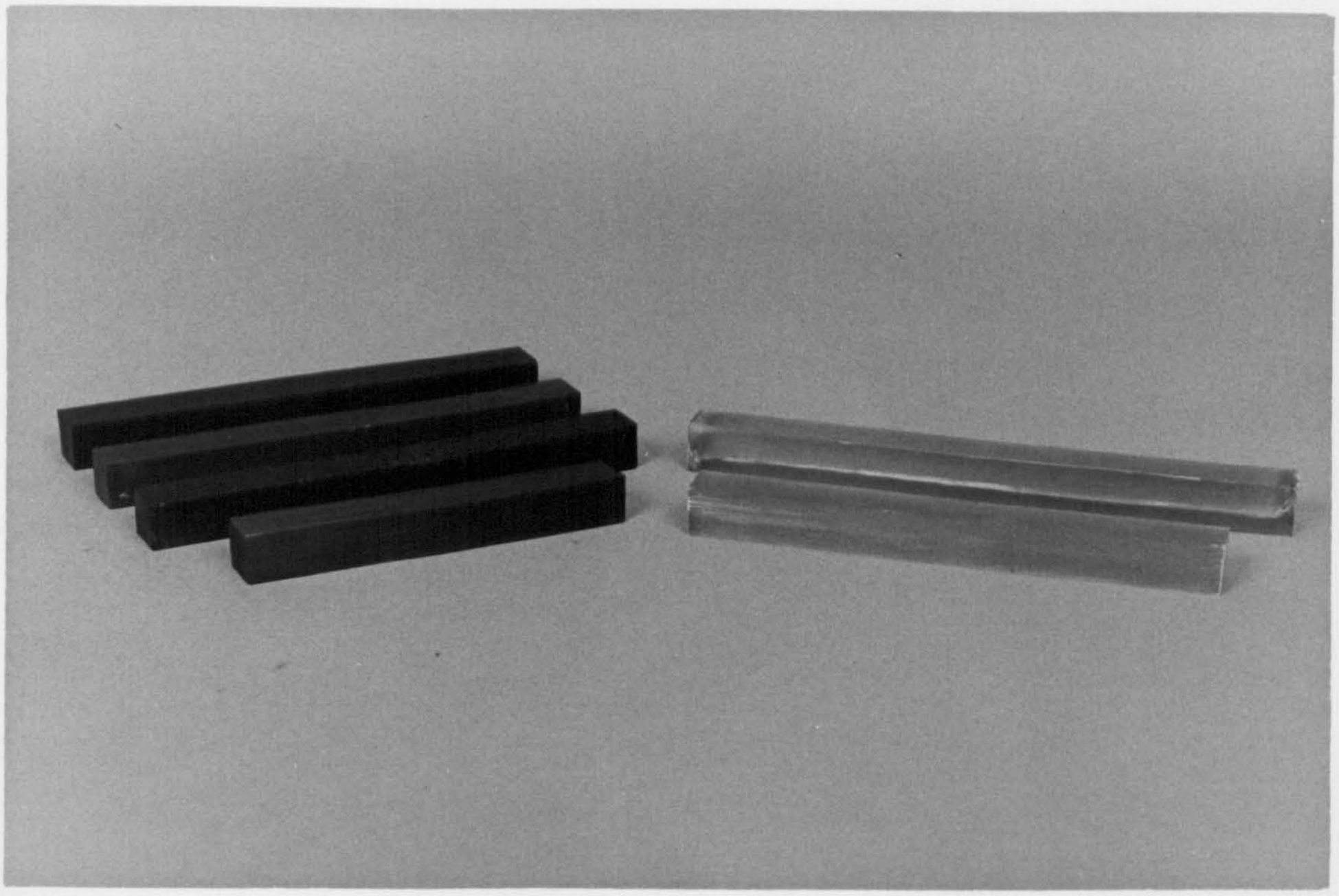

Fig. 3.8

Unidirectional glass and carbon fibre-reinforced epoxy resin specimens.

Fig. 3.9 shows typical photomicrographs of the surface of the CFRP specimens. The void content was visually assessed to be less than about 0.5%, but it is noticeable that the specimen has retained a characteristic of its prepreg origin, displaying bands of resin-rich areas. Such a structure is common in specimens of this type, and was noted by Harris (1980) who also observed curvature of the prepreg layers, due to adhesion to the sides of the mould during compression.

Photographs of specimen sections, such as Fig. 3.9, were used for the calculation of fibre volume fraction. The process of measuring the average value of the area occupied by fibres on a number of photographs was simplified by mounting the print on a microcomputer graphics tablet and digitising the locations of the fibre/resin interfaces along about 15 to 20 straight lines drawn at random on the photograph. The equivalent fibre volume fraction was then calculated by a simplified version of the software employed by Summerscales (1983), who used the system for measuring the distribution of the components of glass/carbon hybrid composites. Mean volume fractions were calculated from a total of 9 photographs of each section.

A total of 6 CFRP specimens were manufactured by the procedure described above, having unidirectional reinforcement orientated at 0^{o}, 5^{o}, 10^{o}, 15^{o}, 20^{o} and 30^{o} to the longitudinal axis of the bar (see Fig. 3.10). As discussed in 2.1.3, the fundamental measurement of temperature gradient in the direction of the heat flux in a material with two-dimensional thermal anisotropy, yields a resistivity

$$R_{11} = \frac{-\partial T/\partial x}{q_x} = \frac{k_{22}}{k_{11}\,k_{22} - k_{12}^{2}} \qquad (3.4)$$

(The components of the thermal conductivity tensor (k_{ij}) were introduced in 2.1.3 and are discussed in more detail in 4.1.1.) In the special case $k_{12} = 0$ (corresponding to the 0^{o} fibre alignment) the measurement of $\frac{\partial T}{\partial x}$ and q_x gives one of the principal thermal conductivities (K_1). In general, however, $\frac{\partial T}{\partial y} \neq 0$, even though the heat flux is one-dimensional, and Equation 2.5 gives

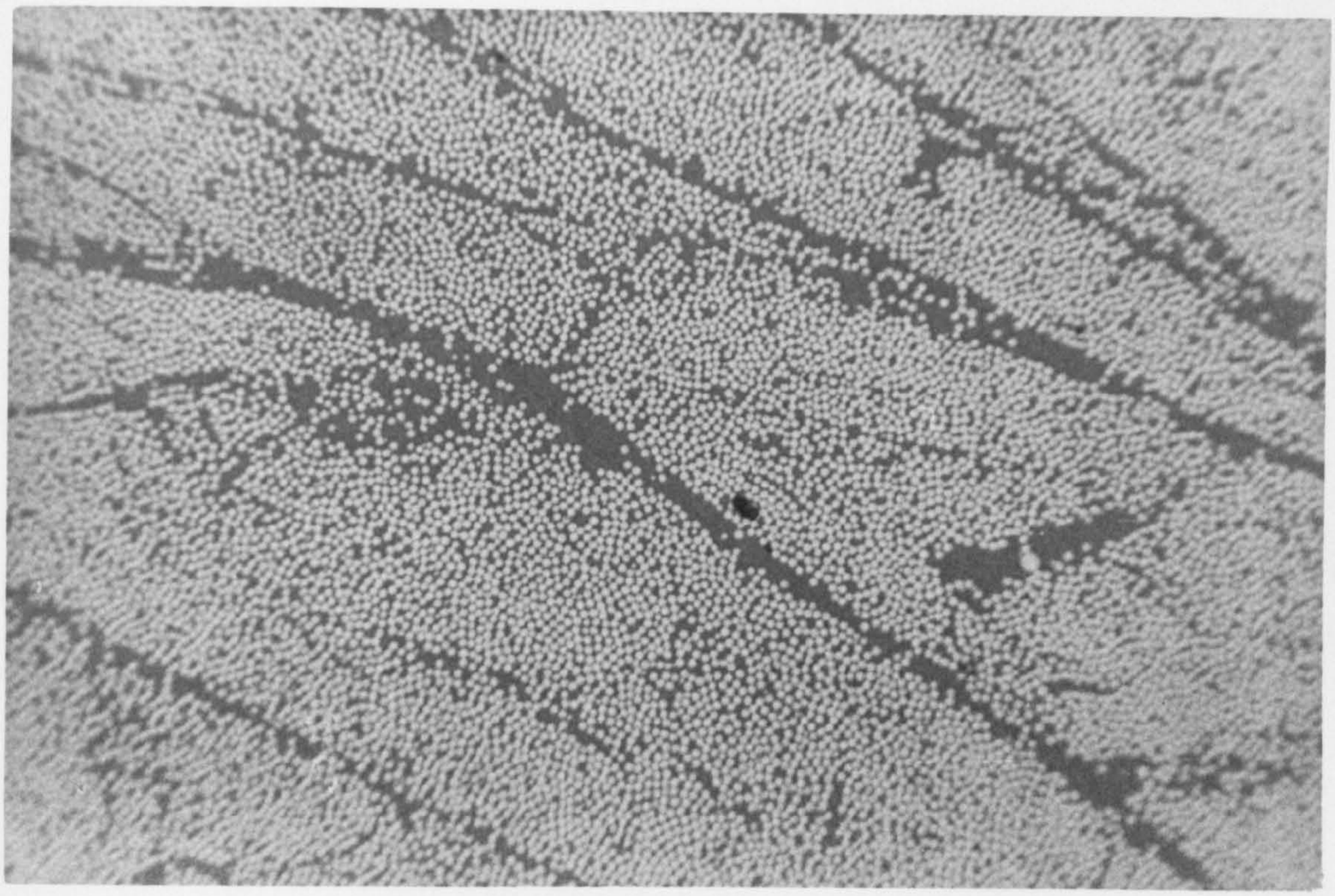

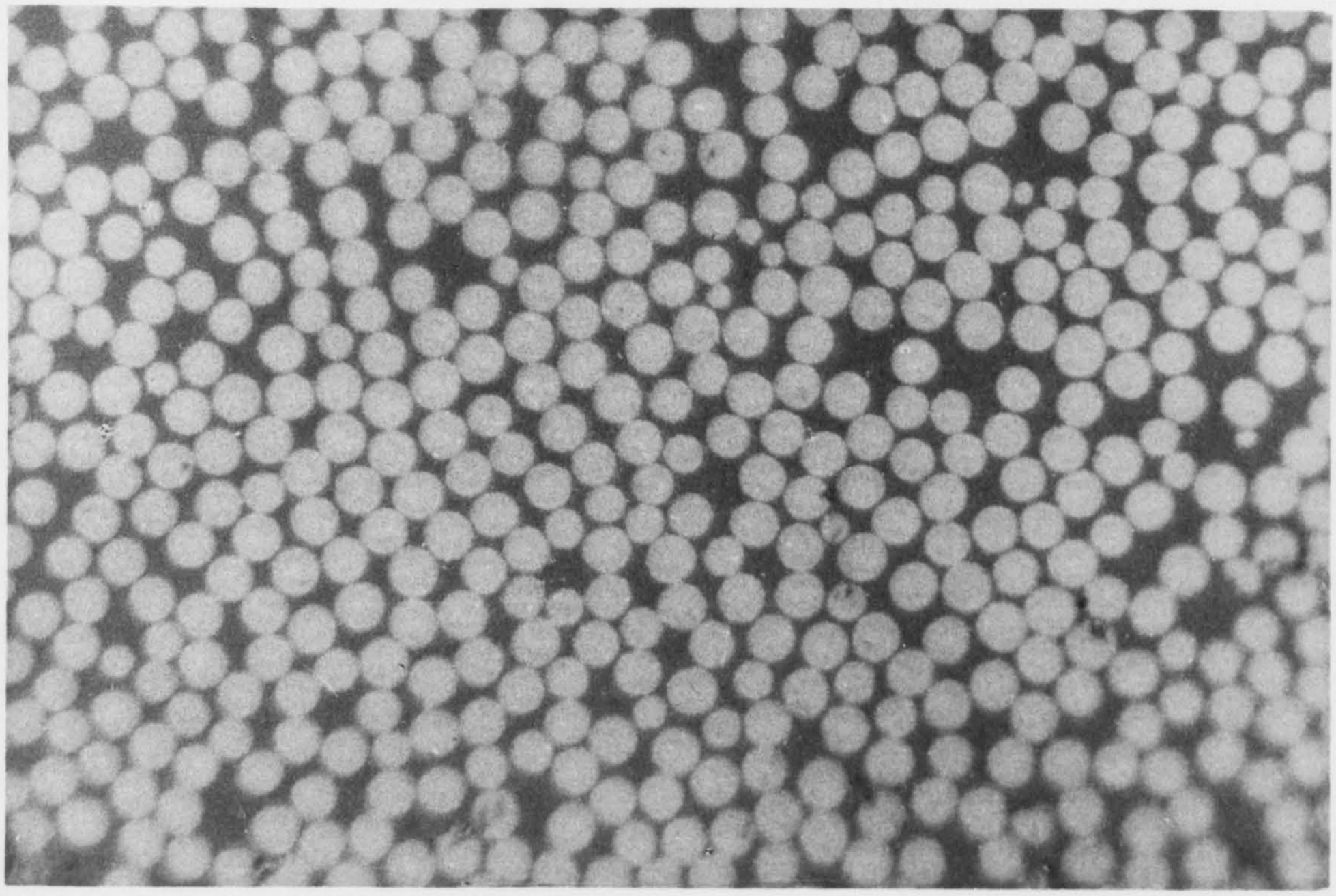

Fig. 3.9

Micrographs of sections of CFRP specimen.

$$R_{12} = \frac{-\partial T/\partial y}{q_x} = \frac{k_{12}}{k_{11}k_{22} - k_{12}^2} \qquad (3.5)$$

The tensor transformations (Equation 4.13) may be used to express the conductivity coefficients in terms of the two principal conductivities (K_1 and K_2) when the fibre reinforcement is at some angle θ to the x-direction. Combining Equations 3.4 and 3.5 gives

$$\chi = \frac{\partial T/\partial y}{\partial T/\partial x} = \frac{k_{12}}{k_{22}} = \frac{(K_1 - K_2)\sin\theta\cos\theta}{K_1\sin^2\theta + K_2\cos^2\theta} = \frac{(\gamma^2 - 1)\sin\theta\cos\theta}{\gamma^2\sin^2\theta + \cos^2\theta} \qquad (3.6)$$

where $\gamma^2 = K_1/K_2$. The transformation may also be applied to Equation 3.4 alone, giving

$$\frac{1}{R_{11}} = \frac{K_1K_2}{K_1\sin^2\theta + K_2\cos^2\theta}, \text{ or } \frac{1/R_{11}}{K_1} = \frac{1}{\gamma^2\sin^2\theta + \cos^2\theta} \qquad (3.7)$$

Thus, having determined K_1 from measurements on the 0° CFRP specimen, an estimate of the ratio of principal conductivities ($\gamma^2 = K_1/K_2$) may be made from similar measurements on the other alignments, using Equation 3.6 or 3.7.

3.1.5 Results

Measurements on the CFRP specimens followed the same calibration and recording procedures described in 3.1.3, although the times required to achieve a steady state were somewhat less than for the mild steel sample.

In an attempt to extend the range of mean specimen temperature, a thermostatically-controlled bath was used to supply cooling water to the heat sink of the apparatus. At a heater power of 4.5 W, a maximum average specimen temperature of 350 K was attained.

Fig. 3.11 shows the measured conductivity (K_1) parallel to the fibre reinforcement (0° specimen) from 295 K to 352 K. Despite the rather large experimental error (compared with the change in conductivity with temperature), the scatter is not severe, and the data appear to be consistent with those of Pilling and others (1979) and of Knibbs and others (1971), which were discussed in 2.3.2. The results are not directly

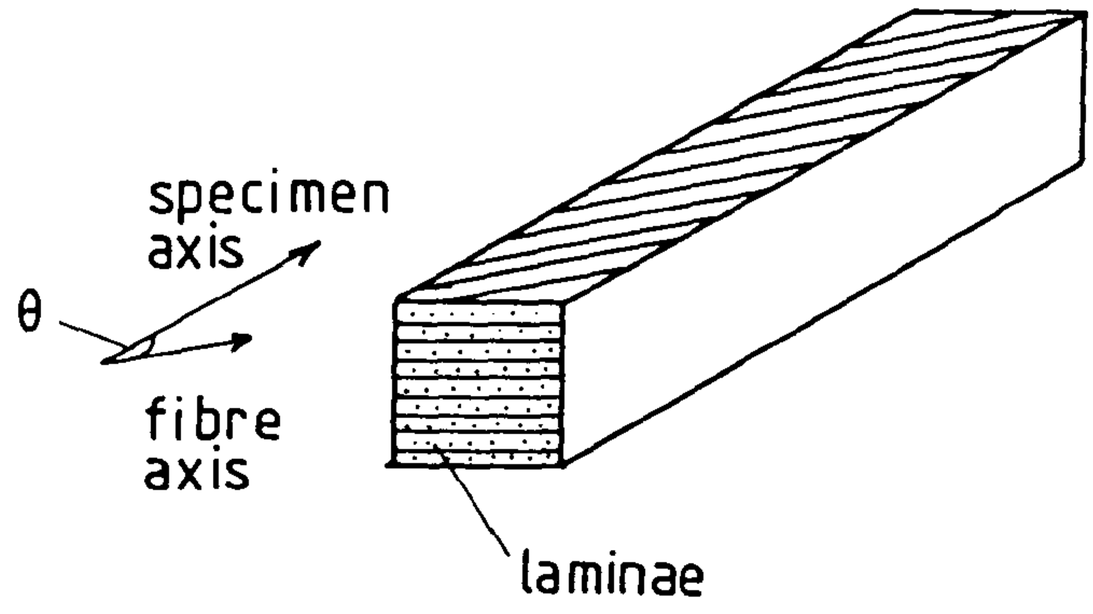

Fig. 3.10

Definition of fibre and specimen axes in 'off-axis' cfrp specimen.

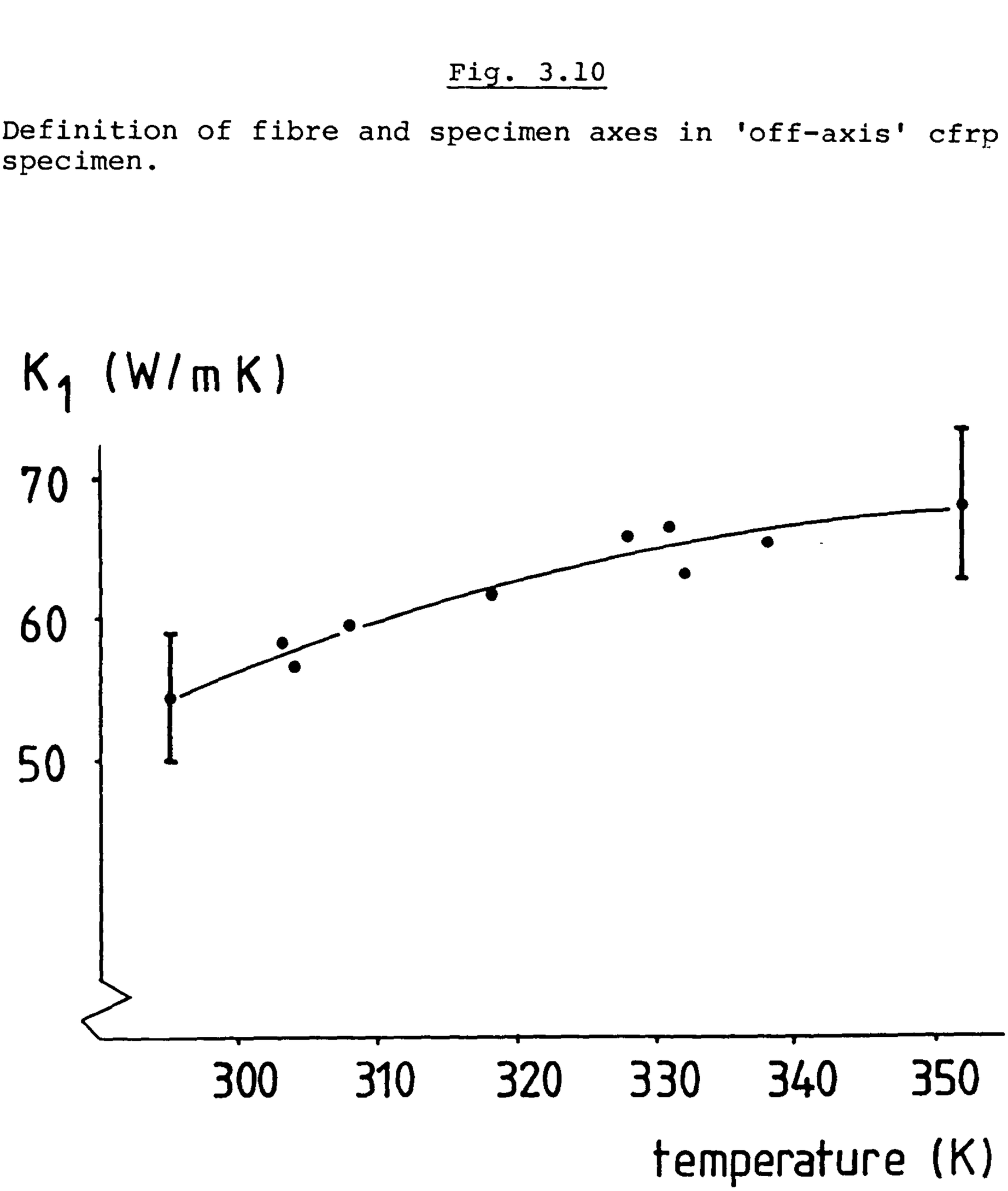

Fig. 3.11

Measured longitudinal thermal conductivity in 0° cfrp specimen.

comparable, however, due to differences in resin systems and fibre origin (compare Tables 2.2 and 3.1).

Measurements on the five 'off-axis' specimens are summarised in Table 3.4. In each case, five measurements were made at varying levels of heater input, but all with cold mains water circulating in the heat sink. The range of mean specimen temperature is considered too small to expect any associated change in thermal properties, so weighted mean values of both χ and $1/R_{11}$ are given. Temperature gradients in the x- and y-directions were determined from four thermocouples, positioned as indicated in Fig. 3.12a.

The random errors associated with measurements on the off-axis specimens are estimated to be $\pm 10\%$ for χ, and $\pm 8\%$ for $1/R_{11}$. The calculation of χ does not involve the value of the heater power, so the error arises solely from the measurement of the two temperature gradients. The uncertainty in the value of $1/R_{11}K_1$ (as used in Equation 3.7) is dependent also on the accuracy of K_1, and could thus be as high as $\pm$ 16%, although both these errors are reduced by taking the average of five readings. However, it should be emphasised that these measurements may be useful only for a crude estimate of the conductivity ratio γ^2. This is because the apparatus is liable to considerable systematic error in specimens where there is an appreciable temperature gradient in the y-direction, since it is not possible for the sample guard to match the temperature distribution along its length. This is indicated schematically in Fig. 3.12b,where one side of the specimen is hotter than the guard and the other side cooler; the effect of such heat flows would be to reduce the measured value of $\frac{\partial T}{\partial y}$ (and hence χ), being particularly severe for orientations at which χ is largest. The results of Table 3.4 should therefore be treated with considerable caution.

In Fig. 3.13 the measured values of $\frac{1}{R_{11}K_1}$ are plotted against fibre orientation (θ). The smooth curve is the Equation 3.7, using a value of $\gamma^2 = 26$, which was found by trial and error to give a minimum mean square deviation from the experimental

Table 3.4

Thermal conductivity measurements on 'off-axis' CFRP specimens

Reinforcement Angle θ^{o}	Mean Temp. K	$\chi = \frac{\partial T}{\partial y}/\frac{\partial T}{\partial x}$	$1/R_{11}$ W/m K
5	298	2.77	50.0
	303	2.82	48.4
	307	2.89	49.7
	311	2.89	50.2
	304	2.85	48.8
mean:		2.84	49.4
10	294	2.70	35.8
	291	2.65	34.4
	299	2.62	35.9
	308	2.87	38.5
	304	2.87	38.3
mean:		2.74	36.6
15	300	2.83	19.6
	298	2.84	18.5
	307	2.91	20.9
	302	2.89	19.9
	303	2.89	20.6
mean:		2.87	19.9
20	312	2.21	12.6
	307	2.07	12.1
	306	2.10	11.8
	310	2.09	12.2
	301	2.02	12.0
mean:		2.10	12.1
30	307	1.60	8.8
	309	1.59	8.7
	302	1.60	8.9
	298	1.57	8.8
	306	1.58	8.8
mean:		1.59	8.8

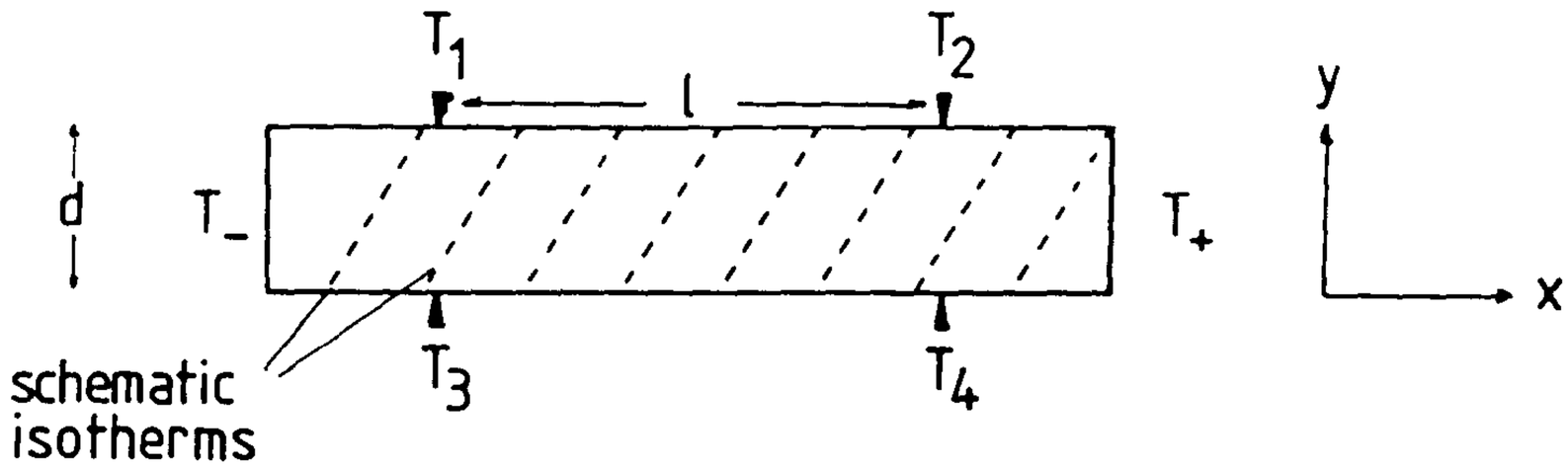

Fig. 3.12(a)

Use of four thermocouples for measurements of x and y-direction temperature gradients on 'off-axis' specimen.

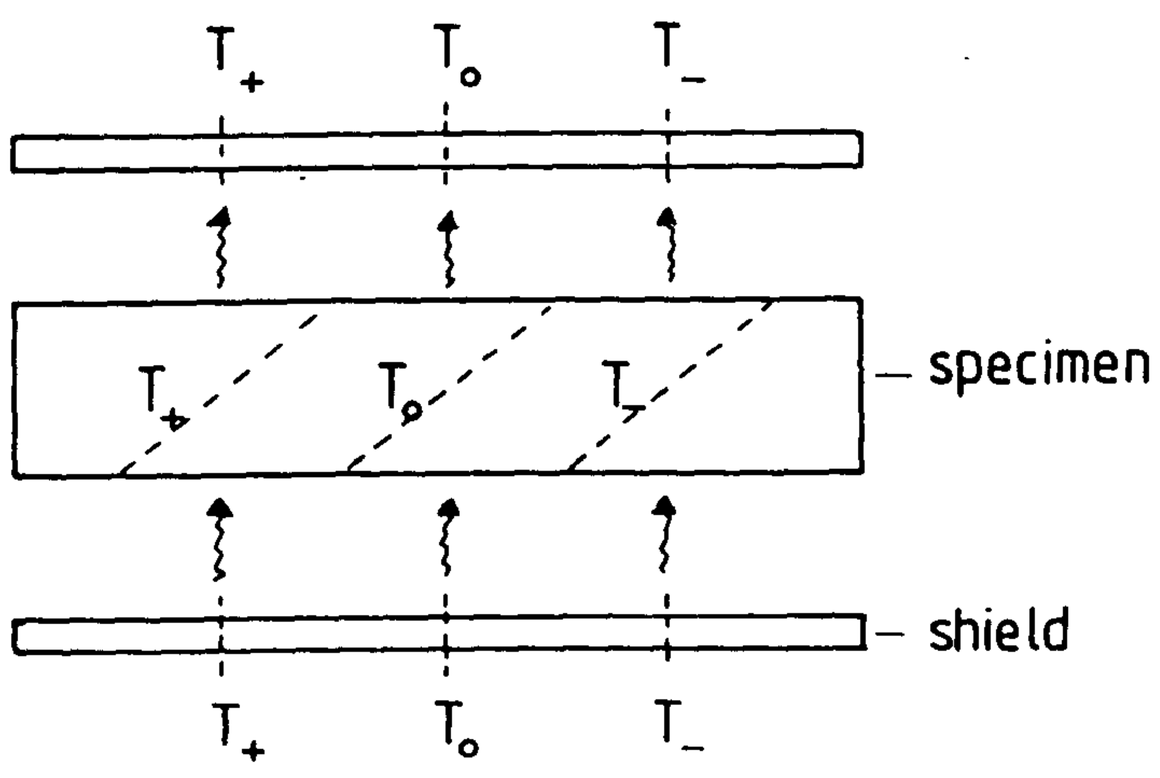

Fig. 3.12(b)

Temperature mismatch between specimen and shield in anisotropic materials.

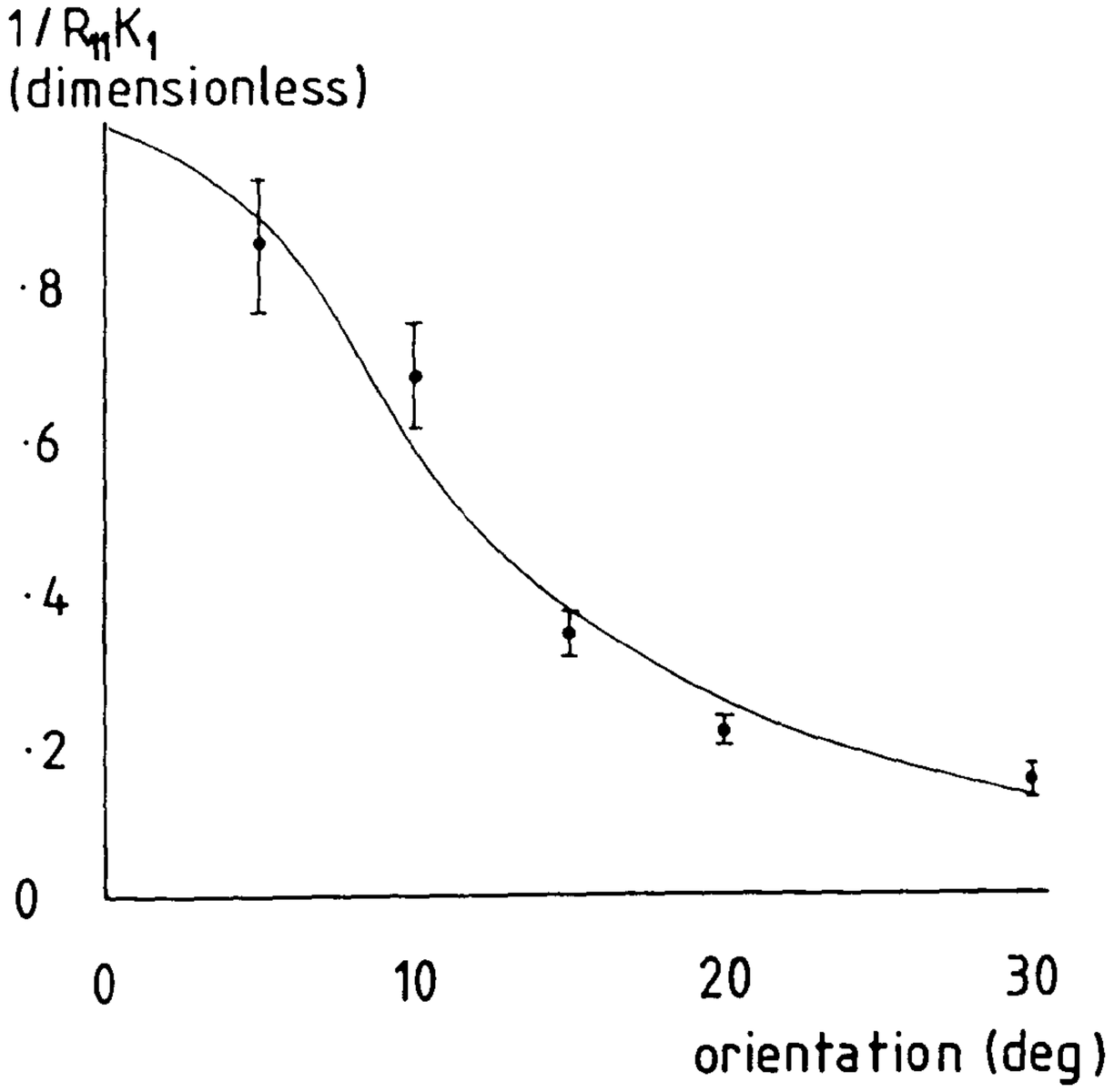

Fig. 3.13

Experimental values of $1/R_{11} K_1$ in off-axis specimens. Smooth curve is Equation 3.7 with $\gamma^2 = 26$.

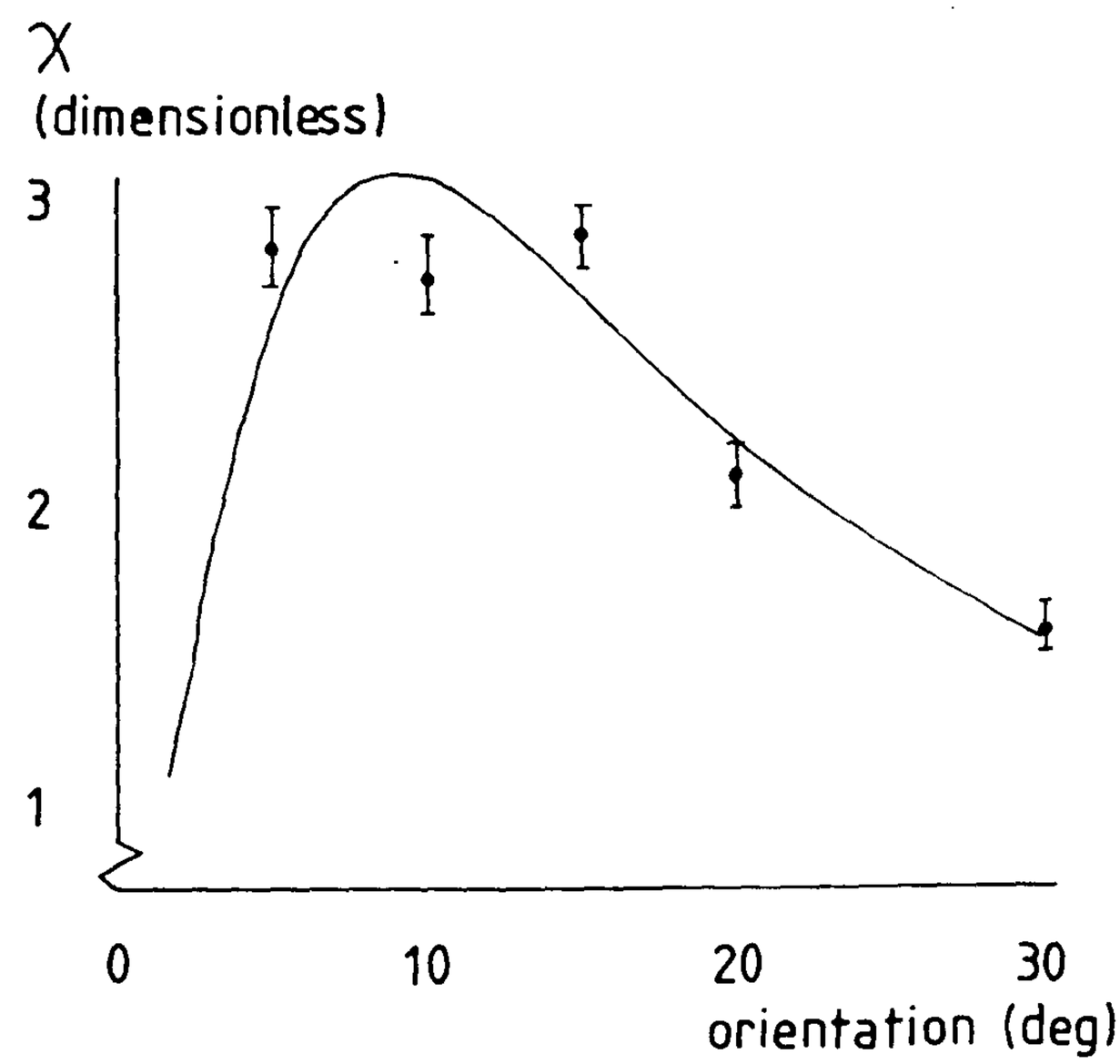

Fig. 3.14

Experimental values of χ for the off-axis specimens. Smooth curve is Equation 3.6.

points. The measurements of X are treated in a similar way; these are plotted against θ in Fig. 3.14, together with the experimental curve (Equation 3.6). In this case, the minimum mean square deviation from the experimental points is obtained with $\gamma^2 = 40$.

The two estimates of γ^2 obtained from these measurements are considerably different, and it is likely that the systematic errors referred to above do not influence X and $1/R_{11}$ to the same extent. It seems possible that the measurement of $1/R_{11}$ is the more reliable, since only one of the temperature gradients is used in the calculation; however, the range of values thus inferred for K_2 (= K_1/γ^2), namely 1.45-2.23, should only be regarded as a rough guide. Nevertheless, it is believed that a redesigned apparatus, incorporating better specimen insulation, would have certain practical advantages, since it could measure both principal conductivities on the same sample geometry.

3.2 MEASUREMENTS PERPENDICULAR TO TEMPERATURE GRADIENT

In order to obtain values of thermal conductivity at right angles to the reinforcement with better accuracy than those deduced from the off-axis specimens in 3.1.5, measurements were performed on a commercial comparative instrument {10}, at the University of Salford. It was also intended to extend the temperature range of measurements up to about 150°C.

3.2.1 Description of Apparatus

The principle of operation of a comparative instrument was outlined in 2.1.1. The specimen is sandwiched between two identical reference samples of known thermal conductivity, and this stack is placed between two heating elements, the temperatures of which are controlled. The resulting heat flux produces temperature gradients in the specimen and reference samples such that, at thermal equilibrium, the unknown thermal conductivity is given by

$$k_s = \frac{d_s}{2\Delta T_s} (q_t + q_b) \qquad (3.8)$$

where q_t and q_b are the heat fluxes through top and bottom

references respectively (see Fig. 3.15). In each case,

$$q_t = k_t \Delta T_t / d_t \text{ and } q_b = k_b \Delta T_b / d_b$$

ΔT is the temperature difference between two thermocouples a distance d apart, and the subscripts $_s$, $_t$ and $_b$ refer to the specimen and top and bottom references respectively.

A linear heat flux through the stack is maintained by a cylindrical guard heater, the top and bottom temperatures being controlled by independent heaters and matched to the upper thermocouple in the top reference and the lower thermocouple in the bottom reference, as shown in Fig. 3.15. Clearly, the temperature gradients in the stack and its guard will only match exactly when the thermal conductivities of reference material and specimen are the same. The overall accuracy of measurement thus depends on the appropriate choice of reference material - the manufacturer suggests that the error will be less than ±10% if the specimen and reference conductivities agree within one order of magnitude. Five reference materials are supplied (obtained from the U.S. National Bureau of Standards) and have well-documented thermal properties. These are:- Pyrex 7740 (for use in the conductivity range 1-2 W/m K); Pyroceram 9606 (3-5 W/m K); Inconel 702 (10-30 W/m K); Inconel 718 (10-25 W/m K) and Armco Iron (30-90 W/m K).

An important feature of the instrument is that thermocouples are installed in the samples themselves; this avoids some of the problems associated with thermal resistance between heater or heat sink and specimens which were referred to in 2.1.1. However, the thermocouples must be as small as possible, in order not to disturb the flow of heat down the stack. Square specimens are required (63.5 mm x 63.5 mm), with thickness between 12.7 mm (½ inch) and 38.1 mm (1½ inch). The specimen thickness should increase with thermal conductivity, so that the temperature gradients produced are large enough for accurate measurement.

In a typical test, thermal equilibrium is reached from 2 to

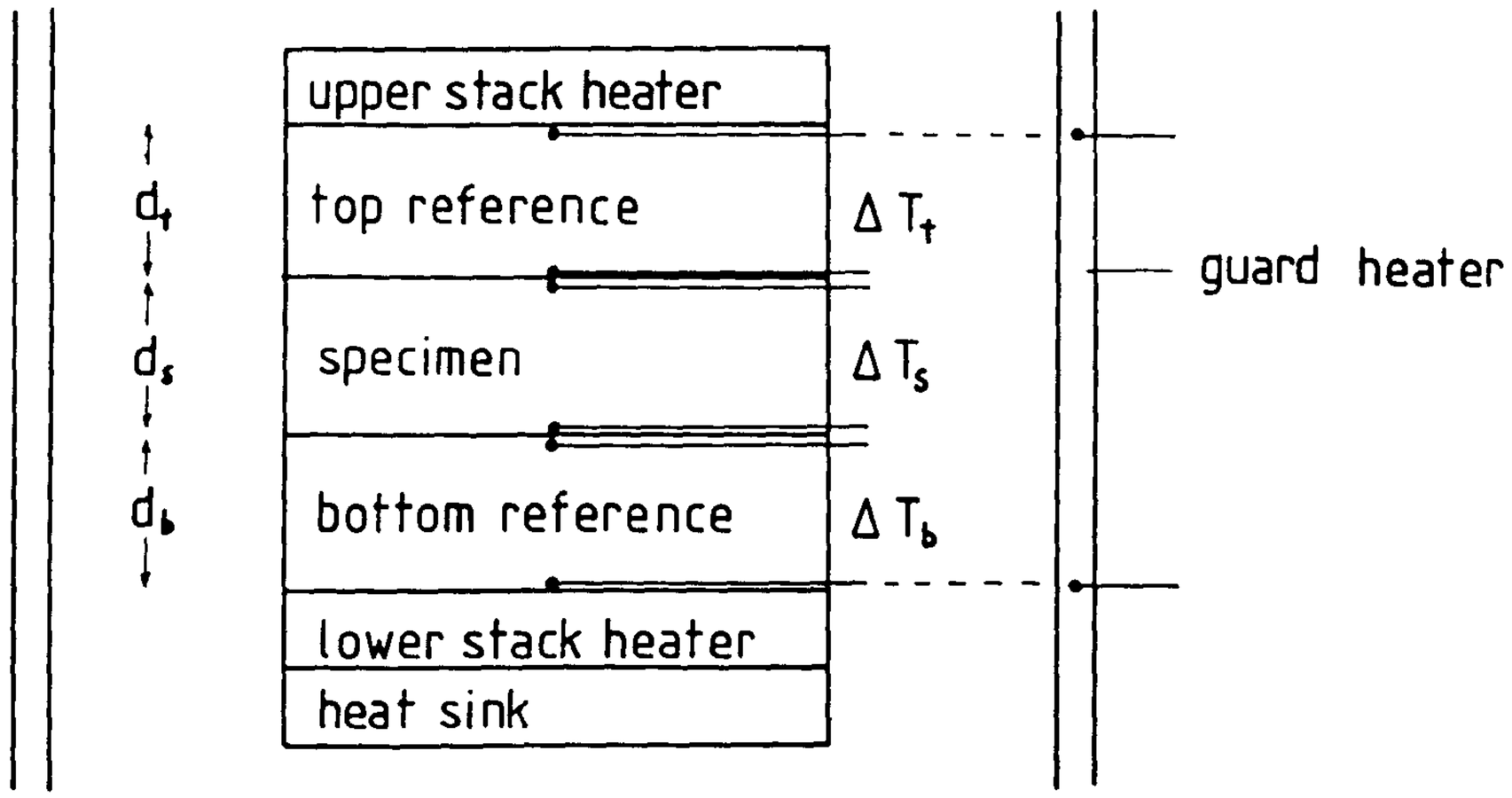

Fig. 3.15

Comparative instrument for measurement of thermal conductivity.

4 hours after starting the measurement. A steady state is usually regarded as a change of less than 1% in ΔT over a period of 30 minutes. All temperatures are scanned manually by a digital voltmeter, giving a precision of 0.025 K for a temperature measurement. It is possible to assess the accuracy of a particular test by comparing the temperature gradients in the two reference materials at equilibrium - if there has been no heat exchange between the stack and the guard, these should be identical, since the heat fluxes will be the same.

3.2.2 Specimen Preparation

As before, CFRP specimens were manufactured by hot compression moulding from prepreg sheets, but in this case the sample geometry necessitated a different mould. Fig. 3.16 shows a heavy-duty steel mould which had originally been designed for vacuum-injection of resin, but was easily adapted for compression moulding by the insertion of square steel blanks in the base - this gave an effective mould size of 102 mm square by 76 mm deep. The use of slightly undersize spacers on the top of the moulding (as shown in Fig. 3.16) allowed the passage of excess resin during compression.

The procedure adopted for moulding was similar to that described in 3.1.4, except that the larger mould had a greater thermal capacity and thus required longer to reach a temperature high enough to cure the resin. In addition, there was some uncertainty regarding the rate at which the composite itself would heat up - if the outer parts of a large moulding were to cure before the centre, some of the excess resin could become trapped. In an extreme case, the centre of the composite may fail to reach the curing temperature at all.

In view of these uncertainties, two pilot mouldings were made, using glass fibre-reinforced epoxy resin prepreg for reasons of economy. As before, the prepreg was supplied at a mould thickness of 0.02 inch for a volume fraction of 60%, so that 150 layers were required for a moulding 3 inch deep.

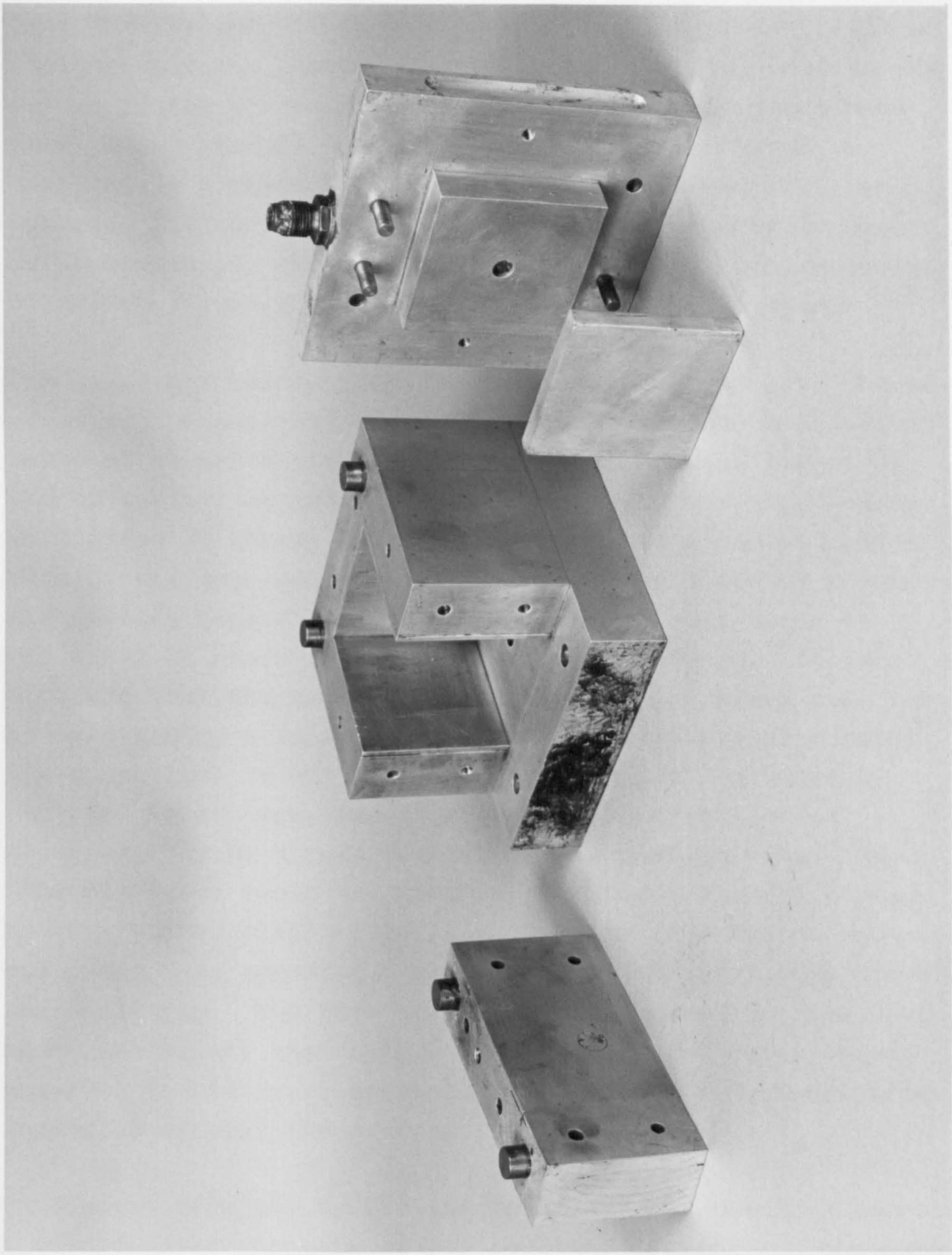

Fig. 3.16

Square steel mould for composite manufacture.

Half way through the lay-up process, a small Chromel-Alumel thermocouple was placed on the layers, with its bead in the centre of the cross-section. The thermocouple leads were then passed through a hole in the side of the mould (originally a resin inlet point) and sealed with silicone rubber. Laying-up then continued, leaving the thermocouple at approximately the centre of the specimen. The assembly of the mould was then completed, and the top located.

The mould was heated prior to compression in an oven set at a nominal temperature of 100°C. A slow rate of heating was selected to avoid premature curing of the outer layers of the composite; at this rate of heating the oven had reached 90°C after 2½ hours. Fig. 3.17 compares the core temperature of the specimen with that of the oven - midway through the heating period the temperature lag is only about 15 K, and after 2½ hours it has virtually disappeared. It is probable that the exothermic curing reaction plays some part in maintaining a reasonably uniform temperature throughout the composite; in any case, the temperature lag would be expected to be even less in a carbon fibre-reinforced material, having a much higher thermal conductivity. At this stage the mould was removed from the oven, and placed between heated platens, as before. Slow compression began, and resin soon appeared flowing through the small gap around the mould top. The core temperature continued to rise, but much more slowly than before (Fig. 3.17), and gelation was observed in the emerging resin about 1 hour 40 minutes after insertion between the platens.

On removal from the mould, the composite was found to contain a considerable quantity of air bubbles. Subsequent mouldings were therefore held under vacuum in the same way as the previous bar specimens. It was also noticed that resin had emerged not only at the top of the mould, but also through the joints between the sides. This was avoided by sealing the edges of the mould with silicone rubber before assembly.

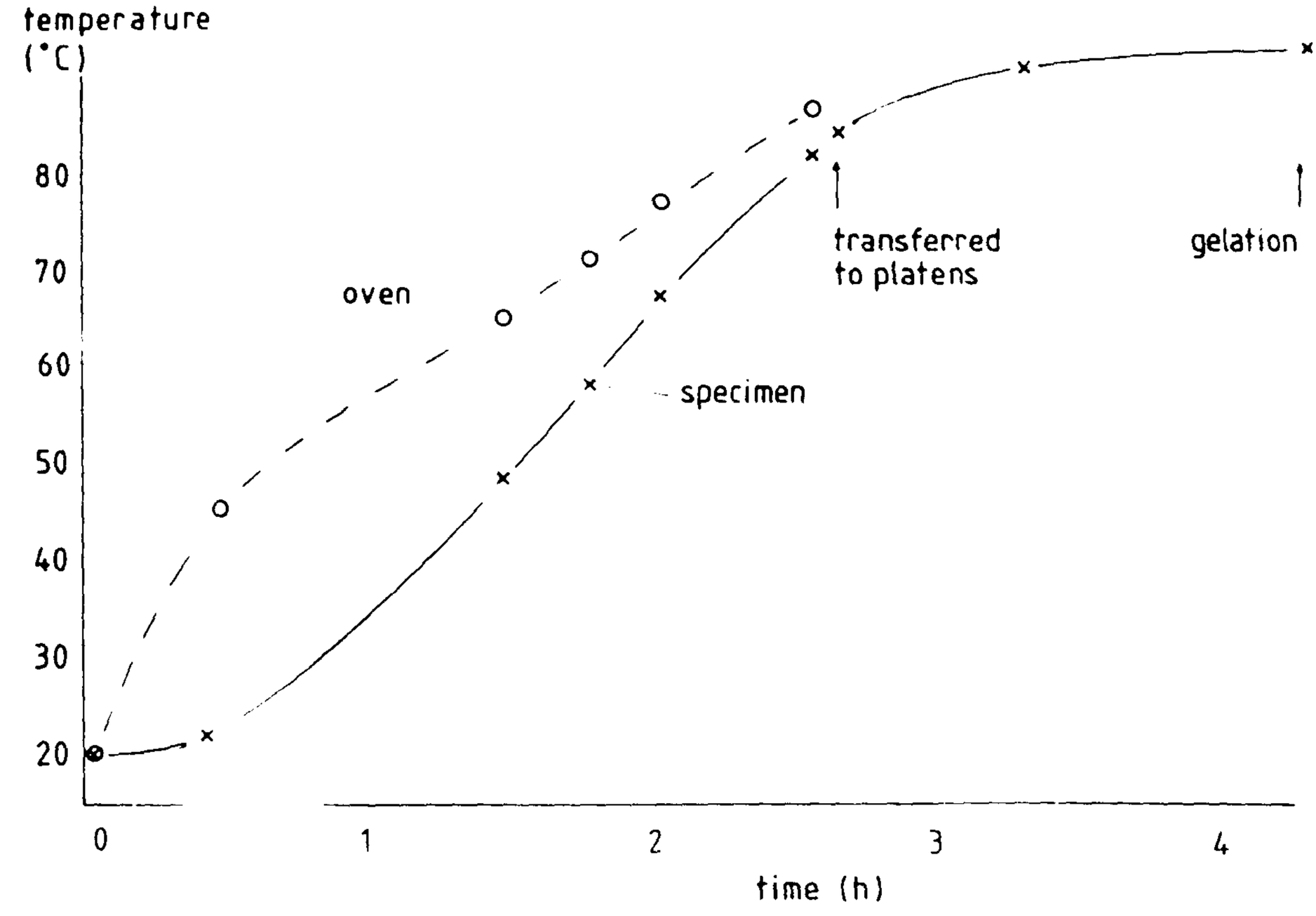

Fig. 3.17

Measurements of temperature rise of oven and centre of specimen in square mould (glass fibre/epoxy prepreg).

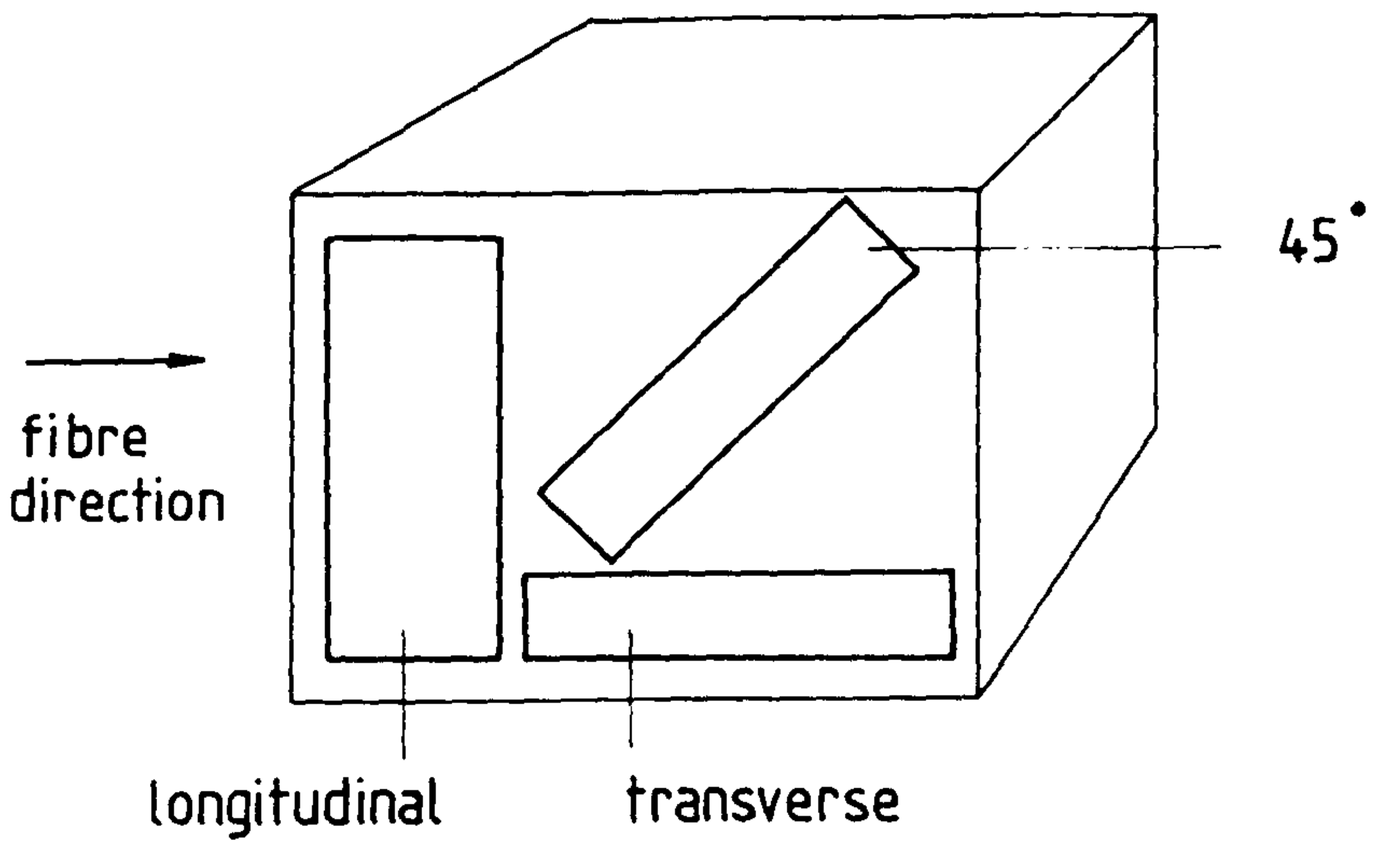

Fig. 3.18

Cutting of large composite block to give three specimens for comparative measurements.

Specimens of the size required by the comparative apparatus were obtained from the large blocks - Fig. 3.18 indicates how samples for the measurement of both principal conductivities (parallel and perpendicular to the reinforcement) could be cut from a single block. Sections were cut slightly over size using a diamond cutting wheel, then ground to the correct dimensions. Very fine Chromel-Alumel thermocouples {11} were selected, having PTFE insulation over 0.003 inch (approx. 0.08 mm) wire. These were butt-welded by the supplier, with a deliberately enlarged bead. A scalpel blade was used to cut a small slot across the centre of opposite faces of the specimens, just big enough to accommodate one of the thermocouple wires. At the mid point of the slot (in the centre of the specimen face) a small hole was drilled by means of a pin chuck into which the thermocouple bead was to fit.

Small quantities of cyanoacrylate adhesive were used to secure the thermocouple in position; when set, the small gaps remaining were carefully filled with epoxy resin adhesive. This was allowed to harden for 24 hours at room temperature before finally polishing the surface with an abrasive paper. Fig. 3.19 shows the prepared specimen, and Fig. 3.20 is a close-up of the thermocouple bead in position.

Surplus material from the original blocks was mounted and polished for microstructural examination and volume fraction determination (see 3.1.4). A section at low magnification is shown in Fig. 3.21, and demonstrates the tendency for resin-rich areas to remain at the interfaces between prepreg layers. The measured volume fraction was 0.60 with a negligible void content.

3.2.3 Results

Fig. 3.22 gives the measured values of thermal conductivity parallel (K_1) and perpendicular (K_2) the carbon fibres. The relatively large experimental errors associated with the former set ($\pm$ 7% to $\pm$ 14%, compared to $\pm$ 4%) arise because the transverse thermal conductivity of the composite was close to that of the Pyrex reference material, whereas the

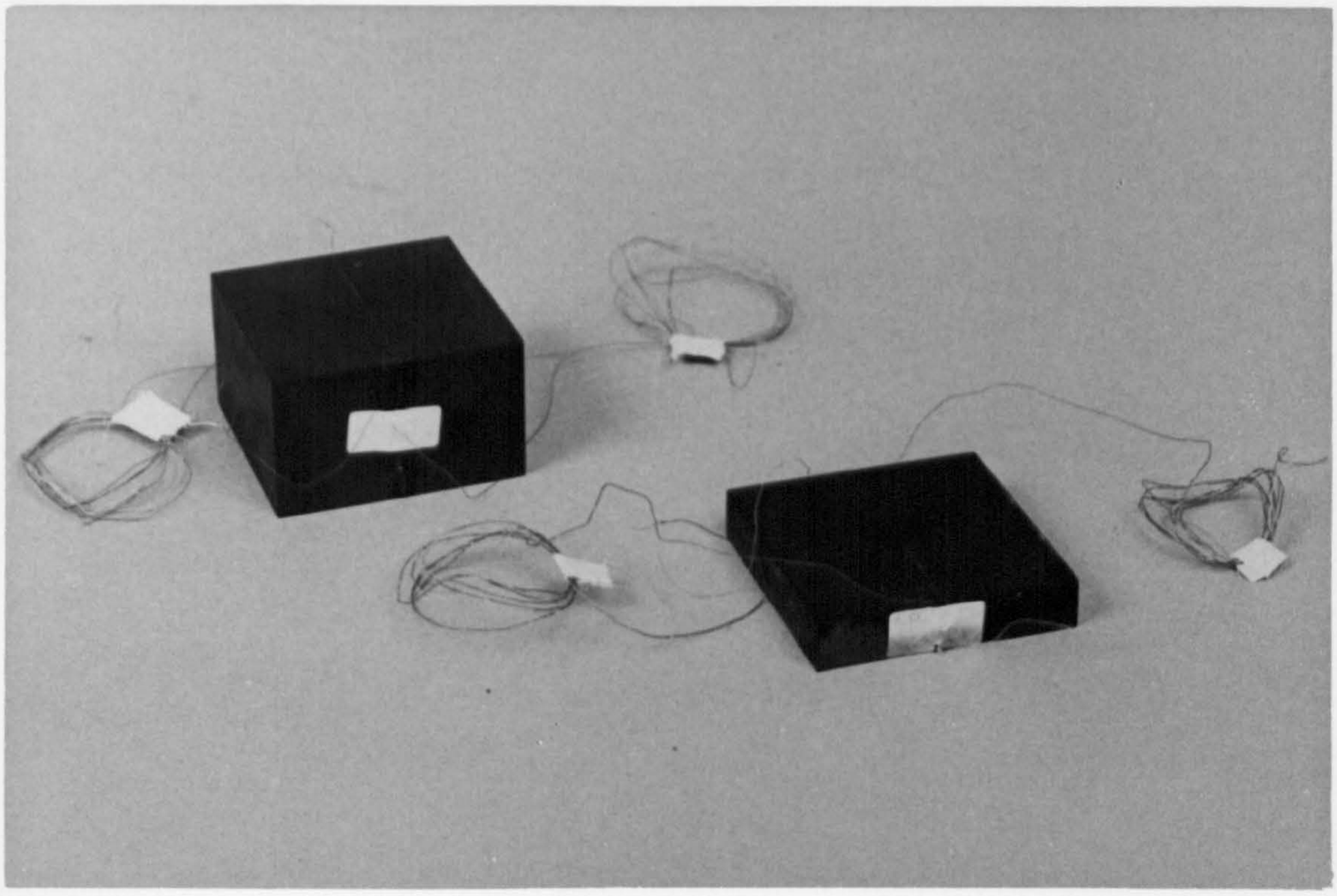

Fig. 3.19

Prepared specimens for comparative measurements.

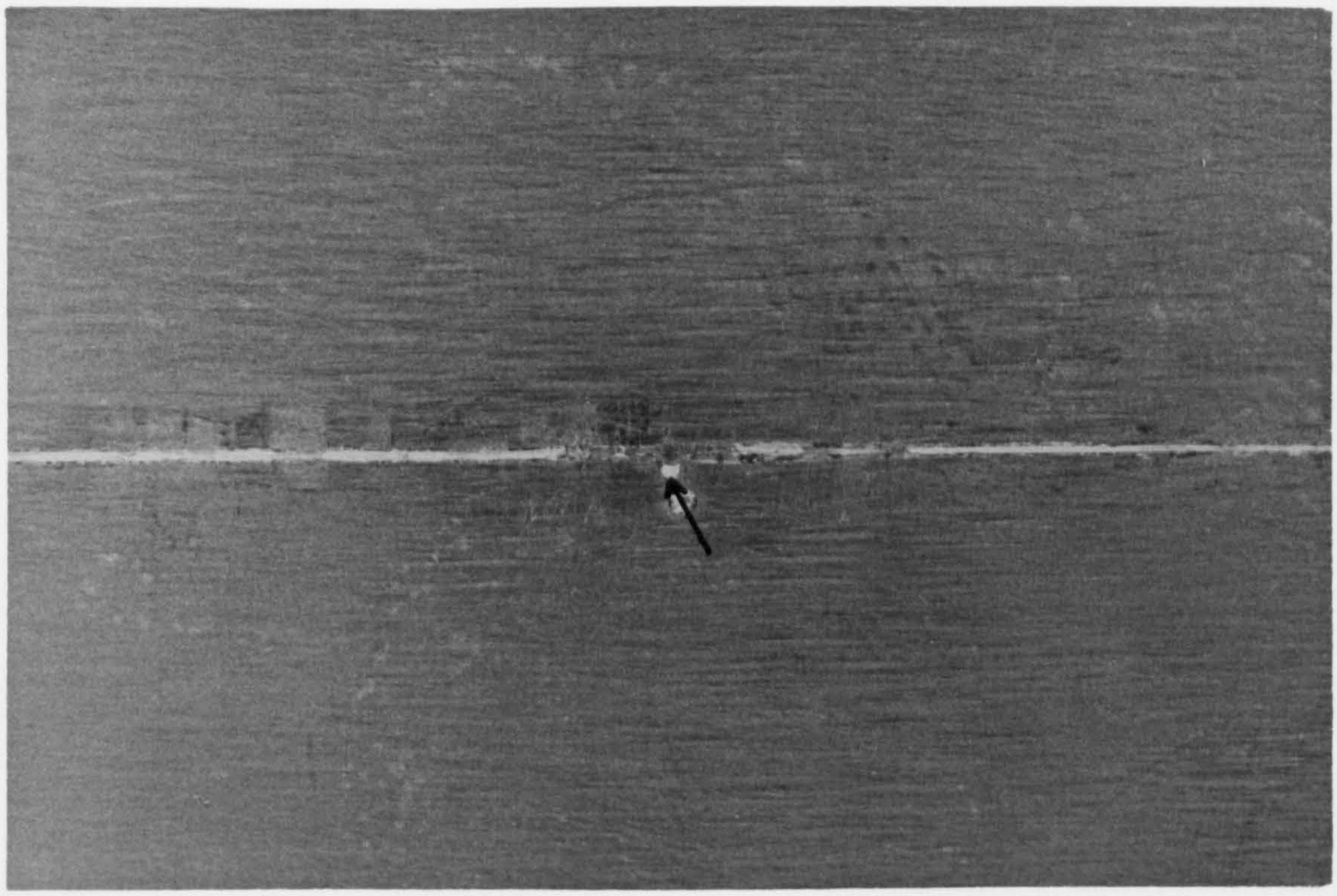

Fig. 3.20

Location of surface thermocouple bead in specimen for comparative measurements.

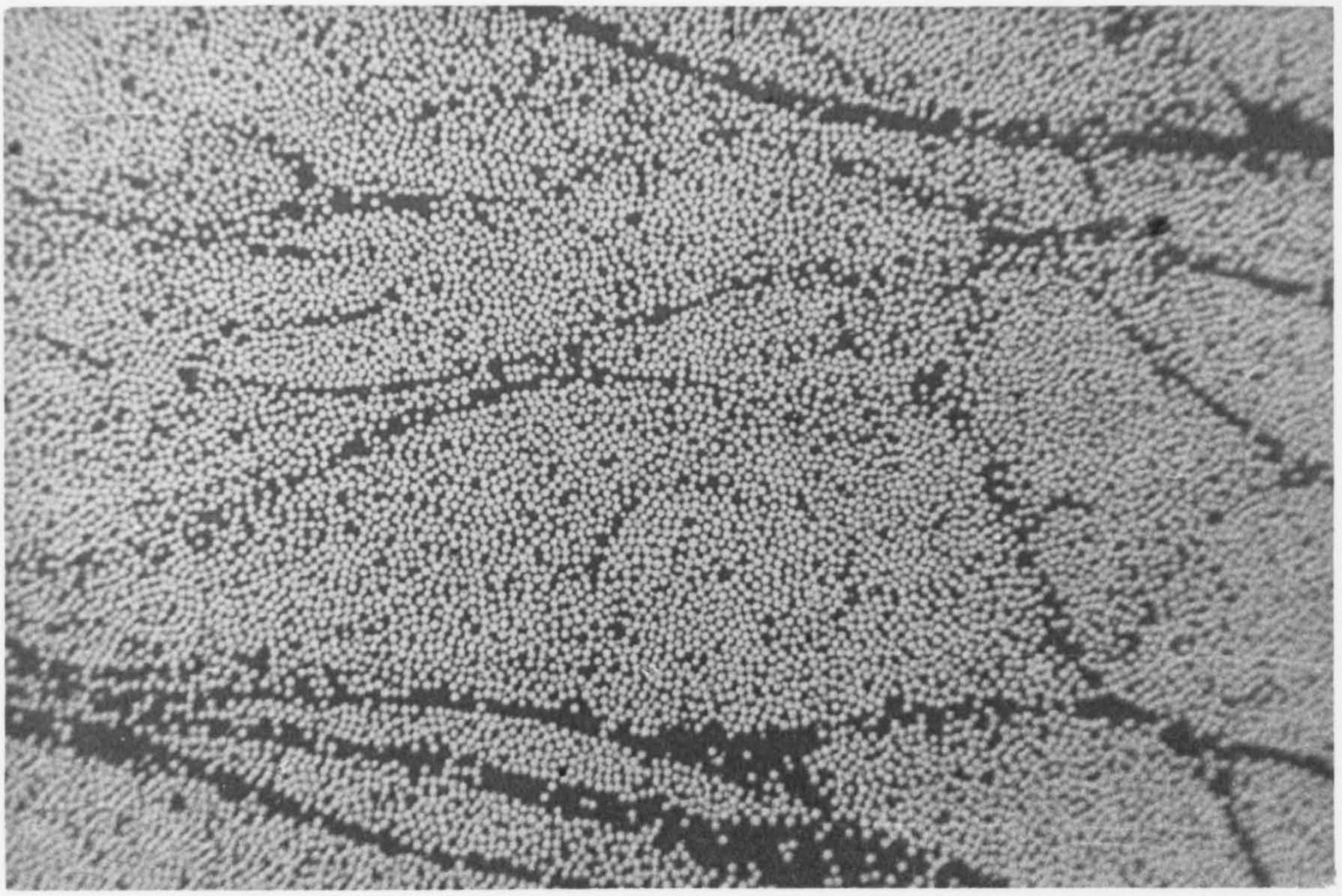

Fig. 3.21

Low magnification section of composite from large square mould.

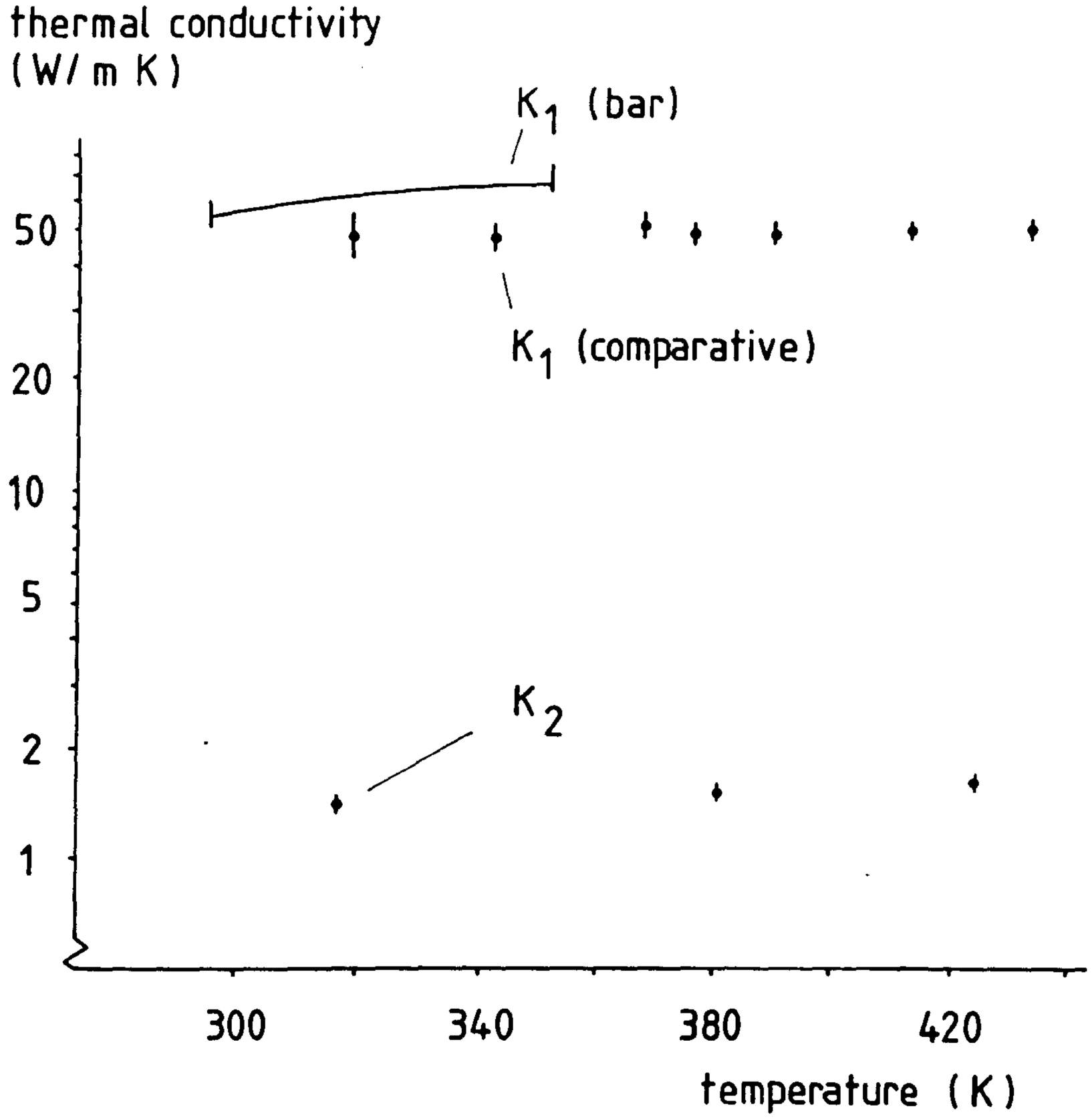

Fig. 3.22

Measured principal thermal conductivities in unidirectional cfrp specimens.

longitudinal value was approximately three times that of the Inconel reference. On the same figure is shown the smooth curve representing measurements of K_1 on the bar specimens (Fig. 3.11).

It will be seen that the conductivity from the comparative apparatus is about 13% lower in the temperature range 20-80°C; moreover the values increase only slightly with temperature. The former discrepancy may be accounted for by the fact that the bar specimen contained a higher volume fraction of carbon fibre than the slab specimen. Since the conductivity in the longitudinal direction is dominated by the fibre, a change in volume fraction of $\Delta\phi$ gives rise to a fractional change in conductivity of $\Delta\phi/\phi$. As reported above, the difference in volume fraction of the two specimens was about 5%, giving an 8% lower conductivity in the slab specimen. Adjusting the measured conductivity of the bar specimen gives a value of about 51 W/m K at 20°C, which is in good agreement with the comparative measurements.

The discrepancy in the temperature-dependence of the two sets of K_1 remains, however. The values obtained from the bar specimen are more consistent with published data for this type of composite (Fig. 2.11) and also with the temperature dependence of the thermal conductivity of carbon fibres (Fig. 2.12). Calculations to be presented in Chapter 7 indicate that these differences have a negligible effect on steady-state temperature distributions up to about 80°C, but the data may require clarification for transient applications at higher temperatures. As pointed out in Chapter 2, there have been very few studies of thermal conductivity at elevated temperatures; this is probably due to the service limitations imposed on most resin systems. For this reason, extrapolation of data obtained below ambient temperatures may be unreliable, and this area will require more experimental work in the future.

The measurements of transverse thermal conductivity (K_2) are consistent both in magnitude and temperature dependence with published values. At room temperatures, the value of the anisotropy ratio ($\gamma^2 = K_1/K_2$) is 35.

CHAPTER 4 : ANISOTROPIC HEAT CONDUCTION - THEORY AND SOLUTIONS

This chapter is concerned with the theoretical aspects of heat conduction in anisotropic solids. It is intended to establish the mathematical basis of the problem as a prelude to the development of the numerical model described in Chapter 5. Published analytic solutions are reviewed before considering the range of approximate numerical methods which have been applied to anisotropic problems. Finally, the advantages of the finite element technique as the basis for a generalised numerical model are discussed.

The theory reviewed in the first sections of this chapter is taken largely from Carslaw and Jaeger (1959) and from Ozisik (1980). Before the widespread use of modern composite materials, the most important anisotropic substances were crystals; the text by Nye (1957) provides an extensive review of their physical properties, and includes the essential mathematics of tensors and the transformation of coordinate axes.

4.1 FUNDAMENTAL EQUATIONS

4.1.1 Heat Flux and Thermal Conductivity in Anisotropic Solids

Fourier's Law for the conduction of heat in an isotropic medium relates the heat flux vector and the temperature gradient by a scalar thermal conductivity:

$$\underline{q} = - k \underline{\nabla} T \qquad (4.1)$$

The generalisation necessary in the case of anisotropic solids is that each component of the flux vector at a given point is a linear function of the components of the temperature gradient at that point. In the cartesian coordinate system:

$$-q_x = k_{11}\frac{\partial T}{\partial x} + k_{12}\frac{\partial T}{\partial y} + k_{13}\frac{\partial T}{\partial z}$$

$$-q_y = k_{21}\frac{\partial T}{\partial x} + k_{22}\frac{\partial T}{\partial y} + k_{23}\frac{\partial T}{\partial z}$$

$$-q_z = k_{31}\frac{\partial T}{\partial x} + k_{32}\frac{\partial T}{\partial y} + k_{33}\frac{\partial T}{\partial z} \qquad (4.2)$$

It follows that the heat flux vector in an anisotropic solid is not necessarily parallel to the temperature gradient. The single thermal conductivity of the isotropic material is replaced by nine conductivity coefficients k_{ij}; these are the components of a second order tensor

$$\bar{k} = \begin{pmatrix} k_{11} & k_{12} & k_{13} \\ k_{21} & k_{22} & k_{23} \\ k_{31} & k_{32} & k_{33} \end{pmatrix} \qquad (4.3)$$

Equations having the form of 4.2, which postulate a linear relationship between "rates" (e.g. flow of heat) and "affinities" (e.g. temperature gradient), are known as phenomenological relations. The coefficients k_{ij} $(i \neq j)$ describe the "interference" of two irreversible processes; in the case of thermal conduction these processes correspond to heat flux and temperature gradient in mutually perpendicular directions. The Onsager reciprocity relations state that $k_{ij} = k_{ji}$ $(i \neq j)$, and may be derived from a consideration of microscopic reversibility (Prigogine, 1967). These relations reduce the number of independent coefficients in Equation 4.3 from nine to six.

Writing the entropy production rate as the product of heat flux and temperature gradient gives, in two dimensions

$$\frac{dS}{dt} = k_{11}\left(\frac{\partial T}{\partial x}\right)^2 + 2k_{12}\,\frac{\partial T}{\partial x}\cdot\frac{\partial T}{\partial y} + k_{22}\left(\frac{\partial T}{\partial y}\right)^2$$

The second law of thermodynamics requires this quantity to be positive; the resulting constraints on the conductivity coefficients are (Prigogine, 1967)

$$k_{11} > 0, \quad k_{22} > 0 \quad \text{and} \quad k_{12}^2 < k_{11}k_{22}$$

Many anisotropic materials, including the majority of crystals, have some characteristic symmetry, and if the coordinate axes are chosen in appropriate directions, the form of the thermal conductivity tensor may be considerably simplified. An example is the monoclinic crystal, which has either a plane of reflection symmetry or a diad (two-fold rotation) axis (such that rotation by 180^{o} about the axis produces congruence). If the z-axis is chosen either as the diad axis or normal to the plane of reflection symmetry then the conductivity tensor may be written

$$\bar{k} = \begin{pmatrix} k_{11} & k_{12} & 0 \\ k_{21} & k_{22} & 0 \\ 0 & 0 & k_{33} \end{pmatrix} \tag{4.4}$$

Probably the most important class of anisotropic material is the orthotropic solid, which has different thermal conductivities in three mutually perpendicular directions (see Fig. 1.1). When the cartesian coordinate axes are chosen to coincide with these directions, the conductivity tensor has the form

$$\bar{k} = \begin{pmatrix} K_1 & 0 & 0 \\ 0 & K_2 & 0 \\ 0 & 0 & K_3 \end{pmatrix} \tag{4.5}$$

Wood, for example, is an orthotropic material in the cylindrical coordinate system, having different thermal conductivities in the directions r, θ and z (corresponding to the rays, rings and axis of the tree).

4.1.2 Differential Equation of Heat Conduction

The differential equation describing the conduction of heat is derived by considering the energy balance on an elemental volume within a continuum. Conservation of energy requires that

$$\text{div } \underline{q} + \rho C_p \frac{\partial T}{\partial t} = \dot{g} \tag{4.6}$$

where the second term represents the change in internal energy and the right hand side is a generation term. Using

the expressions given in Equation 4.2 for the heat flux in an anisotropic solid, the resulting differential equation is

$$k_{11}\frac{\partial^2 T}{\partial x^2} + k_{22}\frac{\partial^2 T}{\partial y^2} + k_{33}\frac{\partial^2 T}{\partial z^2} + 2k_{12}\frac{\partial^2 T}{\partial x \partial y} + 2k_{13}\frac{\partial^2 T}{\partial x \partial z}$$

$$+ 2k_{23}\frac{\partial^2 T}{\partial y \partial z} + \dot{g}(x, y, z, t) = \rho C_p \frac{\partial T}{\partial t} \qquad (4.7a)$$

In two dimensions, the temperature does not vary with the z-coordinate, so the differential equation becomes

$$k_{11}\frac{\partial^2 T}{\partial x^2} + k_{22}\frac{\partial^2 T}{\partial y^2} + 2k_{12}\frac{\partial^2 T}{\partial x \partial y} + \dot{g}(x,y,t) = \rho C_p \frac{\partial T}{\partial t} \qquad (4.7b)$$

Equations 4.7 have been obtained by assuming that the conductivity coefficients are independent of position, so that terms like $\frac{\partial k_{11}}{\partial x}$ etc. are zero. This condition is not imposed in the formulation of the finite element model (Chapter 5).

These Equations have been derived for arbitrarily-orientated cartesian coordinate axes. A transformation to a new set of rectangular coordinates can be found (Carslaw and Jaeger 1959) which removes the cross-derivatives of the space variables. The resulting differential equation is

$$K_1\frac{\partial^2 T}{\partial X} + K_2\frac{\partial^2 T}{\partial Y} + K_3\frac{\partial^2 T}{\partial Z} + \dot{g} = \rho C_p \frac{\partial T}{\partial t} \qquad (4.8)$$

The new axes X, Y, Z are known as the principal axes of conductivity, and K_1, K_2 and K_3 are the principal conductivities; these correspond to the axes of material symmetry referred to in 4.1.1. A further transformation may be made which reduces Equation 4.8 to an isotropic form:

$$\frac{K}{\rho C}\left(\frac{\partial^2 T}{\partial X_1} + \frac{\partial^2 T}{\partial Y_1} + \frac{\partial^2 T}{\partial Z_1}\right) + \dot{g} = \rho C \frac{\partial T}{\partial t} \qquad (4.9)$$

where K is a reference conductivity such that

$$X_1 = \sqrt{\frac{K}{K_1}}X, \quad Y_1 = \sqrt{\frac{K}{K_2}}Y \quad \text{and} \quad Z_1 = \sqrt{\frac{K}{K_3}}Z$$

Poon and Chang (1978) adopted this technique of transforming problems from anisotropic to isotropic in order to facilitate the mathematical solution of the differential equation (see

4.2.1). In practice, the method is of use only in solids of infinite or semi-infinite extent, or when bounded by planes perpendicular to the principal axes of conductivity. In more general problems the boundaries are distorted by application of the transformation, and the boundary conditions become intractable.

4.1.3 Transformation of Axes

In view of the dependence of the thermal conductivity tensor on orientation of axes and material symmetry, it is necessary to be able to relate the conductivity coefficients in any two rectangular coordinate systems.

Consider the cartesian axes Ox, Oy, Oz, in which the conductivity coefficients are k_{ij} (see Fig. 4.1). A new set of axes Ox', Oy', Oz' are defined by direction cosines c_{ij}, where the first subscript refers to the old axes, and the second subscript to the new. For example, c_{13} is the cosine of the angle between Ox and Oz'; c_{22} is the cosine of the angle between Oy and Oy'. As shown by Nye (1957) and by Ozisik (1980), the coefficients in the 'new' coordinate system are given by

$$k'_{ij} = \sum_{r=1}^{3} \sum_{s=1}^{3} c_{ri}\, c_{sj}\, k_{rs} \qquad (4.10)$$

while the inverse relationship ('old' in terms of 'new') is

$$k_{rs} = \sum_{i=1}^{3} \sum_{j=1}^{3} c_{ri}\, c_{sj}\, k'_{ij} \qquad (4.11)$$

However, not all the c_{ij}'s (nine in total) are independent; this arises from the orthogonality relations, which may be written in a single equation as

$$\sum_{k=1}^{3} c_{ik}\, c_{jk} = \delta_{ij} \qquad (4.12)$$

$$\text{where } \delta_{ij} = \begin{cases} 1 , & i = j \\ 0 , & i \neq j \end{cases}$$

Equation 4.12 defines six independent relations between the nine direction cosines, so that only three independent quantities are needed to define the transformation. For

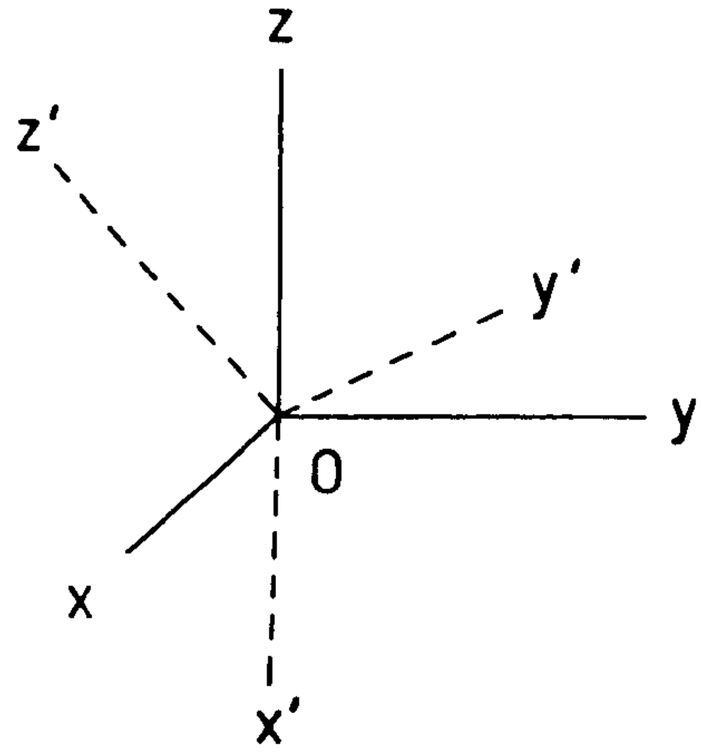

Fig. 4.1

Three-dimensional cartesian axes.

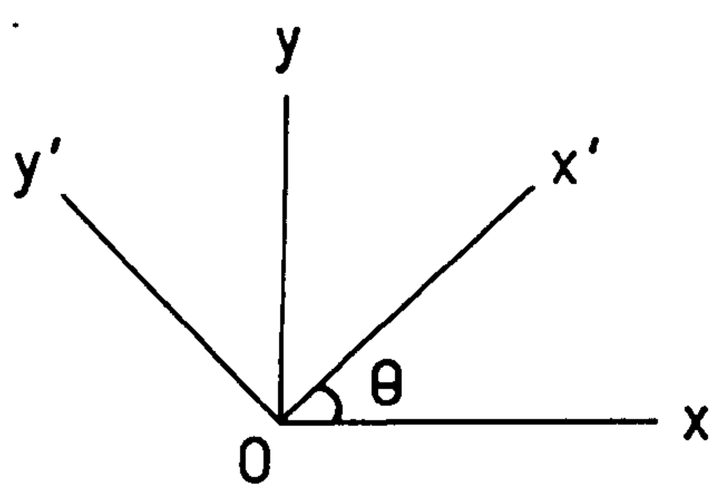

Fig. 4.2

Two dimensional cartesian axes Ox', Oy' after rotation through angle θ.

example, defining the direction of the Ox' axis requires two direction cosines, and automatically fixes the plane in which Oy' and Oz' will lie. The Oy' direction may then be defined by means of a third direction cosine, which simultaneously fixes the Oz' axis (Jaeger, 1966).

A transformation which will be used frequently in later chapters is that for rotation of the two-dimensional cartesian axes, in order to relate the three independent conductivity coefficients k_{11}, k_{12}, k_{22} to the principal conductivities of the orthotropic solid (K_1, K_2). Fig. 4.2 shows the 'new' axes Ox', Oy' corresponding to the principal axes, such that $k'_{11} = K_1$, $k'_{22} = K_2$ and $k'_{12} = 0$. These axes are rotated by angle θ with respect to the 'old' axes Ox, Oy, and the direction cosines are therefore

$$c_{11} = \cos\theta, \quad c_{12} = -\sin\theta, \quad c_{21} = \sin\theta, \quad c_{22} = \cos\theta.$$

Writing Equation 4.11 explicitly in two dimensions,

$$\begin{aligned} k_{rs} = {} & c_{r1}(c_{s1}k'_{11} + c_{s2}k'_{12}) \\ & + c_{r2}(c_{s1}k'_{21} + c_{s2}k'_{22}) \end{aligned}$$

from which

$$\begin{aligned} k_{11} &= K_1\cos^2\theta + K_2\sin^2\theta \\ k_{22} &= K_1\sin^2\theta + K_2\cos^2\theta \\ k_{12} &= (K_1 - K_2)\sin\theta\cos\theta \end{aligned} \tag{4.13}$$

It is useful to express the inverse problem in a convenient form, namely to calculate the principal conductivities and the orientation of the principal axes given values of k_{11}, k_{12} and k_{22}. Ozisik (1980) shows that (in three dimensions) the principal conductivities are the eigenvalues of the equation

$$\begin{vmatrix} k_{11} - K & k_{12} & k_{13} \\ k_{12} & k_{22} - K & k_{23} \\ k_{13} & k_{23} & k_{33} - K \end{vmatrix} = 0$$

In two dimensions this becomes

$$(k_{11} - K)(k_{22} - K) - k_{12}^2 = 0$$

whence $K = \frac{1}{2}(k_{11} + k_{22}) \pm \frac{1}{2}\sqrt{(k_{11} + k_{22})^2 - 4(k_{11}k_{22} - k_{12}^2)}$

The principal conductivities may therefore be written

$$K_1 = \frac{1}{2}(k_{11} + k_{22} + \sqrt{(k_{11} - k_{22})^2 + 4k_{12}^2})$$

$$K_2 = \frac{1}{2}(k_{11} + k_{22} - \sqrt{(k_{11} - k_{22})^2 + 4k_{12}^2}) \qquad (4.14a)$$

with the angle between the appropriate axes given by

$$k_{12} = (K_1 - K_2) \sin\theta \cos\theta$$

or

$$\theta = \frac{1}{2} \sin^{-1}\left(\frac{2k_{12}}{\sqrt{(k_{11} - k_{22})^2 + 4k_{12}^2}} \right) \qquad (4.14b)$$

4.1.4 Boundary Conditions

The generalised linear boundary condition for the heat conduction equation in an isotropic solid may be written

$$\delta\, k\frac{\partial T}{\partial n} + hT = f \quad \text{on the boundary surface S} \qquad (4.15)$$

Here, n is the direction of the outward-drawn normal at the surface, and f may be a function of position and/or time. By setting $\delta = 0$ a boundary condition of the first kind (prescribed temperature) is obtained; if $h = 0$, then the boundary condition is of the second kind (prescribed heat flux). With both δ and h non-zero, the boundary condition is said to be of the third kind, and represents a surface dissipating heat by convection. When the function f is zero, the boundary condition is said to be homogeneous. Nonlinear boundary conditions (for example radiation) involve a power of temperature in one or more of the terms of Equation 4.15.

For the anisotropic solid, the term $k\frac{\partial T}{\partial n}$ (where $\frac{\partial T}{\partial n}$ is the temperature gradient along the outward-drawn normal at the surface S) no longer represents the heat flux at the surface, since the heat flux vector is not necessarily parallel to the temperature gradient. A boundary condition of the second or third kind must therefore incorporate the expressions for the generalised flux (Equations 4.2). Consider, for example,

an insulated surface perpendicular to the x-axis. The condition for no heat flux across this boundary ($q_x = 0$) would be

$$k_{11}\frac{\partial T}{\partial x} + k_{12}\frac{\partial T}{\partial y} + k_{13}\frac{\partial T}{\partial z} = 0$$

which may be written more conveniently as

$$k_{11}\frac{\partial T}{\partial n^*} = 0$$

where $\frac{\partial}{\partial n^*} \equiv \frac{\partial}{\partial x} + \varepsilon_{12}\frac{\partial}{\partial y} + \varepsilon_{22}\frac{\partial}{\partial z}$

and $\varepsilon_{ij} = k_{ij}/k_{11}$.

4.2 SOLUTIONS TO ANISOTROPIC HEAT CONDUCTION PROBLEMS

It has already been mentioned that the presence of cross derivatives of the space variables in the anisotropic heat conduction Equation 4.7 leads to complications in the mathematical solution of boundary value problems. Although the equation may be reduced to an isotropic form by coordinate transformation, the generalised boundary becomes distorted, leaving the problem no nearer a solution. Analytic solutions may be found, however, when the region of interest is of infinite or semi-infinite extent, or when the boundaries are parallel to the coordinate axes. As will be discussed later, the two-dimensional disc is a special case, since certain problems which are anisotropic in cartesian coordinates may be transformed into equivalent orthotropic problems in circular polar coordinates; rotation of the cartesian axes produces no change in the shape of the boundary.

The solution of anisotropic heat conduction problems which may be relevant to the thermal behaviour of engineering components will usually require the use of numerical modelling techniques. Nevertheless, mathematical analyses have two important functions:

i) Analytic solutions may be used to test the validity of a numerical solution technique, and enable experience to be gained concerning its accuracy and efficiency.

ii) At least an approximate mathematical analysis (for example, using an idealised geometry) should always precede the detailed application of a numerical model, particularly when the latter may require large amounts of computer time. This often gives an initial insight into the problem, and increases the efficiency with which, for example, the most appropriate finite element mesh may be obtained.

The following section reviews published treatments of anisotropic heat conduction problems; solutions and techniques which have particular relevance to the development and validation of the generalised finite element model presented in this thesis are considered in greater detail in 4.2.3 to 4.2.6. It has proved impossible to draw a clear distinction between 'analytical' and 'numerical' approaches to boundary value problems - many publications combine a number of solution techniques in order to solve particular problems.

4.2.1 General Review - Analytical Solutions

Padovan (1972) used successive integral transforms and subsequent numerical integration to obtain the temperature distribution in thin-walled bodies of revolution. A similar technique was applied to an anisotropic half-space ($|x|<\infty$, $o<y<\infty$) with a generalised boundary condition at $y = 0$ (Padovan, 1973). The effects of various material properties were demonstrated by imposing a boundary condition of the first kind, namely $T = T_o$, $|x|<L$; $T = 0$, $|x|>L$. Both the technique and the solution are comparable to those given by Ozisik (1980). Padovan (1975b) later developed solutions for the transient temperature distribution in laminated composite slabs and cylinders, composed of any number of distinct, fully anisotropic layers. Each layer of the slab was of infinite length. The solution appears in the form of a complex Fourier series. Previously (Padovan, 1975a) the author illustrated the solution for a three-layer, rectangular laminate, with material properties resembling a fibre-reinforced composite.

Padovan (1974a) also investigated steady-state problems in linear and nonlinear media by a finite element approximation, and results for a laminated slab and cylinder with fixed temperature boundaries were compared with semi-analytic solutions (Padovan, 1974b); this technique avoids the necessity of having to solve a global heat transfer problem when, for example, the temperature is required only at a few points within a given configuration.

Poon (1979) extended the coordinate transformations discussed in 4.1.2 as defined by Poon and Chang (1978) to a general case of layered composite cylinders and plane laminates of anisotropic materials. Poon and others (1979) synthesised several earlier publications and found that the general transformation in circular cylindrical coordinates is only successful for two-dimensional anisotropy, unless $\varepsilon_{23} - \varepsilon_{12}\varepsilon_{13} = 0$ (where $\varepsilon_{ij} = k_{ij}/k_{11}$). This conclusion is in agreement with the work of Ozisik and Shouman (1980), which will be referred to later. The former authors applied their solutions to two specific problems - a ring heat source moving over the surface of an infinite solid cylinder, and steady-state conduction in a rotating solid cylinder.

Turhan and Tuna (1975) presented an approximate heat conduction theory for multilayered cylindrical composites, by replacing the system of discrete cylindrical shells with a homogeneous continuum. The theory was adapted to the case of plane, laminated composites.

Edwards (1980) derived an analytic solution to the problem of heat conduction in a hollow cylinder with anisotropic thermal properties (k_r, k_θ, k_z) and a non-uniform radiation boundary condition at the outer surface - a case which arises in carbon fibre-reinforced booms on space vehicles. By linearising the radiation boundary conditions, and considering a long cylinder with $\partial T/\partial z = 0$, a series solution was obtained, which was used to predict areas of maximum and minimum heating.

Mulholland and Gupta (1975) applied coordinate transformations

to reduce the two-dimensional equation of steady-state conduction to Laplace's equation. The solution was expressed as a series of polynomial functions whose coefficients were determined from the prescribed boundary conditions. They demonstrated detailed solution procedures for a circular region with (i) prescribed surface temperature $T = T_o (1 + \cos\theta)$, and (ii) zero surface temperature and uniform internal heat generation. In a later publication (Mulholland and Gupta, 1977) the method was extended to three dimensions.

Laura and others (1979) discussed the use of conformal mapping techniques to transform certain two-dimensional shapes onto a unit circle. In theory, the method can yield an analytic solution, but in practice there are two important limitations. Firstly, the functional form of the mapping is known for only a few simple shapes (such as regular polygons), and secondly, the transformed boundary condition can often only be expressed in an approximate form. Results for thermally orthotropic square and octagonal plates were compared with a finite element solution with good agreement.

The complication of temperature-dependent thermal properties usually precludes any attempts at analytical solutions to transient anisotropic heat conduction problems. On the other hand, a direct numerical treatment in a three-dimensional domain may be prohibitively expensive. As an alternative, Murakami and others (1980) developed a continuum mixture theory for a periodic hexagonal array of circular fibres, which results in macroscopic diffusion equations in only one spatial variable. With typical values for thermal properties of graphite fibre/epoxy resin matrix, excellent agreement is found between their calculations and a so-called 'exact' solution of a transient problem by means of a finite element program.

Techniques based on the use of Green's functions (see 4.2.3) were employed by Chang and Tsou (1977a,b) and Chang (1977), and the authors were able to derive solutions in an analytic form. In the first two papers, general formulae

were obtained for Green's functions in cylindrical regions, and the results applied to example problems on an infinite solid cylinder with convective and fixed temperature boundaries. In the third paper, formal solutions were applied to regions in the cartesian coordinate system, including the 'half space' (bounded only by a single plane) and the infinite slab (bounded by two parallel planes). The solution for the latter configuration with prescribed temperature on the two boundaries, corresponds to that reported by Tauchert and Akoz (1975) and discussed in 4.2.5.

Wung and Tauchert (1981) obtained an analytic solution for the steady-state temperature distribution in a circular cylindrical vessel with hemispherical ends, having orthotropic thermal properties. This problem arose from a consideration of the use of composite materials in nuclear reactor pressure vessels. Both inner and outer surfaces were subject to convection, with ambient temperature varying axisymmetrically about the centreline of the vessel. Superimposition of solutions for three subproblems (corresponding to the sidewall and the two ends of the vessel) gave an analytic expression for the temperature distribution, although the associated eigenvalue problem requires some numerical computation. The authors verified their analytic solution by comparison with a finite element analysis, finding, in general, good agreement. The largest discrepancies were found in the hemispherical regions of the vessel, and this is explained by the fact that the finite element scheme used a constant angle to describe the principal directions of the orthotropic material in each element. (The model described in chapter 5 reduces this approximation by enabling the thermal conductivity to be specified at each of the four numerical integrating points in a quadratic element - see 5.10.)

Clements and Tauchert (1979) considered the two-dimensional steady-state temperature distribution in an anisotropic material bounded by two parallel planes. Mid-way between these planes, and parallel to them, was a crack of finite length. Boundary temperatures were prescribed along the

edges of the material, while either the heat flux across the crack was specified, or the temperature fixed on the crack surface. The problem is reduced to a pair of integral equations which are solved numerically for the temperature distribution. The geometry of this problem is similar to that discussed in 4.2.5.

Ozisik and Shouman (1980) used an integral transform technique to solve the problem of transient heat conduction in a three-dimensional cylindrical region of infinite length, having boundaries subject to convection into an environment at a specified temperature. The authors present tabulated results for a particular example, but it is not practicable to make direct comparison with the finite element model since they define material anisotropy with respect to the cylindrical coordinate system (their conductivity coefficients k_{ij} are not equivalent to those used in Equation 4.2).

Han (1982) developed a simplified calculation method to study the transient temperature distribution in unidirectional fibre-reinforced composites. He was concerned with heat transfer at the scale of the fibres at small values of time in response to a step change in heat flux or temperature, and considered a cylindrical 'unit cell' of a single fibre surrounded by the matrix. The two components had different thermal properties, but were assumed to be individually isotropic and uniform (this is not the case in, for example, carbon fibres, where the longitudinal thermal conductivity may be an order of magnitude greater than in the transverse direction). He compared the accuracy of his 'heat balance integral method' with exact or detailed finite difference solutions, and identified two significant parametric groups: the first was a transverse conductance, and the second was the thermal capacity ratio of the two materials.

4.2.2 General Review - Numerical Techniques

Katayama and others (1974) have discussed the use of the finite difference method in the solution of two-dimensional transient heat conduction problems in anisotropic solids. Before applying a mesh to the region of interest, they made

the transformation discussed in 4.1.2 to eliminate the cross-differential terms of Equation 4.7b, and the further transformation which yields the isotropic Equation 4.9. The shape of the original domain is thus distorted in response to the material anisotropy and a regular mesh is then fitted. The authors verify their numerical approach by experiments on a multi-crystalline carbon specimen, the extrusion of which had imparted anisotropic properties - the anisotropy ratio (K_1/K_2) was measured as 1.34 at room temperature. The experiment for numerical validation comprised a thin sheet of the material with a heat flow imposed along one edge. Time-varying temperatures were recorded at various locations in the two-dimensional plate, and agreed with numerical calculations to about ± 5%.

McWhorter and Sadd (1980) described the application of a boundary-fitted coordinate technique. The principal advantage of this method is that a coordinate system is generated (by numerical solution of elliptic partial differential equations) which transforms the original domain into a rectangular region, thus allowing simple finite-difference methods to be used to solve the (transformed) differential equation. A qualitative comparison was with solutions given by Chang and others (1973).

4.2.3 Steady State Anisotropic Disc (Chang and others, 1973)

The authors transformed the differential equation of heat conduction into integral equations by means of fundamental Green's functions and Green's second formula, which relates a volume integral to a surface integral. In this way a three-dimensional problem yields two-dimensional boundary-value equations, which require considerably less numerical effort for their solution than would the original differential equation. Similarly, a two-dimensional problem may be reduced to a one-dimensional integral, and the authors present the numerical technique for a region with a boundary condition of the first kind in both transient and steady-state. Fig. 4.3 reproduces calculated temperature distributions on a unit square and unit circle, which clearly demonstrate the effects of thermal anisotropy.

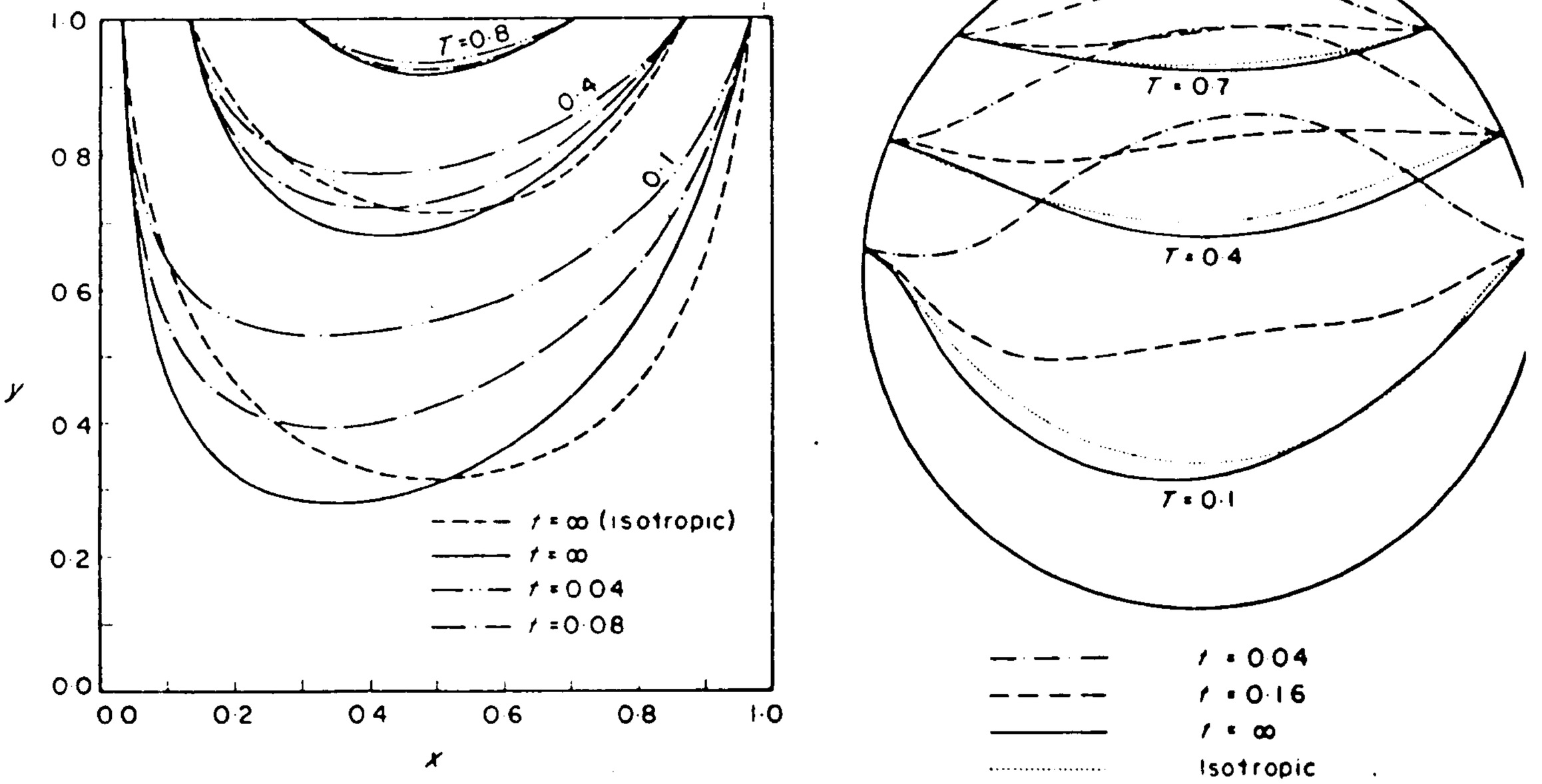

Fig. 4.3

Isotherms on unit square and unit circle (Chang and others, 1973).

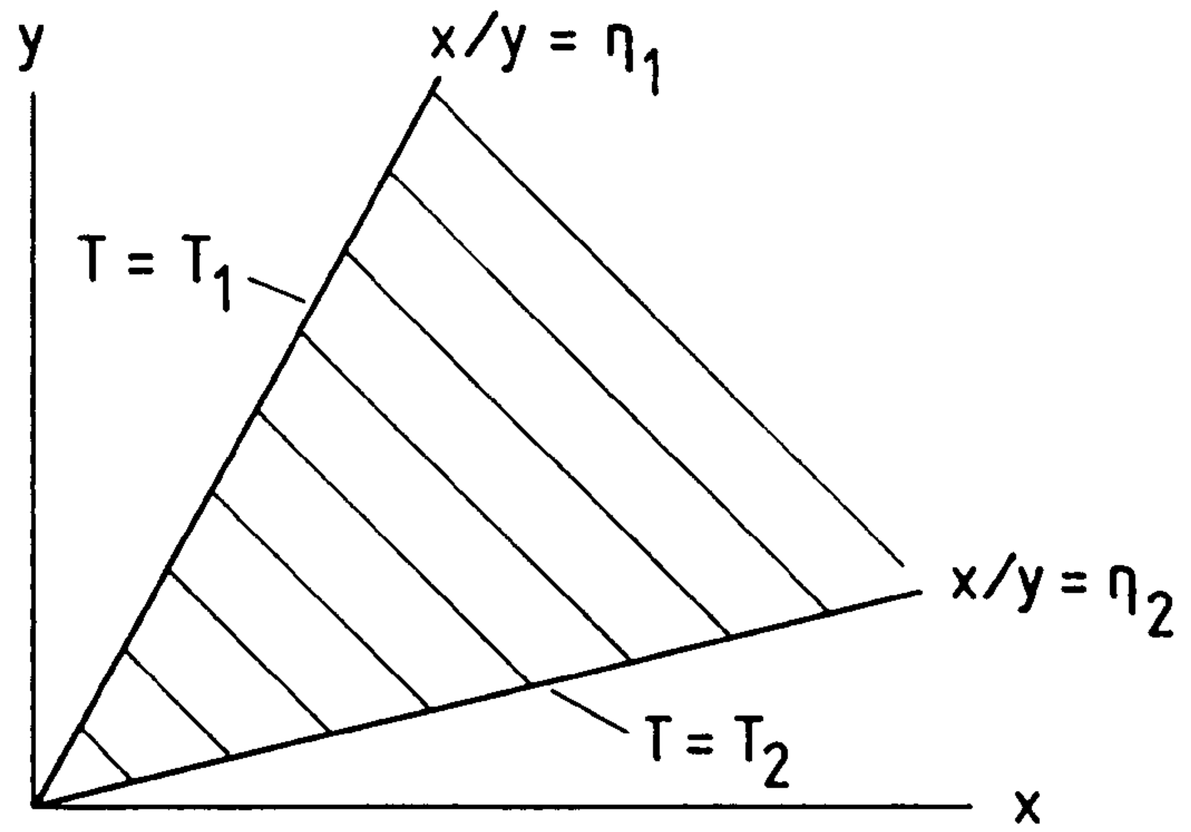

Fig. 4.4

Two-dimensional wedge region, edges defined by x/y = constant.

The authors draw attention to the somewhat surprising result that the temperature distribution on a circular disc of unit radius with the temperature on the boundary fixed by $T\ (r = 1, \theta) = a + b \cos \theta$ (where a and b are constants) is independent of the thermal conductivity. In fact, it is easily seen that the expression

$$T\ (r, \theta) = a + br \cos \theta$$

satisfies both the boundary condition and the differential equation of heat conduction for isotropic and anisotropic media. Since $r \cos \theta \equiv x$ in cartesian coordinates, temperature is independent of y, and the isotherms all lie parallel to the y-axis. This solution is shown in 6.2.2, where it is used in validation of the finite element model.

4.2.4 Steady-State Nonlinear Wedge (Cobble, 1974)

Fig. 4.4 shows a two dimensional wedge-shaped region, with fixed temperatures on the two edges. The thermal conductivity coefficients were allowed to be dependent on temperature, and it was assumed that the temperature distribution in the region could be written $T = T(\eta)$, where $\eta = x/y^n$. Substitution revealed that the differential equation was only satisfied if $n = 1$, so that $\eta \equiv x/y$, and the boundary conditions may be expressed as $T(\eta_1) = T_1$ and $T(\eta_2) = T_2$, where $x/y = \eta_1$ and $x/y = \eta_2$ define the two sides of the wedge. In the general nonlinear case, with $k_{ij} = k_{ij}(T)$, the differential equation was integrated to give

$$\frac{dT}{d\eta} = C_o \left[k_{11}(T) - \eta \{ k_{12}(T) + k_{21}(T) \} + \eta^2 k_{22}(T) \right]^{-1}$$

where C_o is a constant of integration. The author then considered the special case where $k_{ij} = k^o_{ij} \cdot F(T)$, and was thus able to integrate the above equation analytically. Taking $F(T) = 1 + \alpha T$, and letting $T(\eta_2) = T_2 = 0$, the solution is

$$T = \frac{1}{\alpha} (\sqrt{1 + 2\alpha\xi} - 1) \qquad (4.16)$$

where $$\xi = (T_1 + \frac{\alpha}{2} T_1^2) \left[1 - \frac{h(\eta) - h(\eta_1)}{h(\eta_2) - h(\eta_1)} \right]$$

and $$h(\eta) \equiv \arctan (A\eta + B)$$

The constants A and B depend on the 'reference' thermal conductivity coefficients (k^o_{ij}). In general,

$$A = \frac{k^o_{22}}{\sqrt{k^o_{22}\,k^o_{11} - k^{o\,2}_{12}}} \quad \text{and} \quad B = \frac{-\,k^o_{12}}{\sqrt{k^o_{22}\,k^o_{11} - k^{o\,2}_{12}}}$$

As a specific example, the author presents the calculated temperature distribution in a wedge defined by $\eta_1 = 0.1$ and $\eta_2 = 10$, with $T_1 = 100$, for three classes of anisotropic material:

(i) Isotropic - $k_{11} = k_{22} = 1 + 0.001T$; $k_{12} = 0$
(ii) Orthotropic - $k_{11} = 1 + 0.001T$; $k_{22} = 2 + 0.002T$; $k_{12} = 0$
(iii) Anisotropic - $k_{11} = k_{12} = 1 + 0.001T$; $k_{22} = 2 + 0.002T$

Fig. 4.5 shows the temperature distribution as a function of η for the three material types. The effect of the different material properties is more clear on a logarithmic scale (Fig. 4.6); here it can be seen that the anisotropic material (case iii) has a considerably steeper temperature gradient near the centre-line of the wedge. This can be shown to be intuitively correct by considering the material as orthotropic with principal axes parallel and perpendicular to the line $\eta = \eta_o$. Using Equations 4.14 it is found that $K_1 = 2.618$ and $K_2 = 0.382$, with the angle between $\eta = \eta_o$ and the x-axis being $\theta = 31.7^\circ$. Hence $\eta_o = \cot(31.7^\circ) = 1.62$; thus defining the principal axes. In an orthotropic material, the greatest temperature gradients will be found in the direction of lowest thermal conductivity, subject to the imposed boundary conditions. As a result, the isotherms in the anisotropic wedge are compressed away from the edges.

The temperature distributions obtained from Equation 4.16 have been plotted as isotherms in Fig. 4.7. In chapter 6, direct comparison will be made between the finite element model and the analytic solution.

4.2.5 Steady-State Anisotropic Slab (Tauchert and Akoz, 1975)

These authors considered the temperature and stress

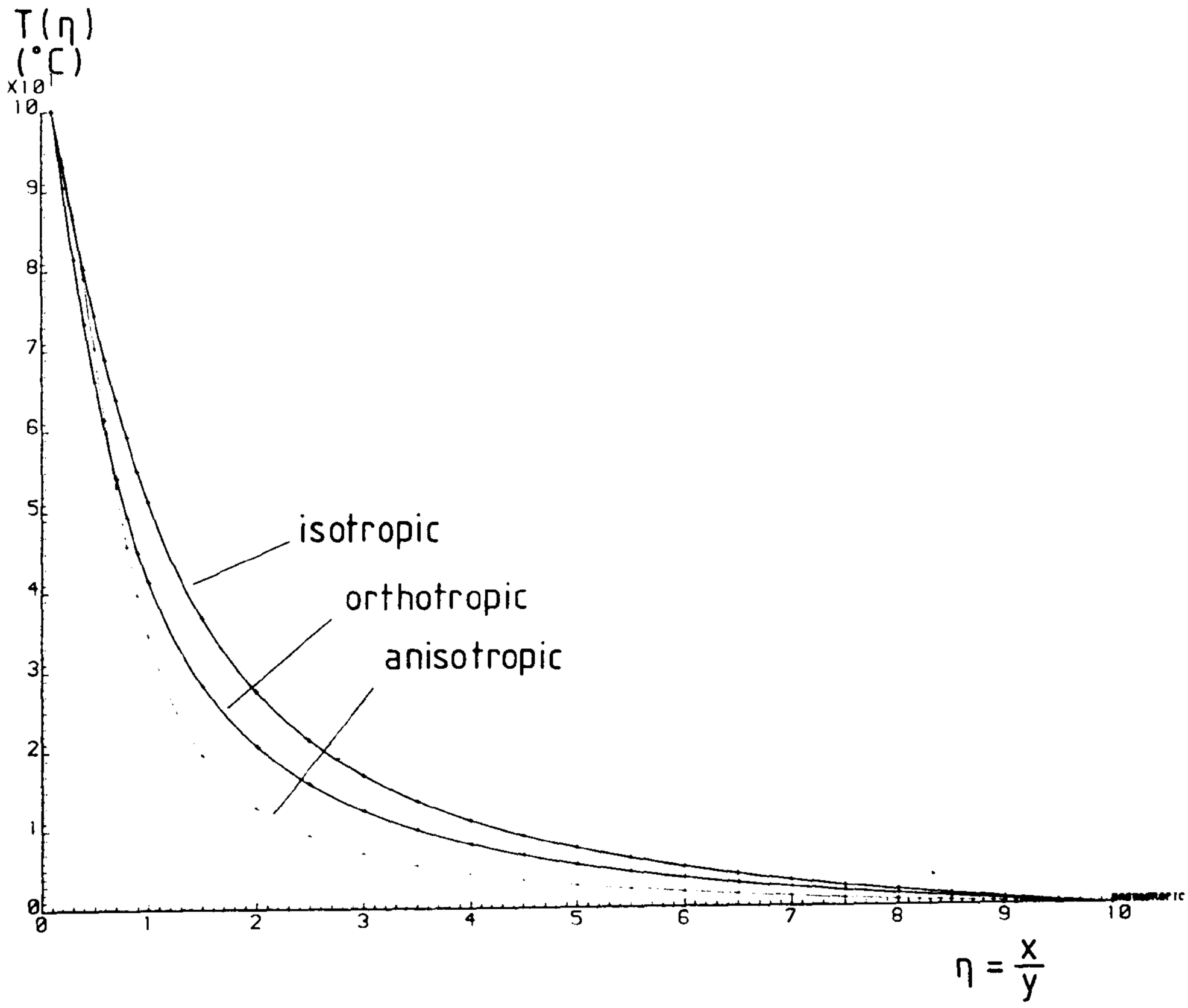

Fig. 4.5

Temperature distribution in wedge region, edges defined by $\eta_1 = 0.1$ and $\eta_2 = 10$.

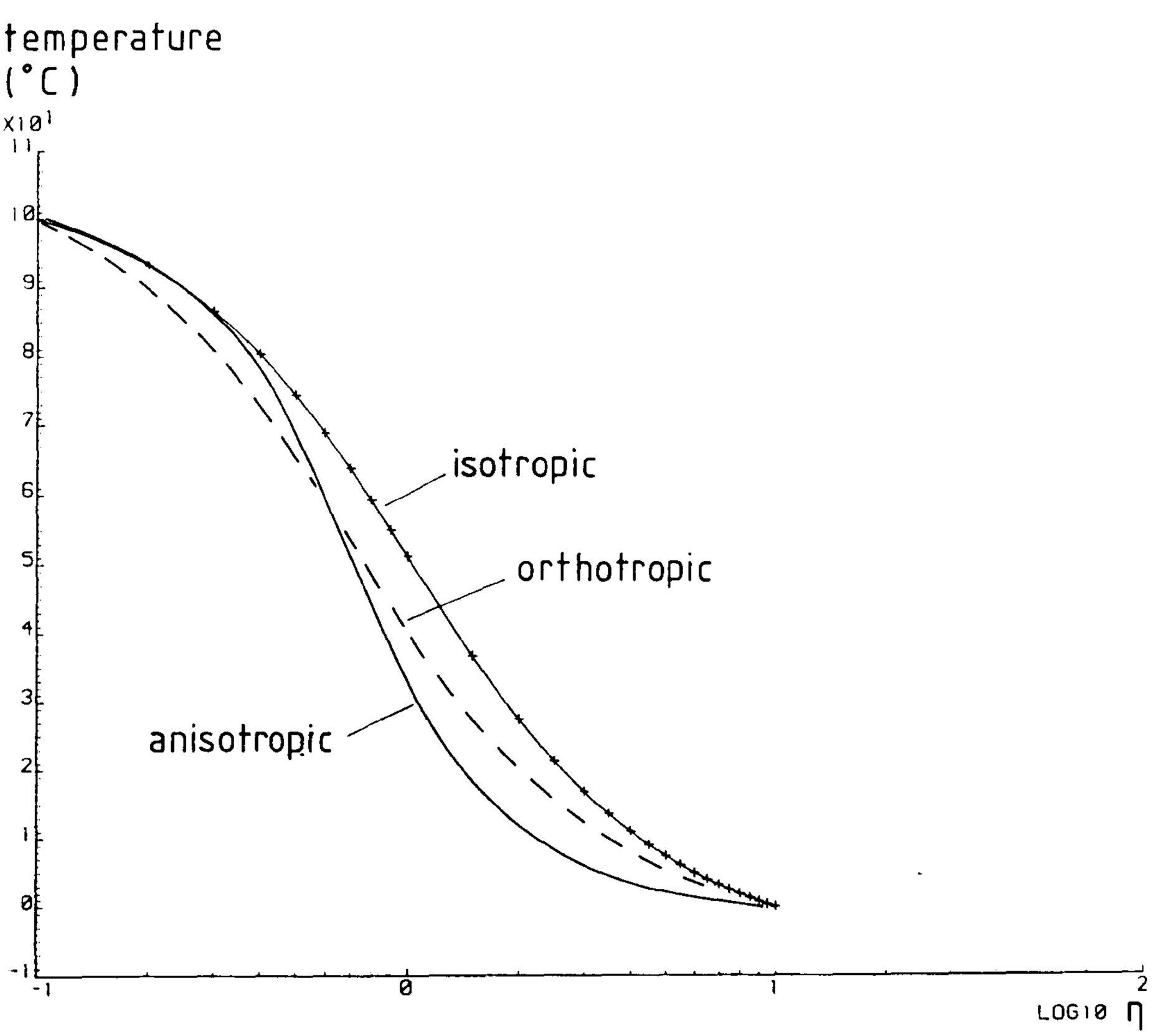

Fig. 4.6

As Fig. 4.5, with logarithmic scale for η.

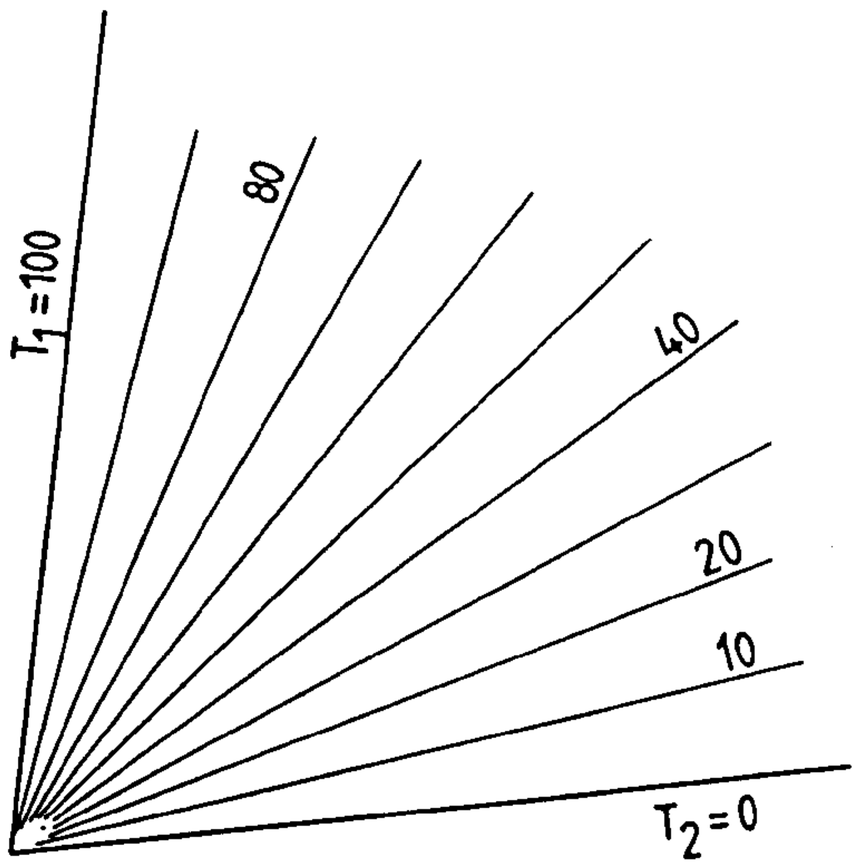

isotropic

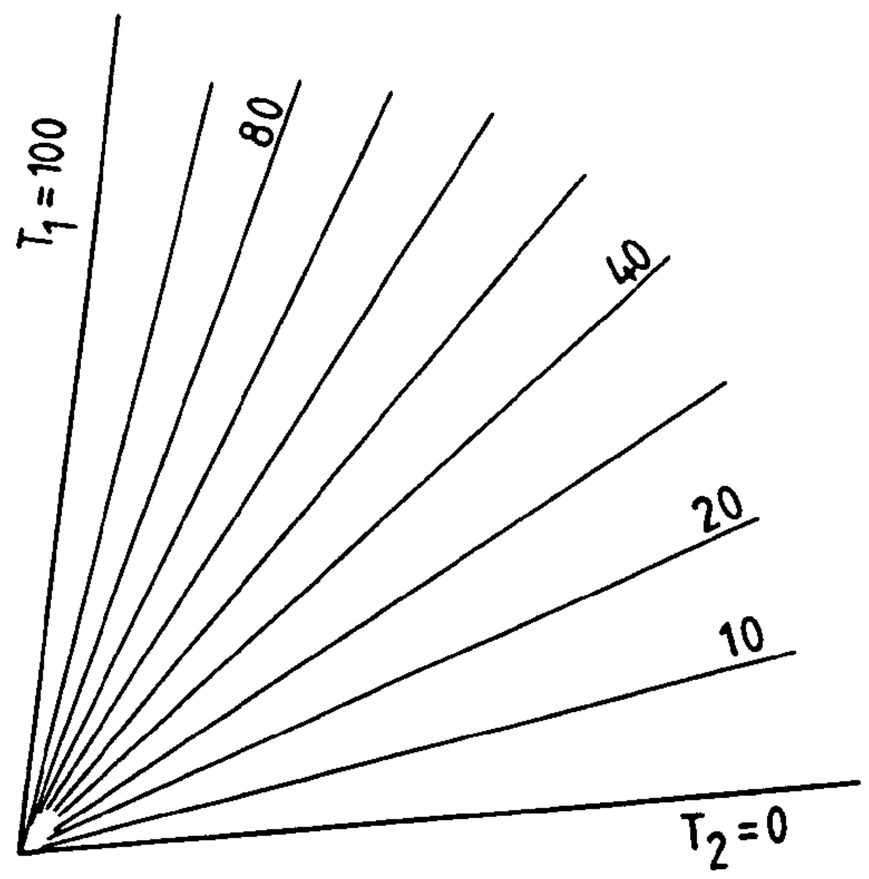

orthotropic

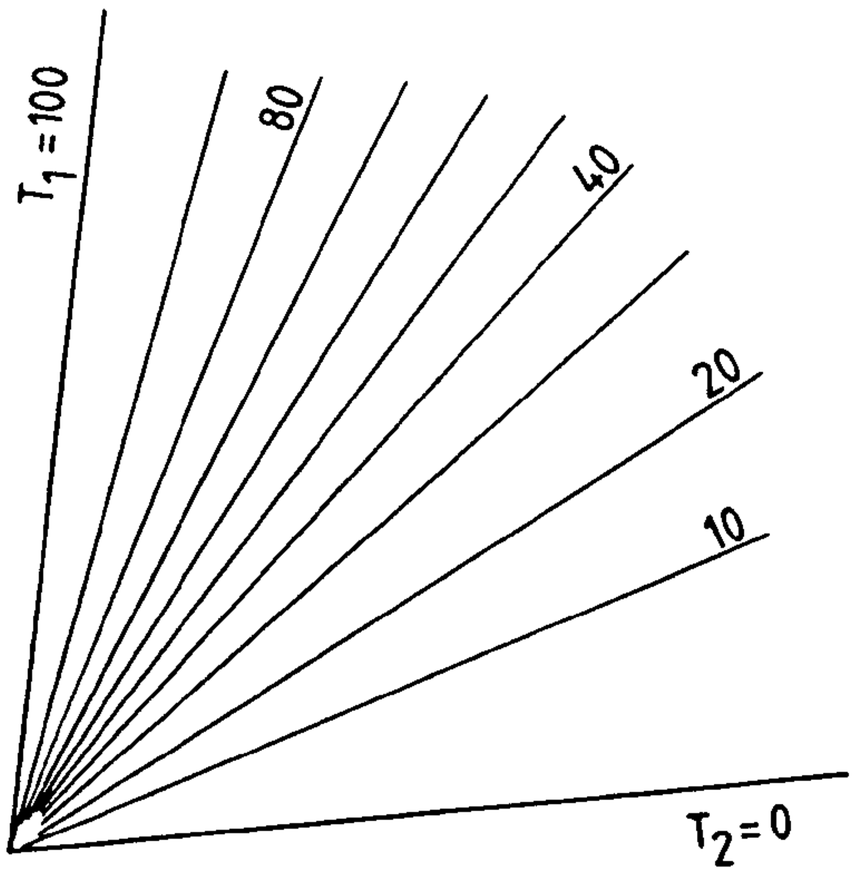

anisotropic

Fig. 4.7

Isotherms on the wedge region. Compared with the isotropic case, the orthotropic material has a greater temperature gradient near the edge at temperature T_1 (see Fig. 4.6).

distributions in an anisotropic slab, bounded by two parallel planes at $y = \pm h$ and extending to $x = \pm \infty$. An integral form of solution (which can be obtained by the application of the Fourier transform to the differential equation of heat conduction) was subjected to a generalised boundary condition, and, except in special cases, required numerical integration to obtain the temperature distribution. The authors completed the calculation for simple boundary conditions of the first kind, and considered the effects of different orthotropic material properties (with $K_1/K_2 = 1$, 10 and 100) on the temperature profile at $x = 0$. Finally, they showed the effect of the orientation of the principal axes for the material with $K_1/K_2 = 100$.

Fig. 4.8 shows the geometry of the region considered, with the generalised boundary conditions. If, as a special case, the temperature at the surface $y = -h$ is zero for all values of x, then the temperature distribution in the slab is given by

$$T(x,y) = \frac{1}{4bh} \int_{-\infty}^{\infty} \frac{f_1(\xi) \sin\frac{\pi}{2h}(y+h) \, d\xi}{\cosh\left[\frac{\pi(x-\xi)-a(y-h)}{2bh}\right] + \cos\frac{\pi}{2h}(y+h)} \qquad (4.17)$$

where $a = \frac{k_{12}}{k_{22}}$ and $b = \frac{k_{11}}{k_{22}} - a^2$

Depending on the form of the function f_1, Equation 4.17 may be integrated analytically. Fig. 4.9 reproduces the authors' results for the temperature profile at $x = 0$, for which they took

$$f_1(x) = \begin{cases} T_o, & |x| \leq h \\ 0, & |x| > h \end{cases}$$

Fig 4.9(a) shows the temperature gradient becoming rapidly steeper near the surface at $y = h$, as the relative thermal conductivity in the x-direction (K_1) increases. As the material takes up an orientation away from the 'orthotropic' position at 0° it can be seen in Fig. 4.9(b) that the temperature profile develops an inflection, as the region of greatest temperature gradient moves further from the hotter surface.

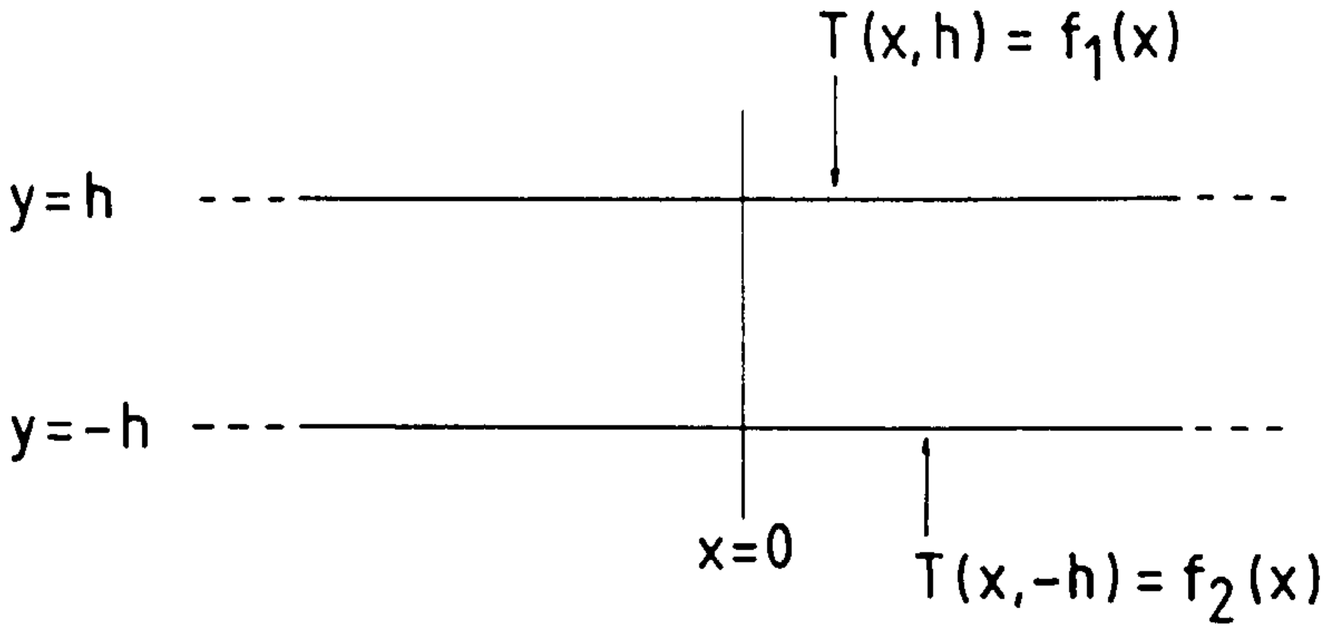

Fig. 4.8

Geometry of semi-infinite slab, with boundary conditions of the first kind.

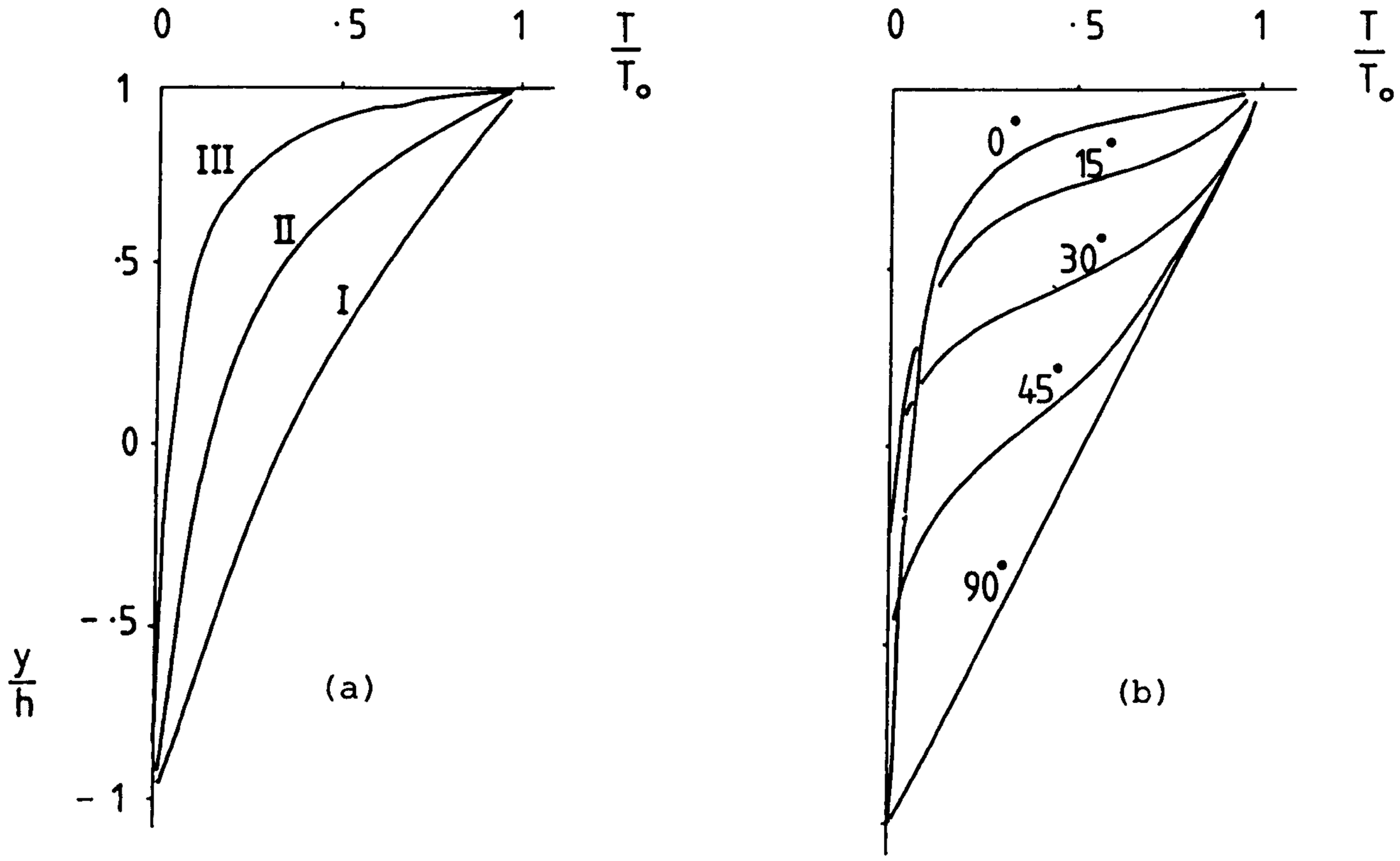

Fig. 4.9

Normalised temperature distribution at x = 0 on semi-infinite slab.

(a) Material I : isotropic
Material II : $K_1/K_2 = 10$
Material III: $K_1/K_2 = 100$

(b) Material III with principal axes at various orientations.

Clearer visualisation of the effect of directional thermal conductivity is provided in Fig. 4.10. Here the temperature along the surface at y = h is given by

$$f_1(x) = \begin{cases} \sin \frac{\pi}{2h} (x + h), & |x| \leqslant h \\ 0, & |x| > h \end{cases}$$

and contours of temperature have been plotted as in 4.2.4. The finite element solution of this problem is discussed in chapter 6.

4.2.6 Transient Anisotropic Half-Space (Ozisik, 1980)

The author's text on heat conduction contains a chapter dealing with anisotropic media, which includes analytical solutions for special cases of time-dependent heat transfer in semi-infinite regions. The favoured technique is the integral transform, which is used in order to remove (successively) the partial derivatives with respect to the space variables. In a time-dependent problem, this leaves a first order differential equation for the transform of the temperature as a function of time. This is subject to the transformed initial condition (that is, the temperature distribution at zero time), and the result is inverted (again successively) to yield a solution for the temperature as a function of the space variables and time.

The example on an anisotropic half space ($0 \leqslant x \leqslant \infty$, $-\infty \leqslant y \leqslant \infty$) has initial temperature $F(x,y)$ and the boundary at $x = 0$ subsequently held at zero temperature. The solution takes the form

$$T(x,y,t) = (4\pi\alpha_{11} t \sqrt{\varepsilon_{22} - \varepsilon_{12}^2})^{-1} \int_{x'=0}^{\infty} \int_{y'=-\infty}^{\infty} F(x',y') \cdot \exp\left(\frac{-[y-y' - \varepsilon_{12}(x-x')]^2}{4\alpha_{11}(\varepsilon_{22} - \varepsilon_{12}^2)t}\right) \left[\exp\left(\frac{-[x-x']^2}{4\alpha_{11}t}\right) - \exp\left(\frac{-[x+x']^2}{4\alpha_{11}t}\right)\right] dy'\, dx' \qquad (4.18)$$

where $\varepsilon_{ij} = \frac{k_{ij}}{k_{11}}$ and $\alpha_{11} = \frac{k_{11}}{\rho C_p}$.

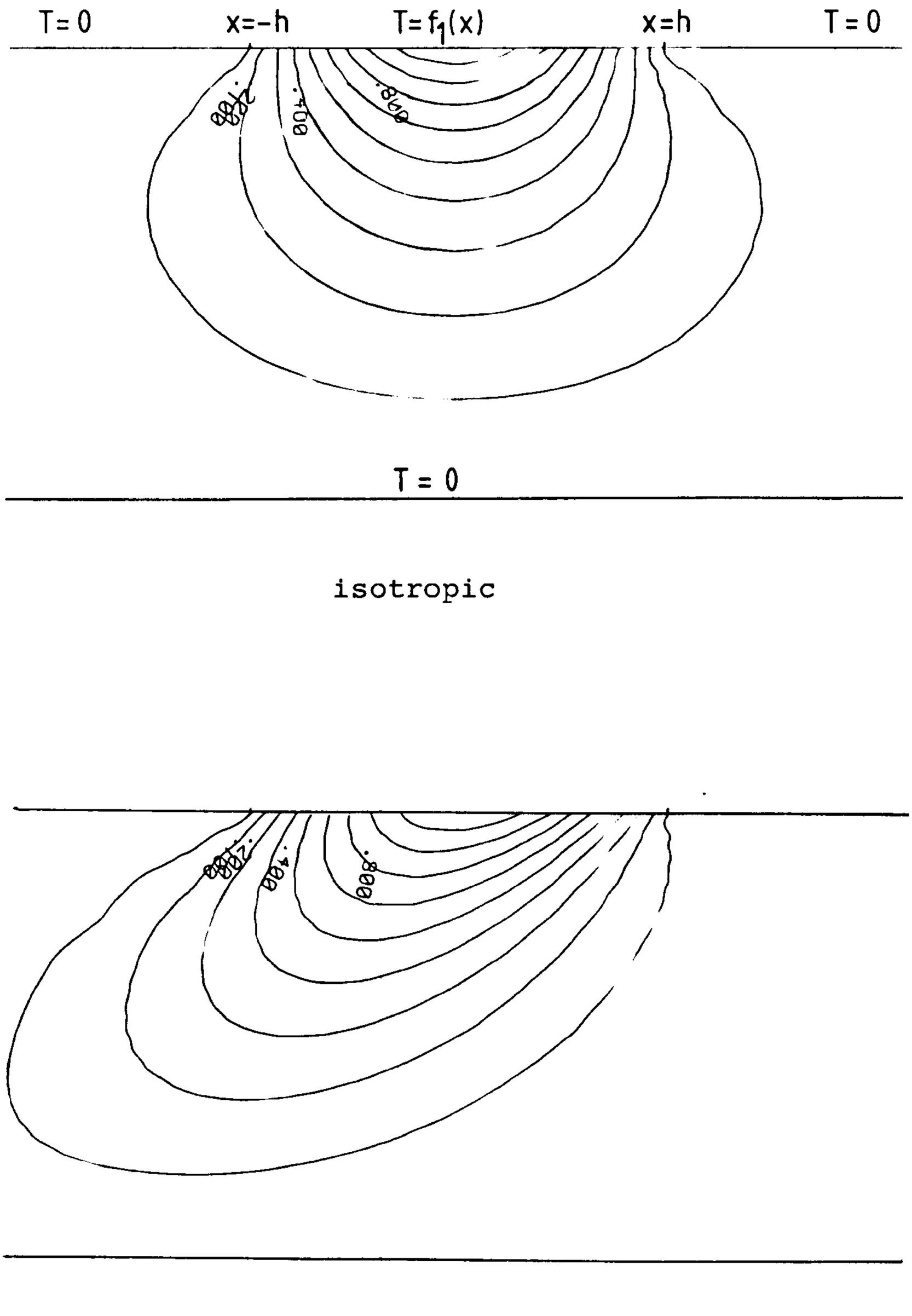

Fig. 4.10

Isotherms on semi-infinite slab for $f_1(x) = \sin \frac{\pi}{2h} (x + h)$, $|x| \leq h$. Anisotropic material has $K_1/K_2 = 5$, at 40° to x-axis.

(It should be noted that in the published text Equation 4.18 contains a number of misprints.)

It is instructive to compare Equation 4.18 with the classical solution for the same problem in an isotropic medium (Carslaw and Jaeger, 1959), where the same form of the exponential functions is obtained (in one dimension).

Even for particularly simple forms of the initial temperature F(x,y), Equation 4.18 requires numerical integration. Comparison with the finite element model is made in Chapter 6.

4.2.7 Circular Orthotropic Disc

In order to test the accuracy of the finite element model in circumstances where the thermal properties of a solid are dependent on position, it is convenient to consider a material which is orthotropic in a different coordinate system. A simple example is a solid circular disc of unit radius, having different thermal conductivities in the directions of the r and θ coordinates; this situation could be representative of timber, or of a composite containing a circular reinforcement, such as would be produced in a filament winding process.

In circular polar coordinates, the steady-state heat conduction equation is

$$\frac{k_r}{r}\frac{\partial}{\partial r}\left(r\frac{\partial T}{\partial r}\right) + \frac{k_\theta}{r^2}\frac{\partial^2 T}{\partial \theta^2} = 0 \qquad (4.19)$$

A substitution of the form $r = e^{-\varepsilon\eta}$ reduces Equation 4.19 to

$$\frac{\partial^2 T}{\partial \eta^2} + \frac{\partial^2 T}{\partial \theta^2} = 0 \qquad (4.20)$$

as long as $\varepsilon^2 = \frac{k_r}{k_\theta}$, on $\eta \geqslant 0$, $0 \leqslant \theta \leqslant 2\pi$

The series solution to Equation 4.20 may be written

$$T(\eta,\theta) = \sum_{n=0}^{\infty} e^{-n\eta}\,(a_n \cos n\theta + b_n \sin n\theta) \qquad (4.21)$$

and with a boundary condition of the first kind (prescribed

temperature) at r = 1 (η = 0),

$$T(0,\theta) = f(\theta) = \sum_{n=0}^{\infty} (a_n \cos n\theta + b_n \sin n\theta) \qquad (4.22)$$

As a specific example, consider the boundary condition studied by Chang and others (1973) and discussed in Section 4.2.3;

$$f(\theta) = \begin{cases} \sin\theta, & 0 \leq \theta \leq \pi \\ 0, & \pi \leq \theta < 2\pi \end{cases}$$

The Fourier coefficients a_n, b_n in Equation 4.22 are evaluated in the usual way, giving the solution for the temperature distribution as

$$T(\eta,\theta) = \frac{1}{\pi} + \frac{e^{-\eta}}{2}\sin\theta + \frac{2}{\pi}\sum_{n=2,4,..}^{\infty} \frac{e^{-n\eta}}{1-n^2}\cos n\theta$$

or, in terms of r and θ,

$$T(r,\theta) = \frac{1}{\pi} + \frac{r^{1/\varepsilon}}{2}\sin\theta + \frac{2}{\pi}\sum_{n=2,4,..}^{\infty} \frac{r^{n/\varepsilon}}{1-n^2}\cos n\theta \qquad (4.23)$$

Fig. 4.11 shows isotherms for three cases of anisotropy, namely isotropic ($\varepsilon = 1$), $k_\theta > k_r$ ($\varepsilon < 1$) and $k_\theta < k_r$ ($\varepsilon > 1$). It can be seen that, as in previous examples, there is a tendency for the isotherms to align parallel to the direction of greatest thermal conductivity.

In the cartesian coordinate system, the above example becomes fully anisotropic, and the values of the thermal conductivity coefficients k_{ij} are dependent on position. In chapter 6, the accuracy of the finite element model in this situation will be assessed by comparison with the analytic solution (Equation 4.23) obtained above.

4.3 THE FINITE ELEMENT METHOD IN THERMAL PROBLEMS

4.3.1 General Principles

The finite element method has its origins in the aircraft industry when, in the early 1940's, it was shown that continuum problems in the field of solid mechanics could be approximated by an arrangement of simple elastic bars (Hrenikoff, 1941). Later, Turner and others (1956) presented

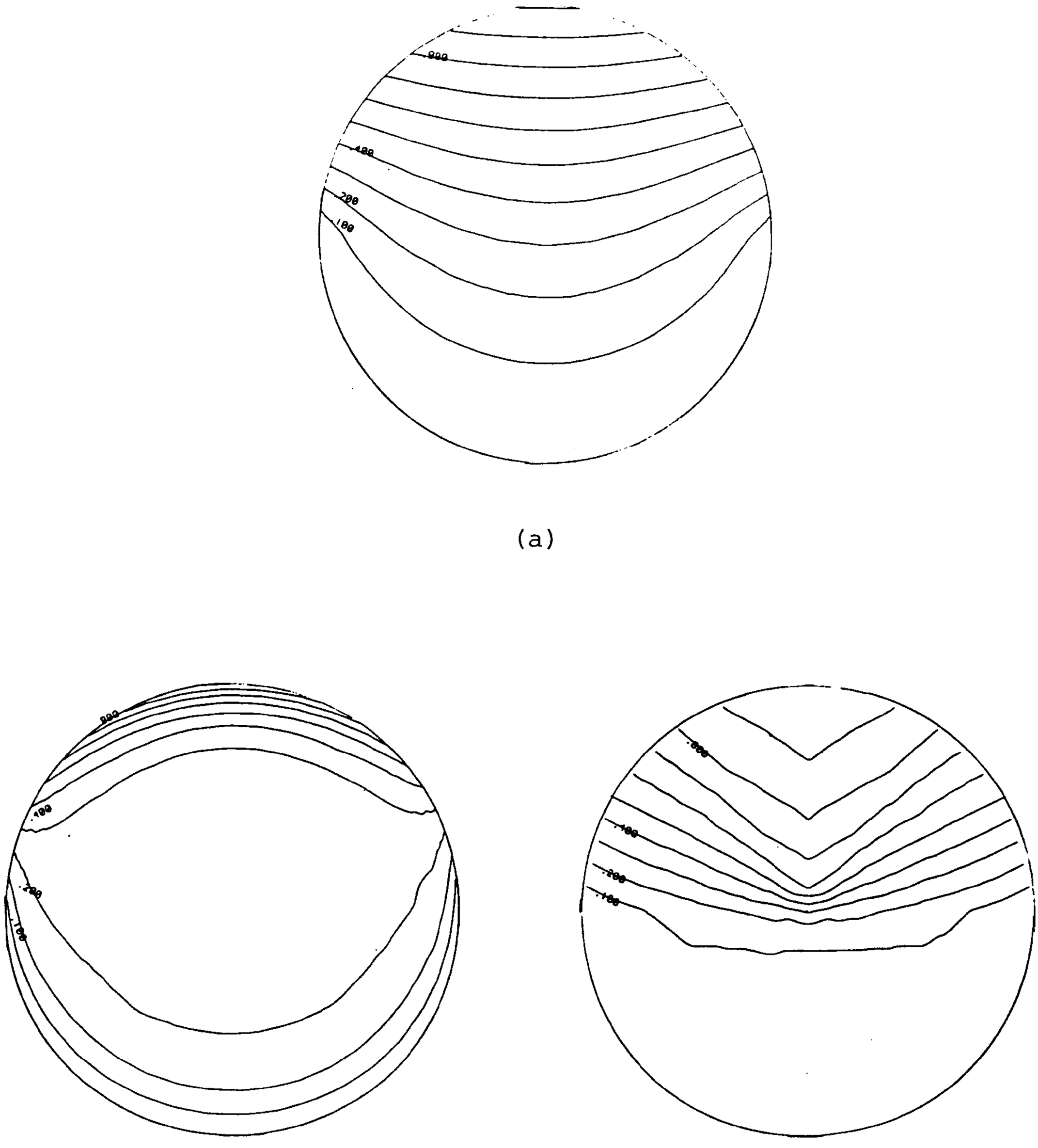

(a)

(b) (c)

Fig. 4.11

Isotherms on unit disc, according to Equation 4.23.

(a) isotropic

(b) $k_\theta > k_r$ ($\varepsilon = 0.03$)

(c) $k_\theta < k_r$ ($\varepsilon = 10$)

a method of stiffness and deflection analysis which involved a direct substitution of properties by considering small elements of a continuum. The method was soon identified with minimisation procedures (in structural mechanics a set of linear equilibrium equations is generated by minimising the potential energy of the system), and was then applied to areas governed by the Laplace and Poisson equations, which are readily expressed in a functional or variational formulation (see Section 5.1). Zienkiewicz and Cheung (1965) were among the first to treat the problem of heat conduction in this manner. A wide range of physical problems are analagous to steady-state heat conduction - some of these are summarised in Table 4.1.

Further development of the theory of finite elements revealed alternative methods of derivation, and Zienkiewicz and Parekh (1970) formulated the general transient field problem in terms of two and three-dimensional finite elements, using the Galerkin approach. As demonstrated by Kao and others (1983), it is also possible to adopt a direct physical approach to the method, based on steady-state energy balances. The finite element method is now regarded as a generalised numerical technique which may be applied to any problem defined by a properly constituted set of differential equations (without the necessity of a functional formulation of the physical problem). In recent years the finite element method has found applications in almost all areas of engineering science (Zienkiewicz, 1977).

The basic steps involved in a finite element analysis are as follows:

i) The continuum is replaced by a mesh of distinct, non-overlapping regions (elements)

ii) Each element is assigned a discrete number of boundary points (nodes), and it is at these points that adjacent elements are connected. The unknown parameters of the problem are the 'degrees of freedom' at the nodes (in thermal problems, the single unknown quantity is temperature).

Table 4.1

Analagous Steady-State Field Problems governed by

(a) the Laplace equation $\frac{\partial}{\partial x}\left(k \frac{\partial \phi}{\partial x}\right) = 0$, or

(b) the Poisson equation $\frac{\partial}{\partial x}\left(k \frac{\partial \phi}{\partial x}\right) + \dot{q} = 0$

Problem	Variable ϕ	Scalar k	Source term $\dot{q}$
Heat conduction	temperature	thermal conductivity	internal heat gen.
Seepage	total head	permeability	
Torsion	stress function	shear modulus	
Irrotational fluid flow	stream function	-	source or sink
Electricity	voltage	electrical conductivity	internal current source
Electrostatic field	potential	permittivity	charge density

iii) A set of functions is chosen to define the variation of (for example) temperature within each element in terms of the values at the nodes.

iv) The material properties of each element and its geometry are used to define a 'stiffness' (or conduction) matrix for that element. These are subsequently assembled into a global matrix representing the whole structure.

v) The physical problem is satisfied by requiring the minimisation of an appropriate quantity. This defines a set of linear simultaneous equations which can be solved for the nodal values of the unknown parameter.

4.3.2 Advantages of the Finite Element Method

Most of the analytic and numerical approaches to heat conduction problems discussed in Section 4.2 suffer from the disadvantage of being applicable only to particular geometries and/or combinations of boundary conditions. Those that are of more general use involve considerable mathematical manipulation, which, while elegant in theory, poses difficulties in practical applications. Many of the attributes of the finite element method arise from the generality of the formulation, and have particular relevance to the study of anisotropic materials.

(i) Thermal properties may vary from one element to another, so that the method can be readily applied to laminated structures, inhomogeneous substances, or the detailed microstructure of a composite material.

(ii) Irregular boundaries are easily modelled by quadratic or higher order elements, which have curved edges, so the method may be applied to any geometry.

(iii) The size of individual elements can be varied at will, allowing the mesh of nodal points to be expanded or refined according to the nature of the

problem.

(iv) A complete range of possible boundary conditions may be incorporated (including nonlinear phenomena such as radiation), and they may be mixed if necessary (for example, combining convective heat loss with an imposed heat flux).

(v) Finite element analysis has become a standard technique for many areas of engineering. There is a considerable advantage in adopting a method which is compatible with other related topics, such as the calculation of thermal stresses.

The most severe limitation to the application of the finite element method is the requirement for substantial computing facilities. Although micro and minicomputers may be able to handle smaller calculations, the complexity of most realistic engineering problems will necessitate the use of a mainframe computer, with its associated software and hardware for the presentation and interpretation of results in a graphical form.

4.3.3 Finite Element Model Development

Having established the necessity of a numerical model for the analysis of heat conduction in composites, and recognised the advantages of the finite element method, work began on a program for the mainframe computer at Plymouth Polytechnic. The commercial finite element system PAFEC 75 was available, and included some facilities for heat transfer calculations, but at that time there was no provision for thermal anisotropy in temperature calculation elements. It was decided, therefore, to develop an independent model of heat conduction incorporating a high level of generality. Additional software was written for data manipulation, enabling, for example, a calculated temperature distribution to be used in a subsequent PAFEC thermal stress calculation.

A later version of PAFEC (Level 4, installed at Plymouth in 1983) included orthotropic temperature calculation elements,

in which the principal thermal conductivities in the directions of the cartesian coordinate axes are specified. In order to represent a material of general anisotropy, it is necessary to define the orientation of the principal axes relative to the coordinate axes within each element. A change of thermal properties in a given problem thus necessitates regeneration and assembly of the element mesh. The procedure adopted in this thesis was to retain the tensorial definition of anisotropy (Equation 4.3), and to permit a different set of conductivity coefficients to be specified for each element. This effectively separates thermal property data from the mesh data, and gives greater flexibility of interchanging materials and structures.

CHAPTER 5 : FINITE ELEMENT MODEL OF ANISOTROPIC CONDUCTION

In this chapter, the variational formulation is used to develop the mathematical basis for a finite element model of transient heat conduction. The procedure follows basic texts on the subject (for example, Segerlind 1976), but retains general anisotropy in terms of the coefficients of the thermal conductivity tensor (Equation 4.3). Notes on the computer implementation of the model, together with a listing of the program FEANCO, are given in Appendices I and II. For clarity, the formulation is given in two dimensions, then generalised to three dimensions in 5.11.

5.1 FUNCTIONAL FORM OF THE CONDUCTION EQUATION

A basic theorem of variational calculus states that the function $F(x, y, z, u, u_x, u_y, u_z)$ which minimises the functional

$$I = \int_V F.\, dV \qquad (5.1)$$

must also satisfy the Euler-Lagrange equation, namely

$$\frac{\partial F}{\partial u} - \frac{\partial}{\partial x}\left(\frac{\partial F}{\partial u_x}\right) - \frac{\partial}{\partial y}\left(\frac{\partial F}{\partial u_y}\right) - \frac{\partial}{\partial z}\left(\frac{\partial F}{\partial u_z}\right) = 0 \qquad (5.2)$$

where $u = u(x,y,z)$ and $u_x = \frac{\partial u}{\partial x}$, $u_y = \frac{\partial u}{\partial y}$ and $u_z = \frac{\partial u}{\partial z}$.

The basis of the variational formulation is to express the equation of heat conduction and its boundary conditions in a form analogous to Equation 5.2 and hence as a functional (Equation 5.1). The temperature distribution may then be obtained by a minimisation procedure.

In two dimensions, the differential equation of heat conduction may be written

$$\frac{\partial}{\partial x}(k_{11}T_x + k_{12}T_y) + \frac{\partial}{\partial y}(k_{12}T_x + k_{22}T_y) + \dot{q} - \rho C_p \frac{\partial T}{\partial t} = 0$$

where $T = T(x,y,t)$, $T_x \equiv \frac{\partial T}{\partial x}$ and $T_y \equiv \frac{\partial T}{\partial y}$ (5.3)

This has the same form as the Euler-Lagrange equation if

$$\frac{\partial F}{\partial T_x} = k_{11} T_x + k_{12} T_y$$

$$\frac{\partial F}{\partial T_y} = k_{12} T_x + k_{22} T_y$$

and $$\frac{\partial F}{\partial T} = -\dot{g} + \rho C_p \frac{\partial T}{\partial t} \qquad (5.4)$$

Integrating each of the three equations in turn gives

$$F = \frac{k_{11} T_x^2}{2} + k_{12} T_x T_y + f_1(T, T_y)$$

$$F = k_{12} T_x T_y + \frac{k_{22} T_y^2}{2} + f_2(T, T_x)$$

$$F = -\dot{g} T + \frac{\rho C_p}{2} \left(\frac{\partial T}{\partial t} \right) T + f_3(T_x, T_y)$$

where f_1, f_2 and f_3 are arbitrary functions.

The functional form of the heat conduction equation may therefore be written as

$$I_c = \int_A \{ \tfrac{1}{2} \left[k_{11} \left(\frac{\partial T}{\partial x} \right)^2 + k_{22} \left(\frac{\partial T}{\partial y} \right)^2 + 2k_{12} \left(\frac{\partial T}{\partial x} \right) \left(\frac{\partial T}{\partial y} \right) \right] - 2 (\dot{g} - \rho C_p \frac{\partial T}{\partial t}) T \} \, dA \qquad (5.5)$$

within the two-dimensional region A.

However, the differential equation is governed by boundary conditions, and these must be incorporated into the functional form before the process of minimisation can be expected to yield the correct temperature distribution. Boundary conditions of the first kind (fixed temperature) are easily imposed at a later stage in the analysis; a prescribed heat flux and/or convection at the surface S gives rise to additional integrals:

$$\text{heat flux: } q \rightarrow \int_S qT \, dS$$

$$\text{convection: } h(T - T_\infty) \rightarrow \int_S \frac{h}{2} (T - T_\infty)^2 \, dS$$

The inclusion of radiative boundaries is discussed in 5.8.

Adopting a matrix notation, with

$$\tilde{\underline{d}} = \left(\frac{\partial T}{\partial x} \; \frac{\partial T}{\partial y} \right) \text{ and } \underline{D} = \begin{pmatrix} k_{11} & k_{12} \\ k_{12} & k_{22} \end{pmatrix} \tag{5.6}$$

the functional form of the problem can be written

$$I = \int_A \tfrac{1}{2}\left[\tilde{\underline{d}} \; \underline{D} \; \underline{d} - (2\dot{g} - \rho C_p \frac{\partial T}{\partial t})T \right] dA + \int_{S_1} qT \; dS + \int_{S_2} \frac{h}{2} (T^2 - 2TT_\infty + T_\infty^2) \; dS \tag{5.7}$$

5.2 DISCRETISATION AND MINIMISATION OF THE FUNCTIONAL

In the process of discretisation, the integrals in Equation 5.7 are replaced by a sum of integrals over the individual elements of the region under consideration. All the variables within the integral are thus replaced by values appropriate to each element, so that

$$I = \sum_{e=1}^{E} I^e$$

$$\text{where } I^e = \int_{A^e} \tfrac{1}{2}\left[\tilde{\underline{d}}^e \; \underline{D}^e \; \underline{d}^e \right] dA + \int_{A^e} T^e \left[\rho C_p{}^e \frac{\partial T^e}{\partial t} - \dot{g}^e \right] dA + \int_{S_1} q^e T^e dS + \int_{S_2^e} \frac{h}{2}^e \left[T^{e\,2} - 2T^e T_\infty{}^e + T_\infty^{e\,2} \right] dS \tag{5.8}$$

The finite element method readily lends itself to problems in which the thermal properties of a medium vary with position; in Equation 5.8 the property matrix $\underline{D}$ as well as h, $\dot{g}$, ρC_p and the other coefficients may be different for each element. This will be considered further in 6.4, where the model is applied to composite materials with a non-uniform distribution of reinforcement.

In Equation 5.8, T^e is the scalar temperature at any point within element e. It is related to the p nodal temperatures of the element by its shape functions:

$$T^e = \underline{N} \cdot \underline{T} = (N_1 \; N_2 \; \ldots \; N_p) \begin{pmatrix} T_1 \\ T_2 \\ \vdots \\ T_p \end{pmatrix} \tag{5.9}$$

The element temperatures in Equation 5.8 are now replaced by Equation 5.9. The element vector $\underline{d}^e$ becomes

$$\underline{d}^e = \begin{pmatrix} \frac{\partial T}{\partial x}^e \\ \frac{\partial T}{\partial y}^e \end{pmatrix} = \begin{pmatrix} \frac{\partial N_1}{\partial x}^e & \frac{\partial N_2}{\partial x}^e & \cdots & \frac{\partial N_p}{\partial x}^e \\ \frac{\partial N_1}{\partial y}^e & \frac{\partial N_2}{\partial y}^e & & \frac{\partial N_p}{\partial y}^e \end{pmatrix} \begin{pmatrix} T_1 \\ T_2 \\ \vdots \\ T_p \end{pmatrix}$$

$$= \underline{B}^e \, \underline{T} \qquad (5.10)$$

$\underline{T}$ is a column vector containing the nodal temperatures for each element; matrix $\underline{B}^e$ contains the derivatives of the shape functions.

By incorporating Equations 5.9 and 5.10 into 5.8, the element integrals may be written

$$I^e = \int_{A^e} \tfrac{1}{2} \, \tilde{\underline{T}} \, \tilde{\underline{B}} \, \underline{D} \, \underline{B} \, \underline{T} \, dA - \int_{A^e} \underline{N} \, \underline{T} \, \dot{g} \, dA$$
$$+ \int_{A^e} \rho C_p \, \underline{N} \, \underline{T} \, \underline{N} \, \frac{\partial \underline{T}}{\partial t} \, dA + \int_{S_1^e} q \, \underline{N} \, \underline{T} \, dS$$
$$+ \int_{S_2^e} \frac{h}{2} \, \tilde{\underline{T}} \, \tilde{\underline{N}} \, \underline{N} \, \underline{T} \, dS - \int_{S_2^e} h T_\infty \, \underline{N} \, \underline{T} \, dS$$
$$+ \int_{S_2^e} \frac{h}{2} \, T_\infty^2 \, dS \qquad (5.11)$$

where, for convenience, the superscript e has been omitted.

The minimisation of the functional is now carried out by differentiating with respect to the nodal temperatures, $\underline{T}$, and setting the result equal to zero.

$$\frac{\partial I}{\partial \underline{T}} = \frac{\partial}{\partial \underline{T}} \sum_{e=1}^{E} I^e = \sum_{e=1}^{E} \frac{\partial I^e}{\partial \underline{T}} = 0 \qquad (5.12)$$

It is easier to perform the differentiation before evaluating the integrals. This is because the equations for the higher-order elements cannot be evaluated analytically, and the required numerical integration is carried out most efficiently within a computer program.

Differentiating Equation 5.11, and using standard theorems

of matrix algebra (see, for example, Segerlind 1976), the element contribution to the total minimisation process is

$$\frac{\partial I}{\partial \underline{T}} = \left(\int_{A^e} \tilde{\underline{B}}\ \underline{D}\ \underline{B}\ dA + \int_{S_2^e} h\ \tilde{\underline{N}}\ \underline{N}\ dS \right) \underline{T} + \left(\int_{A^e} \rho C_p \tilde{\underline{N}}\ \underline{N}\ dA \right) \frac{\partial \underline{T}}{\partial t}$$
$$- \int_{A^e} \dot{g}\ \tilde{\underline{N}}\ dA + \int_{S_1^e} q\ \tilde{\underline{N}}\ dS$$
$$- \int_{S_2^e} h\ T_\infty\ \tilde{\underline{N}}\ dS \qquad (5.13)$$

which may be written

$$\frac{\partial I}{\partial \underline{T}}^e = \underline{k}^e\ \underline{T} + \underline{c}^e\ \frac{\partial \underline{T}}{\partial t} + \underline{f}^e \qquad (5.14)$$

The conventional names for the various matrices in Equation 5.13 derive from the finite element method's original use in structural problems. The 'element stiffness matrix' is

$$\underline{k}^e = \int_{A^e} \tilde{\underline{B}}\ \underline{D}\ \underline{B}\ dA + \int_{S_2^e} h\ \tilde{\underline{N}}\ \underline{N}\ dS \qquad (5.15a)$$

The 'element capacitance matrix' is

$$\underline{c}^e = \int_{A^e} \rho C_p\ \tilde{\underline{N}}\ \underline{N}\ dA \qquad (5.15b)$$

and the 'element force vector' is

$$\underline{f}^e = -\int_{A^e} \dot{g}\ \tilde{\underline{N}}\ dA + \int_{S_1^e} q\ \tilde{\underline{N}}\ dS - \int_{S_2^e} h\ T_\infty \tilde{\underline{N}}\ dS \qquad (5.15c)$$

The final system of equations is obtained by substituting Equation 5.14 into 5.12, so that

$$\frac{\partial I}{\partial \underline{T}} = \sum_{e=1}^{E} \left(\underline{k}^e\ \underline{T} + \underline{c}^e \frac{\partial \underline{T}}{\partial t} + \underline{f}^e \right) = 0$$

or
$$\underline{K}\ \underline{T} + \underline{C}\ \frac{\partial \underline{T}}{\partial t} + \underline{F} = 0 \qquad (5.16)$$

where $\underline{K}$, $\underline{C}$ and $\underline{F}$ are the global matrices, defined by

$$\underline{K} = \sum_{e=1}^{E} \underline{k}^e; \quad \underline{C} = \sum_{e=1}^{E} \underline{c}^e; \quad \underline{F} = \sum_{e=1}^{E} \underline{f}^e$$

Equation 5.16 now represents a system of first-order linear

equations; in the following sections the assembly of the element matrices is described, followed by methods of solving for the temperature field.

5.3 THE EIGHT-NODED QUADRILATERAL ELEMENT

The finite element model presented here uses quadratic elements. The two-dimensional quadrilateral is shown with its shape functions in Fig. 5.1. This is an isoparametric element - the set of eight nodes defines both the element geometry and the locations at which temperatures are to be calculated. The three nodes along each edge permit (quadratic) curvature in cartesian coordinates.

The shape functions in Fig. 5.1 have been written in terms of local coordinates r and s, which greatly facilitate the process of integration over the element. Either r or s is constant along each of the element edges. As indicated in Equation 5.9, the shape functions define the relation between the temperature at any point within the element and the temperature at each of the eight nodes.

5.4 EVALUATION OF THE ELEMENT EQUATIONS

For each element in the discretised region, integration over the area and possibly the edge of the element is required to evaluate the element matrices and vector. In the case of linear elements, the integration may be performed analytically, and general algebraic expressions written for the coefficients of the matrices. This is not so for the quadratic and higher order elements, due to the complexity of the shape functions and their derivatives, so numerical integration is used. Following standard finite element texts (Zienkiewicz 1977), Gauss-Legendre quadrature is used. For each of the integrals in Equation 5.15, the order of the polynomial to be integrated is known, so that the locations and weights of the sampling points are defined for an exact solution.

Equations 5.15 must be expressed in terms of the natural coordinate system (having made the transformation, the

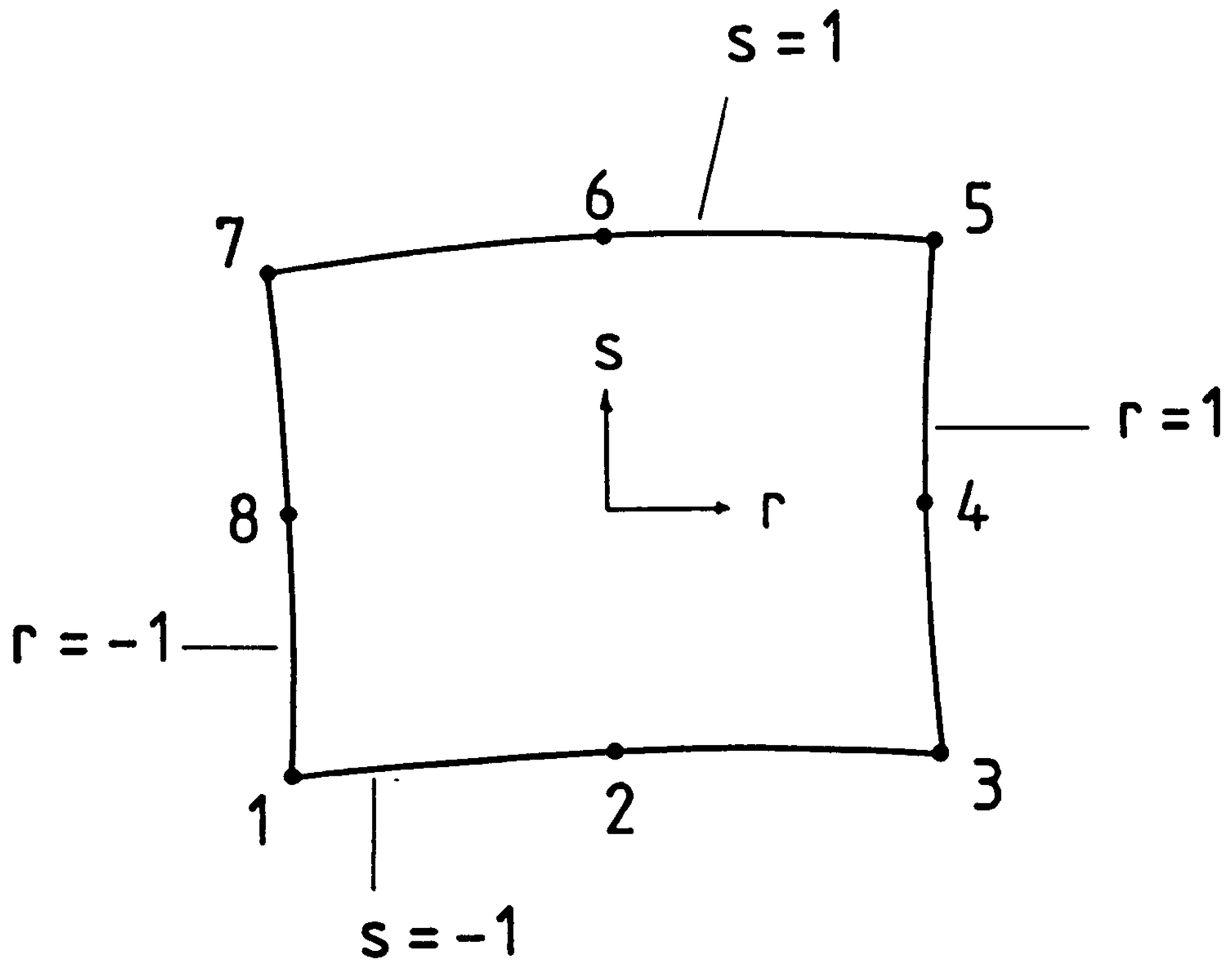

Fig. 5.1

Two-dimensional quadratic quadrilateral element, with local coordinates r and s.

Defining $r_o = rr_i$ and $s_o = ss_i$, shape functions for corner nodes are

$$N_i = \frac{1}{4}(1 + r_o)(1 + s_o)(r_o + s_o - 1)$$

For midside nodes

$$N_i = \frac{1}{2}(1 - r^2)(1 + s_o), \quad r_i = 0$$

and

$$N_i = \frac{1}{2}(1 + r_o)(1 - s^2), \quad s_i = 0$$

limits of integration become particularly simple, since the element is bounded by r = ± 1, s = ± 1). A Jacobian matrix, $\underline{J}$, is defined such that

$$\begin{pmatrix} \frac{\partial N_1}{\partial r} & \frac{\partial N_2}{\partial r} \cdot \cdot \frac{\partial N_8}{\partial r} \\ \frac{\partial N_1}{\partial s} & \frac{\partial N_2}{\partial s} \cdot \cdot \frac{\partial N_8}{\partial s} \end{pmatrix} = \begin{pmatrix} \frac{\partial x}{\partial r} & \frac{\partial y}{\partial r} \\ \frac{\partial x}{\partial s} & \frac{\partial y}{\partial s} \end{pmatrix} \begin{pmatrix} \frac{\partial N_1}{\partial x} & \frac{\partial N_2}{\partial x} \cdot \cdot \frac{\partial N_8}{\partial x} \\ \frac{\partial N_1}{\partial y} & \frac{\partial N_2}{\partial y} \cdot \cdot \frac{\partial N_8}{\partial y} \end{pmatrix} = \underline{J}\ \underline{B} \tag{5.17}$$

which enables the matrix B to be evaluated after inverting $\underline{J}$:

$$\underline{B} = \underline{J}^{-1} \begin{pmatrix} \frac{\partial N_1}{\partial r} & \frac{\partial N_2}{\partial r} \cdot \cdot \frac{\partial N_8}{\partial r} \\ \frac{\partial N_1}{\partial s} & \frac{\partial N_2}{\partial s} \cdot \cdot \frac{\partial N_8}{\partial s} \end{pmatrix} \tag{5.18}$$

Like the shape functions themselves, the matrix of their derivatives with respect to the local coordinates is a function of position within the element, and has to be evaluated at each numerical integration point. The coefficients of the Jacobian are also obtained from the differentiated shape functions, according to

$$x = N_1X_1 + N_2X_2 + N_3X_3 + \ldots + N_8X_8$$

$$\frac{\partial x}{\partial r} = \frac{\partial N_1}{\partial r}X_1 + \frac{\partial N_2}{\partial r}X_2 + \ldots \frac{\partial N_8}{\partial r}X_8 \tag{5.19}$$

and so on, where X_1, X_2 etc. are the global coordinates of each node of the element in question.

The Jacobian is then used to effect a change of variable in the integrals of Equation 5.15 by writing

$$dA = |\underline{J}|\ dr\ ds \tag{5.20}$$

where $|\underline{J}|$ is the determinant of the Jacobian matrix.

The area integrals become

$$\int_{A^e} \underline{\tilde{B}}\ \underline{D}\ \underline{B}\ dA = \int_{-1}^{1}\int_{-1}^{1} \underline{\tilde{B}}\ \underline{D}\ \underline{B}\ |\underline{J}|\ dr\ ds$$

and

$$\int_{A^e} \underline{\tilde{N}}\ \underline{N}\ dA = \int_{-1}^{1}\int_{-1}^{1} \underline{\tilde{N}}\ \underline{N}\ |\underline{J}|\ dr\ ds \tag{5.21}$$

In the process of numerical integration, the two-dimensional integral is replaced by a sum over a finite number of sampling points:

$$\int_{-1}^{1}\int_{-1}^{1} f(r,s)\ dr\ ds \Rightarrow \sum_{i=1}^{n}\sum_{j=1}^{n} W_i W_j f(r_i,s_j) \tag{5.22}$$

where the values of r_i, s_j and the weight coefficients W are defined according to the order of the polynomial f(r,s). As shown in the notes on computer implementation (Appendix I) the function f is evaluated at each of these sampling points, and the resulting contribution is added directly into the global matrix.

The surface (or more precisely, line) integrals in Equation 5.15 are treated in a similar manner. It is possible to integrate the expressions analytically (Segerlind, 1976), but in the case of curved boundaries a numerical method is still required to compute the length of the element edge. Along the element side for which, say, r = constant, the increment of length is

$$dS = \begin{pmatrix} \frac{\partial x}{\partial s} \\ \\ \frac{\partial y}{\partial s} \end{pmatrix} ds \tag{5.23}$$

The magnitude of the column vector in Equation 5.23 is given by $\sqrt{\left(\frac{\partial x}{\partial s}\right)^2 + \left(\frac{\partial y}{\partial s}\right)^2}$, so the length of the side of the element along r = constant is

$$\mathcal{L} = \int_{r=const} dS = \int_{-1}^{1}\sqrt{\left(\frac{\partial x}{\partial s}\right)^2 + \left(\frac{\partial y}{\partial s}\right)^2}\ ds$$

Changing the variable of integration in Equation 5.15 thus gives expressions like

$$\int_{-1}^{1} h\ \underline{\tilde{N}}\ \underline{N}\sqrt{\left(\frac{\partial x}{\partial \eta}\right)^2 + \left(\frac{\partial y}{\partial \eta}\right)^2}\ d\eta\ , \text{ etc.}$$

where $\eta \equiv r$ along s = constant, or $\eta \equiv s$ along r = constant.

These surface integrals are then evaluated numerically in a manner analagous to Equation 5.22.

5.5 TIME INTEGRATION

A two-point, finite difference approximation is used for the time derivative in Equation 5.16. The precise form of the algorithm depends on what point in the time interval Δt is chosen for the evaluation of $\underline{\dot{T}}$ (t) and $\underline{F}$ (t); in general the finite difference form of Equation 5.16 may be written

$$\left(\frac{\underline{C}}{\Delta t} + \underline{K}\,\omega\right)\underline{T}(t + \Delta t) = \left[\frac{\underline{C}}{\Delta t} - \underline{K}(1-\omega)\right]\underline{T}(t) + \underline{F}^* \qquad (5.24)$$

where $\underline{F}^* = \underline{F}(t + \Delta t)\omega + \underline{F}(t)(1-\omega)$

The weighting factor ω defines the degree of implicitness, as follows:

(i) $\omega = 0$ gives an explicit scheme (also known as the Euler or forward difference algorithm).

(ii) $\omega = \frac{1}{2}$ gives the Crank-Nicholson (or central difference) formula.

(iii) $\omega = 1$ gives the Pure Implicit or Backward difference formula.

The two implicit schemes (in which $\omega \geq \frac{1}{2}$) are unconditionally stable, while the explicit algorithm has a maximum time step for a stable solution, which depends on the particular characteristics of the given application. Usually, the Crank-Nicholson algorithm is found to give the most accurate results, but, as discussed by Zienkiewicz (1977), oscillatory results are possible for any value of $\omega < 1$, and the pure implicit scheme can be more accurate than the central difference formula when large time steps are used.

In 6.5.1, the relative stability and accuracy of the three schemes will be compared in the solution of a one-dimensional transient problem.

5.6 ASSEMBLY OF THE GLOBAL EQUATIONS

Each of the element equations 5.15 defines either an 8 x 8 matrix or an 8-row column vector, which are subsequently assembled into the global matrices as defined by Equation 5.16. The dimensions of the global matrices and vector are determined by the total number of nodes in the finite element mesh; n nodes require an n x n matrix or an n-row vector. It is clearly more economical to add the element matrices into the global matrix as soon as they are calculated, rather than store them individually, and this has been implemented in the computer program (Appendix I).

In the process of mesh generation, each node is given a number, and each element of the mesh is defined by its topology, that is the sequence of eight node numbers which lie around its edge. The convention adopted for the two-dimensional element is shown in Fig. 5.1; the topology may be any sequence of node numbers (starting from a corner) moving anticlockwise around the element. In this way, the local node numbers 1 to 8 are each associated with a global node number, and the element topology defines the position within the global matrices to which the coefficients of the element matrix are to be added. This is illustrated in Fig. 5.2, where the global node numbers defining the topology are i, j, k, . . .p. If e_{rs} denotes the coefficient in row r and column s of the element matrix, it can be seen that e_{11} is added to row i, column i; e_{12} to row i, column j, etc., of the global matrix.

Having completed the assembly of the global matrices, Equations 5.24 may be written in the general form

$$\underline{A}\ \underline{T} = \underline{B} \qquad (5.25)$$

where the particular form of $\underline{A}$ and $\underline{B}$ depends on the chosen time integration algorithm. In the case of steady-state problems, Equation 5.16 simplifies to

$$\underline{K}\ \underline{T} = -\underline{F} \qquad (5.26)$$

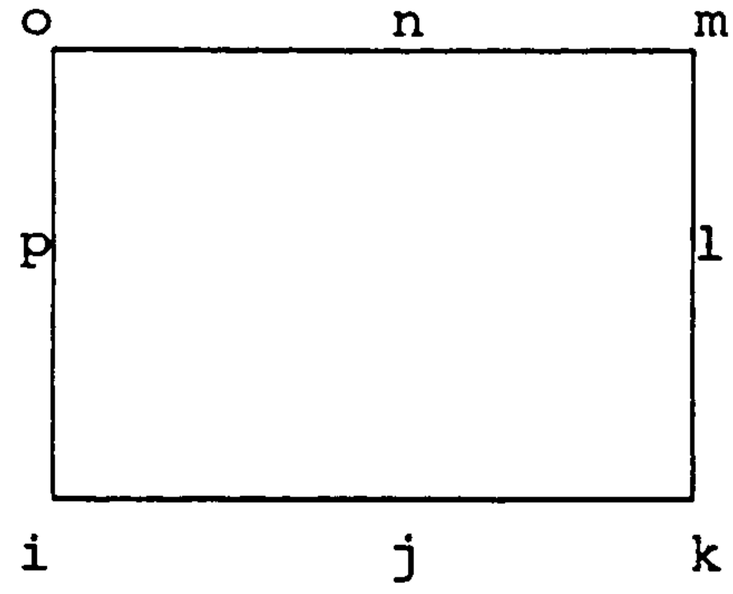

local node numbers

1, 2, 3, ... 8 $\longrightarrow$ i, j, k, ... p

element matrix (8 x 8) $\longrightarrow$ global matrix

$$\begin{pmatrix} e_{11} & e_{12} & e_{13} & \cdots & e_{18} \\ & e_{22} & e_{23} & \cdots & e_{28} \\ & & e_{33} & \cdots & e_{38} \\ & & & & \vdots \\ \text{symmetric} & & & & e_{88} \end{pmatrix}$$

$$\begin{pmatrix} & & \vdots & & \vdots & & \vdots & \\ & & \vdots & & \vdots & & \vdots & \\ \cdots & e_{ii} & \cdots & e_{ij} & \cdots & e_{ik} & \cdots & \\ & & & \vdots & & \vdots & & \\ & & & \vdots & & \vdots & & \\ & & & e_{jj} & \cdots & e_{jk} & \cdots & \\ & & & & & \vdots & & \\ & & & & & \vdots & & \\ & & & & & e_{kk} & \cdots & \\ \text{symmetric} & & & & & & & \text{etc.} \end{pmatrix}$$

Fig. 5.2

Relationship between element and global matrices for the quadrilateral element.

For transient solutions, the amount of computation required at each time step is determined by the nature of the problem. For example, if the material properties and boundary conditions are independent of time and temperature, then the global matrices $\underline{K}$, $\underline{C}$, and $\underline{F}$ are computed only once at the start of the calculation; with time-dependent boundary conditions, both $\underline{K}$ and $\underline{F}$ may have to be re-assembled at each time step.

Before solving the linear system defined by Equation 5.25 or 5.26, modification is required to allow for any nodes at which the temperature is fixed. As shown in standard texts, this may be achieved without disrupting the symmetry of the global matrices (see Appendix I).

5.7 SOLUTION METHODS

Equations 5.25 and 5.26 are equivalent to a set of n simultaneous linear equations, which may be solved for the vector $\underline{T}$, containing the n unknown temperatures at the nodes of the finite element mesh. In general, any appropriate numerical method may be employed for their solution.

One of the commonest direct (as opposed to iterative) methods is Gaussian substitution, which usually incorporates partial pivoting (interchanging rows of the coefficient matrix) to place the largest terms on the diagonal; this avoids division by small numbers and improves the accuracy of the arithmetic. An essentially equivalent technique uses triangular decomposition of the matrix A according to

$$A \equiv \begin{pmatrix} a_{11} & a_{12} & .. & a_{1n} \\ a_{21} & a_{22} & .. & a_{2n} \\ \vdots & & & \\ a_{n1} & a_{n2} & .. & a_{nn} \end{pmatrix} \equiv LU = \begin{pmatrix} \ell_{11} & 0 & .. & 0 \\ \ell_{21} & \ell_{22} & .. & 0 \\ \vdots & & & \\ \ell_{n1} & \ell_{n2} & .. & \ell_{nn} \end{pmatrix} \begin{pmatrix} u_{11} & u_{12} & .. & u_{1n} \\ 0 & u_{22} & .. & u_{2n} \\ \vdots & & & \\ 0 & 0 & .. & u_{nn} \end{pmatrix}$$

where L and U are lower and upper triangular matrices. The solution to the equation $A.T = B \equiv L.U.T$ is then obtained by solving in succession $L\ y = B$ for y by forward substitution, and $U\ T = y$ for T by back substitution.

Two important attributes of the finite element formulation

may be exploited to increase the efficiency with which a solution can be obtained, in terms of both storage requirements and computation time.

The first of these is the symmetry of the global matrices, and hence of the assembled matrices in Equations 5.25 and 5.26. If A is symmetric ($a_{ij} = a_{ji}$) then the decomposition $A \equiv L\ U$ can be performed such that L is the transpose of U, that is $u_{ij} = \ell_{ji}$. Thus, the process of decomposition only needs to generate (and store) the coefficients of the upper triangular matrix.

As noted in 5.6, the location of the coefficients in the global matrices is controlled by the node numbering. The element topology for a given mesh defines a bandwidth for the global and assembled matrices; in a system with one degree of freedom at each node (e.g. temperature), the bandwidth is given by (R + 1), where R is the largest difference between the node numbers in a single element, having considered all the elements in the mesh. Knowledge of the bandwidth of a matrix may be used to reduce the number of calculations in the decomposition, since if certain coefficients are known to be zero, they need not be included in any arithmetic operations.

The symmetry of matrices can be employed throughout the calculation procedure. Only the upper triangle of the global matrices need be accumulated during the assembly, and may be stored in a compact, rectangular matrix. For example, consider a symmetric 5 x 5 matrix with bandwidth 3:

$$M = \begin{pmatrix} a_{11} & a_{12} & a_{13} & 0 & 0 \\ a_{12} & a_{22} & a_{23} & a_{24} & 0 \\ a_{13} & a_{23} & a_{33} & a_{34} & a_{35} \\ 0 & a_{24} & a_{34} & a_{44} & a_{45} \\ 0 & 0 & a_{35} & a_{45} & a_{55} \end{pmatrix} = \begin{pmatrix} a_{11} & a_{12} & a_{13} \\ a_{22} & a_{23} & a_{24} \\ a_{33} & a_{34} & a_{35} \\ a_{44} & a_{45} & x \\ a_{55} & x & x \end{pmatrix}$$

where x denotes an arbitrary value. In large arrays, the economy of space and time may be considerable, since the bandwidth may be as little as a tenth of the total number of nodes.

The chosen numerical technique eventually yields a solution $\underline{T}_o$, say, to the matrix equation $\underline{A}\ \underline{T} = \underline{B}$. Due to rounding errors, this is only an approximation to the true solution $\underline{T}$, although in many cases it will be completely satisfactory. If an 'accurate' solution is required, it is necessary to compute a residual vector $r = \underline{B} - \underline{A}\ \underline{T_o}$, and to obtain a correction vector $\underline{d}$ by solving $\underline{A}\ \underline{d} = \underline{r}$. This leads to a new approximate solution given by $\underline{T_o} + \underline{d}$. The correction process may be continued until convergence, although it should be noted that the 'true' solution may not be meaningful if the coefficients of $\underline{A}$ and $\underline{B}$ are known with certainty to fewer figures than the word length of the computer on which the calculations are carried out.

The finite element program listed in Appendix I makes full use of the bandwidth and symmetry properties of the matrices, which are stored in rectangular form. The solution technique uses decomposition and back-substitution (adapted from Segerlind 1976), and an iterative procedure (to a tolerance of 10^{-5} K) may be selected as an alternative to the direct method.

5.8 RADIATIVE BOUNDARIES

The rate of radiative heat transfer per unit area from a grey body at absolute temperature T and emissivity ε to a black surface at absolute temperature T_∞ is

$$q_R = F\ \varepsilon\ \sigma\ (T^4 - T_\infty{}^4) \qquad (5.27)$$

where F is the shape factor of the grey surface with respect to the black.

By analogy with convection, Equation 5.27 may be expressed in the form

$$q_R = h_R(T - T_\infty) \qquad (5.28)$$

where h_R is a temperature-dependent heat transfer coefficient given by

$$h_R = F\ \varepsilon\ \sigma\ (T^2 + T_\infty{}^2)(T + T_\infty) \qquad (5.29)$$

Radiative heat transfer may thus be included by two additional contributions to the element stiffness matrix and force vector (Equations 5.15), namely

$$\int_{S_3^e} h_R \, \tilde{\underline{N}} \, \underline{N} \, dS \quad \text{and} \quad - \int_{S_3^e} h_R \, T'_\infty \, \tilde{\underline{N}} \, dS \tag{5.30}$$

where T'_∞ is the temperature of the black surface in degrees Centigrade. This adjustment is necessary because the surface temperature T in Equation 5.28 must be expressed in units consistent with other temperatures in Equation 5.13.

S_3^e refers to the radiating surface of element e, but radiation and convection may occur simultaneously from the same surface, in which case $S_2^e \equiv S_3^e$

Because h_R is dependent on the surface temperature T, iteration is required in the calculation; details of the implementation may be found in Appendix I.

5.9 NONLINEAR THERMAL PROPERTIES

In differentiating the element integrals (Equation 5.11) it was assumed that both the property matrix $\underline{D}$ and the heat capacity (ρC_p) were independent of temperature. Nonlinear thermal properties are therefore modelled by iteration. An initial temperature distribution is first calculated using baseline values of k_{ij} and ρC_p; these temperatures are used to obtain corrected values of the thermal properties, which are then used in a second calculation. The process is repeated until convergence of the thermal properties on successive iterations (see Appendix I). A steady-state anisotropic conduction problem with nonlinear thermal conductivity is considered in 6.3.

Zienkiewicz (1977) has shown how certain functional forms of k_{ij} (T) may be incorporated implicitly in the mathematical formulation. Where feasible, this would be computationally more efficient than iteration, but necessarily results in a loss of generality, since the thermal properties of many materials cannot be expressed in a suitable functional

form. As described in Appendix I, the computer model uses a table of values of $k_{ij}(T)$ or $\rho C_p(T)$ as input data, obtaining values at any calculated temperature by linear interpolation.

In Chapter 8, the nonlinear behaviour of heat capacity is used to represent phase changes in a (solid) semicrystalline polymer. Zienkiewicz (1977) has pointed out that a narrow peak in the data could be missed if the calculated temperatures at successive iterations lie on either side. An alternative representation is in terms of specific enthalpy; Fig. 5.3 shows an idealised example with a phase change occurring between T_1 and T_2. Outside this temperature range the specific heat is constant, and a calculation increment from T_o ($< T_1$) to T_3 ($> T_2$), for example, would take no account of the energetics of the phase change. The problem is avoided if the change in specific enthalpy between T_o and T_3 is used to calculate an average specific heat, according to

$$C_p = \frac{\partial h}{\partial T} \simeq \frac{\Delta h}{\Delta T}$$

Both representations have been incorporated in the model (see Appendix I), where, for convenience, enthalpy is expressed as

$$h'(T) = \rho h(T)$$

5.10 INHOMOGENEOUS THERMAL PROPERTIES

As discussed in 1.5, fibre-reinforced composites are assumed to be macroscopically homogeneous. However, many such materials may have thermal properties which are position-dependent; this would be the case with a non-uniform distribution of reinforcement or with fibres aligned parallel to non-cartesian coordinate axes. The finite element formulation presented earlier in this chapter is such that thermal conductivity and heat capacity are defined for each element, and remain within the integrals in Equations 5.15.

The degree to which thermal properties change with position

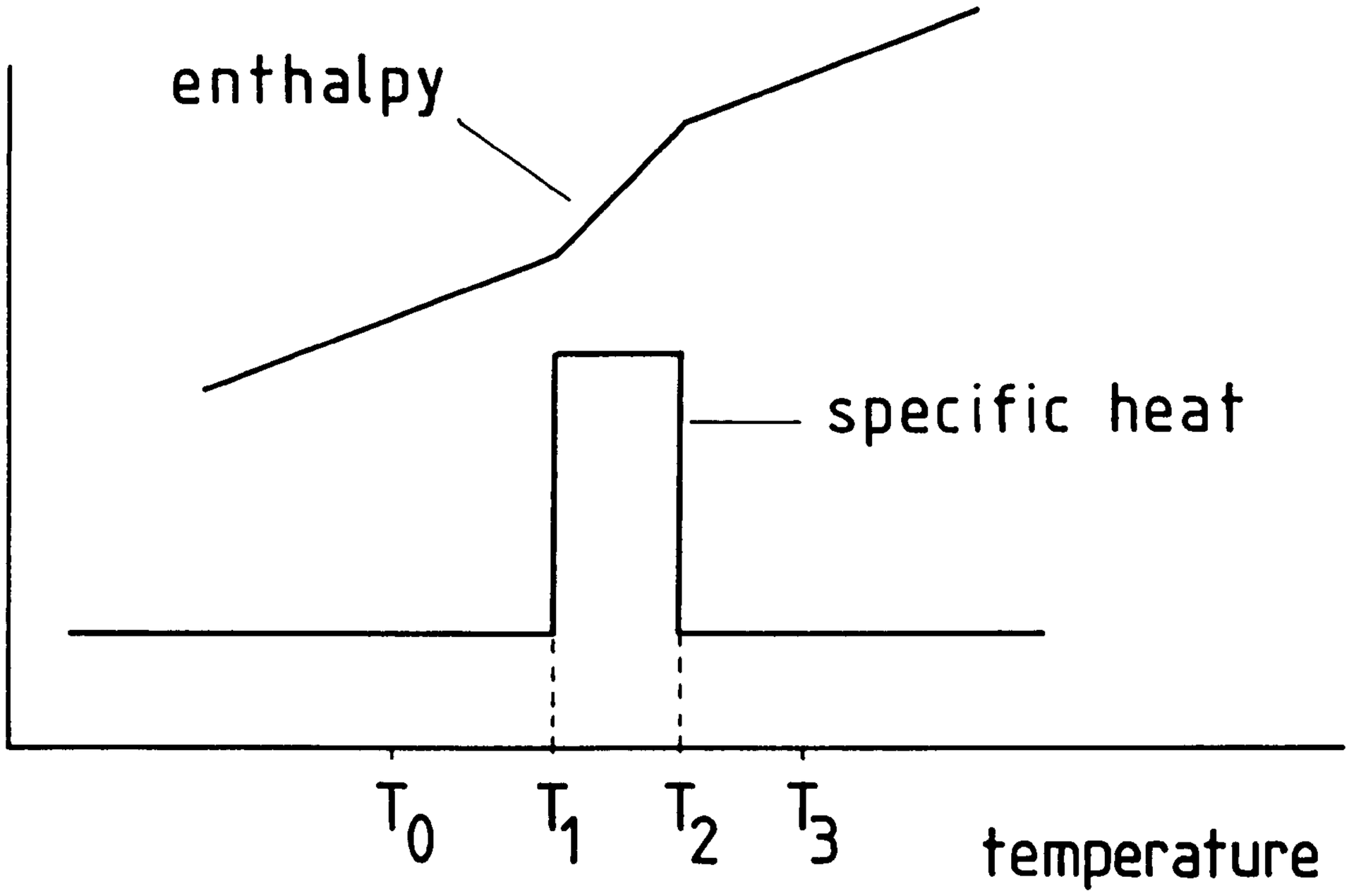

Fig. 5.3

Idealised representation of phase change between temperatures T_1 and T_2 in terms of enthalpy and specific heat.

must be taken into account when assembling the finite element representation of the material. In order to reduce the number of elements which may be required to represent adequately materials with properties which change rapidly with position (such as highly curved reinforcing fibres), thermal conductivity coefficients are defined as input data for each of the numerical integration points in each element of the mesh; there are thus four values for each quadrilateral element (at r = ± .5, s = ± .5). This procedure results in considerable efficiency of calculation compared with the use of average thermal conductivities over each element. This is illustrated by an example problem in 6.4.

5.11 THREE DIMENSIONAL PROBLEMS

Having developed and tested a two-dimensional finite element model, the extension to three dimensions is straightforward. The theoretical basis is outlined here, and notes on the computer implementation are included in Appendix I.

The three-dimensional quadratic element is the 20-noded brick shown in Fig. 5.4. The third dimension involves an additional local coordinate, so that the surfaces of the element (which may be curved in the global cartesian coordinate system) are defined by r = ± 1, s = ± 1 and t = ± 1. The shape functions for this element are also shown in Fig. 5.4, where the generalised form is used for economy.

The three-dimensional element stiffness matrix may be written down by direct analogy with Equation 5.15; it is

$$\underline{k}^e = \int_{V^e} \tilde{\underline{B}}\ \underline{D}\ \underline{B}\ dV + \int_{A_2^e} h\ \tilde{\underline{N}}\ \underline{N}\ dA \qquad (5.31)$$

where V^e represents the volume, and $A_2{}^e$ is the convective surface area of an element. The property matrix becomes

$$\underline{D} = \begin{pmatrix} k_{11} & k_{12} & k_{13} \\ k_{21} & k_{22} & k_{23} \\ k_{31} & k_{32} & k_{33} \end{pmatrix} \qquad (5.32)$$

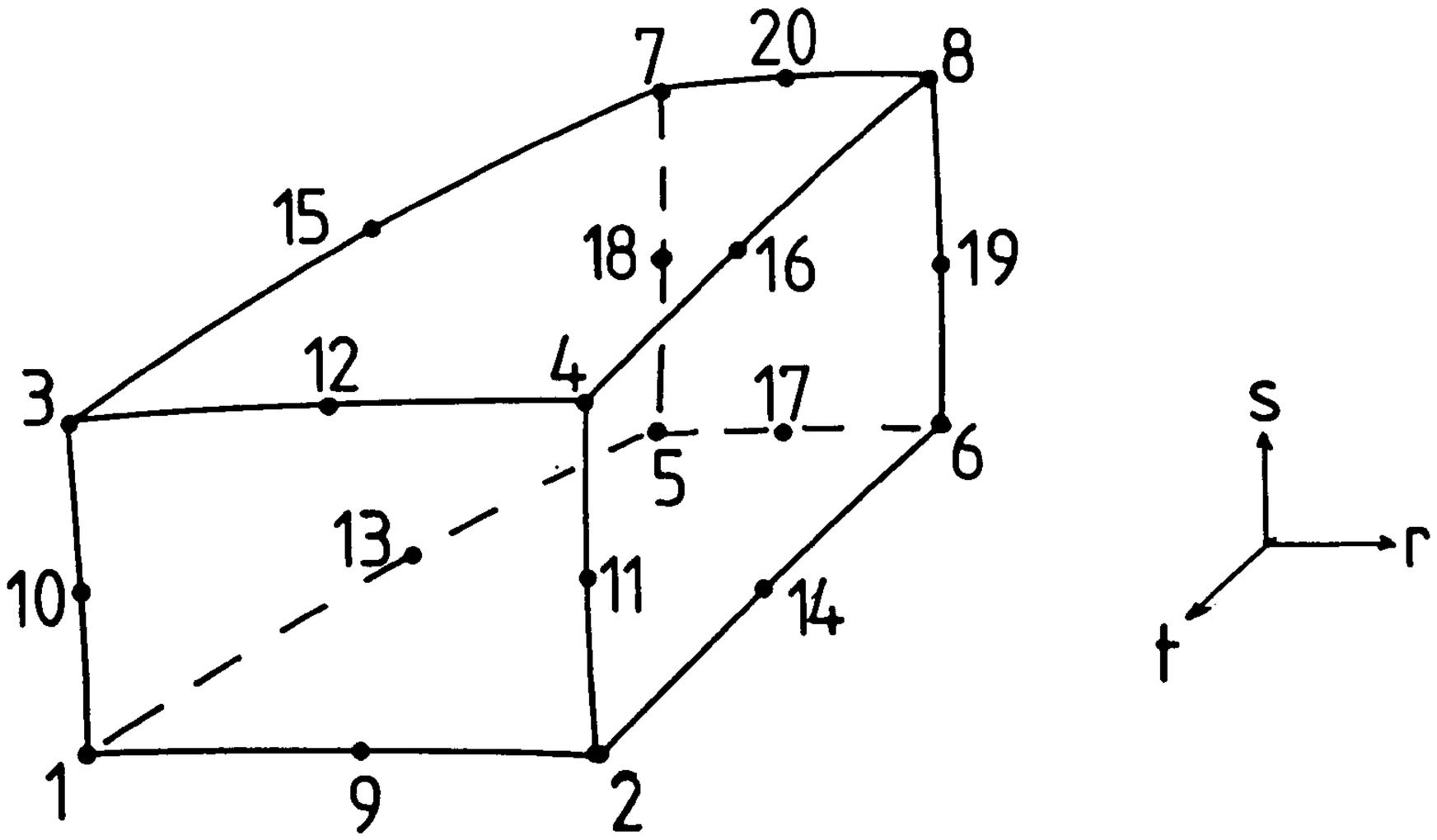

Fig. 5.4

Three-dimensional quadratic element, with local coordinates r, s, t.

Shape functions for corner nodes are

$$N_i = \frac{1}{8}(1 + r_o)(1 + s_o)(1 + t_o)(r_o + s_o + t_o - 2)$$

For midside nodes

$$N_i = \frac{1}{4}(1 - r^2)(1 + s_o)(1 + t_o), \; r_i = 0 \; (s_i = \pm 1, \; t_i = \pm 1)$$

$$N_i = \frac{1}{4}(1 - s^2)(1 + r_o)(1 + t_o), \; s_i = 0 \; (r_i = \pm 1, \; t_i = \pm 1)$$

$$N_i = \frac{1}{4}(1 - t^2)(1 + s_o)(1 + r_o), \; t_i = 0 \; (s_i = \pm 1, \; r_i = \pm 1)$$

with $k_{ij} = k_{ji}$ (see 4.1), and the matrix of shape function derivatives is now defined by

$$\underline{B} = \begin{pmatrix} \frac{\partial N_1}{\partial x} & \cdots & \frac{\partial N_{20}}{\partial x} \\ \frac{\partial N_1}{\partial y} & \cdots & \frac{\partial N_{20}}{\partial y} \\ \frac{\partial N_1}{\partial z} & \cdots & \frac{\partial N_{20}}{\partial z} \end{pmatrix} \tag{5.33}$$

Expressions for the capacitance matrix and the element force vector are obtained in a similar way, replacing the area and line integrals in Equations 5.15 by volume and surface integrals respectively.

As before, the integrals are expressed in terms of the natural coordinate system by means of a Jacobian matrix; the three-dimensional equivalents of Equations 5.17, 5.18 and 5.20 are

$$\begin{pmatrix} \frac{\partial N_1}{\partial r} & \frac{\partial N_2}{\partial r} & \cdots & \frac{\partial N_{20}}{\partial r} \\ \frac{\partial N_1}{\partial s} & \frac{\partial N_2}{\partial s} & \cdots & \frac{\partial N_{20}}{\partial s} \\ \frac{\partial N_1}{\partial t} & \frac{\partial N_2}{\partial t} & \cdots & \frac{\partial N_{20}}{\partial t} \end{pmatrix} = \begin{pmatrix} \frac{\partial x}{\partial r} & \frac{\partial y}{\partial r} & \frac{\partial z}{\partial r} \\ \frac{\partial x}{\partial s} & \frac{\partial y}{\partial s} & \frac{\partial z}{\partial s} \\ \frac{\partial x}{\partial t} & \frac{\partial y}{\partial t} & \frac{\partial z}{\partial t} \end{pmatrix} \begin{pmatrix} \frac{\partial N_1}{\partial x} & \cdots & \frac{\partial N_{20}}{\partial x} \\ \frac{\partial N_1}{\partial y} & \cdots & \frac{\partial N_{20}}{\partial y} \\ \frac{\partial N_1}{\partial z} & \cdots & \frac{\partial N_{20}}{\partial z} \end{pmatrix}$$

$$= \underline{J}.\underline{B} \tag{5.34}$$

so that

$$\underline{B} = \underline{J}^{-1} \begin{pmatrix} \frac{\partial N_1}{\partial r} & \cdots & \frac{\partial N_{20}}{\partial r} \\ \frac{\partial N_1}{\partial s} & \cdots & \frac{\partial N_{20}}{\partial s} \\ \frac{\partial N_1}{\partial t} & \cdots & \frac{\partial N_{20}}{\partial t} \end{pmatrix} \tag{5.35}$$

and the volume element is $dV = |\underline{J}|\ dr\ ds\ dt$ (5.36)

The surface integrals which arise from application of the convective, radiative and heat flux boundary conditions are transformed by writing the area element as a vector product. For example, on the surface t = constant,

$$\underline{dA} = \begin{pmatrix} \frac{\partial x}{\partial r} \\ \frac{\partial y}{\partial r} \\ \frac{\partial z}{\partial r} \end{pmatrix} \hat{} \begin{pmatrix} \frac{\partial x}{\partial s} \\ \frac{\partial y}{\partial s} \\ \frac{\partial z}{\partial s} \end{pmatrix} \; dr \; ds \tag{5.37}$$

and the magnitude of the area vector can be found by applying the usual rules of vector algebra.

The processes of matrix calculation and assembly proceed in an entirely analogous fashion to the two-dimensional case, except that the number of integrating points required in each element is increased; the two-dimensional quadratic element requires $3^2 = 9$ points for the evaluation of $\underline{\tilde{N}}\,\underline{N}$ in the capacitance matrix, while the three-dimensional element requires $3^3 = 27$ points.

Although formulation of the three-dimensional model is straightforward, its use implies considerable increases in both computer storage requirements and calculation time. The scope of this thesis is limited to two-dimensional conduction, but, as discussed in Chapter 9, three-dimensional problems in thermally anisotropic materials are of sufficient importance to justify further effort in this direction. Both the two- and three-dimensional versions of the numerical model are listed in Appendix I.

CHAPTER 6 : THEORETICAL VALIDATION OF THE FINITE ELEMENT MODEL

6.1 INTRODUCTION

The process of validation is an essential stage in the development of any mathematical model, particularly if it is to be used as a generalised design tool and applied to a wide range of problems. Apart from the obvious purpose of isolating gross errors in physical principles, mathematical interpretation and/or computer implementation, validation exercises serve two other functions. Firstly, they provide valuable experience in the mechanics of preparing and executing the model, especially with regard to mesh data preparation and correct specification of the boundary conditions. Secondly, they enable conclusions to be drawn concerning the accuracy and reliability of the model, with regard to its inherent physical and mathematical approximations.

A mathematical model may be validated in one or more of three ways:

i) by comparison with a known analytic solution to a specified problem,

ii) by comparison with controlled experiments,

iii) by comparison with other models.

In this chapter the two-dimensional finite element model is applied to a selection of analytic solutions to anisotropic heat conduction problems which have been reviewed in Chapter 4. Chapter 7 describes experimental measurements of heat transfer in a carbon fibre-reinforced composite and their use in the validation process.

Typically, the approach to a problem for which a finite element solution is required would be to start with a fairly coarse mesh and progressively increase the number of nodes in those regions where the temperature gradient is greatest. A satisfactory solution can be said to exist when the temperature distribution does not change significantly as the mesh

is refined further. In many cases, a preliminary examination of the problem will give some indication of where the greatest temperature gradients are to be found, and the 'first approximation' finite element mesh should reflect this by appropriate modification of elements. Commercial calculations on a large computer are expensive, and every effort should be made to obtain a satisfactory solution as efficiently as possible.

In some of the calculations presented in this chapter, it will be necessary to quantify the accuracy of the finite element solution; this is expressed by the difference between the temperature at a given node ($T_{f.e.}$) and the analytic (exact) value at that point ($T_{anal.}$). The error may also be given as a percentage of an appropriate reference temperature or temperature difference (a simple fractional error, such as $(T_{f.e.} - T_{anal.})/T_{anal.}$, has been avoided since it becomes meaningless as $T_{anal.}$ approaches zero).

The accuracy of a temperature distribution along m nodes in a given mesh is measured by the mean error

$$\bar{\delta} = \frac{1}{m} \sum_i \delta_i \tag{6.1}$$

and by the adjusted root mean square deviation (S), where

$$S^2 = \frac{1}{m-1} \sum_i \delta_i^2 \tag{6.2}$$

In Equations 6.1 and 6.2, δ_i is the error in the temperature at node i. Nodes at which the temperature is specified as a boundary condition are excluded from the summation. These two measures of accuracy have been employed in order to distinguish the phenomena of bias and scatter in the finite element results.

6.2 STEADY-STATE, LINEAR HOMOGENEOUS PROBLEMS

Most of the solutions discussed in Chapter 4 applied only on semi-infinite regions. Solutions to problems involving orthotropic materials in simple geometric shapes with principal conductivities parallel to the cartesian axes may be obtained from the corresponding isotropic solutions (Carslaw and Jaeger, 1959).

6.2.1 Orthotropic Rectangle

Fig. 6.1 shows a rectangular region with orthotropic thermal properties ($\gamma^2 = K_1/K_2$) with boundary conditions of the first kind, namely

$$\left.\begin{aligned} T(x,O) &= f(x) \\ T(x,b) &= O \end{aligned}\right\} \; O < x \leqslant a$$

$$T(O,y) = T(a,y) = O, \quad O \leqslant y \leqslant b$$

The classical method of separation of variables yields a solution in series form for the temperature distribution:

$$T(x,y) = \sum_{n=1}^{\infty} \frac{A_n \sin \frac{n\pi x}{a} \sinh \gamma(b-y)\frac{n\pi}{a}}{\sinh \gamma \frac{n\pi b}{a}} \qquad (6.3)$$

$$\text{with } A_n = \frac{2}{a} \int_o^a f(x') \sin \frac{n\pi x'}{a} \, dx'$$

A particularly simple form of Equation 6.3 results if $f(x) = \sin \pi x/a$, since integration gives

$$A_n = \begin{cases} 1 \;, & n = 1 \\ O \;, & \text{otherwise} \end{cases}$$

The solution for the temperature distribution is

$$T(x,y) = \frac{\sin \frac{\pi x}{a} \sinh \gamma(b-y)\frac{\pi}{a}}{\sinh \gamma \frac{\pi b}{a}} \qquad (6.4)$$

and is illustrated in Fig. 6.2, using the contouring routine described in Appendix I to generate smoothed isotherms from calculated temperatures at specified points. Two rectangular regions with different aspect ratios are considered (a/b = ½ and 2), in combination with two values of the ratio of principal conductivities (γ^2 = 10 and 0.1).

The initial finite element meshes used on this problem are shown in Fig. 6.3; they anticipate areas of highest temperature gradient by 'compressing' the grid near (x = O, y = O), and also take advantage of the symmetry of the problem by

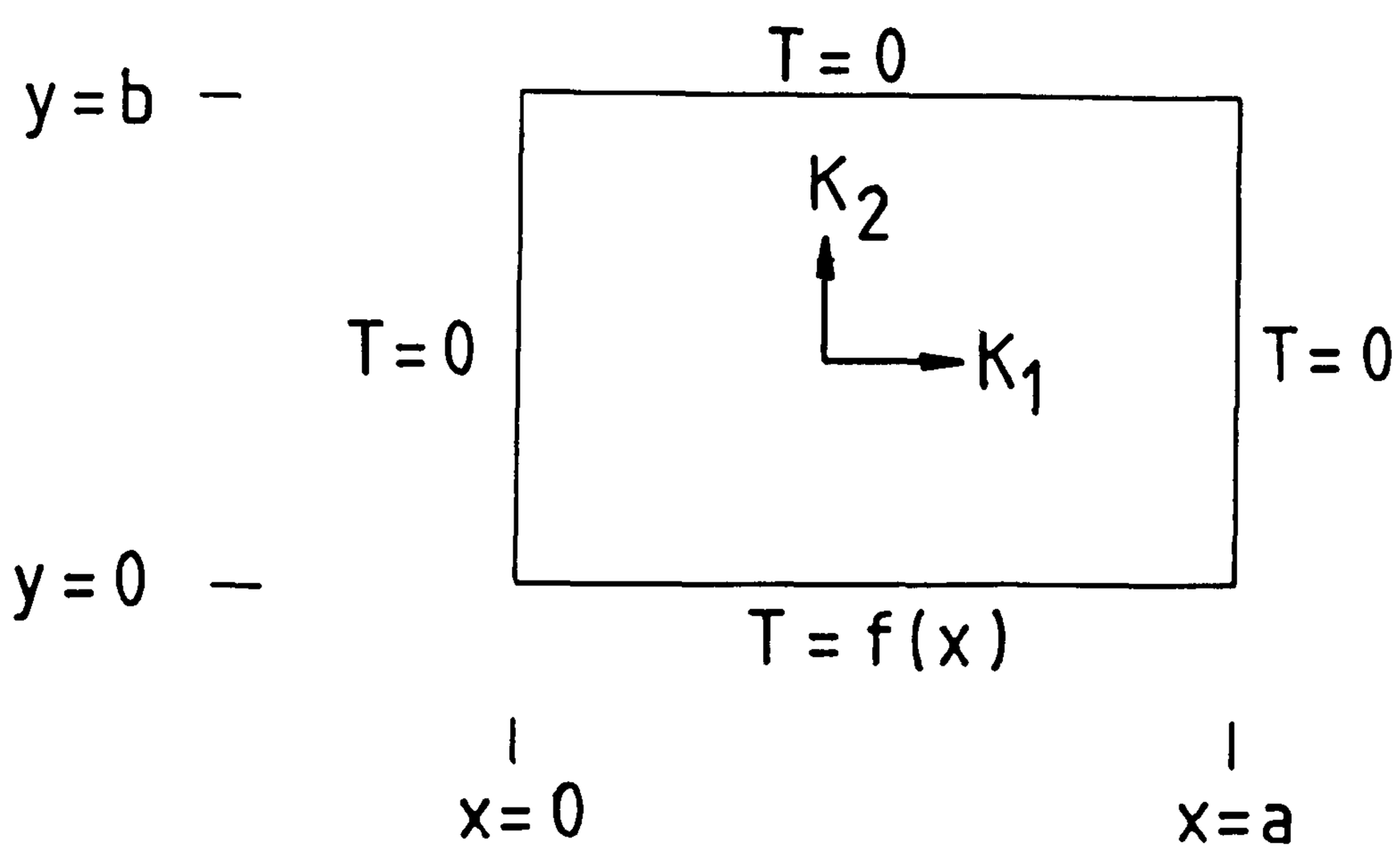

Fig. 6.1

Rectangular region with orthotropic thermal properties and boundary conditions of the first kind.

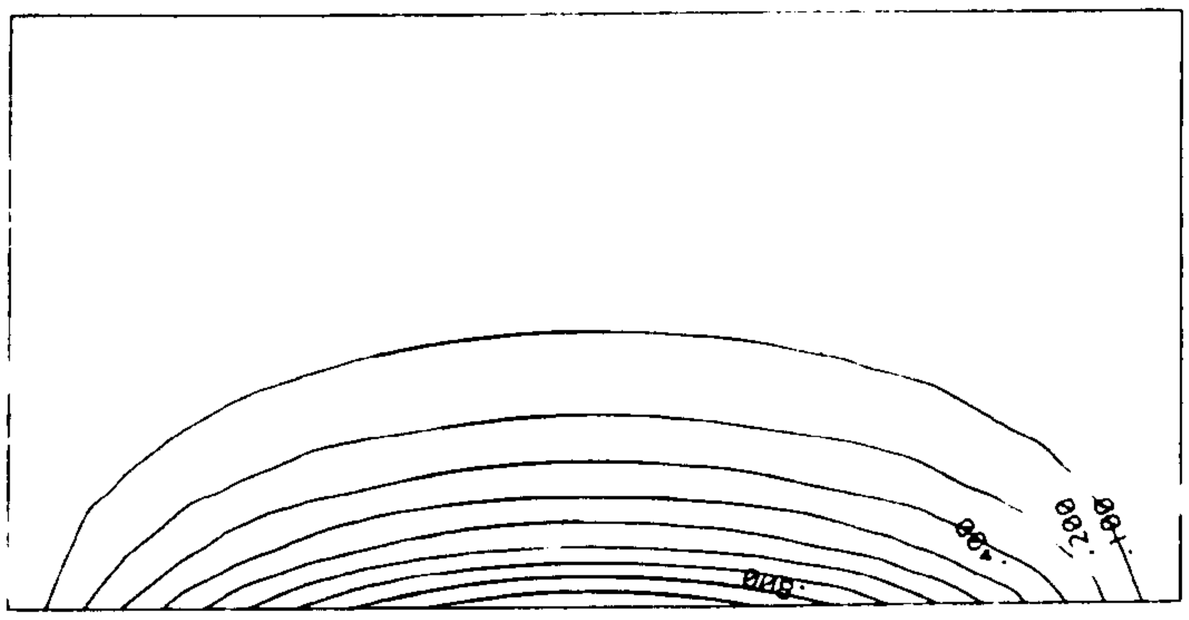

KX/KY=10.0
SCALE 1 IN 10.00

(a)

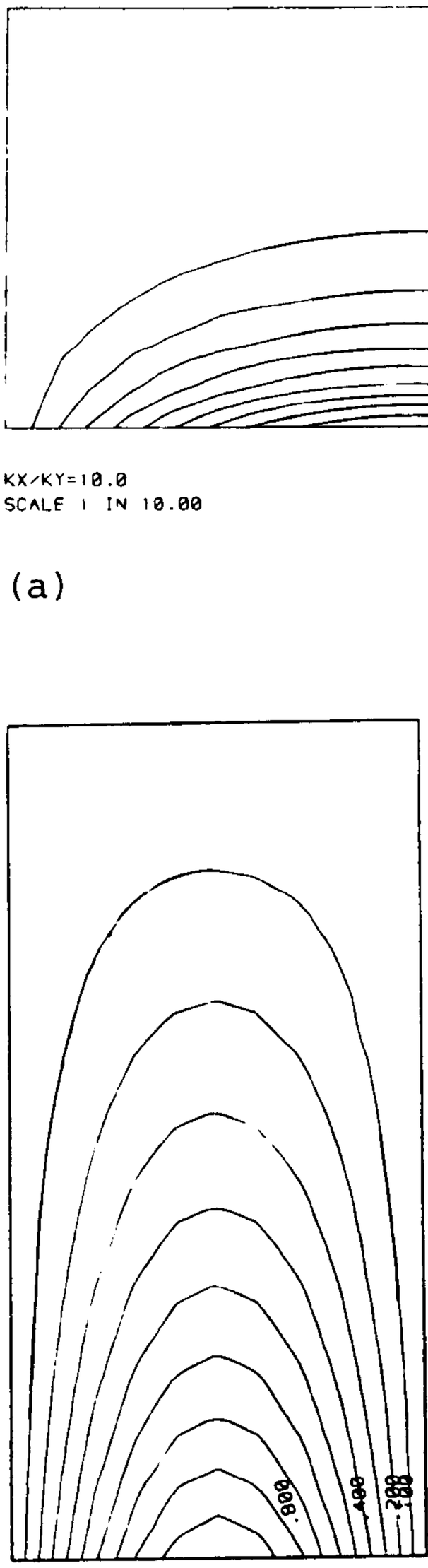

KX/KY=0.1

(c)

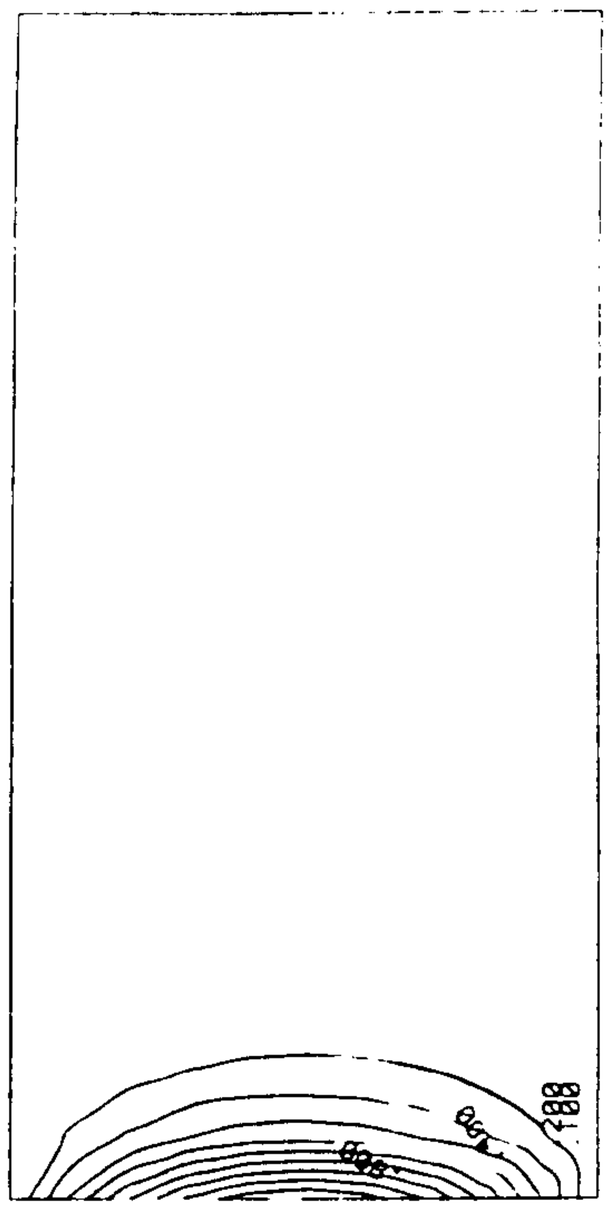

KX/KY=10.
SCALE 1 IN 10.00

(b)

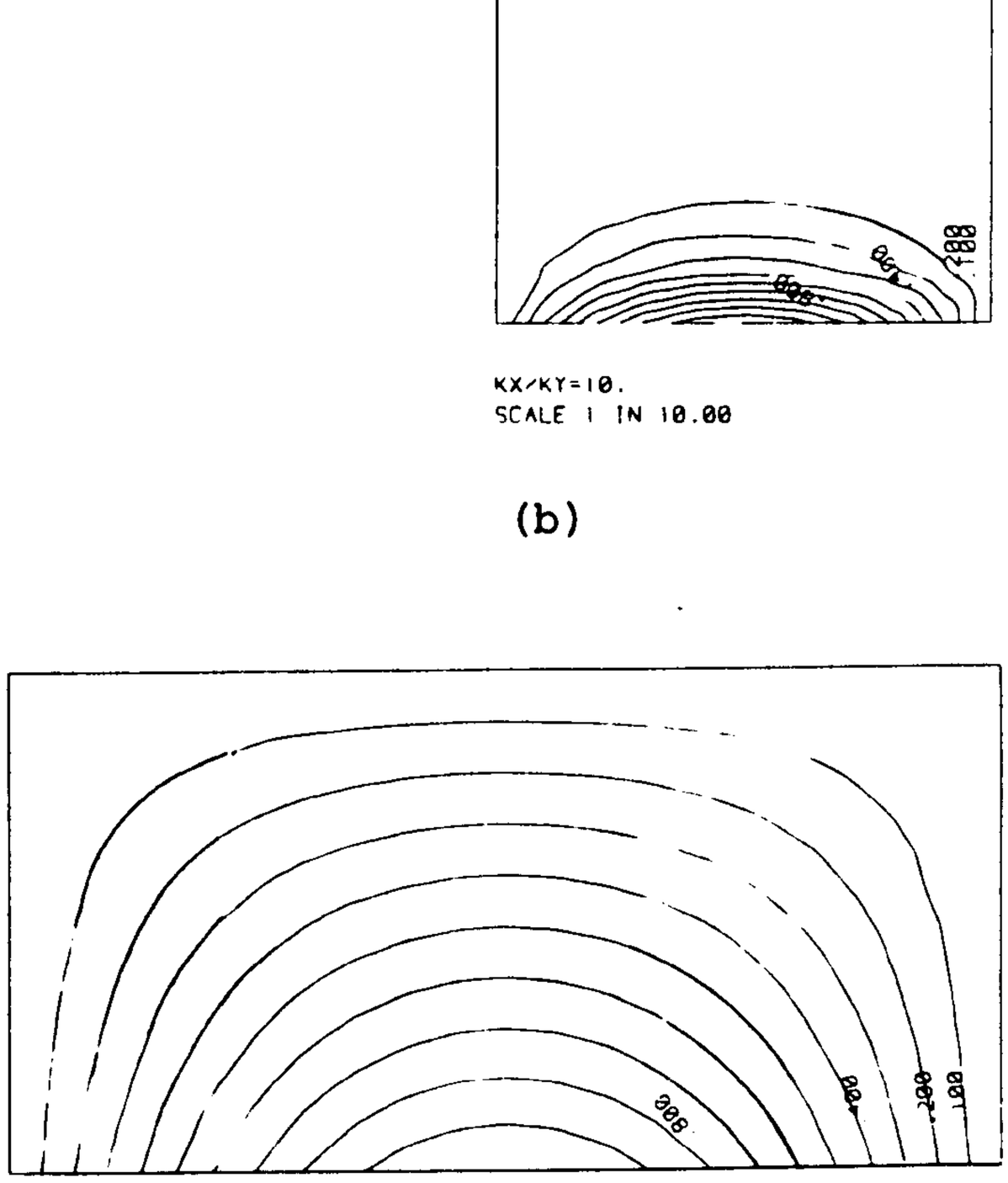

KX/KY=0.1

(d)

Fig. 6.2

Steady-state isotherms on orthotropic rectangle (Equation 6.4)

(a) $a/b = 2$, $K_1/K_2 = 10$

(b) $a/b = \frac{1}{2}$, $K_1/K_2 = 10$

(c) $a/b = \frac{1}{2}$, $K_1/K_2 = 0.1$

(d) $a/b = 2$, $K_1/K_2 = 0.1$

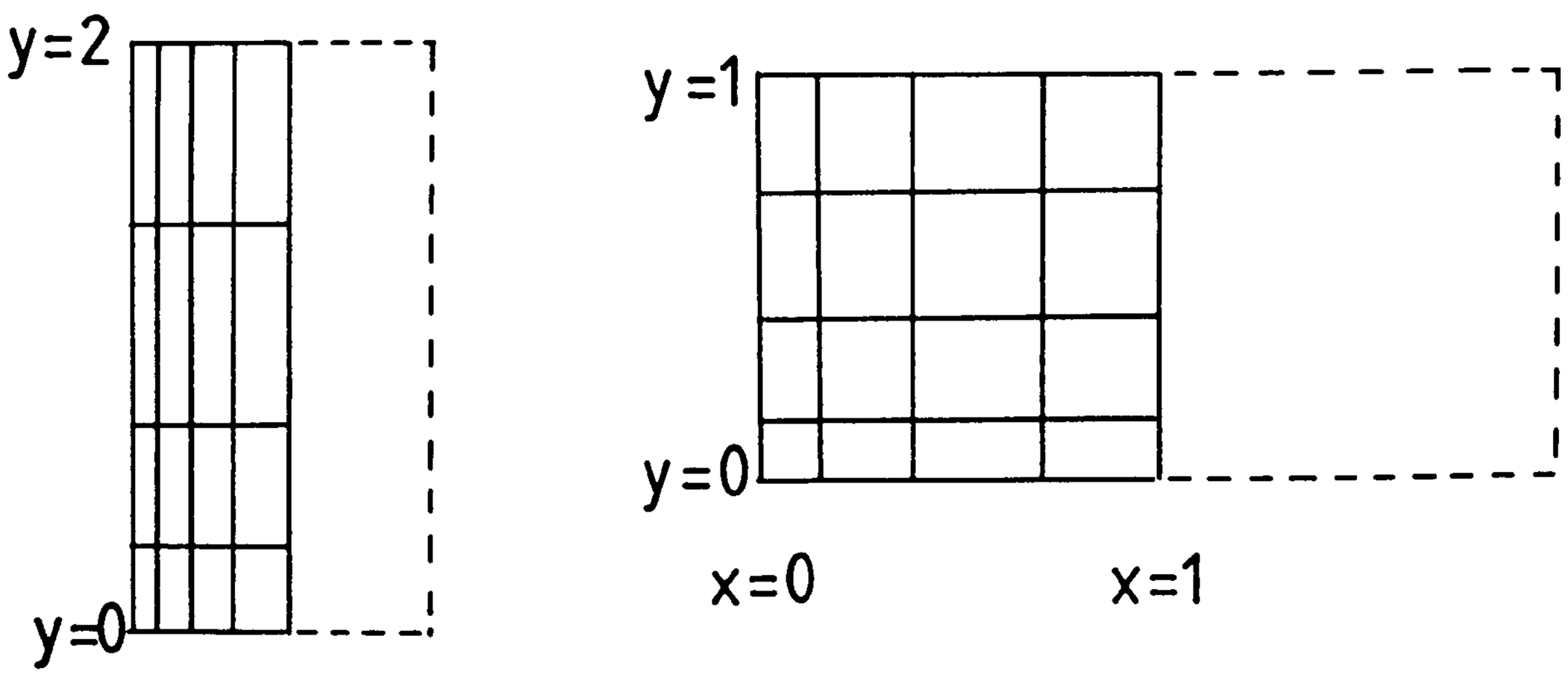

Fig. 6.3

Finite element meshes for the orthotropic rectangles, assuming symmetry about x = a/2.

representing only the region $0 < x < a/2$, $0 < y < b$. In this case the boundary along $x = a/2$ is adiabatic.

The finite element solutions are compared with analytic temperature distributions in Fig. 6.4. For the case $\gamma^2 = 0.1$, the difference between prediction and calculation is negligible; at all nodes on the finite element mesh the discrepancy is nowhere greater than about 10^{-4}. For $\gamma^2 = 10$ the temperature gradient near $y = 0$ is much greater, and a slight deviation from the analytic solution is seen in Fig. 6.4 (c) and (d). The largest differences between analytic and numerical temperatures are between 2 and 3×10^{-2}. Repeating the calculation on the refined mesh shown in Fig. 6.5 (in which the number of elements has been doubled from 16 to 32) the maximum error of the numerical solution is reduced by an order of magnitude to about 3×10^{-3}.

The orthotropic rectangular region of Fig. 6.1 is now considered with a combination of boundary conditions of the first and second kind. The general problem is illustrated in Fig. 6.6, and is defined mathematically by

$$T(x,y=0) = f(x), \quad 0 < x < a$$

$$\left.\begin{aligned} x = 0,\ 0 < y < b \\ y = b,\ 0 < x < a \end{aligned}\right\} \text{ adiabatic}$$

$x = a,\ 0 < y < b$ loses heat by convection, with transfer coefficient h, into a medium at temperature $T_\infty = 0$.

Carslaw and Jaeger (1959) give the steady-state temperature distribution as

$$T(x,y) = \sum_{n=1}^{\infty} \frac{2(h'^2+\beta_n^2)\cos\beta_n x \ \cosh\beta_n\gamma(b-y)}{[(\beta_n^2+h'^2)a + h']\cosh\beta_n\gamma b} \int_0^a f(x)\cos\beta_n x \ dx \qquad (6.5)$$

where $h' = h/K_1$, and the eigenvalues β_n are given by the transcendental equation

$$\beta \tan \beta a = h'$$

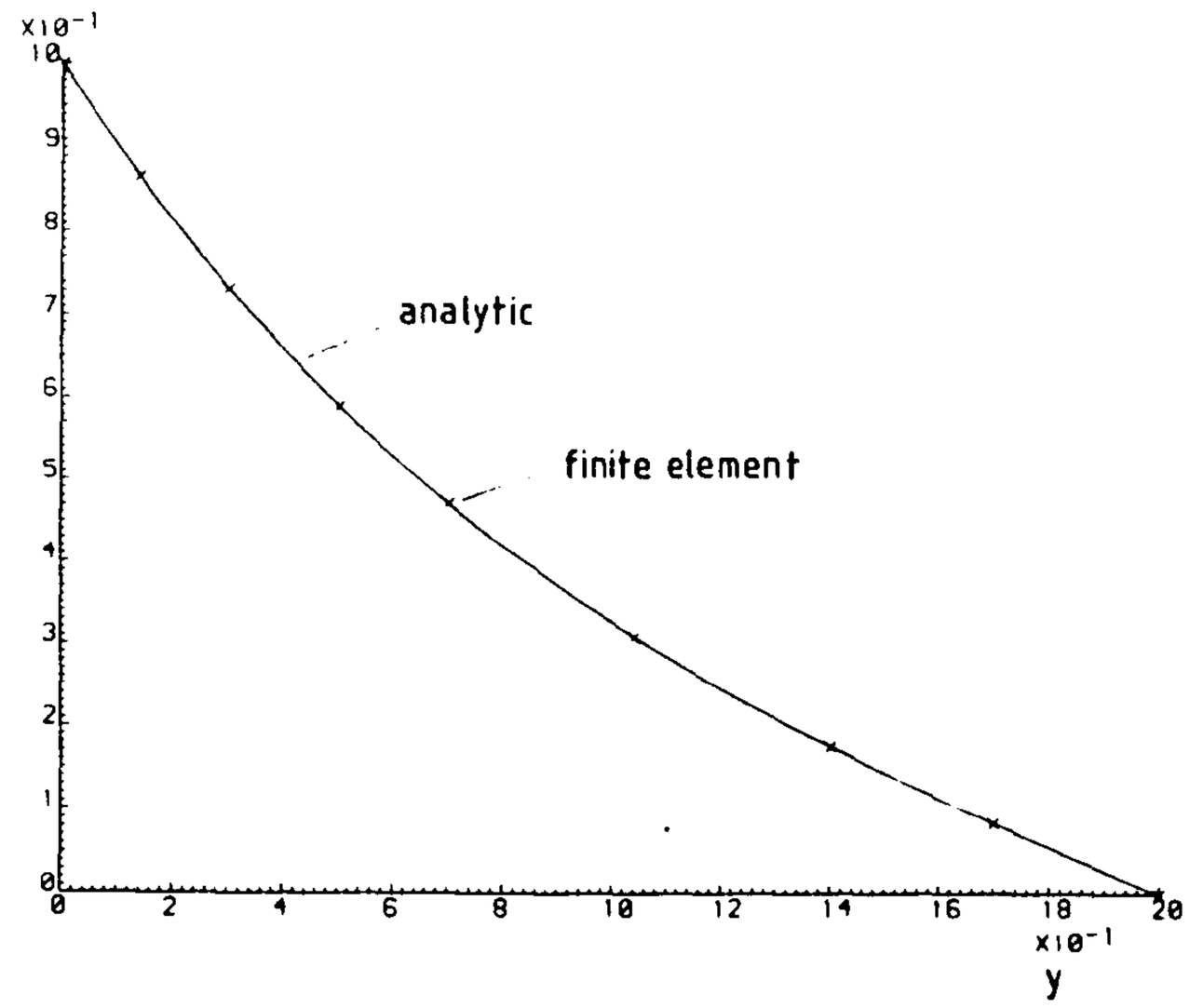

(a)

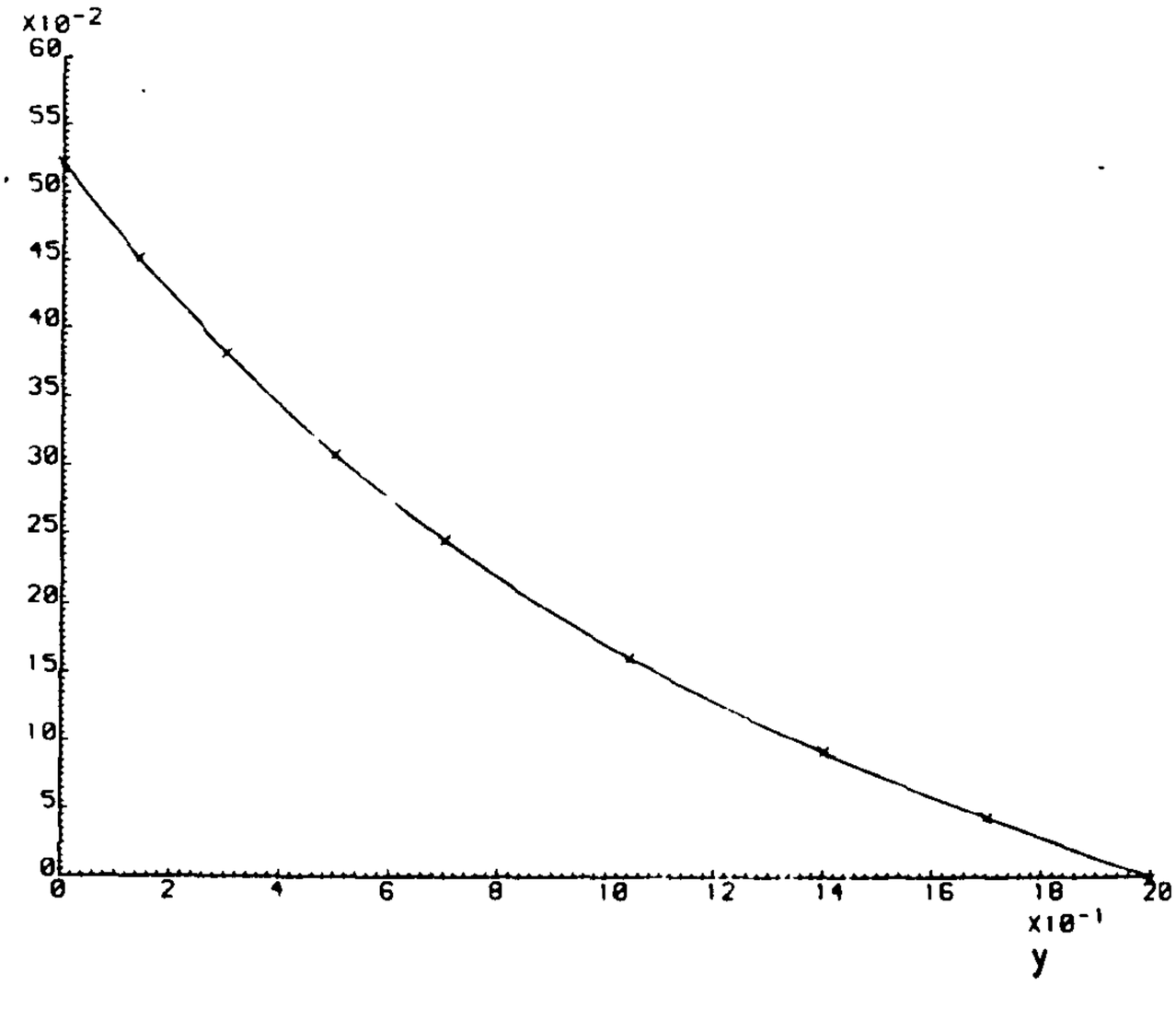

(b)

Fig. 6.4

Comparison between finite element ('X') and analytic temperatures (smooth curve) on rectangle with a/b = ½.

(a) $T(0.5,y)$, $K_1/K_2 = 0.1$

(b) $T(0.175,y)$, $K_1/K_2 = 0.1$

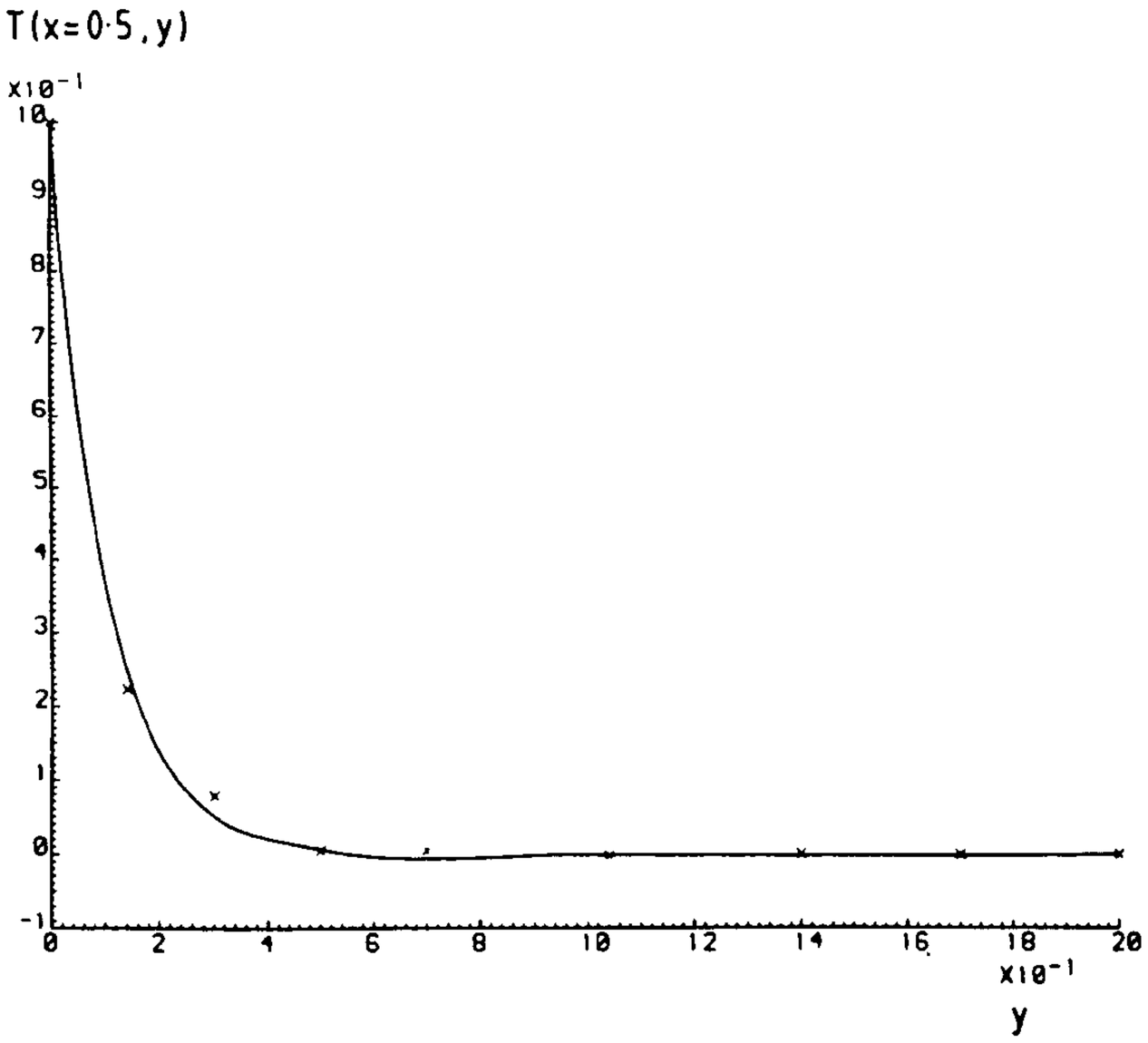

(c)

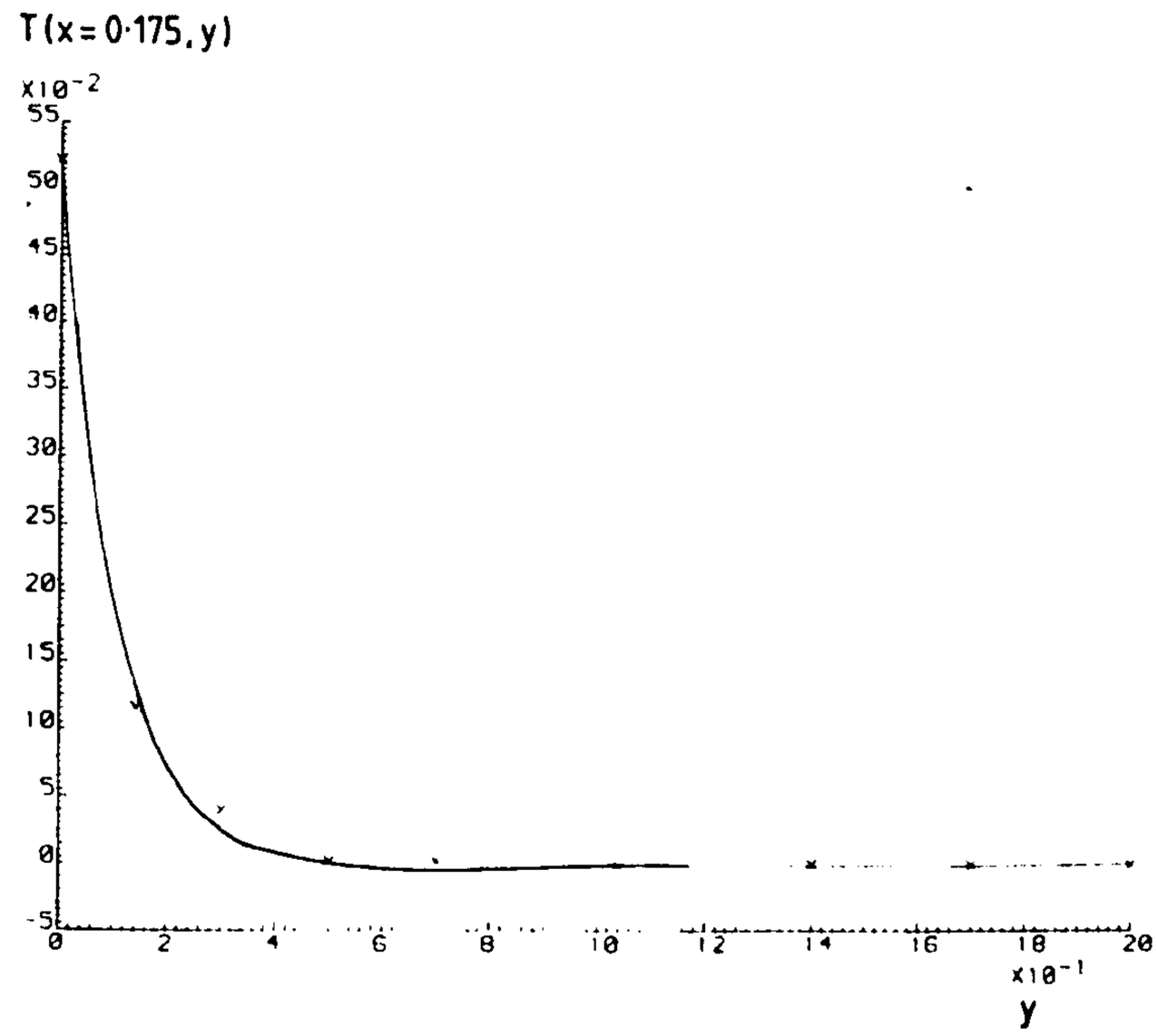

(d)

Fig. 6.4 (cont)

(c) $T(0.5,y)$, $K_1/K_2 = 10$

(d) $T(0.175,y)$, $K_1/K_2 = 10$

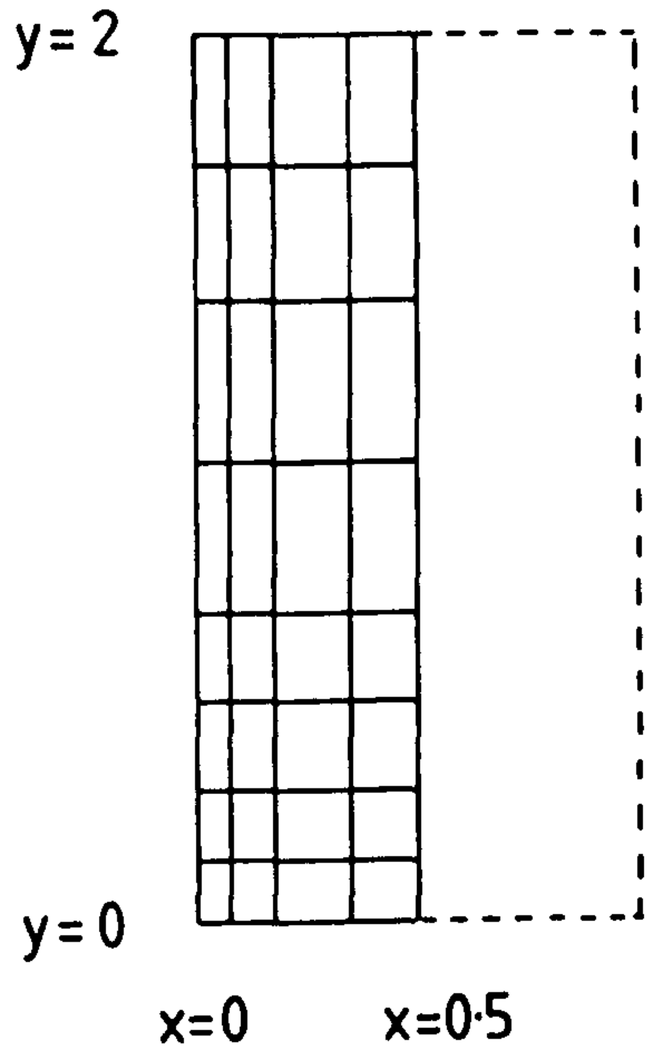

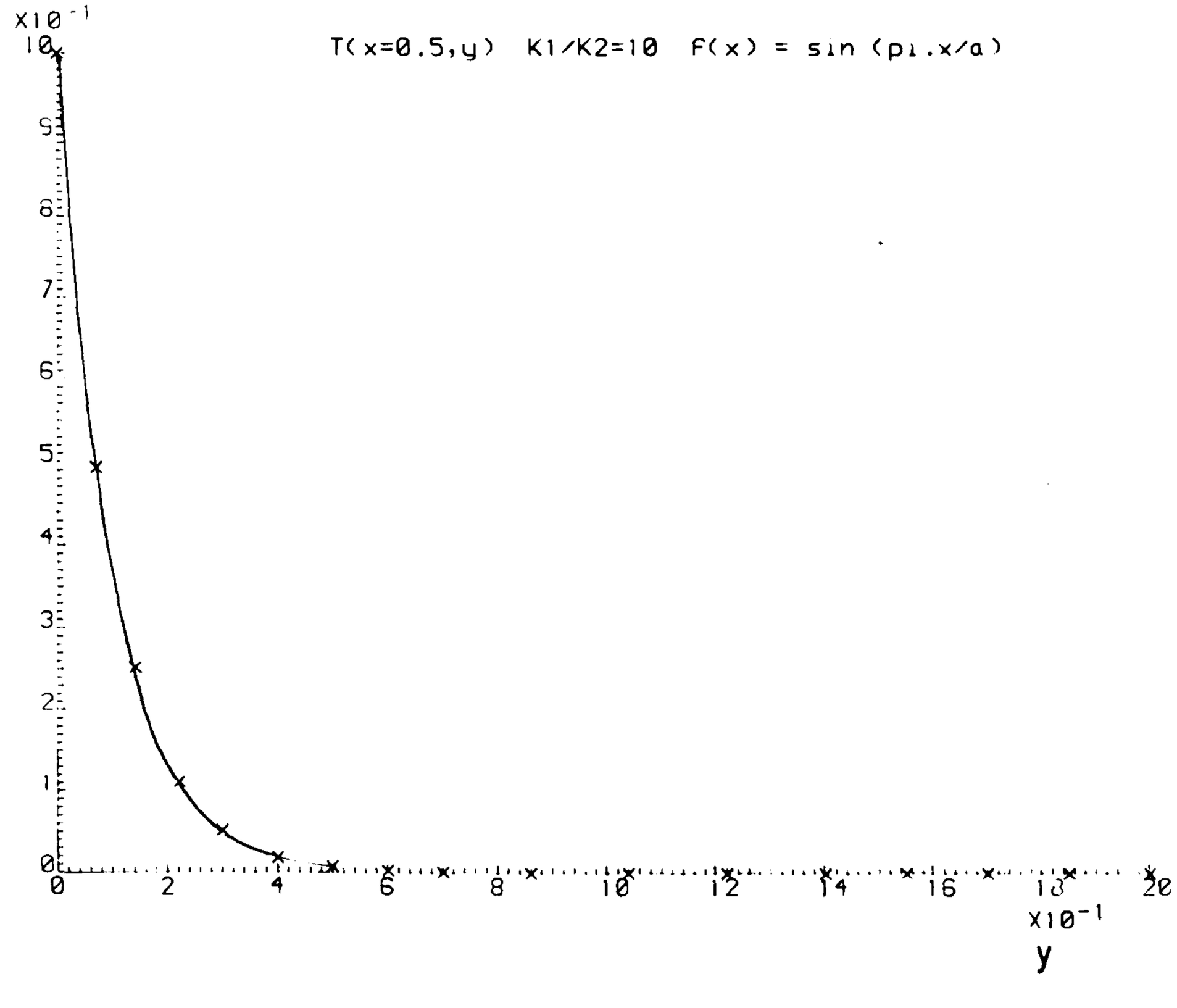

Fig. 6.5

Refined mesh for rectangle with a/b = ½, and improved solution for case (c), Fig. 6.4.

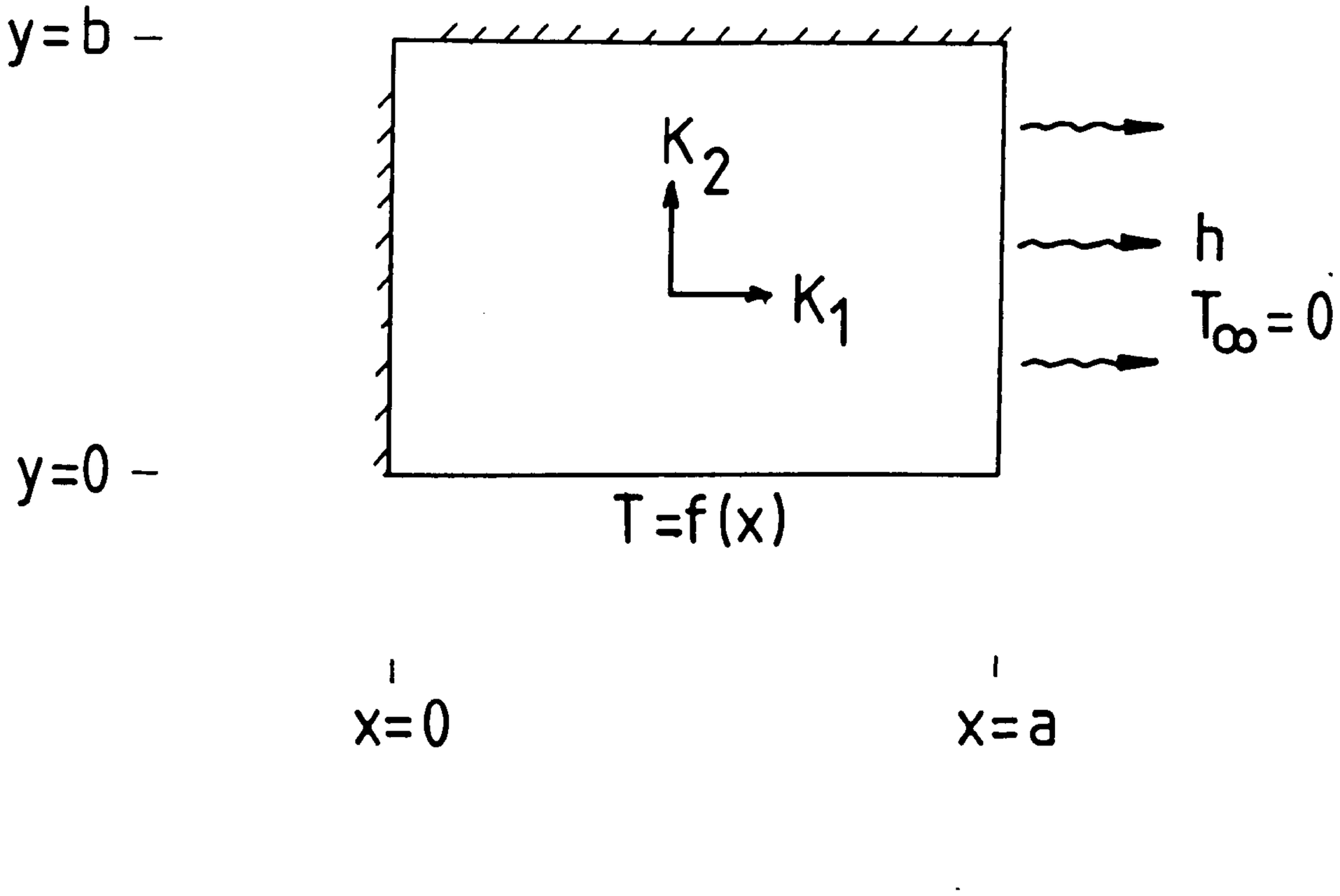

Fig. 6.6

Orthotropic rectangle with mixed boundary conditions.

If $f(x) = T_o$ (a constant temperature), then Equation 6.5 becomes

$$T(x,y) = 2h'T_o \sum_{n=1}^{\infty} \frac{\cos \beta_n x \ \cosh \gamma\beta_n (b-y)}{[(\beta_n^2+h'^2)\ a + h'] \cos \beta_n a \ \cosh \gamma\beta_n b} \qquad (6.6)$$

As in the previous example, two rectangular regions (a/b = 2 and ½) and two thermal conductivity ratios (γ^2 = 10 and 0.1) are considered; Fig 6.7 illustrates the normalised temperature distributions (T_o = 1) for these four combinations, taking h = 5 throughout. In calculating the analytic temperature field it was found necessary to use values of β_n up to n = 20 in order to obtain a precision of 10^{-4}. Convergence was slowest near y = 0.

The initial finite element meshes for this problem are shown in Fig. 6.8, and Fig. 6.9 compares analytic and calculated temperatures along the convecting edge (x = a) for the various combinations of parameters. The agreement obtained is generally good, but discrepancies of up to 0.05 (i.e. 5%) occur near the corner x = a, y = 0, where the temperature gradient is most severe.

In an attempt to quantify the improvement of the numerical solution with mesh refinement, the case a = 2, b = 1, γ^2 = 0.1 has been considered in more detail. The calculation was repeated with increasing numbers of elements in the y-direction whilst retaining the distribution in the x-direction shown in Fig. 6.8. For N elements in the y-direction, element sizes were in the ratio 1 : 2 : 3 : . . . : N. For each mesh, the mean absolute error between analytic and numerical temperatures was calculated for nodes along the convective surface (x = 2). The reduction of the mean error and the adjusted r.m.s. deviation (S) with increasing numbers of elements is shown in Fig. 6.10. Increasing N from 2 to 5 more than halves the mean error, and reduces S by a factor of 3.

A further demonstration of convergence is provided by the error at a fixed point on the convective edge. An example is shown in Fig. 6.11, where the difference between analytic and numerical temperatures at (x = 2, y = 0.1) is shown for

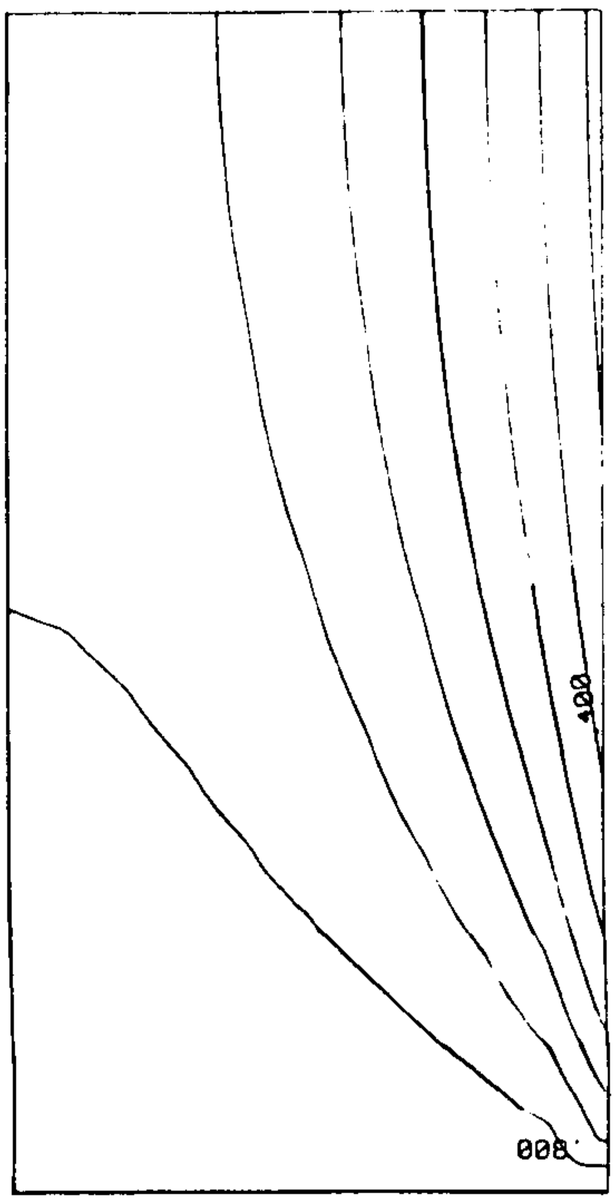

K1/K2=0.1

(a)

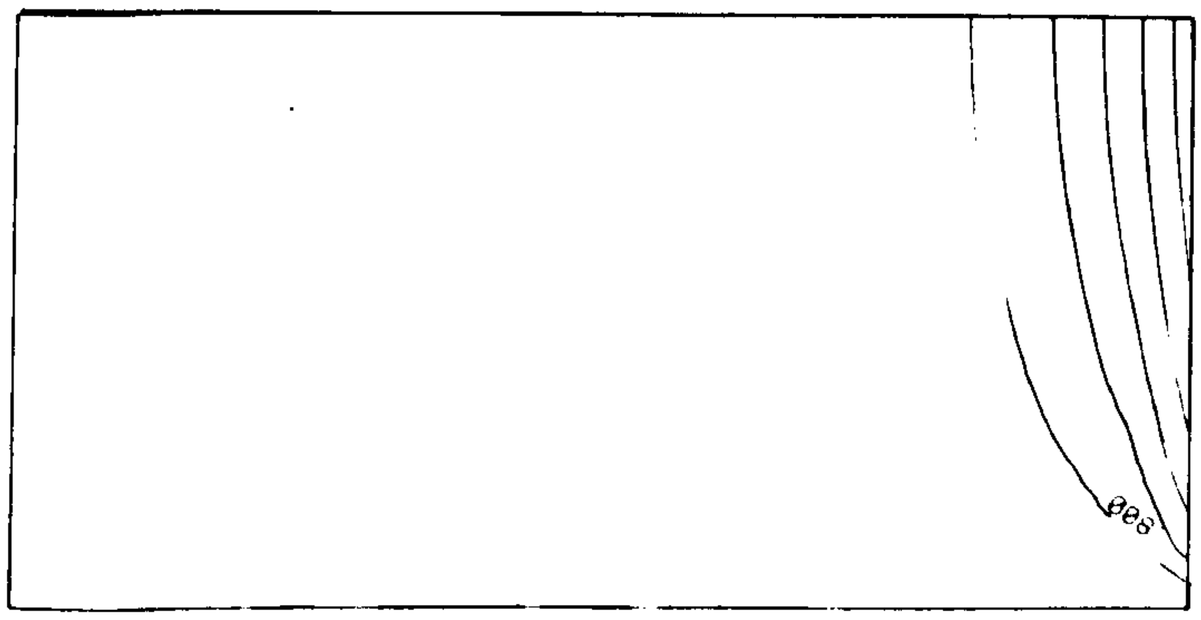

K1/K2=0.1

(b)

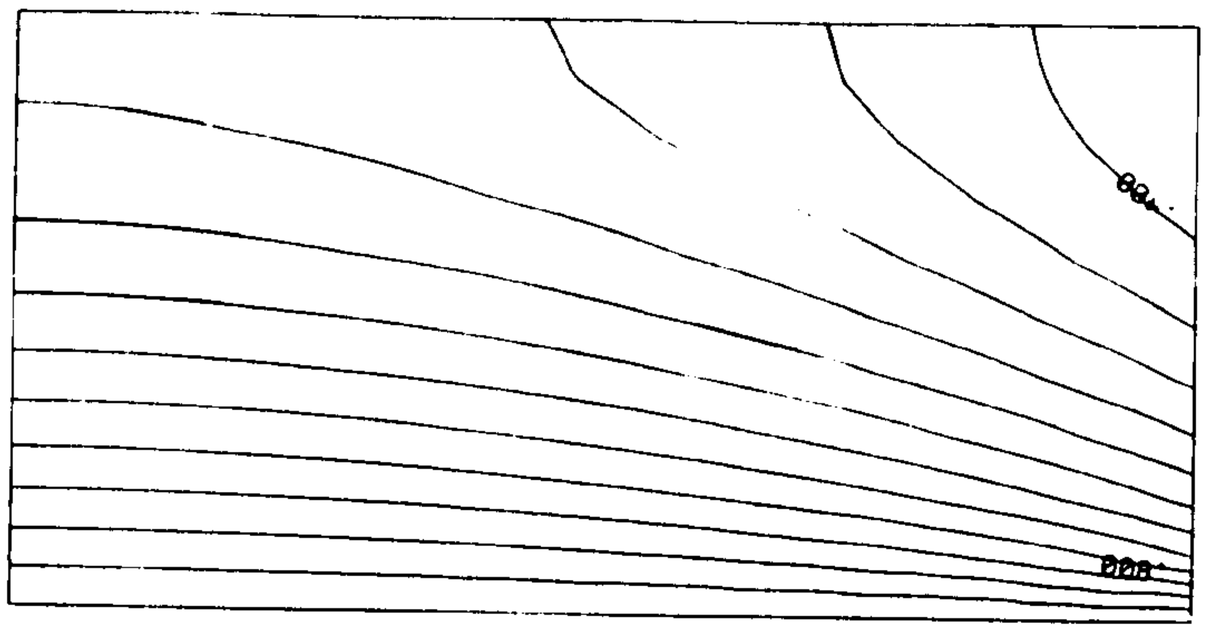

KX/KY=10, H=5

(c)

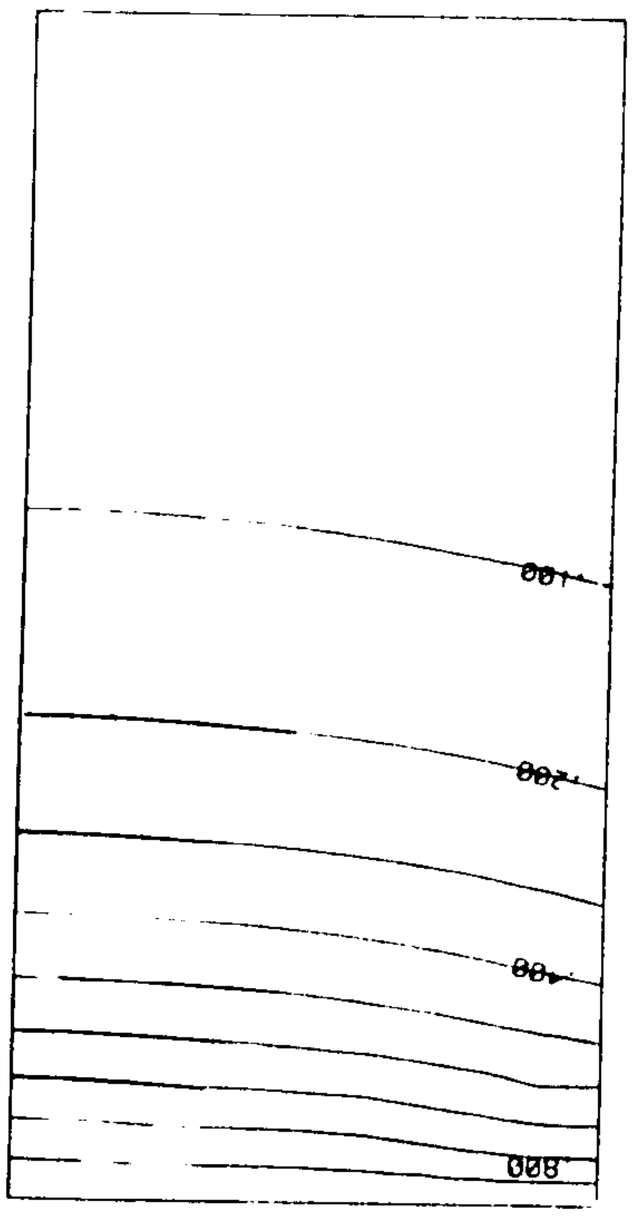

K1/K2=10.0

(d)

Fig. 6.7

Steady-state isotherms on orthotropic rectangle (Equation 6.6)

(a) $a/b = \frac{1}{2}$, $K_1/K_2 = 0.1$

(b) $a/b = 2$, $K_1/K_2 = 0.1$

(c) $a/b = 2$, $K_1/K_2 = 10$

(d) $a/b = \frac{1}{2}$, $K_1/K_2 = 10$

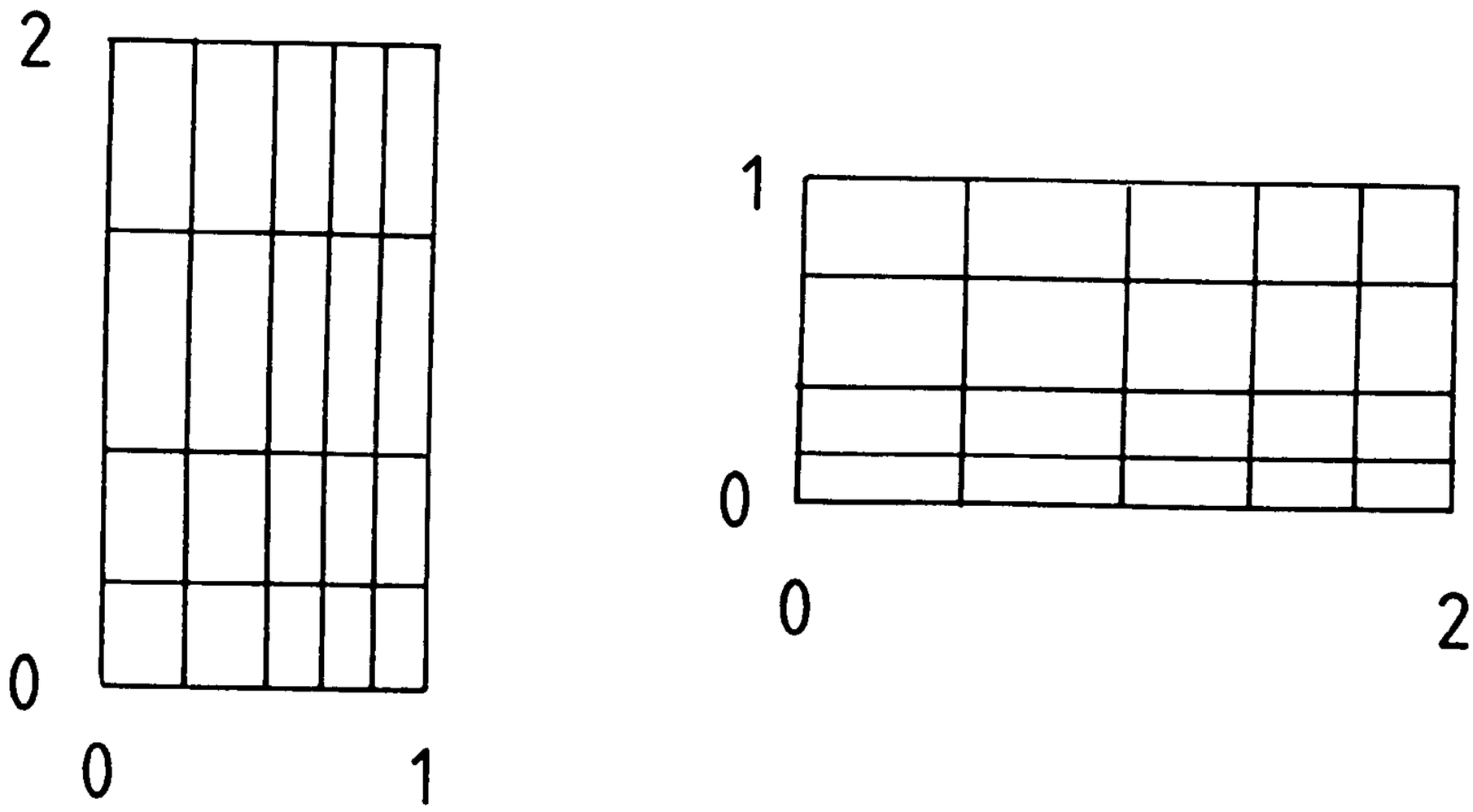

Fig. 6.8

Finite element meshes for orthotropic rectangle.

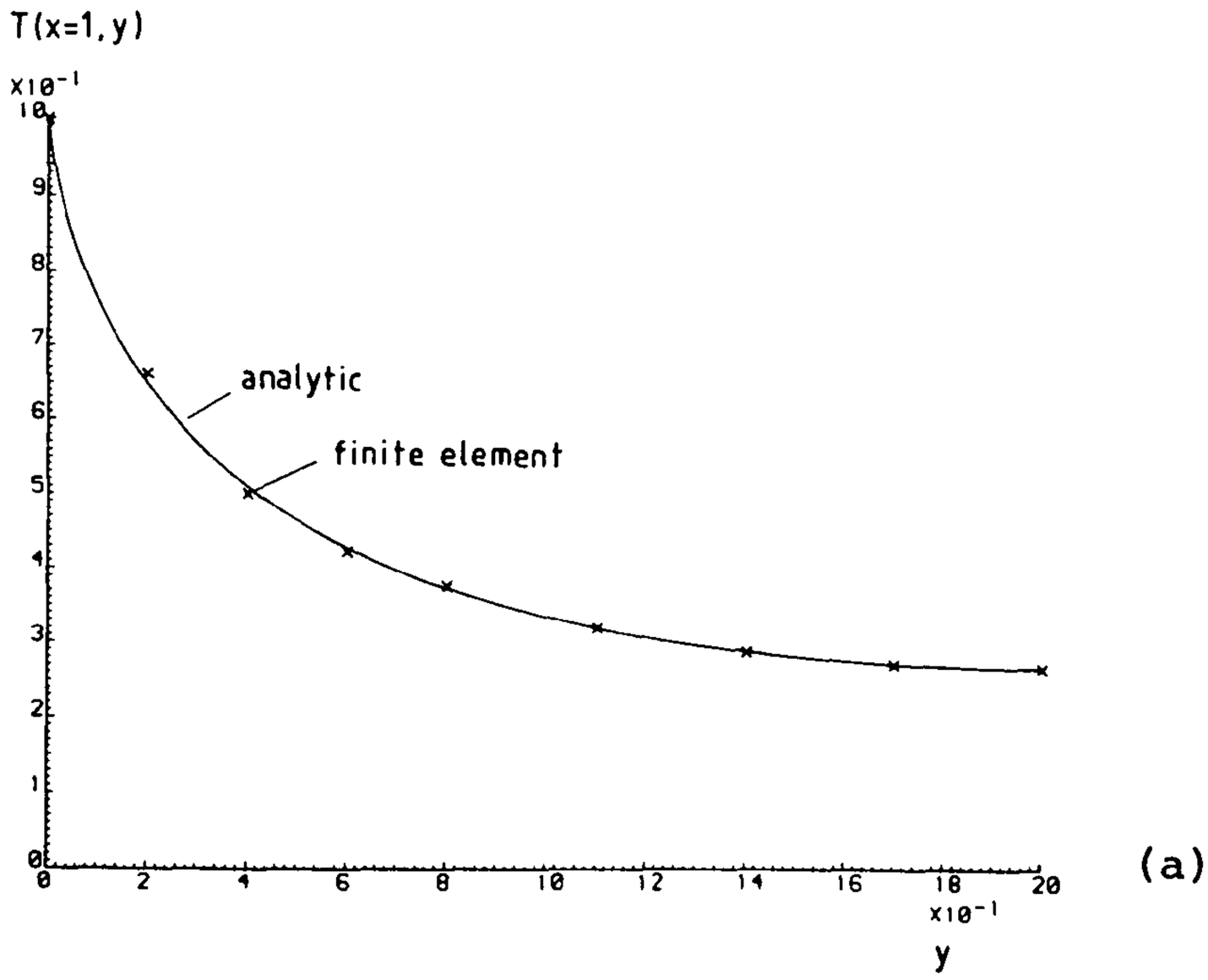

Fig. 6.9

Comparison between finite element and analytic temperatures along the convective edge, x = a.

(a) $a/b = \frac{1}{2}$, $K_1/K_2 = 0.1$

(b) $a/b = 2$, $K_1/K_2 = 0.1$

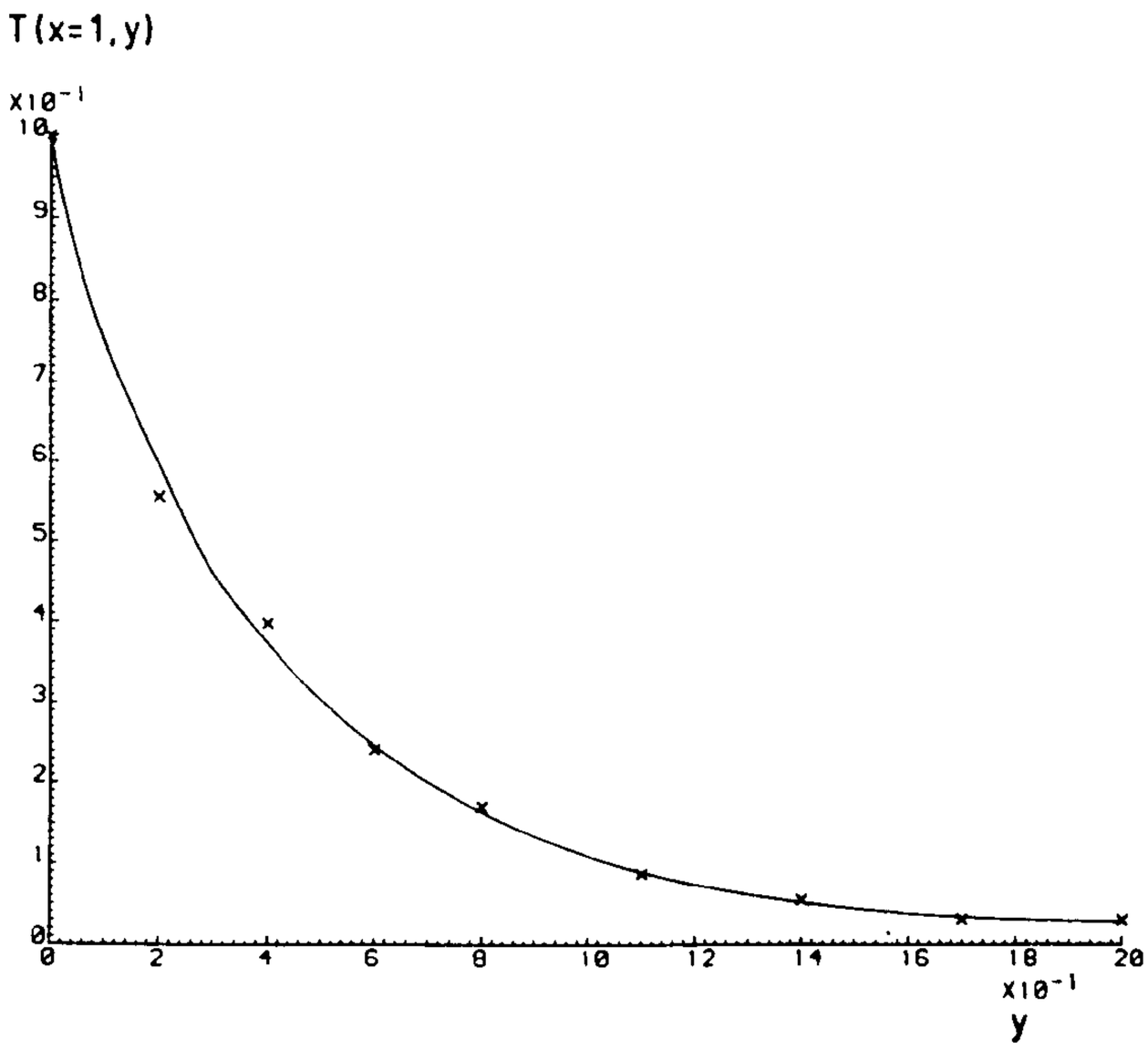

(c)

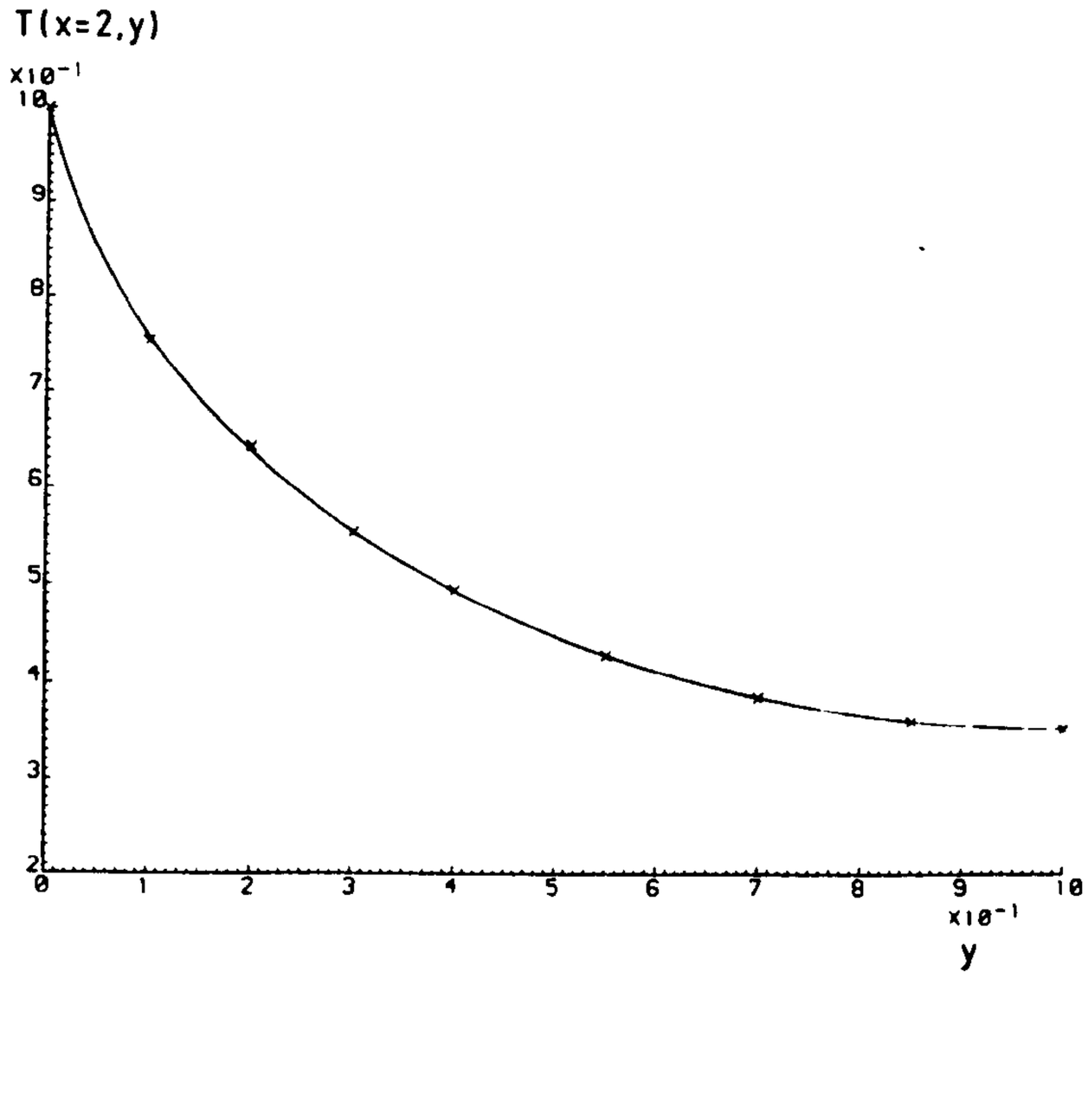

(d)

Fig. 6.9 (cont)

(c) $a/b = \frac{1}{2}$, $K_1/K_2 = 10$

(d) $a/b = 2$, $K_1/K_2 = 10$

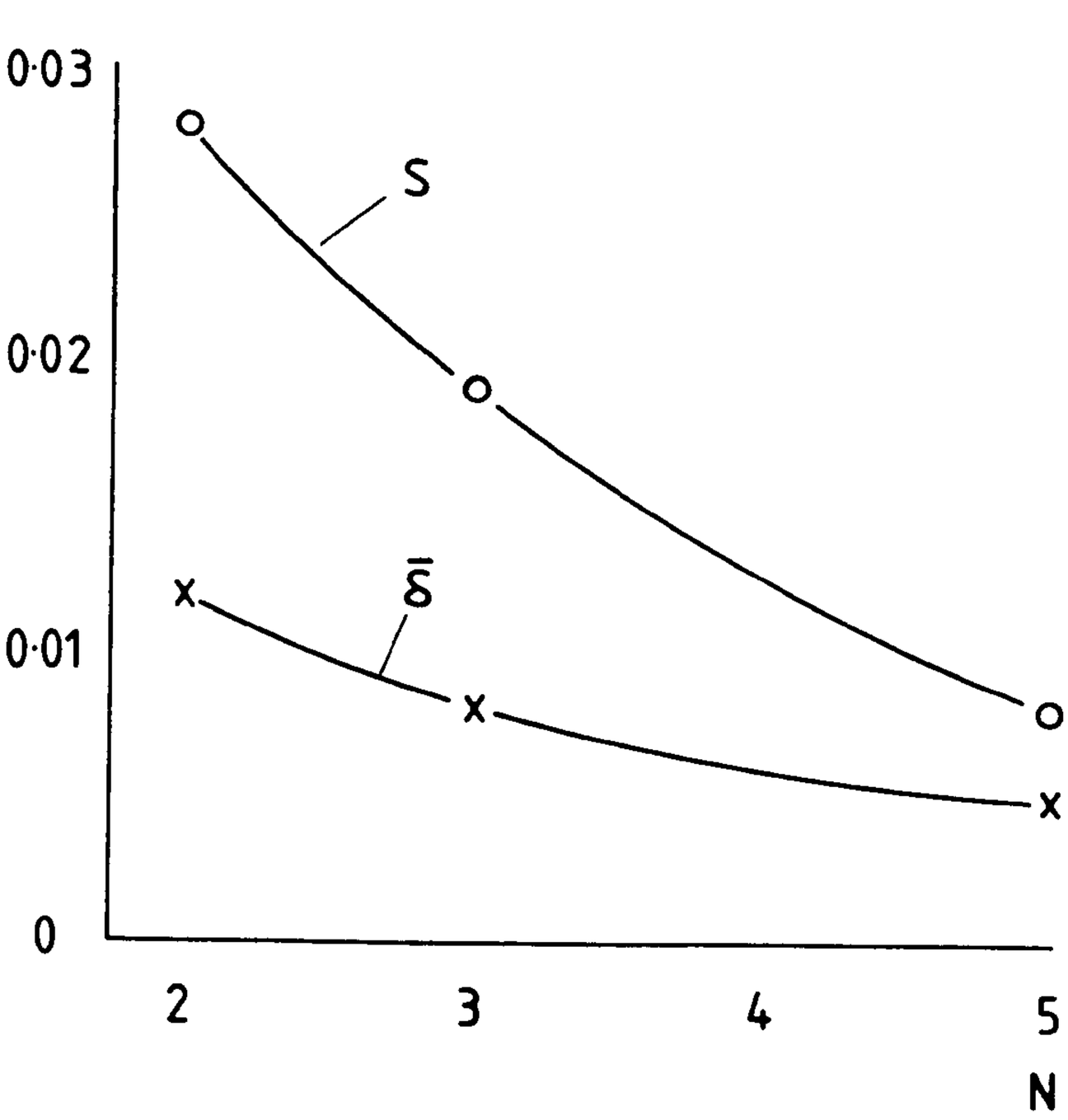

Fig. 6.10

Reduction of mean (absolute) error ($\bar{\delta}$) and adjusted r.m.s. deviation (S) at nodes on convective edge with increasing number of elements in y-direction (N). Case (b), Fig. 6.9.

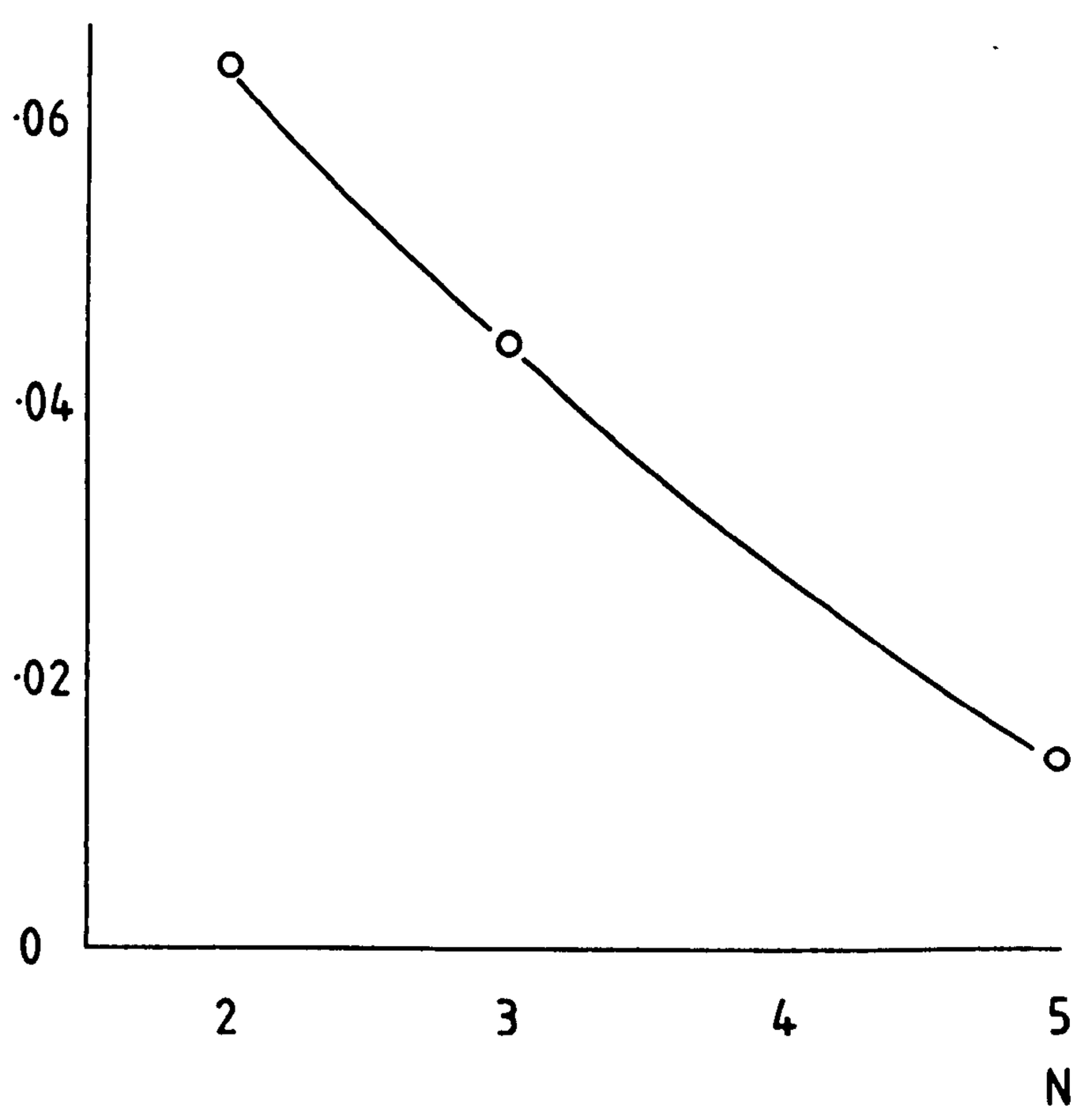

Fig. 6.11

Reduction of the difference between analytic and numerical temperatures at x = a, y/b = 0.1 with increasing N. Case (b), Fig. 6.9.

increasing element numbers. In this case 5 elements (in the y-direction) are required to achieve an accuracy of 1%.

6.2.2 Anisotropic Disc

In 4.2.3 reference was made to a result recognised by Chang and others (1973) concerning the temperature distribution on a circular disc of unit radius, with a boundary temperature fixed by $T(r = 1, \theta) = a + b \cos\theta$, where a and b are arbitrary constants. The solution (by inspection) is

$$T(r, \theta) = a + br\cos\theta = a + bx \qquad (6.7)$$

and is independent of thermal conductivity. The problem and its solution are illustrated in Fig. 6.12, and provide a simple preliminary validation of the numerical model with anisotropic conductivities.

A coarse finite element representation of a unit disc is shown in Fig. 6.13, where curved-sided quadrilateral elements have been used to represent the circle exactly. For convenience, calculations were performed with a = 0 and b = 1 in Equation 6.7, for a range of different thermal properties, ranging from isotropic up to anisotropy ratios (γ^2) of 40, and with various orientations of principal axes. In all cases, the difference between analytic and calculated temperatures at any node was less than about 10^{-5} (that is, 0.001% of the maximum temperature difference across the disc).

6.2.3 Anisotropic Slab

The final problem considered in this section was discussed in 4.2.5 (Tauchert and Akoz, 1975) and illustrated in Figs. 4.8 to 4.10. Following the authors' example, calculations have been performed for the isotropic and two orthotropic cases (K_1/K_2 = 10 and 100), and also with different orientations of principal axes. Fig. 6.14 shows the geometry and parameters considered.

The region of interest in this problem extends to $\pm\infty$ in the x-coordinate direction, and hence requires particular

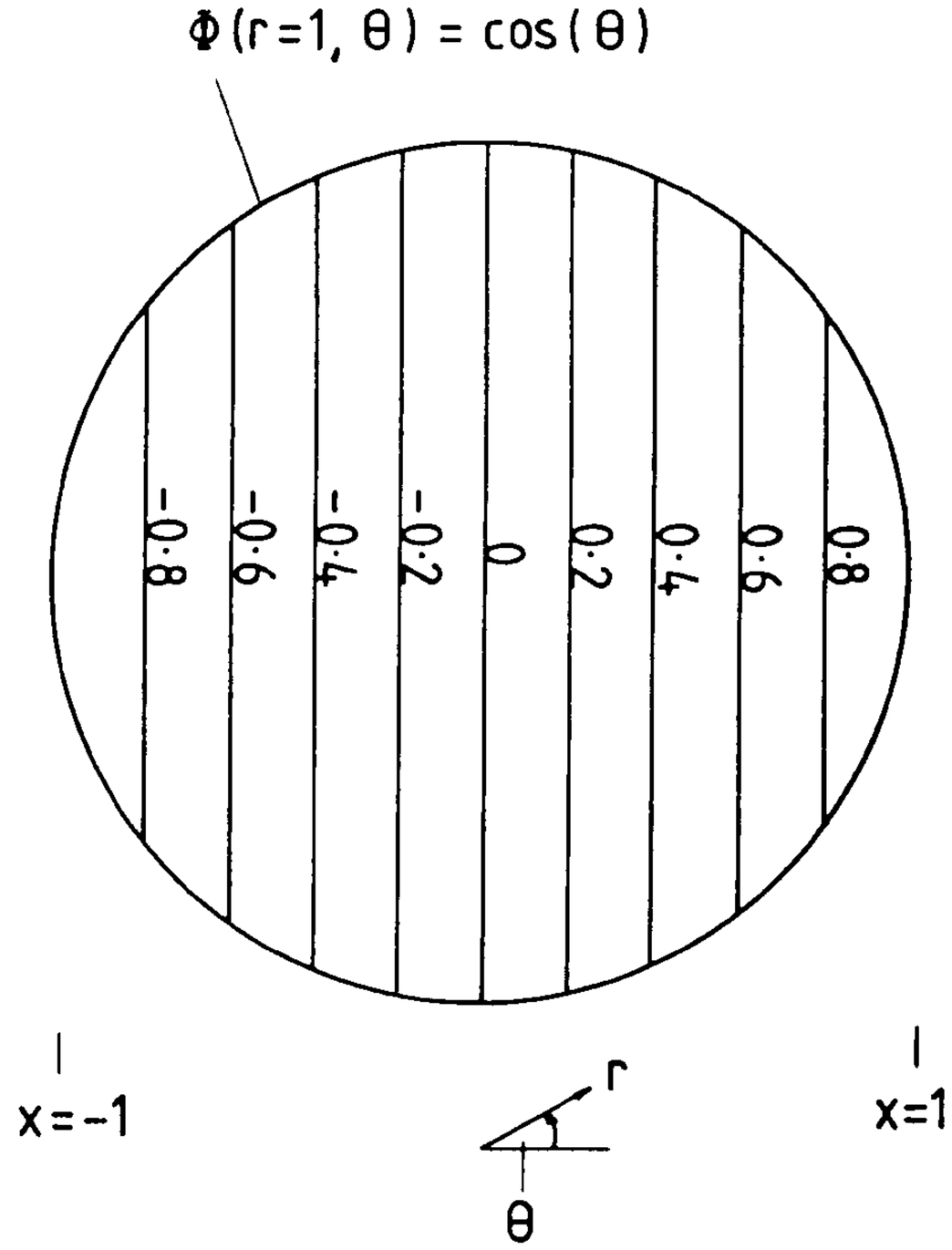

Fig. 6.12

Anisotropic unit disc with fixed surface temperatures, showing isotherms of normalised temperature

$$\Phi(r,\theta) = \frac{T(r,\theta) - a}{b}$$

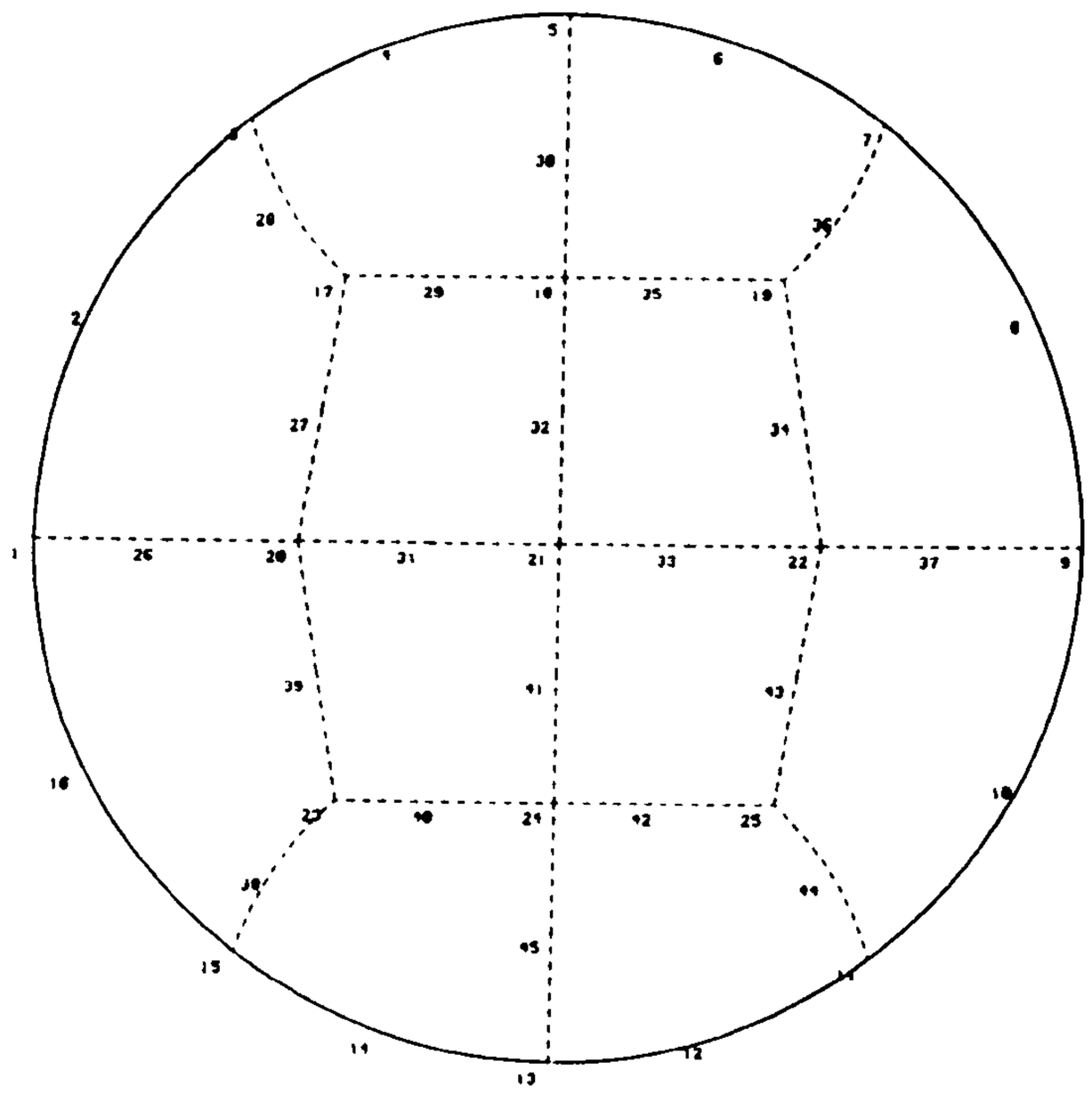

Fig. 6.13

Representation of unit disc by 12 elements.

care in its finite element representation. Mathematical formulations are available for elements of infinite extent (see, for example, Zienkiewicz, 1977) but the approach used here is simply to extend the mesh sideways to some point $x = \pm p$, where, ideally, $p >> h$ (see Fig. 6.14). The artificial boundary so created is taken to be adiabatic, and is assumed not to influence the temperature distribution near x = O. This problem is further complicated by the discontinuity in temperature at $x = \pm h$, y = h, and requires an appropriate reduction in the mesh size, as shown in Fig. 6.14.

Comparisons of finite element and analytic solutions for the temperature distribution at x = O are shown in Fig. 6.15, and are considered to be generally satisfactory, although the large temperature gradients produced by the second orthotropic material (Material III, $\gamma^2 = 100$) require better resolution. This is achieved by the mesh shown in Fig. 6.16, which retains the same number of elements, but reduces their size near y = h. The finite element solution along x = O on this refined mesh is compared with the analytic temperature distribution in Fig. 6.17. The reduction in mean error is small (from .037 to .034) but this does not fully reflect the improvement of the solution in the region $y/h \geq 0.5$, which now gives a considerably better representation of the large temperature gradient near y = h. This is evident in the r.m.s. deviation (S), which is reduced from .042 to .018. Mesh optimisation for other orientations of the orthotropic material could be performed in a similar way, although the position of maximum temperature gradient would be less easy to determine a priori.

The influence of the boundaries at $x = \pm p$ on the temperature distribution at x = O was investigated for the case of isotropic thermal properties. The mesh shown in Fig. 6.14 was used as a basis, and the value of p was varied between 2h and 5h. Fig. 6.18 shows the variation of mean error ($\bar{\delta}$) and deviation (S) for the 7 nodes along x = O. There is a sharp reduction in mean error between p = 2h and 3h, but it

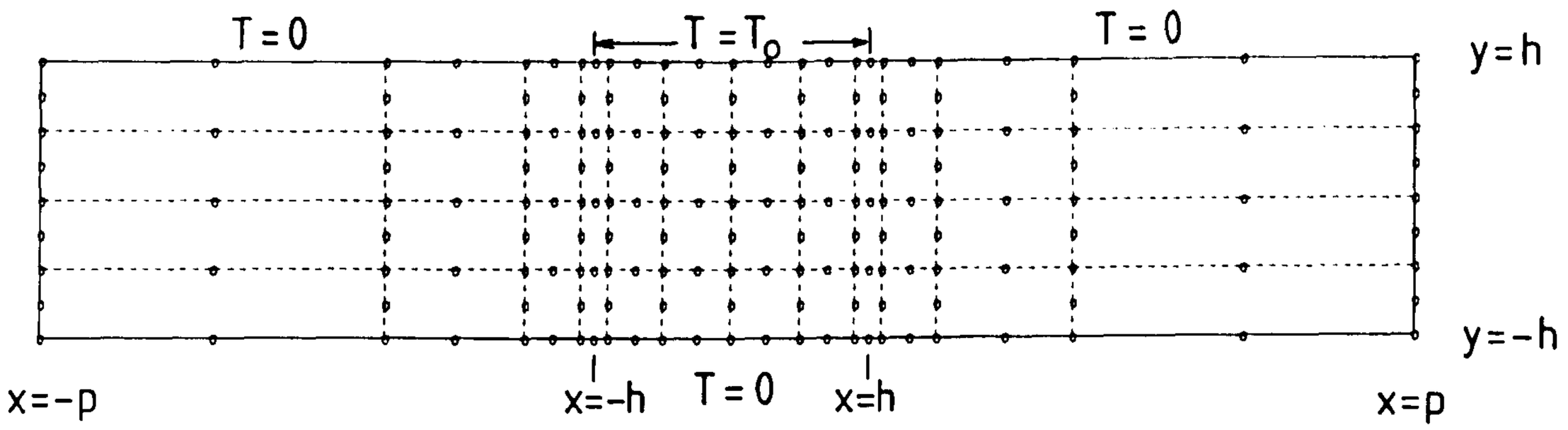

Fig. 6.14

Finite element representation of semi-infinite slab.

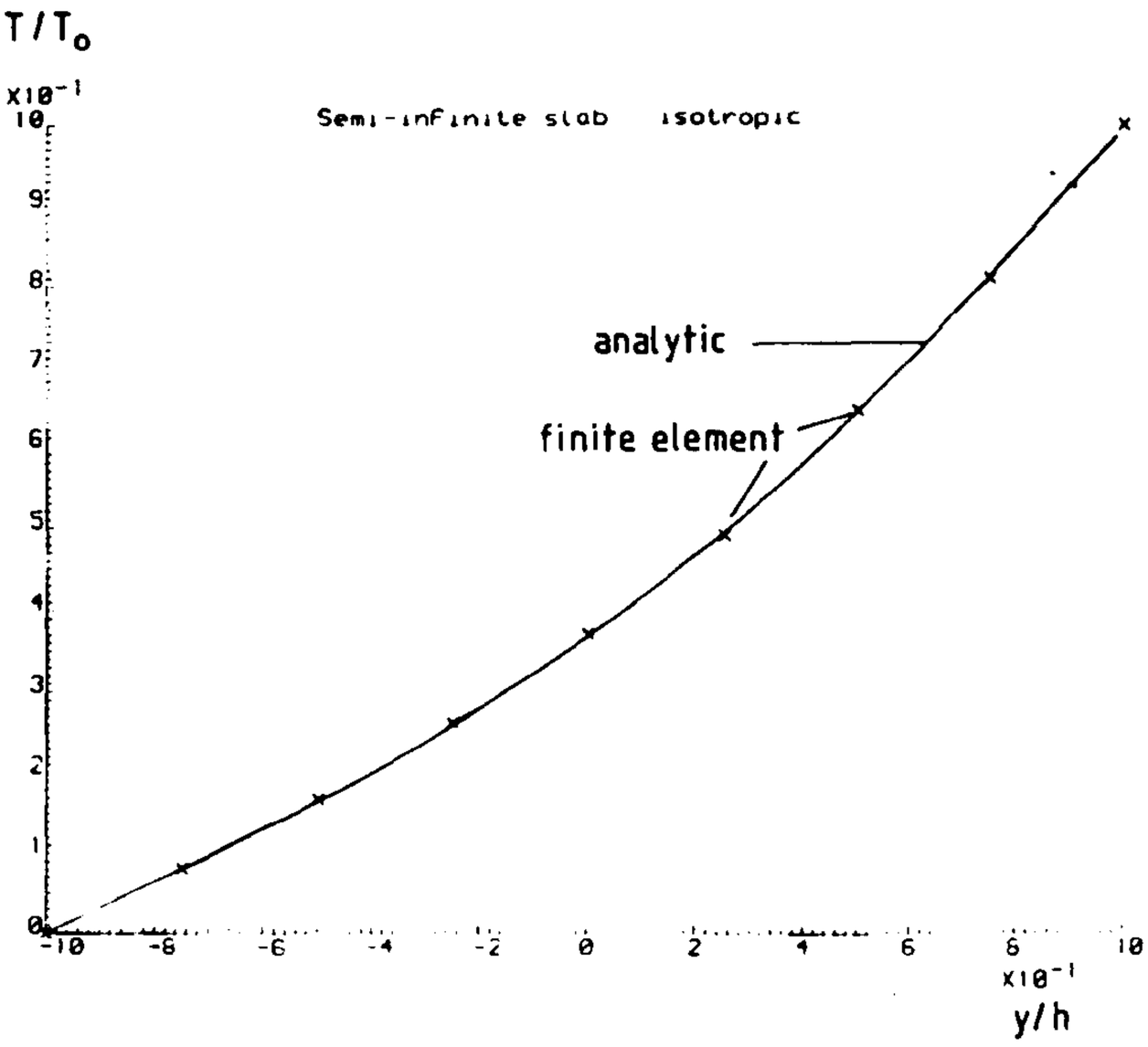

Fig. 6.15

Comparison between finite element and analytic temperatures on semi-infinite slab at x = 0.

(a) Material I (isotropic)

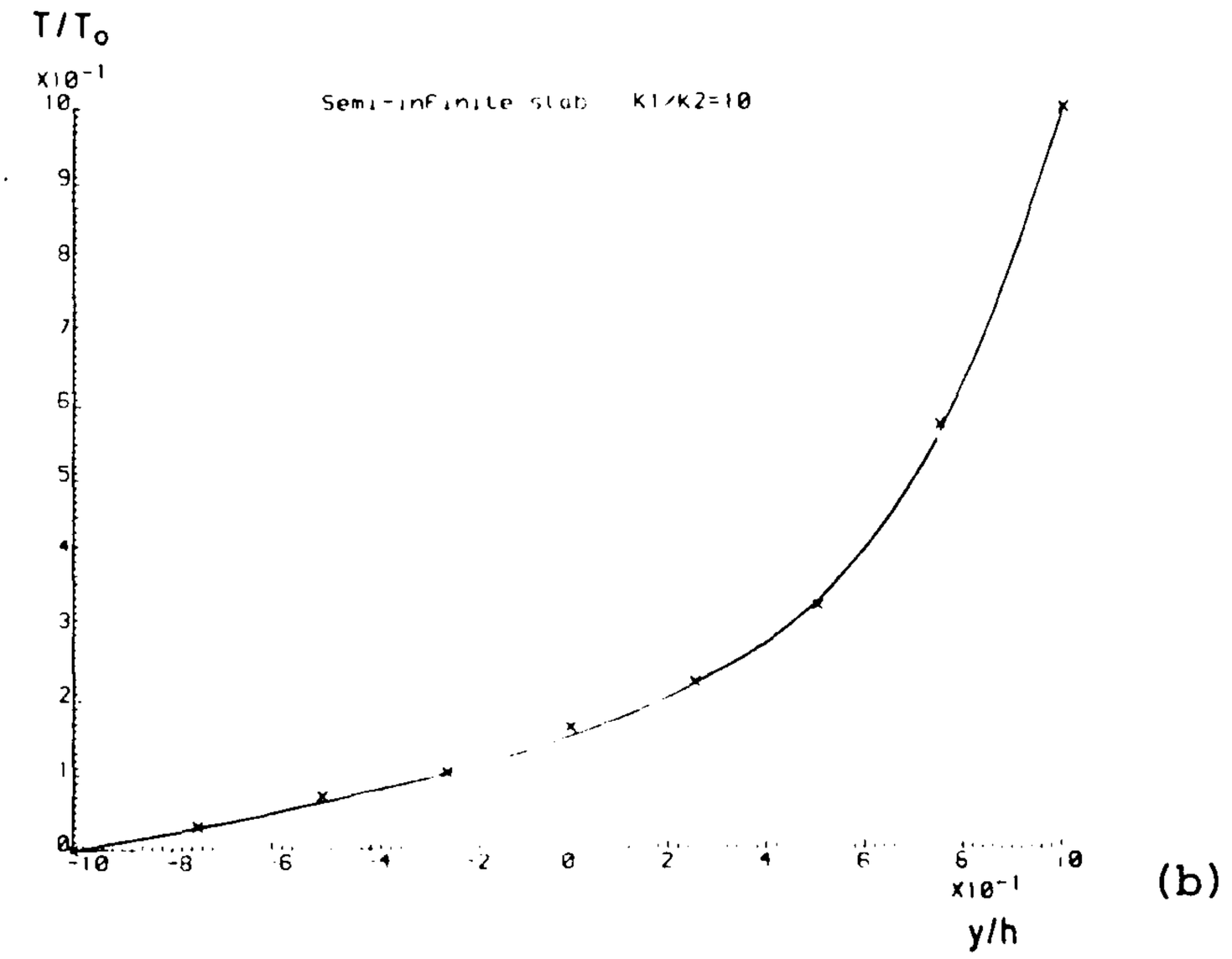

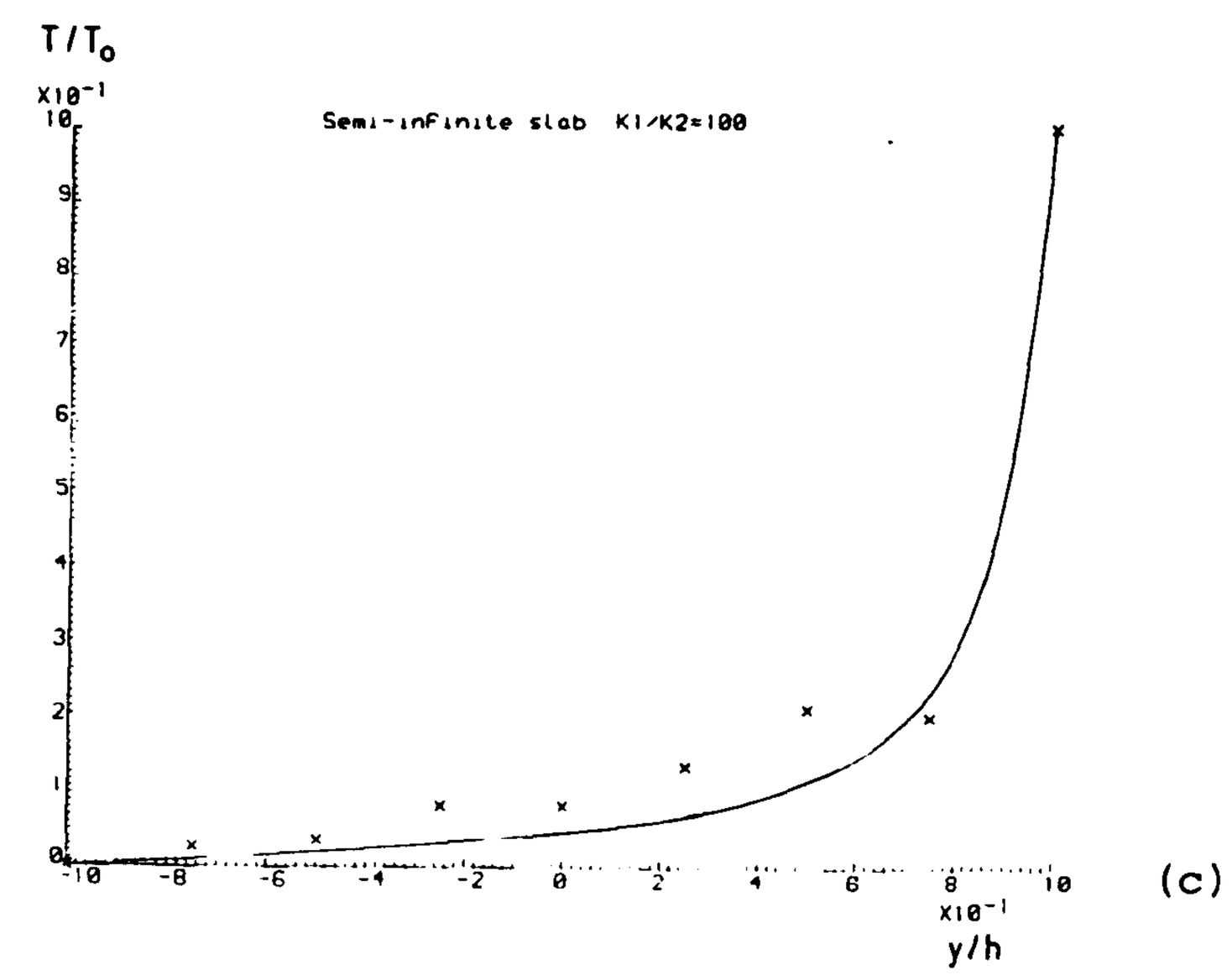

Fig. 6.15 (cont)

(b) Material II (K_1/K_2 = 10)

(c) Material III (K_1/K_2 = 100)

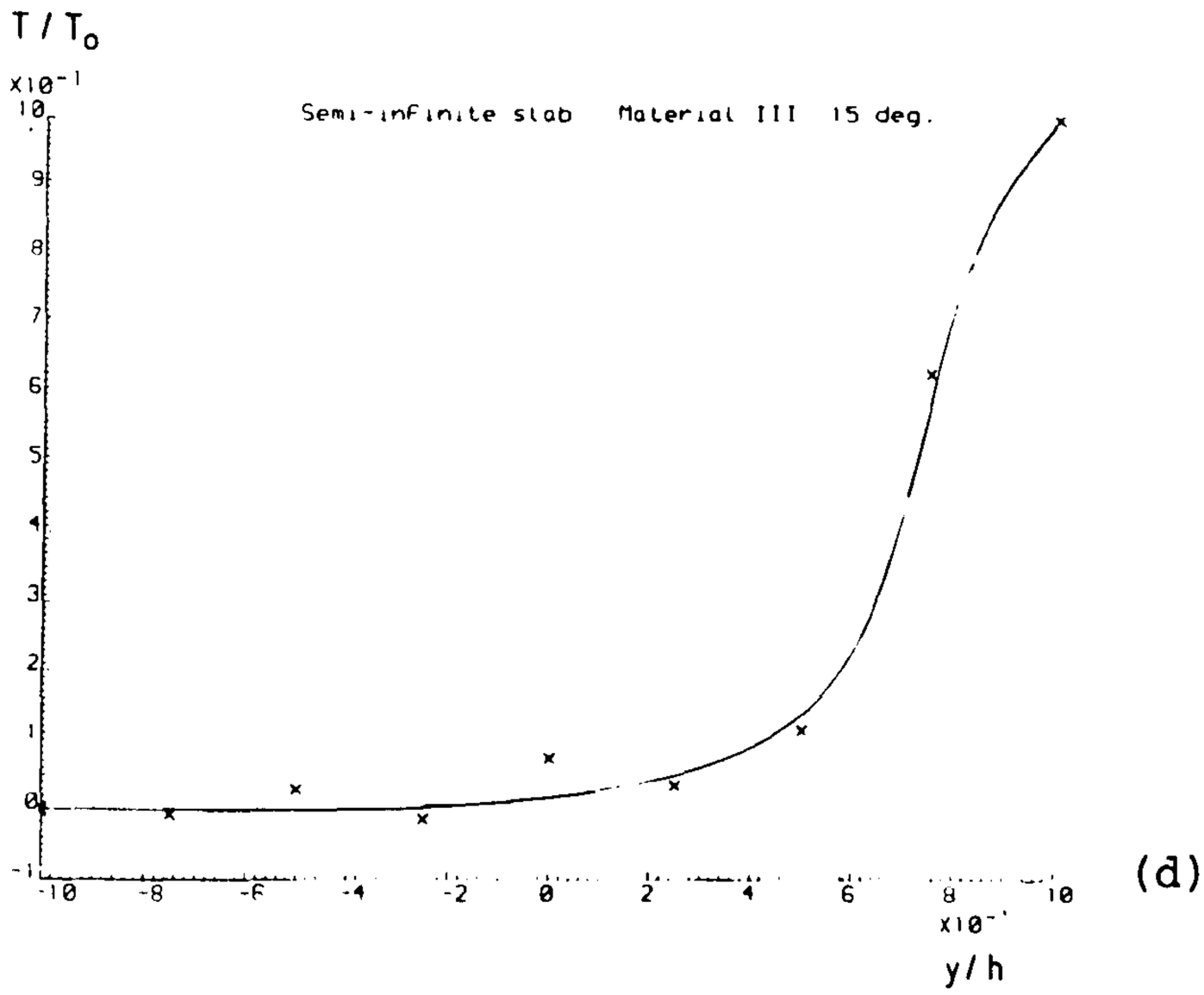

(d)

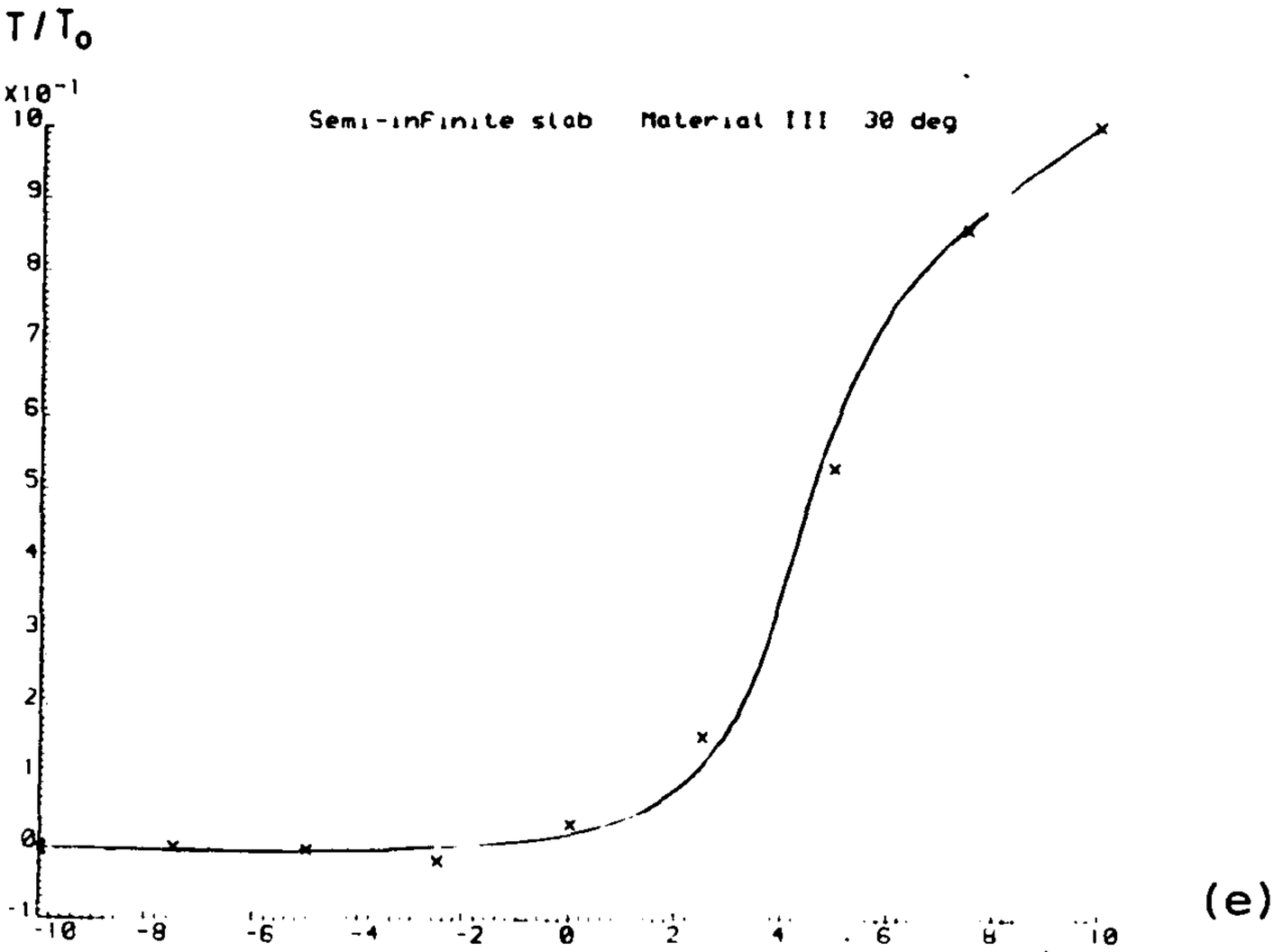

(e)

Fig. 6.15 (cont)

(d) Material III at 15° to x-axis

(e) Material III at 30° to x-axis

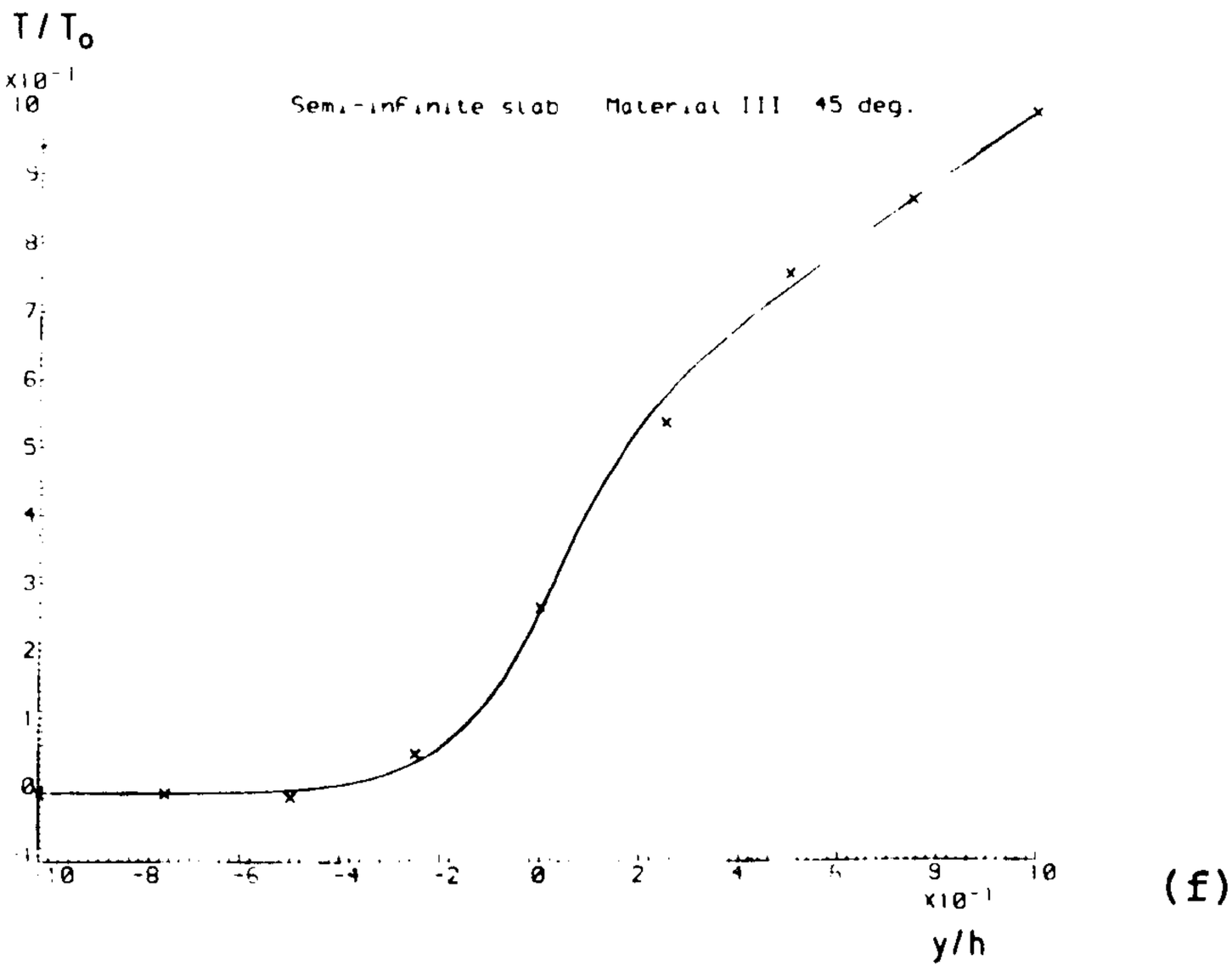

(f)

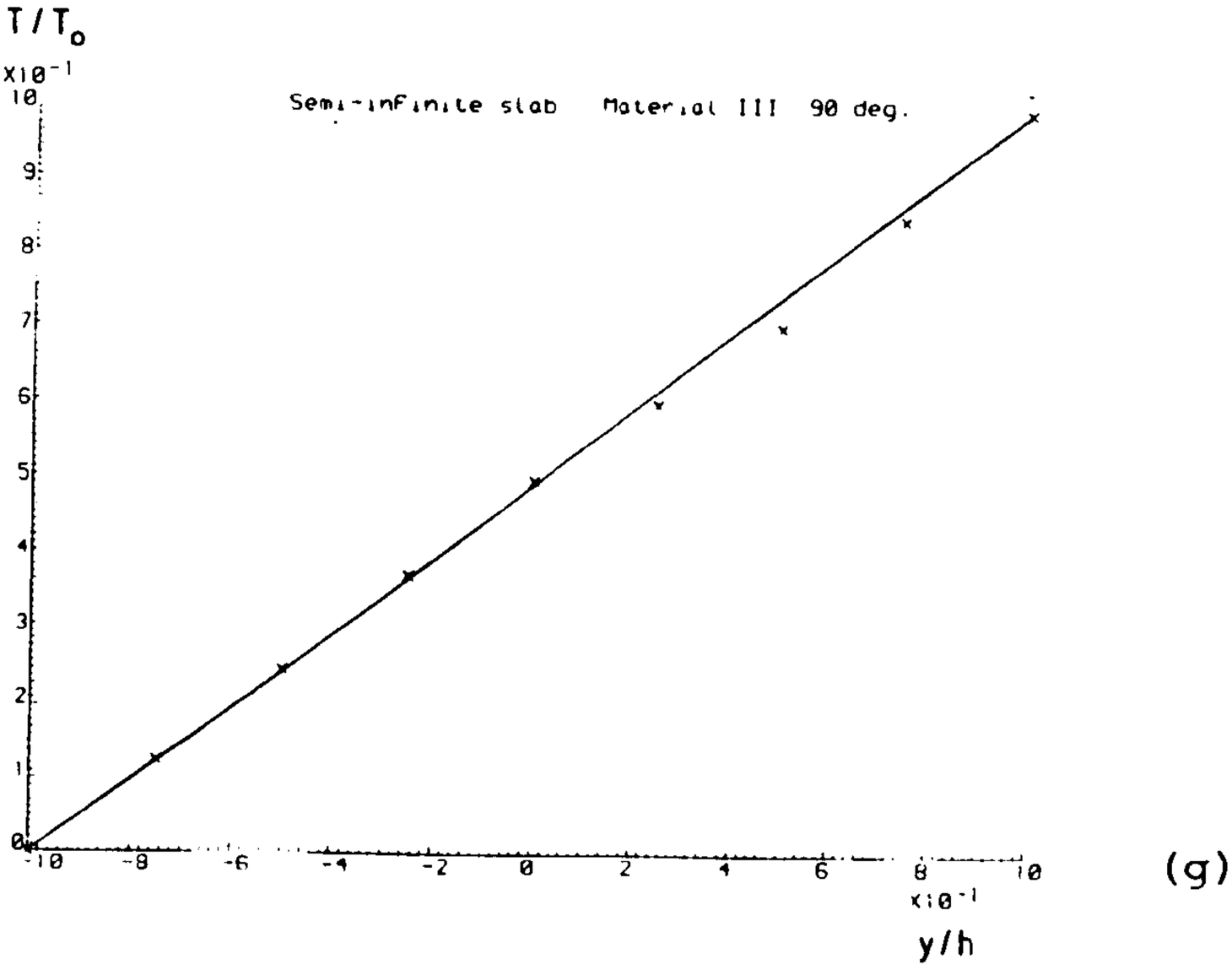

(g)

Fig. 6.15 (cont)

(f) Material III at 45^{o} to x-axis

(g) Material III at 90^{o} to x-axis

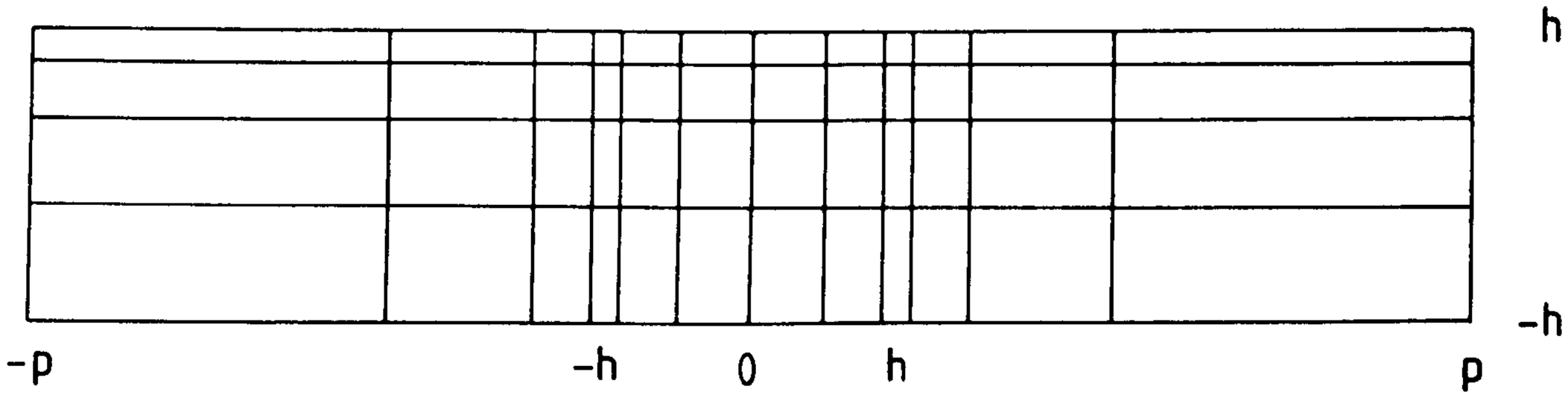

Fig. 6.16

Modified finite element mesh for semi-infinite slab.

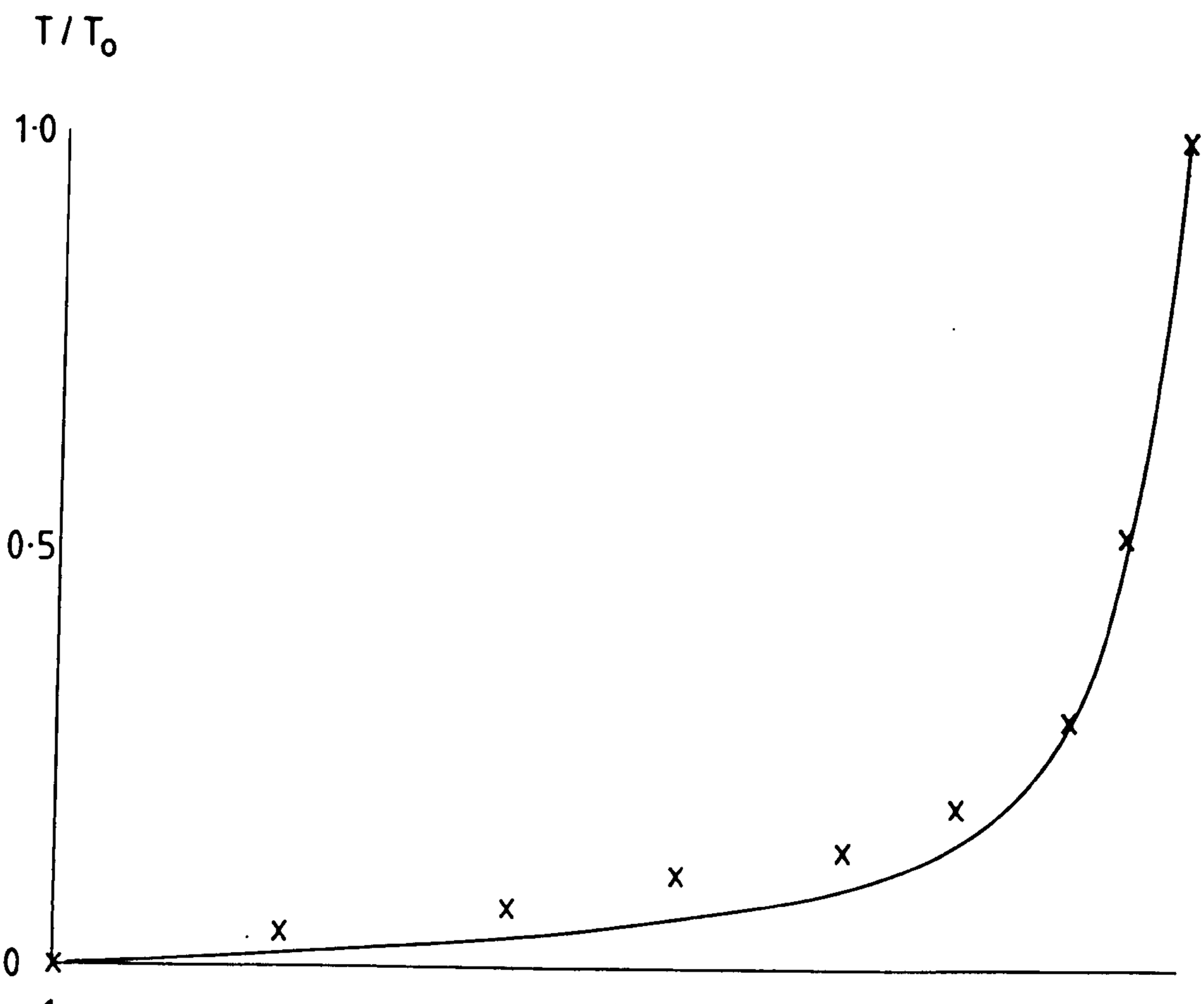

Fig. 6.17

Comparison of finite element and analytic solution at x = 0 on refined mesh (compare Fig. 6.15(c)).

is interesting to note a slight increase at p = 5h. This may be a result of the increasing aspect ratio of elements near the boundary. Even at p = 2h, the maximum difference between analytic and numerical temperatures is less than 0.5% (expressed as a percentage of temperature difference across the faces of the slab).

6.3 STEADY-STATE, NONLINEAR CONDUCTION

Cobble's (1974) solution for steady-state conduction on a wedge-shaped region with temperature-dependent thermal conductivity was discussed in 4.2.4. This problem presents similar difficulties in modelling to that considered in 6.2.3, being a semi-infinite region and containing a discontinuity in the boundary condition at x = 0, y = 0. Fig. 6.19 shows the finite element mesh used for this calculation; the artificial boundaries at x = 10 and y = 10 are adiabatic, and the numerical solution is compared with analytic values along the path shown.

The iterative technique used for temperature-dependent thermal properties is described in 5.9, and the results presented in Fig. 6.20 were obtained with a convergence criterion (on thermal conductivity) of 1%. Agreement between analytic and numerical temperatures is good, the largest difference being approximately 1 K (i.e. 1% of the temperature gradient across the wedge); this occurs near the centreline of the wedge for the orthotropic and anisotropic materials. The calculations were repeated as a check with a convergence criterion of 0.1%, but resulting changes in the nodal temperatures were less than 10^{-4} K.

6.4 STEADY-STATE, SPATIALLY-VARIABLE THERMAL CONDUCTIVITY

In 4.2.7 an analytic solution was derived for the steady-state temperature distribution on a disc with thermal properties orthotropic in the circular coordinate system (k_r and k_θ). In cartesian coordinates, this represents a problem in which the thermal conductivity coefficients (k_{11}, k_{12}, k_{22}) vary continuously with position, since at any point on the disc the principal axes are parallel and perpendicular to the radius vector through that point. As

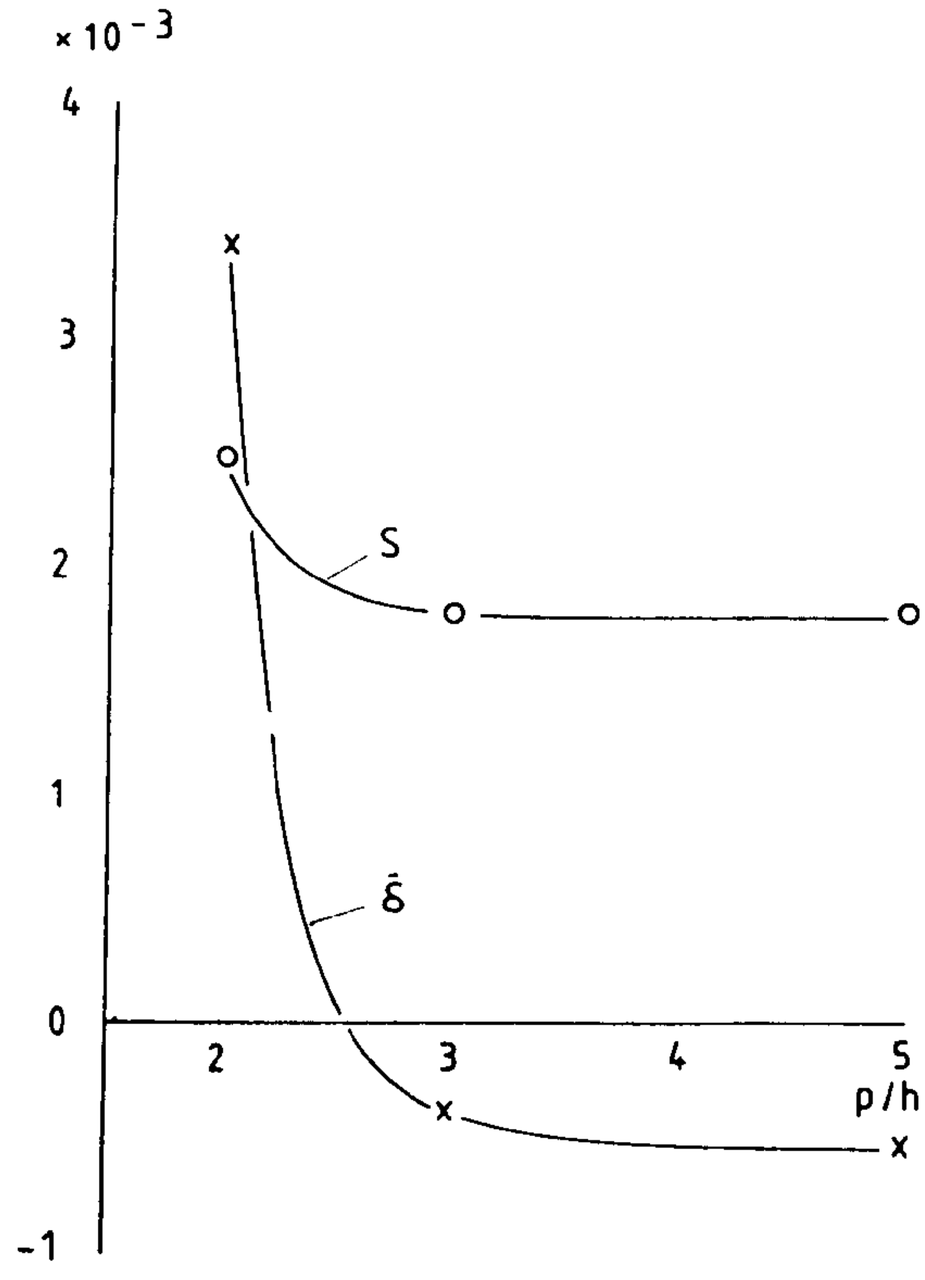

Fig. 6.18

Variation of mean error ($\bar{\delta}$) and deviation (S) at x = 0 with increasing p (see Fig. 6.14).

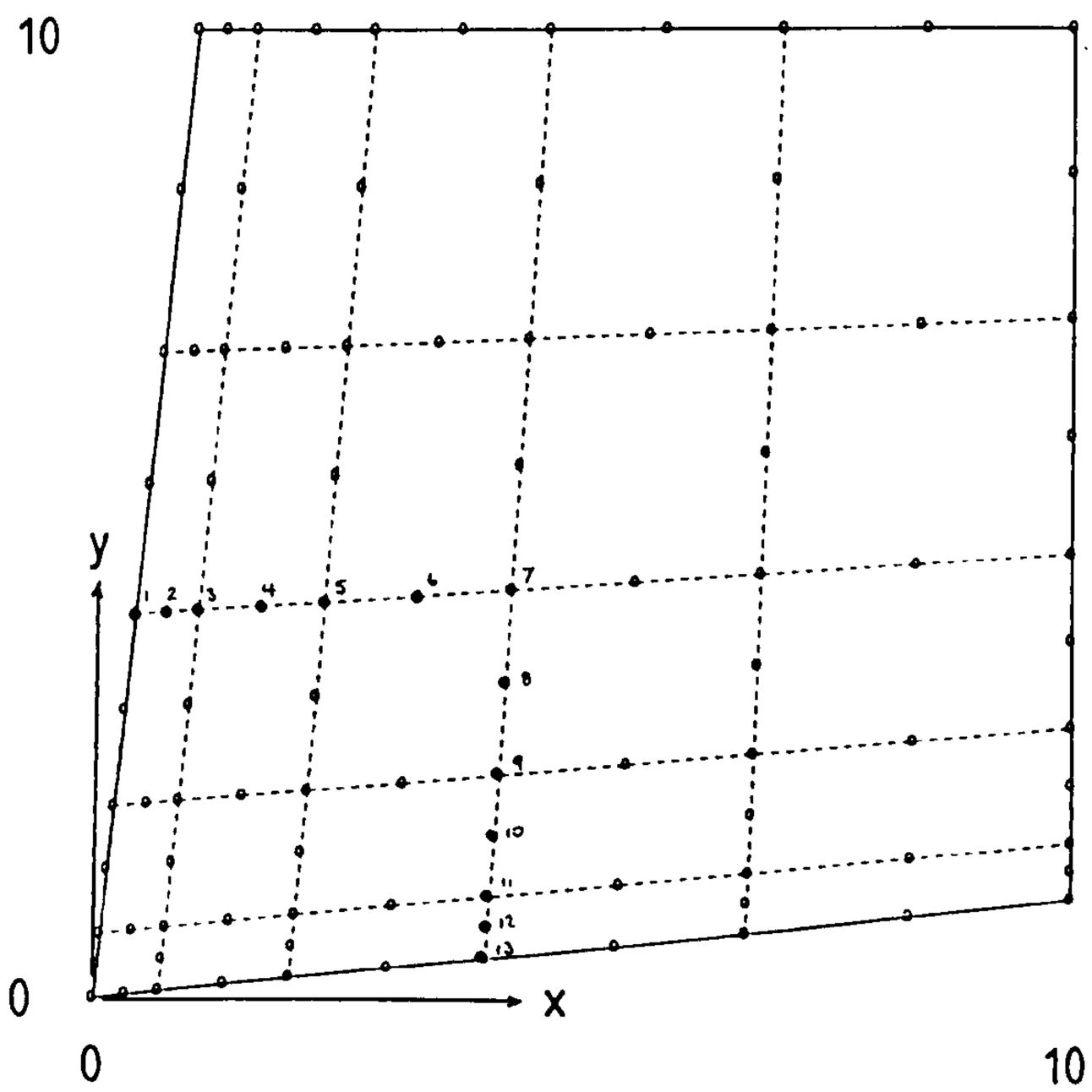

Fig. 6.19

Finite element representation of wedge.

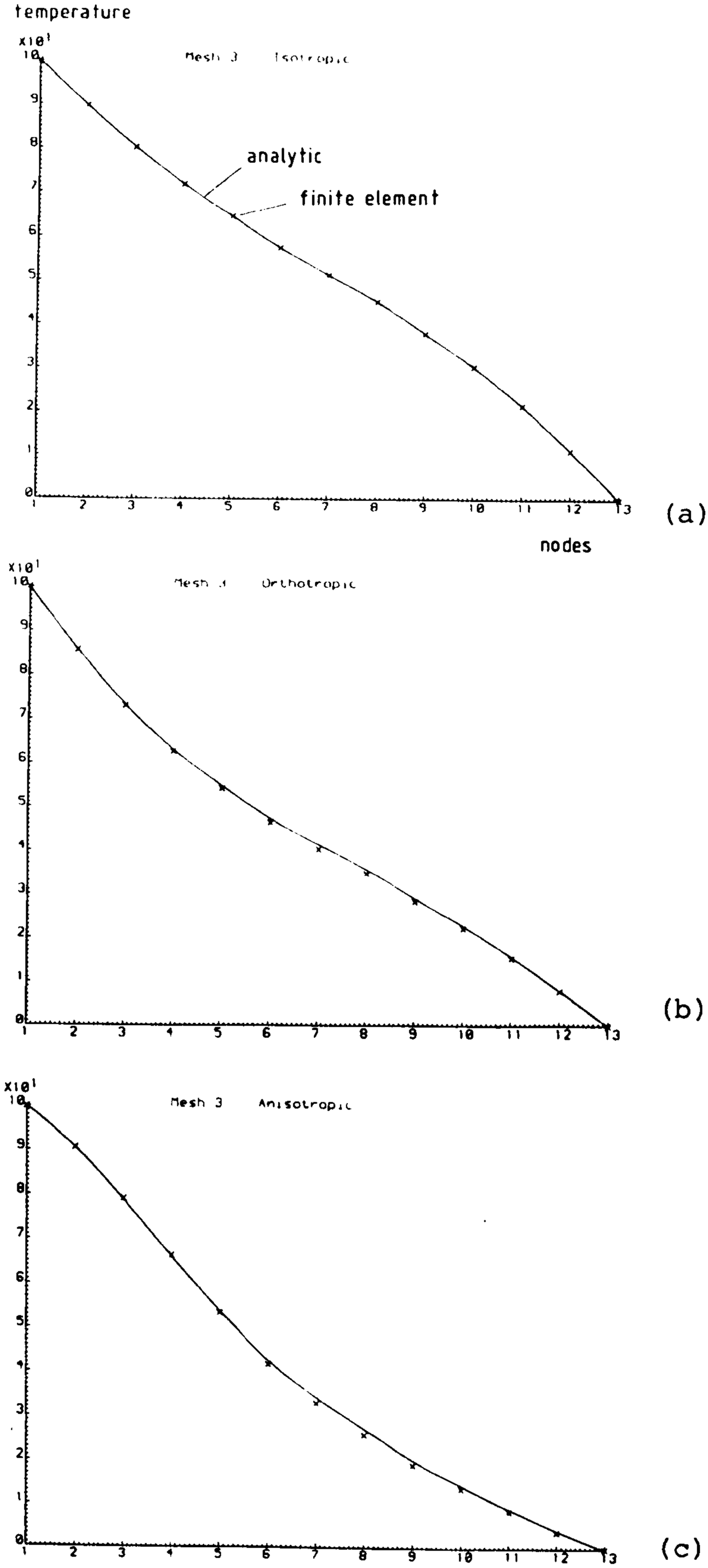

Fig. 6.20

Comparison between finite element and analytic temperatures at nodes indicated in Fig. 6.19.

(a) Isotropic)
(b) Orthotropic) thermal properties defined
(c) Anisotropic) in 4.2.4.

discussed in 5.10, such a situation could be modelled by progressively reducing the size of the mesh until each element was small enough to be represented by a single principal axis orientation. It will be demonstrated here, however, that the problem can be solved much more efficiently by defining thermal properties at each of the four integrating points in each element; this has the effect of increasing the spatial resolution without increasing the total number of elements (and hence the required computation time).

The problem and its boundary condition are defined in Fig. 6.21, and Fig. 6.22 illustrates two contrasting meshes: the first comprises only 45 nodes/12 elements (as used in 6.2.2) while the second uses 183 nodes/52 elements to represent a half-disc (the problem has a plane of symmetry along the diameter $\theta = \pm \pi/2$. Analytic and numerically-calculated temperatures are compared along the diameter defined by $\theta = \pm \pi/2$. Thermal properties typical of a carbon fibre/resin composite are assumed, with $k_\theta / k_r = 35$; the two-dimensional temperature distribution was illustrated in Fig. 4.11.

Firstly, constant thermal conductivities were assumed in each element. These were obtained by locating the mid point of each element (corresponding to r = s = 0 in natural coordinates), calculating the orientation of the tangent to the circular reinforcement at this point, and using this to derive the values of the conductivity coefficients according to Equation 4.13. These values are uniform over each element. Fig. 6.23 shows the calculated temperatures along the disc diameter on the two meshes: the first gives a large systematic error, while the second is much more acceptable. The mean errors between finite element and analytic temperatures were respectively 0.069 and 0.011, while the calculation on the second mesh required approximately 400% more computer time than the first.

Thermal conductivity coefficients were then evaluated at each of the four numerical integration points of the elements

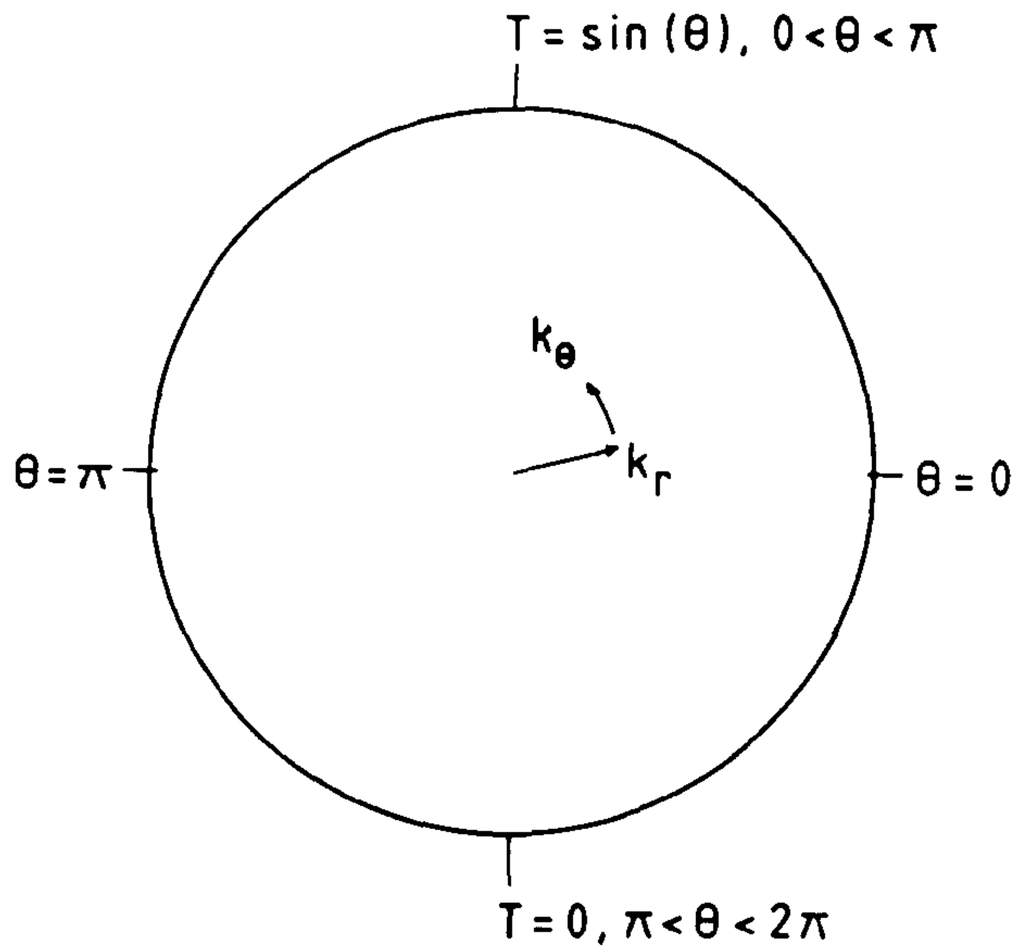

Fig. 6.21

Unit disc with orthotropic thermal properties in circular coordinates and specified boundary temperatures.

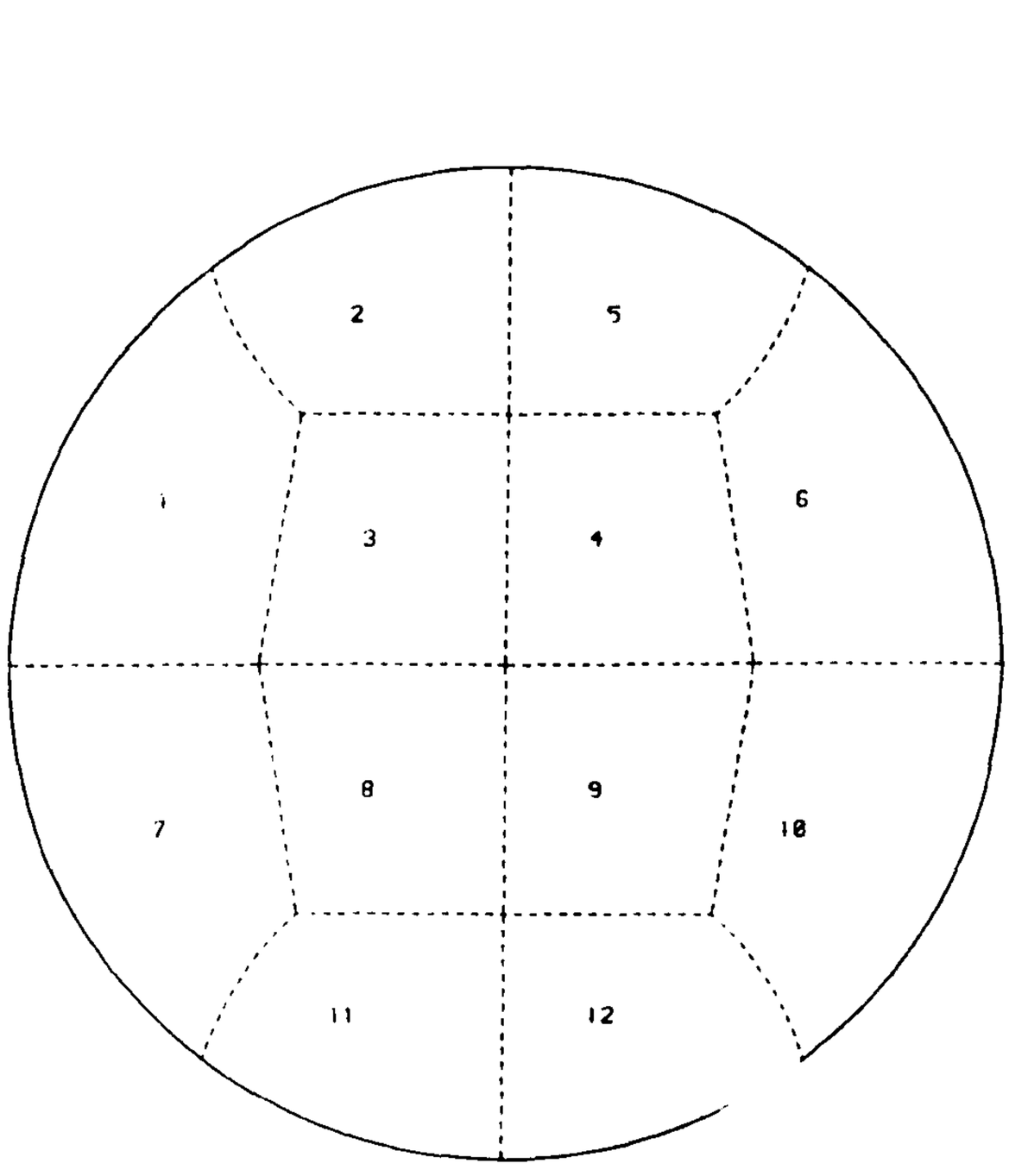

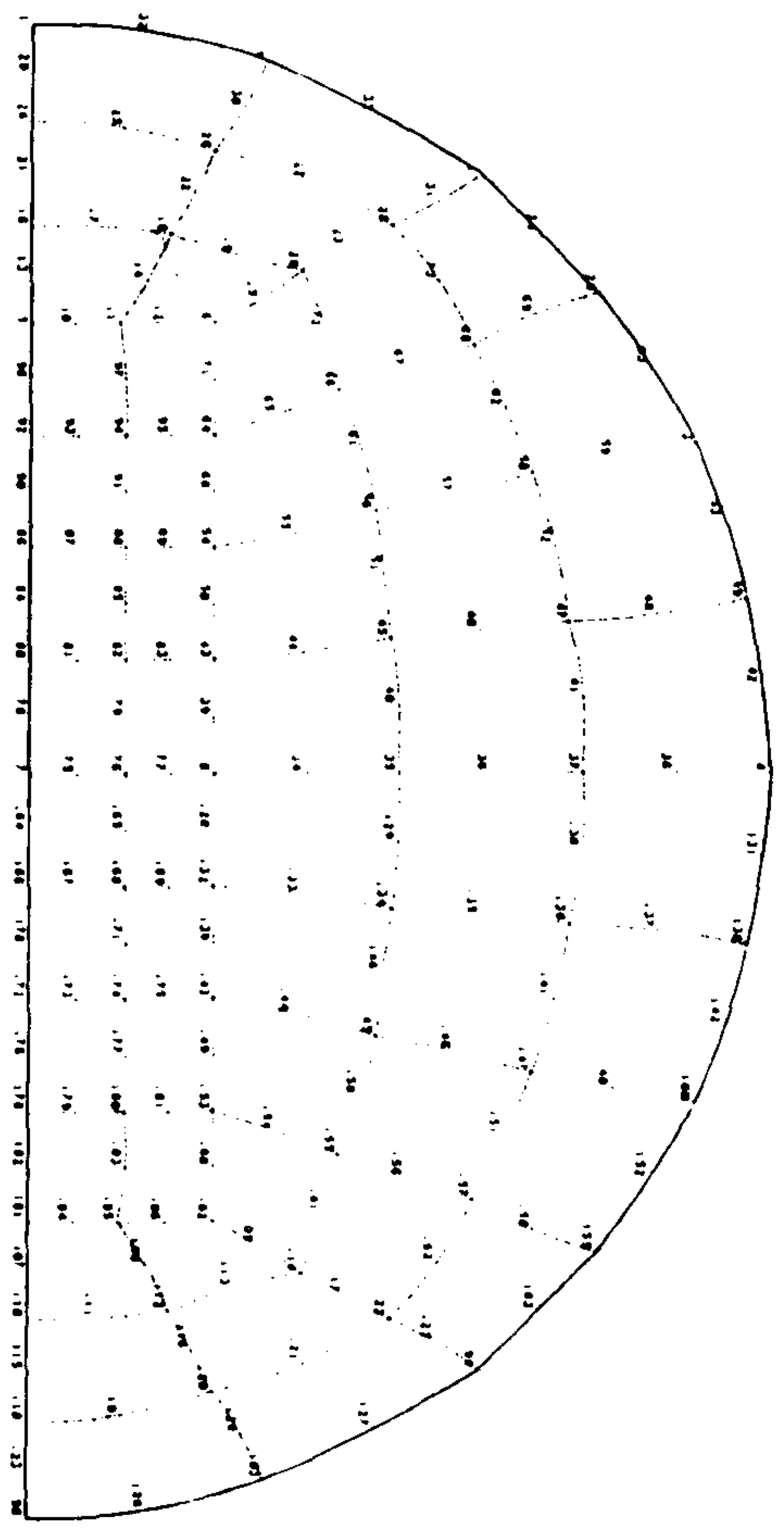

Fig. 6.22

Coarse and fine finite element meshes for the unit disc.

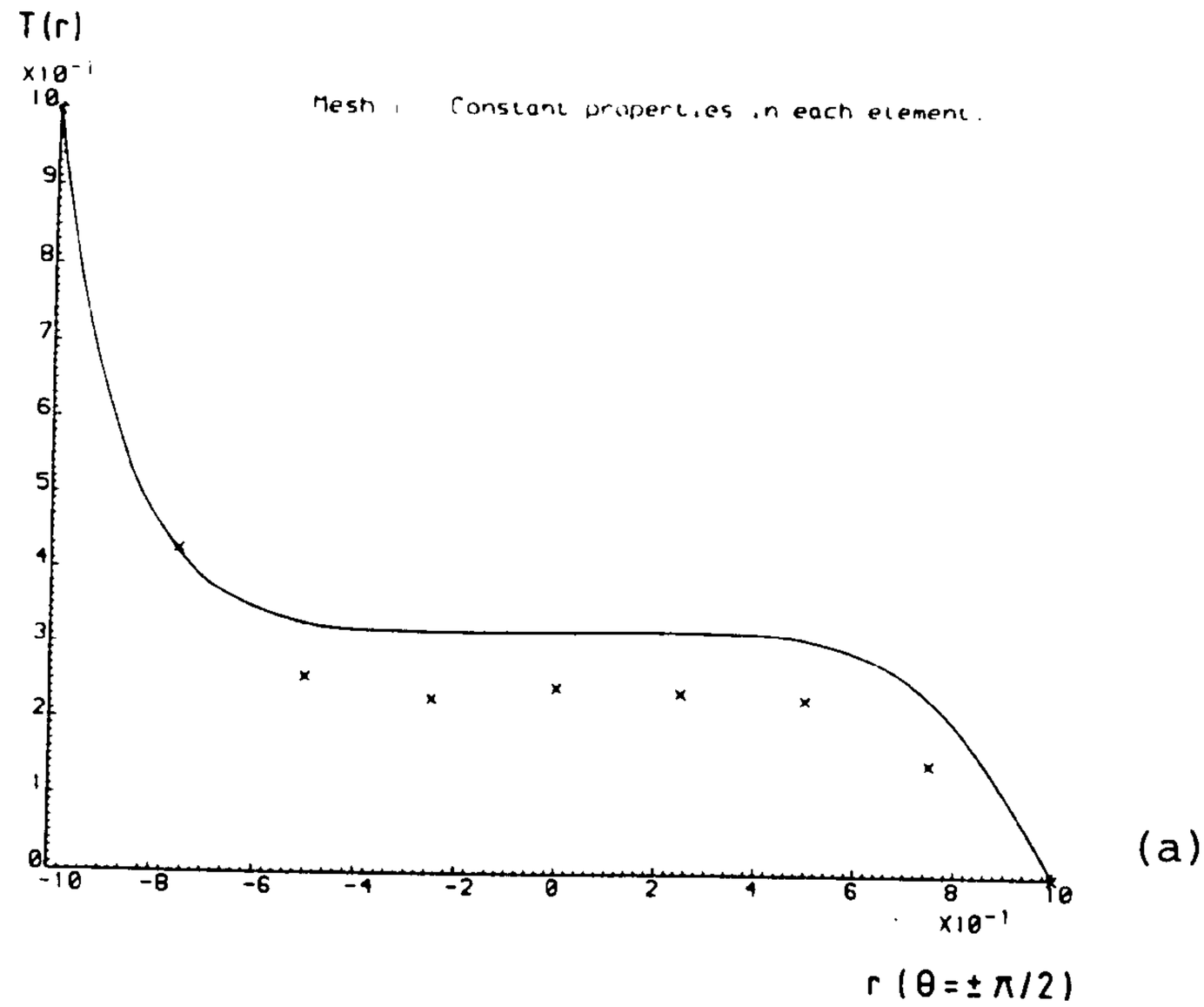

(a)

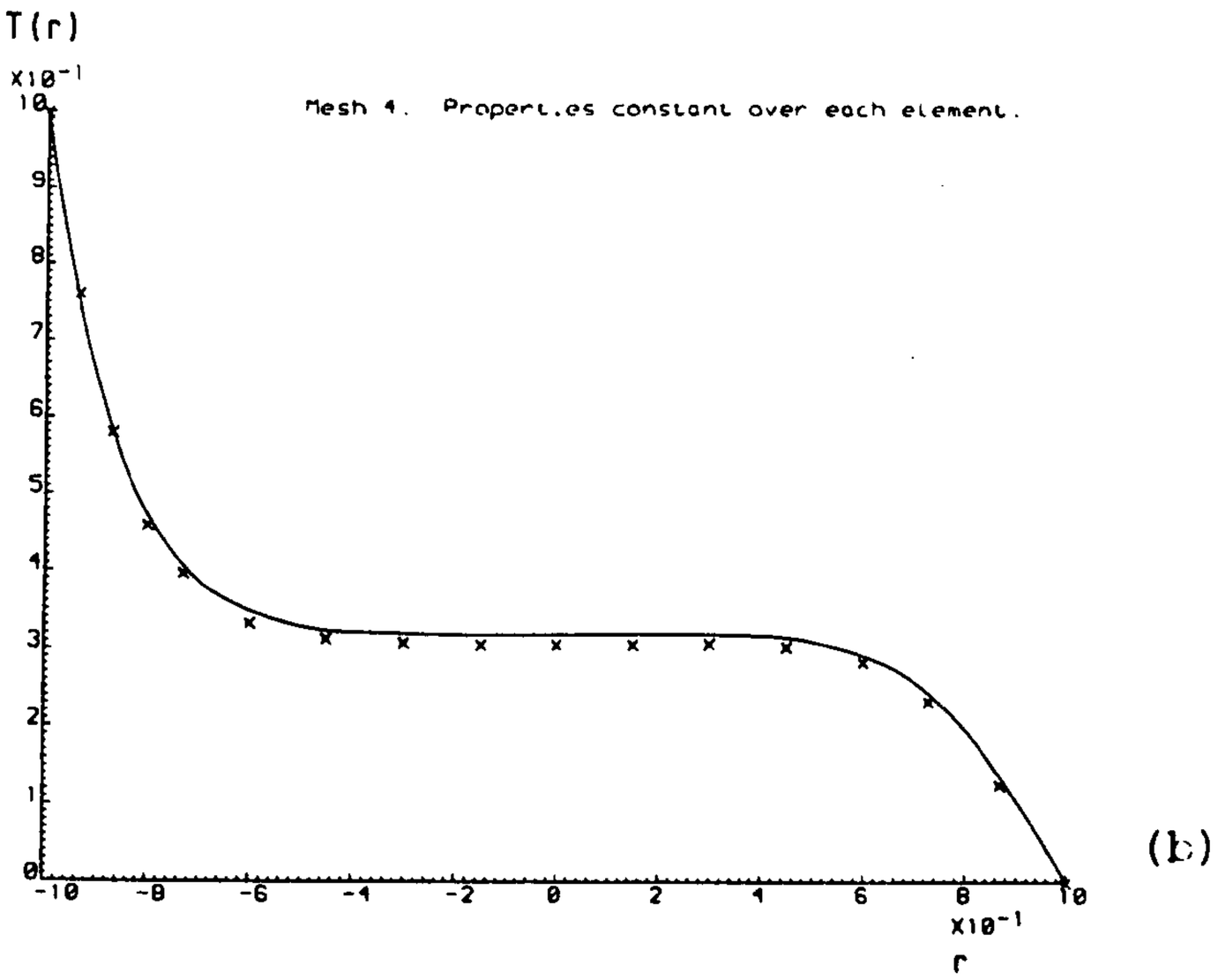

(b)

Fig. 6.23

Comparison of finite element and analytic temperatures along a diameter ($\theta = \pm\pi/2$) of unit disc.

(a) coarse mesh, constant properties
(b) fine mesh, constant properties

of the first mesh, and the calculation repeated with these data. The improved solution is shown in Fig. 6.24. The mean error for temperatures along this diameter has reduced to only 0.006; according to this measure of accuracy, the solution is better than that obtained on the refined mesh, yet requires only about 25% of the computer time.

6.5 TRANSIENT CONDUCTION

Many engineering problems require the calculation of transient temperatures and may involve further complications such as time-dependent boundary conditions. In this section a simple time-dependent heat conduction problem is used to validate and compare different integration algorithms, and the model is then compared with an analytic solution to a time-dependent problem in an anisotropic material.

6.5.1 Comparison of Time Integration Algorithms

Zienkiewicz (1977) demonstrated characteristics of the three integration algorithms by considering a special case of Equation 5.24. With $\underline{K} = \underline{C} = 1$ and $\underline{F} = 0$ it simplifies to

$$T(t + \Delta t) = \frac{1 - \Delta t(1-\omega)}{1 + \Delta t\omega} \; T(t) \qquad (6.8)$$

If the initial condition is $T(0) = 1$, then the problem has the analytic solution $T(t) = \exp(-t)$, and comparison is readily made with 'numerical' solutions. The recurrence relation for this problem (Equation 6.8) yields a stable solution if

$$\left| \frac{1 - \Delta t(1-\omega)}{1 + \Delta t\omega} \right| \leqslant 1 \qquad (6.9)$$

Both the pure implicit ($\omega = 1$) and Crank-Nicholson ($\omega = \frac{1}{2}$) algorithms are unconditionally stable, since Equation 6.9 is satisfied for all positive values of time step (Δt). The forward difference (explicit) algorithm ($\omega = 0$) is unstable if $\Delta t > 2$.

Although a numerical solution may be stable (in that it converges to the 'true' solution as time increases), it is

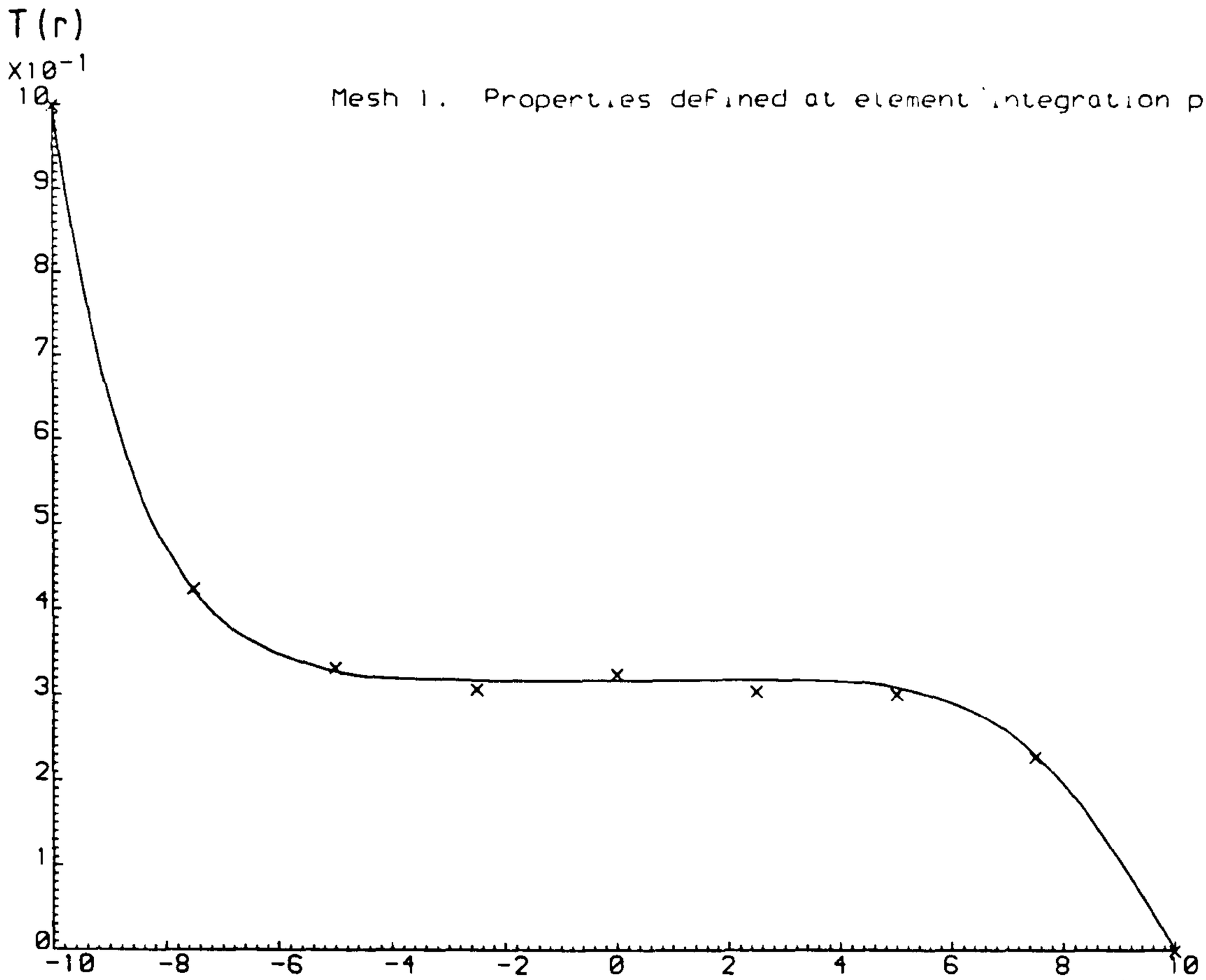

Mesh 1. Properties defined at element integration point

Fig. 6.24

As Fig. 6.23, defining thermal properties at each integration point, coarse mesh.

oscillatory if

$$-1 < \frac{1 - \Delta t(1-\omega)}{1 + \Delta t\omega} < 0$$

The pure implicit solution does not oscillate, since this term is always positive. The forward difference solution is oscillatory for time steps in the range $1 < \Delta t < 2$, while the Crank-Nicholson algorithm gives an oscillatory solution for $\Delta t > 2$. As shown by Zienkiewicz (1977), the highest accuracy for $\Delta t < 2$ is obtained with the Crank-Nicholson algorithm.

Henshell (1975) used a one-dimensional transient problem to test the accuracy of the PAFEC 75 solution routine. A rod of length L has an initial linear temperature distribution given by

$$T(x,\ t = 0) = \frac{100}{L}\ (L - x)$$

At time t = 0, the temperature at x = 0 is reduced to zero, while the end at x = L is kept insulated. Classical separation of variables yields the series solution

$$T(x,t) = \sum_{n=1}^{\infty} A_n \sin\beta_n x\ e^{-\alpha\beta_n^2 t} \qquad (6.10)$$

where $\beta_n = (n-\frac{1}{2})\frac{\pi}{L}$

and $A_n = \frac{200}{L^2\beta_n}\left[L - \frac{(-1)^{n+1}}{\beta_n}\right]$

Fig. 6.25 shows the temperature along a rod of length π at various times from t = 0 to 100, using a diffusivity of 0.01234 (after Henshell, 1975).

The finite element calculation was performed on a uniform mesh of five quadrilateral elements (Fig. 6.26). Results were obtained using each of the three available algorithms (implicit, central-difference and explicit) with a range of time steps. These are compared with the analytic solution at time t = 10s in Table 6.1 (for consistency with Henshell, the error is expressed as a percentage of the analytic solution).

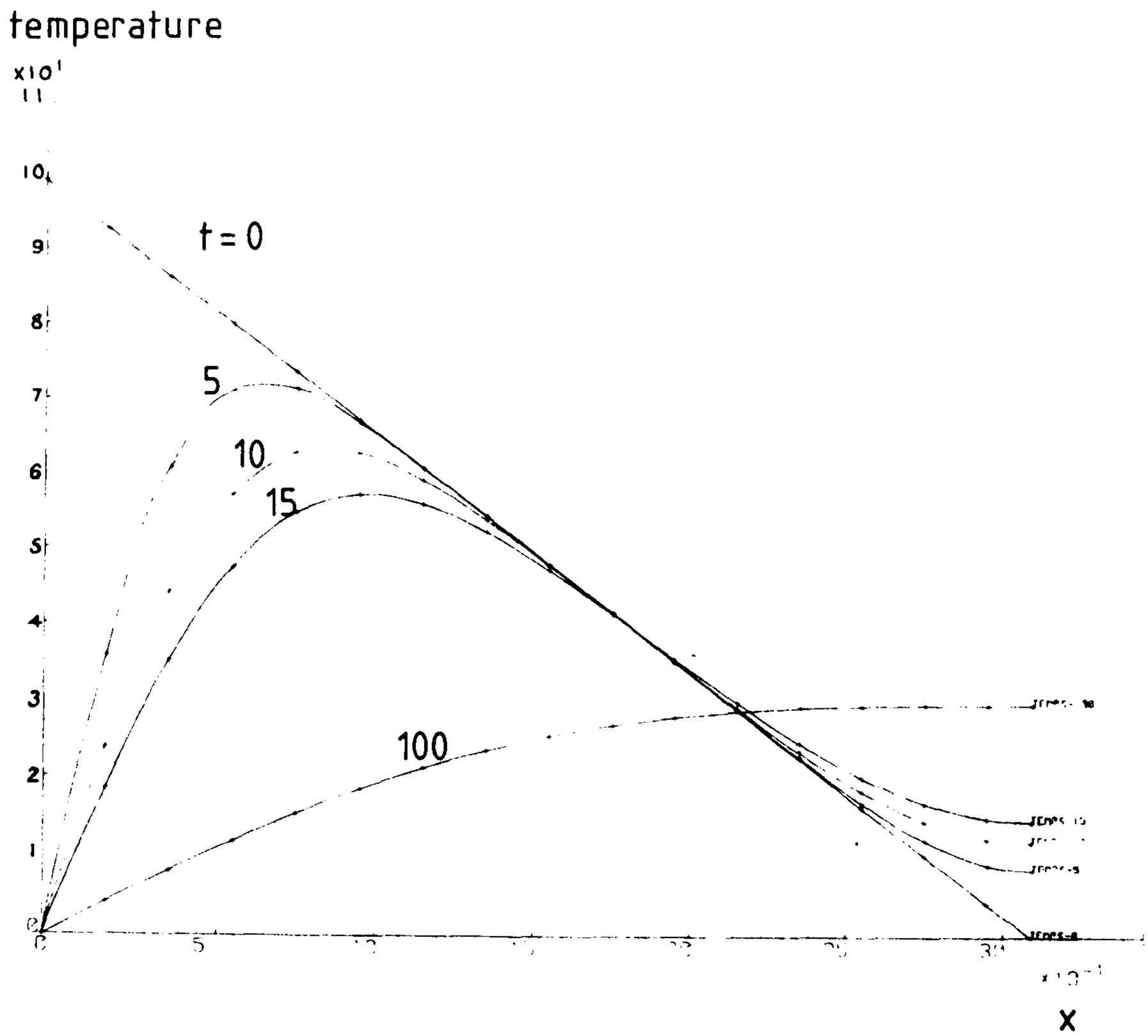

Fig. 6.25

Temperature distribution in one-dimensional rod at various times (t) from 0 to 100.

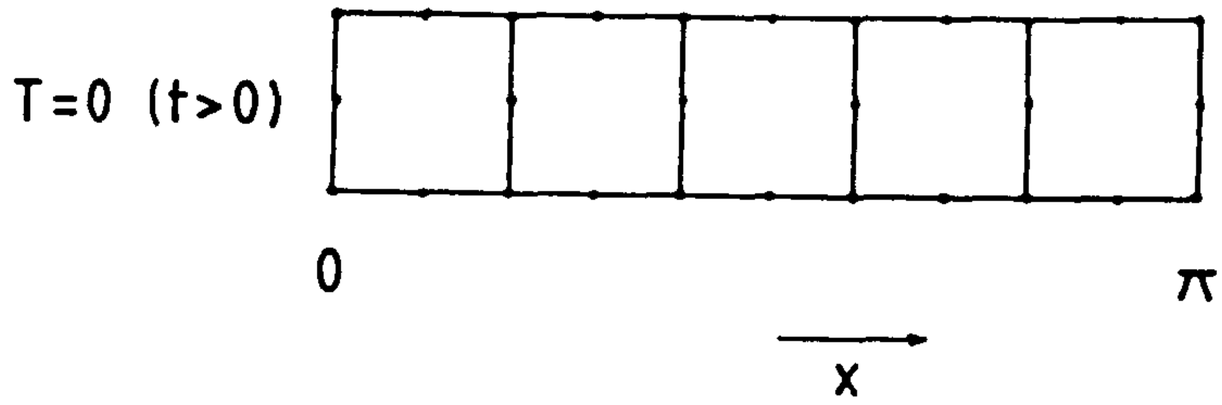

Fig. 6.26

Five-element representation of one-dimensional rod.

DISTANCE ALONG ROD	Forward Difference			Pure Implicit				Crank-Nicholson				
x/L	.5	1	5	.5	1	5	10	.1	.5	1	5	10
.1	1.2	2.1	-174	1.9	3.6	17.2	32	.4	1.5	3.0	10.9	67
.2	1.6	3.2	247	1.1	1.7	5.0	6.1	.5	1.3	2.4	18	20
.3	1.4	2.4	-54.2	.09	-.07	-1.2	-1.7	.3	.7	1.2	4.2	5.2
.4	.7	2.0	74.6	-.3	-.6	-2.0	-2.9	.03	.2	.3	.7	.7
.5	.04	-.3	-14.6	-.3	-.4	-1.1	-1.8	-.15	-.1	-.1	-.03	-.06
.6	-.2	.8	-7.8	-.09	-.08	-.3	-.5	-.1	-.1	-.1	-.02	.02
.7	-.2	-1.1	35.1	.03	.1	.6	.7	-.08	-.07	-.07	-.06	.04
.8	-.3	2.3	-230	-.1	0	.7	1.2	-.2	-.2	-.2	-2.1	-.9
.9	.3	-1.5	268	-.3	-.5	-2.2	-3.8	.01	.01	.01	2.3	-4.9
1	.9	5.3	-687	-.34	-1.0	-6.0	-12.1	.3	.3	.3	-4.5	23
RELATIVE CPU TIME	4.0	2.5	1.5	4.2	2.7	1.3	1	17.0	4.2	2.8	1.3	1.2
mean error ($\bar{\delta}$)	.544	1.52	-6.73	.169	.275	1.07	1.72	.101	.354	.674	2.94	11.01
rms deviation (S)	.712	2.08	278	.741	1.37	6.31	11.59	.251	.612	1.15	6.70	21.75

TABLE 6.1

Percentage errors between finite element and analytic solutions (i.e. $\frac{(T_{f.e.} - T_{anal.})}{T_{anal.}} \times 100\%$) for 1 - d rod at time t = 10 sec.

The maximum stable time step for a one-dimensional finite difference approximation using the explicit integration algorithm is given by

$$\Delta t_{max} = \frac{(\Delta x)^2}{2\alpha} \tag{6.11}$$

where Δx is the smallest distance between adjacent nodes. In the example considered here, $\Delta t_{max} \simeq 4s$, and this accounts for the large errors which occur in Table 6.1 for the forward difference algorithm at $\Delta t = 5s$. As discussed above, the other two algorithms are unconditionally stable, but the central-difference solution gives significantly larger errors than the pure implicit solution at time steps of 5s and above.

The oscillatory nature of the central-difference algorithm is a response to the discontinuous boundary condition at time t = O. As time increases, the influence of the discontinuity will diminish, and solutions of acceptable accuracy may be expected from time steps much longer than Δt_{max}. Fig. 6.27 shows the analytic temperature distribution at t = 500s, together with the numerical solutions at decreasing time steps. At $\Delta t = 25s$, the numerical temperature distribution differs by less than O.5 K along the whole length of the rod.

The choice of time step is thus influenced by the times for which a solution is required, and is also a factor at small times. Fig. 6.28 shows the convergence of the numerical solution with decreasing time step towards the analytic temperatures at x = O.1 L and x = L from time t = O to 10s. At any given time, the accuracy of the numerical solution increases with the number of iterations used (that is, inversely with the length of the time step). A time step of, say, 1s may give an adequate solution at t = 10s, but for comparable accuracy at smaller times would require corresponding reduction. In the case of time-dependent boundaries, the choice of time step must be related to the rate of change of the boundary condition. It should be noted that a convergent numerical solution approaches the

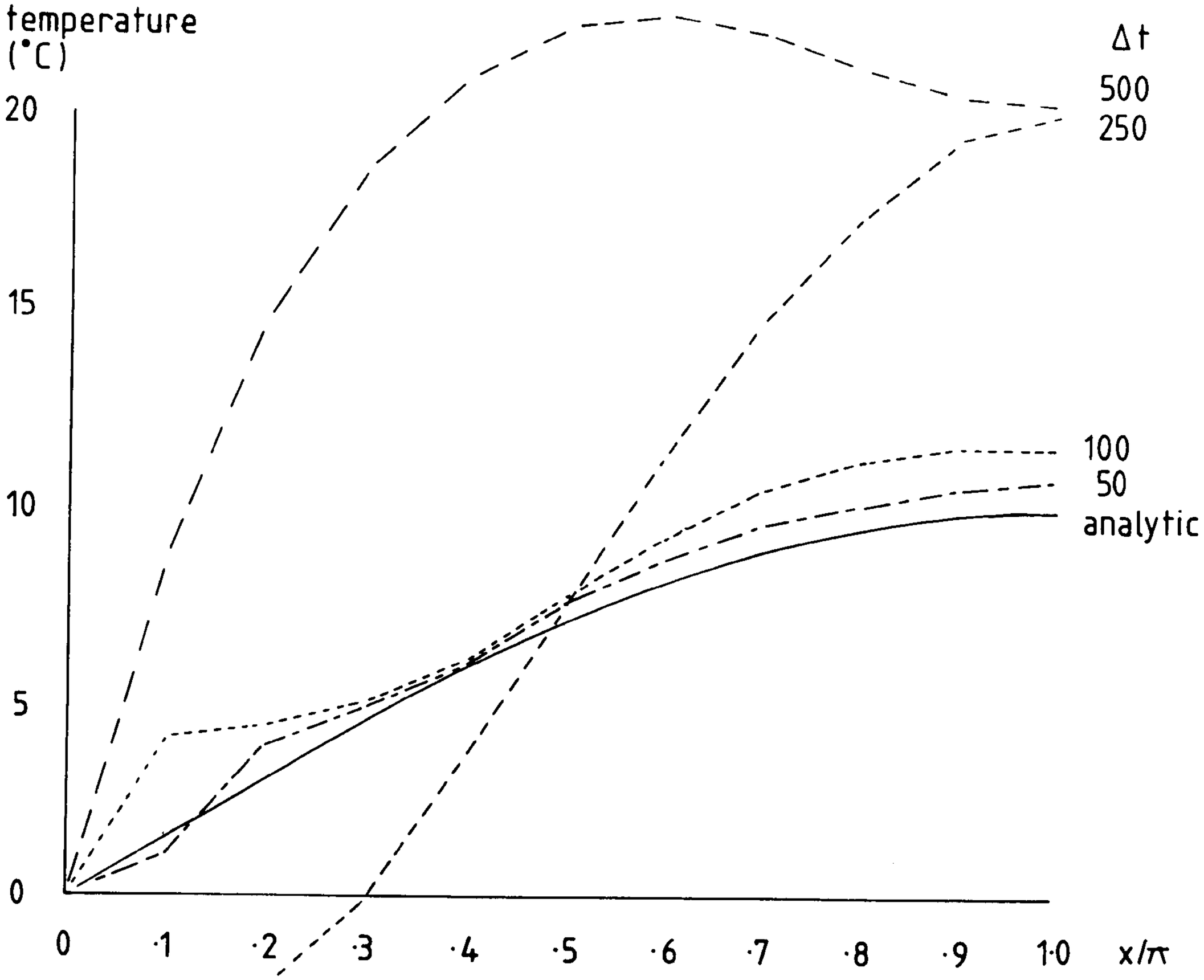

Fig. 6.27

Comparison between analytic and numerical temperature distributions in one-dimensional rod at t = 500 s, showing convergence of finite element solution with decreasing time step (Δt).

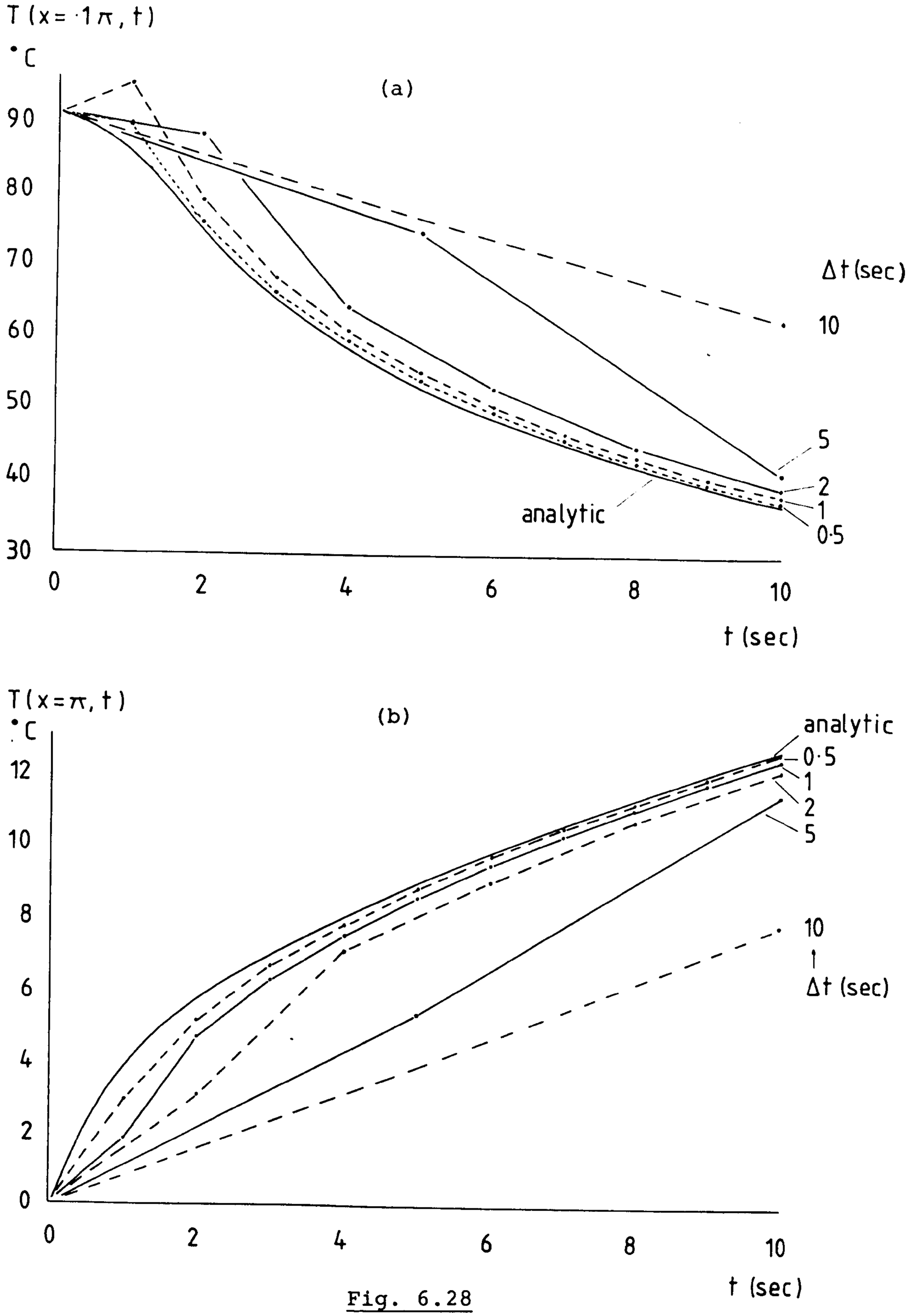

Fig. 6.28

Convergence of numerical solution with decreasing time step (Δt) from time t = 0 to 10 sec.

(a) temperatures at $x = 0.1\,\pi$
(b) temperatures at $x = \pi$

'true' temperature distribution as both the time step and the element size are progressively reduced. Thus, reduction of the time step alone will only improve the accuracy of the solution within the limitations imposed by a given finite element mesh.

It is not possible to deduce general rules for guidance in future transient calculations on the basis of the simple problem examined here; the time step must be considered a variable quantity in the same sense as element size, requiring more than one calculation to ensure a meaningful, convergent solution. As a starting point, the value of Δt_{max} (Equation 6.11) will be used, increasing or decreasing it as necessary to ensure of the order of 10 to 20 iterations within a required solution period.

6.5.2 Transient, Anisotropic Conduction

The final theoretical problem considered in this chapter concerns transient conduction in an anisotropic half space, having initial temperature distribution $F(x,y)$, and the boundary condition $T = 0$ at $x = 0$ for $-\infty < y < \infty$ and $t > 0$. An analytic solution has been derived by Ozisik (1980) and was discussed in 4.2.6.

The initial temperature distribution used in this example calculation is illustrated in Fig. 6.29, and is defined by

$$F(x,y) = \begin{cases} (1 - x/2) \sin \frac{\pi}{2} (1 + y), & 0<x<2, \ |y|<1 \\ 0, & x>2, \ |y| > 1 \end{cases}$$

The temperature is non-zero only within the square $0 < x < 2$, $-1 < y < 1$, and the limits of integration in Equation 4.18 are adjusted appropriately. The analytic solution at chosen points (x, y, t) was evaluated using a Romberg numerical integration procedure given by Gerald (1978). The calculation was performed to a tolerance of 10^{-4}.

Hypothetical material properties were used in the calculations, with $K_1/K_2 = 10$ and $\rho C_p = 1$. Fig. 6.29 illustrates the temperature distribution at time $t = 0.02$ for principal

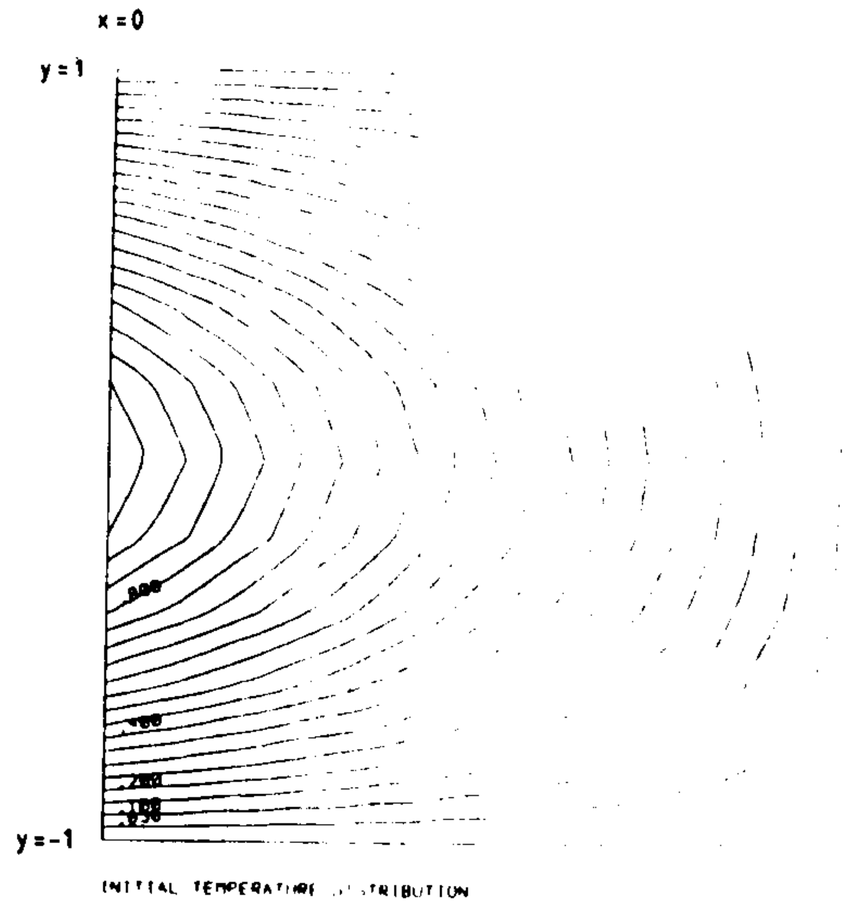

(a)

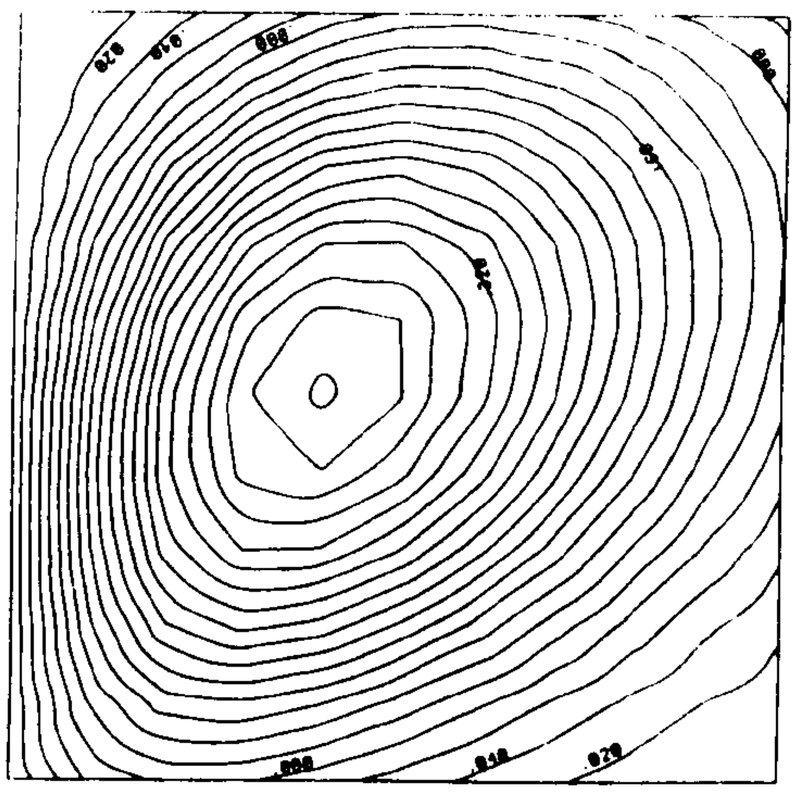

(b)

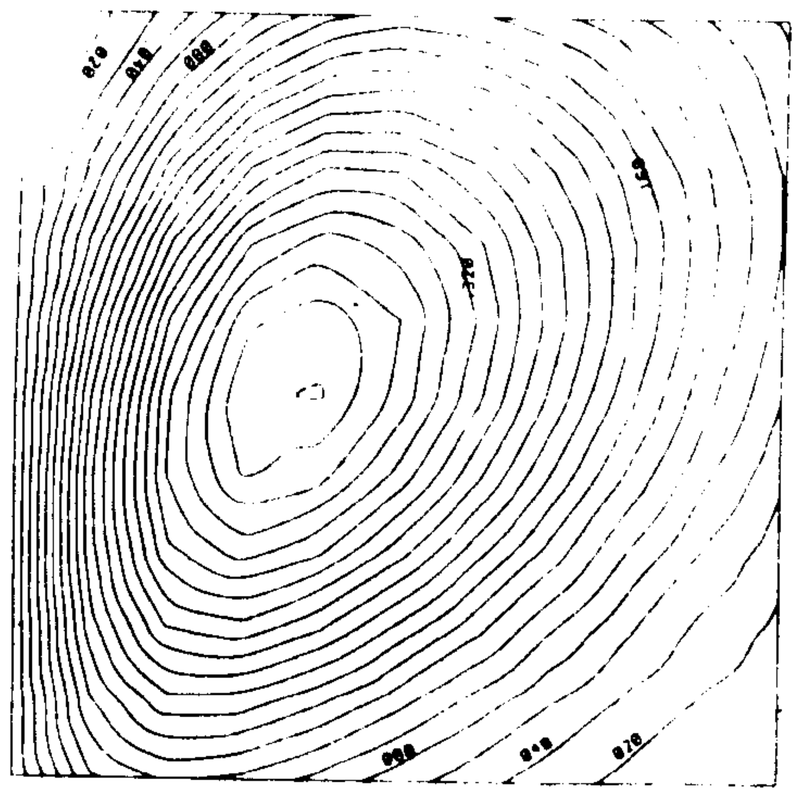

(c)

Fig. 6.29

Analytic temperature distributions within $0 < x < 2$, $|y| < 1$ for transient calculation

(a) Initial temperature ($t = 0$)

(b) Time $t = 0.02$, principal axis at 30° to x-axis

(c) Time $t = 0.02$, principal axis at 45° to x-axis

axis orientations of 30^{o} and 45^{o} (to the x-coordinate axis); the effect of two-dimensional anisotropy is evident in the elongation of the isotherms.

Finite element calculations were first performed on a deliberately coarse mesh, with a total of 61 nodes in the region $0 < x < 5$, $-4 < y < 4$ (Fig. 6.30). The central region of non-zero initial temperature comprises only 4 elements.

Thermal diffusivity is dependent on direction in an anisotropic solid, so that the time step calculated according to Equation 6.11 should assume the maximum value of α. In this example the thermal diffusivities along the two principal axes are 10 and 1, giving the smallest value of Δt_{max} as 0.0125. Since a numerical solution was required at time $t = 0.02$, calculations were first performed with $\Delta t = 0.002$, giving 10 iterations within this period.

Finite element results are compared with the analytic solution in Figs. 6.31 to 6.34, which are for principal axis orientations of 0^{o}, 30^{o}, 45^{o} and 90^{o} respectively. Each figure shows (a) the temperature along $y = 0$ for $0 < x < 2$ at time $t = 0.02$; (b) the temperature along $x = 1$ for $-1 < y < 1$ at $t = 0.02$; and (c) the temperature at $x = 1$, $y = 0$ as a function of time.

For the first three orientations, the agreement with the analytic solution is good, with nodal temperatures at $t = 0.02$ in error by less than about 0.02 (i.e. 2% of the initial temperature difference across the solid). For the 90^{o} orientation, the low effective thermal diffusivity gives rise to steeper temperature gradients in the x-direction, and the finite element solution at $t = 0.02$ is in error by more than 8%. As expected after the discussion in 6.5.1, the solution shows large errors ($\sim$ 10%) at small times, on the first and second iterations.

The numerical solution for the 90^{o} orientation was found to show no improvement in accuracy with reducing time step, and

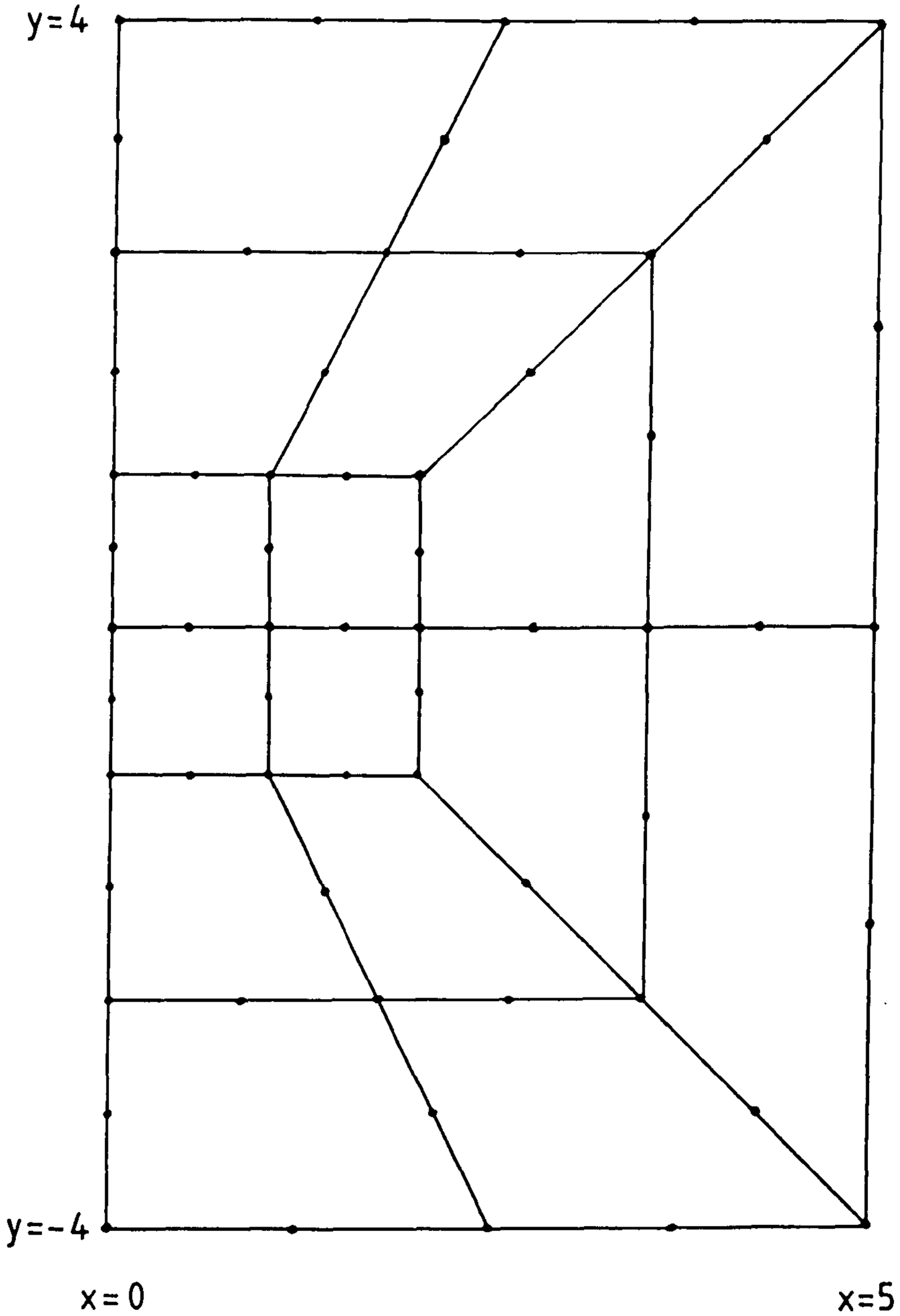

Fig. 6.30

Coarse finite element representation of anisotropic half-space.

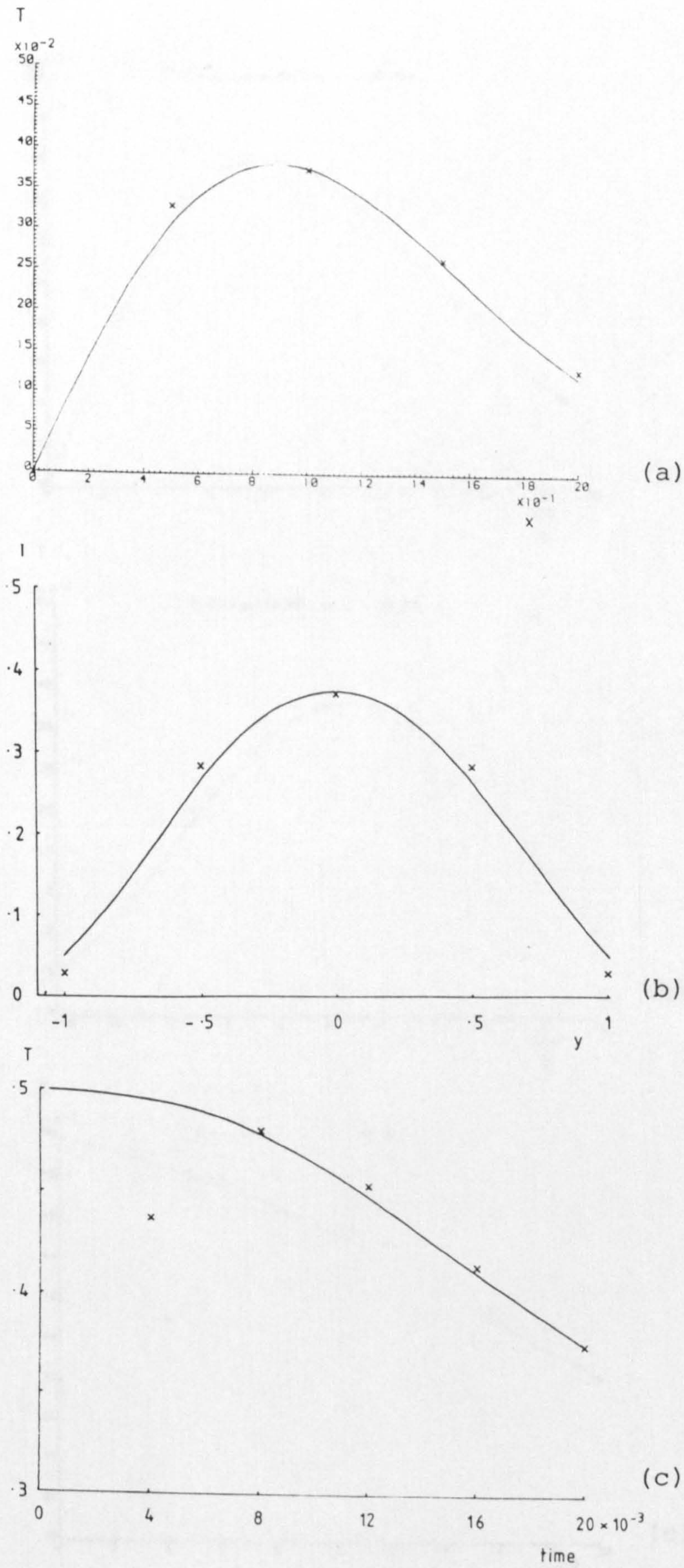

Fig. 6.31

Comparison of finite element and analytic temperatures on anisotropic half-space. 0^{o} orientation.

(a) $T(x, y = 0, t = 0.02)$ vs x

(b) $T(x = 1, y, t = 0.02)$ vs y

(c) $T(x = 1, y = 0, t)$ vs t

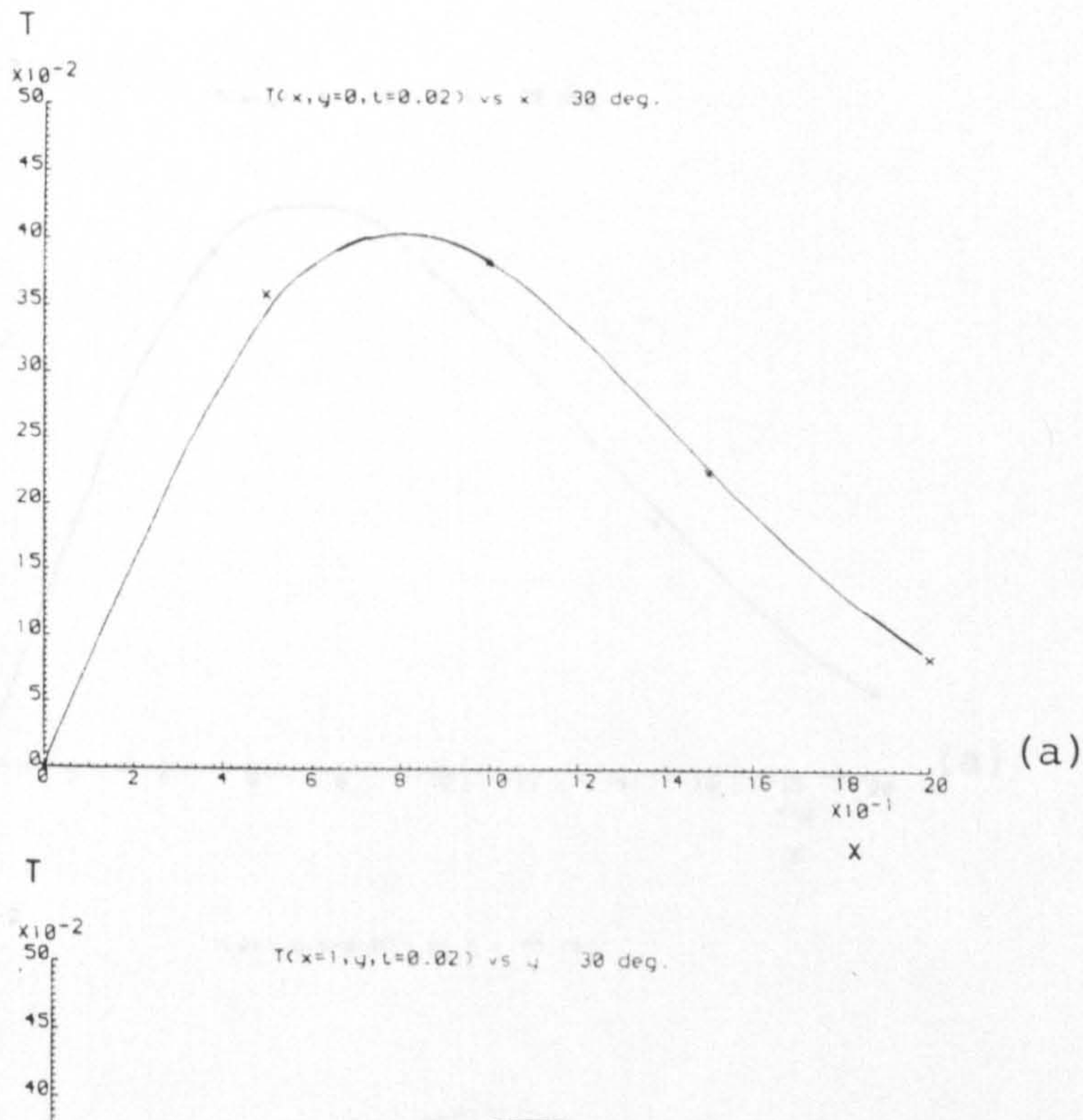

(a)

(b)

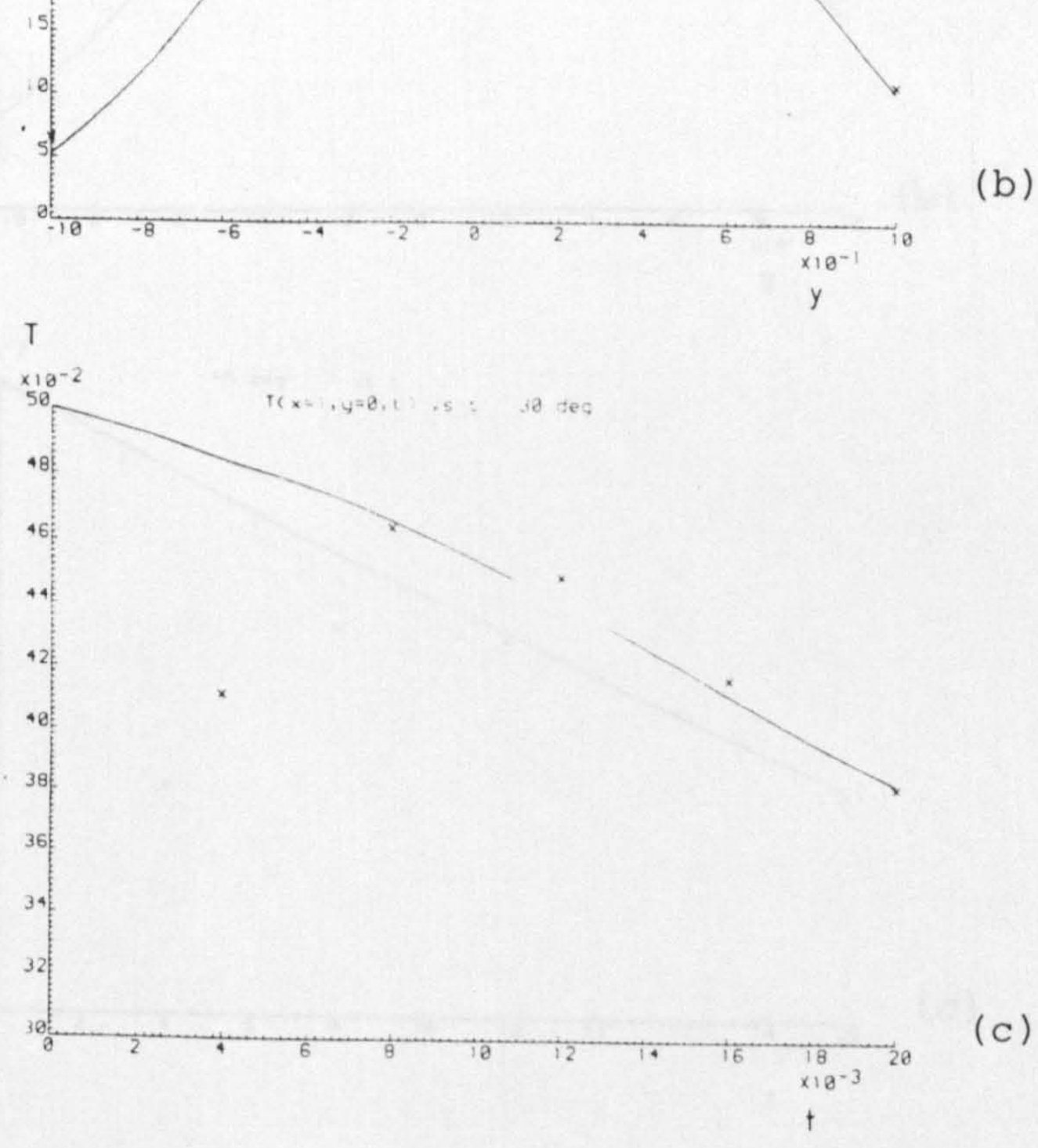

(c)

Fig. 6.32

As Fig. 6.31 for 30° orientation.

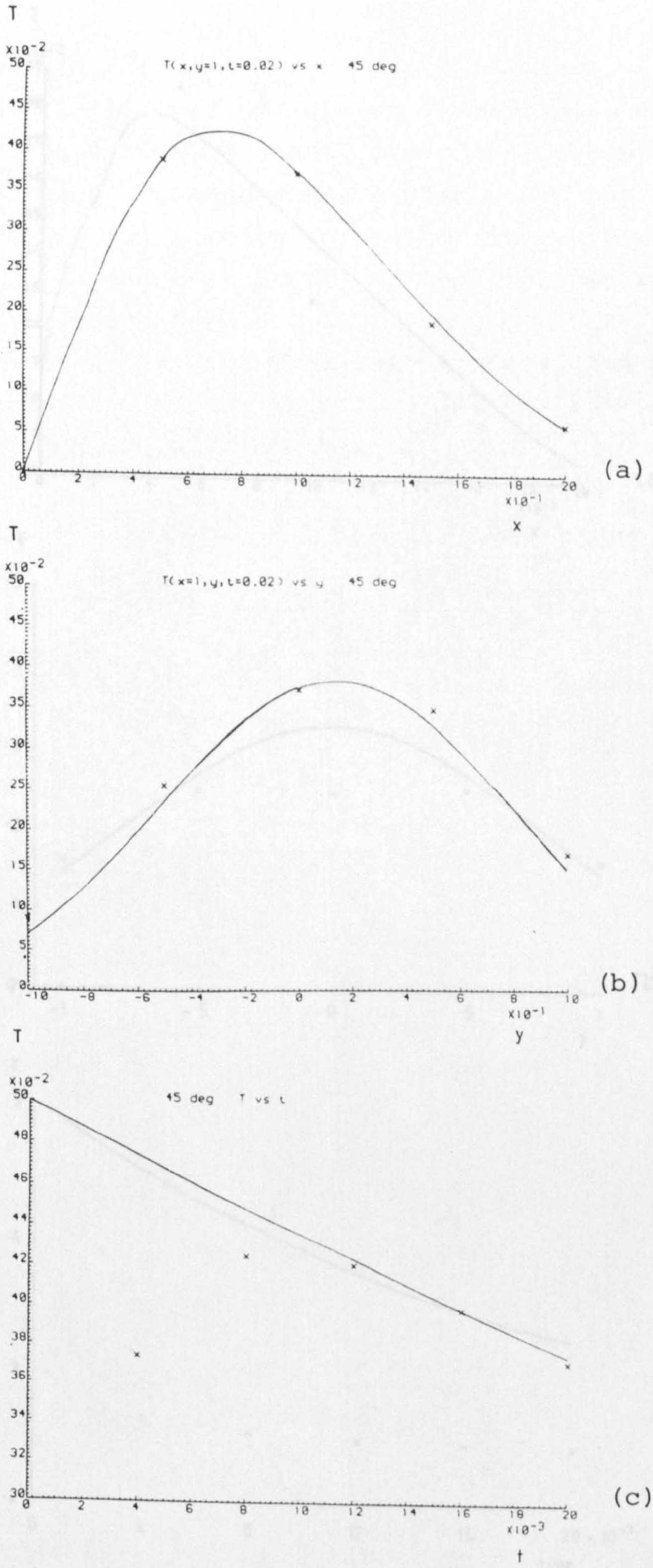

Fig. 6.33

As Fig. 6.31 for 45° orientation.

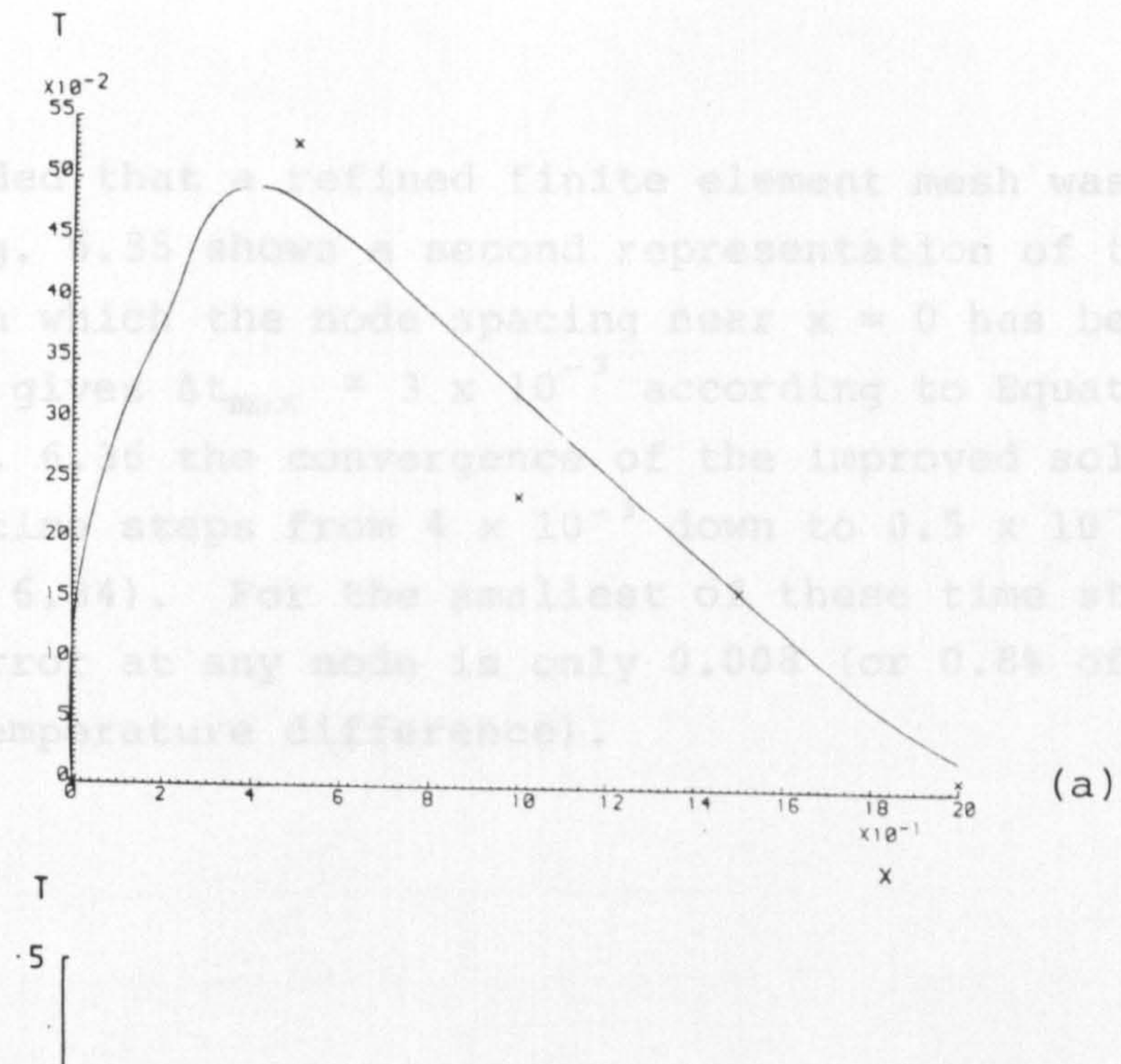

(a)

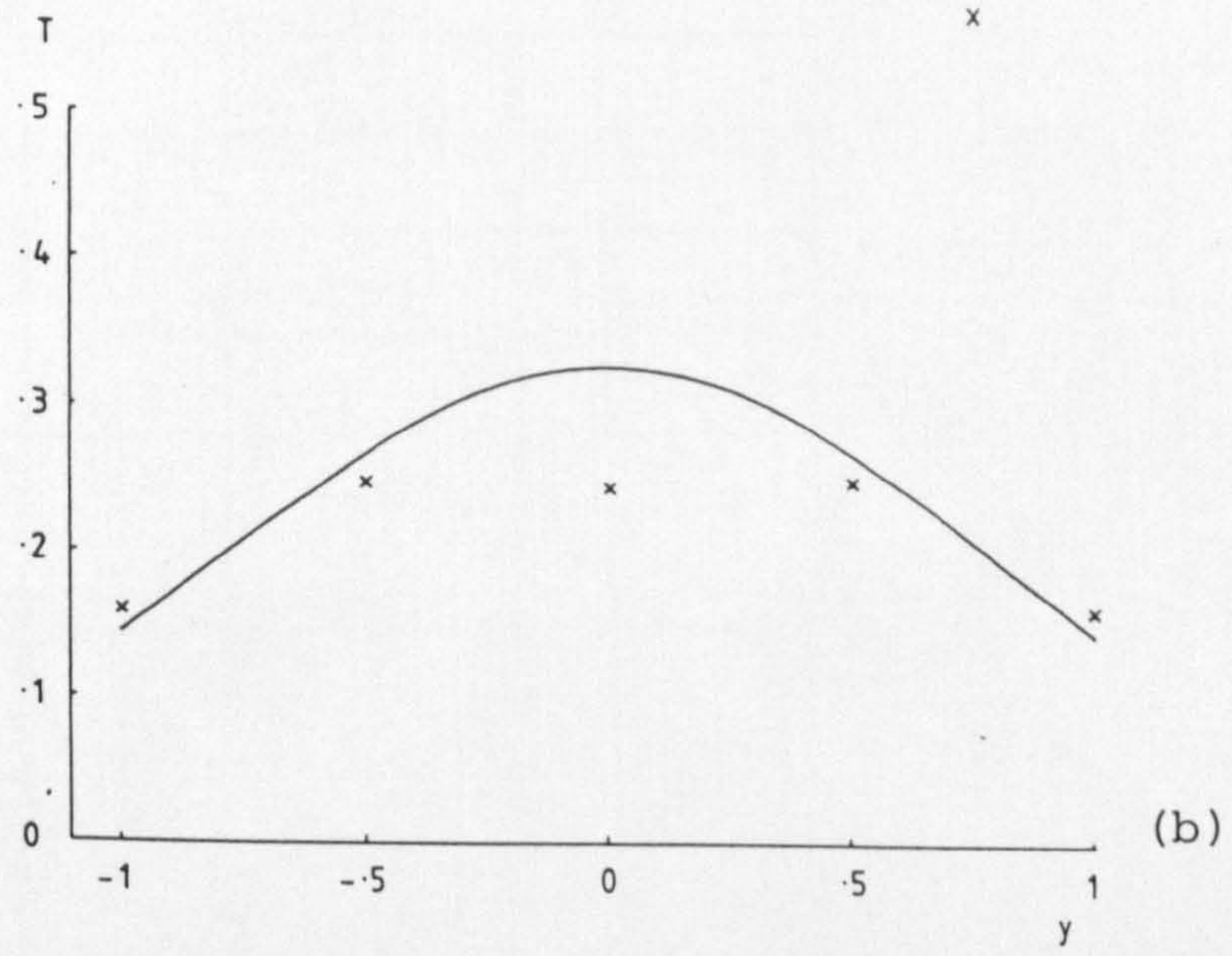

(b)

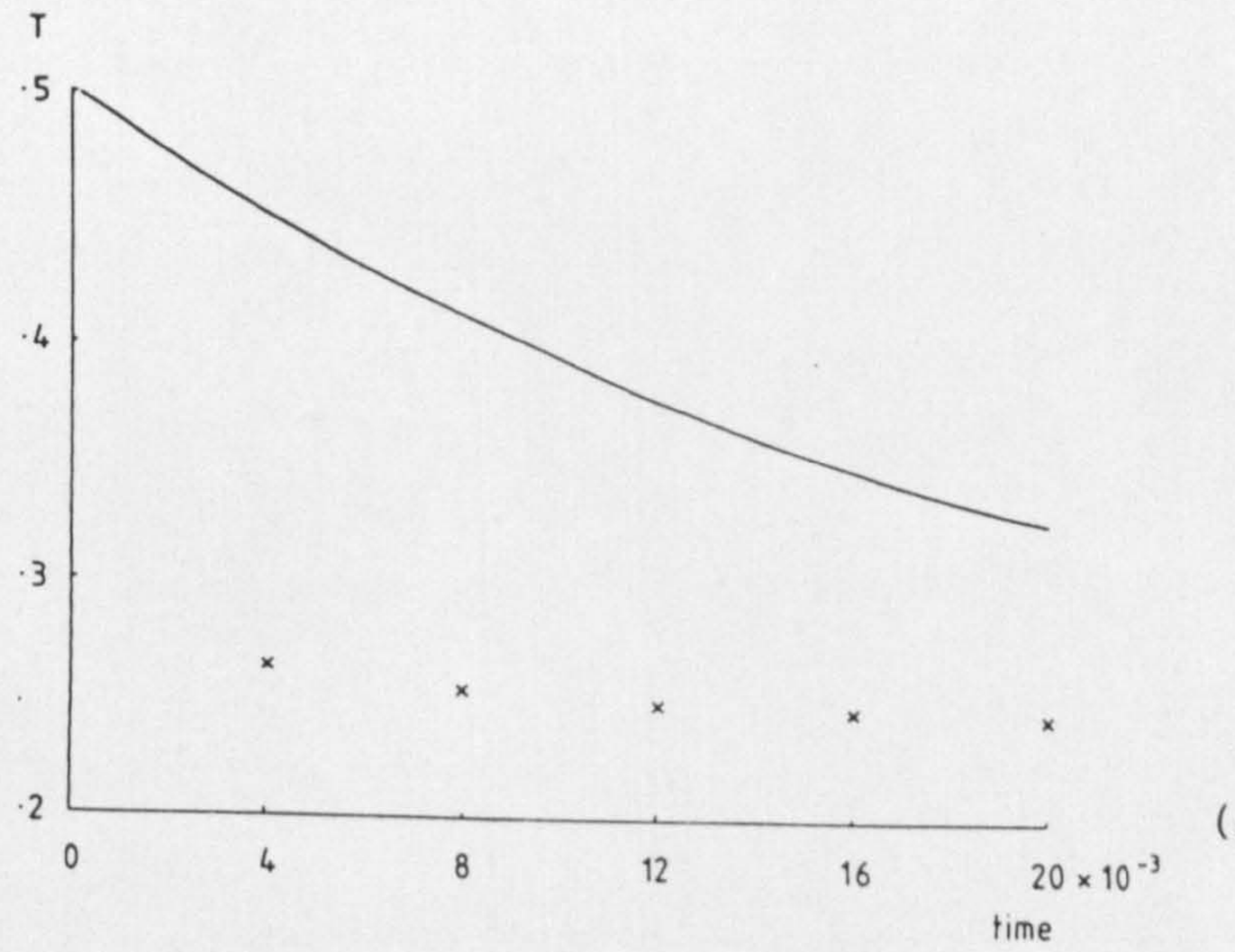

(c)

Fig. 6.34

As Fig. 6.31 for 90° orientation.

it was concluded that a refined finite element mesh was required. Fig. 6.35 shows a second representation of the half-space, in which the node spacing near x = 0 has been halved. This gives $\Delta t_{max} \simeq 3 \times 10^{-3}$ according to Equation 6.11. In Fig. 6.36 the convergence of the improved solution is shown for time steps from 4×10^{-3} down to 0.5×10^{-3} (compare Fig. 6.34). For the smallest of these time steps, the maximum error at any node is only 0.008 (or 0.8% of the initial temperature difference).

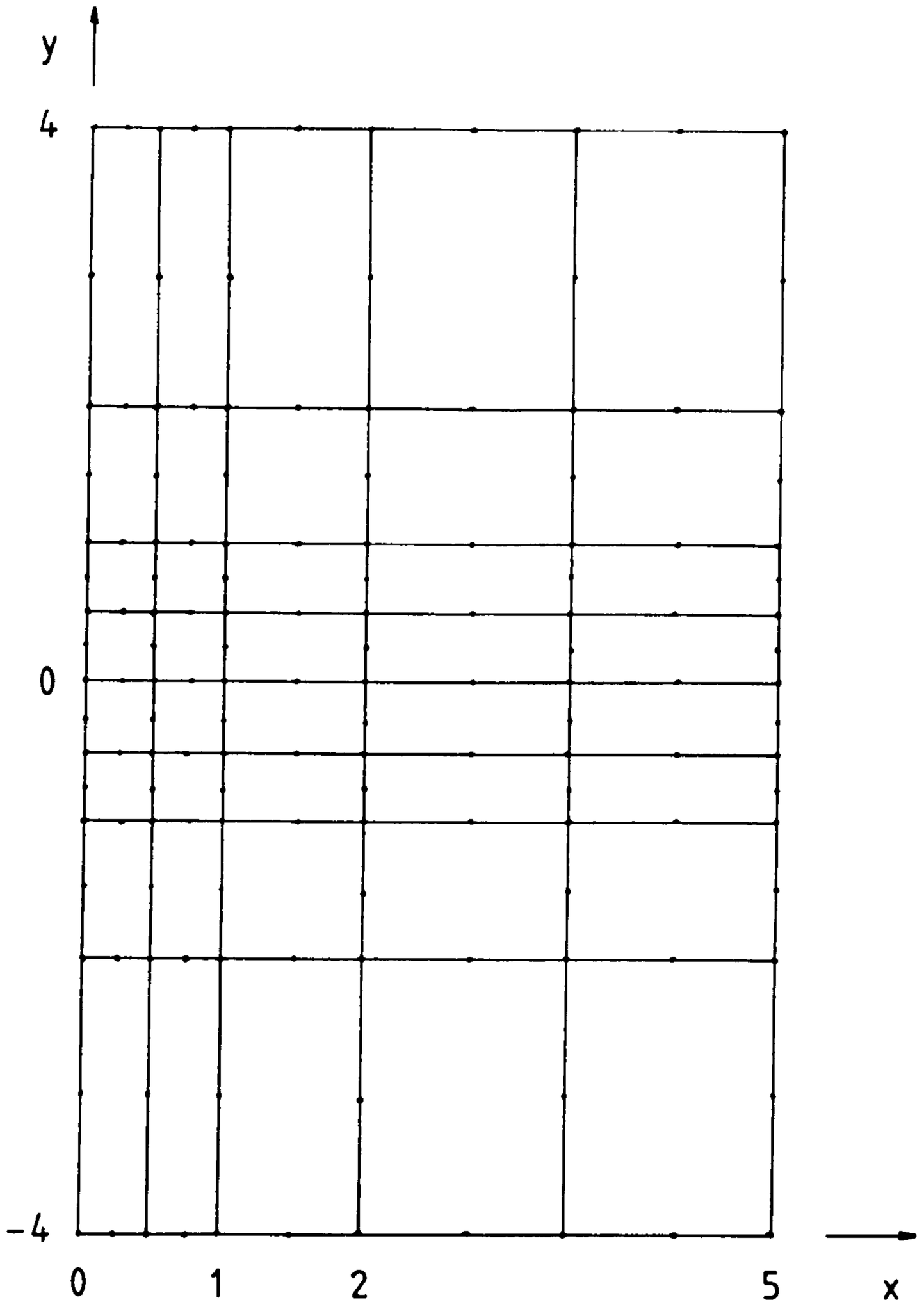

Fig. 6.35

Refined finite element mesh for anisotropic half-space.

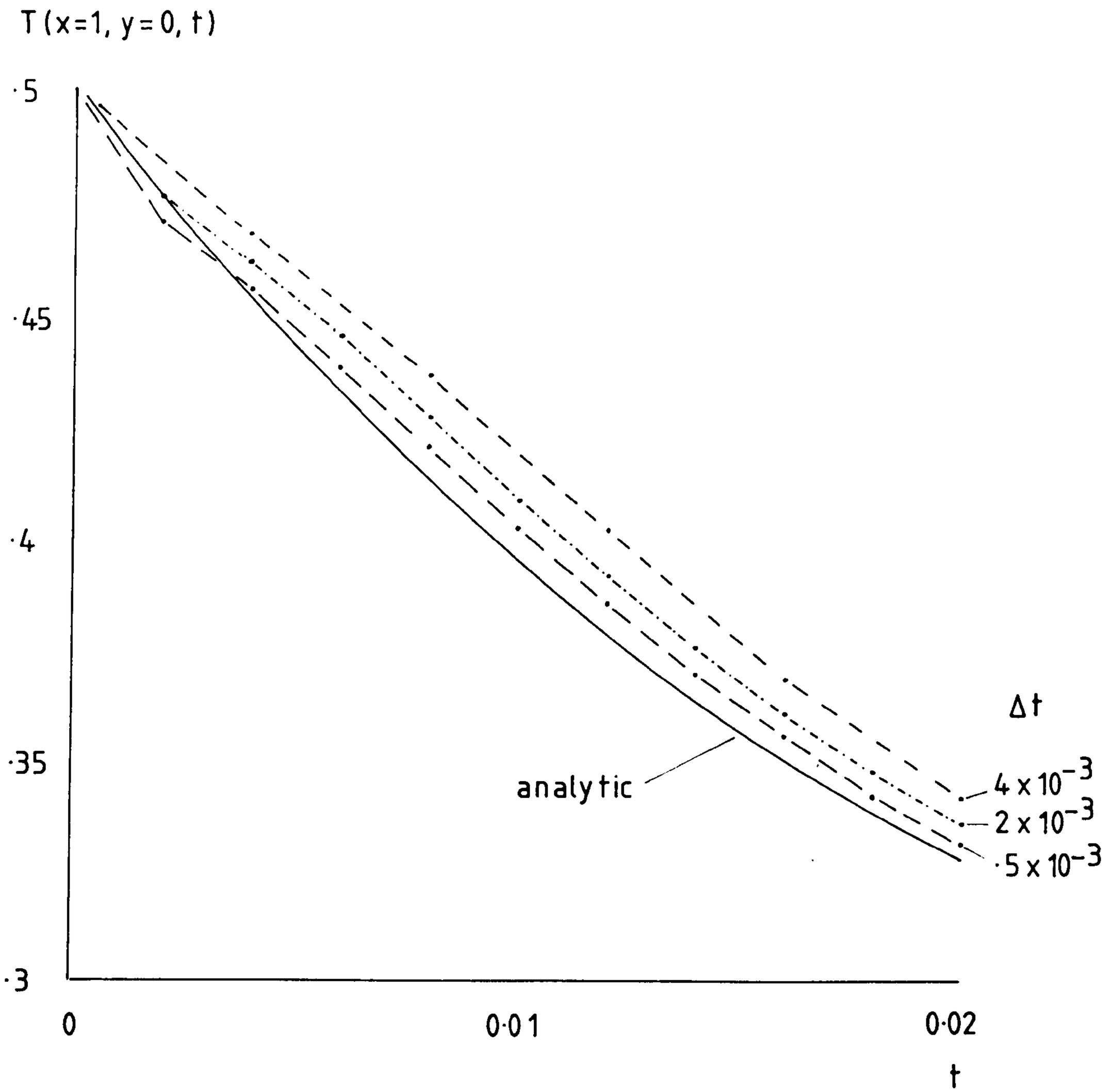

Fig. 6.36

Convergence of numerical solution for T(x = 1, y = 0, t) on refined mesh with decreasing time step, 90° orientation. Compare Fig. 6.34 (c).

CHAPTER 7 : EXPERIMENTAL VALIDATION OF FINITE ELEMENT MODEL

7.1 INTRODUCTION

The experiment described in this chapter was intended primarily to provide data for a validation of the finite element model of anisotropic conduction, using the thermal properties of carbon fibre-reinforced epoxy resin reported in Chapter 3. In addition, it provided an opportunity to gain some experience in the application of finite element techniques to problems involving highly anisotropic materials, and to investigate the sensitivity of temperature distribution to the thermal properties of the material. A basic requirement was flexibility; it was considered important to be able to change the orientation of the composite material relative to a heat source and sink with the minimum of disturbance to the specimen and its instrumentation. Measurements were confined to two dimensions, and were made only under steady state conditions.

Fig. 7.1 shows a schematic, idealised representation of the experiment. The composite material is orthotropic in cartesian coordinates, having long, straight reinforcing fibres, but is of circular geometry. This enables arbitrary orientation of the principal conductivity axes. The boundary condition on the circumference of the disc is a combination of isothermal and adiabatic, the former being maintained by a heat source and heat sink in intimate contact with the surface. This geometry also permits arbitrary variation in the relative positions of source and sink.

Fig. 7.2 illustrates the practical realisation of these concepts. The composite material is in the form of a long circular cylinder, with the reinforcement lying parallel to a diameter. This allows temperature measurements to be made around a circumference well away from either end of the specimen; the region indicated in Fig. 7.2 will experience no 'out-of-plane' temperature gradient, and the heat flow will be two-dimensional. The heat source and heat sink are identical, and were manufactured by milling a serpentine

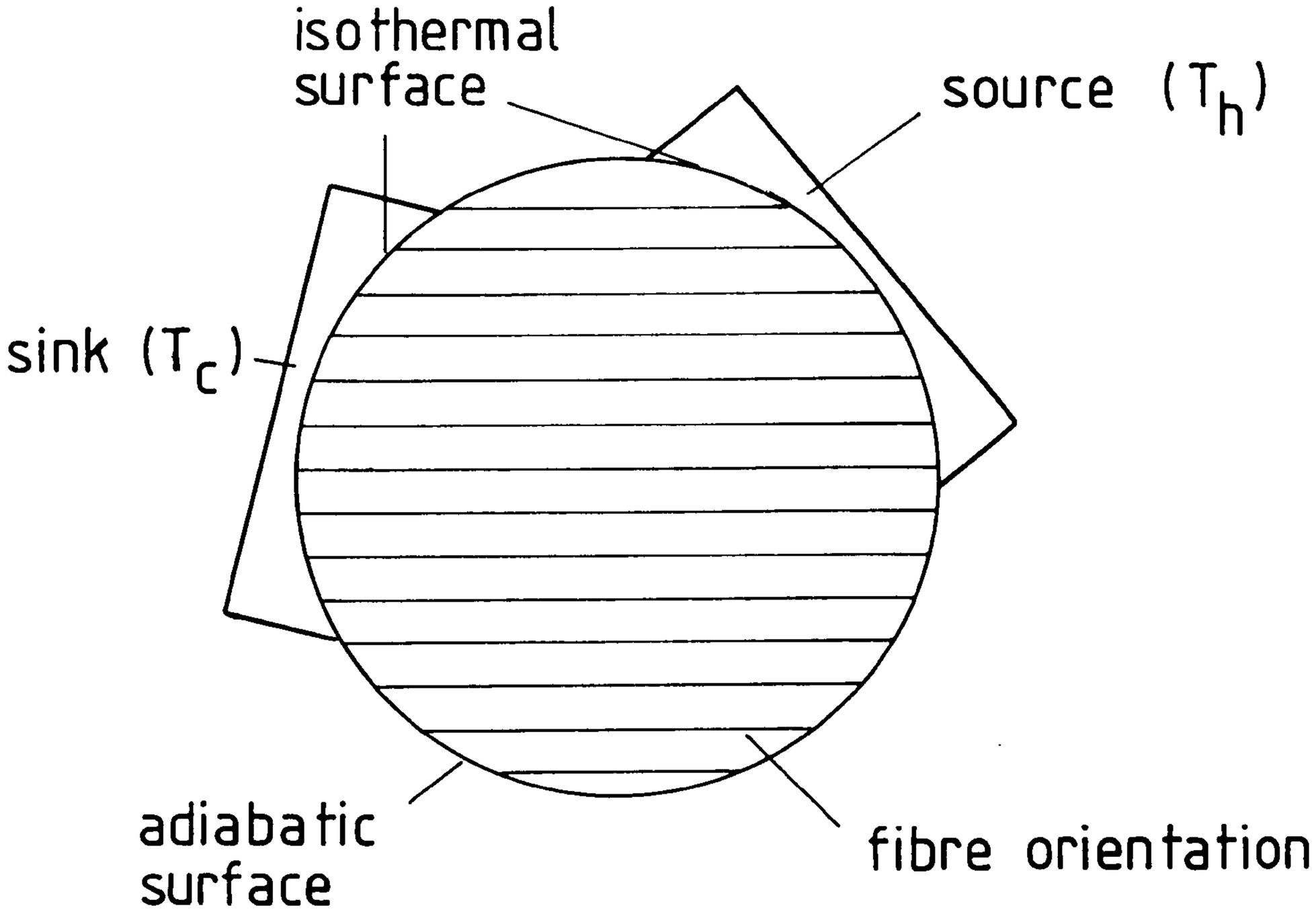

Fig. 7.1

Schematic of validation experiment on orthotropic composite of circular geometry.

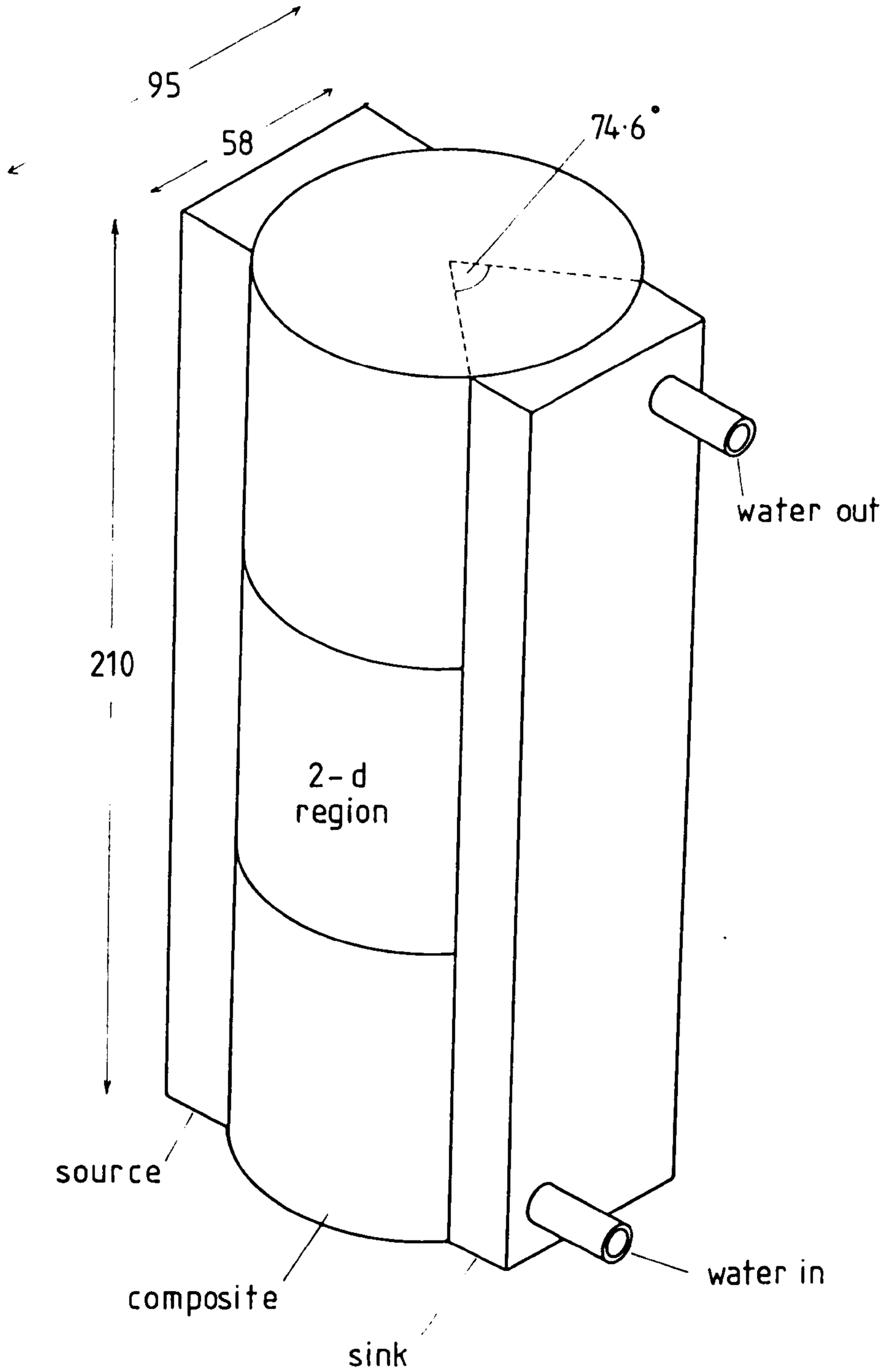

Fig. 7.2

Cylindrical composite with heat source and sink. Dimensions in mm.

channel in a block of aluminium (see 7.2.3). Steady temperatures at the surface of the specimen are maintained by water circulation. The complete assembly is supported inside a large insulated container.

7.2 EXPERIMENTAL DESIGN

7.2.1 Specimen Preparation

The cylinder of composite material illustrated in Fig. 7.2 consisted of three separate cylindrical blocks, each 70mm in length and 95mm in diameter (Fig.7.3). These, in turn, were prepared by hot compression moulding from prepreg sheets in a steel mould of square cross-section - the procedure and materials have already been described fully in 3.2.2.

A 100 mm diameter circular template was attached to one face of the square block with double-sided adhesive tape, and the corners removed with a band-saw. A 75 mm diameter mandrel was then glued securely to one face (after removing the template) using cyanoacrylate adhesive (chosen for its high strength and solubility in water), and inserted into the chuck of a lathe. A second, identical mandrel was inserted in the tail stock, and thus located and glued onto the opposite face. While in the lathe, the specimen was machined to an over-size cylinder, using a high speed steel tool. The specimen assembly was then positioned in a cylindrical grinder and reduced to its final diameter of 95 mm using a silicon carbide grinding wheel. Three identical cylindrical blocks were prepared in this way.

7.2.2 Heater Manufacture

Fig. 7.4 shows the detailed construction of the two aluminium heaters. A serpentine channel, 15 mm wide was milled out of one face of a rectangular block of aluminium to a depth of 10 mm, using a bullnose cutter. This was made water-tight by attaching a rectangular aluminium lid with inlet and outlet, using self-tapping screws together with a sealing compound.

A boring bar was used to machine the opposite face to approximately

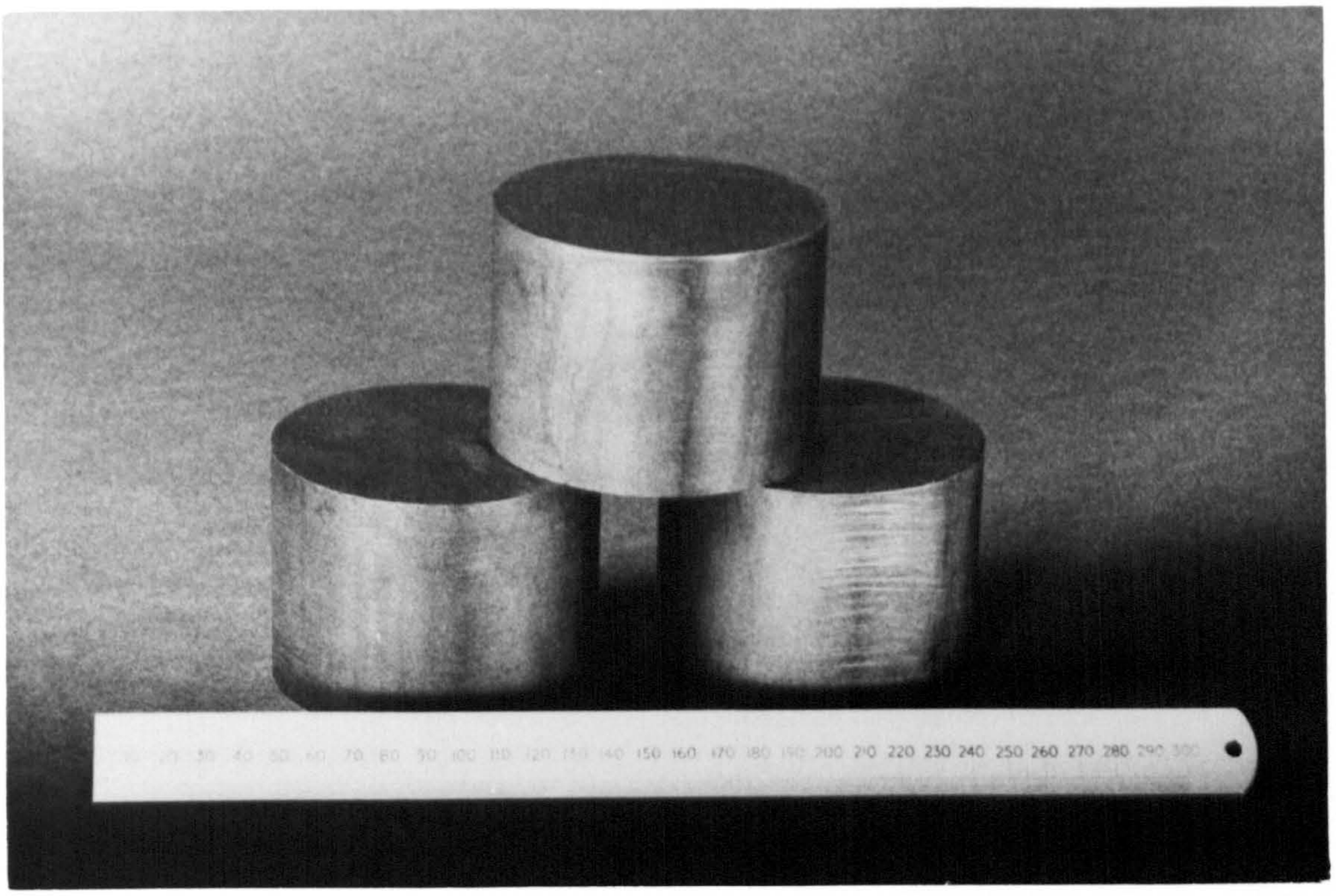

Fig. 7.3

Cylindrical blocks of unidirectional carbon fibre-reinforced epoxy resin.

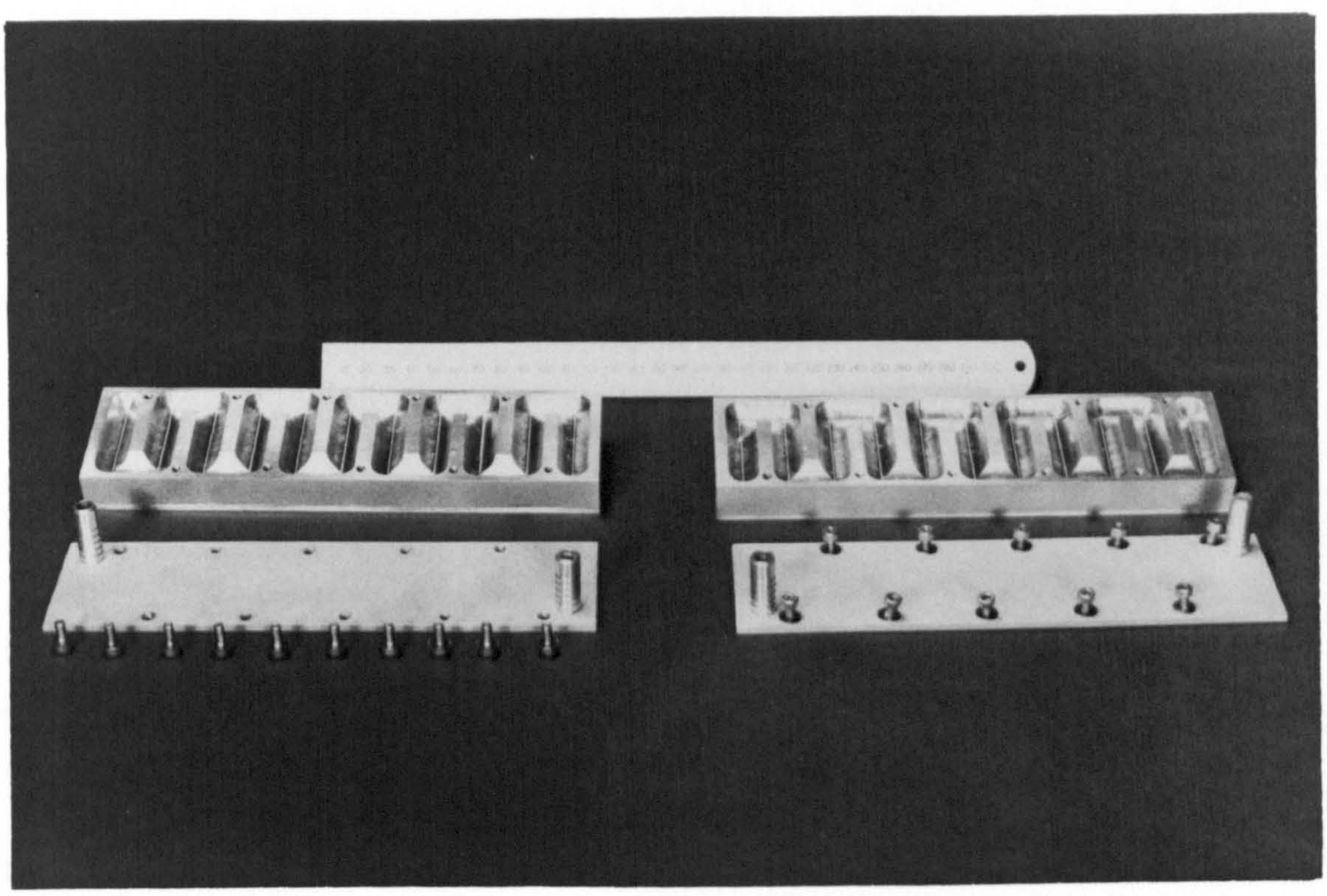

Fig. 7.4

Construction of aluminium heaters.

the same curvature as the cylindrical composite specimens. A steel mandrel was then turned to a diameter of 95 mm and used to lap the heater surface to the correct curvature.

It was required to measure the surface temperatures at the heater/specimen interface, but without disturbing the thermal contact at the surface. This was achieved by inserting thermocouples through the top of the heaters, such that the temperature sensing junction itself became part of the curved heater surface. A total of six aluminium inserts were machined to a diameter of 5 mm, and a 1 mm hole drilled along the centre axis (see Fig. 7.5). A copper-constantan thermocouple was then positioned in the central hole and set in epoxy resin adhesive with the welded bead of the sensing junction just protruding from the base of the insert.

Three holes were drilled through each heater block, as shown in Fig. 7.6, and these were reamed to the same diameter as the thermocouple inserts (5 mm). The inserts were then pushed into the holes and secured with sealing compound such that the end containing the thermocouple bead was fractionally proud of the curved surface. The ends were carefully removed with a bearing scraper then lapped flush with the heater surface.

7.2.3 Experiment Assembly

Before assembly, a series of thin slots were cut with a scalpel blade on the surface of one of the cylindrical blocks. As shown in Fig. 7.7, these were positioned at an angular separation of 20^{o}, and the centre of each slot was enlarged slightly to accommodate the bead of a butt-welded copper-constantan thermocouple.

The three composite blocks were then stacked end-to-end (with a consistent alignment of reinforcement) and positioned in the clamping device illustrated in Fig. 7.8. The curved contact surfaces of the heater blocks were smeared with a zinc oxide-filled silicone heat sink compound before assembly; good thermal contact with the specimen was

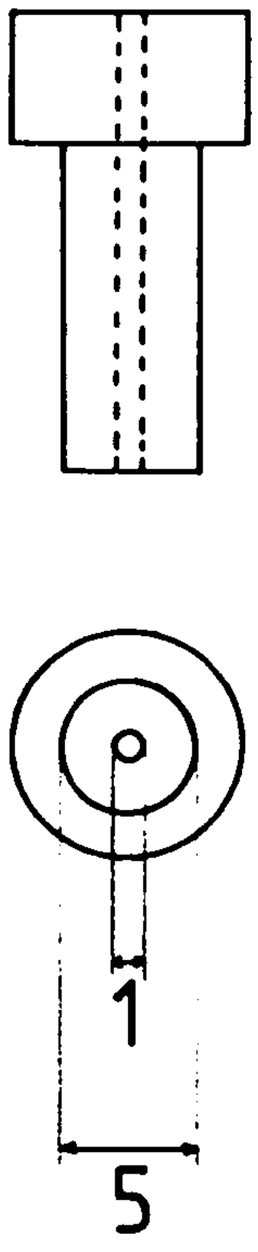

Fig. 7.5

Aluminium insert for thermocouple insertion. Dimensions in mm.

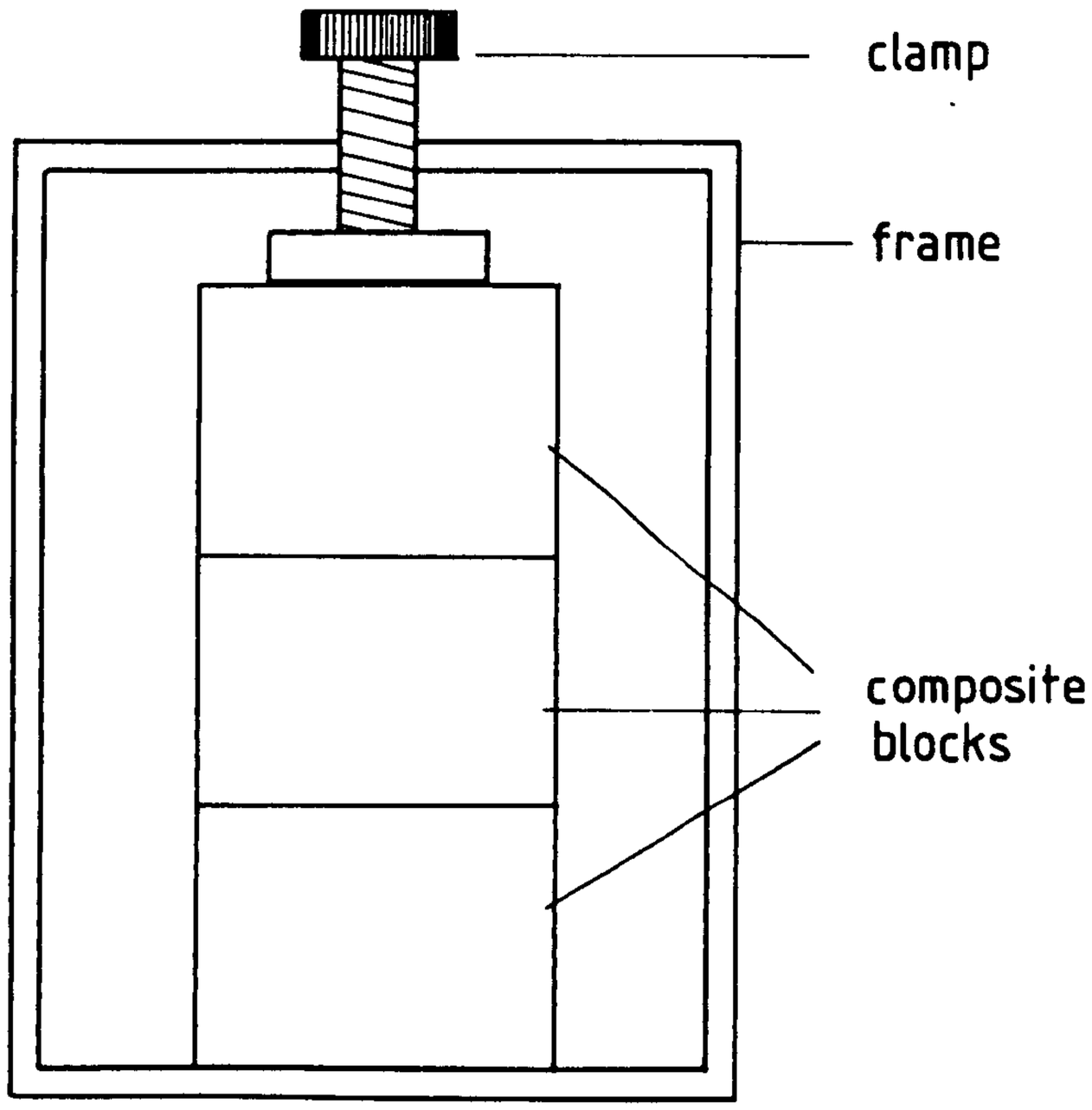

Fig. 7.8

Arrangement of composite blocks in clamping device.

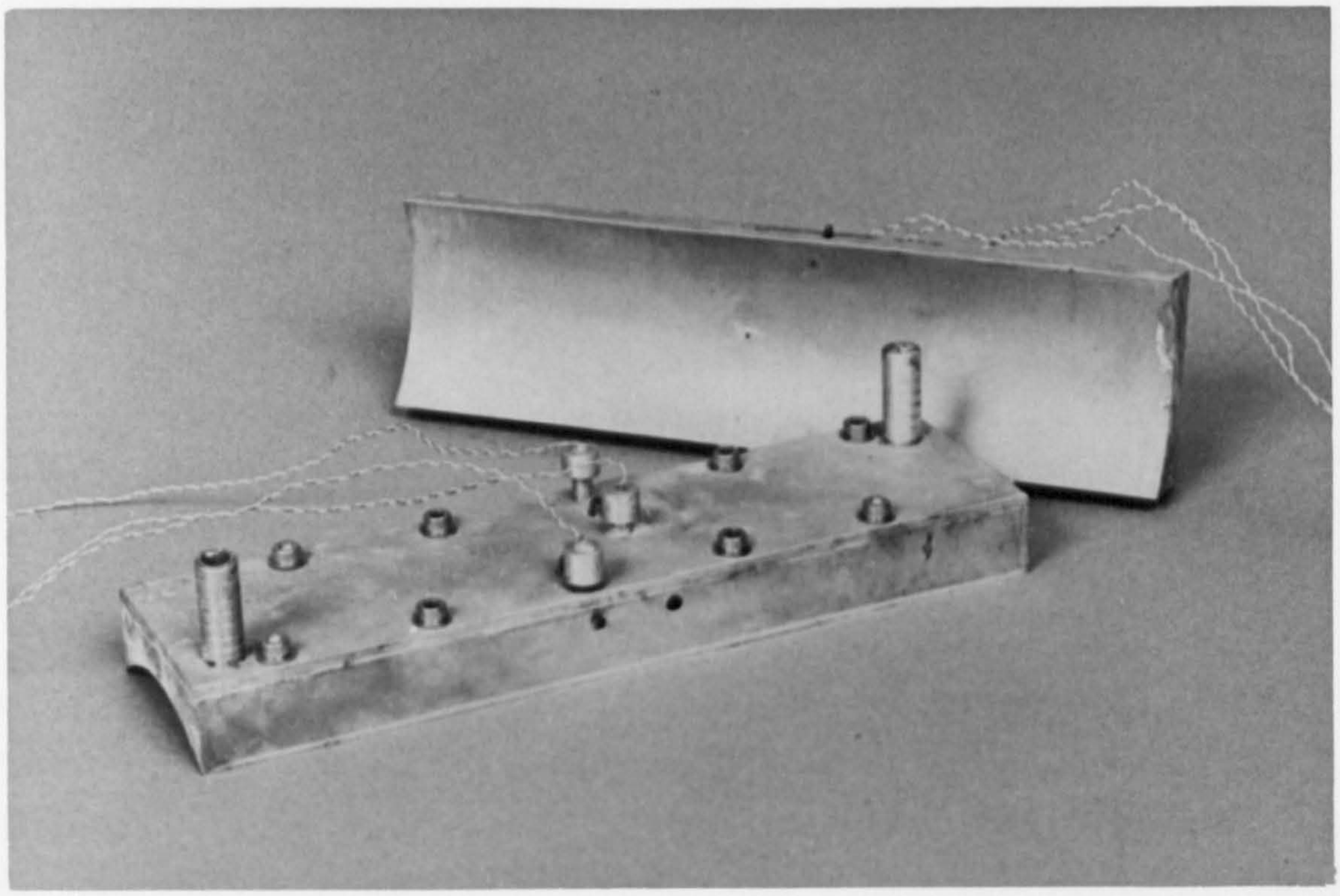

Fig. 7.6

Heater blocks with thermocouple inserts.

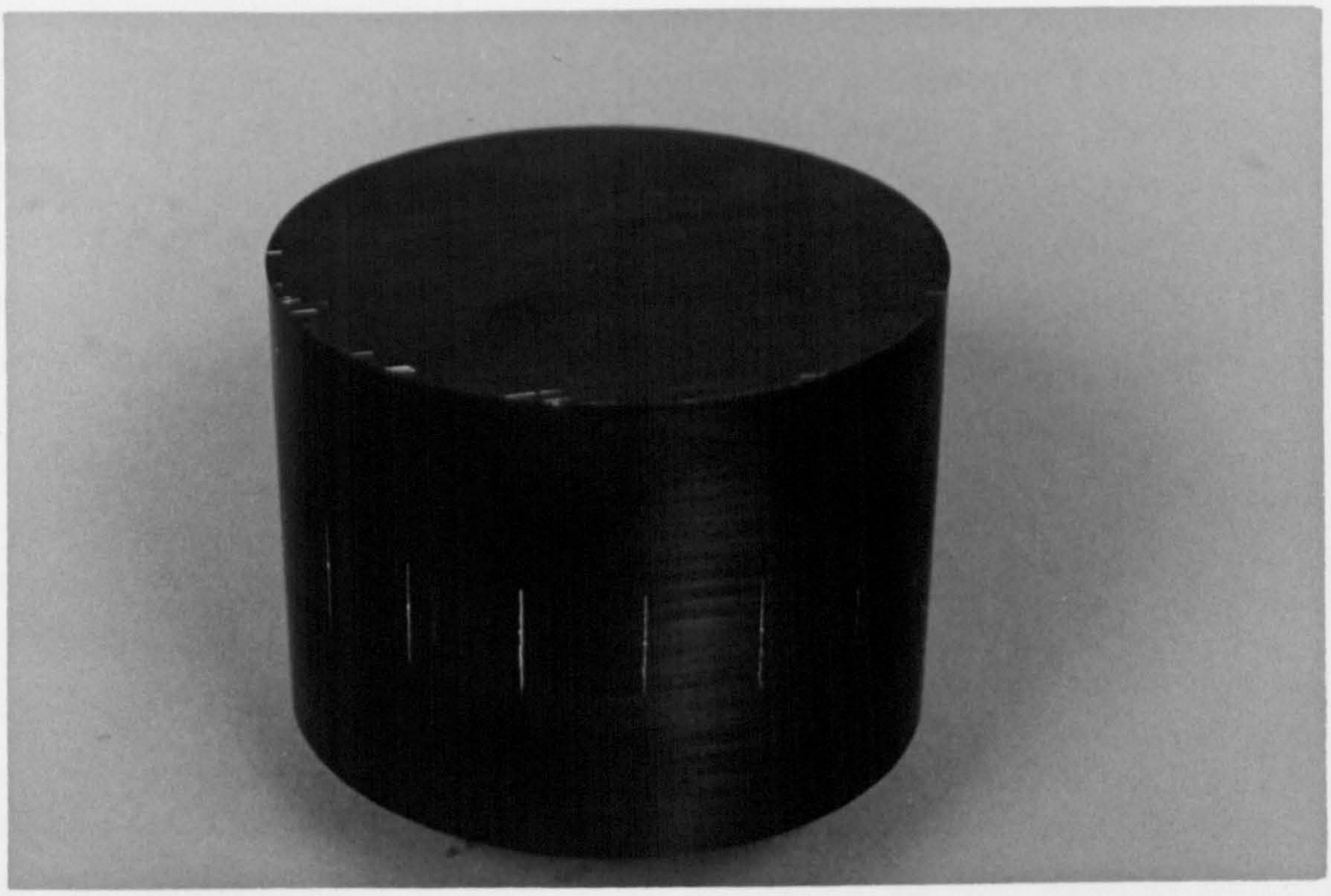

Fig. 7.7

Cylindrical composite showing thermocouple slots.

promoted by means of a G-clamp around the two heaters, which were then located and secured in the desired position.

Thermocouples were located in the slots in the central block and secured in position by a small strip of adhesive tape over the junction. Thermocouples had been previously calibrated by immersion in a stirred water bath (see 3.1.3) using the temperature monitoring system described in 3.1.1, and, as before, the calibrations were checked after each series of measurements.

One heater was connected via a small (23 W) pump to a thermostatically-controlled water bath, using polythene tubing. In operation, the pump achieved a steady flow rate of 1.9 l/min. The other heater was connected directly to the cold water mains supply, which allowed cooling flow rates of up to 2.5 l/min.

Finally, the relative locations of heater, heat sink and specimen were checked and the entire assembly surrounded by loose-fill insulation to a minimum thickness of 10 cm. Pump and water supply were turned on, having set the water bath thermostat to the desired temperature. The system was monitored until a steady-state was achieved; this required a change in any recorded temperature of less than 0.2 K over a period of 15 min. Temperatures were then recorded and averaged over the following 5 min. period. The time required to reach a steady-state depended on specimen orientation and heater temperature, but was typically 15 - 30 min.

7.2.4 Experimental Errors

Before quantifying the random errors associated with the experimental measurements, it is necessary to justify some of the simplifying assumptions involved in the design of the apparatus.

A two-dimensional temperature distribution (that is, in the plane of the cylinder cross-section) at the centre of the

composite stack requires that there should be no variation of temperature in the z-direction (perpendicular to the cross-section) in this region. Such a temperature gradient could arise from significant heat losses from the top and bottom ends of the cylinder, or from a non-uniform temperature distribution along the length of either heater. It is readily shown that the rate of heat loss from each end of the cylinder is of the order of 3×10^{-3} W per unit temperature difference between specimen and environment (assuming 10 cm of insulation with a thermal conductivity of 0.04 W/m K). This may be compared with the smallest typical value of heat flux between the source and sink; at a temperature difference of 10 K this would be about 2 W for the lowest possible value of effective specimen conductivity. It may be concluded, therefore, that end heat losses are generally less than 1% of the heat flux through the specimen.

Similar arguments may be applied to heat losses from the curved specimen surfaces, which will be assumed perfectly insulated in the numerical calculations. The total area of these surfaces is 0.035 m^2, giving a heat loss rate of approximately 10^{-2} W/K through 10 cm of loose-fill insulation.

An important assumption is that there is no significant temperature difference between the heat source and sink and the adjacent specimen surface - in other words, the thermocouples installed in the aluminium heaters record the surface temperature of the composite. This relies on the accuracy with which the radii of curvature of the heaters are matched to the specimen - poor surface contact may be only partially alleviated by the use of the heat sink compound. Fig. 7.9a illustrates (on an exaggerated scale) the effect of the heater radius (r_h) being greater than that of the specimen (r_s) by an amount δr. The largest gap between heater and specimen is indicated by p. Simple trigonometry gives

$$r_s^2 = (\delta r)^2 + (r_h - p)^2 - 2\delta r\,(r_h - p)\cos\theta$$

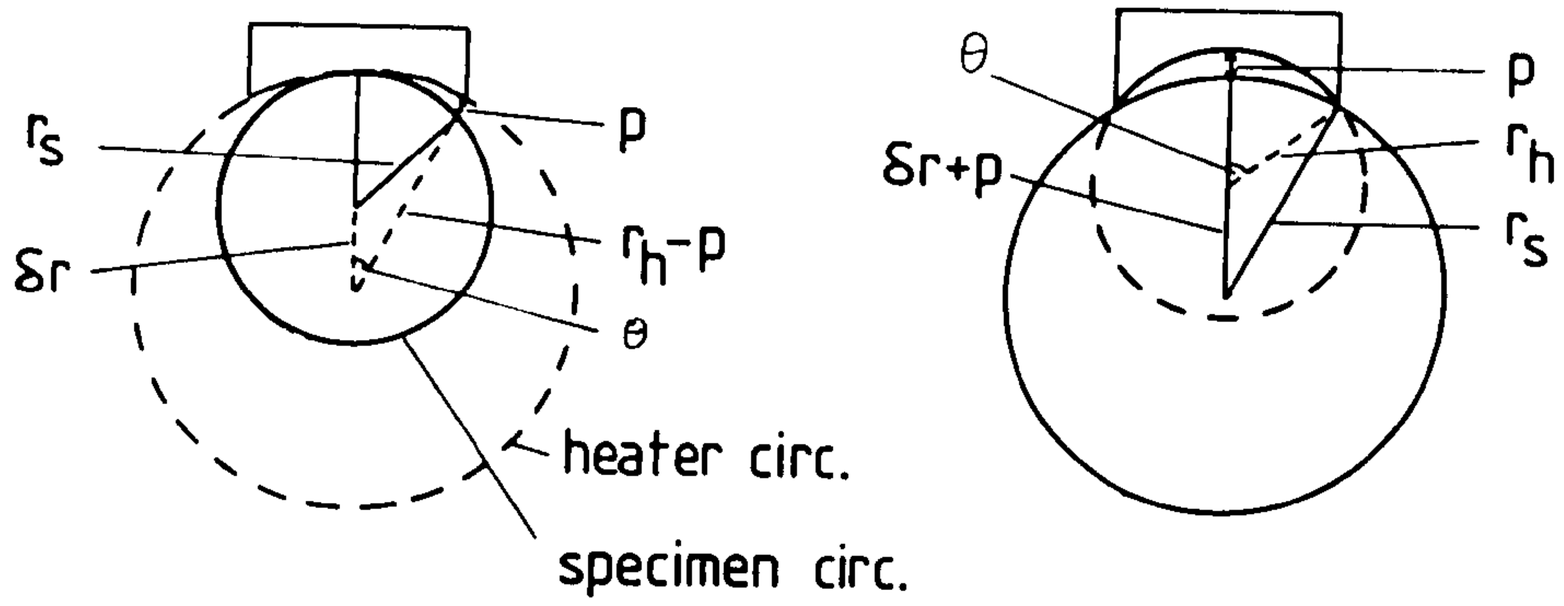

Fig. 7.9

Geometry of specimen and heater with exaggerated difference in radii.

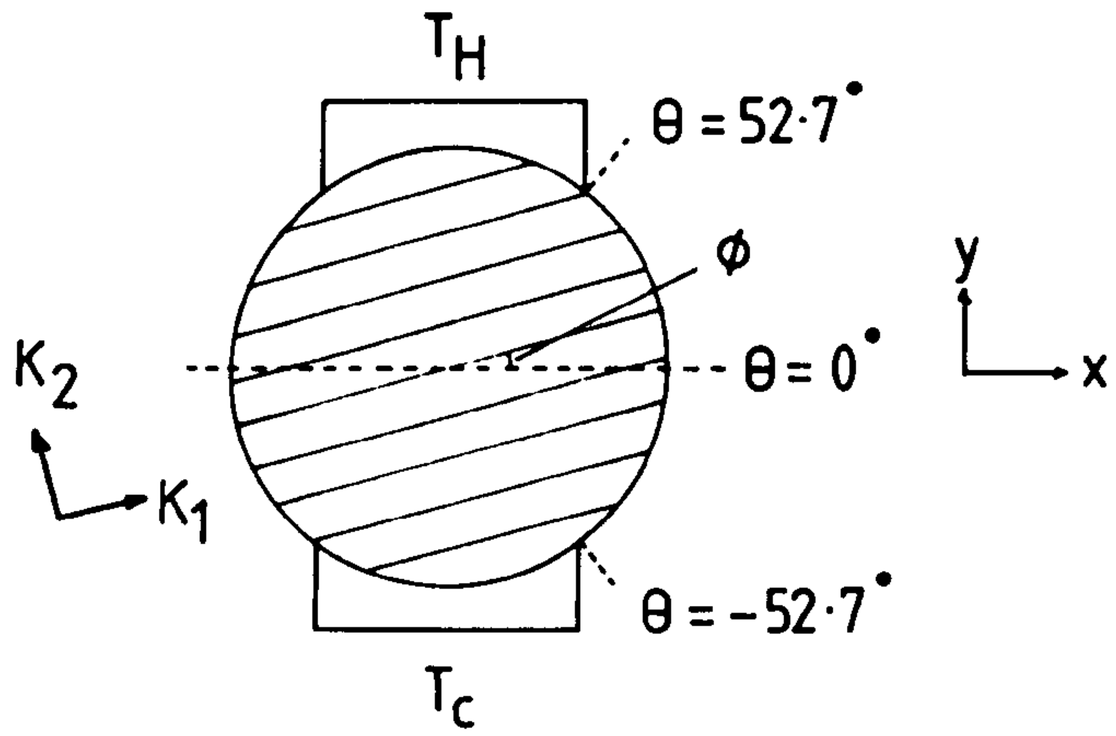

Fig. 7.10

Specimen/heater configuration with source and sink opposed.

whence

$$r_h - p = \delta r \cos\theta \pm\sqrt{r_s^2 - (\delta r)^2 \sin^2\theta} \simeq \delta r \cos\theta \pm r_s$$

giving $p = \delta r\ (1 - \cos\theta)$ (7.1)

For the case where $r_s > r_h$ (Fig. 7.9b), a similar application of the cosine rule gives

$$\delta r + p = r_s \cos\theta \pm\sqrt{r_s{}^2 \cos^2\theta - r_s^2 + r_h{}^2}$$

$$= r_s \cos\theta \pm r_s \cos\theta\ 1 - \left(\frac{(r_s{}^2 - r_h{}^2)}{r_s{}^2 \cos^2\theta}\right)^{\frac{1}{2}}$$

$$\simeq \frac{r_s{}^2 - r_h{}^2}{2r_s\ \cos\theta} = \frac{(r_s - r_h)(r_s + r_h)}{2r_s\ \cos\theta}$$

But $r_s - r_h = \delta r$ and $r_s + r_h \simeq 2r_s$, so that

$$\delta r + p \simeq \frac{\delta r}{\cos\theta}$$

giving $p = \delta r\ (\frac{1}{\cos\theta} - 1)$ (7.2)

As previously indicated in Fig. 7.2, the semi-angle subtended by the heater is $\theta = 37.3^{o}$; using this value in Equations 7.1 and 7.2 gives

$$p = 0.205\ \delta r \quad (r_h > r_s)$$

and $$p = 0.257\ \delta r \quad (r_s > r_h)$$

It is estimated that the radii of the specimen and of the steel mandrel used to lap the heaters was turned to a tolerance of $\pm$ 0.1 mm, giving δr a maximum possible value of 0.2 mm. The value of p could thus be as great as 0.052 mm.

The temperature difference across the gap p is given by

$$\delta T_g = p\ \frac{q}{k_g} \qquad (7.3)$$

where q is the heat flux from heater to specimen, and k_g is

the thermal conductivity of the heat sink compound used to promote thermal contact (the manufacturer's figure is k_g = 0.7 W/m K). At maximum operating temperatures, the heat flux through the specimen will be of the order of 15 kW/m^2, with the heater dissipating about 400 W. With these figures, δT_g amounts to about 1 K, a value which will be correspondingly lower at smaller heat fluxes. The effect of this error on the measured temperature distribution is discussed in 7.5.

The random errors associated with an absolute measurement of surface temperature have already been discussed in 3.1.2; the uncertainty is ± 0.3 K.

The angular position of the thermocouple slots is subject to an estimated error of $\pm 1^o$. A similar uncertainty may be ascribed to the locations of heat source and sink, and the effect of this will be discussed in the context of the numerical results.

7.3 FINITE ELEMENT CALCULATIONS

In this section, some preliminary calculations of the temperature distribution on a two-dimensional disc are presented. They demonstrate the sensitivity of the results to changes in mesh geometry, temperature-dependent thermal conductivity and other experimental variables. Comparison of measured and calculated temperatures is made in 7.4. The configuration considered here is shown in Fig. 7.10, having heat source and sink diametrically opposed. The composite has principal thermal conductivities K_1 (parallel to the reinforcement) and K_2 (perpendicular). For an arbitrary orientation of reinforcement relative to the x-axis (angle ϕ), the conductivity coefficients are given by Equations 4.13, namely

$$k_{11} = K_1 \cos^2\phi + K_2 \sin^2\phi$$
$$k_{22} = K_1 \sin^2\phi + K_2 \cos^2\phi$$
$$k_{12} = (K_1 - K_2) \sin\phi \cos\phi$$

The location of a point on the surface of the disc is denoted by its angular coordinate θ, with the positive x-axis corresponding to $\theta = 0$. The heater and sink are modelled as fixed surface temperatures (T_H and T_C) and it is convenient to define a normalised, dimensionless surface temperature

$$\Phi(\theta) = \frac{T(\theta) - T_C}{T_H - T_C} \qquad (7.4)$$

which varies between 1 at $\theta = 52.7^o$ and 0 at $\theta = -52.7^o$.

Fig. 7.11 shows schematically the distribution of Φ for the two orthotropic configurations of the specimen (that is, with reinforcement aligned parallel to the cartesian axes, corresponding to $\phi = 0^o$ and 90^o), together with the curve for an isotropic solid. For an arbitrary orientation of principal axes ($0^o < \phi < 90^o$) the temperature distribution is asymmetric about $\theta = 0^o$; Fig. 7.12 shows (qualitatively) the transition between the two orthotropic distributions as ϕ takes intermediate values.

7.3.1 Effect of Element Size

Three different meshes were used to represent the two-dimensional disc, having respectively 12, 32 and 104 elements (Fig. 7.13). The first of these is a coarse mesh, with only 5 surface temperatures in the range $-52.7^o < \theta < 52.7^o$ (two of which are fixed by the boundary conditions). The third mesh has 17 such nodes, allowing a more detailed calculation of the surface temperature distribution.

Calculations were made on all three meshes with fibre orientations (angle ϕ in Fig. 7.10) of 0^o, 15.4^o, 27.7^o, 52.7^o and 90^o; these correspond to values used in the experimental measurements discussed in 7.4. Constant (that is, not dependent on temperature) principal thermal conductivities of $K_1 = 48$ W/m K and $K_2 = 1.4$ W/m K were assumed, and Equations 4.13 used to calculate conductivity coefficients where appropriate.

The resulting surface temperature distributions are shown

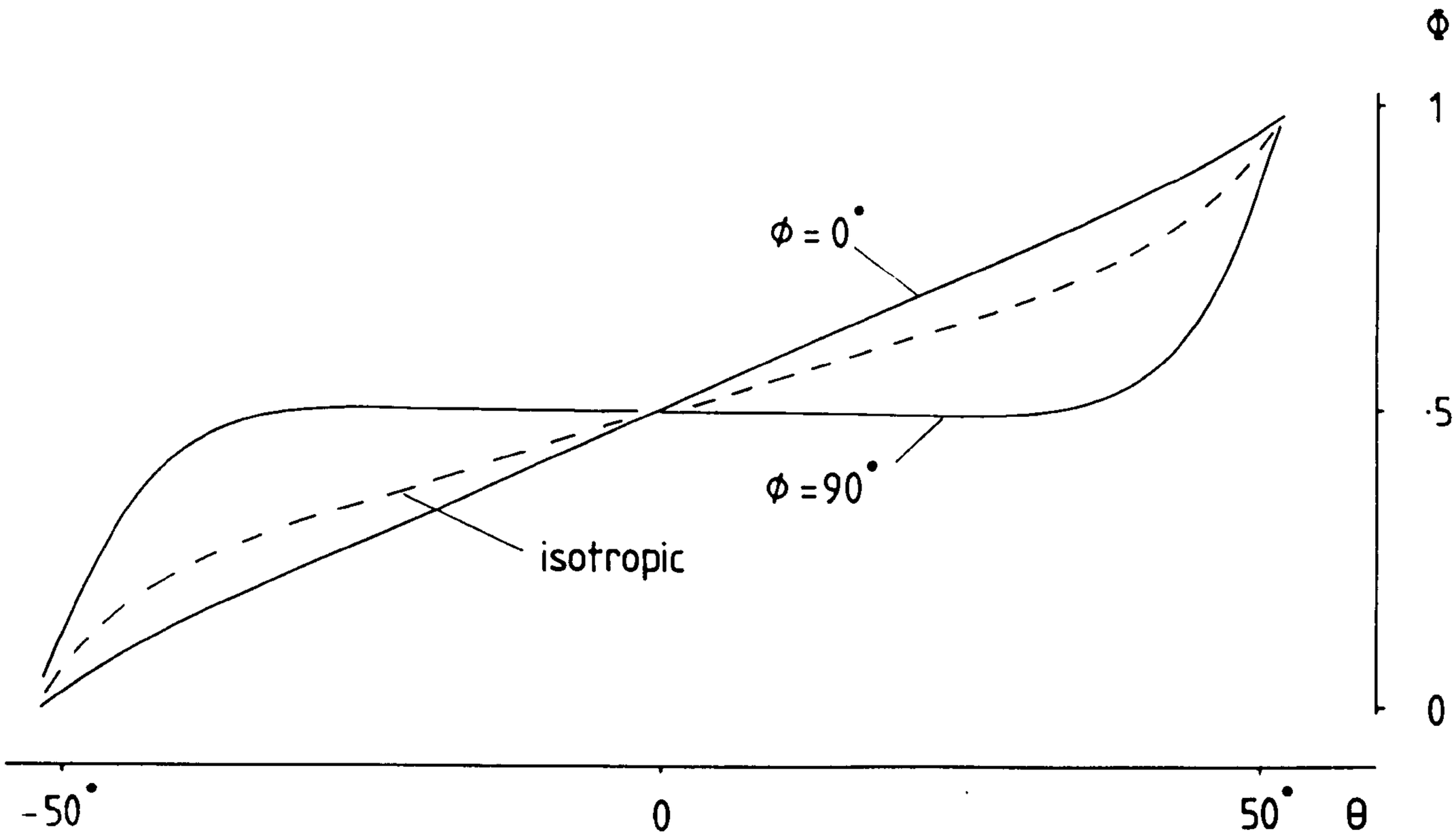

Fig. 7.11

Schematic distribution of normalised surface temperatures for an isotropic material and the two orthotropic configurations.

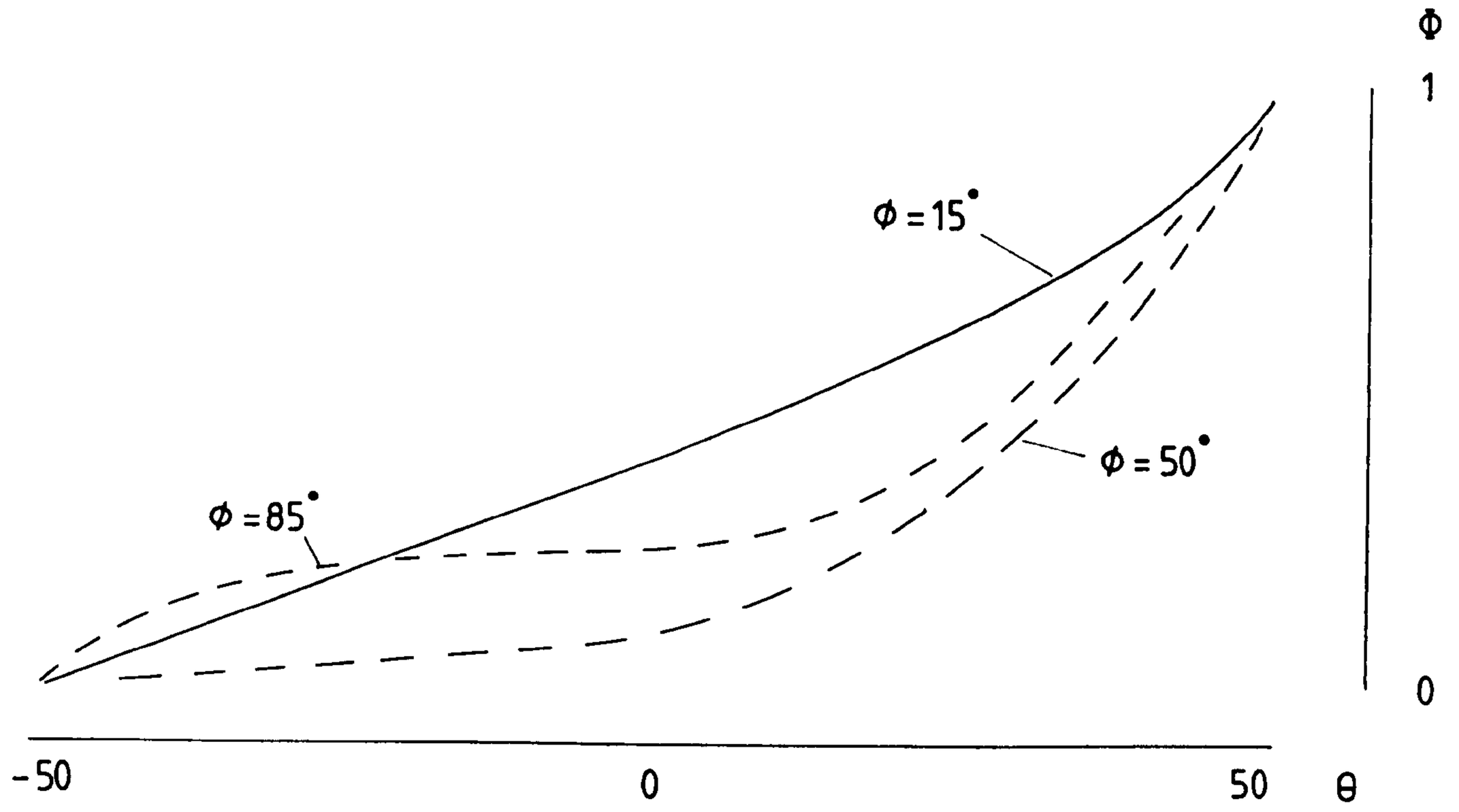

Fig. 7.12

Schematic surface temperatures for intermediate orientations of principal axes.

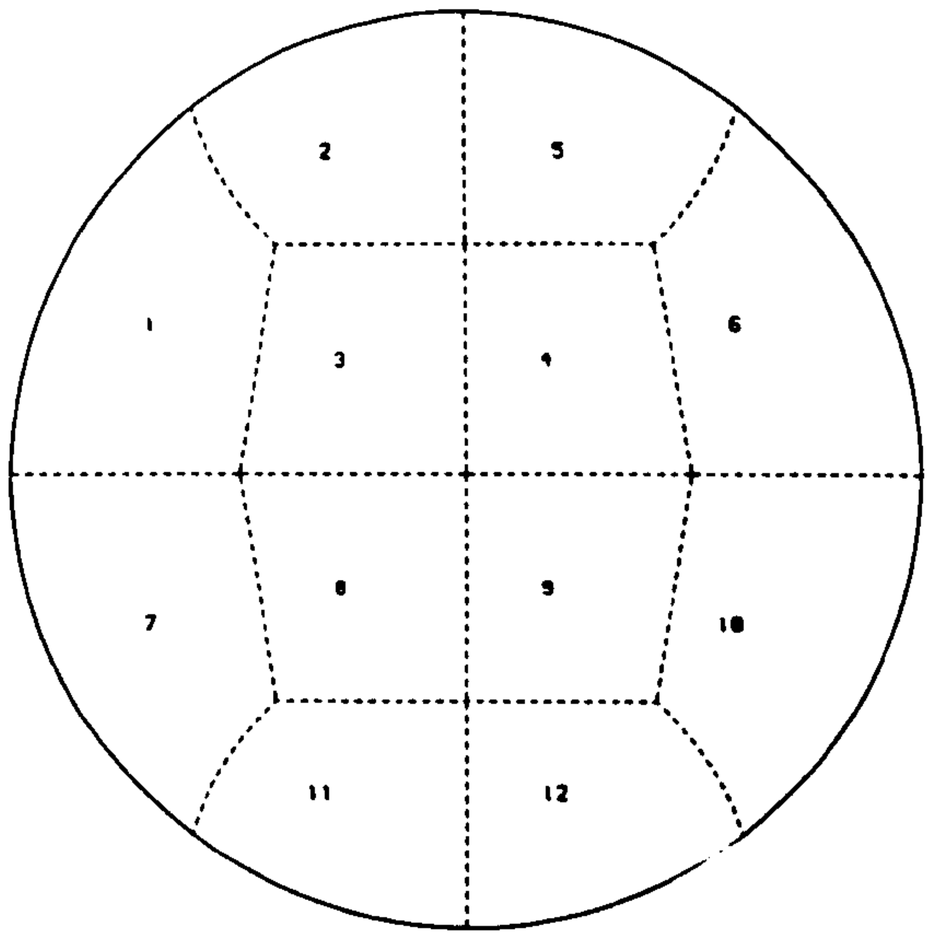

mesh 1

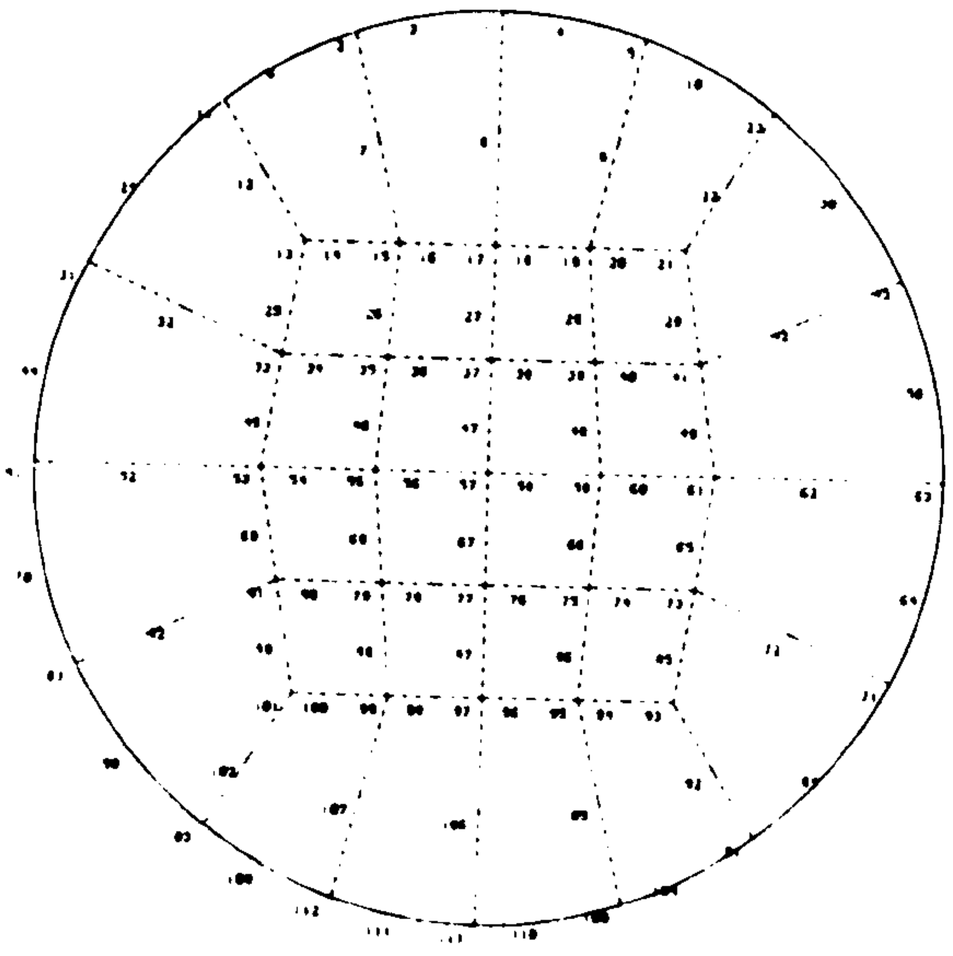

mesh 2

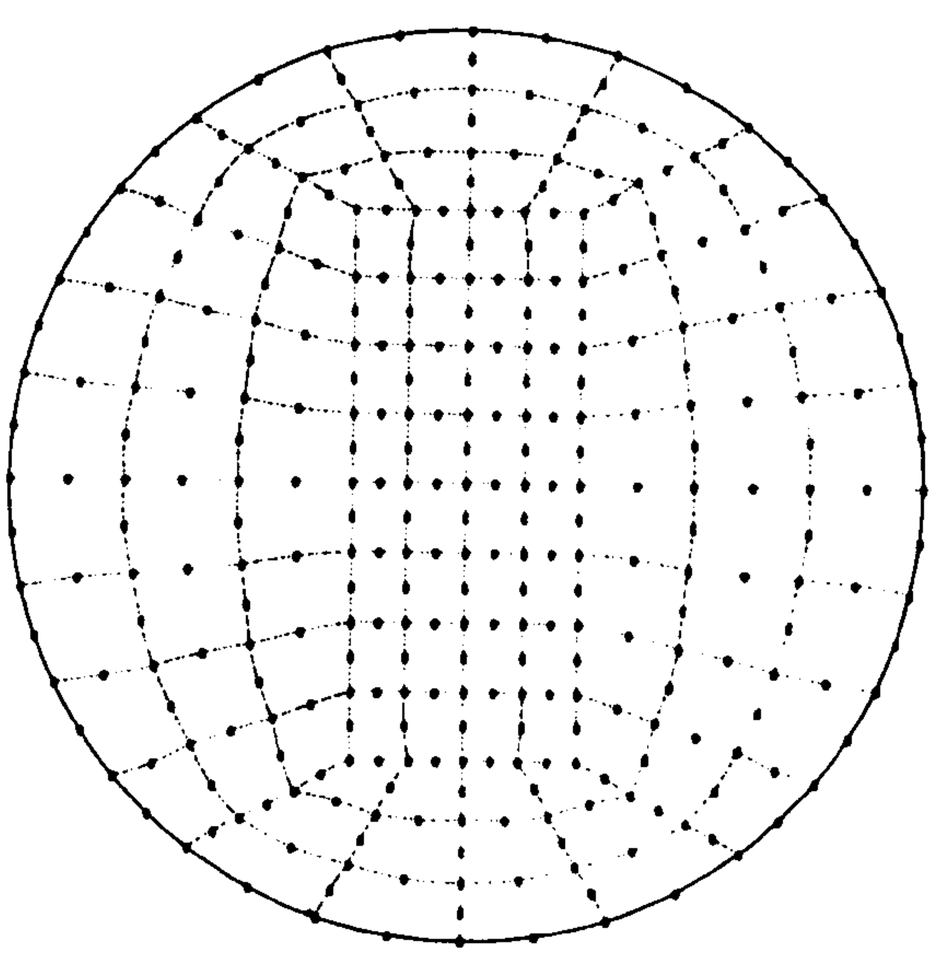

mesh 3

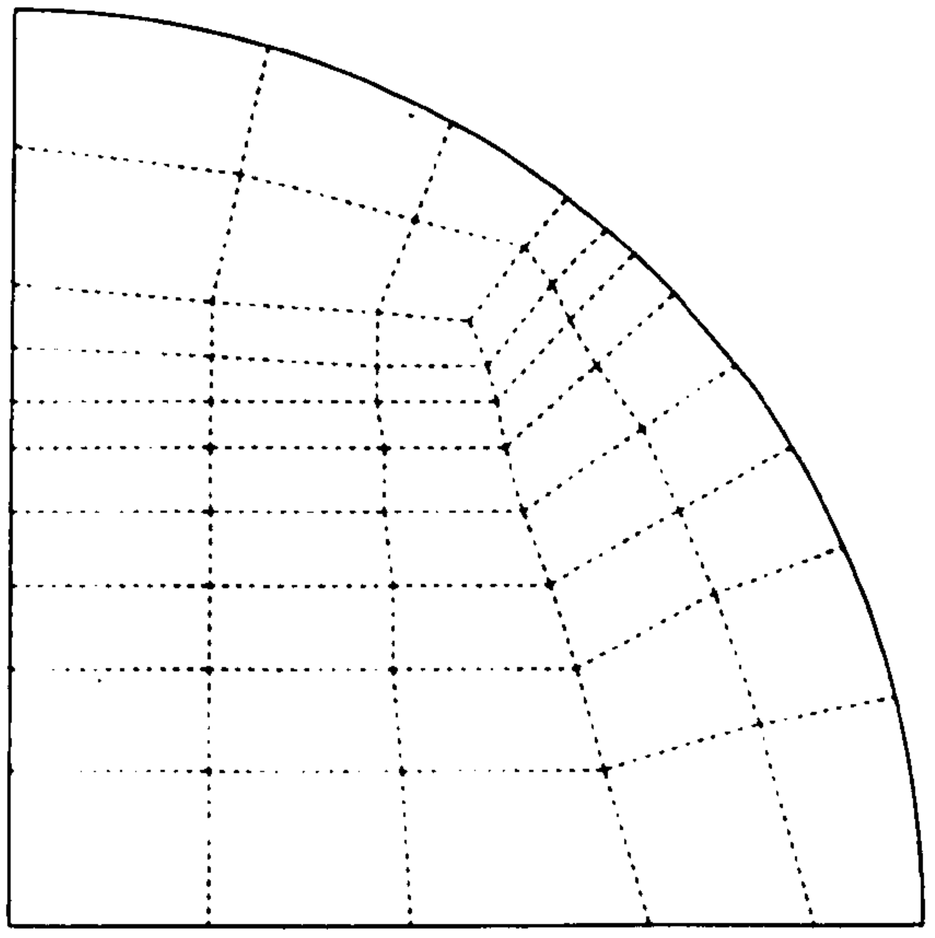

mesh 4

Fig. 7.13

Finite element meshes used for calculations (first configuration).

in Figs. 7.14 to 7.18. For the first four orientations, the calculated surface temperatures appear to converge towards the values obtained on the finest mesh. For $\phi = 0^{o}$, the largest difference between nodal temperatures is about 0.04 (that is 4% of the temperature difference between source and sink). Discrepancies are similar for the other orientations, and in all four cases they are greatest mid way between the centre line ($\theta = 0^{o}$) and the heat source or sink.

However, convergence is not apparent for the last orientation ($\phi = 90^{o}$); at $\theta = \pm 26^{o}$, the nodal temperatures on meshes 1 and 3 agree to within 1%, but the intermediate mesh gives temperatures almost 5% different (Fig. 7.18). These three meshes were prepared as 'general purpose' representations of the disc for use with a range of anisotropic thermal properties, and it seemed probable that not even mesh 3 was appropriate for the very high temperature gradients which occur near $\theta = \pm 52.7^{o}$ at an orientation of $\phi = 90^{o}$. The calculation was therefore repeated on a still finer mesh (also shown in Fig. 7.13). This mesh takes advantage of symmetry and represents only one-quarter of the disc. Element size has been selectively reduced in anticipation of large temperature gradients near the heat source. The surface temperature distribution obtained on this mesh is compared with the three others in Fig. 7.19 (for $0 < \theta < 52.7^{o}$); it confirms the wide region of uniform temperature either side of $\theta = 0^{o}$, and emphasises the large gradients near $\theta = \pm 52.7^{o}$.

7.3.2 Effect of Thermal Properties

The thermal conductivity of the carbon fibre-reinforced epoxy resin composite used in these studies has been discussed in Chapter 3. Numerical calculations were made on the basis of two sets of data:

(i) Constant values of $K_1 = 48$ W/m K, $K_2 = 1.4$ W/m K as used in 7.3.1.

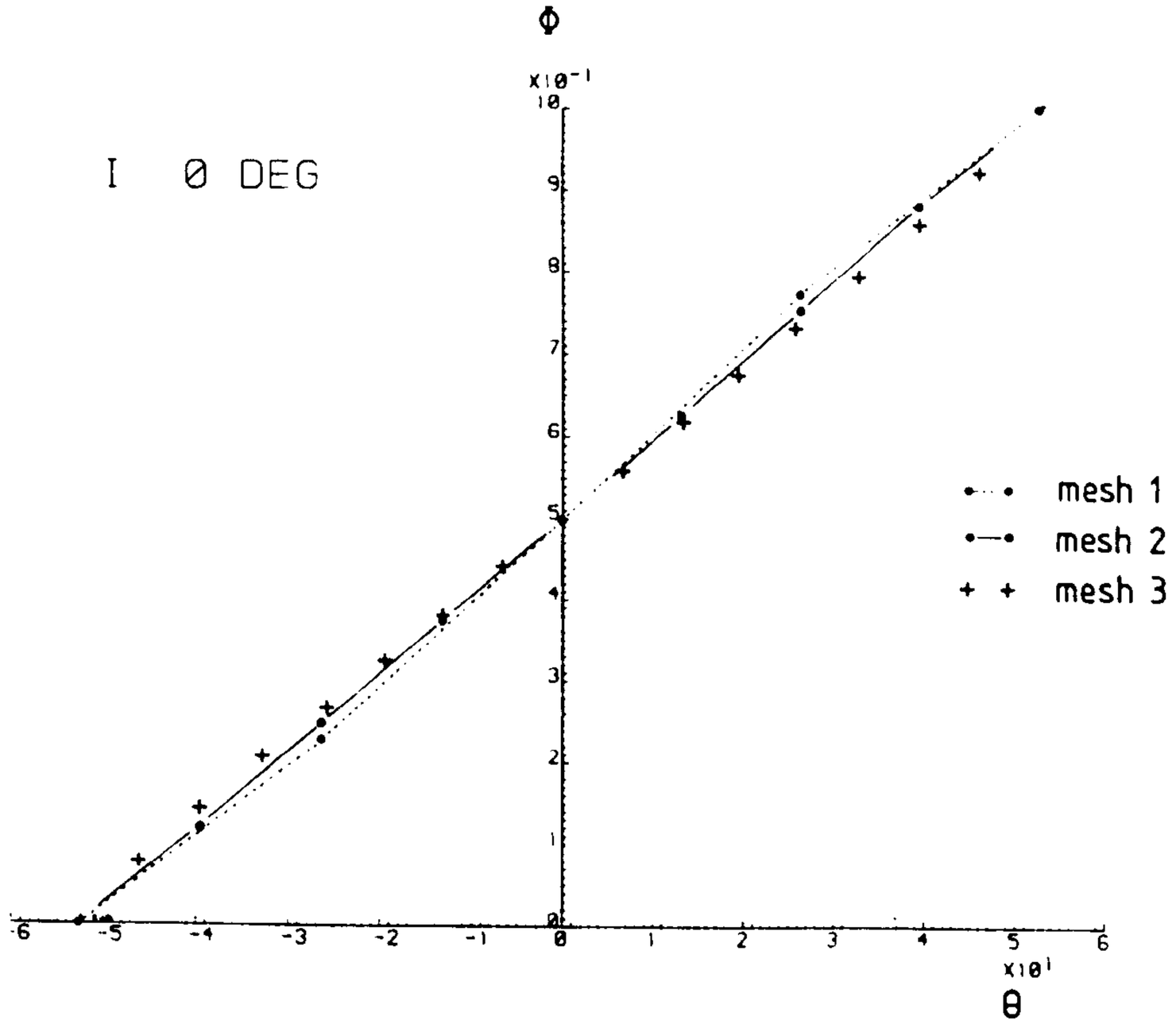

Fig. 7.14

Finite element calculations of surface temperature distribution. $\phi = 0^{o}$.

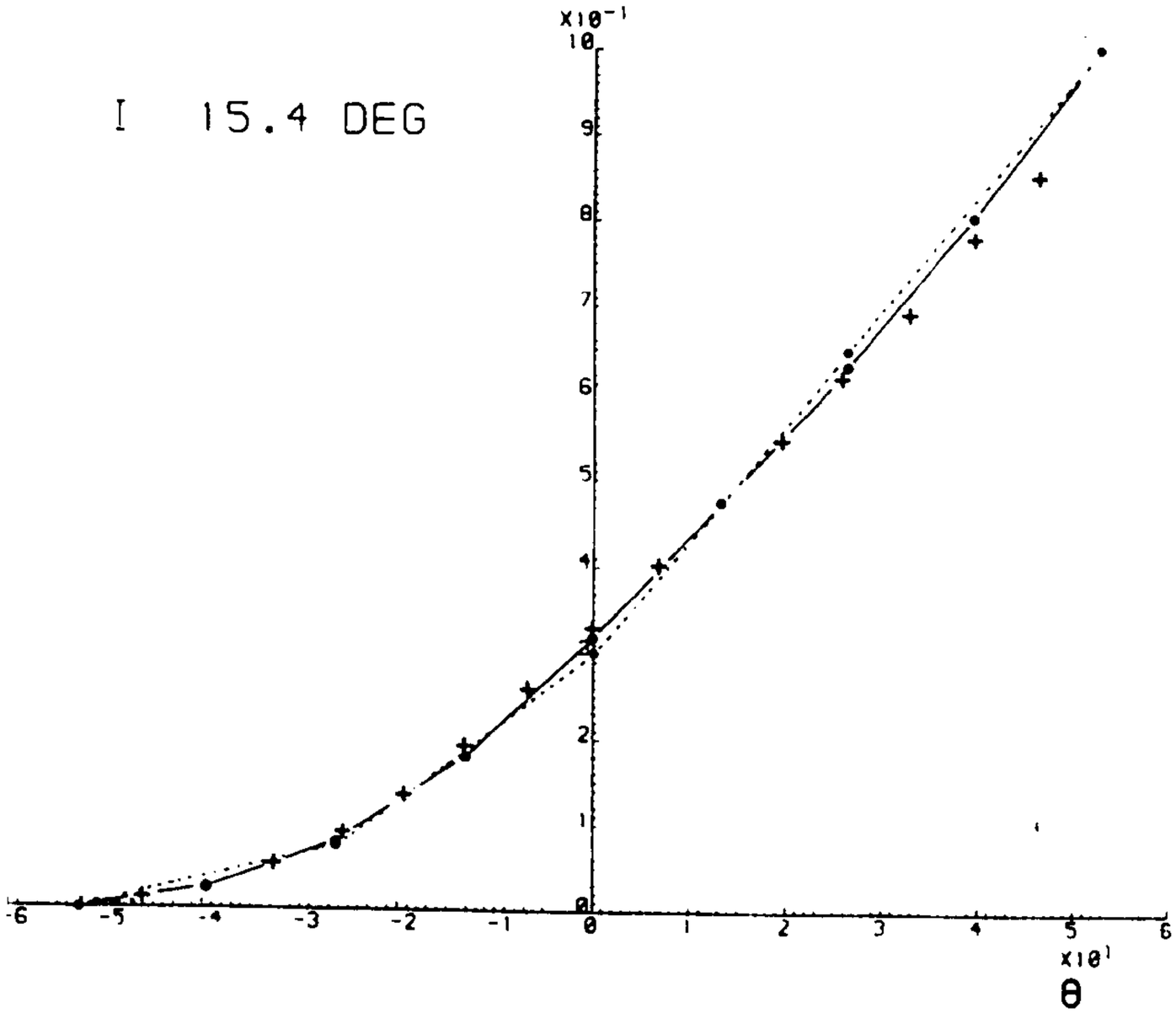

Fig. 7.15

As Fig. 7.14 for $\phi = 15.4^{o}$.

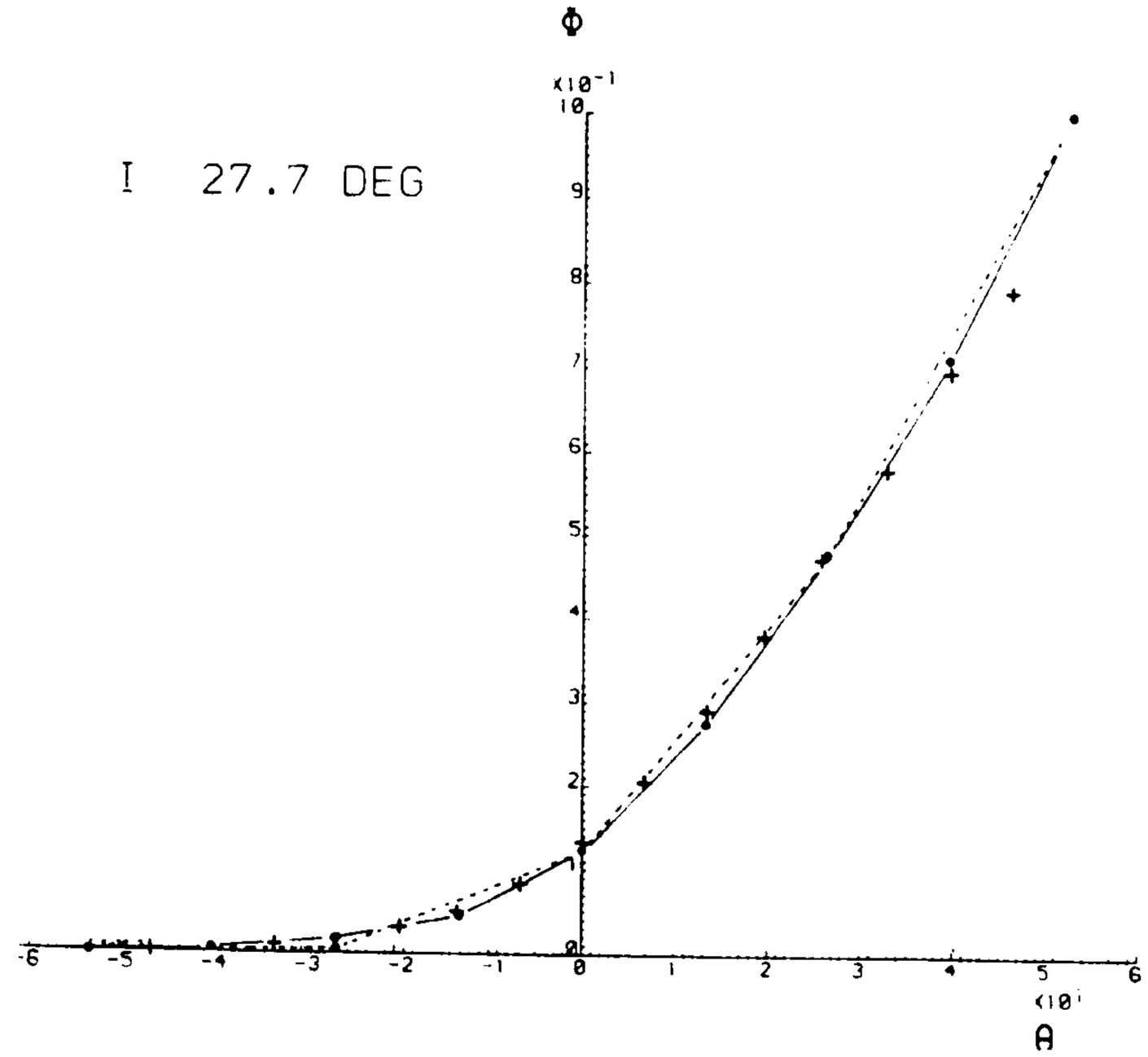

Fig. 7.16

As Fig. 7.14 for $\phi = 27.7^{\circ}$.

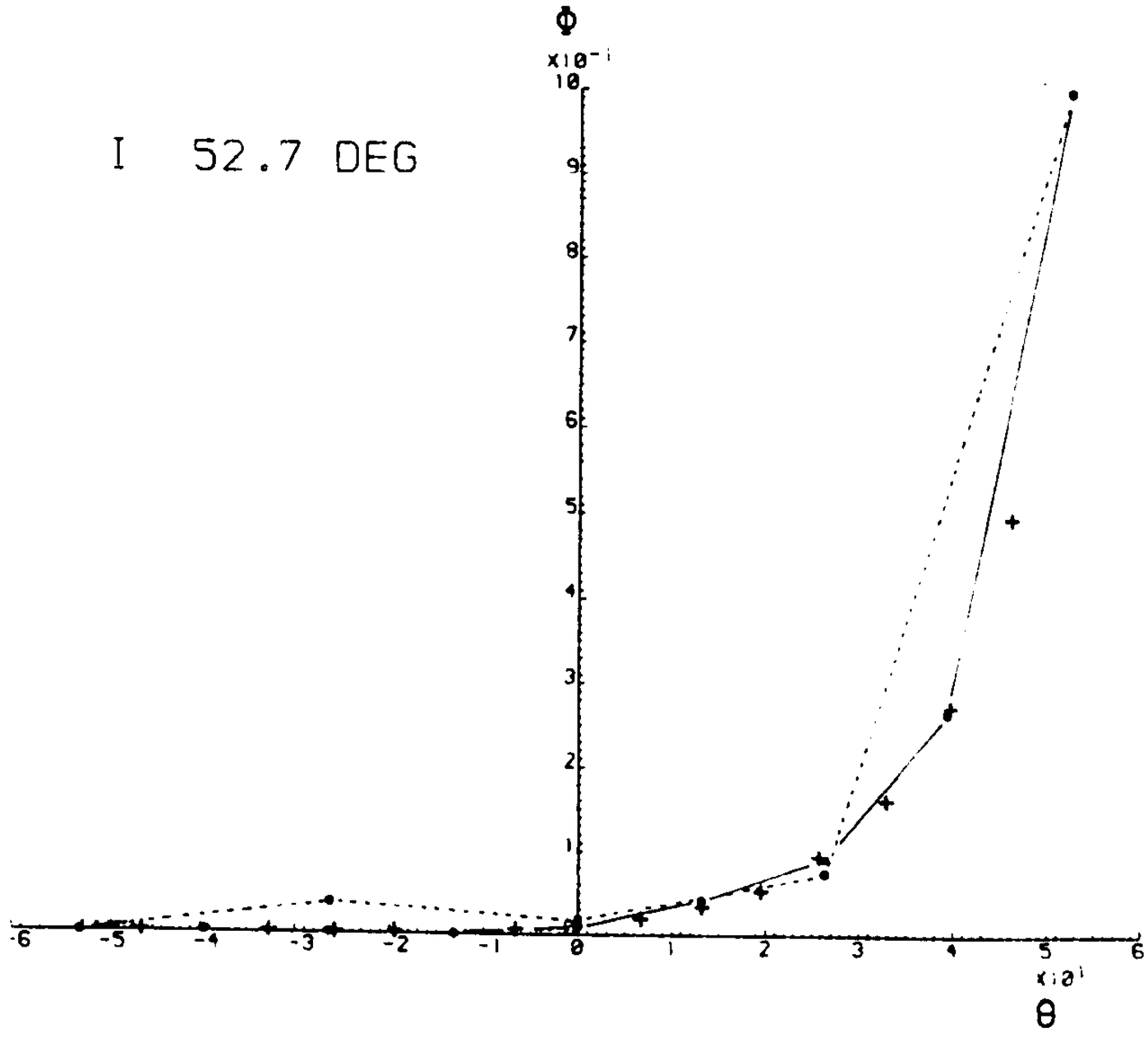

Fig. 7.17

As Fig. 7.14 for $\phi = 52.7^{\circ}$.

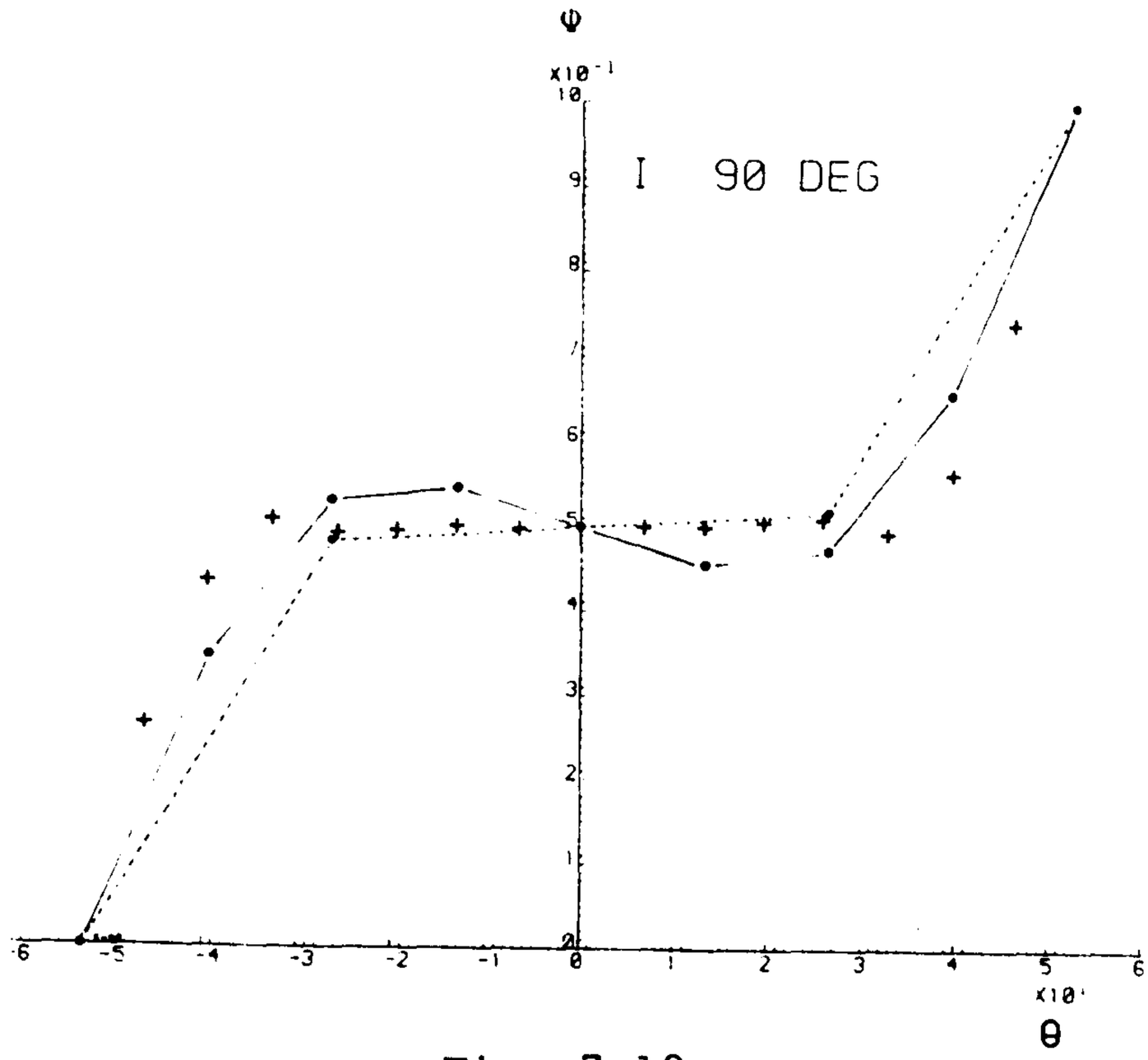

Fig. 7.18

As Fig. 7.14 for $\phi = 90^{o}$.

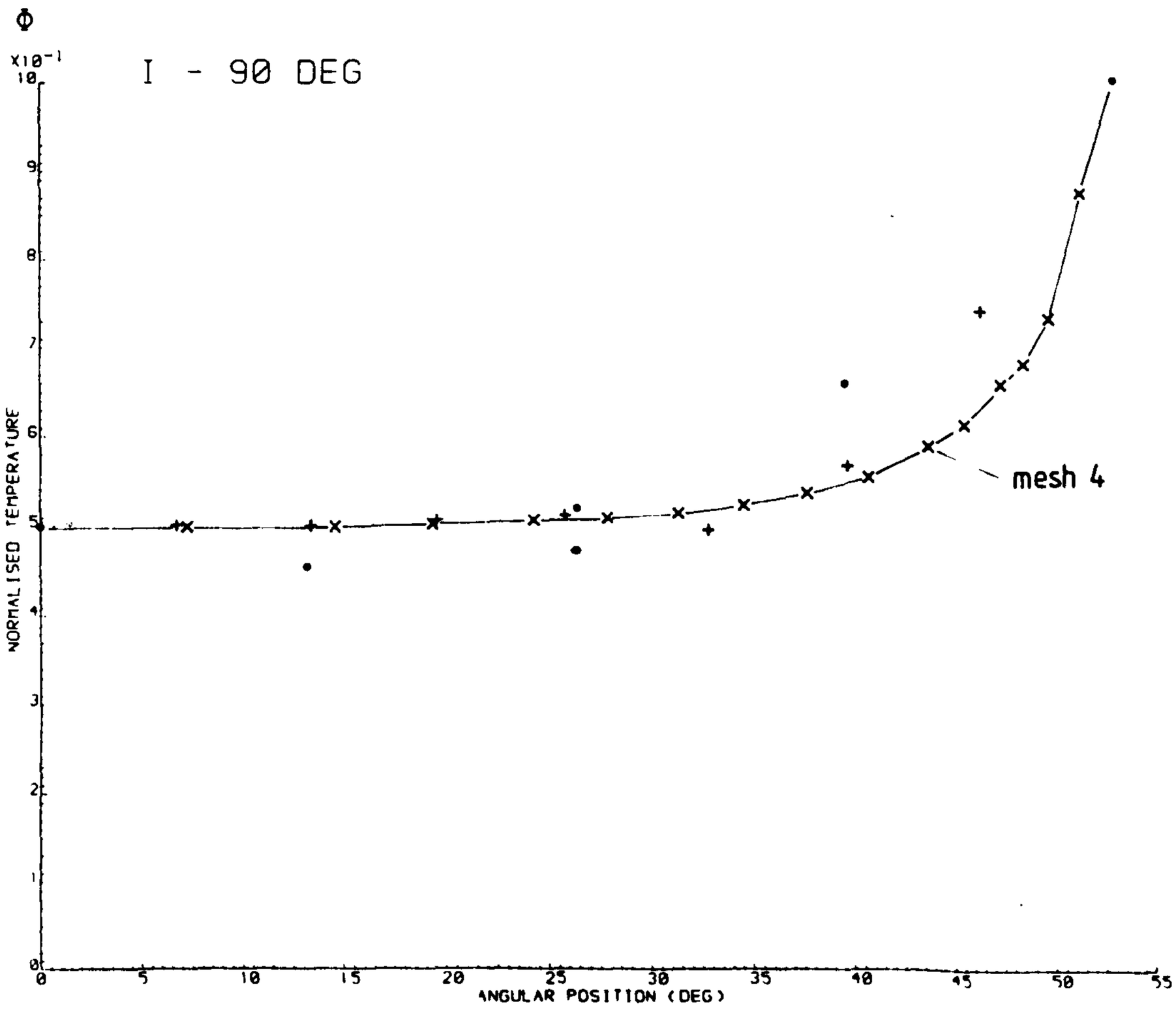

Fig. 7.19

Finite element calculations for surface temperatures on all four meshes (Fig. 7.13) for $\phi = 90^{o}$.

(ii) A constant value of K_2 = 1.4 W/m K, but with K_1 a function of temperature.

The form of $K_1(T)$ as used in (ii) was derived from the data presented in 3.1.5 (and illustrated in Figs. 3.11 and 3.22) by reducing the measured values by 8% to correct for the lower fibre volume fraction (60% compared to 65%). A least-squares quadratic was then fitted to the data, giving

$$K_1(T) = 40.8 + 0.48\ T - 2.682 \times 10^{-3} T^2 \qquad (7.5)$$

The variation of K_2 with temperature was considered to be negligible.

For each of the principal axis orientations considered in 7.3.1, values of the three conductivity coefficients at various temperatures were given by

$$k_{11}(T) = K_1(T)\ \cos^2\phi + K_2\ \sin^2\phi$$
$$k_{12}(T) = \left[K_1(T) - K_2\right]\ \sin\phi\ \cos\phi$$
$$k_{22}(T) = K_1(T)\ \sin^2\phi + K_2\ \cos^2\phi$$

using Equations 7.5 for $K_1(T)$. Least-squares quadratic expressions were thus obtained directly for each calculation.*

However, over the range of temperatures typical of the measurements discussed in 7.4 (approximately 15-45°C) the influence of variable thermal conductivity is very small. The difference in calculated surface temperatures using the two sets of data described above is almost everywhere much less than 1% (of the temperature difference between heater

---

* At the time of these calculations, nonlinear thermal conductivity was represented in the finite element model by specifying the three coefficients of three quadratic expressions for $k_{ij}(T)$. This has since been modified, and, as described in 5.9 and Appendix I, the model now uses linear interpolation between data pairs of T and $k_{ij}(T)$.

and sink). The exception is the case $\phi = 90^{o}$, where calculated surface temperatures near $\theta = 0^{o}$ are almost 1.5% lower using data set (i).

In a highly anisotropic material such as a high modulus carbon fibre-reinforced plastic, the steady-state temperature distribution is determined primarily by the large anisotropy ratio (K_1/K_2). The values of K_1 or K_2 may change considerably, but provided $K_1 >> K_2$, the influence on the temperature distribution is negligible. This has been supported by further calculations in which temperatures around the surface of the disc were found to change by less than 2% as a result of varying K_1/K_2 between 20 and 40.

It was noted on several occasions in Chapter 4 that when the anisotropy ratio is large, the temperature distribution in a two-dimensional geometry tends to adopt a one-dimensional form, with isotherms aligned parallel to the direction of the largest thermal conductivity. In many instances, the effect is masked by the boundary conditions for a given problem, but is demonstrated in Figs. 7.20 to 7.22, which show isotherms on the unit disc for principal axis orientations of $\phi = 0^{o}$, 52.7^{o} and 90^{o}. In Fig. 7.20, the plotted isotherms are everywhere parallel to the x-axis, although some curving must occur in the vicinity of the fixed surface temperatures. Fig. 7.21 shows isotherms lying parallel to the reinforcement axis, and the same effect is also seen in Fig. 7.22, where the combination of boundary conditions and principal axis alignment gives rise to two regions with markedly different temperature gradients.

7.3.3 Effect of Specimen Orientation

One of the potential sources of error, the effect of which is difficult to estimate on the basis of experiment design alone, is the accuracy with which the alignment of the specimen's principal conductivity axes are known. Each of the three cylindrical blocks were inspected for the position of the reinforcement, and small marks made on the curved surface using scriber and protractor at intervals of 20^{o} around the circumference. Each orientation of the specimen

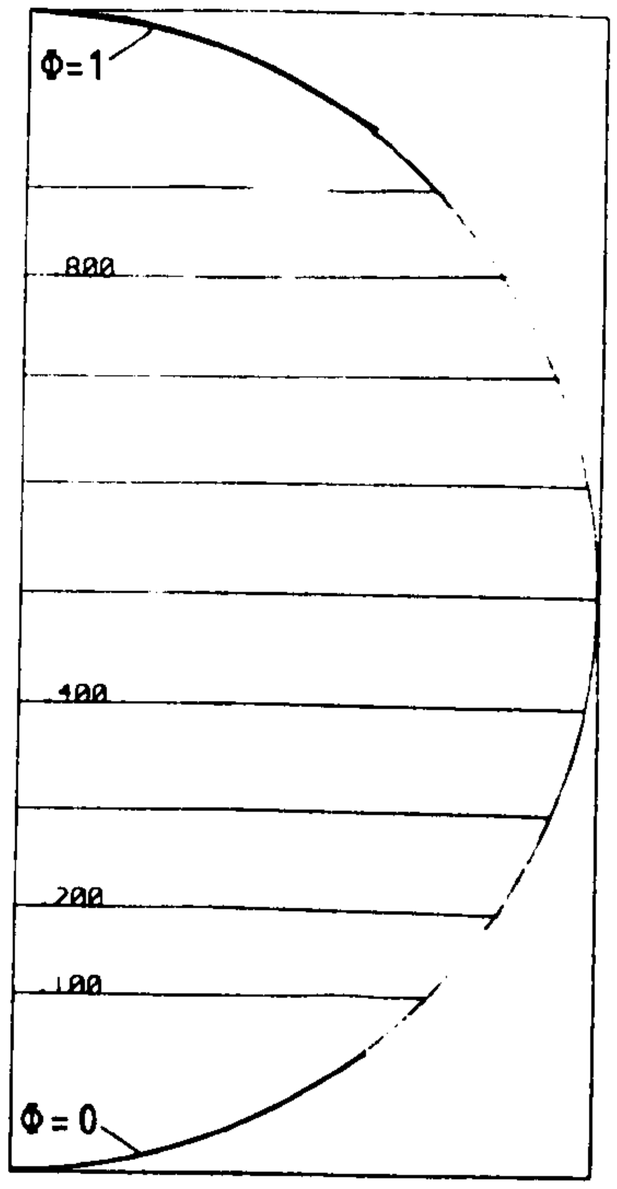

Fig. 7.20

Isotherms for $\phi = 0^{\circ}$ (half disc)

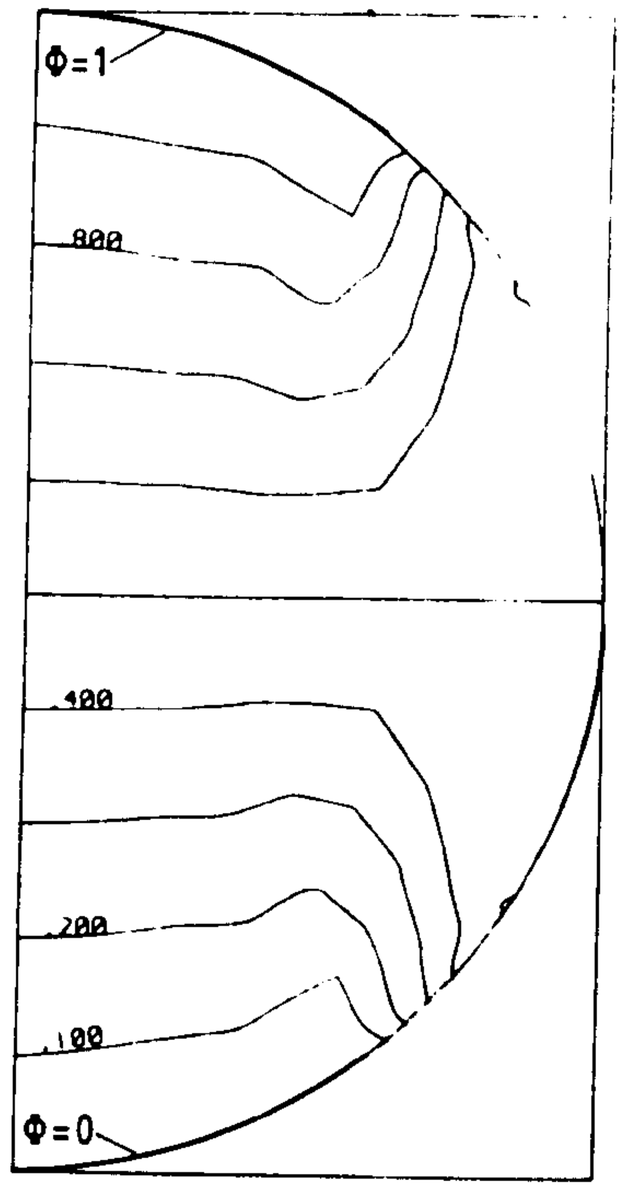

Fig. 7.22

Isotherms for $\phi = 90^{\circ}$.

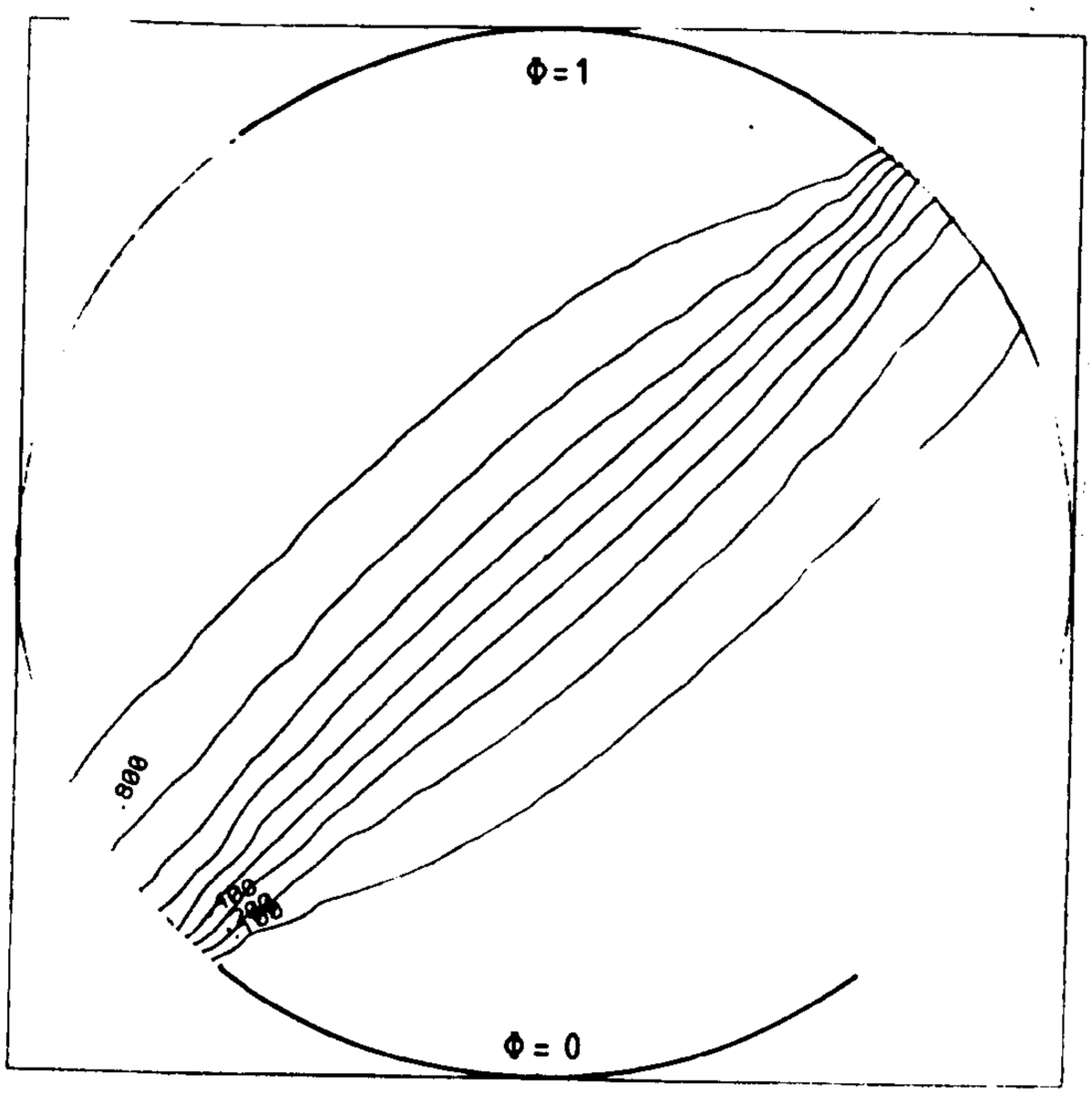

Fig. 7.21

Isotherms for $\phi = 52.7^{\circ}$.

was then set by aligning one of these marks with an edge of the heater block. It is estimated that the combined error in orientation (ϕ) is $\pm 2^{o}$. The effect of this error on surface temperatures was examined by repeating the previous calculations using appropriate perturbations to the orientation angles.

Figs. 7.23 to 7.27 show the effect of a $\pm 2^{o}$ variation in specimen orientation (ϕ) for the five cases considered above. Temperatures at the surface nodes are shown as an error bar, but it should be remembered that such an error is systematic rather than random, since misalignment of the specimen would affect each calculated temperature in the same sense.

The perturbation gives rise to a variation in dimensionless temperature of $\pm$ 2% at $\phi = 0^{o}$ and 52.7^{o} and of $\pm$ 3% at $\phi = 15.4^{o}$ and 27.7^{o}. The effect on the $\phi = 90^{o}$ orientation is, however, very much greater (Fig. 7.27), and over most of the surface is responsible for a 10% variation either side of the unperturbed value.

The relative sensitivity of temperatures at orientation $\phi = 90^{o}$ compared with smaller angles is similar to the variation of elastic moduli (E) in unidirectional composites when tested at different angles to the fibre direction (θ). As shown by Hull (1981), the theoretical curve $E(\theta)$ is highly asymmetric. Measurements on a carbon fibre-epoxy resin composite show the modulus decreasing by 17% between $\theta = 0^{o}$ and 5^{o}, and remaining approximately constant for angles greater than about 45^{o}.

7.4 EXPERIMENTAL MEASUREMENTS AND COMPARISON

7.4.1 First Configuration

The first set of measurements was made with the heater and sink diametrically opposed (Fig. 7.10), using orientation angles of $\phi = 0^{o}$, 15.4^{o}, 27.7^{o}, 52.7^{o} and 90^{o}. Approximately 10 steady-state measurements were made at each orientation, at different mean heater temperatures (the temperature of the heat sink was fixed by the temperature of the mains

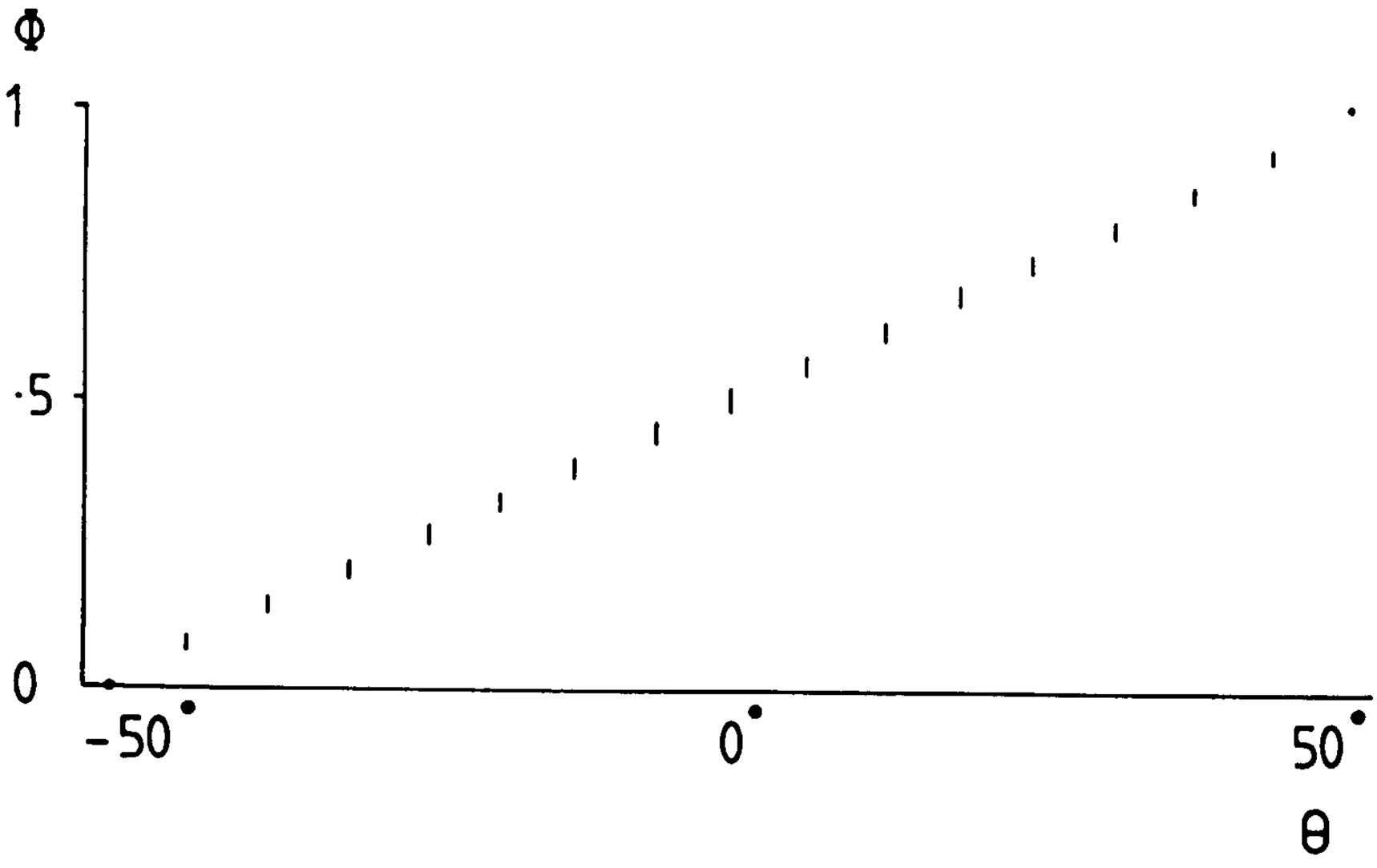

Fig. 7.23

Effect on calculated surface temperatures of a ±2° perturbation in specimen orientation $\phi = 0^{\circ}$.

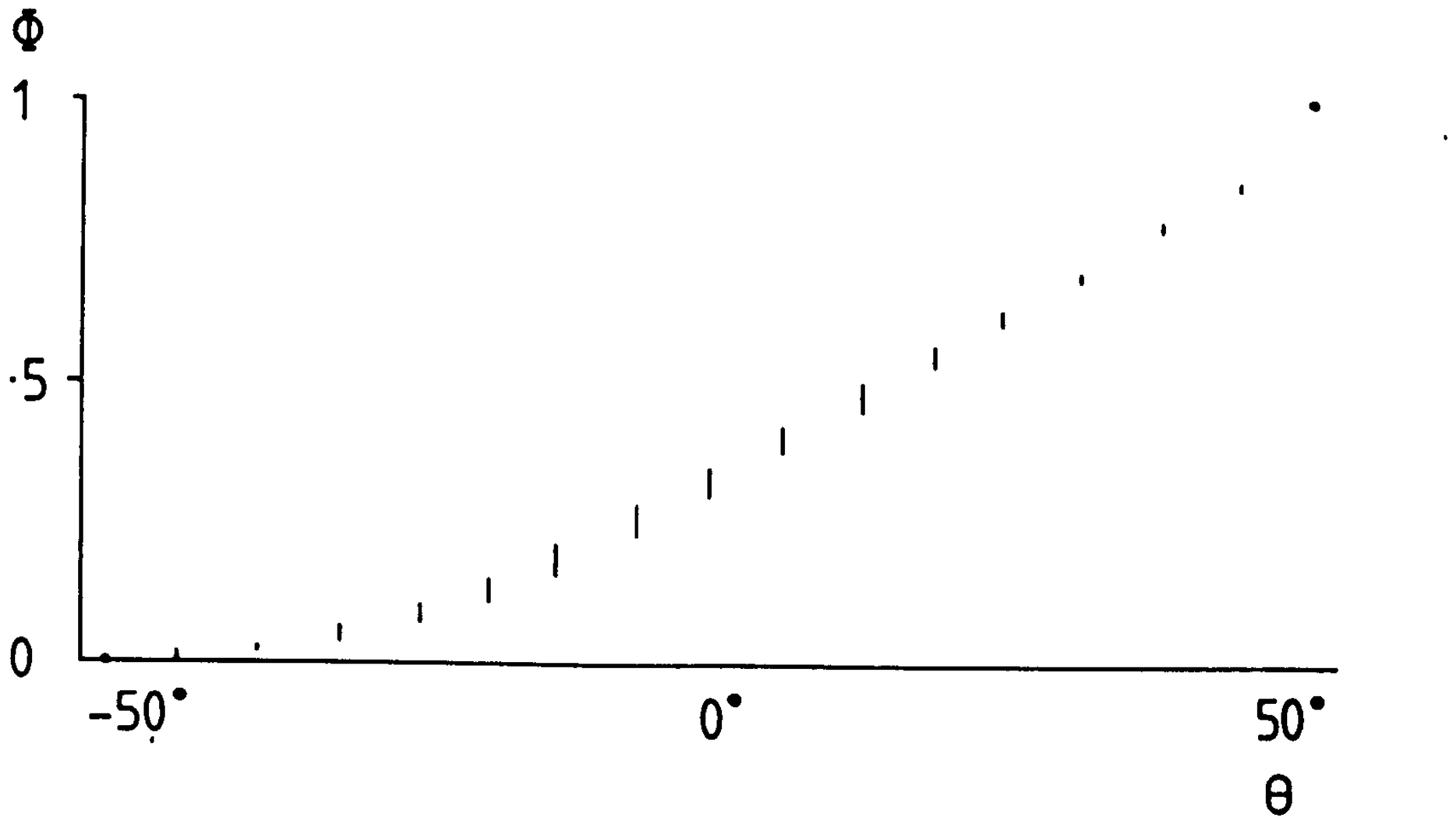

Fig. 7.24

As Fig. 7.23 for $\phi = 15.4^{\circ}$.

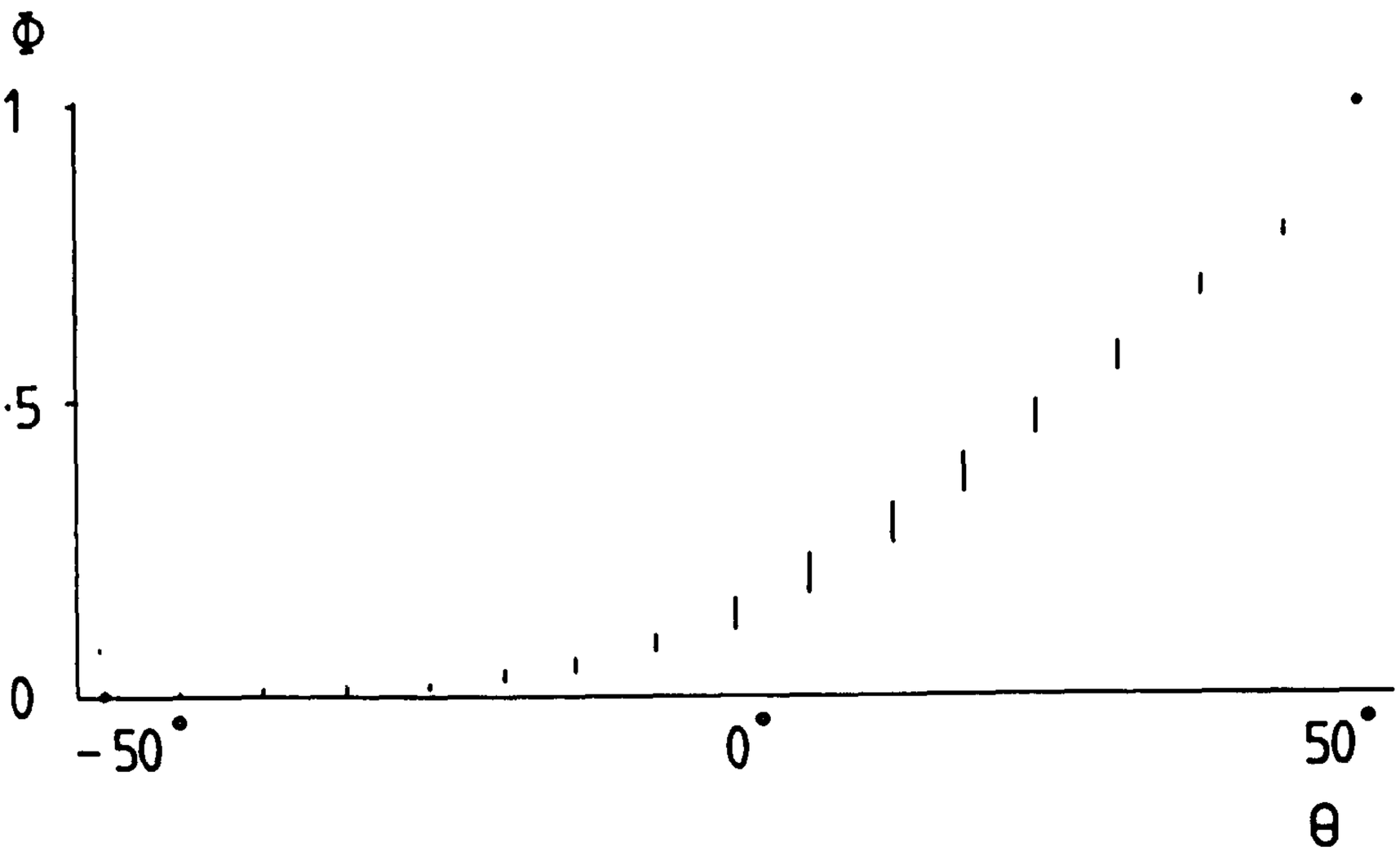

Fig. 7.25

As Fig. 7.23 for $\phi = 27.7^{\circ}$.

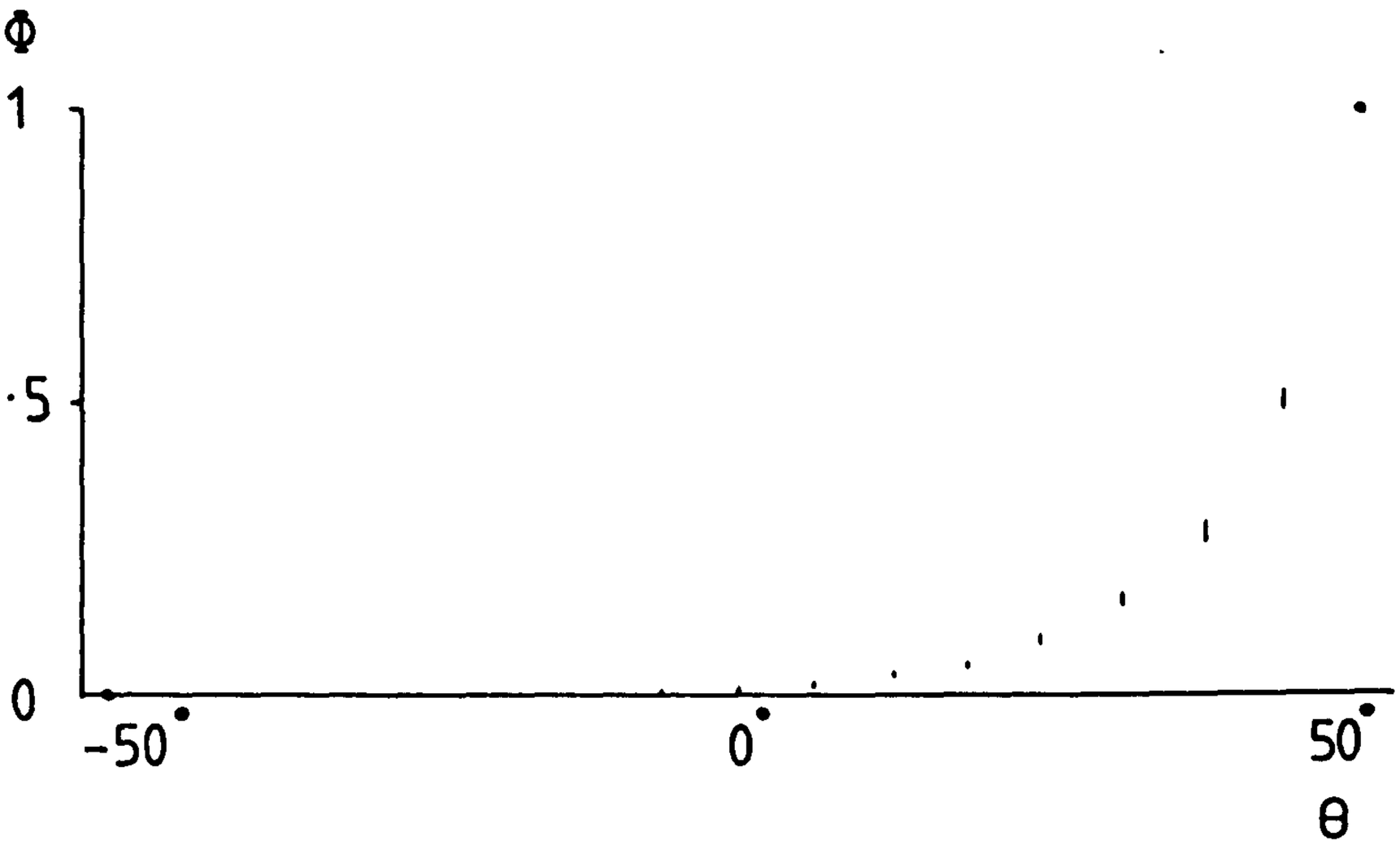

Fig. 7.26

As Fig. 7.23 for $\phi = 52.7^{\circ}$.

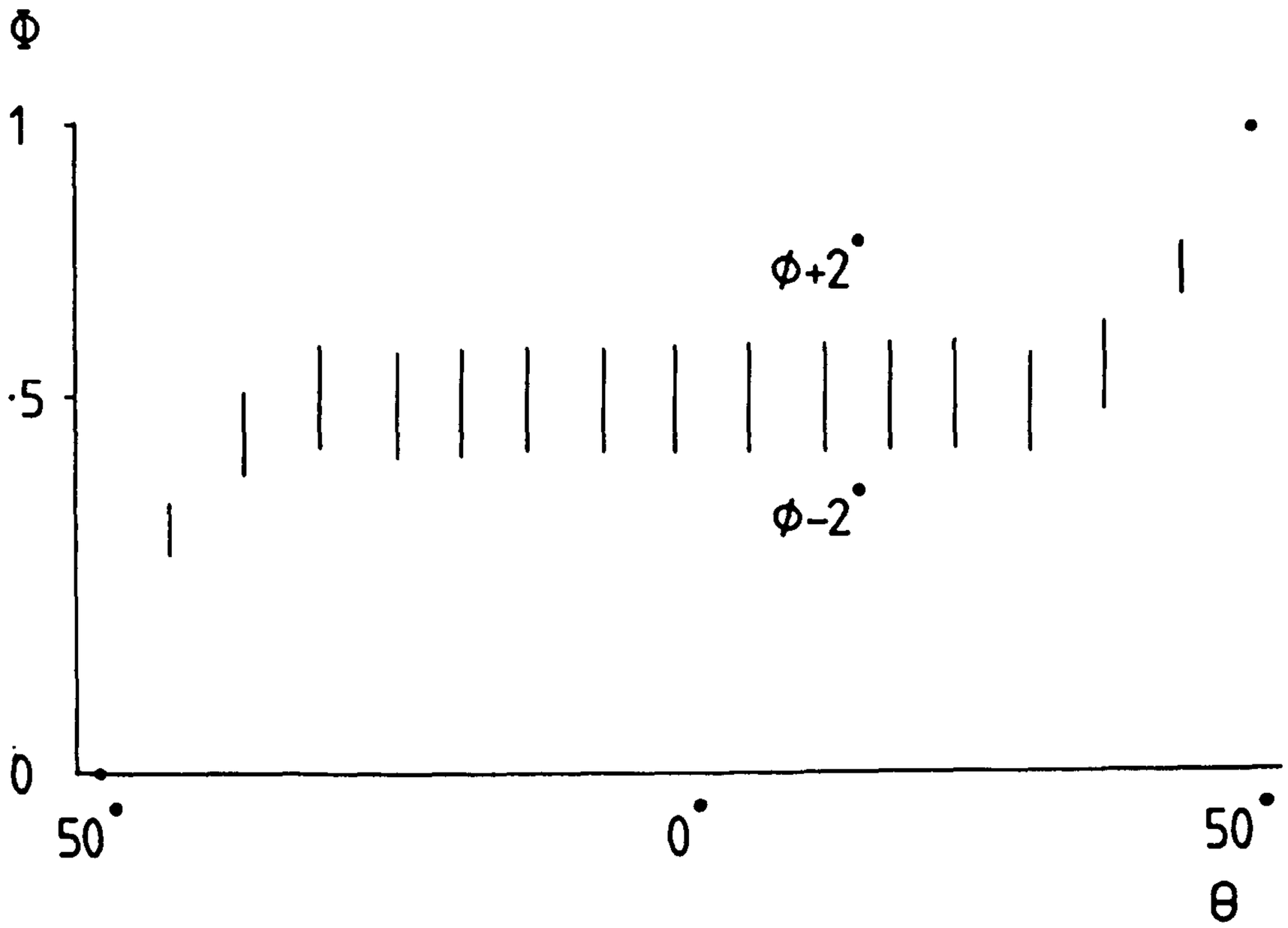

Fig. 7.27

As Fig. 7.23 for $\phi = 90°$.

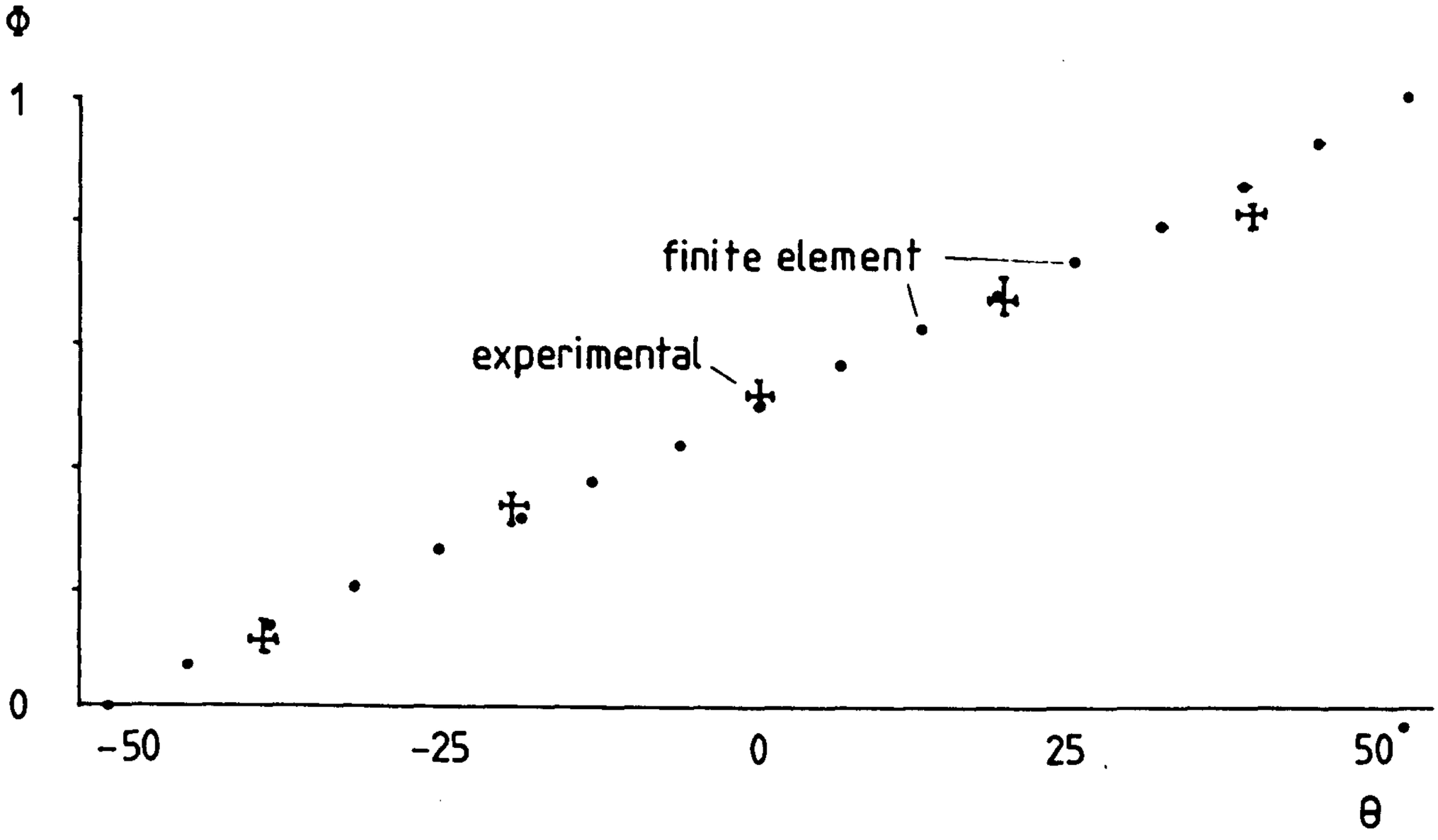

Fig. 7.28

Comparison of measured and calculated surface temperatures (first configuration, Fig. 7.10) $\phi = 0°$.

water supply), and included reversing the roles of heater and sink. The temperature of the heat sink was typically 15-20°C, while that of the heater supply water ranged from 25° to 45°C.

As indicated in 7.2.4, the error in a measurement of temperature is expected to be ± 0.3 K. The dimensionless temperature Φ (defined in Equation 7.4) involves temperature differences, and errors combine to give a maximum uncertainty of $0.6/\Delta T_H$, where $\Delta T_H = T_H - T_C$. Since the error in Φ is dependent on the temperature difference between heater and sink, being smaller at higher values of ΔT_H, it is appropriate to consider a weighted mean value of the measurements at a particular orientation. The weighted mean of a number of measurements $X_n \pm S_n$, $X_m \pm S_m$, $X_\ell \pm S_\ell$, . . . is given by

$$\bar{X} = \frac{1}{S^{-2}}\left(\frac{X_n}{S_n^2} + \frac{X_m}{S_m^2} + \frac{X_\ell}{S_\ell^2} + \ . \ . \ .\right)$$

where S is the standard error, given by

$$S^{-2} = S_n^{-2} + S_m^{-2} + S_\ell^{-2} + \ . \ . \ .$$

Figs. 7.28 to 7.32 show the results for the five orientations, in which the weighted mean experimental points are plotted; the error bars on angular position (θ) correspond to the uncertainty estimated in 7.2.4, while those on the dimensionless temperatures (ϕ) represent the extreme values recorded.

In the first of those five figures ($\phi = 0°$), the experimental points lie within 3-4% of the values obtained from numerical calculations. In Fig. 7.29 ($\phi = 15.4°$), three of the experimental points are in very close agreement with the calculation, while the measurements at $\theta = -25°$ and $-5°$ are 5% and 7% greater (as before, percentage deviations are expressed as a fraction of ΔT_H, since the fractional error in Φ becomes meaningless as Φ approaches zero). Points near $\theta = 0°$ in the surface temperature distribution are similarly higher than calculated for $\phi = 27.7°$, where the discrepancy amounts to 7% on points at $\theta = -12°$ and $+8°$. However, at only one point ($\theta = -12°$) does the numerical

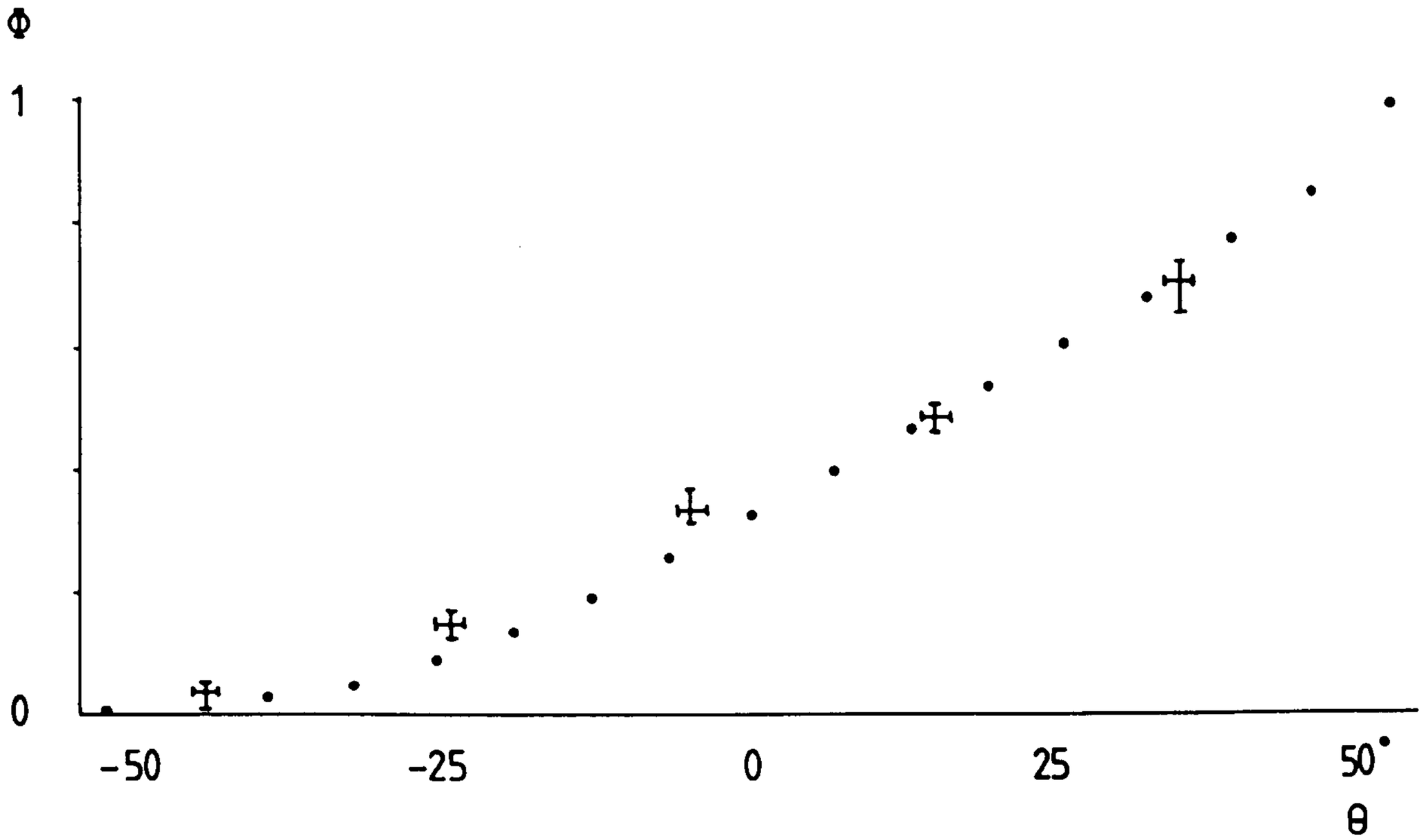

Fig. 7.29

As Fig. 7.28, $\phi = 15.4^{\circ}$.

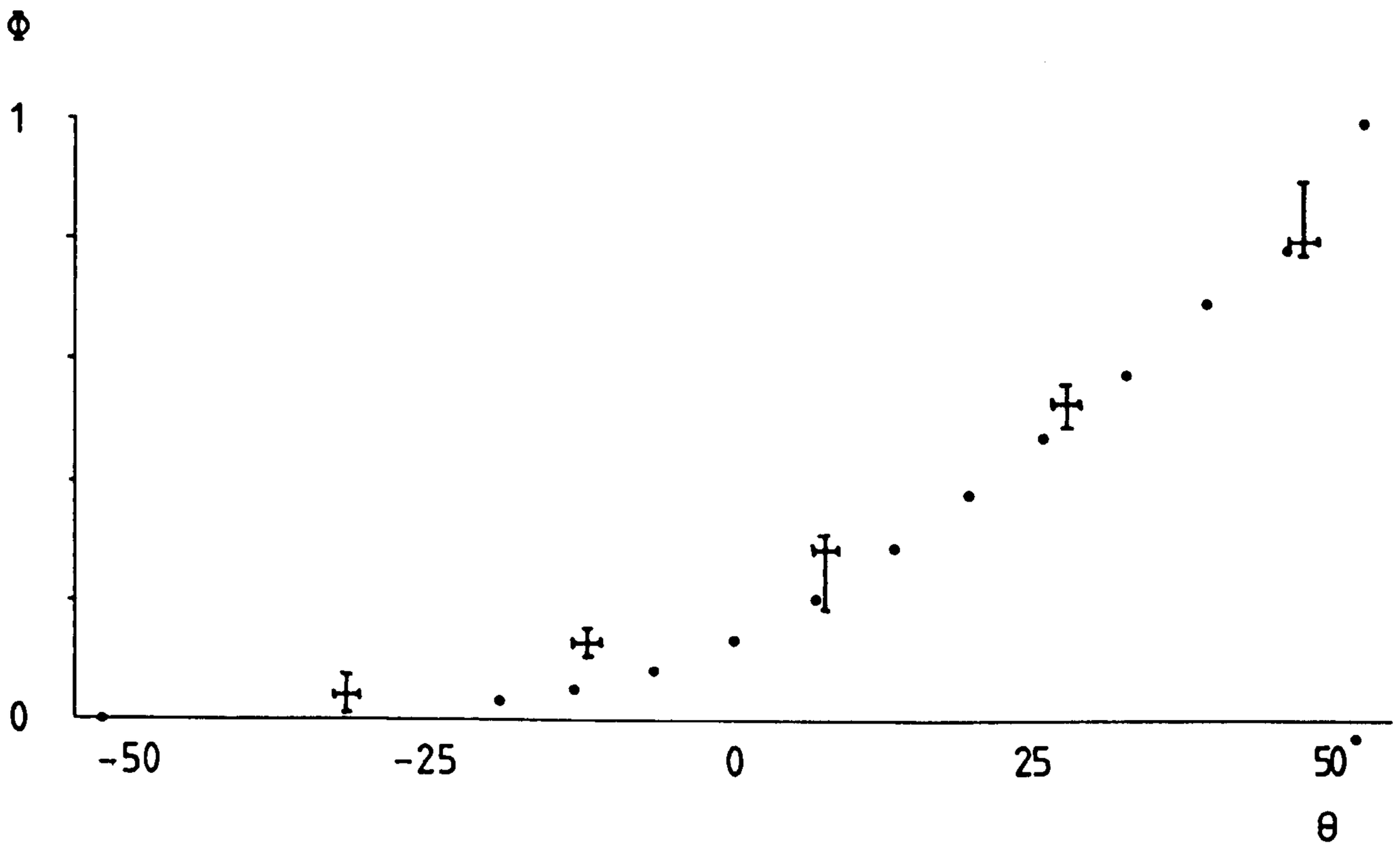

Fig. 7.30

As Fig. 7.28, $\phi = 27.7^{\circ}$.

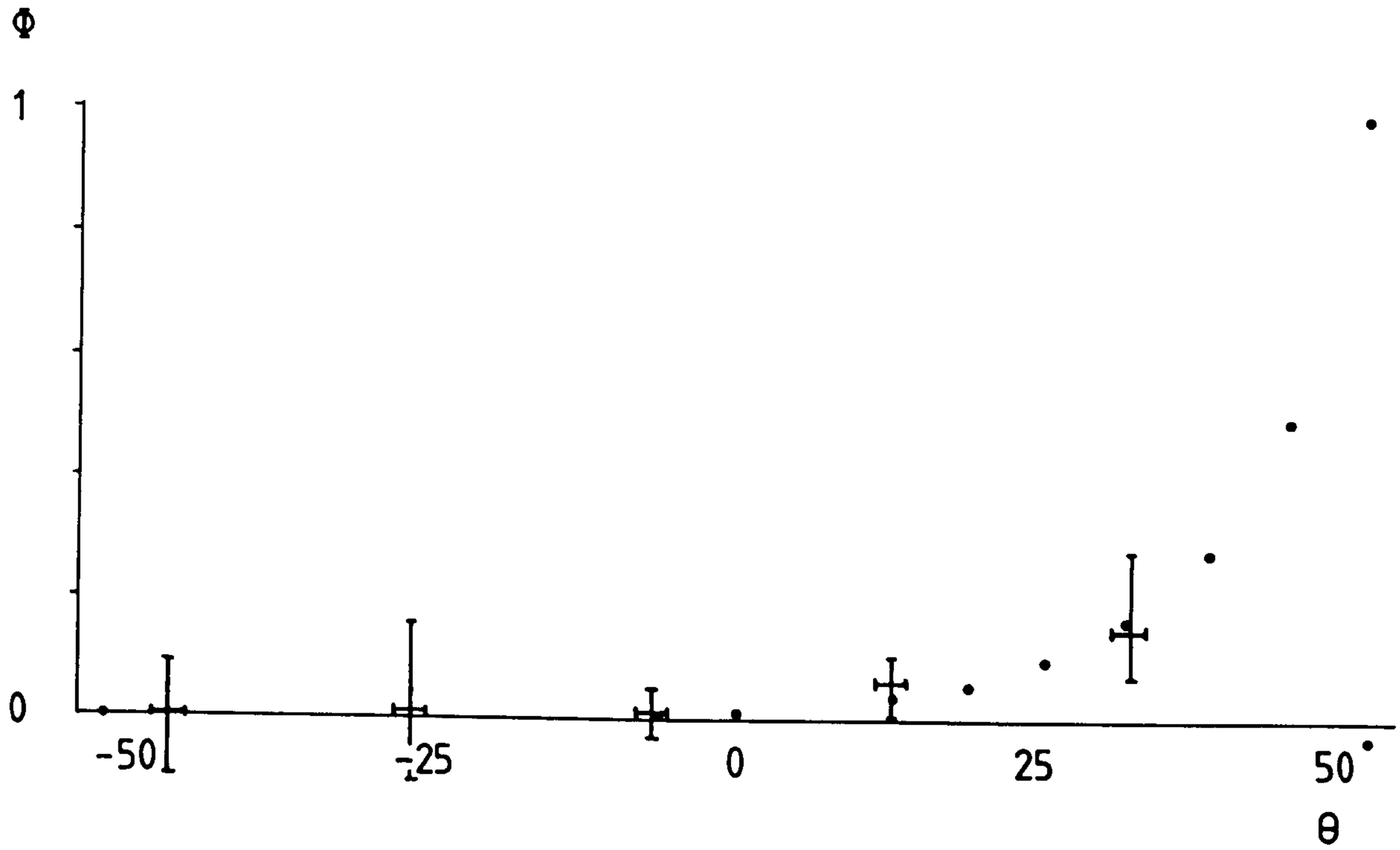

Fig. 7.31

As Fig. 7.28, $\phi = 52.7^{\circ}$.

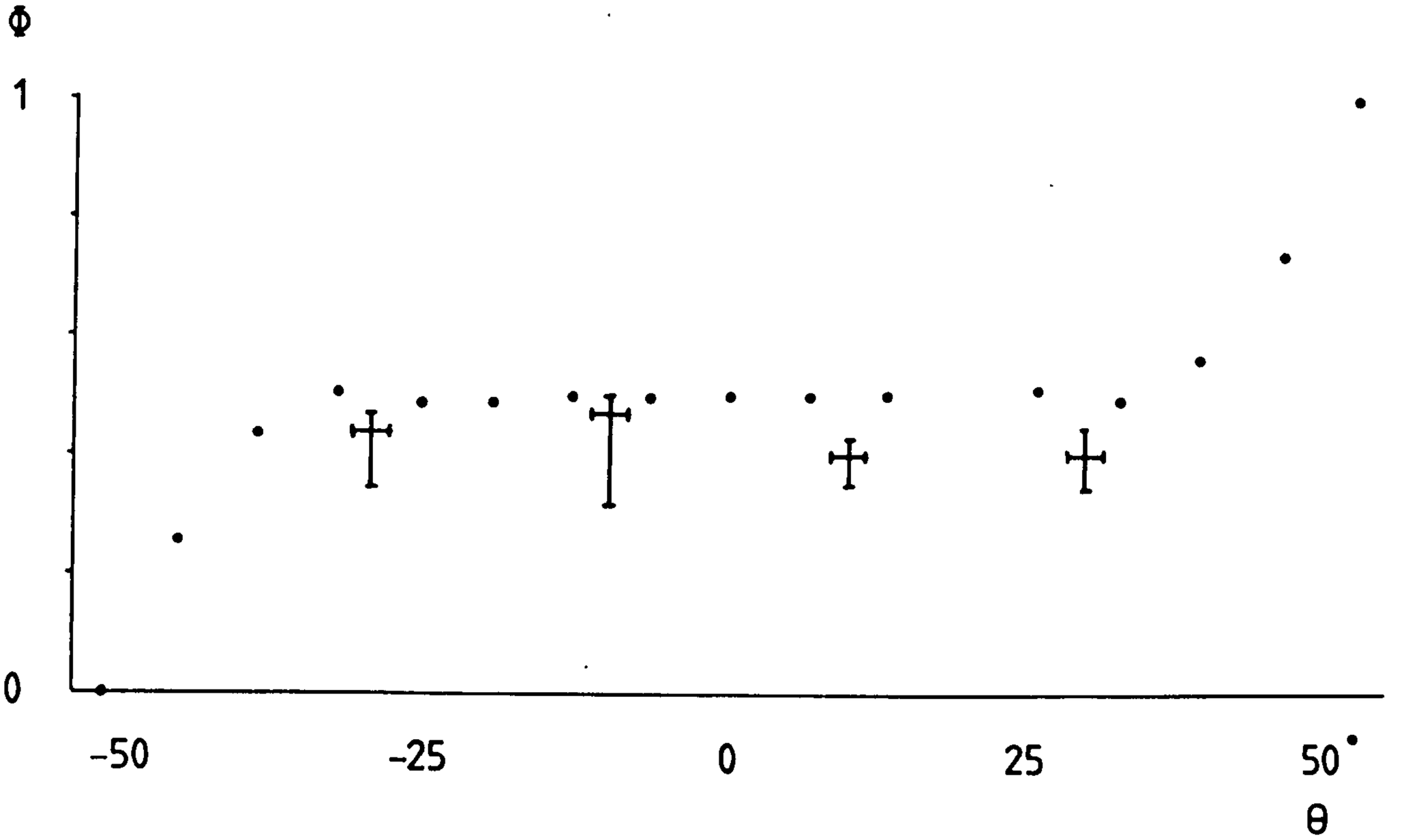

Fig. 7.32

As Fig. 7.28, $\phi = 90^{\circ}$.

value lie outside the range of the error bars; here the discrepancy is 5%. At an orientation $\phi = 52.7^{o}$, the range of temperatures recorded at each point was large (Fig. 7.31), but, encouragingly, the weighted mean values of all points were within 1% of the calculated temperatures.

The least satisfactory measurements were made at a specimen orientation of $\phi = 90^{o}$ (Fig. 7.32). This is the position of greatest effective thermal conductivity between heater and sink, in which surface temperature gradients are concentrated close to the edge of the heater blocks. It proved physically impossible to position thermocouples sufficiently close to the heater blocks to detect these temperature gradients, and all measurements were made in the region of uniform temperature ($\theta = -30^{o}$ to $+30^{o}$). All four measurements lie consistently below the numerical values by up to 10%. A deviation of this magnitude is more acceptable, however, when consideration is given to the large influence of specimen orientation (Fig. 7.27), and the consistently low experimental values of Φ could be explained by only a small ($\sim 1^{o}$) misalignment of the specimen (see 7.3.3).

7.4.2 Second Configuration

A second set of measurements and finite element calculations was made for various specimen orientations with heater and sink positioned at right angles (see Fig. 7.33). As before, the dimensionless surface temperature $\Phi(\theta)$ is defined by Equation 7.4, but in this case the line $\theta = 0$ bisects the angle between the two heater blocks. The range of θ is thus between -97.7^{o} and $+97.7^{o}$.

Finite Element Results

Three meshes were used to examine the effect of element size on calculated surface temperatures, as shown in Fig. 7.34. They anticipate large temperature gradients along the shorter surface between heater and sink by reducing the element size in this region. Calculations were made using constant thermal properties (data set (i) in 7.3.2) with principal axis orientations of $\phi = 0^{o}$, 22.7^{o}, 42.7^{o}, and

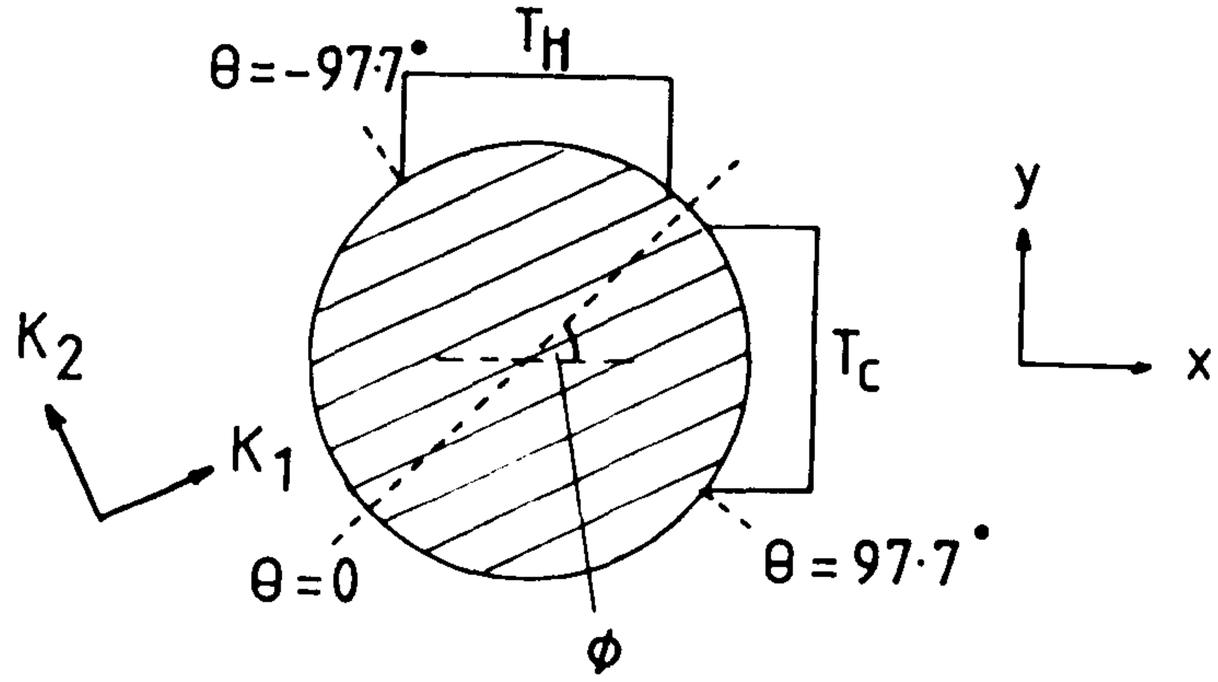

Fig. 7.33

Second experimental configuration, with heater and sink at right angles.

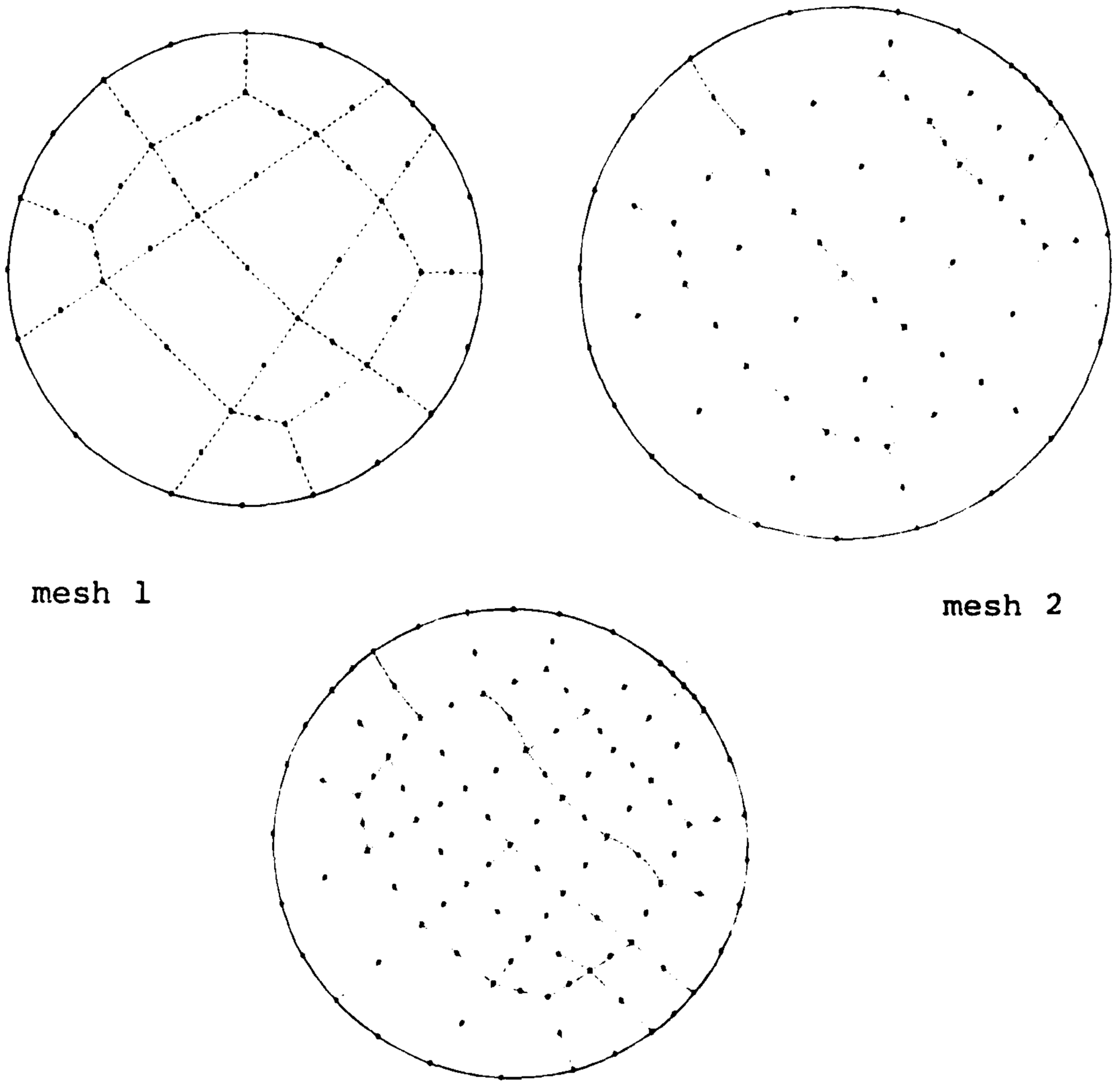

mesh 1

mesh 2

mesh 3

Fig. 7.34

Finite element meshes used for calculations of second configuration.

90^{o} (as before, ϕ is measured anticlockwise from the x-coordinate axis). Fig. 7.35 shows the surface temperature distributions on the three meshes, indicating convergence as the total number of elements is increased. As expected, the biggest differences between meshes are seen at orientations of $\phi = 0^{o}$ and 90^{o}, which give rise to large temperature gradients near the heat source or sink; in this case the greatest change in nodal temperature is approximately 5%.

The effect of a $\pm 2^{o}$ perturbation in specimen orientation is shown by the surface temperature distributions in Fig. 7.36. At orientation $\phi = 0^{o}$, nodal temperatures change by up to 4%, but at $\phi = 22.7^{o}$ and 42.7^{o} this figure increases to as much as 10%.

The calculations were repeated with temperature-dependent thermal conductivities (data set (ii) in 7.3.2) over the appropriate range of temperatures, but as before the influence on the results was negligible, with largest differences being less than 1%.

As in 7.3.2, the temperature difference is dominated by the large anisotropy of thermal conductivity, with isotherms tending to align parallel to the reinforcement direction. Examples of the distribution of isotherms are shown in Fig. 7.37.

Measurements and Comparison

It can be seen from the preceding figures that the temperature gradients along the surface are rather higher than in the first configuration, and it may be expected to be more difficult to obtain reliable measurements. Nevertheless, experiment and calculation were found to be in reasonable agreement, as shown in Figs. 7.38 to 7.40, for specimen orientations of $\phi = 0^{o}$, 22.7^{o} and 42.7^{o} respectively. In the first of these, the greatest discrepancy is about 10% (at $\theta = -83^{o}$), but the other six experimental points are within 3% of the calculated values. Rather more scatter is evident in Fig. 7.39 ($\phi = 22.7^{o}$), notably the points at

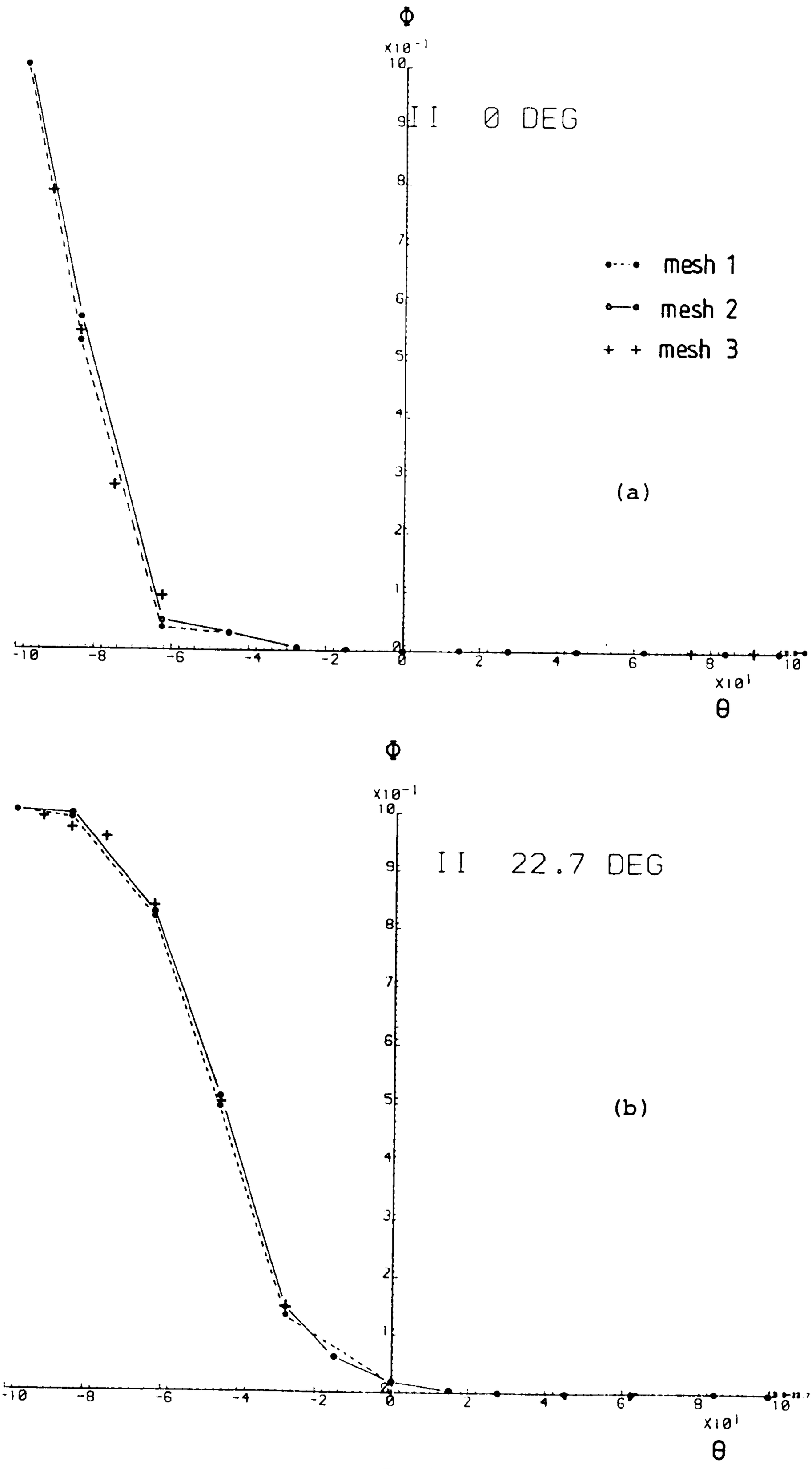

Fig. 7.35

Finite element calculations of surface temperature (second configuration)

(a) $\phi = 0^{o}$
(b) $\phi = 22.7^{o}$

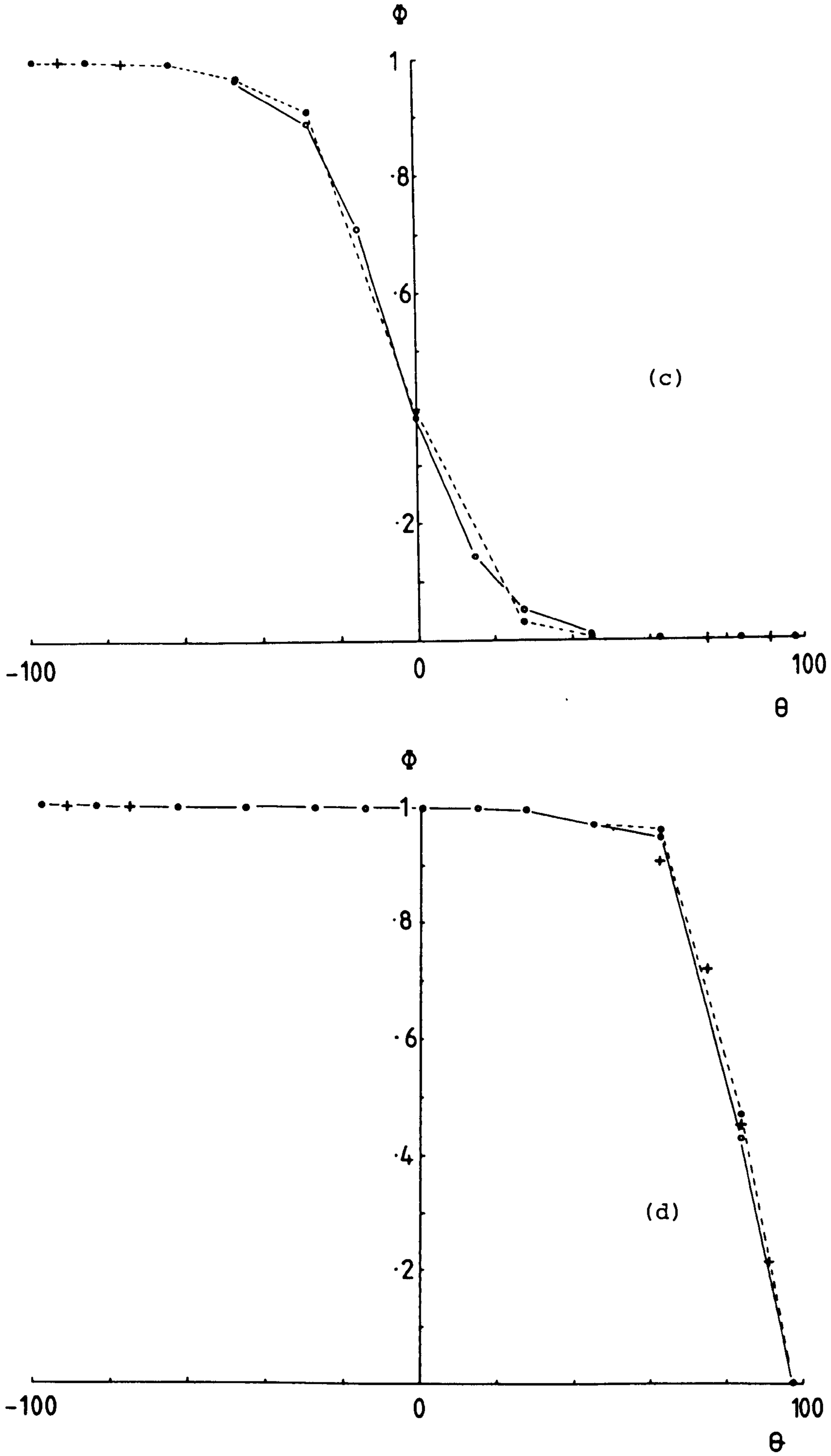

Fig. 6.35 (cont)

(c) $\Phi = 42.7^{o}$

(d) $\Phi = 90^{o}$

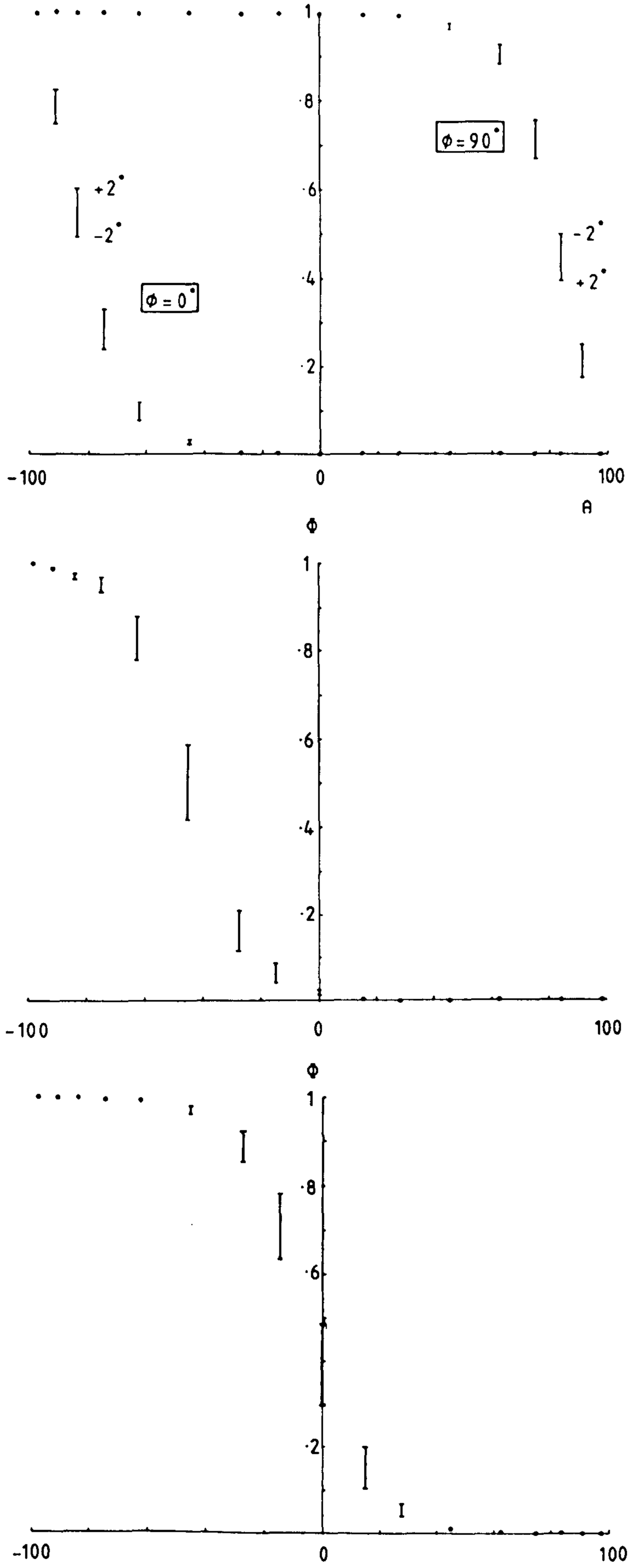

Fig. 7.36

Effect on calculated surface temperatures of a ±2° perturbation in specimen orientation

(a) $\phi = 0^{\circ}$ and 90°
(b) $\phi = 22.7^{\circ}$
(c) $\phi = 42.7^{\circ}$

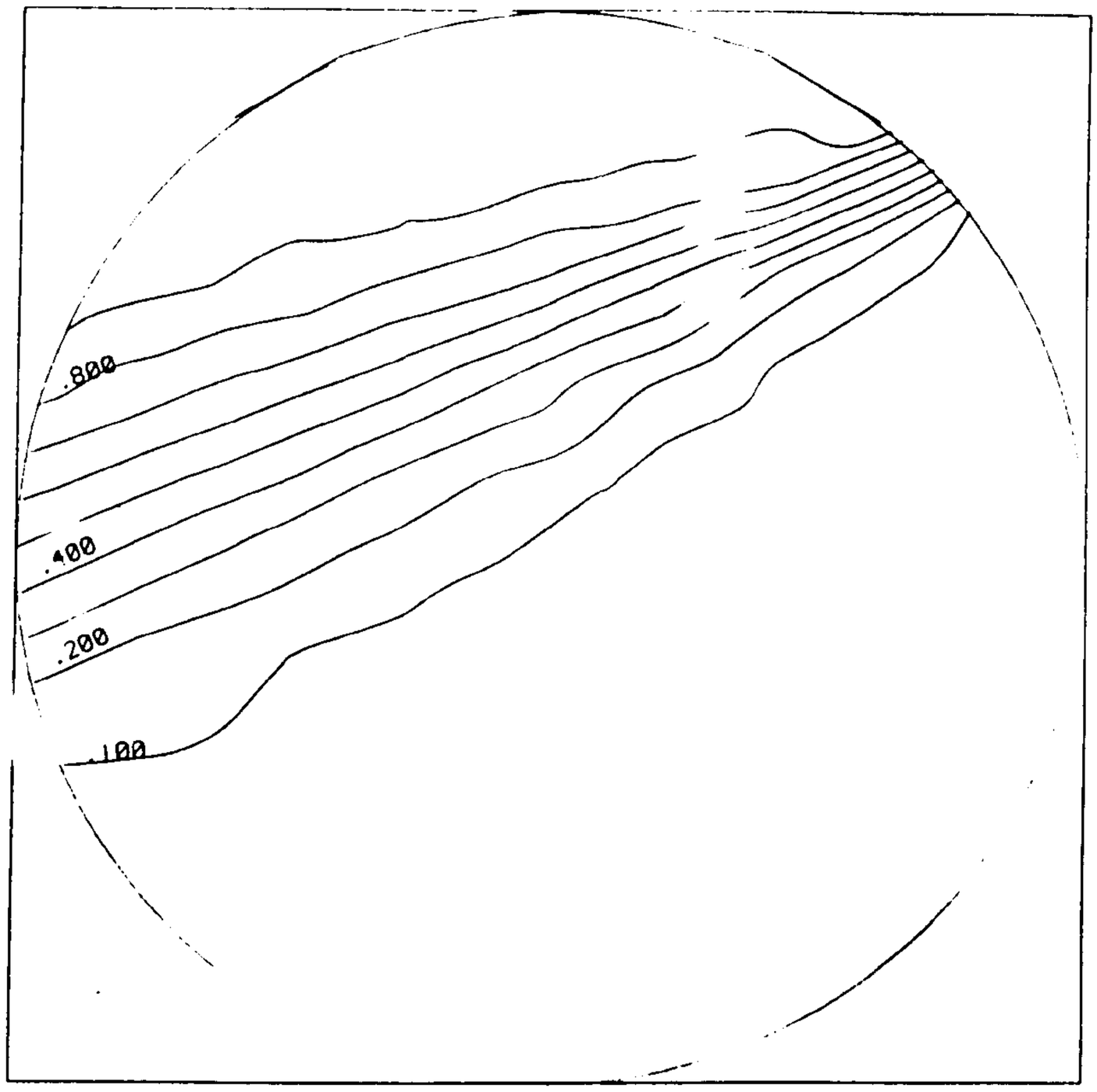

II 22.7 DEG

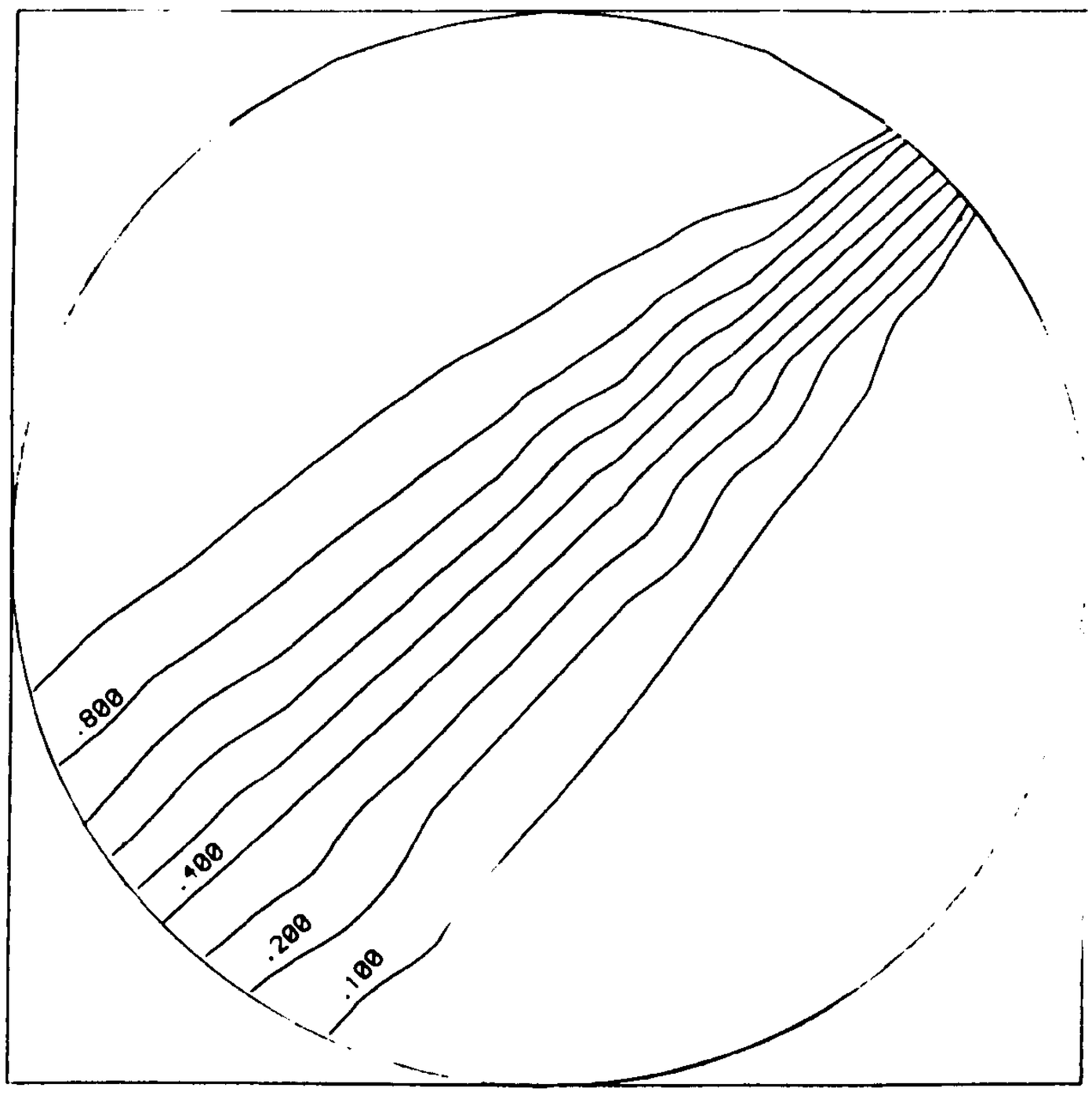

II 42.7 DEG

Fig. 7.37

Temperature distributions for the second configuration with $\phi = 22.7^{o}$ and 42.7^{o}, showing alignment of isotherms parallel to reinforcement direction.

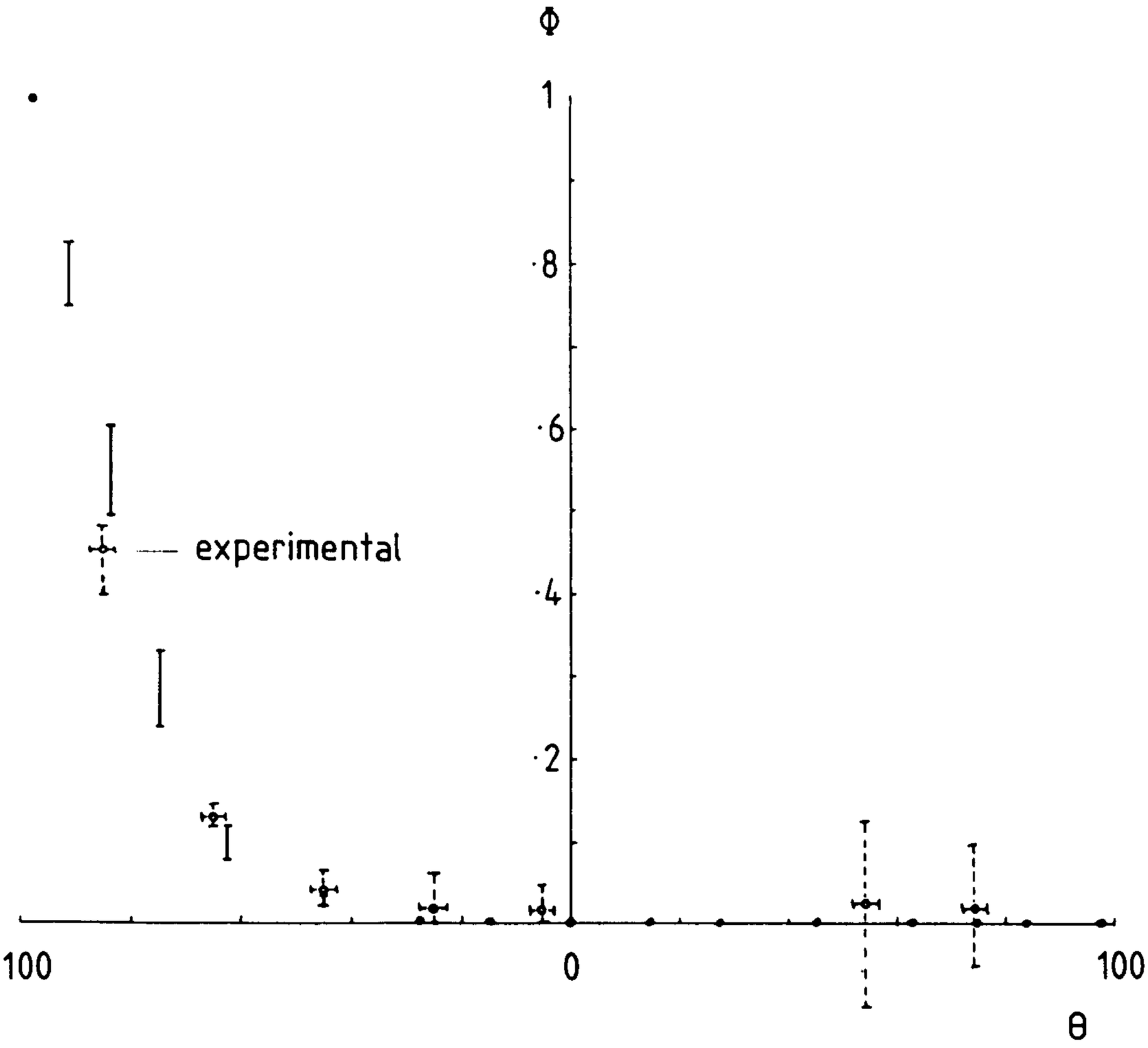

Fig. 7.38

Experimental surface temperatures, superimposed on calculated distribution (with ±2° perturbation). $\phi = 0^{\circ}$

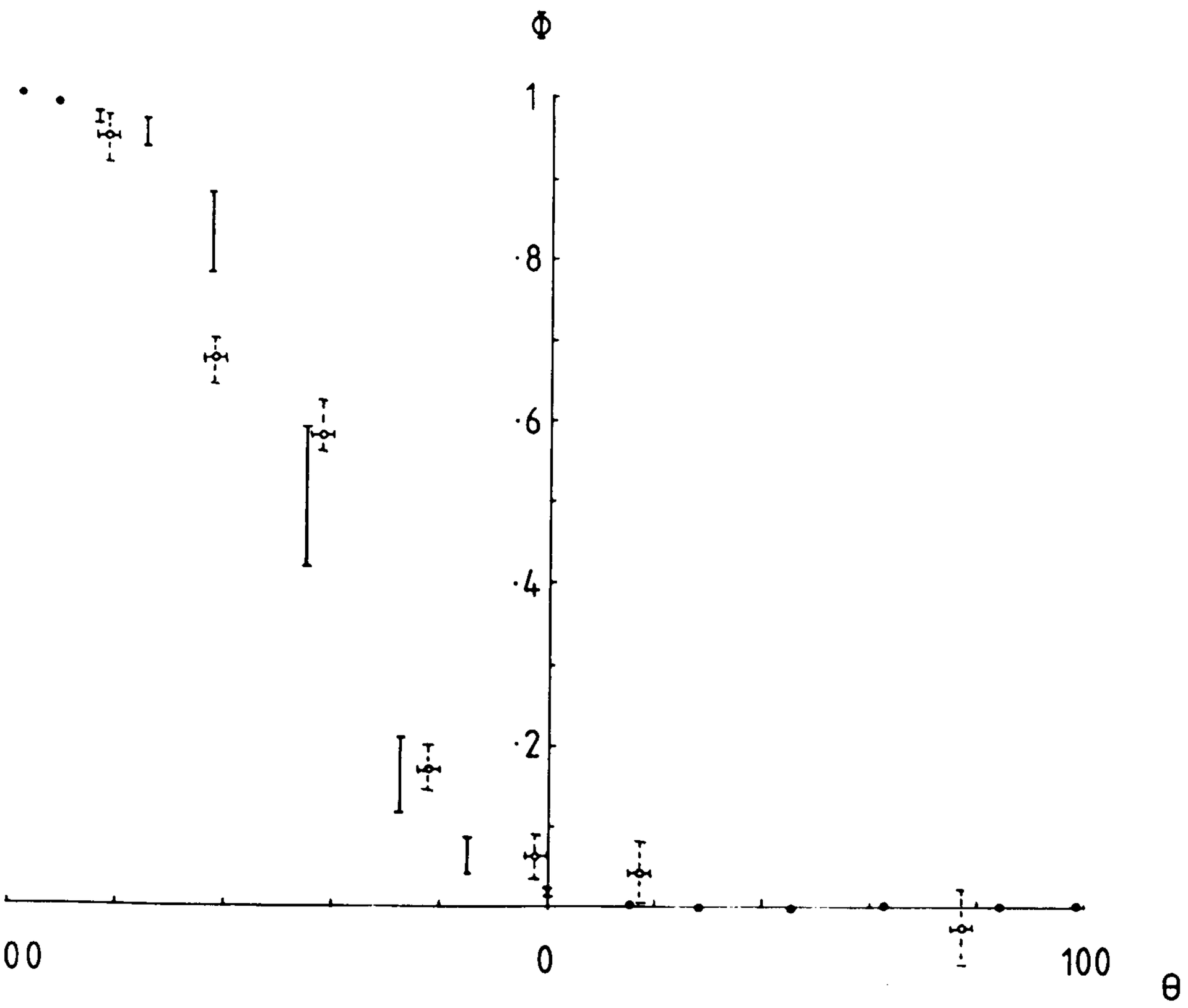

Fig. 7.39

As Fig. 7.38 for $\phi = 22.7°$

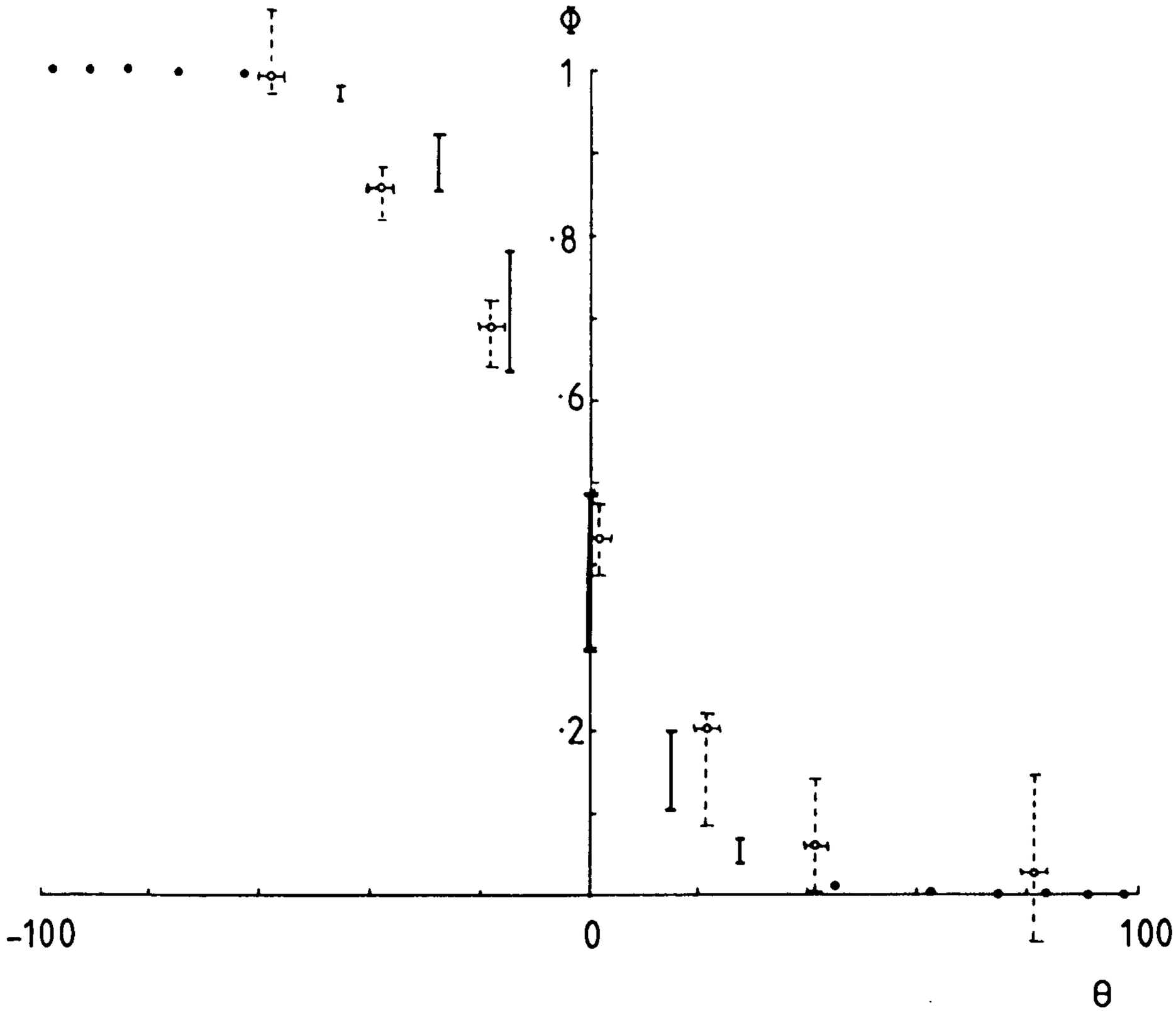

Fig. 7.40

As Fig. 7.39 for $\phi = 42.7^{\circ}$

$\theta = -62^{\circ}$ and -42°, and since the deviations are respectively negative and positive, they cannot be ascribed to errors in specimen alignment. The overall agreement is better at $\phi = 42.7^{\circ}$ (Fig. 7.40), although a smooth curve drawn through the experimental points suggests a mean temperature gradient $(\frac{d\Phi}{d\theta})$ between $\theta = \pm 25^{\circ}$ of only about 75% of the numerical value.

7.5 DISCUSSION

Overall, the experimental measurements on the two configurations agree with numerical calculations to within about 10% (as a fraction of the temperature difference between heater and sink). In some cases, particularly for the second heater/sink arrangement, the discrepancy is rather greater than the estimated experimental uncertainties, and further discussion of possible errors is required.

In 7.2.4, the maximum possible temperature difference between one of the heater blocks and the specimen surface was estimated. The effect of this would be an over-estimation of the (fixed) hot surface temperature and an under-estimation at the cold surface (assuming that both the heater blocks had a slightly different radius of curvature from that of the specimen). If the 'true' fixed surface temperatures become $T_H - \delta T_g$ and $T_C + \delta T_g$, the expression for the dimensionless surface temperature (Equation 7.4) becomes

$$\Phi' = \frac{T - (T_C + \delta T_g)}{T_H - \delta T_g - (T_C + \delta T_g)} = \frac{T - T_C - \delta T_g}{T_H - T_C - 2\delta T_g} \qquad (7.6)$$

The effect of this error is thus asymmetric, with Φ' being less than Φ as T reduces towards T_C, and greater as T approaches T_H. At $\Phi = 0.5$ (that is, $T_H - T_C = 2(T - T_C)$) the errors are self-cancelling, and Φ is unchanged. If the temperature difference δT_g exists at only one of the specimen/heater interfaces, then the result is a consistent bias, increasing from zero to approximately $\delta T_g/\Delta T_H$ at $\Phi = 1$ or reducing from $-\delta T_g/\Delta T_H$ at $\Phi = 0$ to zero, depending on whether the heat source or sink is affected. Fig. 7.41 illustrates these phenomena qualitatively, suggesting that

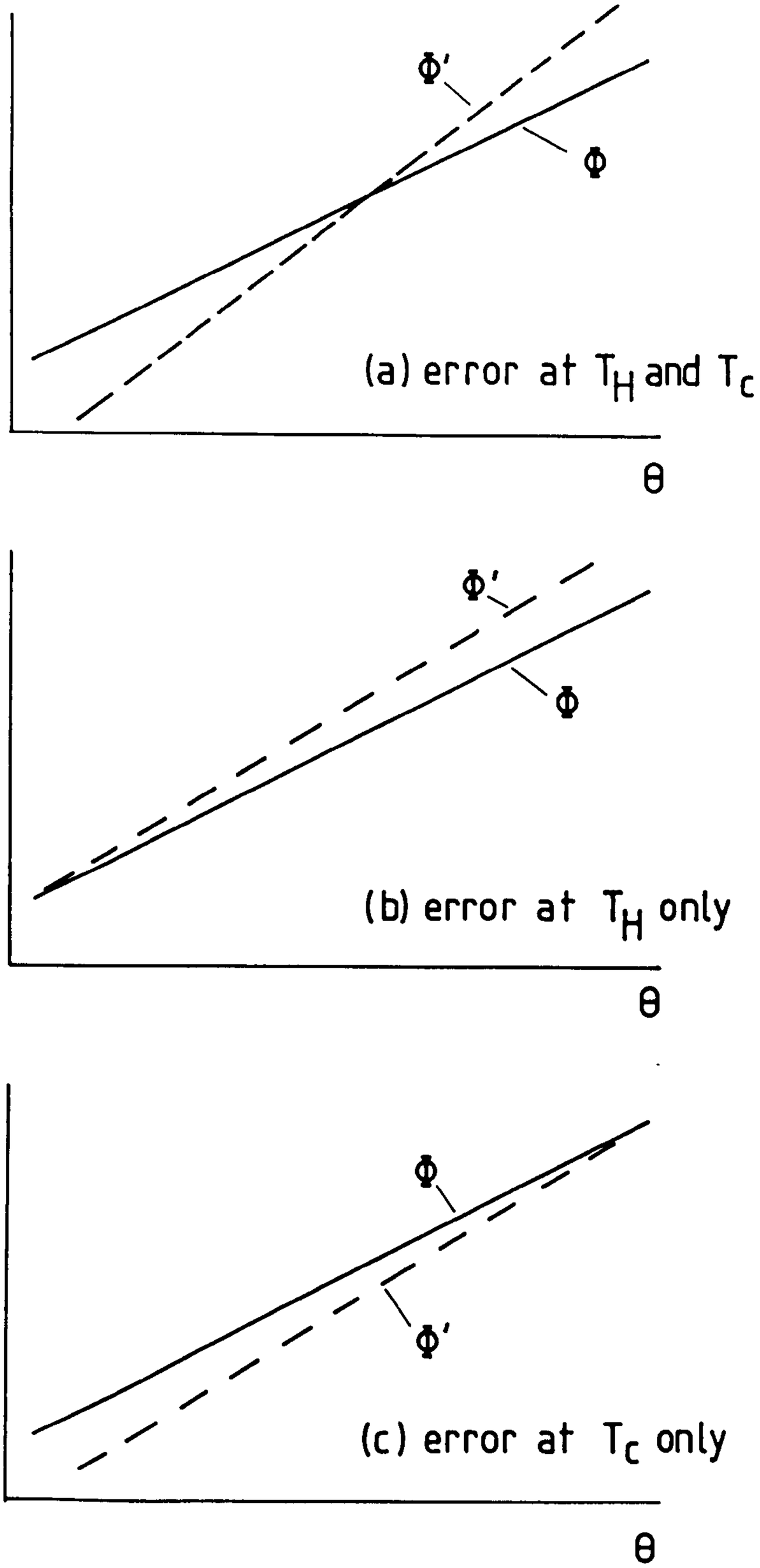

Fig. 7.41

Effect of a temperature difference between heater block and specimen surface. Φ is the 'ideal' temperature distribution, assuming perfect thermal contact between heater and specimen. Φ' is the actual distribution (Equation 7.6).

the experimental values of Φ could lie above the 'true' value as Φ tends towards zero, or below the 'true' value as Φ increases towards unity.

The magnitude of this effect is difficult to estimate, but from Equation 7.3 the maximum error (at $\Phi = 0$ and/or 1) is about

$$\frac{\delta T_g}{\Delta T_H} = \frac{p\ q}{\Delta T_H k_g}$$

The heat flux is dependent on $\Delta T_H = T_H - T_C$, according to

$$q \sim k_{eff}\ \frac{\Delta T_H}{\ell}$$

This applies to the first configuration, where ℓ is the average separation of the heater and sink and k_{eff} is an effective thermal conductivity, depending on the orientation of the specimen (a one-dimensional heat flux is assumed). Taking ℓ as 75 mm, the heat flux varies between about 20 ΔT_H W/m^2 at specimen orientation $\phi = 0^o$ and 650 ΔT_H W/m^2 at $\phi = 90^o$. Using the estimate of p discussed in 7.2.4 gives a maximum error in dimensionless temperature from about 0.002 at the smallest heat flux up to 0.05 at the highest.

Several of the experimental results exhibit trends consistent with an error of this nature, notably those shown in Figs. 7.28, 7.30, 7.39 and 7.40. A correction of the order of magnitude suggested would bring most of the measurements into more acceptable agreement with the numerical calculations.

This series of measurements illustrates a general problem of the experimental validation of a mathematical model, which has been experienced by the author in another context (Dutré, 1984), and is related to the contrasting natures of calculation and measurement. Conceptually, the observation or measurement represents the 'truth' of a physical phenomenon; mathematical models are then constructed upon some logical foundation, and their validity is tested by comparison with the experiment. If the agreement is considered to be

unsatisfactory (according to some previously-defined criteria), the model is re-examined, its fundamental assumptions or approximations modified, and the calculations are then repeated.

In practice, however, the process tends to be reversed, particularly if the model is based on known physical principles and makes use of standard mathematical techniques. Having gained confidence in the validity of the model through a theoretical study (such as that presented in Chapter 6), any discrepancy between calculation and experiment is likely to call into question the accuracy of the measurements rather than that of the numerical technique. Usually, however well-designed the experiment may be, it is relatively easy to invoke some practical short-coming rather than to revise the basis of the model.

Instead, the experiment serves a purpose different from direct validation. If it is assumed that the mathematical model converges towards the 'correct' answer to a problem (as the element size is reduced), then the measurements indicate how well the observed system corresponds to its idealised form which is the subject of the calculation. There are three aspects to this idealisation in the present study. The first is concerned with experimental accuracy, such as the likely error in a measurement of temperature, and can usually be quantified with reasonable confidence. The second aspect relates to the assumptions inherent in the design of the experimental system, such as the two-dimensionality of the heat flux and the negligible heat loss from the specimen surface. Again, they may be quantified, although not so readily as direct measurements. Finally, the question arises of the properties of the specimen material. The fundamental variable, thermal conductivity and its temperature-dependence has been considered in some detail, but there are other assumptions - particularly important in the case of a composite material is that of specimen quality in general and macroscopic homogeneity in particular.

In reviewing both theoretical and experimental aspects of the validation process, it is possible to conclude not only that the numerical model is mathematically valid, but also that the composite under consideration corresponds to the idealised concept of a macroscopically homogeneous material having anisotropic thermal properties. It is emphasised, however, that measurements have been confined to the steady state; under transient conditions, particularly at small values of time following a severe thermal shock, it may be necessary to take the microstructure into account. As discussed in 1.5, Balageas and Luc (1983) have pointed out that the practical limits of thermal property homogenisation must be taken into consideration during mathematical modelling, as well as in transient methods of property measurement (see 2.1.3).

CHAPTER 8 : APPLICATIONS OF THE NUMERICAL MODEL

Following its development, the numerical model has found industrial application in two commercial consultancies carried out at Plymouth Polytechnic. In 1984, the Petrochemicals and Plastics Division of ICI plc requested a numerical study of thermal cycling during tape laying of a continuous carbon fibre-reinforced thermoplastic. In 1985, calculations of the temperature distribution in a composite propeller blade were performed for Dowty Rotol Ltd. Both sponsoring establishments have given permission for a brief description of the work to appear in this thesis.

8.1 TAPE LAYING OF REINFORCED THERMOPLASTICS

8.1.1 Introduction

Carbon fibres have commonly been used as a reinforcement in network or cross-linked polymer systems, such as phenolic or epoxy resins. In recent years, however, considerable interest has arisen in the possibilities offered by carbon fibre-reinforced thermoplastics, which may combine a high specification with ease of processing (Trewin and others, 1980; Cluley, 1983). As discussed in Chapter 1, much of the development and application of composites has occurred in response to the exacting requirements of the aerospace industry, and it was with this market in mind that ICI introduced a carbon fibre-reinforced version of its high performance semi-crystalline thermoplastic PEEK (polyether-etherketone). Known as APC (aromatic polymer composite), the material combines the high specific stiffness and strength expected of a continuous carbon fibre-reinforced polymer with the matrix properties of toughness and chemical resistance.

One of the manufacturing methods under development for this material is tape laying, a brief description of which has been given by Brewster and Cattanach (1983) and ICI (1984). The process uses the thermoplastic equivalent of prepreg, in the form of a tape a few centimetres wide reinforced with long, unidirectional carbon fibre, and is similar to filament

winding, except that the tape is laid by a traversing head onto a relatively flat surface instead of a mandrel. Both filament winding and tape laying are established manufacturing routes for thermosetting composites; after fabrication the component requires curing before removal from its mandrel or open mould. In contrast, the thermoplastic matrix may be subjected to repeated cycles of melting and solidification. This enables tape laying to be performed in a manner analogous to welding. The incoming tape and the substrate are raised to the polymer melting point prior to consolidation, and may be subsequently cooled; in contrast to the bulk curing of a thermosetting resin, only the surfaces to be joined require local heating.

Each layer of prepreg to be laid becomes part of the substrate for the following cycles, and will thus be subjected to a complex series of temperature excursions. Some thermal cycling will take place in the temperature range in which crystallisation of the polymer occurs, so that the final percentage crystallisation and hence the ultimate mechanical properties of the composite may be influenced to some degree by the processing conditions. A further incentive to the study of this problem concerns the optimisation of operating parameters. The 'welding' of tape and substrate is achieved most efficiently (in terms of both energy input and production rate) if only the minimum quantity of material is raised to the polymer melting point, and a numerical model of the process is clearly of considerable value as a design tool.

8.1.2 Thermal Properties of APC

The temperature-dependence of heat capacity (ρC_p) was derived from a combination of measurements of density, specific enthalpy (on cooling) and specific heat (on heating). Enthalpy data had been obtained on a differential scanning calorimeter (DSC), and specific heat data by comparison with an alumina standard by differential thermal analysis (DTA). Fig. 8.1 shows the DSC and DTA-derived curves for $\rho C_p(T)$ from room temperature up to about 400°C. They are reasonably consistent, both showing a small peak at the polymer melting temperature (~340°C). The relatively large exotherm between

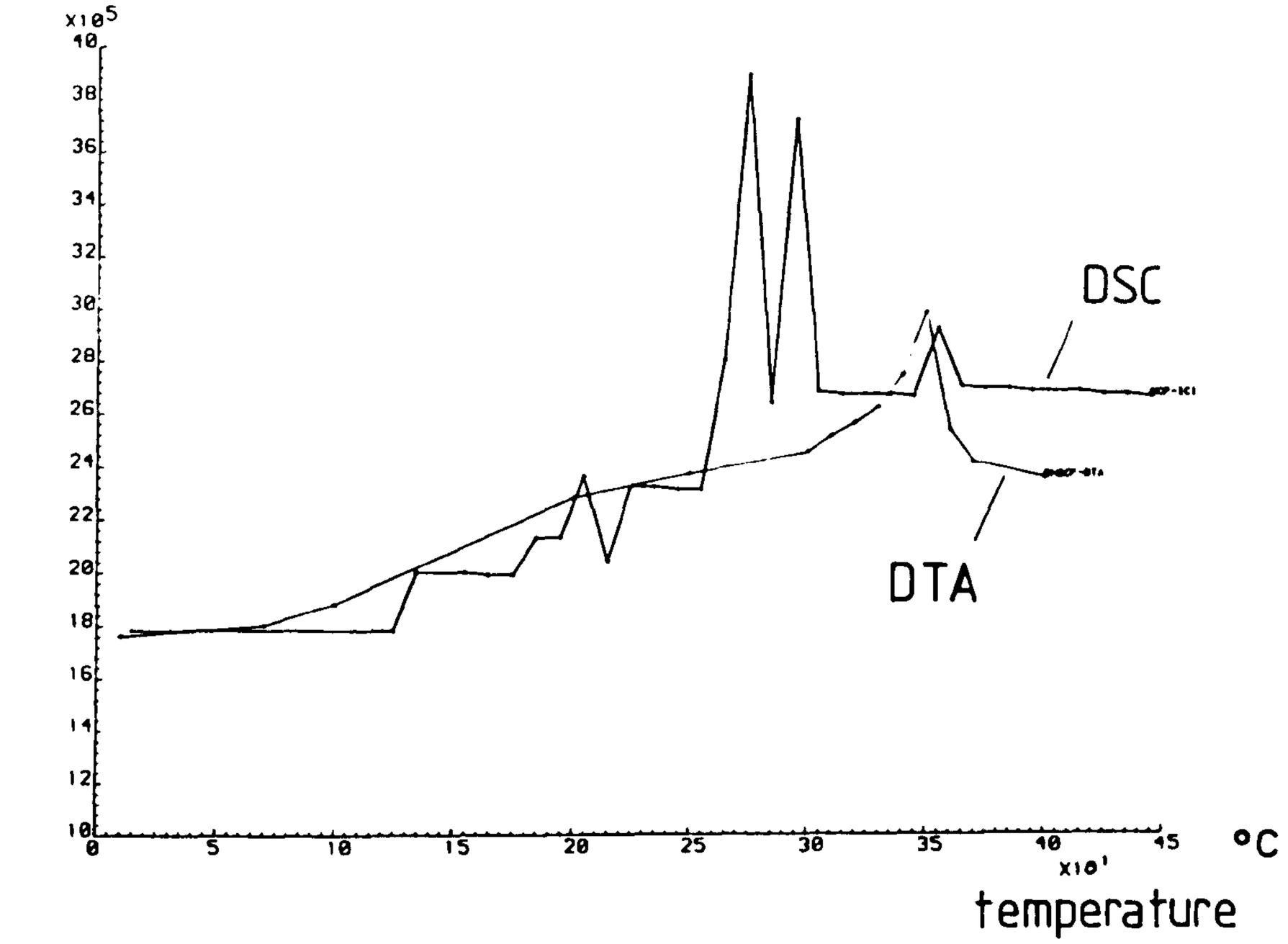

Fig. 8.1

Temperature-dependence of heat capacity of APC as derived from DSC measurements of enthalpy and DTA measurements of specific heat.

250°C and 300°C on the DSC curve is associated with crystallisation during cooling, and corresponds to data reported by Blundell and Osborn (1983) showing a maximum rate of crystal formation in this temperature range. The DTA curve is similar in shape to that described by Tadmor and Gogos (1979) as being typical of crystalline polymers, with no discontinuity around the glass transition and a sharp maximum at the melting point, above which Cp is lower than in the solid phase.

Laser-flash apparatus at the University of Manchester Institute of Science and Technology (described by Taylor, 1980) provided measurements of thermal diffusivity parallel and perpendicular to the unidirectional reinforcement (Fig. 8.2). In the longitudinal direction, diffusivity is dominated by the carbon fibres; only in the transverse direction (where the matrix properties are more significant) is any discontinuity evident due to the melting phase change.

The intention was to derive values of thermal conductivity for use in the numerical model from these separate measurements of diffusivity and heat capacity, but this process requires caution. Apart from the question of the physical validity of an effective macroscopic diffusivity, which was discussed in 1.5, there are also potential inaccuracies associated with combining different sets of data obtained at different times on different samples of material. These may be particularly serious when both diffusivity and heat capacity are changing rapidly with temperature. Fig. 8.3 shows the principal thermal conductivities of APC as derived from diffusivities and (DTA) heat capacity. The sharp peak in $k_{||}$ at about 340°C is illustrative of the difficulties in interpretation; according to the relationship $k = \rho C_p . \alpha$, the thermal conductivity must increase in response to the maximum in heat capacity at the matrix melting temperature. In reality, however, conductivity as well as diffusivity parallel to the reinforcement would be dominated by the carbon fibres. By inserting appropriate values into Equation 1.2 it can be seen that even if the conductivity of the matrix were to undergo a change of, say, 50% on melting,

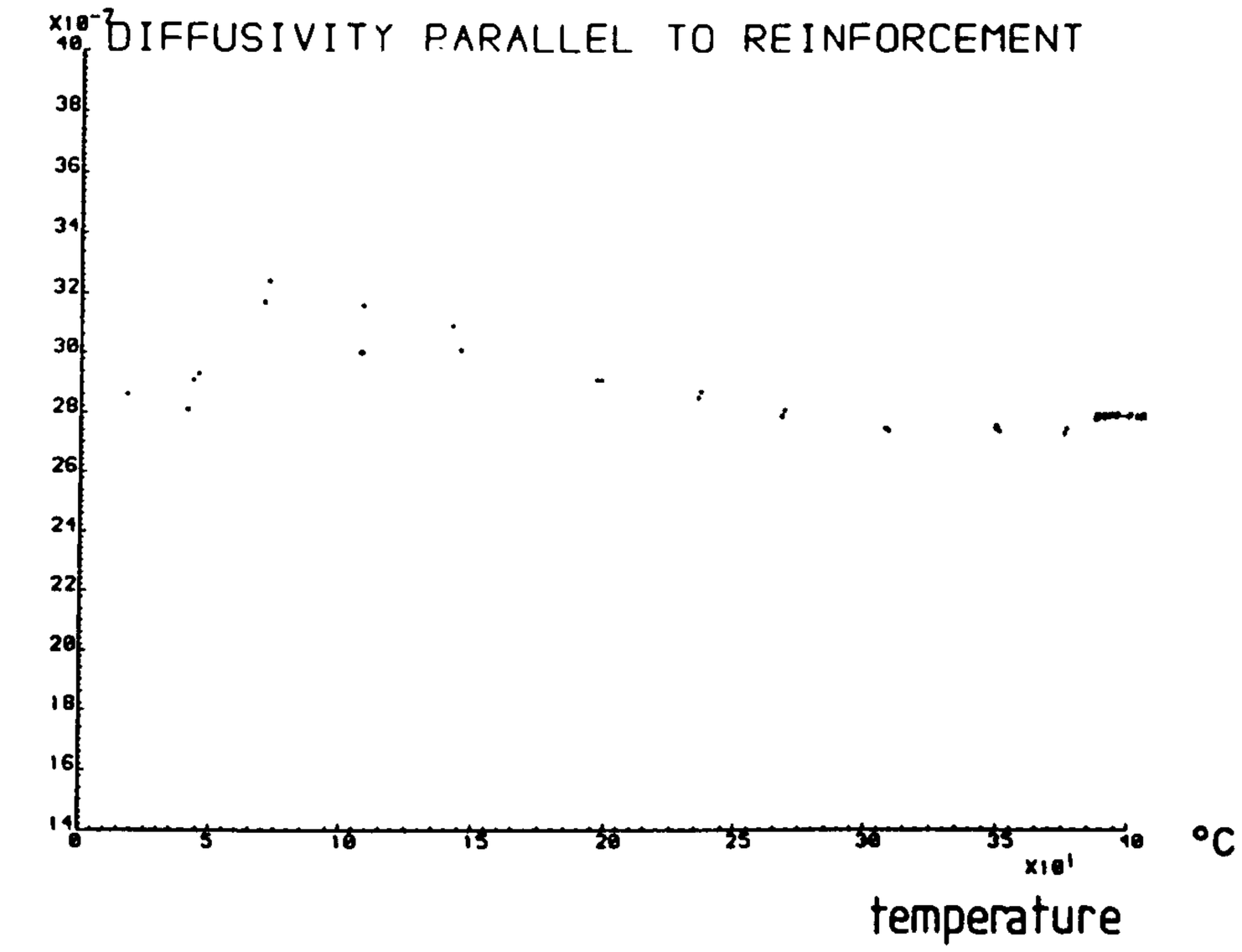

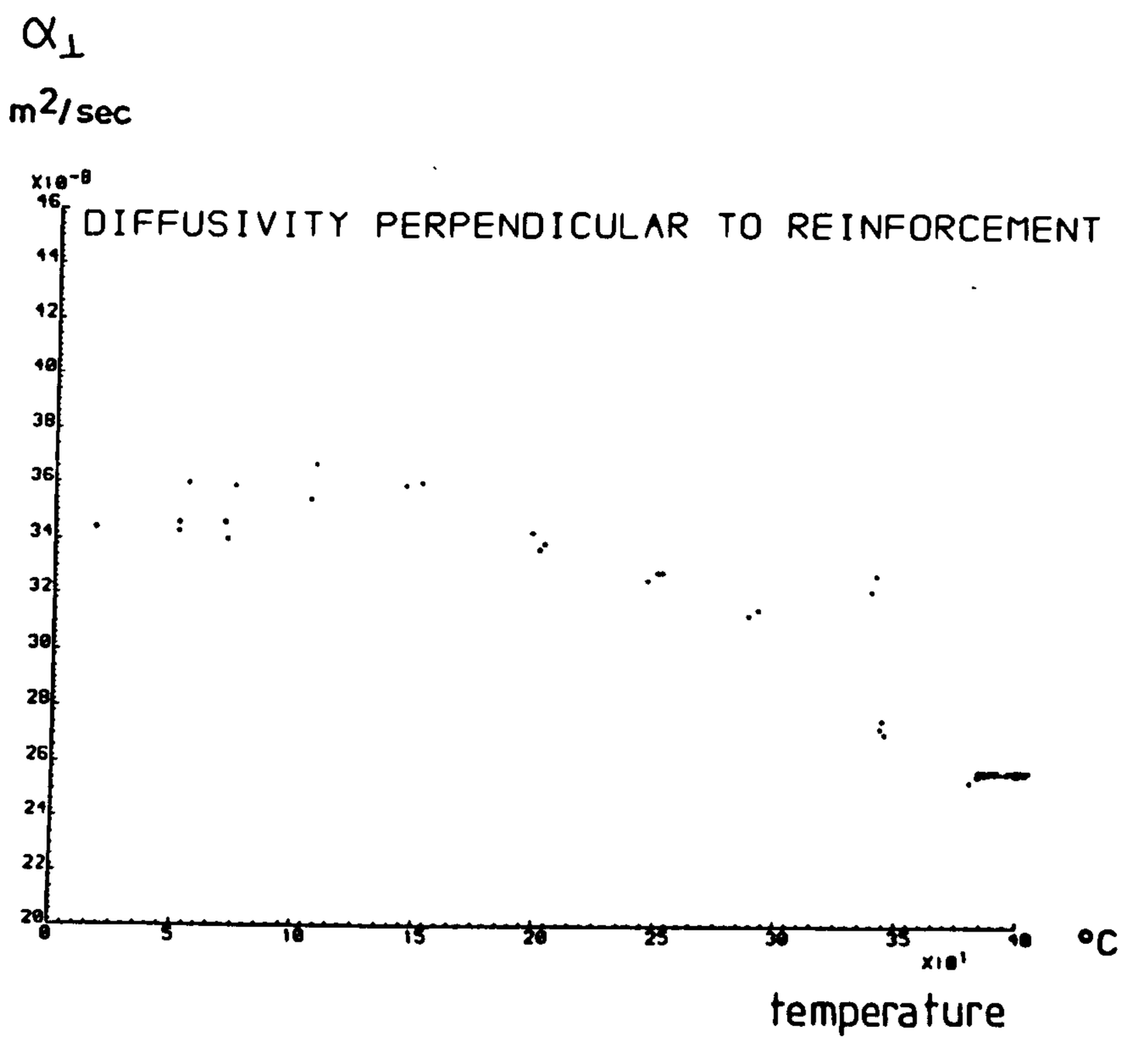

Fig. 8.2

Measured thermal diffusivity of APC parallel and perpendicular to reinforcement.

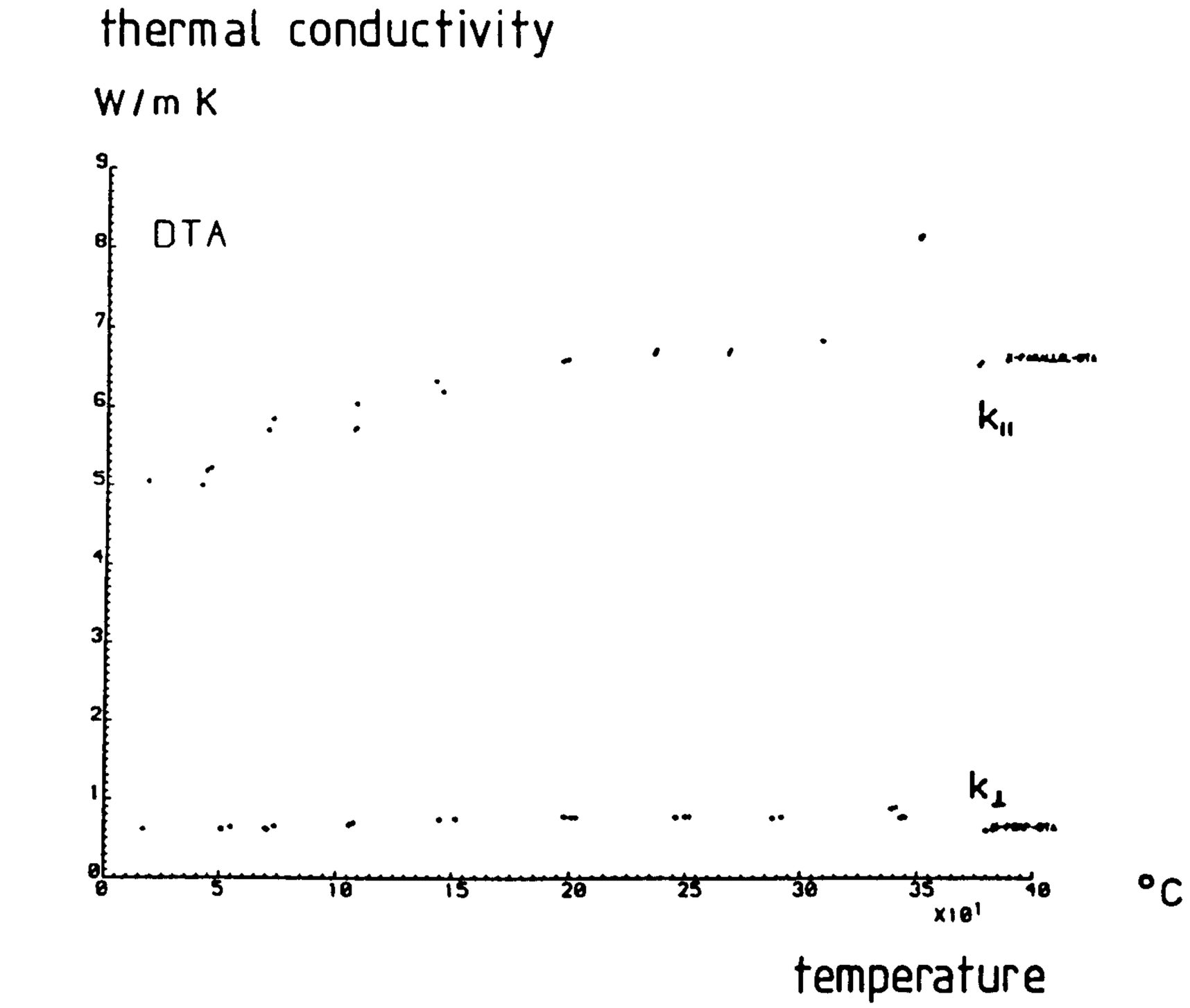

Fig. 8.3

Principal thermal conductivities of APC, as derived from measured thermal diffusivity (Fig. 8.2) and heat capacity (Fig. 8.1).

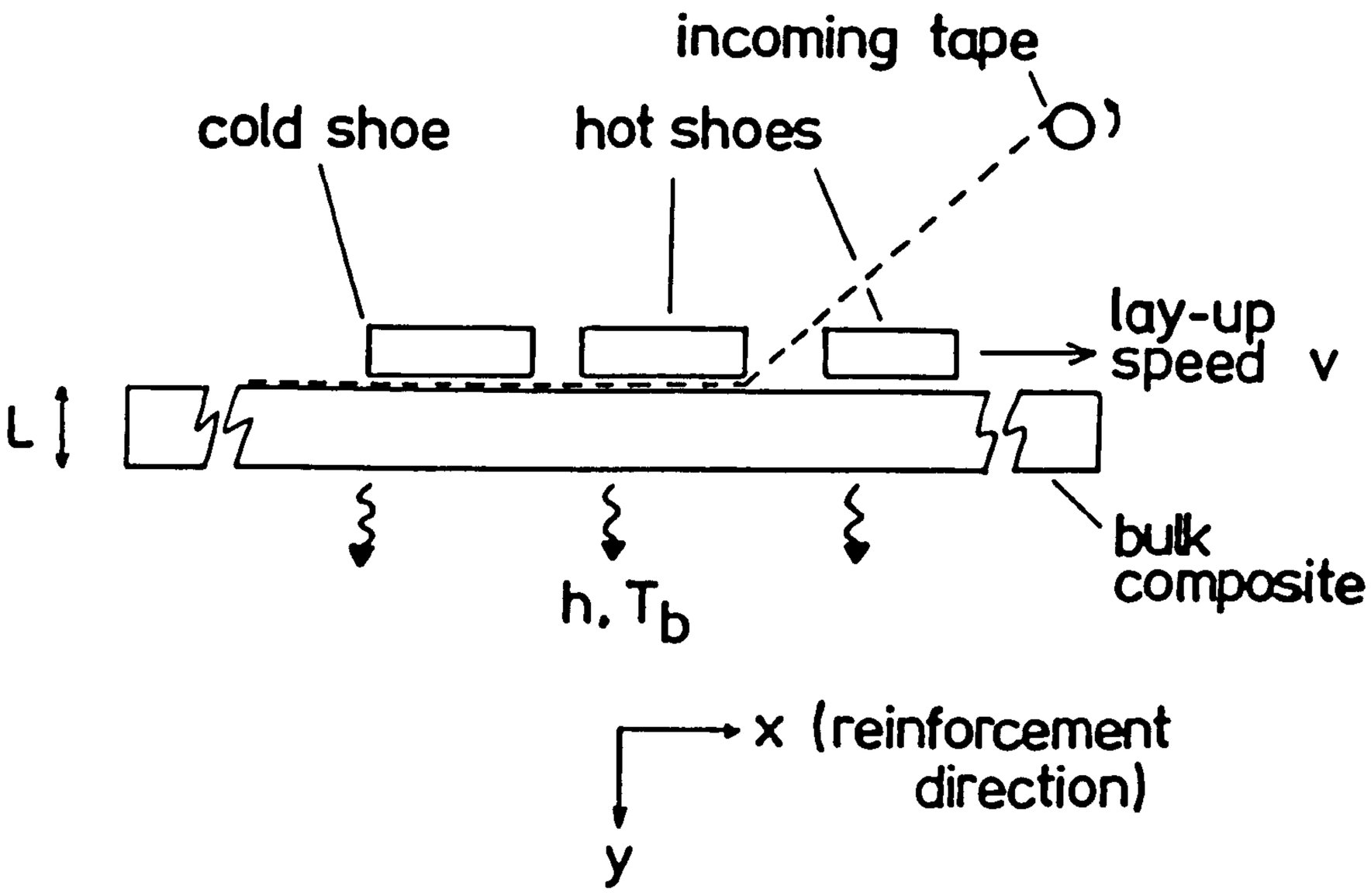

Fig. 8.4

Two-dimensional idealisation of a thermoplastic tape laying process.

the effect on the longitudinal conductivity of the composite would only be about 0.5%. The value of $k_{||}$ at 340°C is therefore considered to be physically unrealistic, and was not included in the data for calculation. A further difficulty arises from the fact that there are differences in measured heat capacity, depending on whether the material is being heated or cooled. Only one set of data at a time can be represented in the numerical model, yet both heating and cooling cycles were expected to be important phases of the tape laying process. In view of the uncertainties surrounding the thermal properties of APC, it was considered desirable to perform all calculations with several alternative sets of data, and to interpret the results accordingly.

8.1.3 Idealisation of Tape Laying Process

Fig. 8.4 shows a schematic, two-dimensional idealisation of a tape laying process. The traversing head comprises three 'shoes'; the leading hot shoe ensures that the surface of the composite is molten, and the second maintains this temperature while consolidating the incoming tape. Welding of the two surfaces is completed by the cold shoe, and the head assembly moves to the right at constant speed v. The composite is assumed to be in contact with a cold substrate at temperature T_b. A finite heat transfer coefficient (h) exists between the material and the substrate, but, in the absence of reliable data, the hot and cold shoes have been represented by fixed temperatures at the top surface of the composite section. This assumption is probably suitable only for preliminary calculations, and will result in faster rates of heating and cooling than would occur in reality.

The thickness of the incoming tape (about 0.1 mm) is much less than that of a typical composite section (between 1 and 5 mm), so that the dimensions of the specimen may be considered constant during a single lay-up cycle. In addition, the length of a section (in the direction of velocity v) is great enough for end heat losses to be neglected, and successive cycles are sufficiently far apart in time for them to be thermally independent (in other words, it is assumed that the temperature of the composite returns to

ambient before the next passage of the tape head).

The two-dimensional region to be modelled is thus rectangular in shape (L_x ~ 50 - 100 cm, L_y ~ 1 - 5 mm) and is thermally orthotropic, with thermal conductivities $k_{||}$ (T) and $k_{\perp}$ (T) in the x and y- directions respectively. There is a convective boundary along $y = L_y$, while the boundary condition at y = 0 is time dependent. The hot and cold shoes are represented by prescribed surface temperatures, while all other nodes on this surface were assumed to be adiabatic.

The choice of calculation time step depends not only on the finite element mesh used, but also on the speed at which the 'tape head' is to move. This movement is not continuous in the model - instead the set of fixed temperatures is advanced along the surface in a discrete fashion. Each change in the boundary conditions constitutes a thermal shock at the surface, and the model requires a period of time in which to stabilise before the tape head can be advanced further. As suggested by the transient calculations in 6.5.1, 5 or more iterations may be required after a change in boundary conditions before the numerical solution at a given time is of acceptable accuracy. As before, the procedure is to select an initial time step, based on node separation and thermal properties, and to investigate the convergence of the solution as its value is reduced. An appropriate preliminary value is based on Δt_{max}, defined in Equation 6.11.

An example of time step selection is provided by the mesh in Fig. 8.5, in which elements near the heated surface have dimensions ℓ_x = 10 mm and ℓ_y = 1 mm. Assuming thermal diffusivities parallel and perpendicular to the reinforcement of $\alpha_x \simeq 3 \times 10^{-6}$ m^2/s and $\alpha_y \simeq 3.5 \times 10^{-7}$ m^2/s, Equation 6.11 indicates time steps for conduction in each direction of $\Delta t_x \simeq 8s$ and $\Delta t_y \simeq 0.7s$. A tape head speed (v) of 1 m/min would require the surface boundary condition to be changed at intervals of $\Delta t_s = \ell_x/v \simeq 0.6s$; a preliminary calculation could thus be made with a time step of 0.6s, but would have

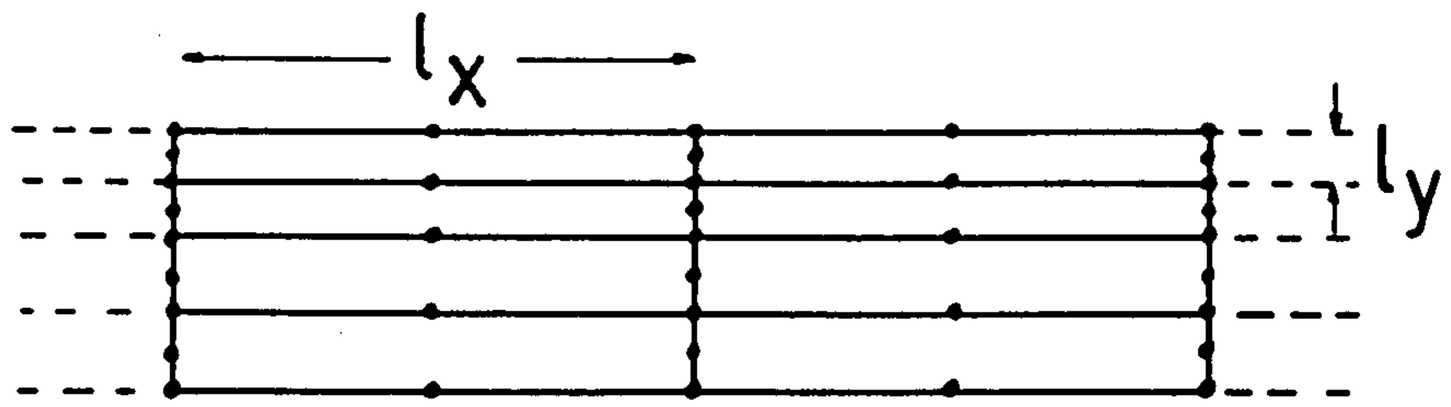

Fig. 8.5

Part of a typical finite element mesh used in the tape laying process.

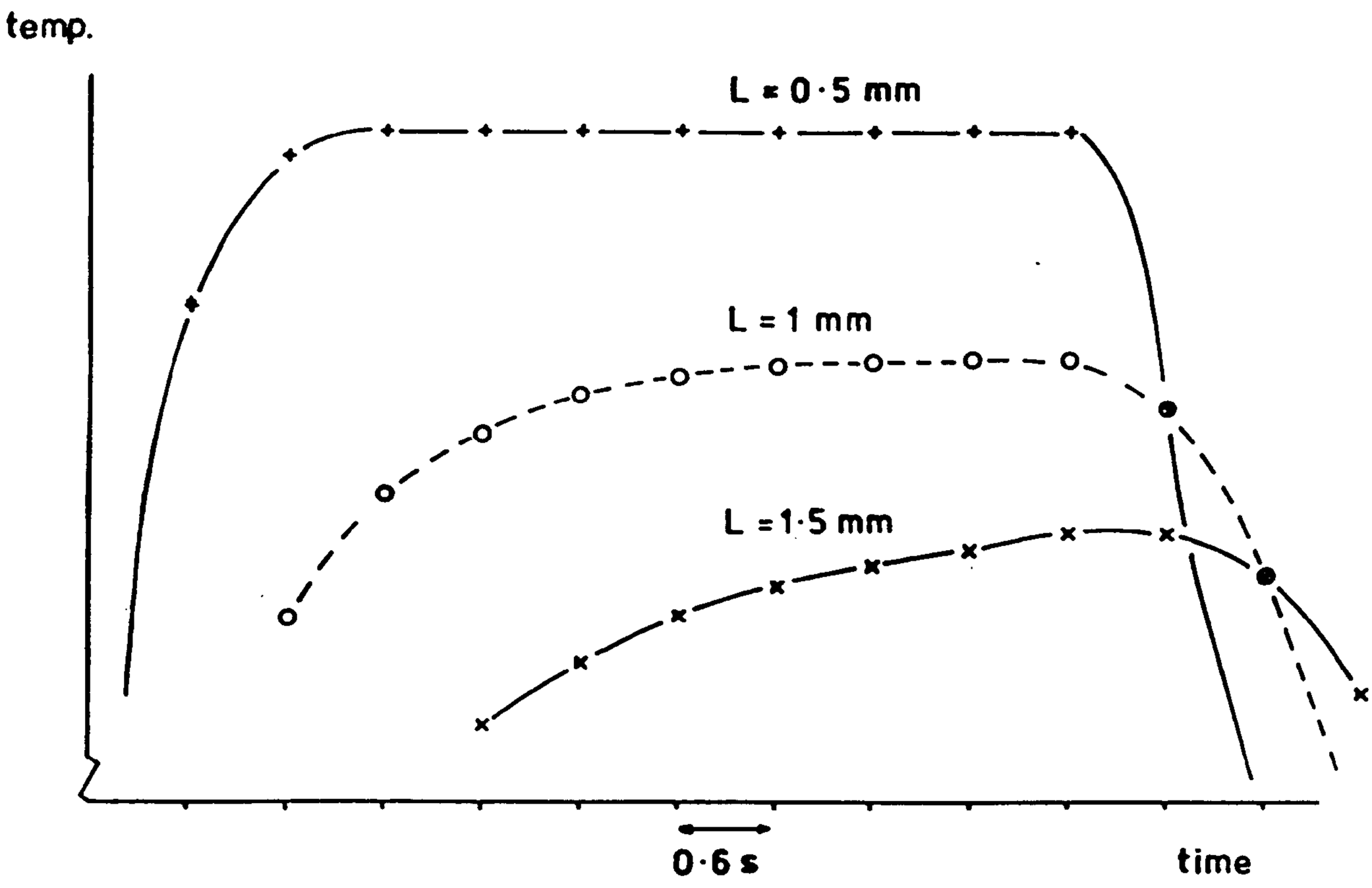

Fig. 8.6

Examples of the thermal response of the base of three sections of different thicknesses to the passage of the tape laying head.

to be reduced appropriately to give a sufficient number of iterations within the interval Δt_s.

It is further assumed that no change in geometry occurs when the melting point of the polymer is reached. The energetics of the phase change are modelled by the temperature-dependence of heat capacity, but no account is taken of polymer flow. This was considered to be a reasonable assumption for the tape laying process, and is further justified by the high melt viscosity of APC.

8.1.4 Thermal Response and Crystallisation

Any point within the bulk of the composite has a characteristic thermal response as a result of the passage of hot and cold shoes along the upper surface. If the point in question is close to the surface, the response will be more discontinuous and reach a higher peak temperature than if it is further away. As the lay up proceeds, therefore, a point within the composite experiences a sequence of thermal shocks which decrease in magnitude (but possibly increase in duration) as further layers are added. Polymer crystallinity is destroyed on melting, and crystallisation proceeds at a variable rate at lower temperatures. Each layer in the composite section will experience a number of cycles within the temperature range of crystal formation, depending on the section thickness (L_y), its proximity to the top or bottom surface and the speed at which lay up proceeds. This process was modelled by a number of separate calculations of the transient temperature distribution in slabs of different thicknesses, in response to a single passage of the tape head across the upper surface. These results were then used to synthesise the thermal history of given layers of tape, having different positions in composites of different final thicknesses.

Qualitative examples of the thermal response of the composite at the base of various sections are shown in Fig. 8.6. In the thinnest section (L = 0.5 mm), the layer in question is closest to the moving tape head, and the thermal response is more rapid than in thicker sections (L = 1 mm and 1.5 mm).

A representation of thermal histories for three layers in a 3 mm thick section is shown in Fig. 8.7, where ℓ_o is the distance from the upper surface. All the material has spent a similar amount of time in the middle of the temperature range, but nearer the upper surface (ℓ_o = 1 mm) there has been much less cycling at lower temperatures. The layer at the base of the section (ℓ_o = 3 mm) has cooled faster from the molten state than other layers, as a result of heat losses to the cold substrate, and this accounts for differences in the three profiles at higher temperatures.

Calculations were also performed to investigate the influence of some of the processing parameters on the thermal response. One indication of the efficiency of the welding process was considered to be the quantity of material which undergoes melting on each passage of the tape head. In practice, ℓ_m (the thickness of molten polymer) must be sufficient to ensure welding of the incoming tape with the previously-consolidated composite, but there is no need to raise more than the top surface to the melting temperature. Calculations indicated that ℓ_m was rather insensitive both to lay-up speed and to the temperature of cold shoe and substrate.

Further discussion of these results has been given by Grove and others (1984). As indicated in 9.2, there is considerable scope for future research in this field, given the current level of interest in processing techniques for high performance thermoplastic composites.

8.2 TEMPERATURE DISTRIBUTION IN COMPOSITE PROPELLER BLADE

8.2.1 Introduction

Fibre-reinforced polymers have been used in the construction of blades for both helicoptor rotors and aircraft propellers for several years (Doe and Holt, 1984; McCarthy, 1981). Current blade designs comprise a lightweight foam core surrounded by a glass cloth-reinforced resin skin. Longitudinal strength is provided by a unidirectional carbon fibre-reinforced spar, extending from root to tip (Fig. 8.8).

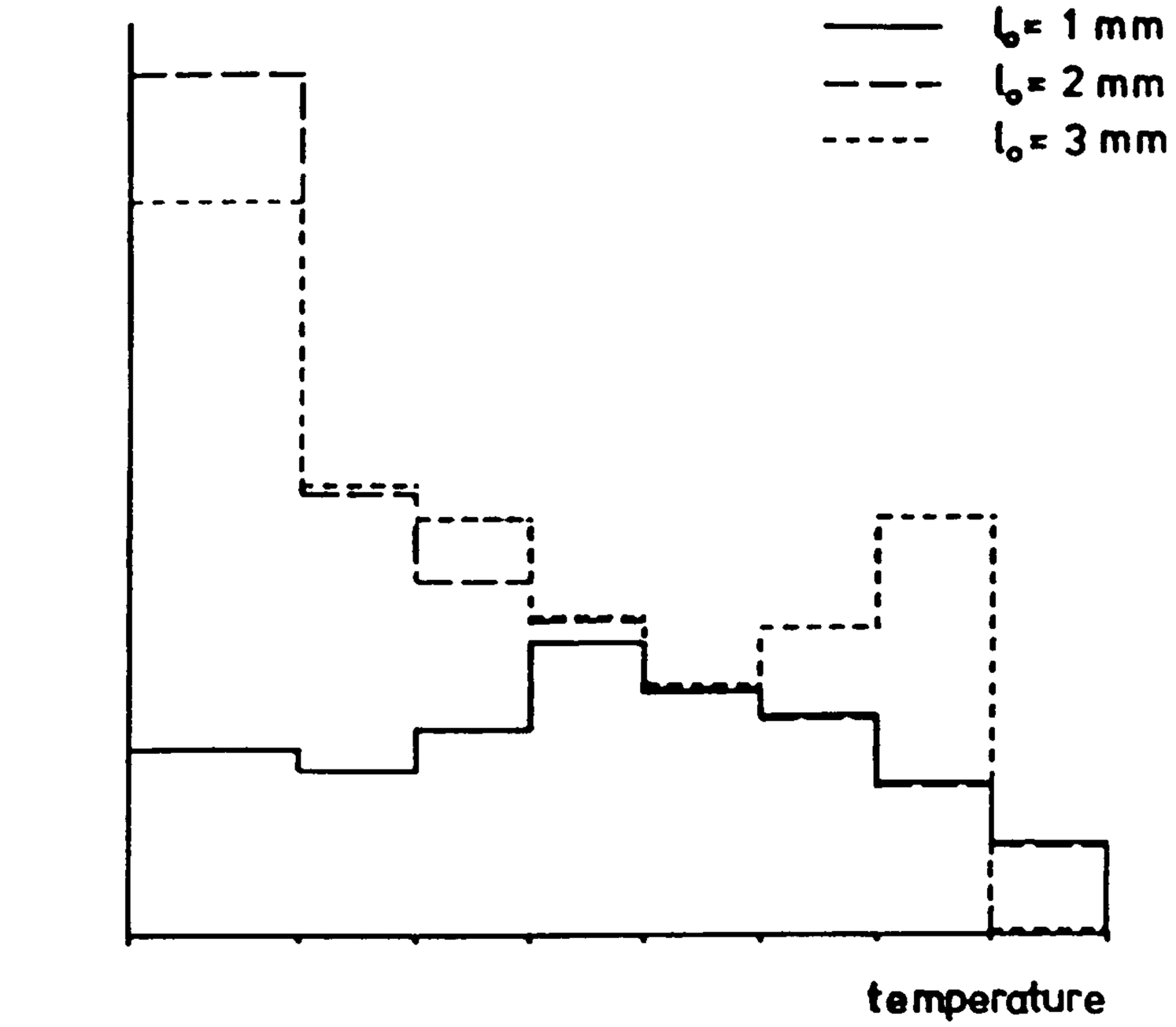

Fig. 8.7

Qualitative thermal histories (cumulative temperature/time distribution) for material at three locations in a 3 mm thick composite.

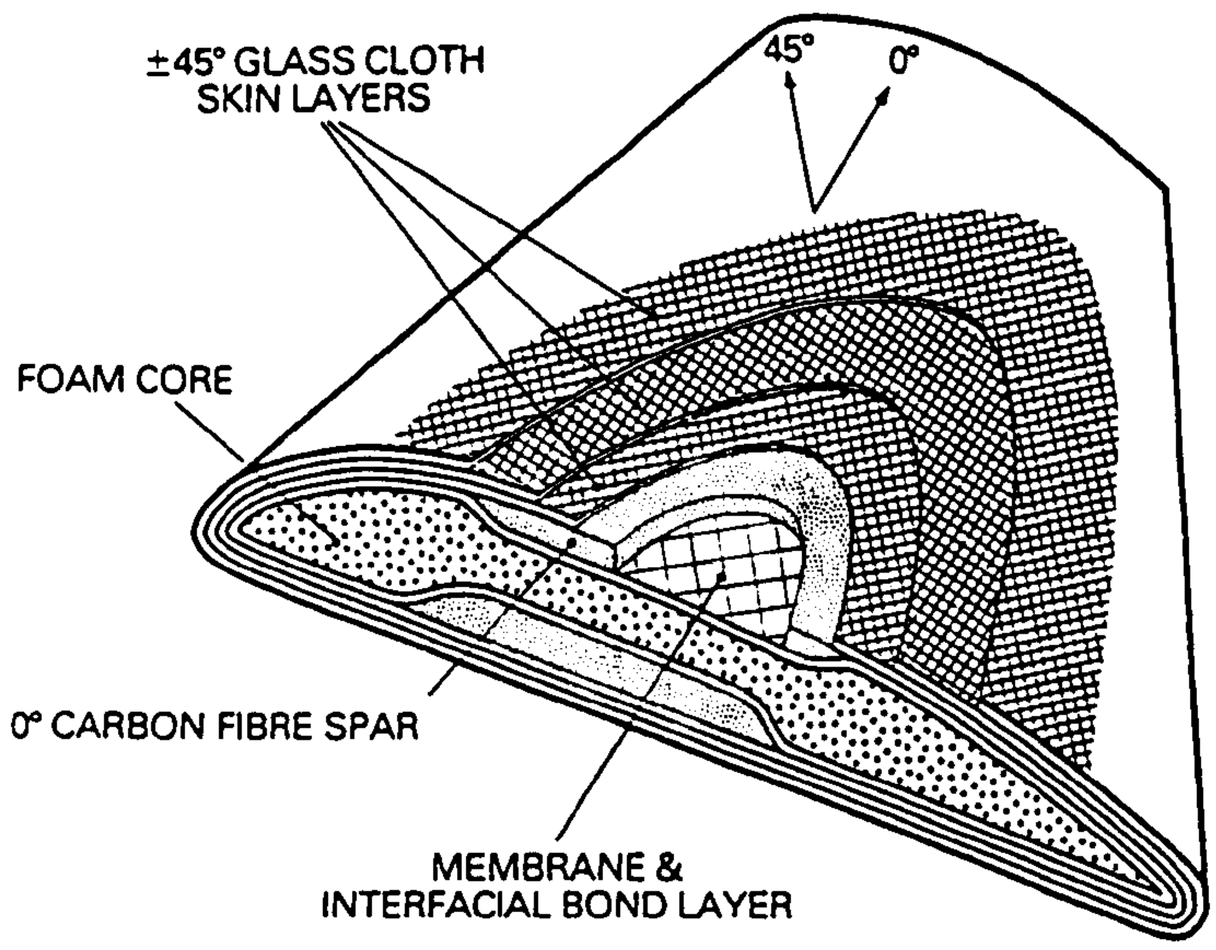

Fig. 8.8

Structure of a composite propeller blade (source: Dowty Rotol Ltd.).

Recent designs of small aircraft incorporate 'pusher' propeller blades which are located to the rear of the wing-mounted engines. At least part of the blade is thereby exposed to exhaust gases from the engine, which, when the aircraft is on the ground, may reach temperatures in the range 100°C - 160°C (Dowty Rotol Ltd., Personal Communication). These temperatures are considerably in excess of those to which common epoxy resins may be exposed in service. The objective of this study, therefore, was to investigate the transient temperature distribution within a composite propeller blade during exposure to a stream of hot exhaust gas, in order to estimate the time required for the epoxy resin-based parts of the structure to reach its limiting temperature. Calculations were confined to a two-dimensional section at a position on the blade considered to be most at risk from the exhaust gas.

8.2.2 Blade Structure and Thermal Properties

Fig. 8.9 shows the section for which calculations were performed. The polyurethane foam core is surrounded by a unidirectional high strength carbon fibre-reinforced epoxy resin, in which the reinforcement runs perpendicular to the plane of the section. The thermal conductivity is therefore isotropic in this plane. The layer of glass fibre-reinforced epoxy resin contains reinforcement in the form of a $\pm 45^{o}$ woven mat, with the plane of the mat lying perpendicular to the section (see Fig. 8.8 for a schematic view). The aerodynamic shape of the blade is provided by an isotropic high-density foam cuff surrounding the glass/epoxy resin skin.

In terms of the rate at which the temperature of the structure increases, the thermal properties of the cuff material are most critical. Measurements of thermal conductivity and specific heat were made by the Yarsley Technical Centre, using a guarded hot plate apparatus and differential scanning calorimetry. At the time the calculations were performed, only values at room temperature were available, and all thermal properties were therefore assumed to be independent of temperature. Later measurements supported this assumption.

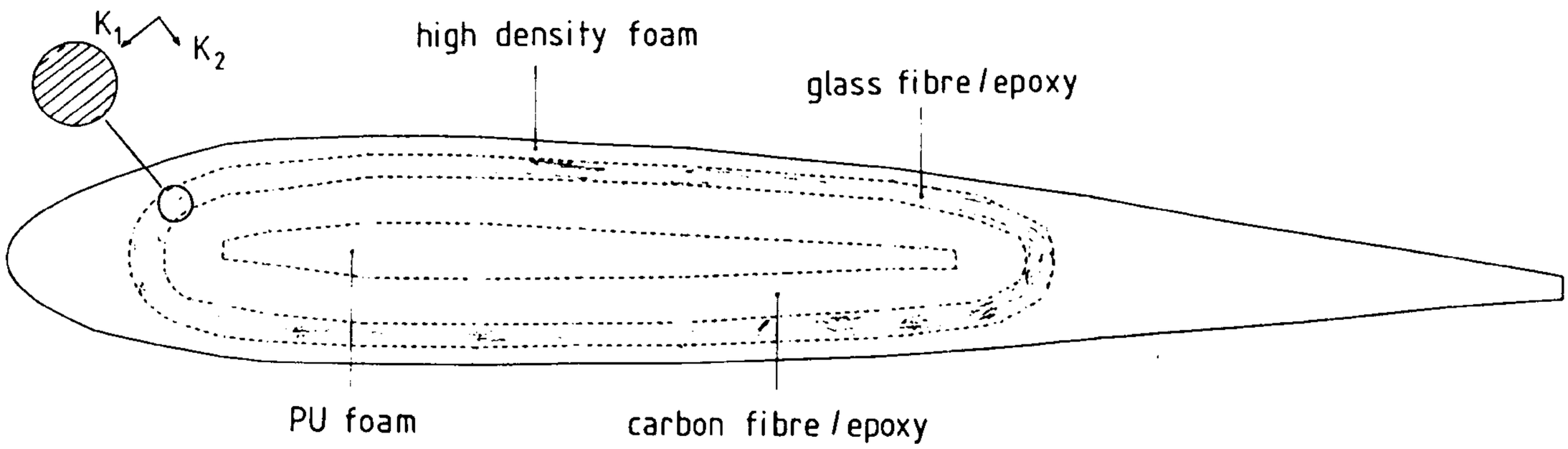

Fig. 8.9

Section of composite blade. The glass fibre/epoxy component is thermally anisotropic, with the direction of principal conductivities (K_1, K_2) varying continuously around the blade.

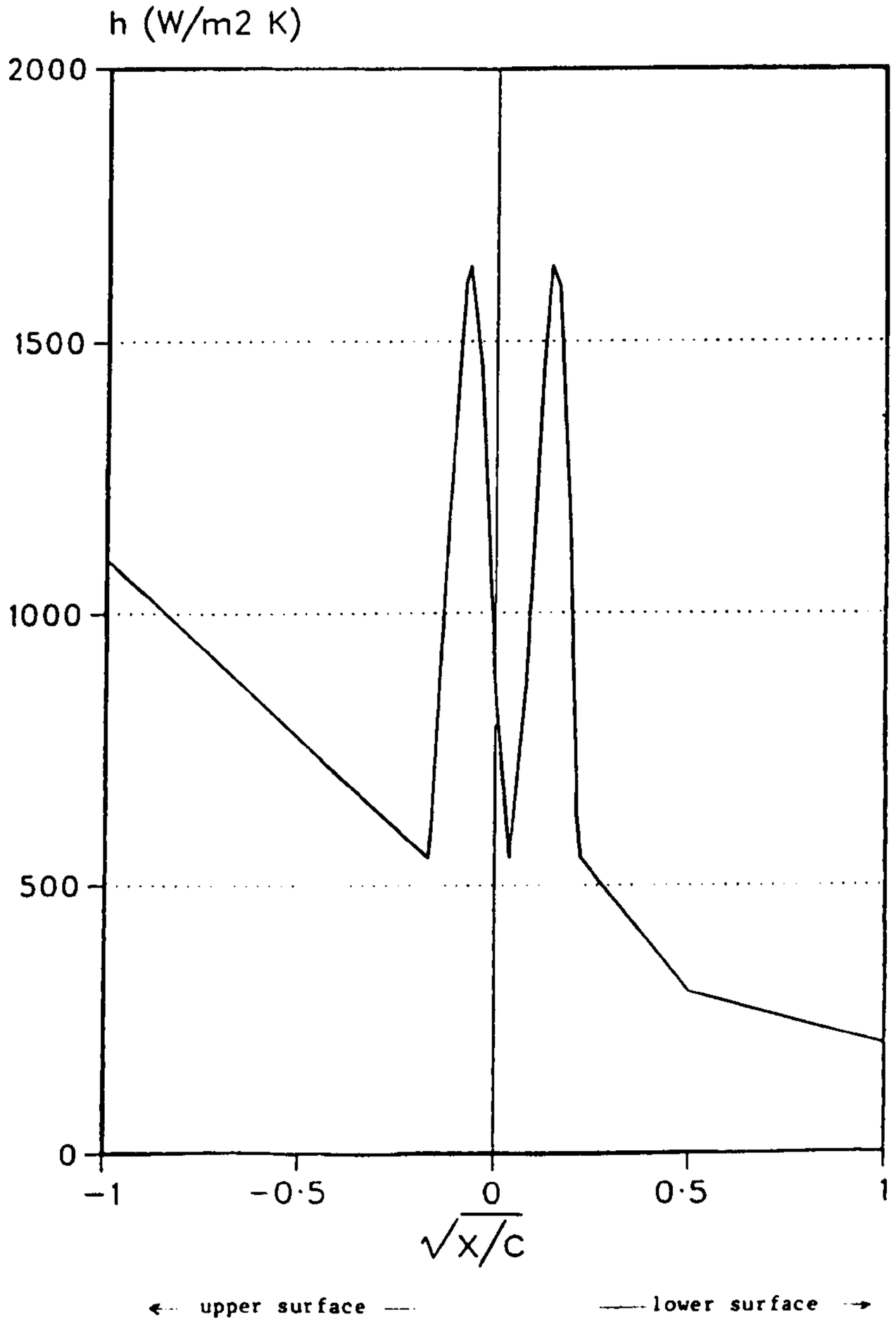

Fig. 8.10

Assumed distribution of convective heat transfer coefficient around blade surface. C is the chord of the blade, and x is measured parallel to C.

Thermal properties of the other component materials were obtained from the open literature (reviewed in 2.3). The principal thermal conductivities of a unidirectional glass fibre-reinforced epoxy resin of 50% volume fraction were taken as 0.7 W/m K and 0.4 W/m K respectively parallel and perpendicular to the reinforcement. The in-plane thermal conductivity of a $\pm 45^{o}$ fibre composite is isotropic, being equal to the mean of the two unidirectional principal conductivities (K_1 = (0.7 + 0.4) / 2 = 0.55 W/m K). Perpendicular to this plane, the thermal conductivity is the same as in the unidirectional composite (K_2 = 0.4 W/m K). The glass fibre-reinforced epoxy component was thus considered to be an orthotropic material, but with principal axes of variable orientation, as indicated in Fig. 8.9. This situation is analogous to the theoretical problem discussed in 4.2.7, concerning an orthotropic material in circular coordinates.

8.2.3 Boundary Conditions

The entire surface of the blade is subjected to convective heat transfer from the surrounding exhaust gas, which was assumed to be at a uniform and constant temperature. A detailed consideration of the air flow around the blade was beyond the scope of this study, and in the absence of published information, values of surface heat transfer coefficient were suggested by Dowty Rotol. These were estimated from Nusselt numbers in flow around a cylinder (to which the leading edge of the blade approximates) and over a flat plate. The profile is shown in Fig. 8.10. A literature search revealed no published data for aerofoils, although several workers (for example, Bayley and Priddy, 1981) have measured heat transfer coefficients around the surface of turbine blades. The form of the distribution is broadly similar, with a peak value in the range 1000 - 2000 W/m^2K at the leading edge. A finite element calculation of the temperature distribution in a cooled turbine blade exposed to a gas at over $1000^{o}C$ was reported by Zienkiewicz and Parekh (1970). They used surface heat transfer coefficients varying from 16.4×10^{3} W/m^2 K to 2.35×10^{3} W/m^2 K between leading and trailing edges.

8.2.4 Finite Element Representation

Two finite element meshes were used for calculations (Fig. 8.11); the first of these (Mesh 1) was constructed with the least number of elements consistent with the high aspect ratio of the section, while the second (Mesh 2) increased the spatial resolution near the surface. On Mesh 1, the minimum node separation was about 1 mm, which, according to Equation 6.11, suggests an initial time step of about 1.6 s. On Mesh 2, the minimum node separation is halved, which reduces Δt_{max} by a factor of 4.

A calculation with spatially-variable thermal properties was described in 6.4, and the same procedure was adopted here. Data files were written containing appropriate thermal conductivity coefficients and heat capacity for each element integration point. For those elements representing the orthotropic glass fibre-reinforced epoxy resin component, the orientation of the principal axes was measured, and the conductivity coefficients calculated according to Equation 4.13.

8.2.5 Results

Since thermal properties were assumed to be independent of temperature, it was convenient to use a normalised temperature, defined by

$$\Phi = \frac{T - T_{init}}{T_\infty - T_{init}}$$

where T_{init} is the initial (uniform) blade temperature, and T_∞ is the temperature of the exhaust gas.

Of primary interest in the calculations was the temperature of the interface between the foam cuff and the glass fibre-reinforced epoxy resin, as here the resin will first reach its limiting temperature. Fig. 8.12 shows the temperatures along this interface at successive times. It will be seen that despite the relatively high heat transfer coefficients at the leading edge of the blade, the interface temperature is lowest in this region, due to the thickness of the cuff.

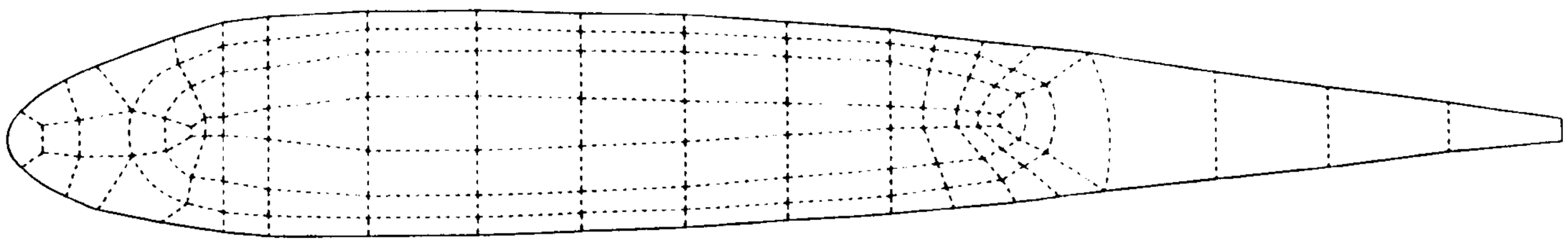

mesh 1

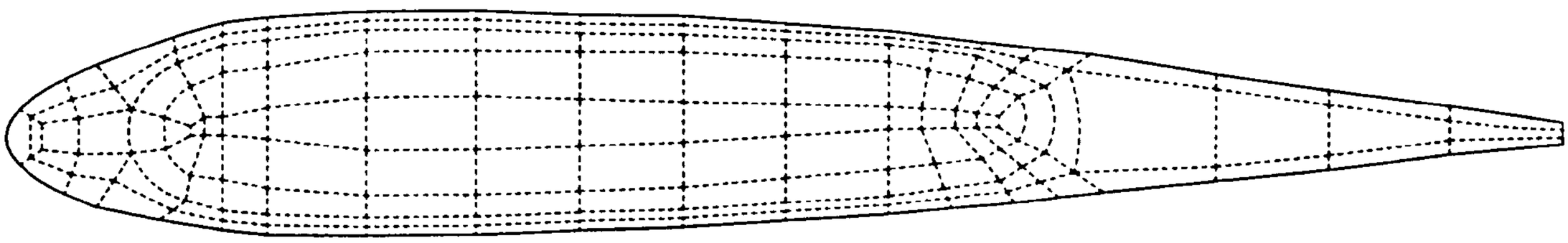

mesh 2

Fig. 8.11

Two finite element representations of the blade section.

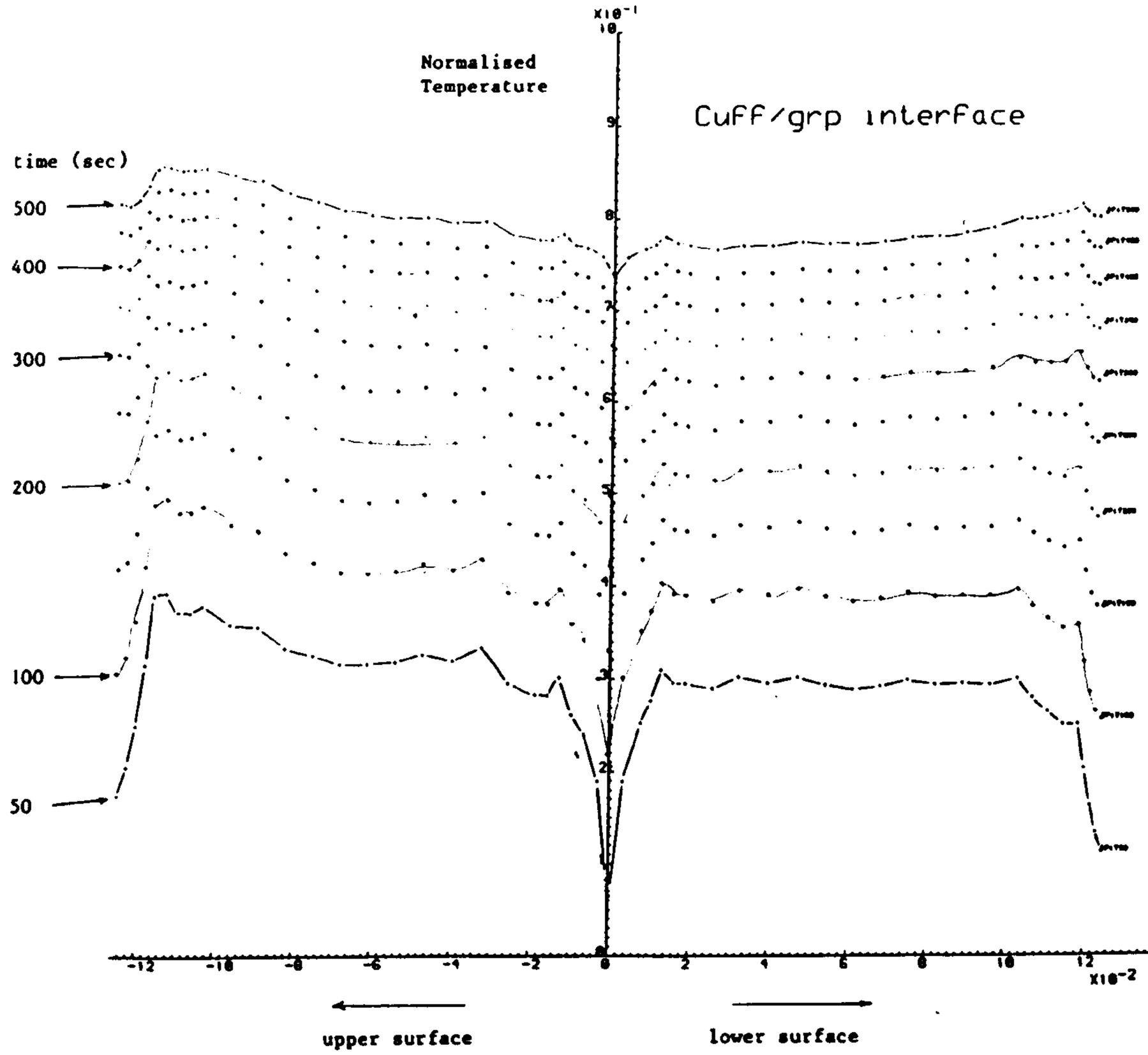

Fig. 8.12

Normalised temperature distribution around the interface between cuff and grp component, from time t = 50s to t = 500s. The ordinate zero corresponds to that part of the interface nearest to the leading edge.

The temperature gradient around the interface decreases as time advances, but throughout the calculation the hottest part of the interface is to be found near the upper surface, at $x/c \simeq 0.6$ (see Fig. 8.12).

The calculation was repeated on Mesh 2, with very little change in nodal temperatures. At the cuff/composite interface the difference in normalised temperature was less than 0.01 (that is, less than 1% of the temperature gradient $T_\infty - T_{init}$).

Having identified the most vulnerable region of the blade, the results were re-interpreted to yield a maximum exposure time for the epoxy resin system, given a limiting service temperature.

Further calculations were made to test the sensitivity of the blade temperature to the rate of heat transfer into the upper surface. It was found that large perturbations to the basic profile, amounting to ± 50% at the trailing edge, affect the maximum exposure time by only about ± 10%. This effect is explained by the low thermal conductivity of the blade cuff - even at the lowest heat transfer coefficients used, the rate of heat removal by conduction from the surface is an order of magnitude less than the rate of convective heating. Heat transfer near the blade surface is thus dominated by convection.

CHAPTER 9 : CONCLUDING REMARKS

This thesis has described the development of a finite element model of transient heat conduction in two and three-dimensional anisotropic solids. The model has been satisfactorily validated in two dimensions by comparison with mathematical solutions to anisotropic conduction problems and by measurements of the steady-state temperature distribution in a carbon fibre-reinforced epoxy resin. Two recent industrial applications of the finite element model have also been described.

9.1 CONCLUSIONS

1. A survey of the literature revealed many theoretical and empirical models of composite properties, which seek to express the effective thermal conductivity in terms of the properties and geometrical arrangement of the constituent phases. For materials of low volume fraction, such models are reasonably consistent, and may indicate useful approximate values of composite thermal conductivity. However, there is increasing divergence at higher volume fractions and in composites where the reinforcement has very different properties from the matrix (as is the case in carbon fibre-reinforced plastics). In addition, few models take into account such factors as variations in packing geometry or the presence of voids, which may depend on the method of manufacture. A more fundamental limitation of the models is that constituent properties may not be known a priori. Measurements of the thermal conductivity of carbon fibre-reinforced plastics also show considerable variation, and there are very few data above room temperature.

2. Principal thermal conductivities in unidirectional carbon fibre-reinforced epoxy resin from room temperature up to 160°C were measured on absolute and comparative apparatus with a typical experimental error of 10%. There was good agreement between the two methods at room temperature. At higher temperatures the comparative method showed very little change in longitudinal conductivity, while the absolute method gave values increasing by about 20% between

room temperature and 80°C. The latter is more consistent with trends extrapolated from published data.

3. The finite element model was validated by comparison with mathematical solutions to various anisotropic conduction problems, including nonlinear, nonhomogeneous (i.e. spatially-variable thermal conductivity) and transient cases in two dimensions. Convergence of the numerical model was demonstrated with respect to mesh size and time step. Several of the analytic solutions proved laborious to implement and often required considerable mathematical manipulation, thus emphasising the value of a reliable numerical model.

4. The experimental validation of the numerical model used measurements of steady-state surface temperatures on a cylindrical carbon fibre-reinforced epoxy resin specimen. The agreement between model and weighted mean measurements was generally within experimental error, although the scatter on individual values was up to ±10%. The temperature distribution in the composite was found to be dominated by the high anisotropy, such that the influence of errors in thermal conductivity or its temperature dependence were negligible. The largest source of uncertainty was specimen orientation.

5. There is evidently a demand in industry for a specialised model of heat conduction in composites, despite the widespread availability of large finite element programs. This resulted in the commercial use of the model in two industrial consultancies. The first was a study of thermal cycling in the fabrication of a reinforced thermoplastic by tape laying. Using measured thermal properties, the model was used to derive 'thermal histories' of the processed material. The second concerned the temperature distribution in a composite propeller blade which was subjected to heating by engine exhaust gases. The model was used to identify regions of the blade most at risk from degradation due to overheating and to estimate maximum exposure times.

9.2 FUTURE RESEARCH

Thermal Conductivity Measurement

In view of the general lack of data and the dependence of thermal properties on manufacturing route, there is a need for improved measurement techniques. An important requirement is the ability to collect large amounts of data more quickly and over a wide range of temperatures, thus permitting detailed investigation of the effects of specimen quality. Transient measurement techniques would appear to be most useful, particularly those which enable the determination of both thermal conductivity and specific heat.

Model Development

Detailed validation of the numerical model has been confined to two-dimensional conduction; although the three-dimensional version is available, more work is required before it may be used with confidence. It is anticipated that large three-dimensional finite element meshes (with more than ~1000 nodes) will be beyond the capability of the direct solution method employed in 'FEANCO-3', and demand a frontal solution technique. Also, complex three-dimensional analyses rely heavily on graphical facilities for visualisation and efficient mesh generation. It is likely, therefore, that a larger three-dimensional version of FEANCO will evolve not as a self-contained program, but as a system which interacts more closely with existing finite element packages such as PAFEC.

Nevertheless, many practical engineering problems may be addressed by a two-dimensional approximation, and useful results obtained without resorting to a computationally expensive three-dimensional analysis. In its present form, 'FEANCO-3' is likely to have a role in the preliminary analysis of heat conduction problems, which would justify the validity or otherwise of two-dimensional approximations.

Processing of Composites

Many aspects of reinforced polymer processing involve the non-isothermal flow of a viscous non-newtonian fluid, and a

complete analysis of such systems is the province of considerably more complex numerical models. In some areas, however, polymer flow is not significant, either because the entire fabrication process is carried out at a very high viscosity (as in tape laying) or because one may consider the process in discrete phases. In thermoplastics, one may isolate the heating of solid material until some or all has melted, and the solidification and cooling of the component after the forming process has been completed. With thermosetting plastics, conduction heat transfer is the dominant mechanism after the mould has been filled. An increasingly important process for thermosetting polymers is reinforced reaction injection moulding (RRIM), which is designed such that the polymerisation reaction takes place almost entirely after filling. This is particularly conducive to the separate analysis of injection and curing, and there is considerable potential for the application of two and three-dimensional anisotropic conduction models.

Thermophysical Properties

Numerical analyses of both composite components in service and polymer processing techniques place considerable demands on the quality and range of thermophysical property data. Reversible crystallisation reactions may be modelled by temperature-dependent heat capacity, while irreversible polymerisation involves internal heat generation at a rate which may depend not only on temperature but also on the recent thermal history of the material. The different molecular structure of polymers before, during and after their processing may affect thermal properties as a result of crystallisation, polymerisation, or, in some cases by stretching. There is a need for more information on polymer properties under conditions representative of those encountered in the processes themselves, which may bear little resemblance to those of the standard measurement techniques. Other necessary data, such as surface heat transfer coefficients are similarly lacking. There is considerable scope for original experimental work in this field, and it is an essential complement to numerical analysis.

REFERENCES

American Society for Testing and Materials (1974)
Steady-State Thermal Transmission Properties by ... the Guarded Hot Plate
Standard Test Method C177

Ashton J E Halpin J C and Petit P H (1969)
Primer on Composite Materials Analysis
Technomic Stamford USA

Assem D and Daniels D H W (1977)
Determination of the Thermal Conductivity of CFRP Sheet Material
Report no NLR TR 77113U Natl. Aerospace Lab. Amsterdam

Balageas D L and Luc A M (1983)
Nonstationary Thermal Behaviour of Directional Reinforced Composites
Paper AIAA-83-1471 18th Thermophysics Conf. Montreal AIAA

Bayley F J and Priddy W J (1981)
Effects of Free-Stream Turbulence ... on Heat Transfer to Turbine Blading
Trans ASME - J Engng for Power 103 60-64

Berrie M A Puttick K E Rider J G Rudman M and Whitehead R D (1981)
Thermal Probe Analysis of Orientation in Polymers and Composites
Plastics & Rubber Processing & Applications 1 129-131

Blundell D J and Osborn B N (1983)
The Morphology of Poly(aryl-ether-ether-ketone)
Polymer 24 953-958

Brennan J J Bentsen L D and Hasselman D P H (1982)
Determination of the Thermal Conductivity ... by the Composite Method
J Materials Sci 17 2337-2342

Brewster I and Cattenach J B (1983)
Engineering with Long Fibre Thermoplastic Composites
paper 3 SAMPE Conf. Engineering with Composites London

British Iron and Steel Research Association (1953)
Physical Constants of Some Commercial Steels at Elevated Temperatures
Butterworths Sci Pubs London

British Standards Institution (1973)
Methods for Determining Thermal Insulating Properties ...
BS 874

Bruggeman D (1935)
Dielectric Constant and Conductivity of Mixtures of Isotope Materials
Ann Phys 24 636

Carslaw H S and Jaeger J C (1959)
Conduction of Heat in Solids
Oxford University Press

Central Statistical Office (1984)
Annual Abstract of Statistics no 120 1984 edition
HMSO London

Chang Y P (1977)
Analytical Solution for Heat Conduction in Anisotropic Media ...
Int J Heat Mass Transfer 20 1019-1028

Chang Y P Kang C S and Chen D J (1973)
The Use of Fundamental Greens Functions ... in Anisotropic Media
Int J Heat Mass Transfer 16 1905-1918

Chang Y P and Tsou R C H (1977a)
Heat Conduction in an Anisotropic Medium ...
Trans ASME - J Heat Transfer 99 41-46

Chang Y P and Tsou R C H (1977b)
Heat Conduction in an Anisotropic Medium ...
Trans ASME - J Heat Transfer 99 132-134

Cheng S C and Vachon R I (1969)
The Prediction of the Thermal Conductivity of ... Mixtures
Int J Heat Mass Transfer 12 249-264

Choy C L (1977)
Thermal Conductivity of Polymers
Polymer 18 984-1004

Clayton W A (1971)
Constituent and Composite Thermal Conductivities of ... Ablators
AIAA Paper no 71-380 AIAA/ASME Conf. Anaheim Calif. USA

Clayton W A Kennedy P B Cotton J E Fransisco A C
  Fabish T J and others (1968)
Thermal Properties of Ablative Chars
US Air Force Materials Lab report AFML-TR-67-413

Clements D L and Tauchert T R (1979)
Stationary Heat Conduction in an Anisotropic Slab
  Containing a Crack
Letters Appl Eng Sci 17 1141-1149

Cluley A P (1983)
Carbon Fibre Reinforced Thermoplastics High Performance
  Engng Materials
paper 5 SAMPE Conf. Engineering with Composites London

Cobble M H (1974)
Nonlinear Anisotropic Temperature Distribution in a Wedge
Int J Heat Mass Transfer 17 379-380

Danielson G C and Sidles P H (1969)
Thermal Diffusivity and Other Non-steady-state Methods
in Thermal Conductivity vol 2 (ed Tye R P) 149-201
  Academic Press

Dawson D M and Briggs A (1981)
Prediction of the Thermal Conductivity of Insulation
  Materials
J Materials Sci 16 3346-3356

Deshpande M S Bogaard R H and Taylor R E (1981)
Variances in the ... Thermal Diffusivity on ...
  Carbon-Carbon Composites ...
Int J Thermophysics 2 357-370

Doe R A and Holt D (1984)
The Composite Technology of a Main Rotor Blade
paper 9 Fibre Reinforced Composites 84 PRI Conf. Liverpool

Donea J (1972)
Thermal Conductivities Based on Variational Principles
J Composite Materials 6 262-266

Dutre W L (1985)
European Modelling Group for Solar Systems
final report CEC contract ESA-M-078-B KU Leuven
  Heverlee Belgium

Edwards D K (1980)
Anisotropic Conduction and Surface Radiation around a Hollow Cylinder
Trans ASME - J Heat Transfer 102 706-708

Edwards M F and Ellis D I (1982)
The Importance of Heat Transfer in Polymer Processing
Physics in Technology 13 91-97

Gerald C F (1978)
Applied Numerical Analysis
Addison-Wesley

German A (1976)
The Thermal Conductivity of some Alloys of Zirconium
PhD Thesis University of Salford

Gille J P (1969)
Development of Advanced Materials for Integrated Tank Insulation System ...
report NASA-CR-102570 US National Aeronautics and Space Admin.

Gogol W and Furmanski P (1980)
Some Investigations of Effective Thermal Conductivity of ... Composites
J Composite Materials 14 167-176

Greig D (1982)
Thermal Conduction in Oriented Polymers
chap 3 of Developments in Oriented Polymers-1 Applied Sci London

Griffin G J L (1974)
Thermally Anisotropic Plastics Bearing Materials
Polymer Science and Tech 5-B 605-621

Grove S M Short D and Bacon D H (1984)
Modelling Heat Transfer in Reinforced Thermoplastics Processing
paper 44 14th Reinforced Plastics Congress British Plastics Fed

Han L S (1982)
Transient Heat Flow along Uni-Directional Fibers in Composites
report AFWAL-TR-82-3061 Wright-Patterson AFB Ohio USA

Han L S and Boyes W F (1983)
Thermal Conductivities and Diffusivities of Graphite-Epoxy Composites
report AFWAL-TR-83-3002 Wright-Patterson AFB Ohio USA

Han L S and Cosner A A (1981)
Effective Thermal Conductivities of Fibrous Composites
Trans ASME - J Heat Transfer 103 387-392

Harris J P (1980)
Thermal Conductivity of High Modulus Fibre Reinforced Composites
PhD Thesis University of Salford

Harris J P Yates B Batchelor J and Garrington P J (1982)
The Thermal Conductivity of Kevlar Fibre-Reinforced Composites
J Materials Sci 17 2925-2931

Henshell R D (1975)
PAFEC 75 Theory, Results
Pafec Ltd Nottingham

Hertz J Christian J L and Varlas M (1972)
Advanced Composite Applications for Spacecraft and Missile
report AFML-TR-71-186 vol 2 US Air Force Materials Lab

Horvay G Mani R Velushami M A and Zinsmeister G E (1973)
Transient Heat Conduction in Laminated Composites
Trans ASME - J Heat Transfer 95 309

Hrenikoff A (1941)
Solution of Problems in Elasticity by the Framework Method
J Appl Mech A8 169-175

Hull D (1981)
An Introduction to Composite Materials
Cambridge University Press

Imperial Chemical Industries plc (1984)
Manufacturing and Fabricating with Aromatic Polymer Composite APC-2
Provisional Data Sheet APC PD4 ICI Petrochem & Plastics Divn Welwyn

Inger-Hansz J (1789)
Journal de Physique 34 380
reported by D'Andrea G PhD Thesis Rensslaer Polytech Inst Troy NY (1969)

Jaeger L G (1966)
Cartesian Tensors in Engineering Science
Pergamon

Johnson W and Watt W (1967)
Structure of High Modulus Carbon Fibre
Nature 215 384-386

Kalnin I L Ram M J and Dix R (1972)
Exploratory Development of Low Thermal Conductivity Carbon Fibre
report AFML-TR-72-151-PT-1 US Air Force Materials Lab

Kao T K Hardisty H and Wallace F J (1983)
An Energy Balance Approach to the Finite Element Method applied to Heat Transfer Analysis
Int J Mech Eng Education 11 1-19

Katayama K Saito A Kobayashi N and Kodama Y (1974)
Transient Heat Conduction in Anisotropic Solids
Bull JSMA 17 1073-1080

Kilian H G and Pietralla M (1978)
Anisotropy of Thermal Diffusivity of Uniaxial Stretched Polyethylenes
Polymer 19 664-672

Kim D H (1972)
The Thermophysical Properties of Fibre Reinforced Plastics
AIAA Paper no 72-366 Proc 13th Conf. (AIAA/ASME/SAE) San Antonio Texas

Knappe W and Martinez-Freire P (1965)
Measuring and Calculating the Thermal Conductivity of GFRP
Kunststoffe 55 776-779 (1965) trans German Plast 55 12-14

Knappe W Ott H-J and Wagner G (1978)
Calculation and Measurement of Thermal Conductivity of GRP
Kunststoffe 68 426-429

Knibbs R H Baker D J and Rhodes S (1971)
The Thermal and Electrical Properties of Carbon Fibre ... Composites
Proc 26th Ann Tech Conf. Soc Plastics Industry section 8-F 1-10

Kozhevnikov I G and Kudryaceva G M (1974)
Thermal Conductivity of some GRPs from 90-470K
Plasticheskie Massy 7 72-73

Laubitz M J (1969)
Measurement of the Thermal Conductivity of Solids ...
in Thermal Conductivity vol 1 (ed Tye R P) Academic Press

Laura P A A Gutierrez G H and Sarmiento G S (1979)
Application of Conformal Mapping to ... Thermally Orthotropic Plates
J Nuclear Eng Design 52 337-342

Lee H J and Taylor R E (1975)
Thermophysical Properties of Carbon/Graphite Fibres
Carbon 13 521-527

Lewis T B and Nielsen L E (1968)
Viscosity of Dispersed and Aggregated Suspensions of Spheres
Trans Soc Rheol 12 421-443

Lovell D R (compiler) and Pamington D (ed) (1982)
World-Wide Carbon Fibre Directory
Pammac Directories Ltd Slough

Maries K (1976)
Prediction of Thermal Conductivity of GRP Laminates
Current Paper CP70/76 Building Research Est Watford

McCarthy R (1981)
Fifteen Years Experience with Composite Propeller Blades
SAMPE Conf (European Chapter) Cannes France

McWhorter J C and Sadd M H (1980)
Numerical Anisotropic Heat Conduction Solutions ...
Trans ASME - J Heat Transfer 102 308-311

Mulholland G P and Gupta B P (1975)
Solution of the Anisotropic Heat Transfer Equation by Orthonormal Polynomials
Trans CSME 3 61-66

Mulholland G P and Gupta B P (1977)
Heat Transfer in a Three-Dimensional Anisotropic Solid of Arbitrary Shape
Trans ASME - J Heat Transfer 99 135-137

Muller F H (1967)
Uniaxial Stretching and Anisotropy
J Polymer Sci (part C) 20 61-76

Murakami H Hegemier G A and Gurtman G A (1980)
A Nonlinear Mixture Theory for ... Fiber Reinforced Composites
Int J Solids Structures 16 421-432

Nielsen L (1974)
The Thermal and Electrical Conductivity of Two-Phase Systems
Ind Eng & Chem Fundam 13 17-20

Nye J F (1957)
Physical Properties of Crystals
Clarendon Press

Ott H J (1981)
Thermal Conductivity of Composite Materials
Plastics and Rubber Processing and Applications 1 9-24

Ozisik M N (1980)
Heat Conduction
Wiley-Interscience

Ozisik M N and Shouman S M (1980)
Transient Heat Conduction in an Anisotropic Medium in Cylindrical Coordinates
J Franklin Inst 309 457-472

Padovan J (1972)
Temperature Distributions in Anisotropic Shells of Revolution
AIAA Journal 10 60-64

Padovan J (1973)
Transient Temperature Distribution of an Anisotropic Half Space
AIAA Journal 11 565-566

Padovan J (1974a)
Steady Conduction of Heat in ... Anisotropic Media by Finite Elements
Trans ASME - J Heat Transfer 96 313-318

Padovan J (1974b)
Solution of Anisotropic Heat Conduction Problems by Monte Carlo Procedures
Trans ASME - J Heat Transfer 96 428-430

Padovan J (1974c)
Quasi-Analytical Finite Element Procedure for ... Anisotropic ... Solids
Int J Num Meth Eng 8 295-310

Padovan J (1975a)
Solution of Transient Temperature Fields in Laminated Anisotropic Slabs ...
Int J Eng Sci 13 247-260

Padovan J (1975b)
Conduction in Multiply Connected Thermally Anisotropic Domains
Letters Heat Mass Transfer 2 371-380

Parrott J E and Stuckes A D (1975)
Thermal Conductivity of Solids
Pion

Pilling M W Yates B Black M A and Tattersall P (1979)
The Thermal Conductivity of Carbon Fibre-Reinforced Composites
J Materials Sci 14 1326-1338

Poon K C (1979)
Transformation of Heat Conduction Problems ... Anisotropic to Orthotropic
Letters Heat Mass Transfer 6 503-511

Poon K C Tsou R C H and Chang Y P (1979)
Solution of Anisotropic Problems ... by Coordinate Transformation
Trans ASME - J Heat Transfer 101 340-345

Poon K C and Chang Y P (1978)
Transformation of Heat Conduction Problems from Anisotropic to Isotropic
Letters Heat Mass Transfer 5 215-221

Powell P C (1983)
Engineering with Polymers
Chapman and Hall

Powell R W and Tye R P (1960)
Thermal and Electrical Conductivities of Nickel-Chromium (Nimonic) Alloys
The Engineer 209 729-732

Prigogine I (1967)
Introduction to the Thermodynamics of Irreversible Processes
Wiley Interscience

Progelhof R C Throne J L and Ruetsch R R (1975)
Methods of Predicting Thermal Conductivity of Composite Systems A Review
Proc Conf Soc Plast Engrs Akron Ohio (October)

Ratcliffe E H (1965)
The Thermal Conductivities of Plastics with ... Fibre Reinforcement
Appl Mater Res 5 200-201

Rayleigh Lord (1892)
On the Influence of Obstacles ... on the Properties of a Medium
Phil Mag 34 481-502

Russell H W (1935)
Principles of Heat Flow in Porous Insulation
J Amer Ceramic Soc 18 1-5

Schneider G E and Romilly D (1979)
The Apparent Thermal Conductivity of Long Cylindrical Fibres in a Matrix
ASME Paper 79-WA/HT-42

Segerlind L J (1976)
Applied Finite Element Analysis
Wiley

Springer G S and Tsai S W (1967)
Thermal Conductivities of Unidirectional Materials
J Composite Materials 1 166-173

Summerscales J (1983)
The Mechanical Properties of ... Hybrid Reinforced Plastics
PhD Thesis CNAA

Tadmor Z and Gogos C G (1979)
Principles of Polymer Processing
Wiley-Interscience

Tanaeva S A Domorod L S and Evseeva S A (1980)
Special Features of Heat Transfer in Carbon and Glass Fibre Materials ...
J Eng Phys 39 1353-1356

Tauchert T R and Akoz A Y (1975)
Stationary Temperature and Stress Fields in an Anisotropic Elastic Slab
Trans ASME - J Appl Mech 97 647-650

Taylor R (1980)
Construction of Apparatus for Heat Pulse Thermal Diffusivity Measurements
J Phys E: Sci Instrum 13 1193-1199

Taylor R and Procter R N (1981)
Measurement of Thermal Diffusivity of Carbon Fibre-Carbon Composites ...
Final Report AFOSR-TR-81-0638 AFOSR Bolling AFB Washington DC

Thornburgh J D and Pears C D (1965)
Prediction of the Thermal Conductivity of Filled and Reinforced Plastics
ASME Paper 65-WA/HT-4

Touloukian Y S and Ho C Y (1977)
Thermophysical Properties of Selected Aerospace Structural Materials pt II
Hemisphere Pubs

Trewin E M Turner R F and Cluley A P (1980)
Carbon Fibre Reinforced Thermoplastics A Cost Effective Material ...
Advances in Composite Materials (ICCM-3) Paris 1796-1813

Truong H V and Zinsmeister G E (1978)
Experimental Study of Heat Transfer in Layered Composites
Int J Heat Mass Transfer 21 905-909

Tsou F K Chou P C and Singh I (1974)
Apparent Tensorial Conductivity of Layered Composites
AIAA Journal 12 1693-1698

Turhan D and Tuna O N (1975)
A Heat Conduction Theory for Layered Composites
METU J Pure Appl Sci 8 69-93

Turner M J Clough R W Martin H C and Topp L J (1956)
Stiffness and Deflection Analysis of Complex Structures
J Aero Sci 23 805-823, 854

Volga V I Frolov V I and Usov V K (1973)
Thermal Conductivity of Carbon Fibre
Inorganic Mater 9 643-644

Voronkov V A Sukhareva L A and Zubov P I (1980)
Apparatus ... to Determine the Anisotropic State of Oriented Polymer Materials
J Eng Phys 37 1202-1205

Willis J R (1977)
Bounds ... for the Overall Properties of Anisotropic Composites
J Mech Phys Solids 25 185-202

Woolman J and Mottram A I M (1964)
The Mechanical and Physical Properties of the British Standard EN Steels Vol 1
Pergamon Press

Wung P M and Tauchert T R (1981)
Stationary Temperature Distribution in an Orthotropic Pressure Vessel ...
Nuclear Eng and Design 64 347-359

Ziebland H (1977)
The Thermal and Electrical Transmission Properties of Polymer Composites
in Polymer Engineering Composites Appl Sci 317-362

Zienkiewicz O C (1977)
The Finite Element Method
McGraw-Hill

Zienkiewicz O C and Cheung Y K (1965)
Finite Elements in the Solution of Field Problems
The Engineer 220 507-510

Zienkiewicz O C and Parekh C J (1970)
Transient Field Problems ... Analysis by Isoparametric Finite Elements
Int J Num Meth Heat Transfer 2 61-71

Zimmerman R H (1981)
Predicting the Transverse Conductivity of Unidirectional ...
report AFWAL-TR-80-3155 Wright-Patterson AFB Ohio USA

APPENDIX I ' FEANCO ' COMPUTER IMPLEMENTATION

This appendix gives details of the computer implementation of the program ' FEANCO ' (Finite Elements for ANisotropic COnduction), and includes a complete listing of the FORTRAN source file. Details are also given of ' FEANCO-3 ', the three-dimensional version of the finite element model.

A-I.1 GENERAL PRINCIPLES

The program is written in FORTRAN 77, and is approximately 1700 lines in length. The storage requirement is quite large - the two-dimensional version listed in A-I.4, which accepts meshes of up to 500 nodes, 200 elements with a maximum bandwidth of 75, occupies about 160 kbytes in executable form on a Prime 9950 mainframe computer. This is due to the fact that the components of the global stiffness matrix and force vector (Equation 4.15) are stored in individual arrays, rather than added directly into the basic conduction matrix as soon as the coefficients have been calculated. Although this procedure is inefficient in terms of storage, it leads to economies in execution time, particularly in transient problems requiring iteration with nonlinear properties. The program listed in A-I.4 is completely self-contained and includes appropriate subroutines for matrix manipulation and equation solving. The definition of parameters for a particular calculation and the names of appropriate data files are contained in a single control file, the structure of which is described in Appendix II.

Fig. A-I.1 illustrates the structure of FEANCO in the form of a flow chart, and is largely self-explanatory. Further description of the important subroutines is given below.

A-I.2 FEANCO SUBROUTINES

Subroutine BASE computes the conduction component

Fig. A-I.1

Flow chart of the finite element program FEANCO

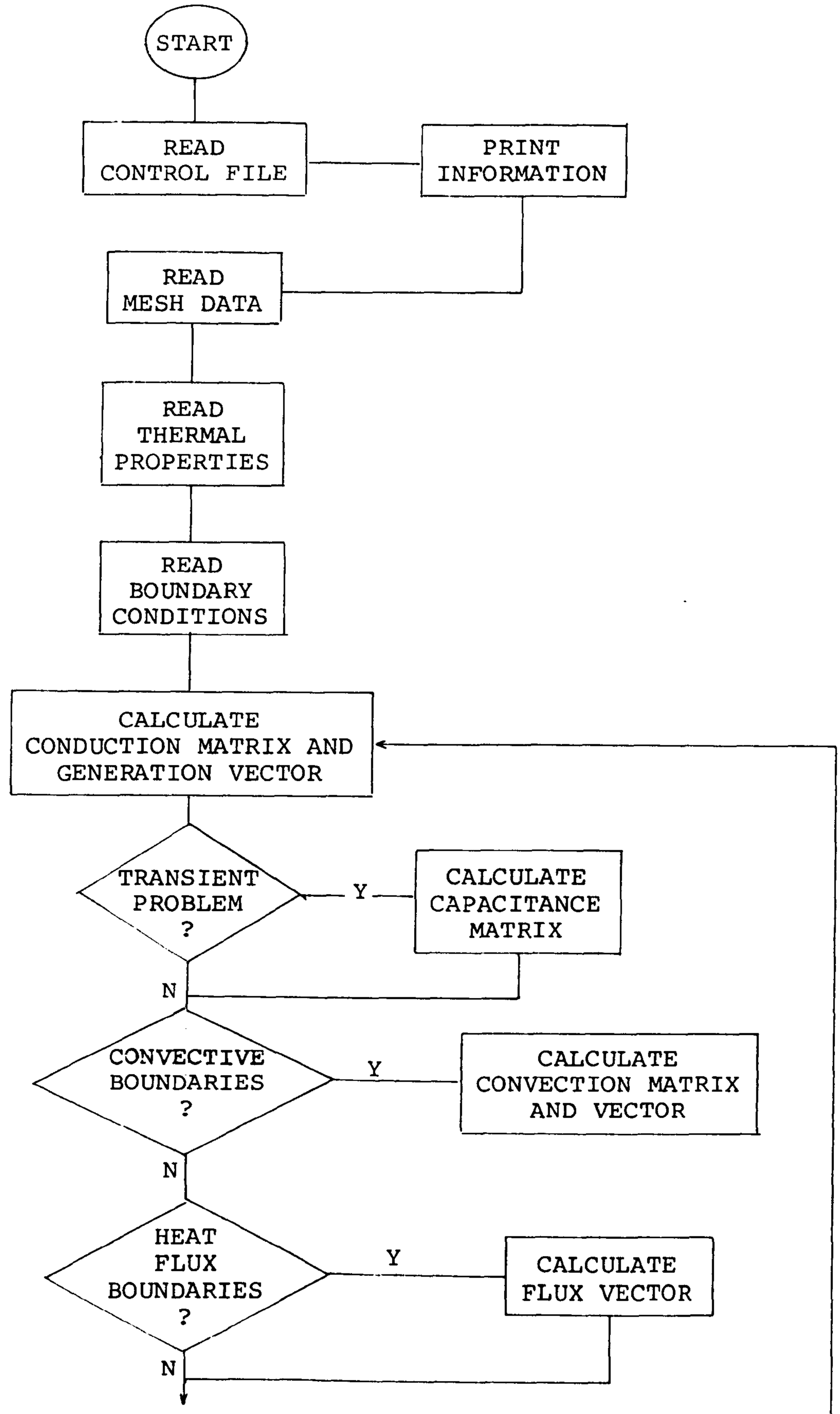

Fig. A-I.1 (cont.)

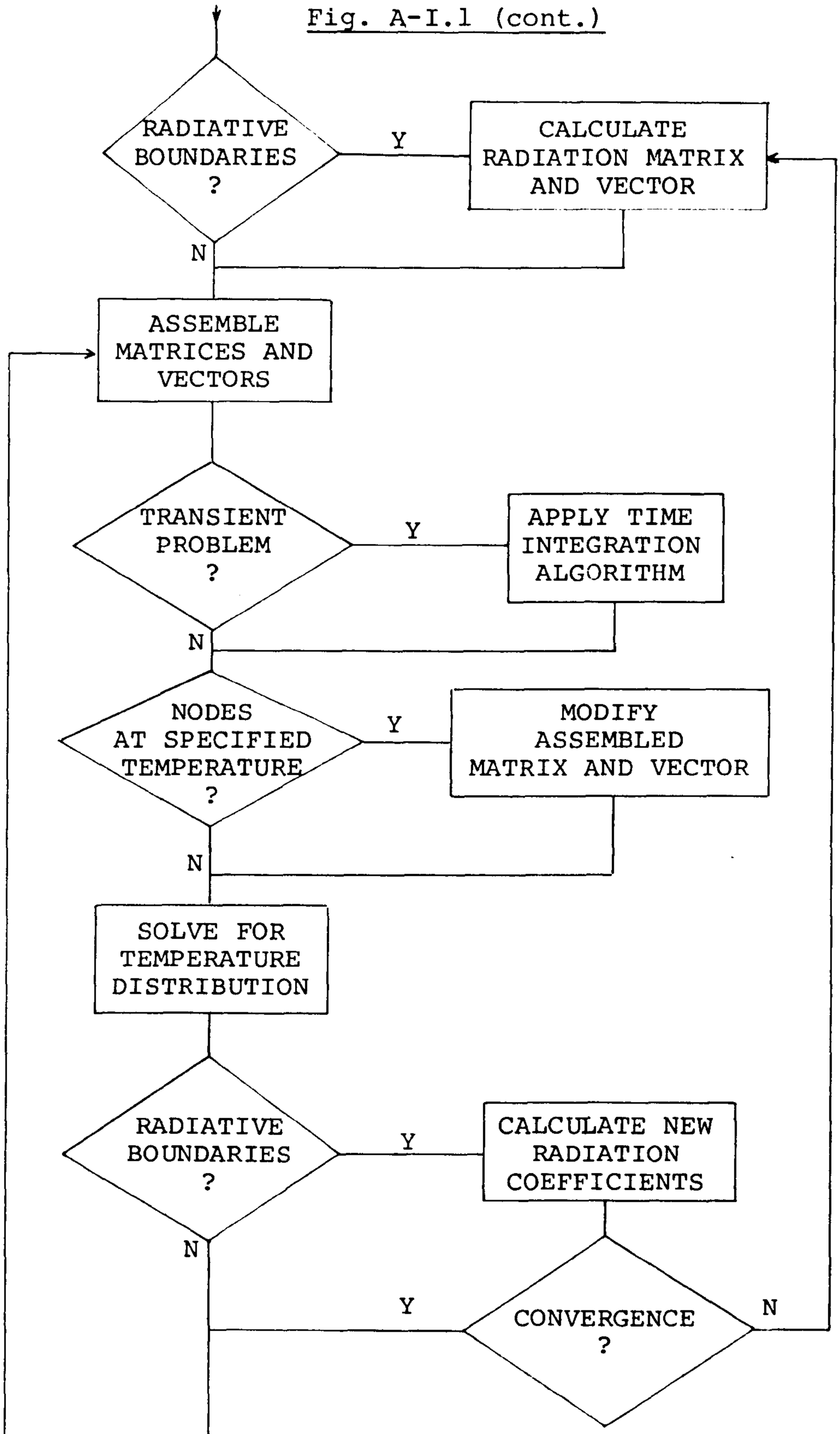
RADIATIVE BOUNDARIES ?
Y
CALCULATE RADIATION MATRIX AND VECTOR
N
ASSEMBLE MATRICES AND VECTORS
TRANSIENT PROBLEM ?
Y
APPLY TIME INTEGRATION ALGORITHM
N
NODES AT SPECIFIED TEMPERATURE ?
Y
MODIFY ASSEMBLED MATRIX AND VECTOR
N
SOLVE FOR TEMPERATURE DISTRIBUTION
RADIATIVE BOUNDARIES ?
Y
CALCULATE NEW RADIATION COEFFICIENTS
N
CONVERGENCE ?
Y
N

Fig. A-I.1 (cont.)

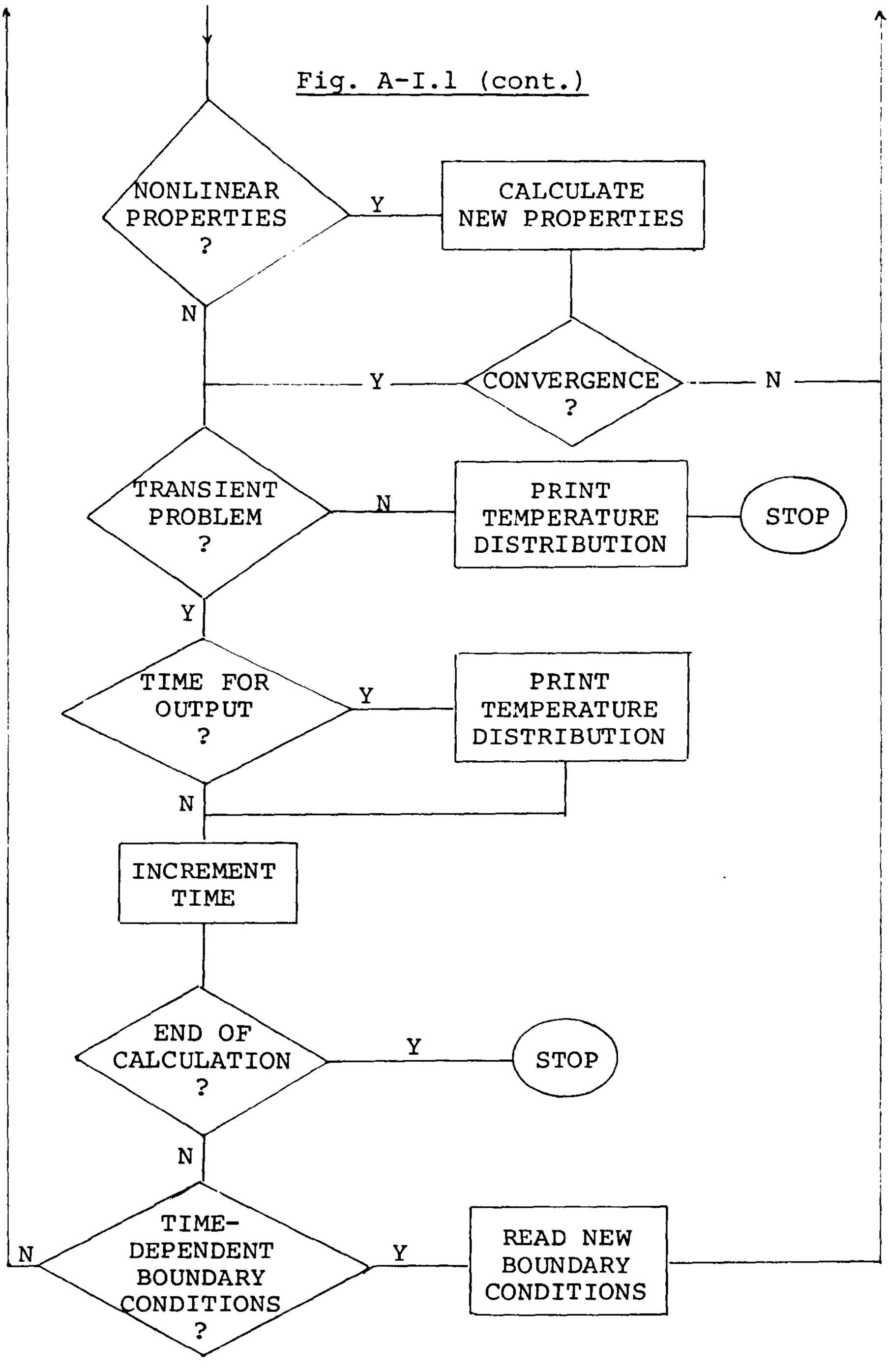
NONLINEAR PROPERTIES ?
Y
CALCULATE NEW PROPERTIES
N
CONVERGENCE ?
Y
N
TRANSIENT PROBLEM ?
N
PRINT TEMPERATURE DISTRIBUTION
STOP
Y
TIME FOR OUTPUT ?
Y
PRINT TEMPERATURE DISTRIBUTION
N
INCREMENT TIME
END OF CALCULATION ?
Y
STOP
N
TIME-DEPENDENT BOUNDARY CONDITIONS ?
N
Y
READ NEW BOUNDARY CONDITIONS

of the global stiffness matrix (the first term in Equation 5.15a) and the contribution to the global force vector due to internal heat generation (the first term in Equation 5.15c). The procedure of numerical evaluation of the element integrals has been detailed in 5.4. In this case, the order of the polynomial to be integrated requires only two values of each of the local coordinates r and s (see Equation 5.22), for which the weight coefficients W_i are unity. The thermal property matrix (Equation 5.6) is established for each of the integrating points, thus allowing an accurate representation of spatially-varying properties, as discussed in 5.10. The individual element matrices (as defined by Equations 5.15) are not calculated as such; instead the contribution from each integrating point is added directly into the global conduction matrix (BM) and the global generation vector (GV). Using the notation of Chapter 5,

$$BM = \sum_{e=1}^{E} \int_{A^e} \tilde{\underline{B}}\ \underline{D}\ \underline{B}\ dA \quad \text{and} \quad GV = \sum_{e=1}^{E} \int_{A^e} \dot{g}\ \tilde{\underline{N}}\ dA \,. \tag{AI.1}$$

where the integrals over each element are evaluated according to Equations 5.21 and 5.22.

The operation of subroutine CAP in transient calculations is similar to that of BASE, except that the polynomial under the area integral for the capacitance matrix (Equation 5.15b) requires three numerical values of each of the local coordinates and has weight coefficients less than unity. The heat capacity (ρC_p) is taken to be constant over each element. The global capacitance matrix is defined by Equation 5.16 .

Subroutine CONV deals with the contributions to the global stiffness matrix and the global force vector due to convection (the second and third terms in Equations 5.15a and 5.15c respectively). As in subroutine CAP, the form of the polynomial requires three points for numerical integration.

Here, however, the integration is to be performed along the convective edge of the element in question, so the subroutine first locates this edge in terms of local node numbers and fixes the value of the appropriate natural coordinate (either r or s = - 1 or + 1). Integration is then carried out accordingly to Equations 5.23.

The procedure in subroutines FLUX and RADN for the heat flux vector (QV) and the radiation matrix (RM) and vector (RV) is entirely analogous to that described above. The global stiffness matrix and force vector are then assembled in subroutine ASSMBL. In the notation of Chapter 5

$$\underline{C} = BM + CM + RM \quad \text{and} \quad \underline{F} = GV + CV - QV + RV$$

In the FORTRAN program, $\underline{C}$ and $\underline{F}$ are stored in the arrays A (I,J) and B (I). For transient calculations, the finite difference algorithm (Equation 5.24) is then applied in subroutine INTGRT, so that matrix A now contains the quantity $(\underline{C}/\Delta t + \underline{K}\omega)$, while the vector B becomes the right hand side of Equation 5.24.

All the matrices referred to here are characterised by the bandwidth calculated from the mesh data in the main program, and are stored in the compact form described in 5.7. Subroutine MODIFY alters coefficients in matrix A and vector B to account for nodes at which the temperature has been prescribed, and is a more compact version of the listing given by Segerlind (1976).

The matrix equation (A.T = B) is now ready for solution, following the standard procedure of decomposition described in 5.7. Again, FORTRAN listings given by Segerlind (1976) have been adapted in subroutine SOLVE. If an 'accurate' solution is requested, this subroutine also calculates the residual vector and iterates until every component of the correction vector (see 5.7) is less than 10^{-5}.

Before the current solution (stored in vector T1) is accepted

as the final temperature distribution, further iteration may be required if a radiative boundary is present or if nonlinear thermal properties are involved. In the former instance, the newly-calculated temperatures are used to obtain a new set of radiation heat transfer coefficients according to Equation 5.29, having evaluated the mean of the three nodal temperatures along a radiating edge (subroutine COEFFS). Convergence (in subroutine CONVRG) requires that each pair of new and old coefficients differ by 1% or less; if not, the program returns to subroutine RADN, and the calculation is stopped if more than 10 iterations occur.

If thermal conductivity and/or heat capacity are temperature-dependent, new properties are calculated in subroutines NEWK and NEWCP respectively and tested for convergence by comparison with the current values. These values are obtained by linear interpolation in subroutines INTERK and INTER, using input data comprising thermal properties at given temperatures (see Appendix II). If any of the thermal properties so calculated differ by more than 1% from the current values, then these are returned to subroutine BASE and the temperature distribution is re-solved.

The remainder of the program is mostly concerned with output, and requires no detailed explanation. If the problem includes time-dependent boundary conditions, then subroutine NEWBC is entered. Here, the appropriate data file is opened and read sequentially until information for time beyond the current value is found; control then returns to the main program with the previous block of boundary condition data.

A-I.3 PRINCIPAL FORTRAN VARIABLES

Two and three dimensional arrays and one-dimensional vectors are denoted by indices I, J, K. Figures in brackets refer to equations in the main text.

Main Program

A(I,J)	assembly of global stiffness matrices for solution	(5.25)
B(I)	assembly of global vectors	(5.25)
BCNAME	name of data file containing intitial boundary conditions	
BCTIME	name of data file giving time-dependent boundary conditions	
BM(I,J)	conduction component of global stiffness matrix	(5.15)
BOLD(I)	global vector at previous time step	(5.24)
C(I,J,K)	thermal conductivity coefficients (k_{11}, k_{12}, k_{13})	
CAPM(I,J)	global capacitance matrix	(5.15)
CM(I,J)	convection component of stiffness matrix	(5.15)
CP(I)	density x specific heat at temperature TCP(I) (data)	
CPTEMP	name of data file containing $\rho C_p(T)$	
CV(I)	convection component of global vector	(5.15)
DT	time step	
EPS(I)	emissivity	(5.27)
FLNAME	name of file for element heat fluxes	

FNAME	name of control data file
GEN(I)	internal heat generation rate
GV(I)	generation component of global vector (5.15)
H(I)	convective heat transfer coefficient
HEADER	first line of control data file
HRNEW(I)	radiative heat transfer coefficient for next time step
HROLD(I)	radiative heat transfer coefficient (5.29)
IBAND	mesh bandwidth
ICONV1,ICONV2	flags denoting convergence with nonlinear thermal properties
IFFLUX	Flag requesting calculation of element heat fluxes
IFH	Flag indicating form of $\rho C_p(T)$ data
IFHOMG	Flag for nonhomogeneous thermal properties
IFINIT	Flag for uniform initial temperature distribution
IFPLOT	Flag requesting isotherm plot file
IFTEMP	Flag indicating nonlinear thermal properties
IFTIME	Flag indicating time-dependent boundary conditions

IFTRNS	flag indicating transient calculation
INODE (I,J)	element topology
INTALG	code for time integration algorithm (5.24)
IP	numerical integration point within element
ISOLVE	code for solution method
ITNAME	name of data fild containing initial temperature distributions
MENAME	name of mesh data file
MIDC(I)	number of midside node on convective edge of element
MIDQ(I)	number of midside node in element with heat flux
MIDR(I)	number of midside node cn radiative edge of element
NCE(I)	number of Ith convective element
NCP	number of values in $\rho C_p(T)$ data
NDT	time step counter
NECT	total number of convective elements
NEGEN(I)	number of Ith element with heat generation
NEQT	total number of elements with heat flux
NER(I)	number of Ith radiative element

NERT	total number of radiative elements
NET	Total number of elements
NFT(I)	number of Ith node at prescribed temperature
NGEN	total number of elements with heat generation
NITER	iteration counter (radiative boundary)
NNFT	total number of nodes at prescribed temperature
NNT	total number of nodes
NQE(I)	number of Ith element with heat flux
NSTEPS	requested frequency of printed output (every NSTEPS time steps)
PFNAME	name of isotherm plot file
Q(I)	element heat flux (positive into solid)
QV(I)	heat flux component of global vector (5.15)
RHOCP(I)	heat capacity of Ith element
RM(I,J)	radiation component of stiffnes matrix (5.30)
RV(I)	radiation component of global vector (5.30)
T(I)	temperature of Ith node
T1(I)	newly-calculated temperature of Ith node

TCP(I)	temperature in ρC_p (T) data
TFIX(I)	prescribed temperature at Ith such node
THNAME	name of nonhomogeneous thermal properties data file
TIME	current time in transient calculation (starts from t = 0)
TIMEND	duration of transient calculation
TINF(I)	'fluid' temperature for convection from Ith such element
TINIT	initial (uniform) temperature
TITLE	title (first line) of data files
TK(I),THCOND(J,I)	nonlinear thermal property data: $T, k_{ij}(T)$
TMID(I)	calculated temperature at mid point of an element
TRAD(I)	enclosure temperature (deg C) in radiation problems (5.27)
X(I),Y(I)	cartesian coordinates of node I

Subroutines

B(2,8)	matrix of shape function derivatives	(5.10,5.18)
BE(8,8)	element matrix	(5.15)
BTRAND(8,2)	product of BTRANS and D	

BTRANS(8,2)	transpose of B	
CC(2,8)	matrix of shape function derivatives (natural coords.)	(5.17)
D(2,2)	property matrix	(5.6)
DETJAC	determinant of Jacobian (JAC)	(5.20)
DNR(8), DNS(8)	derivatives of shape functions w.r.t. natural coords.	(5.17 - 5.1
IC	column in global matrix corresponding to ICOL	
ICOL	column in element matrix	
INT(2)	natural coordinates at numerical integration points	(5.22)
IR	row in global matrix corresponding to IROW	
IROW	row in element matrix	
JAC(2,2)	Jacobian matrix	(5.17)
JACINV(2,2)	inverse of Jacobian	
N(8)	element shape functions	(5.9)
R,S	natural coordinates within element ($-1 \leq R,S \leq +1$)	
WC(I)	weight factors for numerical integration	(5.22)

A-I.4 FORTRAN LISTING OF FEANCO

NOTE: This program is copyright © Stephen Grove 1985. Prospective users should contact the author in the first instance.

```
C  Anisotropic conduction in two dimensions.
C  February 1984 version.

C  Common blocks and dimension statements

      COMMON/MATB/BM(500,125)
      COMMON/MATC/CM(500,125)
      COMMON/MATR/RM(500,125)
      COMMON/MATRIX/A(500,125),B(500)
      COMMON/MATCAP/CAPM(500,125)
      COMMON/VECTRS/QV(500),CV(500),RV(500),QV(500)
      COMMON/TEMP/T(500),T1(500)
      COMMON/MESH/X(500),Y(500),INODE(8,200)
      COMMON/COND/C(3,4,200),RHOCP(200)
      DIMENSION NFT(100),TFIX(100),NCE(100),MIDC(100),
     +   TINF(100),EPS(100),TRAD(100),MIDR(100),NER(100),
     +   HROLD(100),HRNEW(100),NQE(100),MIDQ(100),Q(100),
     +   H(100),NEGEN(200),GEN(200),TK(20),THCOND(3,20),BOLD(500),
     +   TCP(20),CP(20),TMID(200)
      CHARACTER*40 TITLE,FNAME,MENAME,THNAME,BCNAME,ITNAME,
     +    FLNAME,HEADER,PFNAME,BCTIME,CPTEMP,KTEMP

C  Get name of control file

      WRITE(1,20)
      READ(1,'(A)')FNAME

C  Open file and read control parameters

      OPEN(5,FILE=FNAME,STATUS='OLD')
      READ(5,'(A)')HEADER
      READ(5,*)IFTRNS
      READ(5,*)ISOLVE
      READ(5,*)IFHOMG
      IF(IFHOMG.EQ.1)THEN
       READ(5,'(A)')THNAME
       ELSE
       READ(5,*)(C(K,1,1),K=1,3),RHOCP(1)
       END IF
      READ(5,*)IFTEMP
      IF(IFTEMP.EQ.1.OR.IFTEMP.EQ.3) READ(5,'(A)') KTEMP
      IF(IFTEMP.GT.1) THEN
       READ(5,'(A)') CPTEMP
       READ(5,*) IFH
      END IF
      READ(5,'(A)')MENAME
      READ(5,'(A)')BCNAME
      IF(IFTRNS.NE.1) THEN
       READ(5,*)IFPLOT
       IF(IFPLOT.EQ.1) READ(5,'(A)')PFNAME
       READ(5,*)IFFLUX
       IF(IFFLUX.EQ.1) READ(5,'(A)')FLNAME
       GO TO 100
      END IF
      READ(5,*)DT,TIMEND,NSTEPS,INTALG
      READ(5,*)IFINIT
```

```
      IF(IFINIT.EQ.1)THEN
       READ(5,'(A)')ITNAME
       OPEN(6,FILE=ITNAME,STATUS='OLD')
       READ(6,*)NNT
       DO 1 IT=1,NNT
1      READ(6,*)NT,T(NT)
       CLOSE(6)
       ELSE
       READ(5,*)T(1)
       DO 2 IT=2,500
2      T(IT)=T(1)
       END IF
       READ(5,*)IFTIME
       IF(IFTIME.EQ.1)READ(5,'(A)')BCTIME
       NSTART=0
       READ(5,*,END=100) NSTART,NSTOP,NINT
 100   CLOSE(5)

C  Output basic information about this run

       CALL INFO(HEADER,THNAME,ITNAME,IFTRNS,ISOLVE,IFHOMG,IFTEMP,IFTIME,
     +   CPTEMP,IFH,BCTIME,
     +   IFINIT,KTEMP,DT,TIMEND,NSTEPS,INTALG)

C  Read the mesh data - node coordinates and topology - and compute bandwidth

       OPEN(5,FILE=MENAME,STATUS='OLD')
       READ(5,'(A)')TITLE
       WRITE(1,21)MENAME,TITLE
       READ(5,*)NNT
       IF(NNT.GT.500) CALL TOOBIG(1)
       DO 3 I=1,NNT
3      READ(5,*)NN,X(NN),Y(NN)
       READ(5,*)NET
       IF(NET.GT.200) CALL TOOBIG(2)
       DO 4 I=1,NET
4      READ(5,*)NE,(INODE(J,NE),J=1,8)
       READ(5,*,END=44)IBAND
       GO TO 45
 44    IBAND=1
       DO 444 NE=1,NET
       NMIN=NNT
       NMAX=1
       DO 445 II=1,8
       IN=INODE(II,NE)
       IF(IN.LT.NMIN) NMIN=IN
 445   IF(IN.GT.NMAX) NMAX=IN
       IB=NMAX-NMIN+1
 444   IF(IB.GT.IBAND) IBAND=IB
 45    CLOSE(5)
       IF(IBAND.GT.125) CALL TOOBIG(3)

C  Read thermal properties

       IF(IFHOMG.EQ.1)THEN
        OPEN(5,FILE=THNAME,STATUS='OLD')
        READ(5,'(A)')TITLE
        WRITE(1,22)THNAME,TITLE
        DO 5 NE=1,NET
        DO 5 IP=1,4
5       READ(5,*)(C(K,IP,NE),K=1,3),RHOCP(NE)
        CLOSE(5)
       ELSE
        DO 55 NE=1,NET
        RHOCP(NE)=RHOCP(1)
        DO 55 IP=1,4
        DO 55 K=1,3
55      C(K,IP,NE)=C(K,1,1)
       END IF
```

```
      IF(IFTEMP.GT.1) THEN
       OPEN(5,FILE=CPTEMP,STATUS='OLD')
       READ(5,*) NCP
       IF(NCP.GT.20) CALL TOOBIG(6)
       READ(5,*)(TCP(I),CP(I),I=1,NCP)
       CLOSE(5)
       DO 551 NE=1,NET
551    CALL ELTEMP(0.,0.,NE,TMID(NE))
      END IF

      IF(IFTEMP.EQ.1 .OR.  IFTEMP.EQ.3) THEN
       OPEN(5,FILE=KTEMP,STATUS='OLD')
       READ(5,*)NK
       IF(NK.GT.20) CALL TOOBIG(6)
       READ(5,*)(TK(I),(THCOND(J,I),J=1,3),I=1,NK)
       CLOSE(5)
      END IF

C  Read boundary conditions

      OPEN(5,FILE=BCNAME,STATUS='OLD')
      READ(5,'(A)')TITLE
      WRITE(1,23)BCNAME,TITLE
      READ(5,*)NNFT
      IF(NNFT.GT.100) CALL TOOBIG(4)
      CALL TITLE1(NNFT)
      IF(NNFT.EQ.0)GO TO 150
      DO 6 IT=1,NNFT
      READ(5,*)NFT(IT),TFIX(IT)
 6    CALL TITLE2(NFT(IT),TFIX(IT))

 150  READ(5,*)NECT
      IF(NECT.GT.100) CALL TOOBIG(5)
      CALL TITLE3(NECT)
      IF(NECT.EQ.0)GO TO 200
      DO 7 I=1,NECT
      READ(5,*)NCE(I),MIDC(I),H(I),TINF(I)
 7    CALL TITLE4(NCE(I),MIDC(I),H(I),TINF(I))

 200  READ(5,*)NEQT
      IF(NEQT.GT.100) CALL TOOBIG(5)
      CALL TITLE5(NEQT)
      IF(NEQT.EQ.0)GO TO 300
      DO 8 I=1,NEQT
      READ(5,*)NQE(I),MIDQ(I),Q(I)
8     CALL TITLE6(NQE(I),MIDQ(I),Q(I))

 300  READ(5,*)NERT
      IF(NERT.GT.100) CALL TOOBIG(5)
      CALL TITLE7(NERT)
      IF(NERT.EQ.0)GO TO 400
      DO 9 I=1,NERT
      HROLD(I)=0.
      READ(5,*)NER(I),MIDR(I),EPS(I),TRAD(I)
9     CALL TITLE8(NER(I),MIDR(I),EPS(I),TRAD(I))
      NITER=0
      ITER=0

 400  READ(5,*)NGEN
      IF(NGEN.GT.200) CALL TOOBIG(2)
      CALL TITLE9(NGEN)
      IF(NGEN.EQ.0)GO TO 500
      DO 10 IG=1,NGEN
      READ(5,*)NEGEN(IG),GEN(NEGEN(IG))
10    CALL TITL10(NEGEN(IG),GEN(NEGEN(IG)))
500   CLOSE(5)
```

```
C  Initialise vectors

       CALL VZERO(NNT)

       TIME=DT
       NDT=0

 600   CALL BASE(NNT, IBAND, NET, NEGEN, GEN)

       IF(IFTRNS.EQ.1) THEN
        CALL CAP(NNT, IBAND, NET)
        IF(TIME.EQ.DT) CALL ZERO(NNT, IBAND, BOLD)
       END IF

       IF(NECT.GT.0) CALL CONV(NCE, MIDC, H, TINF, NECT, NNT, IBAND)

       IF(NEQT.GT.0) CALL FLUX(NQE, MIDQ, Q, NEQT, NNT)

 700   IF(NERT.GT.0) CALL RADN(NER, MIDR, HROLD, TRAD, NERT, NNT, IBAND)

 800   CALL ASSMBL(NNT, IBAND)

       IF(IFTRNS.EQ.1) CALL INTGRT(NNT, IBAND, DT, INTALG, BOLD)

       IF(NNFT.GT.0) CALL MODIFY(NNT, IBAND, NNFT, NFT, TFIX)

       CALL SOLVE(NNT, IBAND, ISOLVE)

       IF(NERT.EQ.0)GO TO 900

        CALL COEFFS(NER, MIDR, EPS, TRAD, HRNEW, NERT)

        CALL CONVRG(HRNEW, HROLD, NERT, ICONV)
        IF(ICONV.EQ.1)GO TO 900
        NITER=NITER+1
        IF(NITER.EQ.10)CALL FAIL
        DO 11 I=1, NERT
 11     HROLD(I)=HRNEW(I)
       GO TO 700

 900   IF(IFTEMP.EQ.0)GO TO 1000
       ICONV1=1
       ICONV2=1
       IF(IFTEMP.GT.1) CALL NEWCP(ICONV1, NET, NCP, TCP, CP, TMID, IFH)
       IF(IFTEMP.EQ.1.OR.IFTEMP.EQ.3) CALL NEWK(ICONV2, NET, NK, TK, THCOND)
       IF(ICONV1.EQ.0.OR.ICONV2.EQ.0) GO TO 600

 1000 NDT=NDT+1
       CALL UPTEMP(NNT)
       IF(IFTRNS.EQ.0)THEN
        CALL OUTPUT(NNT, IFTRNS, TIME, NSTART, NSTOP, NINT)
        IF(IFFLUX.EQ.1) CALL HTFLUX(NNT, NET, FLNAME)
        IF(IFPLOT.EQ.1) CALL PLOTOP(PFNAME, HEADER, NNT)
        CALL EXIT
        END IF

       IF(NDT.EQ.NSTEPS)THEN
        IF(IFTIME.EQ.1)CALL OUTBC(TIME, NNFT, NFT, TFIX, NECT, NCE, H, TINF,
     +   NEQT, NQE, Q, NERT, NER, EPS, TRAD, NQEN, NEQEN, GEN, MIDC, MIDR, MIDQ)
        CALL OUTPUT(NNT, IFTRNS, TIME, NSTART, NSTOP, NINT)
        NDT=0
        END IF

       TIME=TIME+DT
       IF(TIME.GT.TIMEND) CALL EXIT
       IF(IFTIME.EQ.1)THEN
        CALL NEWBC(BCTIME, TIME, NNFT, NFT, TFIX, NECT, NCE, MIDC, H, TINF,
     +   NEQT, NQE, MIDQ, Q, NERT, HROLD, NER, MIDR, EPS, TRAD, NITER, ITER,
     +   NQEN, NEQEN, GEN)
        GO TO 600
        END IF

       GO TO 800
```

```
 20    FORMAT(//'MASTER DATA FILE NAME?',/)
 21    FORMAT(//'READING MESH DATA FROM FILE ',(A),/(A)/)
 22    FORMAT(//'READING THERMAL DATA FROM FILE ',(A),/(A)/)
 23    FORMAT(//'READING BOUNDARY CONDITIONS FROM FILE ',(A),/(A)/)

       END

CCCCCCCCCCCCCCCCCCCCCCCCCCCCCCCCCCCCCCCCCCCCCCCCCCCCCCCCCCCCCCCCCCCCCCCC

       SUBROUTINE INFO(TITLE,THNAME,ITNAME,IFTRNS,ISOLVE,IFHOMG,IFTEMP,
     +   IFTIME,CPTEMP,IFH,BCTIME,
     +   IFINIT,KTEMP,DT,TIMEND,NSTEPS,INTALG)
       COMMON/COND/C(3,4,200),RHOCP(200)
       COMMON/TEMP/T(500),T1(500)
       CHARACTER*40 TITLE,THNAME,ITNAME,CPTEMP,BCTIME,KTEMP

       WRITE(1,10)TITLE
       IF(IFTRNS.EQ.1)THEN
        WRITE(1,11)TIMEND
        WRITE(1,12)DT,NSTEPS
        IF(INTALG.EQ.0)WRITE(1,13)
        IF(INTALG.EQ.1)WRITE(1,14)
        IF(INTALG.EQ.2)WRITE(1,15)
        IF(IFINIT.EQ.1)WRITE(1,16)ITNAME
        IF(IFINIT.LT.1)WRITE(1,17)T(1)
       ELSE
       WRITE(1,18)
       END IF

       IF(IFHOMG.EQ.1)THEN
        WRITE(1,19)THNAME
       ELSE
       WRITE(1,20)(C(K,1,1),K=1,3),RHOCP(1)
       END IF

       IF(IFTEMP.EQ.1.OR.IFTEMP.EQ.3) WRITE(1,22) KTEMP
       IF(IFTEMP.GT.1) THEN
        WRITE(1,25) CPTEMP
        IF(IFH.EQ.0) WRITE(1,251)
        IF(IFH.EQ.1) WRITE(1,252)
       END IF

       IF(IFTIME.EQ.1)WRITE(1,24)BCTIME

       IF(ISOLVE.EQ.6) WRITE(1,30)
       IF(ISOLVE.EQ.7) WRITE(1,31)

       RETURN

 10    FORMAT(/////'FEANCO: FINITE ELEMENTS FOR ANISOTROPIC',
     +   ' CONDUCTION'/,50('-'),//,'TITLE:  ',(A),///)
 11    FORMAT('TRANSIENT CALCULATION OVER ',F8.3,' SECS'/)
 12    FORMAT('TIME STEP ',F6.3,'; OUTPUT EVERY ',I3,' STEPS'/)
 13    FORMAT('FORWARD-DIFFERENCE INTEGRATION ALGORITHM'/)
 14    FORMAT('PURE IMPLICIT INTEGRATION ALGORITHM'/)
 15    FORMAT('CRANK-NICOLSON INTEGRATION ALGORITHM'/)
 16    FORMAT('INITIAL TEMPERATURE DISTRIBUTION FROM FILE ',(A),/)
 17    FORMAT('UNIFORM INITIAL TEMPERATURE OF ',F8.3,/)
 18    FORMAT('STEADY-STATE CALCULATION'//)
 19    FORMAT(/'INHOMOGENEOUS THERMAL PROPERTIES READ FROM FILE ',
     +   (A),/)
 20    FORMAT(/'HOMOGENEOUS THERMAL PROPERTIES: ',/,5X,'K11=',
     +   F7.3,'  K12=',F7.3,'  K22=',F7.3,'  RHO.CP=',E10.5,//)
 22    FORMAT('TEMPERATURE-DEPENDENT THERMAL CONDUCTIVITY DATA',
     +   ' FROM FILE ',(A)/)
 25    FORMAT(/'RHO.CP(T) FROM FILE ',(A),/)
 251   FORMAT('(DATA ARE ACTUAL RHO.CP)'//)
 252   FORMAT('(DATA ARE ENTHALPY VALUES)'//)
 24    FORMAT(//'TIME-DEPENDENT BOUNDARY CONDITIONS FROM FILE ',(A),///)
 30    FORMAT(//'SOLUTION OBTAINED BY DECOMPOSITION OF SYMMETRIC',
     +   ' BANDED MATRIX'///)
 31    FORMAT(//'ACCURATE SOLUTION (TO 1E-5)'///)

       END
```

```
CCCCCCCCCCCCCCCCCCCCCCCCCCCCCCCCCCCCCCCCCCCCCCCCCCCCCCCCCCCCCCCCCCCCCCCCCCCCCCCCCCCCCCC

      SUBROUTINE TITLE1(NNFT)
      WRITE(1,10)
      WRITE(1,11)NNFT
      IF(NNFT.EQ.0)RETURN
      WRITE(1,12)
 10   FORMAT(///'BOUNDARY CONDITIONS:'/)
 11   FORMAT(///'THERE ARE ',I3,' NODES AT A FIXED TEMPERATURE')
 12   FORMAT(/'NODE NUMBER      TEMPERATURE')
      END

CCCCCCCCCCCCCCCCCCCCCCCCCCCCCCCCCCCCCCCCCCCCCCCCCCCCCCCCCCCCCCCCCCCCCCCCCCCCCCCCCCCCCCC

      SUBROUTINE TITLE2(NN,TFIX)
      WRITE(1,10)NN,TFIX
 10   FORMAT(I7,9X,F8.3)
      RETURN
      END

CCCCCCCCCCCCCCCCCCCCCCCCCCCCCCCCCCCCCCCCCCCCCCCCCCCCCCCCCCCCCCCCCCCCCCCCCCCCCCCCCCCCCCC

      SUBROUTINE TITLE3(NECT)
      WRITE(1,10)NECT
      IF(NECT.EQ.0)RETURN
      WRITE(1,11)
      RETURN
 10   FORMAT(//'THERE ARE ',I3,' CONVECTIVE ELEMENTS')
 11   FORMAT(/'ELEMENT  MIDSIDE NODE      H      FLUID TEMP.')
      END

CCCCCCCCCCCCCCCCCCCCCCCCCCCCCCCCCCCCCCCCCCCCCCCCCCCCCCCCCCCCCCCCCCCCCCCCCCCCCCCCCCCCCCC

      SUBROUTINE TITLE4(NE,MIDC,H,TINF)
      WRITE(1,10)NE,MIDC,H,TINF
 10   FORMAT(2(I4,7X),F7.1,1X,F8.3)
      RETURN
      END

CCCCCCCCCCCCCCCCCCCCCCCCCCCCCCCCCCCCCCCCCCCCCCCCCCCCCCCCCCCCCCCCCCCCCCCCCCCCCCCCCCCCCCC

      SUBROUTINE TITLE5(NEQT)
      WRITE(1,10)NEQT
      IF(NEQT.EQ.0)RETURN
      WRITE(1,11)
      RETURN
 10   FORMAT(//'THERE ARE ',I3,' ELEMENTS WITH A SPECIFIED HEAT FLUX')
 11   FORMAT(/'ELEMENT  MIDSIDE NODE  HEAT FLUX')
      END

CCCCCCCCCCCCCCCCCCCCCCCCCCCCCCCCCCCCCCCCCCCCCCCCCCCCCCCCCCCCCCCCCCCCCCCCCCCCCCCCCCCCCCC

      SUBROUTINE TITLE6(NE,MIDQ,Q)
      WRITE(1,10)NE,MIDQ,Q
 10   FORMAT(2(I4,7X),F7.1)
      RETURN
      END

CCCCCCCCCCCCCCCCCCCCCCCCCCCCCCCCCCCCCCCCCCCCCCCCCCCCCCCCCCCCCCCCCCCCCCCCCCCCCCCCCCCCCCC

      SUBROUTINE TITLE7(NERT)
      WRITE(1,10)NERT
      IF(NERT.EQ.0)RETURN
      WRITE(1,11)
      RETURN
 10   FORMAT(//'THERE ARE ',I3,' RADIATIVE ELEMENTS')
 11   FORMAT(/'ELEMENT  MIDSIDE NODE  EMISSIVITY  T-INFINITY')
      END

CCCCCCCCCCCCCCCCCCCCCCCCCCCCCCCCCCCCCCCCCCCCCCCCCCCCCCCCCCCCCCCCCCCCCCCCCCCCCCCCCCCCCCC

      SUBROUTINE TITLE8(NER,MIDR,EPS,TRAD)
      WRITE(1,10)NER,MIDR,EPS,TRAD
 10   FORMAT(2(I4,7X),2X,F7.2,3X,F8.3)
      RETURN
      END
```

```
CCCCCCCCCCCCCCCCCCCCCCCCCCCCCCCCCCCCCCCCCCCCCCCCCCCCCCCCCCCCCCCCCCCCCCCCCCCCCCC

      SUBROUTINE TITLE9(NGEN)
      WRITE(1,10)NGEN
      IF(NGEN.EQ.0)RETURN
      WRITE(1,11)
      RETURN
 10   FORMAT(//'THERE ARE ',I3,' ELEMENTS WITH HEAT GENERATION')
 11   FORMAT(/'ELEMENT    RATE (W/m3)')
      END

CCCCCCCCCCCCCCCCCCCCCCCCCCCCCCCCCCCCCCCCCCCCCCCCCCCCCCCCCCCCCCCCCCCCCCCCCCCCCCC

      SUBROUTINE TITL10(NEGEN,GEN)
      WRITE(1,10)NEGEN,GEN
      RETURN
 10   FORMAT(I4,6X,E10.4)
      END

CCCCCCCCCCCCCCCCCCCCCCCCCCCCCCCCCCCCCCCCCCCCCCCCCCCCCCCCCCCCCCCCCCCCCCCCCCCCCCC

      SUBROUTINE BASE(NNT,IBAND,NET,NEGEN,GEN)

C  Evaluation of global conduction matrix and generation vector.

      COMMON/MATB/BM(500,125)
      COMMON/VECTRS/GV(500),CV(500),RV(500),QV(500)
      COMMON/MESH/X(500),Y(500),INODE(8,200)
      COMMON/COND/C(3,4,200),RHOCP(200)

      REAL JAC(2,2),JACINV(2,2),N(8),INT(2)
      DIMENSION CC(2,8),B(2,8),BTRANS(8,2),D(2,2),
     +  DNR(8),DNS(8),BE(8,8),BTRAND(8,2),NEGEN(200),GEN(200)

C  Initialise matrix and vector.

      DO 1 IROW=1,NNT
      QV(IROW)=0.
      DO 1 ICOL=1,IBAND
 1    BM(IROW,ICOL)=0.

C  Define points for numerical integration (natural coords.).  Weights are unity.

      INT(1)=-.577350269189626
      INT(2)=-INT(1)

C  For each element...

      DO 2 NE=1,NET

C  ...and each integration point...

      IP=0
      DO 2 I=1,2
      R=INT(I)
      DO 2 J=1,2
      S=INT(J)
      IP=IP+1

C  Set up property matrix.

      D(1,1)=C(1,IP,NE)
      D(1,2)=C(2,IP,NE)
      D(2,1)=D(1,2)
      D(2,2)=C(3,IP,NE)

C  Evaluate shape functions, derivatives and Jacobian for this point.

      CALL SHAPE(R,S,N)
      CALL DERIV(R,S,DNR,DNS)
      CALL JACOB(R,S,JAC,NE,DNR,DNS)

C  Evaluate inverse of J and det J.

      CALL DET(JAC,DETJAC)
      CALL INV(JAC,DETJAC,JACINV)
```

```
C  Set up matrix of shape function derivatives.

      DO 3 ICOL=1,8
      CC(1,ICOL)=DNR(ICOL)
 3    CC(2,ICOL)=DNS(ICOL)

C  Transform from natural to cartesian coords.  B=inv J . CC

      CALL MULT(JACINV,CC,B,2,8,2)

C  Evaluate transpose of B

      CALL TRANS(B,BTRANS,2,8)

C  Multiply by D, store result in BTRAND.

      CALL MULT(BTRANS,D,BTRAND,8,2,2)

C  Multiply by B to give element matrix BE.

      CALL MULT(BTRAND,B,BE,8,8,2)

C  Add BE.det J to global matrix, and g.N.det J to generation vector.

      DO 2 IROW=1,8
      IR=INODE(IROW,NE)
      GV(IR)=GV(IR) + N(IROW)*DETJAC*GEN(NE)
      DO 2 ICOL=IROW,8
      IC=INODE(ICOL,NE)
      IF(IR.LE.IC)THEN
       BM(IR,IC-IR+1)=BM(IR,IC-IR+1) + BE(IROW,ICOL)*DETJAC
       ELSE
       BM(IC,IR-IC+1)=BM(IC,IR-IC+1) + BE(ICOL,IROW)*DETJAC
      END IF
 2    CONTINUE

      RETURN

      END

CCCCCCCCCCCCCCCCCCCCCCCCCCCCCCCCCCCCCCCCCCCCCCCCCCCCCCCCCCCCCCCCCCCCCCCCCCCC

      SUBROUTINE CAP(NNT,IBAND,NET)

C  Evaluation of capacitance matrix (3rd order numerical integration).

      COMMON/MESH/X(500),Y(500),INODE(8,200)
      COMMON/COND/C(3,4,200),RHOCP(200)
      COMMON/MATCAP/CAPM(500,125)

      REAL JAC(2,2),N(8),INT(3)
      DIMENSION WC(3),DNR(8),DNS(8)

C  Initialise matrix

      DO 1 IROW=1,NNT
      DO 1 ICOL=1,IBAND
 1    CAPM(IROW,ICOL)=0.

C  Define integration points and weight coefficients

      INT(1)=-.774596669241483
      INT(2)=0.
      INT(3)=-INT(1)
      WC(1)=5./9.
      WC(2)=8./9.
      WC(3)=WC(1)

C  For each element:

      DO 2 NE=1,NET

C  For each integration point:

      DO 2 I=1,3
      R=INT(I)
      DO 2 J=1,3
      S=INT(J)
```

```
C  Evaluate shape functions, Jacobian, etc.

      CALL SHAPE(R,S,N)
      CALL DERIV(R,S,DNR,DNS)
      CALL JACOB(R,S,JAC,NE,DNR,DNS)

C  Evaluate det J.

      CALL DET(JAC,DETJAC)

C  Form capacitance matrix:

      DO 2 IROW=1,8
      IR=INODE(IROW,NE)
      DO 2 ICOL=IROW,8
      IC=INODE(ICOL,NE)
      IF(IR.LE.IC) THEN
       CAPM(IR,IC-IR+1) = CAPM(IR,IC-IR+1) +
     +   N(IROW)*N(ICOL)*DETJAC*RHOCP(NE)*WC(I)*WC(J)
       ELSE
       CAPM(IC,IR-IC+1) = CAPM(IC,IR-IC+1) +
     +   N(IROW)*N(ICOL)*DETJAC*RHOCP(NE)*WC(I)*WC(J)
       END IF
 2    CONTINUE

      RETURN

      END

CCCCCCCCCCCCCCCCCCCCCCCCCCCCCCCCCCCCCCCCCCCCCCCCCCCCCCCCCCCCCCCCCCCCCCCC

      SUBROUTINE ZERO(NNT,IBAND,BOLD)

C  Set initial value of generation vector  BOLD=BM.T

      COMMON/MATB/BM(500,125)
      COMMON/TEMP/T(500),T1(500)
      DIMENSION BOLD(500)

      DO 1 IROW=1,NNT
      BOLD(IROW)=0.
      K=IROW-1
      DO 2 ICOL=2,IBAND
      M=ICOL+IROW-1
      IF(M.LE.NNT) BOLD(IROW)=BOLD(IROW) + T(M)*BM(IROW,ICOL)
      IF(K.LE.0) GO TO 2
      BOLD(IROW)=BOLD(IROW) + T(K)*BM(K,ICOL)
      K=K-1
 2    CONTINUE
 1    BOLD(IROW)=BOLD(IROW) + T(IROW)*BM(IROW,1)

      RETURN
      END

CCCCCCCCCCCCCCCCCCCCCCCCCCCCCCCCCCCCCCCCCCCCCCCCCCCCCCCCCCCCCCCCCCCCCCCC

      SUBROUTINE DET(A,DETA)

C  Determinant of 2 x 2 matrix.

      DIMENSION A(2,2)

      DETA=A(1,1)*A(2,2)-A(1,2)*A(2,1)

      RETURN
      END

CCCCCCCCCCCCCCCCCCCCCCCCCCCCCCCCCCCCCCCCCCCCCCCCCCCCCCCCCCCCCCCCCCCCCCCC
```

```
      SUBROUTINE INV(A,DETA,AINV)

C  Calculates inverse of 2 x 2 matrix.

      DIMENSION A(2,2),AINV(2,2)

      AINV(1,1)=A(2,2)/DETA
      AINV(1,2)=-A(1,2)/DETA
      AINV(2,1)=-A(2,1)/DETA
      AINV(2,2)=A(1,1)/DETA

      RETURN
      END

CCCCCCCCCCCCCCCCCCCCCCCCCCCCCCCCCCCCCCCCCCCCCCCCCCCCCCCCCCCCCCCCCCCCCCCCCC

      SUBROUTINE SHAPE(R,S,N)

C  Shape functions in natural coordinates for 8 noded quadrilateral.

      REAL N(8)

      RM1=1.-R
      SM1=1.-S
      RP1=1.+R
      SP1=1.+S
      N(1)=-RM1*SM1*(R+SP1)/4.
      N(2)=RM1*RP1*SM1/2.
      N(3)=RP1*SM1*(R-SP1)/4.
      N(4)=SM1*SP1*RP1/2.
      N(5)=RP1*SP1*(R-SM1)/4.
      N(6)=RM1*RP1*SP1/2.
      N(7)=-RM1*SP1*(R+SM1)/4.
      N(8)=SM1*SP1*RM1/2.

      RETURN
      END

CCCCCCCCCCCCCCCCCCCCCCCCCCCCCCCCCCCCCCCCCCCCCCCCCCCCCCCCCCCCCCCCCCCCCCCCCC

      SUBROUTINE DERIV(R,S,DNR,DNS)

C  Derivatives of shape functions for 8-noded quadrilateral.

      DIMENSION DNR(8),DNS(8)

      RM1=1.-R
      RP1=1.+R
      SM1=1.-S
      SP1=1.+S
      DNR(1)=SM1*(2.*R+S)/4.
      DNS(1)=RM1*(2.*S+R)/4.
      DNR(2)=-SM1*R
      DNS(2)=-RM1*RP1/2.
      DNR(3)=SM1*(2.*R-S)/4.
      DNS(3)=RP1*(2.*S-R)/4.
      DNR(4)=SM1*SP1/2.
      DNS(4)=-RP1*S
      DNR(5)=SP1*(2.*R+S)/4.
      DNS(5)=RP1*(2.*S+R)/4.
      DNR(6)=-SP1*R
      DNS(6)=RP1*RM1/2.
      DNR(7)=SP1*(2.*R-S)/4.
      DNS(7)=RM1*(2.*S-R)/4.
      DNR(8)=-SM1*SP1/2.
      DNS(8)=-RM1*S

      RETURN
      END
```

```
cccccccccccccccccccccccccccccccccccccccccccccccccccccccccccccccccccccccccc

      SUBROUTINE MULT(A,B,C,M,N,P)

C  Forms matrix product A.B=c

      INTEGER P
      DIMENSION A(M,P),B(P,N),C(M,N)

      DO 1 IROW=1,M
      DO 1 ICOL=1,N
      C(IROW,ICOL)=0.
      DO 1 J=1,P
 1    C(IROW,ICOL)=C(IROW,ICOL) + A(IROW,J)*B(J,ICOL)

      RETURN
      END

cccccccccccccccccccccccccccccccccccccccccccccccccccccccccccccccccccccccccc

      SUBROUTINE TRANS(A,B,M,N)

C  Forms transpose of A(M,N).

      DIMENSION A(M,N),B(N,M)

      DO 1 IROW=1,M
      DO 1 ICOL=1,N
 1    B(ICOL,IROW)=A(IROW,ICOL)

      RETURN
      END

cccccccccccccccccccccccccccccccccccccccccccccccccccccccccccccccccccccccccc

      SUBROUTINE JACOB(R,S,JAC,NE,DNR,DNS)

C  Forms Jacobian matrix from shape function derivatives.

      COMMON/MESH/X(500),Y(500),INODE(8,200)

      REAL JAC(2,2),DNR(8),DNS(8)

      DO 1 I=1,2
      DO 1 J=1,2
 1    JAC(I,J)=0.

      DO 2 I=1,8
      IN=INODE(I,NE)
      JAC(1,1)=JAC(1,1) + DNR(I)*X(IN)
      JAC(1,2)=JAC(1,2) + DNR(I)*Y(IN)
      JAC(2,1)=JAC(2,1) + DNS(I)*X(IN)
 2    JAC(2,2)=JAC(2,2) + DNS(I)*Y(IN)

      RETURN
      END
```

```
CCCCCCCCCCCCCCCCCCCCCCCCCCCCCCCCCCCCCCCCCCCCCCCCCCCCCCCCCCCCCCCCCCCCCCCCCCCCCCC

      SUBROUTINE CONV(NCE,MIDC,H,TINF,NECT,NNT,IBAND)

C  Evaluates global convection matrix and vector.

      COMMON/MATC/CM(500,125)
      COMMON/VECTRS/QV(500),CV(500),RV(500),QV(500)
      COMMON/MESH/X(500),Y(500),INODE(8,200)

      DIMENSION NCE(NECT),MIDC(NECT),H(NECT),TINF(NECT)
      REAL LENGTH,N(8),DNR(8),DNS(8),JAC(2,2),INT(3),WC(3)

      INT(1)=-.774596669241483
      INT(2)=0.
      INT(3)=-INT(1)
      WC(1)=5./9.
      WC(2)=8./9.
      WC(3)=WC(1)

C  Initialise

      DO 1 IROW=1,NNT
      CV(IROW)=0.
      DO 1 ICOL=1,IBAND
 1    CM(IROW,ICOL)=0.

C  For each element with a convective side...

      DO 2 IEL=1,NECT

      JC=MIDC(IEL)
      NE=NCE(IEL)
      R=0.
      S=0.

C  Locate convective side and check for numbering error.

      IF(JC.EQ.INODE(2,NE)) S=-1.
      IF(JC.EQ.INODE(4,NE)) R=1.
      IF(JC.EQ.INODE(6,NE)) S=1.
      IF(JC.EQ.INODE(8,NE)) R=-1.
      IF(S.EQ.0..AND.R.EQ.0.) CALL CONERR(NE)

      DO 2 I=1,3
      IF(ABS(R).EQ.1.) THEN
       S=INT(I)
       IJ=2
       ELSE
       R=INT(I)
       IJ=1
       END IF
      CALL SHAPE(R,S,N)
      CALL DERIV(R,S,DNR,DNS)
      CALL JACOB(R,S,JAC,NE,DNR,DNS)
      LENGTH=WC(I)*SQRT(JAC(IJ,1)**2+JAC(IJ,2)**2)
      TERM=LENGTH*H(IEL)

      DO 2 IROW=1,8
      IR=INODE(IROW,NE)
      CV(IR)=CV(IR) + N(IROW)*TERM*TINF(IEL)
      DO 2 ICOL=IROW,8
      IC=INODE(ICOL,NE)
      IF(IR.LE.IC) THEN
       CM(IR,IC-IR+1)=CM(IR,IC-IR+1) + N(IROW)*N(ICOL)*TERM
       ELSE
       CM(IC,IR-IC+1)=CM(IC,IR-IC+1) + N(IROW)*N(ICOL)*TERM
       END IF

 2    CONTINUE

      RETURN
      END
```

```
CCCCCCCCCCCCCCCCCCCCCCCCCCCCCCCCCCCCCCCCCCCCCCCCCCCCCCCCCCCCCCCCCCCCCCCCCCC

      SUBROUTINE CONERR(NE)
      WRITE(1,10)NE
 10   FORMAT(///'SURFACE NODE NUMBERING ERROR IN ELEMENT ',I3,///)
      RETURN
      END

CCCCCCCCCCCCCCCCCCCCCCCCCCCCCCCCCCCCCCCCCCCCCCCCCCCCCCCCCCCCCCCCCCCCCCCCCCC

      SUBROUTINE FLUX(NQE,MIDQ,Q,NEQT,NNT)

C  Evaluates global flux vector.

      COMMON/VECTRS/QV(500),CV(500),RV(500),QV(500)
      COMMON/MESH/X(500),Y(500),INODE(8,200)

      DIMENSION NQE(NEQT),MIDQ(NEQT),Q(NEQT)
      REAL LENGTH,N(8),DNR(8),DNS(8),JAC(2,2),INT(3),WC(3)

      INT(1)=-.774596669241483
      INT(2)=0.
      INT(3)=-INT(1)
      WC(1)=5./9.
      WC(2)=8./9.
      WC(3)=WC(1)

C  Initialise

      DO 1 IROW=1,NNT
 1    QV(IROW)=0.

C  For each element with heat flux...

      DO 2 IEL=1,NEQT

      JC=MIDQ(IEL)
      NE=NQE(IEL)
      R=0.
      S=0.

C  Locate side and check for numbering error.

      IF(JC.EQ.INODE(2,NE)) S=-1.
      IF(JC.EQ.INODE(4,NE)) R=1.
      IF(JC.EQ.INODE(6,NE)) S=1.
      IF(JC.EQ.INODE(8,NE)) R=-1.
      IF(S.EQ.0..AND.R.EQ.0.) CALL CONERR(NE)

      DO 2 I=1,3
      IF(ABS(R).EQ.1.) THEN
       S=INT(I)
       IJ=2
       ELSE
       R=INT(I)
       IJ=1
       END IF
      CALL SHAPE(R,S,N)
      CALL DERIV(R,S,DNR,DNS)
      CALL JACOB(R,S,JAC,NE,DNR,DNS)
      LENGTH=WC(I)*SQRT(JAC(IJ,1)**2+JAC(IJ,2)**2)
      TERM=LENGTH*Q(IEL)

      DO 2 IROW=1,8
      IR=INODE(IROW,NE)
 2    QV(IR)=QV(IR) + N(IROW)*TERM

      RETURN
      END
```

```
CCCCCCCCCCCCCCCCCCCCCCCCCCCCCCCCCCCCCCCCCCCCCCCCCCCCCCCCCCCCCCCCCCCCCCCCCCC

      SUBROUTINE RADN(NER,MIDR,H,TRAD,NERT,NNT,IBAND)

C  Evaluates global radiation matrix and vector.

      COMMON/MATR/RM(500,125)
      COMMON/VECTRS/GV(500),CV(500),RV(500),QV(500)
      COMMON/MESH/X(500),Y(500),INODE(8,200)

      DIMENSION NER(NERT),MIDR(NERT),H(NERT),TRAD(NERT)
      REAL LENGTH,N(8),DNR(8),DNS(8),JAC(2,2),INT(3),WC(3)

      INT(1)=-.774596669241483
      INT(2)=0.
      INT(3)=-INT(1)
      WC(1)=5./9.
      WC(2)=8./9.
      WC(3)=WC(1)

C  Initialise

      DO 1 IROW=1,NNT
      RV(IROW)=0.
      DO 1 ICOL=1,IBAND
1     RM(IROW,ICOL)=0.

C  For each element with a radiative side...

      DO 2 IEL=1,NERT

      JC=MIDR(IEL)
      NE=NER(IEL)
      R=0.
      S=0.

C  Locate radiative side and check for numbering error.

      IF(JC.EQ.INODE(2,NE)) S=-1.
      IF(JC.EQ.INODE(4,NE)) R=1.
      IF(JC.EQ.INODE(6,NE)) S=1.
      IF(JC.EQ.INODE(8,NE)) R=-1.
      IF(S.EQ.0..AND.R.EQ.0.) CALL CONERR(NE)

      DO 2 I=1,3
      IF(ABS(R).EQ.1.) THEN
       S=INT(I)
       IJ=2
       ELSE
       R=INT(I)
       IJ=1
       END IF

      CALL SHAPE(R,S,N)
      CALL DERIV(R,S,DNR,DNS)
      CALL JACOB(R,S,JAC,NE,DNR,DNS)
      LENGTH=WC(I)*SQRT(JAC(IJ,1)**2+JAC(IJ,2)**2)

      TERM=LENGTH*H(IEL)

      DO 2 IROW=1,8
      IR=INODE(IROW,NE)
      RV(IR)=RV(IR) + N(IROW)*TERM*TRAD(IEL)
      DO 2 ICOL=IROW,8
      IC=INODE(ICOL,NE)
      IF(IR.LE.IC) THEN
       RM(IR,IC-IR+1)=RM(IR,IC-IR+1) + N(IROW)*N(ICOL)*TERM
       ELSE
       RM(IC,IR-IC+1)=RM(IC,IR-IC+1) + N(IROW)*N(ICOL)*TERM
       END IF

2     CONTINUE

      RETURN
      END
```

```
      SUBROUTINE ASSMBL(NNT, IBAND)
      COMMON/MATRIX/A(500, 125), B(500)
      COMMON/MATB/BM(500, 125)
      COMMON/MATC/CM(500, 125)
      COMMON/MATR/RM(500, 125)
      COMMON/VECTRS/GV(500), CV(500), RV(500), QV(500)

      DO 1  IROW=1, NNT
      B(IROW)=GV(IROW)+CV(IROW)+RV(IROW)-QV(IROW)
      DO 1  ICOL=1, IBAND
 1    A(IROW, ICOL)=BM(IROW, ICOL)+CM(IROW, ICOL)+RM(IROW, ICOL)

      RETURN
      END

cccccccccccccccccccccccccccccccccccccccccccccccccccccccccccccccccccccc

      SUBROUTINE INTGRT(NNT, IBAND, DT, INTALG, BOLD)
      COMMON/MATRIX/A(500, 125), B(500)
      COMMON/MATCAP/CAPM(500, 125)
      COMMON/TEMP/T(500), T1(500)
      DIMENSION BOLD(500)

      R=INTALG
      IF(INTALG. EQ. 2) R=. 5

      DO 1 IROW=1, NNT
      F=B(IROW)
      B(IROW)=B(IROW)*R + BOLD(IROW)*(1. -R)
      BOLD(IROW)=F
      K=IROW-1
      DO 2 ICOL=2, IBAND
      M=ICOL+IROW-1
      IF(M. LE. NNT) B(IROW)=B(IROW) +
     +  T(M)*(CAPM(IROW, ICOL)/DT - (1. -R)*A(IROW, ICOL))
      IF(K. LE. 0) GO TO 2
      B(IROW)=B(IROW) +
     +  T(K)*(CAPM(K, ICOL)/DT - (1. -R)*A(K, ICOL))
      K=K-1
 2    CONTINUE
 1    B(IROW)=B(IROW) +
     +  T(IROW)*(CAPM(IROW, 1)/DT - (1. -R)*A(IROW, 1))

      DO 3 IROW=1, NNT
      DO 3 ICOL=1, IBAND
 3    A(IROW, ICOL)=CAPM(IROW, ICOL)/DT + A(IROW, ICOL)*R

      RETURN
      END

cccccccccccccccccccccccccccccccccccccccccccccccccccccccccccccccccccccc

      SUBROUTINE MODIFY(NNT, IBAND, NNFT, NFT, TFIX)
      COMMON/MATRIX/A(500, 125), B(500)
      DIMENSION NFT(100), TFIX(100)

      DO 1 IT=1, NNFT

      IROW=NFT(IT)
      TF=TFIX(IT)
      K=IROW-1
      DO 2 J=2, IBAND
      M=IROW+J-1
      IF(M. GT. NNT) GO TO 100
      B(M)=B(M) - TF*A(IROW, J)
      A(IROW, J)=0.
 100  IF(K. LE. 0) GO TO 2
      B(K)=B(K) - TF*A(K, J)
      A(K, J)=0.
      K=K-1
 2    CONTINUE

 1    B(IROW)=TF*A(IROW, 1)

      RETURN
      END
```

```
CCCCCCCCCCCCCCCCCCCCCCCCCCCCCCCCCCCCCCCCCCCCCCCCCCCCCCCCCCCCCCCCCCCCCCCCCCCC

      SUBROUTINE SOLVE(N,IBAND,ISOLVE)

C  Solution by triangular decomposition, utilising symmetry and bandwidth

      COMMON/MATRIX/A(500,125),B(500)
      COMMON/TEMP/T(500),T1(500)
      DIMENSION R(500),E(500)

C  Decompose banded matrix

      CALL DECOMP(N,IBAND)

C  Decompose rhs vector

      CALL DECRHS(N,IBAND)

C  Solve by back substitution

      CALL SOLVB(N,IBAND,T1,B)

      IF(ISOLVE.EQ.6) RETURN

C  Calculate residual

 100  DO 2 I=1,N
      R(I)=B(I)-A(I,1)*T1(I)
      M=I
       DO 22 J=2,IBAND
       M=M+1
       IF(M.GT.N) GO TO 2
 22    R(I)=R(I)-A(I,J)*T1(M)
 2    CONTINUE

C  Solve for correction vector

      CALL SOLVB(N,IBAND,E,R)

C  Correct temperature and check accuracy

      ICONV=1
      DO 3 I=1,N
      IF(ABS(E(I)).GT.1.E-5) ICONV=0
 3    T1(I)=T1(I)+E(I)
      IF(ICONV.EQ.0) GO TO 100
      RETURN
      END

CCCCCCCCCCCCCCCCCCCCCCCCCCCCCCCCCCCCCCCCCCCCCCCCCCCCCCCCCCCCCCCCCCCCCCCCCCCC

      SUBROUTINE DECOMP(N,IBAND)

C  Decomposes A to upper triangular form

      COMMON/MATRIX/A(500,125)

      NP1=N-1
      DO 1 I=1,NP1
      MJ=I+IBAND-1
      IF(MJ.GT.N) MJ=N
      NJ=I+1
      MK=IBAND
      IF((N-I+1).LT.IBAND) MK=N-I+1
      ND=0
      DO 1 J=NJ,MJ
      MK=MK-1
      ND=ND+1
      NL=ND+1
      DO 1 K=1,MK
      NK=ND+K
1     A(J,K)=A(J,K) - A(I,NL)*A(I,NK)/A(I,1)

      RETURN
      END
```

```
CCCCCCCCCCCCCCCCCCCCCCCCCCCCCCCCCCCCCCCCCCCCCCCCCCCCCCCCCCCCCCCCCCCCCCCCCCCCCCC

      SUBROUTINE SOLVB(N, IBAND, T, B)

      COMMON/MATRIX/A(500, 125)
      DIMENSION T(500), B(500)

C  Form solution by back-substitution

      T(N)=B(N)/A(N, 1)
      DO 2 I=N-1, 1, -1
      MJ=IBAND
      IF((I+IBAND-1). GT. N) MJ=N-I+1
      SUM=0.
       DO 3 J=2, MJ
       NN=I+J-1
 3      SUM=SUM + A(I, J)*T(NN)
 2     T(I)=(B(I)-SUM)/A(I, 1)

      RETURN
      END

CCCCCCCCCCCCCCCCCCCCCCCCCCCCCCCCCCCCCCCCCCCCCCCCCCCCCCCCCCCCCCCCCCCCCCCCCCCCCCC

      SUBROUTINE DECRHS(N, IBAND)

      COMMON/MATRIX/A(500, 125), B(500)

C  Decompose column vector

      DO 1 I=1, N-1
      MJ=I+IBAND-1
      IF(MJ. GT. N) MJ=N
      NJ=I+1
      L=1
      DO 1 J=NJ, MJ
      L=L+1
 1     B(J)=B(J) - A(I, L)*B(I)/A(I, 1)

      RETURN

      END

CCCCCCCCCCCCCCCCCCCCCCCCCCCCCCCCCCCCCCCCCCCCCCCCCCCCCCCCCCCCCCCCCCCCCCCCCCCCCCC

      SUBROUTINE COEFFS(NER, MIDR, EPS, TRAD, HR, NERT)
      COMMON/TEMP/T(500), T1(500)
      COMMON/MESH/X(500), Y(500), INODE(8, 200)
      DIMENSION NER(NERT), MIDR(NERT), EPS(NERT), TRAD(NERT), HR(NERT)
      DATA STEFAN/5. 67E-8/

      DO 1 IEL=1, NERT
      NE=NER(IEL)
      JR=MIDR(IEL)
      DO 2 I=2, 8, 2
      IF(JR. EQ. INODE(I, NE)) THEN
       IR=I-1
       KR=I+1
       IF(KR. EQ. 9) KR=1
       IR=INODE(IR, NE)
       KR=INODE(KR, NE)
       END IF
 2     CONTINUE

      TAVE=(T1(IR)+T1(JR)+T1(KR))/3.  + 273. 16
      TR=TRAD(IEL) + 273. 16
 1     HR(IEL)=STEFAN*EPS(IEL)*(TAVE**2+TR**2)*(TAVE+TR)

      RETURN
      END
```

```
CCCCCCCCCCCCCCCCCCCCCCCCCCCCCCCCCCCCCCCCCCCCCCCCCCCCCCCCCCCCCCCCCCCCCCCCC

      SUBROUTINE CONVRG(HRNEW,HROLD,NERT,ICONV)
      DIMENSION HRNEW(100),HROLD(100)
      DATA DELTA/.01/

      ICONV=0

      DO 1 IEL=1,NERT
      IF(HROLD(IEL).EQ.0.) RETURN
      TEST=ABS((HRNEW(IEL)-HROLD(IEL))/HROLD(IEL))
 1    IF(TEST.GT.DELTA)RETURN

      ICONV=1

      RETURN
      END

CCCCCCCCCCCCCCCCCCCCCCCCCCCCCCCCCCCCCCCCCCCCCCCCCCCCCCCCCCCCCCCCCCCCCCCCCCC

      SUBROUTINE FAIL
      WRITE(1,10)
 10   FORMAT(/////'RADIATIVE BOUNDARY - NO CONVERGENCE AFTER',
     +  ' 10 ITERATIONS'/////)
      CALL EXIT
      END

CCCCCCCCCCCCCCCCCCCCCCCCCCCCCCCCCCCCCCCCCCCCCCCCCCCCCCCCCCCCCCCCCCCCCCC

      SUBROUTINE NEWK(KCONV,NET,NK,TK,THCOND)
      COMMON/COND/C(3,4,200),RHOCP(200)
      COMMON/MESH/X(500),Y(500),INODE(8,200)
      DIMENSION TK(NK),THCOND(3,NK)
      REAL INT(2)

      INT(1)=-.577350269189626
      INT(2)=-INT(1)
      TOL=.01

      DO 1 NE=1,NET
      IP=0
      DO 1 I=1,2
      R=INT(I)
      DO 1 J=1,2
      S=INT(J)
      IP=IP+1

      CALL ELTEMP(R,S,NE,TIP)

      DO 1 K=1,3
      IF(C(K,IP,NE).EQ.0.) GO TO 1
      CALL INTERK(NK,TK,THCOND,K,TIP,CNEW)
      IF(ABS(CNEW-C(K,IP,NE))/C(K,IP,NE).GT.TOL) KCONV=0
      C(K,IP,NE)=CNEW
 1    CONTINUE

      RETURN

      END
```

```
CCCCCCCCCCCCCCCCCCCCCCCCCCCCCCCCCCCCCCCCCCCCCCCCCCCCCCCCCCCCCCCCCCCCCCCCCCCCCCCC

      SUBROUTINE NEWCP(KCONV,NET,NCP,TCP,CP,TMID,IFH)

      COMMON/COND/C(3,4,200),RHOCP(200)
      COMMON/MESH/X(500),Y(500),INODE(8,200)

      DIMENSION TCP(NCP),CP(NCP),TMID(NET)

      TOL=0.01

      DO 1 NE=1,NET

      CALL ELTEMP(0.,0.,NE,TM)

      IF(IFH.EQ.1) THEN
       CALL INTER(NCP,TCP,CP,TM,H1)
       CALL INTER(NCP,TCP,CP,TMID(NE),H2)
       CPNEW=RHOCP(NE)
       DH=H1-H2
       DT=TM-TMID(NE)
       IF(ABS(DH).GT.0..AND.ABS(DT).GT.0.01) CPNEW=DH/DT
       TMID(NE)=TM
      ELSE
       CALL INTER(NCP,TCP,CP,TM,CPNEW)
      END IF
      IF(ABS(CPNEW-RHOCP(NE))/RHOCP(NE).GT.TOL) KCONV=0
 1    RHOCP(NE)=CPNEW

      RETURN

      END
CCCCCCCCCCCCCCCCCCCCCCCCCCCCCCCCCCCCCCCCCCCCCCCCCCCCCCCCCCCCCCCCCCCCCCCCCC

      SUBROUTINE OUTPUT(NNT,IFTRNS,TIME,NSTART,NSTOP,NINT)
      COMMON/MESH/X(500),Y(500),INODE(8,200)
      COMMON/TEMP/T(500),T1(500)
      IF(IFTRNS.EQ.0) WRITE(1,10)
      IF(IFTRNS.EQ.1) WRITE(1,11)TIME
      WRITE(1,12)
      IF(NSTART.EQ.0) GO TO 100
      DO 2 I=NSTART,NSTOP,NINT
 2    WRITE(1,13)I,X(I),Y(I),T(I)
      GO TO 200
 100  DO 1 I=1,NNT
 1    WRITE(1,13)I,X(I),Y(I),T(I)
 200  WRITE(1,14)

      RETURN

 10   FORMAT(///'STEADY-STATE TEMPERATURES',/,25('-'))
 11   FORMAT(///'TEMPERATURES AT TIME = ',F9.3,' SEC.',
     +  /,37('-'))
 12   FORMAT(/'NODE     X-COORDINATE     Y-COORDINATE      ',
     +  'TEMPERATURE')
 13   FORMAT(I4,3(5X,F12.5))
 14   FORMAT(/////'****************************************',
     + '***************')

      END
```

```
CCCCCCCCCCCCCCCCCCCCCCCCCCCCCCCCCCCCCCCCCCCCCCCCCCCCCCCCCCCCCCCCCCCCCCCCCC

      SUBROUTINE OUTBC(TIME,NNFT,NFT,TFIX,NECT,NCE,H,TINF,NEQT,NQE,Q,
     +  NERT,NER,EPS,TRAD,NGEN,NEGEN,GEN,MIDC,MIDR,MIDQ)
      DIMENSION NFT(100),TFIX(100),NCE(100),H(100),TINF(100),
     +  NQE(100),Q(100),NER(100),EPS(100),TRAD(100),NEGEN(200),GEN(200),
     +  MIDC(100),MIDR(100),
     +  MIDQ(100)

      WRITE(1,10)TIME
      CALL TITLE1(NNFT)
      IF(NNFT.EQ.0)GO TO 100
      DO 1 IT=1,NNFT
 1    CALL TITLE2(NFT(IT),TFIX(IT))

 100  CALL TITLE3(NECT)
      IF(NECT.EQ.0) GO TO 200
      DO 2 I=1,NECT
 2    CALL TITLE4(NCE(I),MIDC(I),H(I),TINF(I))

 200  CALL TITLE5(NEQT)
      IF(NEQT.EQ.0) GO TO 300
      DO 3 I=1,NEQT
 3    CALL TITLE6(NQE(I),MIDQ(I),Q(I))

 300  CALL TITLE7(NERT)
      IF(NERT.EQ.0) GO TO 400
      DO 4 I=1,NERT
 4    CALL TITLE8(NER(I),MIDR(I),EPS(I),TRAD(I))

 400  CALL TITLE9(NGEN)
      IF(NGEN.EQ.0)RETURN
      DO 5 I=1,NGEN
 5    CALL TITL10(NEGEN(I),GEN(NEGEN(I)))

      RETURN

 10   FORMAT(/////'BOUNDARY CONDITIONS AT TIME = ',F9.3,' SEC.',/,
     +  44('-'),/)

      END

CCCCCCCCCCCCCCCCCCCCCCCCCCCCCCCCCCCCCCCCCCCCCCCCCCCCCCCCCCCCCCCCCCCCCCCCCC

      SUBROUTINE NEWBC(BCTIME,TIME,NNFT,NFT,TFIX,
     +  NECT,NCE,MIDC,H,TINF,NEQT,NQE,MIDQ,Q,NERT,HROLD,NER,MIDR,
     +  EPS,TRAD,NITER,ITER,NGEN,NEGEN,GEN)

      DIMENSION NFT(100),TFIX(100),NCE(100),MIDC(100),H(100),TINF(100),
     + NQE(100),MIDQ(100),Q(100),HROLD(100),MIDR(100),EPS(100),NER(100),
     + TRAD(100),NEGEN(200),GEN(200)
      CHARACTER*40 BCTIME

      OPEN(5,FILE=BCTIME,STATUS='OLD')

 100  READ(5,*,END=700)T
      IF(TIME.LE.T)THEN
       CLOSE(5)
       RETURN
       END IF
      READ(5,*)NNFT
      IF(NNFT.EQ.0)GO TO 200
      IF(NNFT.GT.100) CALL TOOBIG(4)
      DO 1 I=1,NNFT
 1    READ(5,*)NFT(I),TFIX(I)
 200  READ(5,*)NECT
      IF(NECT.EQ.0)GO TO 300
      IF(NECT.GT.100) CALL TOOBIG(5)
      DO 2 I=1,NECT
 2    READ(5,*)NCE(I),MIDC(I),H(I),TINF(I)
 300  READ(5,*)NEQT
      IF(NEQT.EQ.0)GO TO 400
      IF(NEQT.GT.100) CALL TOOBIG(5)
```

```
       DO 3 I=1,NEQT
 3     READ(5,*)NQE(I),MIDQ(I),Q(I)
 400   READ(5,*)NERT
       IF(NERT.EQ.0)GO TO 500
       IF(NERT.GT.100) CALL TOOBIG(5)
       DO 4 I=1,NERT
       HROLD(I)=0.
 4     READ(5,*)NER(I),MIDR(I),EPS(I),TRAD(I)
       NITER=0
       ITER=0
 500   READ(5,*)NGEN
       IF(NGEN.EQ.0)GO TO 600
       IF(NGEN.GT.200) CALL TOOBIG(2)
       DO 5 I=1,NGEN
 5     READ(5,*)NEGEN(I),GEN(NEGEN(I))

 600   GO TO 100

 700   CLOSE(5)

       RETURN

       END

CCCCCCCCCCCCCCCCCCCCCCCCCCCCCCCCCCCCCCCCCCCCCCCCCCCCCCCCCCCCCCCCCCCCCCCCCC

       SUBROUTINE HTFLUX(NNT,NET,FLNAME)

       COMMON/TEMP/P(500),T1(500)
       COMMON/MESH/X(500),Y(500),INODE(8,200)
       COMMON/COND/C(3,4,200),RHOCP(200)

       REAL N(8),JAC(2,2),JACINV(2,2),DNR(8),DNS(8),CC(2,8),B(2,8)
       CHARACTER*40 FLNAME

C  Open data file

       OPEN(6,FILE=FLNAME)

       DO 1 NE=1,NET

C  Shape fns, derivs etc at r=s=0

       CALL SHAPE(0.,0.,N)
       CALL DERIV(0.,0.,DNR,DNS)
       CALL JACOB(0.,0.,JAC,NE,DNR,DNS)
       CALL DET(JAC,DETJAC)
       CALL INV(JAC,DETJAC,JACINV)

       DO 2 ICOL=1,8
       CC(1,ICOL)=DNR(ICOL)
 2     CC(2,ICOL)=DNS(ICOL)

C  Transform to cartesians

       CALL MULT(JACINV,CC,B,2,8,2)

       XX=0.
       YY=0.
       DTX=0.
       DTY=0.
       DO 3 I=1,8
       IN=INODE(I,NE)
       DTX=DTX+B(1,I)*T(IN)
       DTY=DTY+B(2,I)*T(IN)
       XX=XX+N(I)*X(IN)
 3     YY=YY+N(I)*Y(IN)

       QX=-C(1,1,NE)*DTX-C(2,1,NE)*DTY
       QY=-C(2,1,NE)*DTX-C(3,1,NE)*DTY

 1     WRITE(6,20)XX,YY,QX,QY

 20    FORMAT(2(F10.5,3X),2(F12.4,2X))

       CLOSE(6)
       RETURN

       END
```

```
cccccccccccccccccccccccccccccccccccccccccccccccccccccccccccccccccccccccccccc

      SUBROUTINE PLOTOP(PFNAME,TITLE,NNT)

      COMMON/MESH/X(500),Y(500),INODE(8,200)
      COMMON/TEMP/T(500),T1(500)
      CHARACTER*40 PFNAME,TITLE

C  Find contour interval and boundaries

      XMIN=1.E10
      YMIN=XMIN
      TMIN=XMIN
      XMAX=-1.E10
      YMAX=XMAX
      TMAX=XMAX

      DO 1 I=1,NNT
      IF(X(I).LT.XMIN) XMIN=X(I)
      IF(X(I).GT.XMAX) XMAX=X(I)
      IF(Y(I).LT.YMIN) YMIN=Y(I)
      IF(Y(I).GT.YMAX) YMAX=Y(I)
      IF(T(I).LT.TMIN) TMIN=T(I)
 1    IF(T(I).GT.TMAX) TMAX=T(I)

      CINT=(TMAX-TMIN)/10.
      INT=CINT*100.+.5
      CINT=FLOAT(INT)/100.

      OPEN(5,FILE=PFNAME)

      WRITE(5,10)
      DO 2 I=1,NNT
 2    WRITE(5,20)X(I),Y(I),T(I)
      WRITE(5,30)XMIN,XMAX,YMIN,YMAX,CINT
      WRITE(5,40)TITLE

      CLOSE(5)
      RETURN

 10   FORMAT('*GENESYS'/'*START ''RANDOM/1'''/'JOB ISOTHERM PLOT'/
     +  'LIMIT ROWS TO 400'/'*TABLES'/'''TEMPERATURES'''/
     +  'X    Y    LEVEL')
 20   FORMAT(3(F10.5,3X))
 30   FORMAT('*MASTER'/'SET BOUNDARY FOR TABLE ''TEMPERATURES'' ...'/
     +  '     USING X LIMITS ',F5.1,',',F5.1,' ...'/
     +  9X,'Y LIMITS ',F5.1,',',F5.1/
     +  'INTERVAL FOR CONTOURS ',F5.2)
 40   FORMAT('PLOT TABLE ''TEMPERATURES'' SCALE 10 ...'/
     +  '     SHOWING CONTOURS ...'/'   USING CURVE SMOOTHING ...'/
     +  '     TITLE ''',(A),''' ...'/'    ANNOTATION OF CONTOURS'/
     +  '*FINISH')

      END

ccccccccccccccccccccccccccccccccccccccccccccccccccccccccccccccccccccccccccccccc

      SUBROUTINE TOOBIG(I)

      IF(I.EQ.1) WRITE(1,1)
      IF(I.EQ.2) WRITE(1,2)
      IF(I.EQ.3) WRITE(1,3)
      IF(I.EQ.4) WRITE(1,4)
      IF(I.EQ.5) WRITE(1,5)
      IF(I.EQ.6) THEN
       WRITE(1,7)
       GO TO 100
      END IF
      WRITE(1,6)

 100  CLOSE(5)
      CALL EXIT
```

```
 1     FORMAT(///'TOO MANY NODES! '/)
 2     FORMAT(///'TOO MANY ELEMENTS! '/)
 3     FORMAT(///'BANDWIDTH TOO BIG! '/)
 4     FORMAT(///'TOO MANY FIXED TEMPERATURES! '/)
 5     FORMAT(///'TOO MANY BOUNDARY ELEMENTS! '/)
 6     FORMAT('Modify mesh data, or redimension program'//,
     +  40('*'),//)
 7     FORMAT(///'Too many entries in KTEMP or CPTEMP - max. 20! '//,
     +  40('*'),//)

       END

CCCCCCCCCCCCCCCCCCCCCCCCCCCCCCCCCCCCCCCCCCCCCCCCCCCCCCCCCCCCCCCCCCCCCCCCCCCC

       SUBROUTINE INTER(N,X,Y,XX,YY)

       DIMENSION X(N),Y(N)

       DO 1 I=2,N
 1     IF(XX.LE.X(I)) GO TO 100
 100   IF(I.GT.N) I=N
       YY=Y(I)+(Y(I)-Y(I-1))*(XX-X(I))/(X(I)-X(I-1))

       RETURN

       END

CCCCCCCCCCCCCCCCCCCCCCCCCCCCCCCCCCCCCCCCCCCCCCCCCCCCCCCCCCCCCCCCCCCCCCCCCCCC

       SUBROUTINE INTERK(N,TK,TH,K,T,CNEW)
       DIMENSION TK(N),TH(3,N)

       DO 1 I=2,N
 1     IF(T.LE.TK(I)) GO TO 100
 100   IF(I.GT.N) I=N
       CNEW=TH(K,I) + (TH(K,I)-TH(K,I-1))*(T-TK(I))/
     +    (TK(I)-TK(I-1))

       RETURN

       END

CCCCCCCCCCCCCCCCCCCCCCCCCCCCCCCCCCCCCCCCCCCCCCCCCCCCCCCCCCCCCCCCCCCCCCCCCCCC

       SUBROUTINE ELTEMP(R,S,NE,TT)

       COMMON/MESH/X(500),Y(500),INODE(8,200)
       COMMON/TEMP/T(500),T1(500)
       REAL N(8)

       CALL SHAPE(R,S,N)
       TT=0.
       DO 1 K=1,8
       IN=INODE(K,NE)
 1     TT=TT+T1(IN)*N(K)

       RETURN

       END
```

```
CCCCCCCCCCCCCCCCCCCCCCCCCCCCCCCCCCCCCCCCCCCCCCCCCCCCCCCCCCCCCCCCCCCCCCCCCCCCCCC

      SUBROUTINE UPTEMP(NNT)

      COMMON/TEMP/T(500),T1(500)

      DO 1  I=1,NNT
 1    T(I)=T1(I)

      RETURN

      END

CCCCCCCCCCCCCCCCCCCCCCCCCCCCCCCCCCCCCCCCCCCCCCCCCCCCCCCCCCCCCCCCCCCCCCCCCCCCCCC

      SUBROUTINE VZERO(NNT)

      COMMON/VECTRS/QV(500),CV(500),RV(500),QV(500)

      DO 1  I=1,NNT
      CV(I)=0.
      RV(I)=0.
 1    QV(I)=0.

      RETURN

      END

CCCCCCCCCCCCCCCCCCCCCCCCCCCCCCCCCCCCCCCCCCCCCCCCCCCCCCCCCCCCCCCCCCCCCCCCCCCCCCC
```

A-I.5 THREE-DIMENSIONAL CONDUCTION

The theoretical and experimental validation work presented in this thesis has been confined to transient anisotropic conduction in two dimensions. However, as discussed in 5.11, the extension of the finite element model to three dimensions is straightforward, and the program 'FEANCO-3' has been established on the Prime Computer at Plymouth. The program has been adapted directly from FEANCO, and has the same wide range of capabilities. At the time of writing, however, it has only been subjected to limited validation calculations, and prospective users should regard it with caution.

The FORTRAN listing of the three-dimensional program is not given in full here, since much of the coding is identical to that of FEANCO (A-I.4). Instead, the essential differences are outlined, and relevant extracts from the program given in A-I.6.

The three-dimensional quadratic element (Fig 5.3) requires a third cartesian coordinate (z) and 20 nodes. This increases the numerical integration points from 4 to 8, and from 9 to 27 in subroutines BASE and CAP respectively, and there are 6 independent thermal conductivity coefficients (Equation 5.31). Convection and other boundary conditions are applied over a surface instead of an element edge, and these are identified by the numbers of the nodes at opposite corners of the face. Volume and surface elements are transformed according to Equations 5.35 and 5.36, and the three-dimensional analogy of Equation 5.22 for integration over an element is

$$\int_{-1}^{1}\int_{-1}^{1}\int_{-1}^{1} f(r,s,t)\,dr\,ds\,dt = \sum_{i=1}^{n}\sum_{j=1}^{n}\sum_{k=1}^{n} W_i W_j W_k f(r_i, s_j, t_k)$$

The procedures for assembly, time integration, modification and solution of the global matrices and vector are identical to those discussed in A-I.2.

A-I.6 EXTRACTS FROM FORTRAN LISTING OF FEANCO-3

A-I.6.1 Main Program (up to call to BASE)

```
C  Anisotropic conduction in three dimensions.
C  July 1984 version.

C  Common blocks and dimension statements

      COMMON/MATB/BM(500,125)
      COMMON/MATC/CM(500,125)
      COMMON/MATR/RM(500,125)
      COMMON/MATRIX/A(500,125),B(500)
      COMMON/MATCAP/CAPM(500,125)
      COMMON/VECTRS/QV(500),CV(500),RV(500),QV(500)
      COMMON/TEMP/T(500),T1(500)
      COMMON/MESH/X(500),Y(500),Z(500),INODE(20,200)
      COMMON/COND/C(6,8,200),RHOCP(200)
      DIMENSION NFT(100),TFIX(100),NCE(100),MIDC(2,100),
     +  TINF(100),EPS(100),TRAD(100),MIDR(2,100),NER(100),
     +  HROLD(100),HRNEW(100),NQE(100),MIDQ(2,100),Q(100),
     +  H(100),NEQEN(200),QEN(200),TK(20),THCOND(6,20),BOLD(500),
     +  TCP(20),CP(20),TMID(200)
      CHARACTER*40 TITLE,FNAME,MENAME,THNAME,BCNAME,ITNAME,
     +   HEADER,BCTIME,CPTEMP,KTEMP

C  Get name of control file

      WRITE(1,20)
      READ(1,'(A)')FNAME

C  Open file and read control parameters

      OPEN(5,FILE=FNAME,STATUS='OLD')
      READ(5,'(A)')HEADER
      READ(5,*)IFTRNS
      READ(5,*)ISOLVE
      READ(5,*)IFHOMQ
      IF(IFHOMQ.EQ.1)THEN
       READ(5,'(A)')THNAME
       ELSE
       READ(5,*)(C(K,1,1),K=1,6),RHOCP(1)
       END IF
      READ(5,*)IFTEMP
      IF(IFTEMP.EQ.1.OR.IFTEMP.EQ.3) READ(5,'(A)') KTEMP
      IF(IFTEMP.QT.1) THEN
       READ(5,'(A)') CPTEMP
       READ(5,*) IFH
      END IF
      READ(5,'(A)')MENAME
      READ(5,'(A)')BCNAME
      IF(IFTRNS.NE.1) GO TO 100
      READ(5,*)DT,TIMEND,NSTEPS,INTALQ
      READ(5,*)IFINIT
      IF(IFINIT.EQ.1)THEN
       READ(5,'(A)')ITNAME
       OPEN(6,FILE=ITNAME,STATUS='OLD')
       READ(6,*)NNT
       DO 1 IT=1,NNT
1      READ(6,*)NT,T(NT)
       CLOSE(6)
       ELSE
       READ(5,*)T(1)
       DO 2 IT=2,500
2      T(IT)=T(1)
       END IF
      READ(5,*)IFTIME
      IF(IFTIME.EQ.1)READ(5,'(A)')BCTIME
```

```
      NSTART=0
      READ(5,*,END=100) NSTART,NSTOP,NINT

  100 CLOSE(5)

C  Output basic information about this run

      CALL INFO(HEADER,THNAME,ITNAME,IFTRNS,ISOLVE,IFHOMG,IFTEMP,IFTIME,
     +  CPTEMP,IFH,BCTIME,
     +  IFINIT,KTEMP,DT,TIMEND,NSTEPS,INTALG)

C  Read the mesh data - node coordinates and topology - and compute bandwidth

      OPEN(5,FILE=MENAME,STATUS='OLD')
      READ(5,'(A)')TITLE
      WRITE(1,21)MENAME,TITLE
      READ(5,*)NNT
      IF(NNT.GT.500) CALL TOOBIG(1)
      DO 3 I=1,NNT
    3 READ(5,*)NN,X(NN),Y(NN),Z(NN)
      READ(5,*)NET
      IF(NET.GT.200) CALL TOOBIG(2)
      DO 4 I=1,NET
    4 READ(5,*)NE,(INODE(J,NE),J=1,20)
      READ(5,*,END=44)IBAND
      GO TO 45
   44 IBAND=1
      DO 444 NE=1,NET
      NMIN=NNT
      NMAX=1
      DO 445 II=1,20
      IN=INODE(II,NE)
      IF(IN.LT.NMIN) NMIN=IN
  445 IF(IN.GT.NMAX) NMAX=IN
      IB=NMAX-NMIN+1
  444 IF(IB.GT.IBAND) IBAND=IB
   45 CLOSE(5)
      IF(IBAND.GT.125) CALL TOOBIG(3)

C  Read thermal properties

      IF(IFHOMG.EQ.1)THEN
       OPEN(5,FILE=THNAME,STATUS='OLD')
       READ(5,'(A)')TITLE
       WRITE(1,22)THNAME,TITLE
       DO 5 NE=1,NET
       DO 5 IP=1,8
    5  READ(5,*)(C(K,IP,NE),K=1,6),RHOCP(NE)
       CLOSE(5)
      ELSE
       DO 55 NE=1,NET
       RHOCP(NE)=RHOCP(1)
       DO 55 IP=1,8
       DO 55 K=1,6
   55  C(K,IP,NE)=C(K,1,1)
      END IF

      IF(IFTEMP.GT.1) THEN
       OPEN(5,FILE=CPTEMP,STATUS='OLD')
       READ(5,*) NCP
       IF(NCP.GT.20) CALL TOOBIG(6)
       READ(5,*)(TCP(I),CP(I),I=1,NCP)
       CLOSE(5)
       DO 551 NE=1,NET
  551  CALL ELTEMP(0.,0.,0.,NE,TMID(NE))
      END IF

      IF(IFTEMP.EQ.1 .OR. IFTEMP.EQ.3) THEN
       OPEN(5,FILE=KTEMP,STATUS='OLD')
       READ(5,*) NK
       IF(NK.GT.20) CALL TOOBIG(6)
       READ(5,*) (TK(I),(THCOND(J,I),J=1,6),I=1,NK)
       CLOSE(5)
      END IF
```

```
C  Read boundary conditions

      OPEN(5,FILE=BCNAME,STATUS='OLD')
      READ(5,'(A)')TITLE
      WRITE(1,23)BCNAME,TITLE
      READ(5,*)NNFT
      IF(NNFT.GT.100) CALL TOOBIG(4)
      CALL TITLE1(NNFT)
      IF(NNFT.EQ.0)GO TO 150
      DO 6 IT=1,NNFT
      READ(5,*)NFT(IT),TFIX(IT)
 6    CALL TITLE2(NFT(IT),TFIX(IT))

 150  READ(5,*)NECT
      IF(NECT.GT.100) CALL TOOBIG(5)
      CALL TITLE3(NECT)
      IF(NECT.EQ.0)GO TO 200
      DO 7 I=1,NECT
      READ(5,*)NCE(I),MIDC(1,I),MIDC(2,I),H(I),TINF(I)
 7    CALL TITLE4(NCE(I),MIDC(1,I),MIDC(2,I),H(I),TINF(I))

 200  READ(5,*)NEQT
      IF(NEQT.GT.100) CALL TOOBIG(5)
      CALL TITLE5(NEQT)
      IF(NEQT.EQ.0)GO TO 300
      DO 8 I=1,NEQT
      READ(5,*)NQE(I),MIDQ(1,I),MIDQ(2,I),Q(I)
 8    CALL TITLE6(NQE(I),MIDQ(1,I),MIDQ(2,I),Q(I))

 300  READ(5,*)NERT
      IF(NERT.GT.100) CALL TOOBIG(5)
      CALL TITLE7(NERT)
      IF(NERT.EQ.0)GO TO 400
      DO 9 I=1,NERT
      HROLD(I)=0.
      READ(5,*)NER(I),MIDR(1,I),MIDR(2,I),EPS(I),TRAD(I)
 9    CALL TITLE8(NER(I),MIDR(1,I),MIDR(2,I),EPS(I),TRAD(I))
      NITER=0
      ITER=0

 400  READ(5,*)NGEN
      IF(NGEN.GT.200) CALL TOOBIG(2)
      CALL TITLE9(NGEN)
      IF(NGEN.EQ.0)GO TO 500
      DO 10 IG=1,NGEN
      READ(5,*)NEGEN(IG),GEN(NEGEN(IG))
 10   CALL TITL10(NEGEN(IG),GEN(NEGEN(IG)))
 500  CLOSE(5)

C  Initialise vectors

      CALL VZERO(NNT)

      TIME=DT
      NDT=0

 600  CALL BASE(NNT,IBAND,NET,NEGEN,GEN)
```

A-I.6.2. Subroutine BASE

```
CCCCCCCCCCCCCCCCCCCCCCCCCCCCCCCCCCCCCCCCCCCCCCCCCCCCCCCCCCCCCCCCCCCCCCCCCCCCCCC

      SUBROUTINE BASE(NNT,IBAND,NET,NEGEN,GEN)

C  Evaluation of global conduction matrix and generation vector.

      COMMON/MATB/BM(500,125)
      COMMON/VECTRS/GV(500),CV(500),RV(500),QV(500)
      COMMON/MESH/X(500),Y(500),Z(500),INODE(20,200)
      COMMON/COND/C(6,8,200),RHOCP(200)

      REAL JAC(3,3),JACINV(3,3),N(20),INT(2)
      DIMENSION CC(3,20),B(3,20),BTRANS(20,3),D(3,3),DNR(20),
     +   DNS(20),DNT(20),BE(20,20),BTRAND(20,3),NEGEN(200),GEN(200)
```

```
C   Initialise matrix and vector.

        DO 1  IROW=1,NNT
        GV(IROW)=0.
        DO 1  ICOL=1,IBAND
 1      BM(IROW,ICOL)=0.

C   Define points for numerical integration (natural coords.).  Weights are unity.

        INT(1)=-.577350269189626
        INT(2)=-INT(1)

C   For each element...

        DO 2 NE=1,NET

C   ...and each integration point...

        IP=0
        DO 2 I=1,2
        R=INT(I)
        DO 2 J=1,2
        S=INT(J)
        DO 2 K=1,2
        T=INT(K)
        IP=IP+1

C   Set up property matrix.

        D(1,1)=C(1,IP,NE)
        D(2,2)=C(4,IP,NE)
        D(3,3)=C(6,IP,NE)
        D(1,2)=C(2,IP,NE)
        D(2,1)=D(1,2)
        D(1,3)=C(3,IP,NE)
        D(3,1)=D(1,3)
        D(2,3)=C(5,IP,NE)
        D(3,2)=D(2,3)

C   Evaluate shape functions, derivatives and Jacobian for this point.

        CALL SHAPE(R,S,T,N)
        CALL DERIV(R,S,T,DNR,DNS,DNT)
        CALL JACOB(R,S,T,DNR,DNS,DNT,NE,JAC)

C   Evaluate inverse of J and det J.

        CALL DET(JAC,DETJAC)
        CALL INV(JAC,DETJAC,JACINV)

C   Set up matrix of shape function derivatives.

        DO 3 ICOL=1,20
        CC(1,ICOL)=DNR(ICOL)
        CC(2,ICOL)=DNS(ICOL)
 3      CC(3,ICOL)=DNT(ICOL)

C   Transform from natural to cartesian coords.  B=inv J . CC

        CALL MULT(JACINV,CC,B,3,20,3)

C   Evaluate transpose of B

        CALL TRANS(B,BTRANS,3,20)

C   Multiply by D, store result in BTRAND.

        CALL MULT(BTRANS,D,BTRAND,20,3,3)
```

```
C  Multiply by B to give element matrix BE.

      CALL MULT(BTRAND, B, BE, 20, 20, 3)

C  Add BE.det J to global matrix, and g.N.det J to generation vector.

      DO 2 IROW=1, 20
      IR=INODE(IROW, NE)
      GV(IR)=GV(IR) + N(IROW)*DETJAC*GEN(NE)
      DO 2 ICOL=IROW, 20
      IC=INODE(ICOL, NE)
      IF(IR.LE. IC)THEN
       BM(IR, IC-IR+1)=BM(IR, IC-IR+1) + BE(IROW, ICOL)*DETJAC
       ELSE
       BM(IC, IR-IC+1)=BM(IC, IR-IC+1) + BE(ICOL, IROW)*DETJAC
      END IF
 2    CONTINUE

      RETURN

      END
```

A-I.6.2. Subroutine CAP

```
      SUBROUTINE CAP(NNT, IBAND, NET)

C  Evaluation of capacitance matrix (3rd order numerical integration).

      COMMON/MESH/X(500), Y(500), Z(500), INODE(20, 200)
      COMMON/COND/C(6, 8, 200), RHOCP(200)
      COMMON/MATCAP/CAPM(500, 125)

      REAL JAC(3, 3), N(20), INT(3)
      DIMENSION WC(3), DNR(20), DNS(20), DNT(20)

C  Initialise matrix

      DO 1 IROW=1, NNT
      DO 1 ICOL=1, IBAND
 1    CAPM(IROW, ICOL)=0.

C  Define integration points and weight coefficients

      INT(1)=-.774596669241483
      INT(2)=0.
      INT(3)=-INT(1)
      WC(1)=5./9.
      WC(2)=8./9.
      WC(3)=WC(1)

C  For each element:

      DO 2 NE=1, NET

C  For each integration point:

      DO 2 I=1, 3
      R=INT(I)
      DO 2 J=1, 3
      S=INT(J)
      DO 2 K=1, 3
      T=INT(K)

C  Evaluate shape functions, Jacobian, etc.

      CALL SHAPE(R, S, T, N)
      CALL DERIV(R, S, T, DNR, DNS, DNT)
      CALL JACOB(R, S, T, DNR, DNS, DNT, NE, JAC)

C  Evaluate det J.

      CALL DET(JAC, DETJAC)
```

```
C  Form capacitance matrix:

      DO 2 IROW=1,20
      IR=INODE(IROW,NE)
      DO 2 ICOL=IROW,20
      IC=INODE(ICOL,NE)
      IF(IR.LE.IC) THEN
       CAPM(IR,IC-IR+1) = CAPM(IR,IC-IR+1) +
     +   N(IROW)*N(ICOL)*DETJAC*RHOCP(NE)*WC(I)*WC(J)*WC(K)
       ELSE
       CAPM(IC,IR-IC+1) = CAPM(IC,IR-IC+1) +
     +   N(IROW)*N(ICOL)*DETJAC*RHOCP(NE)*WC(I)*WC(J)*WC(K)
       END IF
 2    CONTINUE

      RETURN

      END
```

A-I.6.3 Subroutine CONV

```
CCCCCCCCCCCCCCCCCCCCCCCCCCCCCCCCCCCCCCCCCCCCCCCCCCCCCCCCCCCCCCCCCCCCCCCCCCCCCCC

      SUBROUTINE CONV(NCE,MIDC,H,TINF,NECT,NNT,IBAND)

C  Evaluates global convection matrix and vector.

      COMMON/MATC/CM(500,125)
      COMMON/VECTRS/GV(500),CV(500),RV(500),QV(500)
      COMMON/MESH/X(500),Y(500),Z(500),INODE(20,200)

      DIMENSION NCE(NECT),MIDC(2,NECT),H(NECT),TINF(NECT)
      REAL N(20),DNR(20),DNS(20),DNT(20),JAC(3,3),INT(3),WC(3)

      INT(1)=-.774596669241483
      INT(2)=0.
      INT(3)=-INT(1)
      WC(1)=5./9.
      WC(2)=8./9.
      WC(3)=WC(1)

C  Initialise

      DO 1 IROW=1,NNT
      CV(IROW)=0.
      DO 1 ICOL=1,IBAND
 1    CM(IROW,ICOL)=0.

C  For each element with a convective side...

      DO 2 IEL=1,NECT

      NE=NCE(IEL)
      R=0.
      S=0.
      T=0.
      IC=0
      JC=0

C  Locate convective side and check for numbering error.

      DO 3 I=1,8
      IF(MIDC(1,IEL).EQ.INODE(I,NE)) IC=I
 3    IF(MIDC(2,IEL).EQ.INODE(I,NE)) JC=I
      IF((IC*JC).EQ.0) CALL CONERR(NE)
      ISUM=IC+JC
      IF(ISUM.EQ.5) R=1.
      IF(ISUM.EQ.13) R=-1.
      IF(ISUM.EQ.10) S=1.
      IF(ISUM.EQ.8) S=-1.
      IF(ISUM.EQ.11) T=1.
      IF(ISUM.EQ.7) T=-1.
```

```
      DO 2 I=1,3
      IJ1=2
      IJ2=3
      IF(ABS(T).EQ.1.) THEN
       R=INT(I)
       IJ1=1
       IJ2=2
       END IF
      IF(ABS(S).EQ.1.) THEN
       IJ1=1
       IJ2=3
       T=INT(I)
       END IF
      IF(ABS(R).EQ.1.) S=INT(I)

      DO 2 J=1,3
      IF(ABS(T).EQ.1.) S=INT(J)
      IF(ABS(S).EQ.1.) R=INT(J)
      IF(ABS(R).EQ.1.) T=INT(J)

      CALL SHAPE(R,S,T,N)
      CALL DERIV(R,S,T,DNR,DNS,DNT)
      CALL JACOB(R,S,T,DNR,DNS,DNT,NE,JAC)

      TERM1=JAC(IJ1,2)*JAC(IJ2,3) - JAC(IJ1,3)*JAC(IJ2,2)
      TERM2=JAC(IJ1,3)*JAC(IJ2,1) - JAC(IJ1,1)*JAC(IJ2,3)
      TERM3=JAC(IJ1,1)*JAC(IJ2,2) - JAC(IJ1,2)*JAC(IJ2,1)

      AREA=WC(I)*WC(J)*SQRT(TERM1**2+TERM2**2+TERM3**2)
      TERM=AREA*H(IEL)

      DO 2 IROW=1,20
      IR=INODE(IROW,NE)
      CV(IR)=CV(IR) + N(IROW)*TERM*TINF(IEL)
      DO 2 ICOL=IROW,20
      IC=INODE(ICOL,NE)
      IF(IR.LE.IC) THEN
       CM(IR,IC-IR+1)=CM(IR,IC-IR+1) + N(IROW)*N(ICOL)*TERM
       ELSE
       CM(IC,IR-IC+1)=CM(IC,IR-IC+1) + N(IROW)*N(ICOL)*TERM
       END IF

2     CONTINUE

      RETURN
      END
```

A-I.6.4. Subroutines SHAPE, DERIV, JACOB

```
CCCCCCCCCCCCCCCCCCCCCCCCCCCCCCCCCCCCCCCCCCCCCCCCCCCCCCCCCCCCCCCCCCCCCCCCCCCC

      SUBROUTINE SHAPE(R,S,T,N)

C  Shape functions for 20-node 3-d element, using 'PAFEC' topology.

      REAL N(20),RBETA(20),SBETA(20),TBETA(20)
      DATA RBETA/4*1.,4*-1.,4*1.,4*0.,4*-1./,
     +     SBETA/-1.,1.,-1.,1.,-1.,1.,-1.,1.,0.,-1.,1.,0.,-1.,1.,
     +           -1.,1.,0.,-1.,1.,0./,
     +     TBETA/2*-1.,2*1.,2*-1.,2*1.,-1.,2*0.,1.,2*-1.,2*1.,
     +           -1.,2*0.,1./

C  Corner nodes  1-8

      DO 1 I=1,8
      RO=RBETA(I)*R
      SO=SBETA(I)*S
      TO=TBETA(I)*T
1     N(I)=(1.+RO)*(1.+SO)*(1.+TO)*(RO+SO+TO-2.)/8.
```

```
C  Midside nodes

      DO 2 I=13,16
      SO=SBETA(I)*S
      TO=TBETA(I)*T
 2    N(I)=(1.-R*R)*(1.+SO)*(1.+TO)/4.

      DO 3 I1=9,17,8
      I2=I1+3
      DO 3 I=I1,I2,3
      RO=RBETA(I)*R
      TO=TBETA(I)*T
 3    N(I)=(1.-S*S)*(1.+TO)*(1.+RO)/4.

      DO 4 I1=10,18,8
      I2=I1+1
      DO 4 I=I1,I2
      RO=RBETA(I)*R
      SO=SBETA(I)*S
 4    N(I)=(1.-T*T)*(1.+RO)*(1.+SO)/4.

      RETURN
      END
cccccccccccccccccccccccccccccccccccccccccccccccccccccccccccccccccccccccc

      SUBROUTINE DERIV(R,S,T,DNR,DNS,DNT)

C  Derivatives of shape functions

      DIMENSION RBETA(20),SBETA(20),TBETA(20),DNR(20),DNS(20),DNT(20)
      DATA RBETA/4*1.,4*-1.,4*1.,4*0.,4*-1./,
     +     SBETA/-1.,1.,-1.,1.,-1.,1.,-1.,1.,0.,-1.,1.,0.,-1.,1.,
     +           -1.,1.,0.,-1.,1.,0./,
     +     TBETA/2*-1.,2*1.,2*-1.,2*1.,-1.,2*0.,1.,2*-1.,2*1.,
     +           -1.,2*0.,1./

C  Corner nodes  1-8

      DO 1 I=1,8
      RO=RBETA(I)*R
      SO=SBETA(I)*S
      TO=TBETA(I)*T
      DNR(I)=DCORN(RO,SO,TO)*RBETA(I)
      DNS(I)=DCORN(SO,TO,RO)*SBETA(I)
 1    DNT(I)=DCORN(TO,RO,SO)*TBETA(I)

C  Midside nodes

      DO 2 I=13,16
      SO=SBETA(I)*S
      TO=TBETA(I)*T
      DNR(I)=DMID1(R,SO,TO)
      DNS(I)=DMID2(R,TO)*SBETA(I)
 2    DNT(I)=DMID2(R,SO)*TBETA(I)

      DO 3 I1=9,17,8
      I2=I1+3
      DO 3 I=I1,I2,3
      RO=RBETA(I)*R
      TO=TBETA(I)*T
      DNS(I)=DMID1(S,TO,RO)
      DNT(I)=DMID2(S,RO)*TBETA(I)
 3    DNR(I)=DMID2(S,TO)*RBETA(I)

      DO 4 I1=10,18,8
      I2=I1+1
      DO 4 I=I1,I2
      RO=RBETA(I)*R
      SO=SBETA(I)*S
      DNT(I)=DMID1(T,RO,SO)
      DNR(I)=DMID2(T,SO)*RBETA(I)
 4    DNS(I)=DMID2(T,RO)*SBETA(I)

      RETURN
      END
```

```
      FUNCTION DCORN(RO, SO, TO)
      DCORN=(2. *RO+SO+TO-1. )*(1. +SO)*(1. +TO)/8.
      RETURN
      END

      FUNCTION DMID1(RO, SO, TO)
      DMID1=-RO*(1. +SO)*(1. +TO)/2.
      RETURN
      END

      FUNCTION DMID2(RO, TO)
      DMID2=(1. -RO*RO)*(1. +TO)/4.
      RETURN
      END
```

```
CCCCCCCCCCCCCCCCCCCCCCCCCCCCCCCCCCCCCCCCCCCCCCCCCCCCCCCCCCCCCCCCCCCCCCCCCCCC
```

```
      SUBROUTINE JACOB(R, S, T, DNR, DNS, DNT, NE, JAC)

C  Jacobian matrix for 3-d element

      COMMON/MESH/X(500), Y(500), Z(500), INODE(20, 200)
      REAL JAC(3, 3), DNR(20), DNS(20), DNT(20)

      DO 1 I=1, 3
      DO 1 J=1, 3
 1    JAC(I, J)=0.

      DO 2 I=1, 20
      IN=INODE(I, NE)
      JAC(1, 1)=JAC(1, 1) + DNR(I)*X(IN)
      JAC(1, 2)=JAC(1, 2) + DNR(I)*Y(IN)
      JAC(1, 3)=JAC(1, 3) + DNR(I)*Z(IN)
      JAC(2, 1)=JAC(2, 1) + DNS(I)*X(IN)
      JAC(2, 2)=JAC(2, 2) + DNS(I)*Y(IN)
      JAC(2, 3)=JAC(2, 3) + DNS()*Z(IN)
      JAC(3, 1)=JAC(3, 1) + DNT(I)*X(IN)
      JAC(3, 2)=JAC(3, 2) + DNT(I)*Y(IN)
 2    JAC(3, 3)=JAC(3, 3) + DNT(I)*Z(IN)

      RETURN
      END
```

A-I.6.5. Subroutine COEFFS

```
CCCCCCCCCCCCCCCCCCCCCCCCCCCCCCCCCCCCCCCCCCCCCCCCCCCCCCCCCCCCCCCCCCCCCCCCCCCCCCC

      SUBROUTINE COEFFS(NER,MIDR,EPS,TRAD,HR,NERT)
      COMMON/TEMP/T(500),T1(500)
      COMMON/MESH/X(500),Y(500),Z(500),INODE(20,200)
      DIMENSION NER(NERT),MIDR(2,NERT),EPS(NERT),TRAD(NERT),HR(NERT)
      DATA STEFAN/5.67E-8/

      DO 1 IEL=1,NERT
      NE=NER(IEL)
      IC=0
      JC=0
      DO 2 I=1,8
      IF(MIDR(1,IEL).EQ.INODE(I,NE)) IC=I
2     IF(MIDR(2,IEL).EQ.INODE(I,NE)) JC=I
      ISUM=IC+JC
      IF(ISUM.EQ.5) THEN
       TAVE=(T1(INODE(1,NE))+T1(INODE(2,NE))+T1(INODE(3,NE))
     +    +T1(INODE(4,NE)))/4.  + 273.16
       GO TO 100
       END IF
      IF(ISUM.EQ.13) THEN
       TAVE=(T1(INODE(5,NE))+T1(INODE(6,NE))+T1(INODE(7,NE))
     +    +T1(INODE(8,NE)))/4.  + 273.16
       GO TO 100
       END IF
      IF(ISUM.EQ.10) THEN
       TAVE=(T1(INODE(2,NE))+T1(INODE(4,NE))+T1(INODE(6,NE))
     +    +T1(INODE(8,NE)))/4.  + 273.16
       GO TO 100
       END IF
      IF(ISUM.EQ.8) THEN
       TAVE=(T1(INODE(1,NE))+T1(INODE(3,NE))+T1(INODE(5,NE))
     +    +T1(INODE(7,NE)))/4.  + 273.16
       GO TO 100
       END IF
      IF(ISUM.EQ.11) THEN
       TAVE=(T1(INODE(3,NE))+T1(INODE(4,NE))+T1(INODE(7,NE))
     +    +T1(INODE(8,NE)))/4.  + 273.16
      GO TO 100
       END IF
      IF(ISUM.EQ.7) TAVE=(T1(INODE(1,NE))+T1(INODE(2,NE))
     +    +T1(INODE(5,NE))+T1(INODE(6,NE)))/4.  + 273.16

100   TR=TRAD(IEL) + 273.16

1     HR(IEL)=STEFAN*EPS(IEL)*(TAVE**2+TR**2)*(TAVE+TR)

      RETURN
      END
```

APPENDIX II RUNNING THE FINITE ELEMENT PROGRAMS

This appendix contains a detailed description of the various input data files used by FEANCO and FEANCO-3 and contains sufficient information for an inexperienced user to perform calculations. A complete example problem is defined in A-II.5 and extracts from input and output are reproduced.

A-II.1 GENERAL PRINCIPLES

The programs have been operated at Plymouth Polytechnic on a Prime computer system, but they are self-contained, and require no system-dependent facilities. The necessary data resides in sequential files, all of which are held in the user's disc storage space and can be accessed interactively, with output directly to the user terminal; transient problems, however, usually require batch processing. In the latter case, the batch job file contains the same commands which would have been used in an interactive session, ensuring that a 'COMOUTPUT' file has been opened. This file will then contain a record of the run, including everything which the program would otherwise have written to the user terminal. Table A-II.1 is an example of a batch job file.

On execution of the finite element program (the command 'RUN77') the name of a master data file is requested, and this appears on line 4 in Table A-II.1. This data file contains a complete definition of the required calculation, as described below, and execution cannot proceed without it. In an interactive mode, the file name would be entered directly from the terminal in response to the prompt. Alternatively, the entire batch job may be run from the terminal by passing control to the job file with the command 'CO jobfilename'. The last line in Table A-II.1 ensures that control returns to the terminal on completion.

Table A-II.1

A typical file for the batch execution of FEANCO

COMO filename	opens the 'COMOUTPUT' file
DATE	prints date and time of run
RUN77 FEANCO	command to execute program
master filename	name of master data file
T	prints elapsed and CPU time for the run
COMO -E	closes the 'COMOUTPUT' file
SPOOL filename.COMO	produces hard copy of the 'COMOUTPUT' file
CO -TTY	returns control to the user's terminal

A-II.2 MASTER DATA FILE

This file comprises integers, which select various calculation options, and the names of appropriate data files. The contents are shown in Table A-II.2, and the parameters are defined below.

IFTRNS is 0 for a steady-state or 1 for a transient calculation.

ISOLVE selects the equation solution method - 6 for the direct 'approximate' procedure and 7 for iteration (see 5.7).

IFHOMG is 0 for uniform (homogeneous) thermal properties, or 1 to indicate a spatial variation. A value of 0 is followed by k_{11}, k_{12}, k_{22} and ρC_p, while 1 is followed by the name of the data file giving the thermal properties (THNAME). In the former case, a value of ρC_p must always be present, even in a steady-state calculation.

IFTEMP is greater than 0 if any of the thermal properties are temperature-dependent. The convention is

(a) IFTEMP = 1 : k_{ij} (T) only
(b) IFTEMP = 2 : ρC_p (T) only
(c) IFTEMP = 3 : k_{ij} (T) and ρC_p (T)

If (a) or (c) is the case, then the next line contains the name of the data file for thermal conductivity (KTEMP). If (b) or (c) is the case, the next line contains the name of the data file describing the temperature-dependence of specific heat (CPTEMP); this must be followed by IFH, a value of 0 or 1 indicating that that data are to be interpreted as ρC_p or ρh respectively, where h is the specific enthalpy (see A-I.2).

The following two lines give the names of the mesh data file (MENAME) and the boundary conditions file (BCNAME).

In a steady-state calculation, IFPLOT and IFFLUX are either

Table A-II.2

Structure of the master data file.

Title

IFTRNS

ISOLVE

IFHOMG

either k_{11}, k_{12}, k_{22}, ρC_p (if IFHOMG = 0)

or THNAME (if IFHOMG = 1)

IFTEMP

KTEMP (if IFTEMP = 1 or 3)

CPTEMP) (if IFTEMP = 2 or 3)

IFH) (if IFTEMP = 2 or 3)

MENAME

BCNAME

If IFTRNS = 0

IFPLOT

PFNAME (if IFPLOT = 1)

IFFLUX

FLNAME (if IFFLUX = 1)

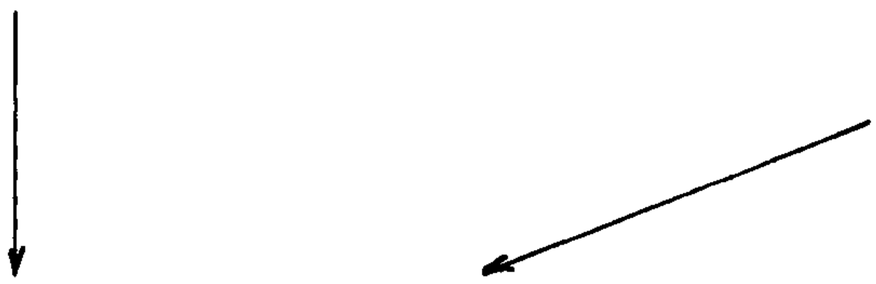

NSTART, NSTOP, NINT (optional)

end of file

If IFTRNS = 1

DT, TIMEND, NSTEPS, INTALG

IFINIT

either ITNAME (if IFINIT = 1)

or TINIT (if IFINIT = 0)

IFTIME

BCTIME (if IFTIME = 1)

0 or 1, and request the preparation of particular output files (see A-II.4). These options are not available in transient calculations, and the remainder of the file is used to define aspects of the time-dependent solution. All the variables have been explained in A-I.3. The code INTALG has three possible values:

(a) INTALG = 0 : forward-difference algorithm
(b) INTALG = 1 : pure-implicit algorithm
(c) INTALG = 2 : central difference (Crank-Nicholson) algorithm.

The final line, which is optional, requests output of temperatures at node numbers NSTART, NSTART + NINT,..... NSTOP only.

In three-dimensional problems, the options relating to IFPLOT and IFFLUX are not available. Thermal properties (line 5) are given in the order k_{11}, k_{12}, k_{13}, k_{22}, k_{23}, k_{33}, ρC_p. Otherwise, the format of the file is identical.

A-II.3 INPUT DATA FILES

The content of all the input files is summarised in Table A-II.3, following the nomenclature of A-I.3.

In the mesh data file (MENAME), the node coordinates and element topologies may be listed in any order, although the contents of each line must be as given in Table A-II.3.

The topology of two-dimensional (8-noded) and three-dimensional (20-noded) quadratic elements is described in 5.3 and 5.11. For many two-dimensional problems, finite element meshes may be generated manually or by simple computer programs. Three-dimensional meshes are more complex, and the use of commercial mesh-generating software is recommended; the 20-noded element used here adopts the topology used in the PAFEC system. In the author's experience, most of the errors in problem solving have occurred in mesh data preparation, and

Table A-II.3

Format of the input data files.

1. THNAME

Title

k_{11}, k_{12}, k_{22}, ρC_p

One line of thermal properties for each of the four integrating points in each element. For three-dimensional problems, each line contains k_{11}, k_{12}, k_{13}, k_{22}, k_{23}, k_{33}, ρC_p and there are eight points in each element.

2. CPTEMP

no. of data pairs (min.2, max.20)

T_1, CP_1 , T_2, CP_2, ...

CP_i is the value of ρC_p or ρh at temperature T_i

3. KTEMP

no. of data sets (min 2, max. 20)

T_1, $k_{11}(T_1)$, $k_{12}(T_1)$, $k_{22}(T_1)$

T_2 , $k_{11}(T_2)$, $k_{12}(T_2)$, $k_{22}(T_2)$, etc.

In 3 dimensions, each temperature is followed by six thermal conductivity coefficients.

4.1 MENAME (2 - d)

Title

NNT

I, X(I), Y(I))
. . .) NNT lines of data
. . .)
. . .)

```
NET
I, INODE(1,I)  INODE(2,I), ...  INODE(8,I)  )   NET lines
.      .           .                .       )   of
.      .           .                .       )   data
.      .           .                .       )
IBAND          (optional)
```

4.2 MENAME(3-d)

```
Title
NNT
I, X(I), Y(I), Z(I)     )
.   .      .      .      )   NNT lines of data
.   .      .      .      )
.   .      .      .      )

NET
I, INODE(1,I), INODE(2,I), ...  INODE(20,I)  )   NET lines
.      .           .                .        )
.      .           .                .        )
.      .           .                .        )
IBAND          (optional)
```

5. BCNAME(2-d)

```
Title
NNFT
NFT(1), TFIX(1)   )
   .        .     )   NNFT lines of data
   .        .     )
   .        .     )

NECT
NCE(1), MIDC(1), H(1), TINF(1)   )
   .        .        .       .    )   NECT lines of data
   .        .        .       .    )
   .        .        .       .    )

NEQT
NQE(1), MIDQ(1), Q(1)   )
   .        .       .   )   NEQT lines of data
   .        .       .   )
   .        .       .   )
```

```
NERT
NER(1), MIDR(1), EPS(1), TRAD(1)  )
   .        .        .       .     )  NERT lines
   .        .        .       .     )
   .        .        .       .     )  of data

NGEN
NEGEN(1), GEN(NEGEN(1))   )
   .          .           )  NGEN lines of data
   .          .           )
   .          .           )

          end of file
```

In 3-d problems, MIDC(I) is replaced by MIDC(1,I), MIDC(2,I), etc.

6. ITNAME

```
          NNT
   node number, temperature   )
      .            .          )  NNT lines
      .            .          )
                              )
```

7. BCTIME

```
          time t(1)
          NNFT
          NFT(1), TFIX(1)
             .       .
             .       .
          (as BCNAME)
             .       .
          time t(2)
          NNFT
             .       .
             .       .
          (as BCNAME)
             .       .
          time t(i)
             .       .
             .       .
```

the maximum possible use should be made of available graphical facilities. If the bandwidth of the mesh is known, it may be inserted as the last line of the data file; in its absence, the calculation is performed in the main program.

The file BCTIME is required in problems with time-dependent boundary conditions. In these cases, BCNAME would contain the initial (at time = 0) boundary conditions, and the first block of data in BCTIME would apply from the time given in the first line. Continuously-changing boundary conditions are thus approximated by a sequence of constant conditions between t(i) and t(i + 1); this, in effect, introduces a discrete time step into the data, and the user should experiment with different values, taking into account the time step of the transient calculation itself (see the discussions in Chapters 6 and 8).

A-II.4 PROGRAM OUTPUT

If a (two-dimensional) plot of steady-state isotherms is requested by setting IFPLOT = 1, the program writes the file PFNAME. This serves as an input file for the GENESYS 'Random/1' contour plotting routines. Examples of graphical output produced in this way may be found in Chapters 4 and 6. The system has certain limitations on spatial resolution (being designed for surveying applications) and it is sometimes necessary to apply a scaling factor to the finite element mesh. Negative node coordinates are not accepted. FEANCO calculates an appropriate contour interval, giving about 10 isotherms, but this and other parameters may be modified before processing.

When IFFLUX = 1, heat fluxes at the mid point of each element (r = s = 0) are computed from the steady-state temperature distribution, according to Equation 4.2. The two cartesian components of the temperature gradient are obtained by differentiating Equation 5.9:

$$\frac{\partial T}{\partial x} = \sum_{i=1}^{8} \frac{\partial N_i}{\partial x} T_i \quad \text{and} \quad \frac{\partial T}{\partial y} = \sum_{i=1}^{8} \frac{\partial N_i}{\partial y} T_i$$

where N_i are the element shape functions and T_i the nodal temperatures. Each line of the heat flux file (FLNAME) contains the cartesian coordinates of the mid point of the element and the components of the flux: x, y, q_x, q_y. These data have been processed by a separate program which calculates the magnitude and direction of the flux vectors and plots them as an 'arrow' symbol using GINO-F subroutines.

A-II.5 EXAMPLE CALCULATION

The preparation of data files and production of output is illustrated by a simple one-dimensional transient conduction problem. A rod, length 0.1m, has an initial temperature of 20^{o}C. For time t>0, one end is maintained at a steady temperature of 100^{o}C, while the other end loses heat by convection into a medium at 0^{o}C with a heat transfer coefficient of 50 W/m^{2}K. The material has an isotropic thermal conductivity of 10 W/m K and $\rho C_p = 10^6$ J/m^{3}K.

Fig. A-II.1 shows the representation of the one-dimensional problem with 5 two-dimensional elements. The width (y-direction) of the mesh is arbitrary, since there are no temperature gradients in this direction - the value of 0.02 m is chosen to give square elements. Table A-II.4 lists the mesh data file (called 'EXAMPLE-MESH') and Table A-II.5 the boundary conditions ('EXAMPLE-B.C.'). The master data file is shown in Table A-II.6, and requests a transient calculation over 100 sec. with a time step of 5 sec. using the Crank-Nicholson integration algorithm. The program output is reproduced in Fig. A-II.2, giving, as requested, the temperature distribution at t = 50 and 100 sec. (that is, every 10 time steps).

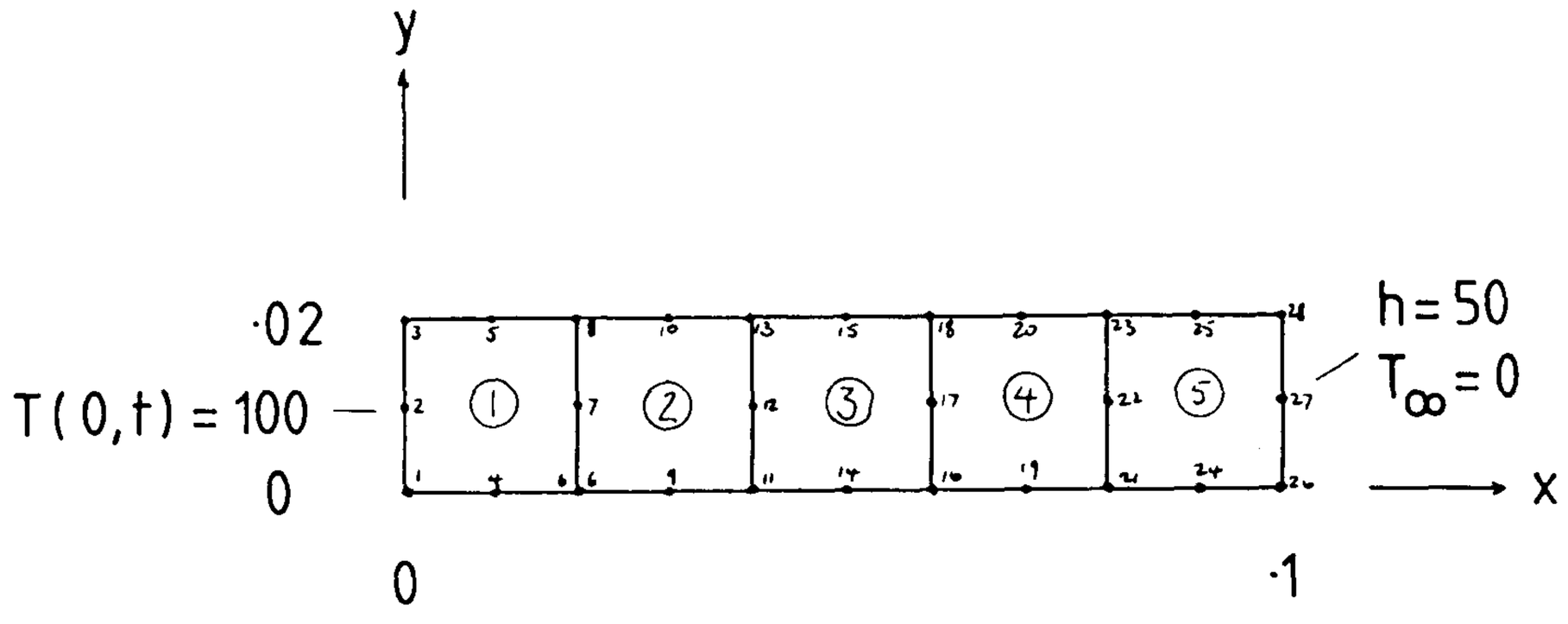

Fig. A-II.1

Five-element representation of 1-d rod, with node and element numbers.

```
1-D ROD (5 ELEMENTS)
 28
  1      0.000000      0.000000
  2      0.000000      0.010000
  3      0.000000      0.020000
  4      0.010000      0.000000
  5      0.010000      0.020000
  6      0.020000      0.000000
  7      0.020000      0.010000
  8      0.020000      0.020000
  9      0.030000      0.000000
 10      0.030000      0.020000
 11      0.040000      0.000000
 12      0.040000      0.010000
 13      0.040000      0.020000
 14      0.050000      0.000000
 15      0.050000      0.020000
 16      0.060000      0.000000
 17      0.060000      0.010000
 18      0.060000      0.020000
 19      0.070000      0.000000
 20      0.070000      0.020000
 21      0.080000      0.000000
 22      0.080000      0.010000
 23      0.080000      0.020000
 24      0.090000      0.000000
 25      0.090000      0.020000
 26      0.100000      0.000000
 27      0.100000      0.010000
 28      0.100000      0.020000
  5
  1     1     4     6     7     8     5     3     2
  2     6     9    11    12    13    10     8     7
  3    11    14    16    17    18    15    13    12
  4    16    19    21    22    23    20    18    17
  5    21    24    26    27    28    25    23    22
```

Table A-II.4

Mesh data file 'EXAMPLE-MESH'

```
5 ELEMENT ROD.  FIXED TEMP + CONV
3
1   100.0
2   100.0
3   100.0
1
5   27   50.0   0.0
0
0
0
```

Table A-II.5

Boundary conditions file 'EXAMPLE-BC'

```
EXAMPLE CALCULATION
1
6
0
10.0   0.0   10.0   1 E6
0
EXAMPLE-MESH
EXAMPLE-BC
5.0   100.0   10   2
0
20.0
0
```

Table A-II.6

Master data file 'C-EXAMPLE'

Fig. A-II.2

Computer output from example calculation.

```
OK. DATE
03 Jun 85 10:47:00 Monday
OK. RUN77 FEANCO-N

MASTER DATA FILE NAME?
C_EXAMPLE


FEANCO: FINITE ELEMENTS FOR ANISOTROPIC CONDUCTION
--------------------------------------------------

TITLE: EXAMPLE CALCULATION


TRANSIENT CALCULATION OVER   100.000 SECS

TIME STEP   5.000, OUTPUT EVERY   10 STEPS

CRANK-NICOLSON INTEGRATION ALGORITHM

UNIFORM INITIAL TEMPERATURE OF    20.000

HOMOGENEOUS THERMAL PROPERTIES:
     K11=  10.000   K12=   0.000   K22=  10.000   RHO.CP=  10000D+07


SOLUTION OBTAINED BY DECOMPOSITION OF SYMMETRIC BANDED MATRIX

READING MESH DATA FROM FILE EXAMPLE-MESH
1-D ROD (5 ELEMENTS)

READING BOUNDARY CONDITIONS FROM FILE EXAMPLE-BC
5 ELEMENT ROD: FIXED TEMP + CONV
```

BOUNDARY CONDITIONS

THERE ARE 3 NODES AT A FIXED TEMPERATURE

NODE NUMBER	TEMPERATURE
1	100.000
2	100.000
3	100.000

THERE ARE 1 CONVECTIVE ELEMENTS

ELEMENT	MIDSIDE NODE	H	FLUID TEMP
5	27	50.0	0.000

THERE ARE 0 ELEMENTS WITH A SPECIFIED HEAT FLUX

THERE ARE 0 RADIATIVE ELEMENTS

THERE ARE 0 ELEMENTS WITH HEAT GENERATION

TEMPERATURES AT TIME = 50.000 SEC.

NODE	X-COORDINATE	Y-COORDINATE	TEMPERATURE
1	0.00000	0.00000	100.00000
2	0.00000	0.01000	100.00000
3	0.00000	0.02000	100.00000
4	0.01000	0.00000	79.66429
5	0.01000	0.02000	79.66429
6	0.02000	0.00000	61.31350
7	0.02000	0.01000	61.31350
8	0.02000	0.02000	61.31350
9	0.03000	0.00000	46.40454
10	0.03000	0.02000	46.40454
11	0.04000	0.00000	35.44916
12	0.04000	0.01000	35.44916
13	0.04000	0.02000	35.44916
14	0.05000	0.00000	28.20518
15	0.05000	0.02000	28.20518
16	0.06000	0.00000	23.80642
17	0.06000	0.01000	23.80642
18	0.06000	0.02000	23.80642
19	0.07000	0.00000	21.30711
20	0.07000	0.02000	21.30711
21	0.08000	0.00000	19.83603
22	0.08000	0.01000	19.83603
23	0.08000	0.02000	19.83603
24	0.09000	0.00000	18.81264
25	0.09000	0.02000	18.81264
26	0.10000	0.00000	17.90838
27	0.10000	0.01000	17.90838
28	0.10000	0.02000	17.90838

TEMPERATURES AT TIME = 100.000 SEC.

NODE	X-COORDINATE	Y-COORDINATE	TEMPERATURE
1	0.00000	0.00000	100.00000
2	0.00000	0.01000	100.00000
3	0.00000	0.02000	100.00000
4	0.01000	0.00000	85.62380
5	0.01000	0.02000	85.62380
6	0.02000	0.00000	71.94561
7	0.02000	0.01000	71.94561
8	0.02000	0.02000	71.94561
9	0.03000	0.00000	59.56369
10	0.03000	0.02000	59.56369
11	0.04000	0.00000	48.88574
12	0.04000	0.01000	48.88574
13	0.04000	0.02000	48.88574
14	0.05000	0.00000	40.11070
15	0.05000	0.02000	40.11070
16	0.06000	0.00000	33.22078
17	0.06000	0.01000	33.22078
18	0.06000	0.02000	33.22078
19	0.07000	0.00000	28.05050
20	0.07000	0.02000	28.05050
21	0.08000	0.00000	24.34676
22	0.08000	0.01000	24.34676
23	0.08000	0.02000	24.34676
24	0.09000	0.00000	21.85285
25	0.09000	0.02000	21.85285
26	0.10000	0.00000	20.37170
27	0.10000	0.01000	20.37170
28	0.10000	0.02000	20.37170

****

OK, COMO -E

APPENDIX III : 'BASIC' TEMPERATURE LOGGING PROGRAM

Listed below is the BASIC program used for logging temperatures on the PCI 1002 thermocouple converter. In this configuration, channels 4 and 5 were used for microvolt inputs. Channel 3 is the (internal) cold junction temperature, leaving channels 6 to 15 available for thermocouple inputs.

The PCI 1002 gives an output which is linear in microvolts (V), rather than temperature (T). The conversion to temperature uses the polynomial

$$T = A_o + A_1 V + A_2 V^2 + A_3 V^3 + A_4 V^4$$

where the values of the linearisation coefficients are given in lines 145 and 146.

```
1 DIMOP(16),CN(16),V(15):ON=13
100 PRINT"■GENERALISED DATA LOGGING PROGRAM":PRINT:PRINT
105 INPUT"RANGE - 10 30 OR 100 MV";R
106 IFR<10ORR>100THEN105
107 IFR>10ANDR<30THEN105
108 IFR>30ANDR<100THEN105
110 INPUT"HOW MANY CHANNELS IN USE";NC:PRINT
120 FORI=1TONC:INPUT"CHANNEL NO.";CN(I):NEXT:CN(0)=3
130 PRINT:INPUT"TEMPS AS MICROVOLTS OR DEG C (M OR D)";I$
140 IFI$="M"THEN150
141 REM
142 REM LINEARISATION COEFFICIENTS FOR TYPE T THERMOCOUPLES
143 REM
145 A(0)=0:A(1)=2.5661297E-2:A(2)=-6.1954869E-7
146 A(3)=2.2181644E-11:A(4)=-3.55009E-16:CK=40.25
147 REM
150 PRINT:INPUT"AVERAGED OUTPUT";O$
160 IFO$="N"THEN170
165 PRINT:INPUT"PERIOD (SEC)";OT
170 PRINT:INPUT"OUTPUT TO PRINTER";OP$
180 IFOP$="N"THEN200
181 REM
182 REM OPEN CHANNELS TO PRINTER AND SET FORMAT
183 REM
185 CLOSE4:OPEN4,4:CLOSE2:OPEN2,4,1:CLOSE3:OPEN3,4,2
186 FORI=1TO5:PRINT#4:NEXT
187 A$="  TIME          CHANNEL NUMBER":PRINT#4,A$:A$="                "
188 FORI=1TONC:S$=STR$(CN(I)):S$=RIGHT$(S$,2):A$=A$+"    "+S$+"   ":NEXTI
190 PRINT#4,A$:L=LEN(A$):A$="":FORI=1TOL:A$=A$+"-":NEXT:PRINT#4,A$:PRINT#4
195 A$="AAAAAAAA ":FORI=1TONC
196 IFCN(I)>=6ANDI$="D"THENA$=A$+" S999.9":GOTO199
197 A$=A$+" S9999"
198 NEXTI:PRINT#3,A$
199 REM
200 REM INITIALISE ARRAYS AND TIME
201 REM
205 FORI=1TONC:V(I)=0:NEXT
210 NS=0:T0=TI:PRINT"■"
211 REM
212 REM CURRENT TIME
213 REM
220 T$=LEFT$(TI$,2)+"-"+MID$(TI$,3,2)+"-"+RIGHT$(TI$,2)
230 PRINT"■TIME:";T$:PRINT:PRINT"CHANNEL    VALUE":PRINT"-------    -------"
```

```
231 REM
232 REM SCAN INPUT CHANNELS
233 REM
240 FORI=0TONC:CH=CN(I):GOSUB10000:NEXT
250 FORI=1TONC:CH=CN(I):IFCH>2THENGOSUB11000
260 V(I)=V(I)+OP(CH)
262 IF5>=CHORI$="M"THENOP(CH)=INT(OP(CH)+.5):GOTO270
264 OP(CH)=INT(OP(CH)*10+.5)/10
270 PRINT"   ";CH;TAB(10);"          ▮▮▮▮▮▮▮▮";OP(CH):NEXT
271 REM
272 REM OPTION TO START PRINTING
273 REM
275 GETG$:IFG$<>"@"THEN280
276 IFOP$="N"THENOP$="Y":GOTO185
277 OP$="N"
278 REM
280 NS=NS+1:IFOP$="N"THEN220
285 IFO$="N"THEN295
287 DT=(TI-T0)/60:IFDT>DTTHEN220
292 REM
293 REM CALCULATE AVERAGED VALUES AND PRINT
294 REM
295 GOSUB12000:GOTO220
300 END
10000 REM
10010 REM*** OPERATING SUBROUTINE***
10020 REM
10030 OPEN1,DN,CH
10040 GET#1,J$,K$
10050 K=ASC(K$)-224
10060 IFK<0THEND=(K+32)*-1
10070 IFK>=0THEND=K
10080 D=D*256
10090 IFJ$=""THENJ=0:GOTO10110
10100 J=ASC(J$)
10110 IFK<0THENJ=J*-1
10120 OP(CH)=J+D
10130 CLOSE1
10140 RETURN
11000 REM
11010 REM***BITS TO DEGC SUBROUTINE***
11020 REM
11030 CJ=CK*(OP(3)*R/400):REM GIVES CJC IN MICROVOLTS
11040 OP(CH)=OP(CH)*R/4:REM GIVES O/P IN MICROVOLTS
11045 IF6>CHTHENRETURN
11050 OP(CH)=OP(CH)+CJ:IFI$="M"THENRETURN
11060 T=A(4):FORII=3TO0STEP-1:T=T*OP(CH)+A(II):NEXTII
11100 OP(CH)=T:RETURN
12000 REM
12001 REM***AVERAGING SUBROUTINE***
12002 REM
12005 T$=LEFT$(TI$,2)+"-"+MID$(TI$,3,2)+"-"+RIGHT$(TI$,2):C$=CHR$(29)
12010 FORI=1TONC:V(I)=INT(V(I)/NS*10+.5)/10:NEXT
12020 PRINT#2,T$,C$,V(1),V(2),V(3),V(4),V(5),V(6),V(7),V(8),V(9),V(10),V(11)
12030 FORI=1TONC:V(I)=0:NEXT
12040 NS=0:T0=TI:RETURN
50000 CLOSE1:CLOSE2:CLOSE3:CLOSE4:GOTO170
```